



HAL
open science

Out-of-equilibrium dynamics in 1D Bose gases

Maximilian Schemmer

► **To cite this version:**

Maximilian Schemmer. Out-of-equilibrium dynamics in 1D Bose gases. Optics [physics.optics]. Université Paris Saclay (COMUE), 2019. English. NNT : 2019SACLO002 . tel-02128579

HAL Id: tel-02128579

<https://pastel.hal.science/tel-02128579v1>

Submitted on 14 May 2019

HAL is a multi-disciplinary open access archive for the deposit and dissemination of scientific research documents, whether they are published or not. The documents may come from teaching and research institutions in France or abroad, or from public or private research centers.

L'archive ouverte pluridisciplinaire **HAL**, est destinée au dépôt et à la diffusion de documents scientifiques de niveau recherche, publiés ou non, émanant des établissements d'enseignement et de recherche français ou étrangers, des laboratoires publics ou privés.

Out-of-equilibrium dynamics in 1D Bose gases

Thèse de doctorat de l'Université Paris-Saclay
préparée à l'Institut d'Optique Graduate School

École doctorale n° 572
Ondes et Matière (EDOM)

Thèse soutenue à Palaiseau, le 22 mars 2019, par

Maximilian Schemmer

Composition du jury:

M. Nicolas Pavloff	Président	LPTMS
M. Jérôme Beugnon	Rapporteur	LKB
M. Hanns-Christoph Nägerl	Rapporteur	Universität Innsbruck
Mme Hélène Perrin	Examinatrice	LPL
M. Tim Langen	Examineur	Universität Stuttgart
Mme Isabelle Bouchoule	Directrice de thèse	LCF
M. Jérôme Dubail	Invité	LPCT

Contents

Introduction	3
1 Theory	7
1.1 1D Physics	7
1.2 Lieb-Liniger Hamiltonian	8
1.2.1 Two particle problem	9
1.2.2 N-particle Bethe ansatz	11
1.2.3 Thermodynamic limit	14
1.2.3.1 Yang-Yang equation of state	15
1.2.4 The equilibrium regimes	16
1.2.4.1 Ideal Bose gas	17
1.2.4.2 Quasi-condensate regime	18
1.2.4.3 Tonks gas	19
1.2.4.4 Correlation functions	19
1.3 Linearized theory in the quasi-condensate	21
1.3.1 Homogeneous system	21
1.3.1.1 Wigner representation	24
1.3.1.2 First order correlation function	25
1.3.2 Trapping potential	26
1.3.2.1 Local Density Approximation (LDA)	26
1.3.2.2 Bogoliubov in a harmonic trap	26
1.3.3 High density 3D effects	27
1.3.3.1 Bogoliubov Hamiltonian with 3D effects	29
1.3.4 Classical field	30
1.4 Dynamics of 1D Bose gases	30
1.4.1 Dynamics of the linearized theory in the quasi-condensate regime	30
1.4.2 Coarse grained description	31
1.4.3 Conventional Hydrodynamics (CHD)	32
1.4.4 Generalized Hydrodynamics (GHD)	32
1.4.4.1 Collision of two wave-packets	33
1.4.4.2 The GHD equations	33

1.5	Losses	35
1.5.1	Quantum Monte-Carlo wave-function method	36
2	The atomchip experiment	39
2.1	The experimental setup	39
2.2	Preparation scheme	40
2.3	Magnetic trapping	42
2.3.1	Wire geometries for trapping neutral atoms	42
2.3.1.1	Potential by a single wire	42
2.3.1.2	Three wire geometry and modulated guide	44
2.3.2	Longitudinal trapping	47
2.3.2.1	Harmonic trapping potential	50
2.3.2.2	Double well potential	51
2.3.2.3	Potential roughness	57
2.4	Genetic algorithms	57
2.4.1	The algorithm	58
2.5	Heating and losses	60
2.5.1	Background gas losses	60
2.5.2	Technical noise	61
2.5.3	Switching-mode power devices	62
2.6	Technical instabilities	63
2.6.1	Mechanical instabilities	63
2.6.2	Magnetic stability	65
2.7	Imaging system	65
2.7.1	Time-of-flight images	66
2.7.2	In situ images	67
2.8	Analysis methods	70
2.8.1	Density ripple analysis	70
2.8.1.1	Density ripples power spectrum	70
2.8.1.2	Filter for Bogoliubov modes	72
2.8.1.3	Density ripple thermometry	73
2.8.1.4	Local density approximation	75
2.8.1.5	Bogoliubov in a trap	76
2.8.1.6	Imaging system	77
2.8.1.7	Interactions during time-of-flight	78
2.8.2	Yang-Yang thermometry	78
2.8.3	Momentum space distribution	80
2.8.4	Comment about temperature measurements in the system	82
2.9	Parameter calibration	82

3	Interaction quench	85
3.1	Quenches in integrable systems	85
3.2	The Experiment	88
3.2.1	Interaction quench in the quasi-condensate regime	90
3.3	Momentum space	91
3.3.1	Light-cone like effect on the one-body correlation function	91
3.3.1.1	Relation to the Vienna experiment	93
3.3.2	Experimental observation in momentum space	93
3.4	Density ripple analysis	95
3.4.1	Squeezed Bogoliubov modes	95
3.4.2	Experimental realization	97
3.4.3	Beyond the light-cone	98
3.4.4	Mode damping	100
3.4.5	Amplitude reduction	102
3.4.6	Recurrences in a harmonic trap	104
3.4.6.1	Experimental realization	105
4	Losses in a Bose gas	109
4.1	j -body loss in a quasi-condensate	110
4.2	Quantum Monte-Carlo	111
4.2.1	Generalization to all cells	115
4.2.2	Effect of the Bogoliubov Hamiltonian	119
4.2.3	Average over different trajectories	119
4.3	Simplified approach	122
4.4	Cooling by three body losses	126
4.4.1	The evolution of the peak density n_p under three-body losses	126
4.4.2	The phonon temperature	128
4.4.2.1	Comparison to theory	129
4.4.2.2	Evolution towards the asymptotic ratio	132
4.4.2.3	The phase diagram	133
4.4.3	Yang-Yang thermometry	135
4.5	Cooling by one-body losses	137
4.5.1	Cooling a single cloud into the 1D regime	137
4.5.2	Experimental results for $j = 1$	139
4.6	Quartic potentials	140
4.7	Quantum Feedback	141
4.8	Outlook	143

5	Generalized Hydrodynamics (GHD)	147
5.1	GHD experiment	147
5.1.1	The experiments	149
5.1.2	Expansion from harmonic trap	149
5.1.3	Expansion from double well	152
5.1.4	Release from double-well into harmonic potential	156
5.2	Outlook	158
	Conclusion	161
A	Appendix	165
A.1	Values of ^{87}Rb	165
A.2	Chip layout	165
A.3	Longitudinal anti-confining term	168
A.4	Atom losses	169
A.4.1	The Lindblad operators	169
A.4.2	New Gaussian state	170
A.5	Phase space occupation	171
B	Résumé en français	173
C	Publications	177

Acknowledgement

There are so many people which made this thesis possible and which made out of this PhD such a good memory which I will never forget. It will be impossible for me to give everyone the attention they merit.

First of all, I want to thank Isabelle very much for the last three and a half years: For your constant support, the time you took to answer my stupid questions and the spend in the lab. I wish you a safe and great journey to Svalbard and back!

I would also like to thank Aisling very much. Thank you for introducing me to the experiment and thank you for your works on the experiment prior to my arrival on which I could built up during my thesis. I am already looking forward to the time in Vienna and Berlin! I was also lucky to have had generations of very talented former PhD and Post-Docs on the chip experiment and I especially want to thank Bess. I also worked together with fantastic internship students, where I especially would like to thank Raphael, Grégoire, Huan, Pierre and Aghilas.

During my PhD we also collaborated closely with theoreticians: Benjamin, Carsten, Duncan, Jérôme and Ryan. I especially want to highlight the contribution from Jérôme and thank him for his help and his input on the GHD project. I also thank a lot Ryan and Duncan for welcoming me in Hamilton and I wish you good physics with the project on mode damping.

This work would have been impossible without the surrounding of this incredible team of gaz quantique which made me feel comfortable at work. The permanent staff Alain, Chris, David, Denis, Marc, Thomas and Vincent, and especially the PhD students and Post-Docs: Adrien, Alessandro, Alexandre, Amaudric, Anaïs, Antoine, Baptiste, Cécile Carcy, Cécile Crosnier, Clémence, Guillaume, Hugo, Julien, Marco, Maxime, Mukhtar, Pierre, Quentin, Rockson, Valentin, Vasiliki, Vincent and Ziyad. C'était vraiment génial avec vous !

Such an experimental research would have been impossible without the technical support from the electronic, technical and optical workshop. Here, I especially would like to thank André Villing, André Guilbaud, Florence, Jean-René and Frédéric for their support.

This thesis was also made possible through the support of the German Academic Scholarship foundation who I like to thank for its ideal support as well as for its fi-

nancial support. A special thanks to Silke for help and advises. At this point I would also like to thank all of her group members for the time spent outside of the lab.

I had the chance to be able to teach during my PhD and I want to thank everyone who helped me during this experience: Cédric, Nathalie, Thierry and Vincent (TP optique); Charles, Hervé and Mukhtar (Matlab); Julien, Maxime, Cécile, Clémence, Sylvain, Baptiste (EITI); Anaïs, Philipp and Yvan (cours laser). Merci à tous de m'avoir aidé et soutenu en toutes circonstances. En particulier, ce n'était pas évident de commencer à enseigner dans une langue que tout l'amphithéâtre maîtrise parfaitement, excepté l'enseignant.

I also thank the rapporteurs and all the members of the jury for reviewing my thesis and for giving my very helpful comments and remarks on my manuscript.

Such a thesis would have been impossible without the mental support from good friends: Thank you very much for that great time here in Paris: Anis, Clément, David, François, Guillaume Fabre, Guillaume Rieu, Jean-Baptiste, Laure, Laurène, Margaux, Mathieu, Paul, Pierre, Rachel, Sibille and Victor. Vous m'avez fait adorer mon temps à Paris avec toutes les soirées et sorties. A special thanks to Jean-Baptiste for introducing me to Jupyter. And a very special thanks to all of my flatmates who had to listen to me when I was complaining about electronic noise and other weird experimental physics words and a special thanks to Pierre for listening to such simple things as experimental physics problems.

I also thank my old friends from Waldkirch who supported me during this journey of long studies: Felix, Matthias, Max, Philip, Raffael, Sandra, Simon and Stephan. Es ist wirklich besonders für mich, dass wir auch nach all den Jahren und trotz der Entfernung den Kontakt weiterhin so halten. Auf noch viele weitere durchzechte Nächte!

Furthermore I would like to thank my mentors of physics in early years who orientated me towards science: Jürgen Wiemann, Wolfgang Mattig and Thino Kornhaß.

I also want to thank my family in France, la famille Bonneton and Gilles for coming to my defense from far away.

Finally, I thank my family: This PhD would not have been possible without the constant mental support by my mum, my dad and my brother. But especially I want to thank you for the organization and preparation of the incredible buffet at my defense. Last, I would like to thank Melisa for her support during all my PhD. Danke, dass du meine Launen all die Zeit ertragen hast und das mit mir durchgemacht hast. Insbesondere auch für deine Mühen, die du mit den häufigen Flügen auf dich genommen hast. Danke an euch alle, ohne euch wäre ich nie soweit gekommen!!!

Introduction

Integrable systems have fascinated physicist and mathematicians for centuries. Starting from "simple" integrable models, as the Kepler problem [1], they already played a fundamental role in the early development of physics and are still the first examples physics students face in their curriculum.

A classically integrable model with N degrees of freedom possesses N constants of motion. These constants of motion impose severe constraints on the system's time evolution and can lead to very particular behavior: Integrable systems lack ergodicity and are completely determined by their initial values. One needs to take into account the values of the N constants of motion to predict the properties of the system. Consequently they lack the ability to thermalize which is a phenomenon that is very far from our every day experience.

The concept of integrability can be extended to quantum systems. The precise definition of quantum integrability is subject to scientific debates [2, 3]. In this thesis I will refer to integrable quantum systems, as systems that are solvable by the Bethe-Ansatz [4]. The Bethe-Ansatz is an analytic technique introduced 1931 by Hans Bethe in the context of the one-dimensional (1D) Heisenberg model. It allows to calculate the exact eigenvalues and eigenvectors and it has been subsequently generalized to many different 1D systems. One example is the 1D system of Bosons with contact interactions [5] which I will be studying in this thesis.

For a long time research of quantum integrable systems remained a theoretician's playground. This situation changed with the realization of isolated many-body integrable systems in cold atom experiments [6–13]. Apart from its experimental importance and its use as a testbed for theoretical predictions [14], these experimental realizations also stimulated new theoretical progress. One example is the recent theoretical breakthrough in the description of the out-of-equilibrium dynamics of quantum integrable systems which is called Generalized HydroDynamics (GHD) [15–17]. This new GHD theory (2016) is one of the subject of this thesis (see Chap. 5).

In this thesis I experimentally study the integrable model of Bosons with repulsive contact interactions in 1D, named the Lieb-Liniger model. For this purpose we use an atomchip setup with magnetic microwire traps to strongly confine ^{87}Rb atoms in two dimensions. We then freeze out these two dimensions to create a 1D

Bose gas. Besides their theoretical motivation, 1D systems are interesting to study on their own. 1D systems can exhibit phenomena that are very different from higher dimensions: There is no Bose-Einstein condensation in 1D and interactions lead to a new phenomena – the quasi-condensation. The experiments in this thesis focus on clouds which are in the quasi-condensate regime. A particularly counter-intuitive example of the difference of 1D is the regime of strong interactions. It is reached for low densities and in the strongly interacting regime the bosonic atoms start to behave as fermions. Additionally, 1D systems can also be interesting because of their conceptual simplicity.

This thesis focuses on three experimental studies of the dynamics of bosons in 1D. The three studies are the following: the study of the out-of-equilibrium dynamics after an interaction quench, the cooling by three-body losses and the first experimental study of the theory of GHD. Each of these studies is presented in a different chapter (Chap. 3-5) and the first two chapters introduce the theoretical and experimental basis for those three studies.

The first chapter gives an introduction to the theoretical tools in the Lieb-Liniger model; such as the Bethe-Ansatz and approximate theories inside quasi-condensate regime. Furthermore, I discuss corrections arising from the 3D world. In contrast to the theoretical toy model of the Lieb-Liniger model, experimental artifacts from the 3D world can not always be completely neglected. At the end of this chapter I introduce the treatment of losses with the wavefunction Quantum Monte-Carlo (QMC) method. Furthermore, I introduce the tools to study the out-of-equilibrium dynamics, with a focus on GHD.

The second chapter introduces the experimental setup and highlights the experimental difficulties encountered during my PhD. Furthermore it discusses experimental analysis methods, such as the density ripple analysis and the Yang-Yang thermometry.

The following three chapters (3-5) are mostly independent from each other, and each chapter focusses on the detailed description of one of the previously mentioned experimental studies. The third chapter introduces an experimental attempt to address the problem of thermalization in an integrable model. We therefore suddenly change the interaction parameter of the system and observe the subsequent time evolution. Our results are in agreement with an approximated model of independent harmonic oscillator – the Bogoliubov Hamiltonian [18]. We cannot establish direct links to the integrability of Lieb-Liniger Hamiltonian, still the description in terms of the the Bogoliubov Hamiltonian represents a "trivially" integrable model.

The fourth chapter focuses on energy-independent losses. At the beginning of my PhD a surprising experimental and theoretical result was published in the atom-chip group in Vienna [19, 20]. It was shown that energy-independent losses can lead to a cooling of a 1D Bose gas. Inspired by these results, our group published several

papers on this subject [21–24]. With these papers we developed different theoretical approaches to the problem and I give a theoretical description of the problem with the wavefunction Monte-Carlo method, which we introduced in [21]. These theoretical results are experimentally verified by the first experimental observation of the cooling of a 1D Bose gas by three-body losses [24]. Special attention is paid to the cooling limit of the energy-independent loss process which we observed for the first time in [24]. According to the theoretical approaches, introduced at the beginning of the chapter, the cooling mechanisms should also exist in higher dimensions. However, these cooling mechanisms have never been observed in higher dimensions. This difference is probably due to the integrability of the 1D system.

The last chapter describes the first experimental study of the previously mentioned GHD theory [25]. We therefore prepare 1D Bose gases at equilibrium inside different initial trapping potentials and follow their time evolution after a sudden modification of the longitudinal confinement. The obtained results can be well explained by the newly introduced theory of GHD which takes into account the complete set of conserved charges of the integrable model. At the same time "older" theories, such as the conventional hydrodynamics approach, fail to describe the experimental results. Additionally, we reproduce the famous Newton's cradle experiment [26] in which the theory of conventional hydrodynamics is unable to produce results.

Chapter 1

Theory

In this chapter I will introduce the theoretical tools necessary to describe the 1D physics that will be studied in the following chapters. I will start with the transition from 3D to the 1D world by the freezing out of the transverse degrees of freedom. Most of the physics can be understood by considering a homogeneous system of size L . For precise calculation, the effect of the slowly varying longitudinal potential needs to be taken into account, while leading to the same overall physical picture. Therefore, I will mainly focus on homogeneous 1D systems and take into account the longitudinal trapping potential in a later step. In the homogeneous case our system can be described by the Lieb-Liniger Hamiltonian, whose eigenstates, obtained by Bethe-Ansatz, are discussed starting from a pedagogical example of two particles. It is followed by a discussion of the exact thermodynamics of the Lieb-Liniger model, the Yang-Yang equation of state and the different regimes obtained from it. Then, I will focus on the linearized model – the Bogoliubov approach – within the experimentally important quasi-condensate regime. Furthermore, I explain how corrections to the 1D model, arising from the 3D world which are experimentally always present, can be taken into account. In the last part I discuss out-of-equilibrium theories, the main topic of this thesis.

1.1 1D Physics

Consider a single component Bose gas trapped in three dimensions in a harmonic trapping confinement with trapping frequencies $\omega_x, \omega_y, \omega_z$ and a many-body wavefunction denoted as $\Psi(\mathbf{x}_1, \mathbf{x}_2, \dots, \mathbf{x}_N)$. In the following we will assume that $\omega_x = \omega_y = \omega_\perp \gg \omega_z$. Then, if all the relevant energy scales, namely the chemical potential μ and the energy scale $k_B T$ given by the temperature T , are much smaller than the energy gap to the first excited state in the transverse direction, i.e.

$$k_B T, \mu \ll \hbar\omega_\perp, \tag{1.1}$$

the system can be treated as a 1D system: The transverse degrees of freedom are frozen out and the dynamics is restricted to the longitudinal direction $\omega_{\parallel} = \omega_z$. In such a situation the wave function factorizes into its transverse and longitudinal part

$$\Psi(\mathbf{x}_1, \mathbf{x}_2, \dots, \mathbf{x}_N) = \Psi(z_1, z_1, \dots, z_N) \prod_{n=1}^N \phi_0(x_i, y_i) \quad (1.2)$$

and the system can be described as a 1D system with a longitudinal wave function $\Psi(z_1, z_1, \dots, z_N)$. The ground state wave function in the transverse directions $\phi_0(x_i, y_i)$ is a Gaussian function¹ of width $l_{\perp} = \sqrt{\hbar/m\omega_{\perp}}$.

For 3D cold bosonic gases at low enough temperatures s-wave scattering dominates [27, 28] and the scattering is completely characterized by the 3D scattering length a_{3D} and the pseudo potential

$$U(\mathbf{x} - \mathbf{x}')\Psi = g_{3D}\delta^3(\mathbf{x} - \mathbf{x}')\frac{\partial}{\partial r}(r\Psi), \quad (1.3)$$

where $g_{3D} = 4\pi\hbar^2 a_{3D}/m$ and m is the mass of the atoms. When the transverse degrees of freedom are frozen out, this can be related to an effective 1D interaction parameter g with a 1D scattering potential.

$$V(z - z') = g\delta(z - z'), \quad (1.4)$$

with

$$g = \frac{2\hbar a_{3D}\omega_{\perp}}{1 - C\frac{a_{3D}}{l_{\perp}}}. \quad (1.5)$$

The constant C can be calculated with the Riemann zeta function $C = \zeta(1/2) = 1.46\dots$ [29]. For experimentally relevant parameters $a_{3D} \ll l_{\perp}$ Eq. (1.5) reduces to

$$g = 2\hbar a_{3D}\omega_{\perp}. \quad (1.6)$$

In situations where $Ca_{3D}/l_{\perp} \simeq 1$ a confinement induced resonance appears which are for ⁸⁷Rb experimentally out of reach. For Cesium atoms, where Feshbach resonances can be used to tune a_{3D} , confinement induced resonances have been observed [30].

1.2 Lieb-Liniger Hamiltonian

With Eq. (1.4) one can write the Hamiltonian describing the gas in the longitudinal direction

$$\hat{H} = -\frac{\hbar^2}{2m} \sum_i^N \frac{\partial^2}{\partial z^2} + g \sum_{i<j} \delta(z_i - z_j). \quad (1.7)$$

¹3D correlations between atoms at distances smaller than l_{\perp} are neglected.

Equivalently, \hat{H} writes in the second quantized version

$$\hat{H} = \int \hat{\Psi}^\dagger(z) \left[-\frac{\hbar^2}{2m} \frac{\partial^2}{\partial z^2} + \frac{g}{2} \hat{\Psi}^\dagger(z) \hat{\Psi}(z) \right] \hat{\Psi}(z) dz, \quad (1.8)$$

where the bosonic fields $\hat{\Psi}^{(\dagger)}(z)$ fulfill the standard commutation relations

$$[\hat{\Psi}(z), \hat{\Psi}(z')^\dagger] = \delta(z - z'), \quad [\hat{\Psi}(z), \hat{\Psi}(z')] = [\hat{\Psi}^\dagger(z), \hat{\Psi}^\dagger(z')] = 0. \quad (1.9)$$

Since 1963 this Hamiltonian is well known in the literature when it was introduced by Lieb and Liniger [5, 31]. Lieb and Liniger showed that the system was solvable via the Bethe-ansatz. In 1969 C.N. Yang and C.P. Yang showed that the Bethe-ansatz solution form a complete set of solutions and at the same time developed the exact thermodynamic equations starting from the microscopic model of Eq. (1.7). This so-called Yang-Yang thermodynamics or Thermodynamic Bethe-ansatz (TBA) is discussed in Sec. 1.2.3.1. Note that in this manuscript I will always consider situations where $g > 0$, leading to repulsive interactions between atoms.

1.2.1 Two particle problem

Before discussing the solution of Eq. (1.7) found by Lieb and Liniger [5, 31], let me start for pedagogical reasons with the two-particle problem

$$H = -\frac{\hbar^2}{2m} \left[\frac{\partial^2}{\partial z_1^2} + \frac{\partial^2}{\partial z_2^2} \right] + g\delta(z_1 - z_2), \quad (1.10)$$

which can be rewritten in the center of mass frame

$$H = -\frac{\hbar^2}{m} \frac{\partial^2}{\partial z^2} + g\delta(z), \quad (1.11)$$

where $z = z_1 - z_2$. Solutions to Eq. (1.11) are plane waves with a discontinuity in the first derivative at $z = 0$ (see Fig. 1.1). For bosons $\Psi(z)$ must be even in z and up to a normalization constant the solution can be written

$$\Psi(z) = \sin(k|z| + \theta(k)). \quad (1.12)$$

Using the continuity condition on the first derivative

$$\left. \frac{\partial \Psi}{\partial z} \right|_{0^+} - \left. \frac{\partial \Psi}{\partial z} \right|_{0^-} = \frac{mg}{\hbar^2} \Psi(0) \quad (1.13)$$

we obtain the scattering phase of the two particle problem

$$\tan[\theta(k)] = \frac{2\hbar^2 k}{mg}. \quad (1.14)$$

The phase shift $\theta(k)$ for free particles is $\pi/2$ and interaction change $\theta(k)$ to lower values. This phase shift is central to integrable models solved by the Bethe-ansatz. It is worth to look at certain limits on this simple solution. In the limit $g \rightarrow \infty$ the phase shift becomes zero and the wave function develops strong kinks at $z = 0$ with $\Psi(0) = 0$ which resembles the Pauli exclusion principle of free Fermions (see Fig. 1.1). In the limit weakly interacting limit $g \rightarrow 0$ or in the high energy limit $k \rightarrow \infty$, the phase shift become $\pi/2$ and the wave function becomes a pure sinusoidal.

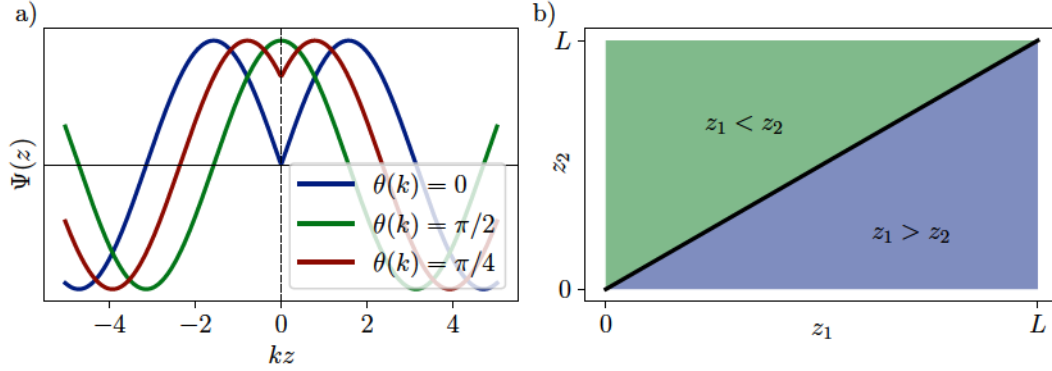


Figure 1.1 – a) Wave function of the two particle problem: The wavefunction is sinusoidal for $z \neq 0$ and shows a kick at $z = 0$. The kink is the strongest for $\theta(k) = 0$ with $\Psi(0) = 0$ (blue line) and vanishes for $\theta(k) = \pi/2$ (green line). The red line shows the intermediate behavior. b) Representation of the two particle problem Bethe-Ansatz. The black line indicates the position of the discontinuity of the derivative. In the green shaded region the plane wave solution for $z_2 > z_1$ applies and in the blue region $z_1 > z_2$ respectively.

Two-particle Bethe Ansatz The solution of the two-particle problem in relative coordinates Eq. (1.12) can be rewritten, such that it can be later extended to N particles. This is the so-called Bethe-Ansatz for two particles. The generic solution for bosons can be written as

$$\Psi(z_1, z_2) = f(z_1, z_2)\theta_H(z_2 - z_1) + f(z_2, z_1)\theta_H(z_1 - z_2) \quad (1.15)$$

by dividing the space into the subspace $z_1 < z_2$ and $z_2 < z_1$ as shown in Fig. 1.1. The Heaviside step function $\theta_H(z)$ of Eq. 1.15 is defined by:

$$\theta_H(z) = \begin{cases} 1 & z > 0 \\ 0 & z < 0. \end{cases} \quad (1.16)$$

Introducing the Bethe-Ansatz for two particles, the most general solution writes as a superposition of plane waves

$$f(z_1, z_2) = Ae^{i(k_1 z_1 + k_2 z_2)} + Be^{i(k_2 z_1 + k_1 z_2)}. \quad (1.17)$$

Injecting the solution Eq. (1.17) together with Eq. (1.15) into the Hamiltonian of Eq. (1.10) and using $\partial_z \theta_H(z) = \delta(z)$ and $f(z) \partial_z \delta(z) = -\partial_z f(z) \delta(z)$ (valid under integral), we obtain a solution if

$$\frac{A}{B} = \frac{i(k_1 - k_2) + \frac{mg}{\hbar^2}}{i(k_1 - k_2) - \frac{mg}{\hbar^2}} = e^{i\tilde{\theta}(k_1 - k_2)}, \quad (1.18)$$

with the phase shift $\tilde{\theta}(k)$

$$\tilde{\theta}(k) = 2 \arctan\left(\frac{\hbar^2 k}{mg}\right). \quad (1.19)$$

The phase shift introduced in Eq. (1.14) is related to the phase shift introduced above with $\tilde{\theta}(k)/2 = \theta(k/2)$. When considering periodic boundary conditions in a box of length L , the wave-function needs to be invariant under $z_j \rightarrow L + z_j$. Let us consider the case $\Psi(0, z_2) = \Psi(L, z_2)$ which implies

$$e^{ik_1 L} = \frac{A}{B} \quad \text{and} \quad e^{ik_2 L} = \frac{B}{A}. \quad (1.20)$$

Eq. (1.20) are called the *Bethe equations* which can be rewritten in logarithmic form

$$2\pi I_1 = Lk_1 + \tilde{\theta}(k_1 - k_2) \quad \text{and} \quad 2\pi I_2 = Lk_2 + \tilde{\theta}(k_2 - k_1) \quad (1.21)$$

which leads to the introduction of two integers, called the Bethe-integers I_1 and I_2 [2, 32, 33].

1.2.2 N-particle Bethe ansatz

The main result of Lieb and Liniger [5] consists of a generalization of these previous results from two particles to N -particles. For the N particle problem let us restrict to the subspace $z_1 < z_2 < \dots < z_N$ which writes with the Bethe-Ansatz

$$\Psi(z_1, z_2, \dots, z_N) = \sum_p \mathcal{A}_p e^{i(k_{p(1)} z_1 + \dots + k_{p(N)} z_N)} \quad \text{for} \quad z_1 < z_2, \dots, z_N \quad (1.22)$$

where the sum is taken over all permutations p . \mathcal{A}_p is a prefactor which needs to be determined. The complete solution can then be deduced by the corresponding permutation of the $\{z_i\}$. This wave-function is an eigenvector of the Lieb-Liniger Hamiltonian Eq. 1.7 with energy $E = \sum_j \hbar^2 k_j^2 / (2m)$. Note that the k_j are not the true momenta and are called rapidities or quasi-momenta. The sum $P = \hbar \sum_j k_j$ on the other hand is the total momentum.

The prefactor \mathcal{A}_p can be determined by considering two permutations p and p' , interchanging the two rapidities k and k' and in analogy to Eq. (1.18) one finds

$$\frac{\mathcal{A}_p}{\mathcal{A}_{p'}} = e^{i\tilde{\theta}(k-k')}. \quad (1.23)$$

This relation leads to

$$\mathcal{A}_p = \alpha \prod_{n < m} \left[i \left(k_{p(n)} - k_{p(m)} + \frac{mg}{\hbar^2} \right) \right], \quad (1.24)$$

where α is a normalization factor. Again the periodic boundary conditions need to be respected and we obtain in analogy to Eq. (1.20) the Bethe equations

$$e^{ik_j L} = \prod_{j \neq p}^N \frac{i(k_j - k_p) - \frac{mg}{\hbar^2}}{i(k_j - k_p) + \frac{mg}{\hbar^2}}. \quad (1.25)$$

The Bethe equations are a non trivial set of N coupled non-linear equations which can be rewritten by taking the logarithm. Thus we obtain a set of equations, where due to the periodicity of the complex logarithm the Bethe integers² I_j are introduced:

$$2\pi I_j = Lk_j + \sum_{n \neq j}^N [\tilde{\theta}(k_j - k_n)]. \quad (1.26)$$

The eigenstates of the Lieb-Liniger Hamiltonian are then uniquely characterized by a set of Bethe integers $\{I_1, I_2, \dots, I_N\}$ and from which the quasi-momenta k_j can be numerically calculated. Since $\tilde{\theta}(k)$ is an odd function, the total momentum writes $P = 2\pi\hbar/L \sum_j I_j$.

Ground state The ground state of the system is given by the symmetrically distributed Bethe integers

$$\{I_j\} = \left\{ -\frac{N-1}{2}, \dots, \frac{N-1}{2} \right\}, \quad (1.27)$$

with a total momentum $P = 0$. The ground state is also called the *Fermi sea* in analogy to condensed matter physics, while the use of this interpretation will become more clear in the following; let us stick to this nomenclature. In the limit $g \rightarrow \infty$, these Bethe integers correspond to the quasi-momenta

$$k_j = \frac{2\pi I_j}{L}. \quad (1.28)$$

²The use of the name *integers* is abusive. For N even, the Bethe integers are half integers and for N odd, they are integers.

Excitations Starting from the ground state, the simplest excitations correspond in changing one of the Bethe integers. Then, two types of excitations can be distinguished: *Type I* excitations correspond to the creation of a new particle to the Fermi sea at $k > k_{\max}$, the so-called *particle excitations*. In terms of the Bethe integers, this corresponds to adding a new particle³ above the edge of the Fermi sea

$$\{I_j^{\text{Type I}}\} = \left\{ -\frac{N}{2}, -\frac{N}{2} + 1, \dots, \frac{N}{2} - 1, \frac{N}{2} + s \right\}, \quad (1.29)$$

with $s > 0$ and total momentum $q = 2\pi\hbar s/L$. For low values of q , it can be shown that these collective modes are characterized by a sound-wave like dispersion relation which becomes quadratic for higher q as shown in Fig. 1.2 b). In the case of weak interactions, these excitations can be also obtained from Bogoliubov calculations as introduced in Sec. 1.3 .

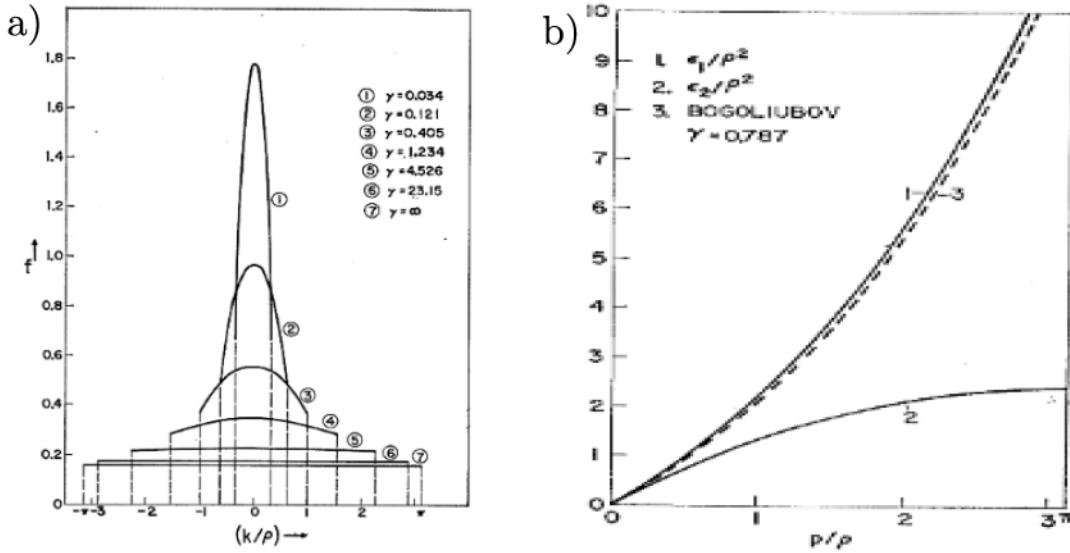


Figure 1.2 – a) Quasi-momentum occupation $f(k)$ for different $\gamma = \frac{mg}{\hbar^2 n}$ with $n = N/L$ the density. In the limit $\gamma \rightarrow \infty$ the quasi-momentum occupation corresponds to a Fermi sea, while for $\gamma \ll 1$ the Fermi sea gets deformed into an inverted parabola with a smaller cut off momentum.

b) The excitation spectrum of the Lieb-Liniger model with type I and type II excitations for $\gamma = 0.8$. In the weakly interacting regime these excitation are very close to the Bogoliubov spectrum, calculated in Sec. 1.3. Here ρ is the density in real space. Both figures taken from [31].

Type II excitations are also called *hole excitations*, where within the Fermi sea one

³Note that adding a new particle tuns the half-integer Bethe numbers into integers

Bethe integer is displaced just above the the Fermi sea

$$\{I_j^{\text{Type II}}\} = \left\{ -\frac{N}{2} + 1, -\frac{N}{2} + 1, \dots, \frac{N}{2} - s - 1, \frac{N}{2} - s + 1, \dots, \frac{N}{2} - 1, \frac{N}{2} \right\}, \quad (1.30)$$

creating a hole at $\frac{N}{2} - s$, again with total momentum $q = 2\pi\hbar s/L$. Type II excitations are not sound waves, and it has been argued that, in the weak interactions limit, they correspond to dark solitons of the Gross-Pitaevskii equation [34]. Its dispersion relation can be seen in Fig. 1.2 b).

An excitation, i.e. a general eigenstate, is then a combination of the type I and type II excitation with certain number of holes and particles, characterized by a set of numbers $\{I_j\}$. The corresponding k_j can then be calculated by the solving the Bethe equations Eq. (1.26).

1.2.3 Thermodynamic limit

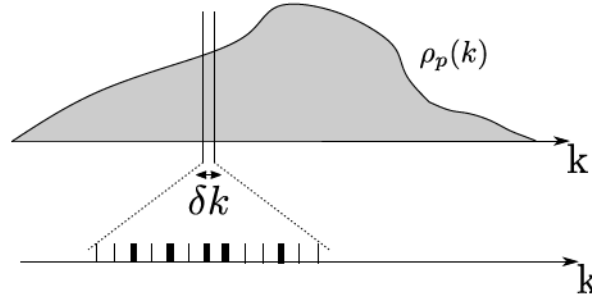


Figure 1.3 – In the thermodynamic limit one can introduce the continuous function of the particle density $\rho_p(k)$ as depicted above. A zoom into a small zone δk shows the individual states which can be occupied with a particle (thick lines) or unoccupied, leading to a hole (thin line). Note that the local density of state $\rho_s(k)$ depends on the function $\rho_p(k)$.

In the thermodynamic limit of $N, L \rightarrow \infty$ with $n = N/L$ constant, the k_j can be represented with the quasi-momentum distribution as sketched in Fig. 1.3

$$\rho_p(k) = 1/L \sum_j \delta(k - k_j), \quad (1.31)$$

where p stands for particle and which counts the number of particles $\rho_p(k)dk$ in the interval dk . The quasi-momentum distribution is linked to the $I(k)$ by

$$\frac{k}{2\pi} + \int \frac{dk'}{2\pi} \tilde{\theta}(k - k') \rho_p(k') = \frac{1}{L} I(k). \quad (1.32)$$

In the strongly interacting limit $g \rightarrow \infty$ and for the ground state, this corresponds to a Fermi sea, where $\rho_p(k) = 1/(2n\pi)$ for $|k| < k_{\max} = n\pi$ and zero everywhere else. For finite g , the Fermi sea becomes deformed and turns into an inverted parabola in the weakly interacting regime as shown in Fig. 1.2 a). In the thermodynamic limit we can also introduce the density of state $\rho_s(k)$ which is defined as

$$\rho_s(k) = \frac{1}{L} \frac{dI}{dk}. \quad (1.33)$$

By differentiating Eq. (1.32) the integral equation

$$\frac{1}{2\pi} + \int \frac{dk'}{2\pi} \Delta(k-k') \rho_p(k') = \rho_s(k) \quad (1.34)$$

links $\rho_s(k)$ to $\rho_p(k)$ where the differential scattering phase

$$\Delta(k) = \frac{2mg\hbar^2}{(mg)^2 + \hbar^4 k^2} \quad (1.35)$$

was introduced. In analogy to the density of quasi-particles, one can introduce the density of holes

$$\rho_s(k) = \rho_h(k) + \rho_p(k). \quad (1.36)$$

Note that the density of state is a non-trivial function (Eq. (1.34)) of the particle density $\rho_p(k)$. The change of the particle density $\rho_p(k)$ affects the density of state $\rho_s(k)$ in the whole k space.

1.2.3.1 Yang-Yang equation of state

For generic physical systems only rare examples exist where the equilibrium thermodynamic properties can be exactly calculated starting from the microscopic properties. With the previously introduced exact solutions, Yang and Yang⁴ showed how the equilibrium properties at temperature T can be calculated in the Lieb-Liniger model [35]. For this task, they calculated for a given $\rho_p(k)$ the number of possible microstates and from which the entropy S of the system can be calculated. Furthermore, they calculated the maximum entropy under the constraints of fixed energy E and particle numbers N . They maximized the quantity $S - \frac{\mu N}{T} - \frac{E}{T}$, with the Lagrange multiplier μ which is the chemical potential. From the maximization condition, they obtain that the density of holes $\rho_h(k)$ and the density of particles $\rho_p(k)$ obey the following equation:

$$\frac{\rho_h(k)}{\rho_p(k)} = e^{\beta\epsilon(k)}, \quad (1.37)$$

⁴Yang and Yang refers to C.N. Yang and C.P. Yang where the former is the nobel laureate, maybe better known from the Yang-Mills theory.

where $\beta = 1/(k_B T)$ is the inverse temperature and $\epsilon(k)$ the so-called pseudo-energy. The pseudo-energy $\epsilon(k)$ depends on all the other states and can be calculated from the implicit equation

$$\epsilon(k) = -\mu + \frac{\hbar^2 k^2}{2m} - \frac{1}{\beta} \int \frac{dk'}{2\pi} \Delta(k-k') \ln(1 + e^{\beta\epsilon(k')}). \quad (1.38)$$

From Eq. (1.38) one can then calculate the particle density in a second implicit equation

$$\rho_p(k) (1 + e^{\beta\epsilon(k)}) = \frac{1}{2\pi} + \int \frac{dk'}{2\pi} \Delta(k-k') \rho_p(k'). \quad (1.39)$$

Eq. (1.38) & (1.39) form the Yang-Yang equations and can be solved numerically by iteration (see [36] or [14] for details of numerical implementation). The density in real space n is then given by

$$n = \int dk \rho_p(k). \quad (1.40)$$

The Yang-Yang equations allow to calculate numerically in a reasonable time the equation of state $n(\mu, T)$, from which the thermodynamic quantities of interest can be deduced. For the pressure P one can deduce the formula:

$$P = \frac{1}{\beta} \int \frac{dk}{2\pi} \ln(1 + e^{-\beta\epsilon(k)}), \quad (1.41)$$

which will be used in Chap. 4 [2, 32, 33, 35].

1.2.4 The equilibrium regimes

Depending on the temperature T , the density n and the interaction strength g , different regimes of the Lieb-Liniger model can be distinguished. These different regimes can be distinguished within the phase diagram spanned by the adimensional temperature t_{YY} ⁵ and the adimensional interaction parameter γ

$$t_{YY} = \frac{2\hbar^2 k_B T}{mg^2} \quad \text{and} \quad \gamma = \frac{mg}{\hbar^2 n}. \quad (1.42)$$

Here, the use of the word *phase diagram* should not to be taken by the thermodynamic sense of phase transitions. The Mermin-Wagner theorem forbids phase transitions for $T > 0$ in 1D [37–39] and so the different regimes at finite temperature are separated by smooth cross-overs [40]. The boundaries between the regimes can be calculated from the exact Yang-Yang thermodynamics. The values which will be given in the following should be understood as typical values for which the cross-over occurs.

⁵The subscript YY stands for Yang-Yang and is introduced to not confuse with the time, usually denoted t in out-of-equilibrium experiments.

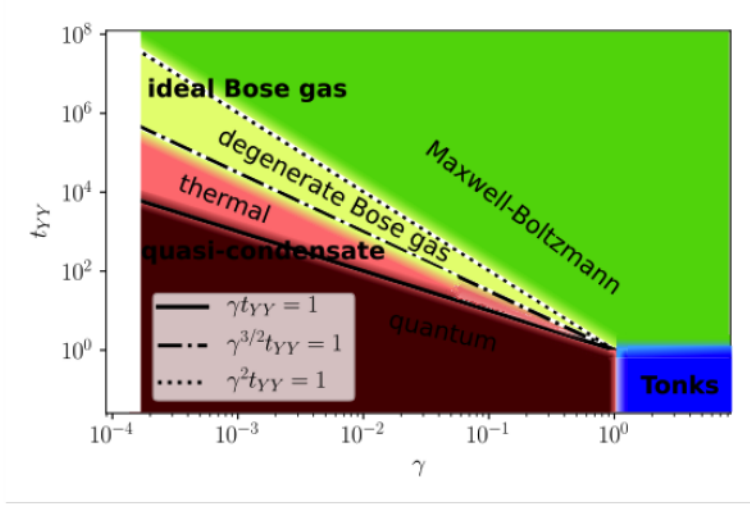


Figure 1.4 – Equilibrium phase diagram with the three regimes and its subregimes. The lines separating the regimes indicate the smooth crossovers.

The historical approach to distinguish the different regimes uses the normalized two-body correlation function

$$g^{(2)}(z) = \frac{\langle \hat{\Psi}^\dagger(z) \hat{\Psi}^\dagger(0) \hat{\Psi}(z) \hat{\Psi}(0) \rangle}{n_0^2} \quad (1.43)$$

at zero-distance $g^{(2)}(0)$ where the mean density is given by $n_0 = \langle \hat{\Psi}^\dagger(z) \hat{\Psi}(z) \rangle$. The two-body correlation function $g^{(2)}(0)$ can be calculated via the Hellman-Feynman theorem which relates the former to the free energy $F = U - TS$

$$\frac{dF}{dg} = \frac{1}{2} \int dz \langle \hat{\Psi}^\dagger(z) \hat{\Psi}^\dagger(0) \hat{\Psi}(z) \hat{\Psi}(0) \rangle = \frac{Ln_0^2}{2} g^{(2)}(0). \quad (1.44)$$

From $g^{(2)}(0)$ three different main regimes can be distinguished [41]: the **ideal Bose gas** regime (IBG) where $g^{(2)}(0) \simeq 2$, the **strongly interacting** regime, also known as the Tonks-Girardeau gas ($g^{(2)}(0) \ll 1$), and the **quasi-condensate** regime ($g^{(2)}(0) \simeq 1$). Those regimes are show in Fig. 1.4 and their properties are discussed in more detail in the following sections.

1.2.4.1 Ideal Bose gas

For $\gamma^{3/2} t_{YY} \gg 1$ and $t \gg 1$ the gas is in the ideal Bose gas regime where $g^{(2)}(0) \simeq 2$: The particles bunch and a particle has twice the probability to be at the position of another particle, than far apart. The occupation number of each momentum state q

is given by the Bose-Einstein statistic for a non-interacting gas:

$$n_q = \frac{1}{e^{\beta(\frac{\hbar^2 q^2}{2m} - \mu)} - 1}. \quad (1.45)$$

From latter one can obtain the equation of state, here expressed in the form $n(\mu, T)$, by integrating over dq

$$n = \frac{1}{\lambda_{\text{dB}}} g_{\frac{1}{2}}(e^{\beta\mu}), \quad (1.46)$$

with the de-Broglie wave length $\lambda_{\text{dB}} = \sqrt{2\pi\hbar^2/(mk_B T)}$ and the Bose-Einstein function $g_{\frac{1}{2}}(x) = \sum_{j=0}^{\infty} x^j j^{-1/2}$. Note that the 1D Bose-Einstein function does not show the characteristics of condensation: The density n diverges when $|\mu|$ approaches zero. In contrast to 3D, no phase transition driven by degeneracy occurs.

The ideal Bose gas can be further divided in two sub-regimes: For $\gamma^2 t_{\text{YY}} \gg 1$ the gas is in the classical regime where it is described by the Maxwell-Boltzmann statistics, and the interparticle distance is larger than the thermal de Broglie wave length λ_{dB} . For $\gamma^2 t_{\text{YY}} \ll 1$ the gas becomes a degenerate Bose gas.

1.2.4.2 Quasi-condensate regime

When decreasing the interactions or decreasing the temperature, interactions start to prevent the bosonic bunching and $g^{(2)}(0) \approx 1$. This crossover occurs at about $\gamma^{3/2} t_{\text{YY}} \approx 1$ and is called the quasi-condensate cross-over⁶. Within the quasi-condensate regime large density fluctuations are suppressed due to interactions, i.e. $\delta n \ll n_0$, while, in contrast to 3D condensate, phase fluctuations are big and prevent true long range order. Within the quasi-condensate the equation of state is well approximated by

$$\mu = gn, \quad (1.47)$$

which does not depend on the temperature.

The quasi-condensate can also be separated in two subregimes. When considering $g^{(2)}(0)$, for $\gamma t_{\text{YY}} \gg 1$ thermal fluctuations dominate, while for $\gamma t_{\text{YY}} \ll 1$ quantum fluctuations dominate. Within this thesis the scientific results are all obtained around this crossover $\gamma t_{\text{YY}} \sim 1$. It turns out that for many observable of interest, such as the one-body correlation function $g^{(1)}(z)$, the quantum fluctuations do not play a role around the cross-over $\gamma t_{\text{YY}} \sim 1$. See Sec. 1.2.4.4 and for a more detailed discussion [42].

⁶The cross-over condition $\gamma^{3/2} t_{\text{YY}} \approx 1$ can be derived from the condition that density fluctuations are small.

1.2.4.3 Tonks gas

For $\gamma \gg 1$ and $t \ll 1$ the gas is in the strongly interacting regime, also called Tonks(-Girardeau) gas. In this regime the particles interact so strongly that they force the many-body wave-function to vanish for $z_i = z_j$ (see Fig. 1.1). This mimics the Pauli-exclusions principle and leads to an almost vanishing two-body correlation function at zero distance $g^{(2)}(0)$. There exists a mapping of the many-body wavefunction $\Psi(z_1, z_2, \dots, z_N)$ onto the wave function of non-interacting fermions $\Psi_F(z_1, z_2, \dots, z_N)$

$$\Psi(z_1, z_2, \dots, z_N) = \Psi_F(z_1, z_2, \dots, z_N) \prod_{1 \leq i < j \leq N} \text{sgn}(z_i - z_j) \quad (1.48)$$

called fermionization. The bosonic and the fermionic many-body wavefunction only differ by a sign and therefore quantities which depends on the absolute value of the many-body wavefunction, can be directly calculated by the fermionic wavefunctions. This justifies the interpretation of the Tonks regime as the regime of free fermions in certain situations. The energy and the thermodynamic quantities are the same as for free fermions.

1.2.4.4 Correlation functions

Correlation functions are an important tool to characterize the equilibrium properties of a system. In this section I give a brief overview and summary of the correlation functions. For the experimentally most relevant quasi-condensate regime, detailed calculations are performed in Sec. 1.3.

One-body correlation The one-body correlation function

$$g_1(z) = \langle \hat{\Psi}^\dagger(0) \hat{\Psi}(z) \rangle \quad (1.49)$$

can be accessed experimentally in a homogeneous system via the Fourier transform of the momentum distribution

$$\langle \hat{\Psi}^\dagger(q) \hat{\Psi}(q) \rangle = \int dz g_1(z) e^{iqz}, \quad (1.50)$$

where

$$\hat{\Psi}(q) = \frac{1}{\sqrt{2\pi}} \int dz \hat{\Psi}(z) e^{iqz}. \quad (1.51)$$

In the following I discuss the one-body correlation function in different regimes.

The one-body correlation function inside the ideal Bose gas regime The one-body correlation function inside the ideal Bose gas regime can be calculated by using the inverse relation of Eq. (1.50) and the Bose occupation Eq. (1.45). In the two sub-regimes Maxwell-Boltzmann (M-B) and degenerate Bose gas (deg. Bose) analytical formulas can be found and which are given by

$$g_1^{\text{M-B}} = n_0 e^{-\pi \frac{z^2}{\lambda_{\text{dB}}^2}} \quad \text{and} \quad g_1^{\text{deg. Bose}} = n_0 e^{-2\pi \frac{|z|}{n_0 \lambda_{\text{dB}}^2}}. \quad (1.52)$$

The one-body correlation function inside the quasi-condensate regime In the quasi-condensate (q.-C.) regime the one-body correlation function is given by

$$g_1^{\text{q.-C.}} = n_0 e^{-\frac{|z|}{l_c}}, \quad (1.53)$$

where the phase correlation length $l_c = \frac{2\hbar^2 n_0}{mk_B T} = \frac{2n_0 \lambda_{\text{dB}}^2}{2\pi}$ has been introduced. The explicit calculation of Eq. (1.53) can be found in Sec. 1.3.1.2. Note that the behavior in the degenerate ideal Bose gas, only differs by a factor of 1/2 from the quasi-condensate regime. The crossover between the two regimes is however not a simple extrapolation [40]. It is important to note that Eq. (1.53) stays valid inside the quasi-condensate up to very low temperatures where $g_2(0)$ is already dominated by quantum fluctuations. The effect of quantum fluctuations on the $g_1(z)$ function for distances larger than the thermal phonon wavelength $l_T = \lambda_{\text{dB}}^2 / \xi$ leads to a reduction by a prefactor $(l_T / \xi)^{-\sqrt{\gamma}/(2\pi)}$, where $\sqrt{\gamma}/(2\pi)$ is typically very small inside the quasi-condensate-regime. Let us calculate this effect. The temperature T_Q for which the g_1 -function is decreased by a prefactor 1/2 from the quantum fluctuations is given by $\frac{k_B T_Q}{gn} = 2^{-2\pi/\sqrt{\gamma}}$. The temperature T_Q correspond to experimentally unreachable temperatures [42].

Higher order correlation functions Higher order correlation functions at zero distance $g^{(j)}(0)$ can be an important tool to characterize the Bose gas. As previously introduced, the different regimes are characterized by the two-body correlation function at zero distance $g^{(2)}(0)$ and the the three-body loss rate depends on the three-body correlation function at zero distance $g^{(3)}(0)$ (Sec. 4.4).

In the ideal Bose gas regime the interaction part of the Lieb-Liniger Hamiltonian Eq. (1.8) can be neglected, making the Hamiltonian quadratic in $\hat{\Psi}$. At thermal equilibrium this allows to use the Wick theorem, and calculate for example the second order correlation function

$$g_{\text{IBG}}^{(2)}(z) = 1 + |g^{(1)}(z)|^2, \quad (1.54)$$

from which we obtain $g_{\text{IBG}}^{(2)}(0) = 2$, since $g_{\text{IBG}}^{(1)}(0) = 1$ in all subregimes of the ideal Bose gas (see Eq. (1.52)). Higher order correlation functions can be expressed similarly which leads to e.g. $g_{\text{IBG}}^{(3)}(0) = 6$.

In the quasi-condensate regime the field operator $\hat{\Psi}$ can be approximated by $\sqrt{n_0}e^{i\theta}$ where density fluctuations are neglected. This leads to higher order correlation functions at zero distance which are close to one. Most importantly for Chap. 4 the normalized third order correlation function at zero distance is

$$g_{\text{q-c.}}^{(3)}(0) = \frac{\langle \Psi^{\dagger 3}(0)\Psi^3(0) \rangle}{\langle n \rangle^3} \simeq 1. \quad (1.55)$$

Concerning the Tonks-Girardeau regime, calculations of correlation functions can be involved and I refer to the reviews [43, 44]. When approaching the Tonks-Girardeau regime, the probability of finding more than one particle at the same place drops to zero which can be used as an experimental signature [7].

1.3 Linearized theory in the quasi-condensate

1.3.1 Homogeneous system

Inside the quasi-condensate regime the Bogoliubov treatment can be applied, where the Hamiltonian is rewritten as

$$H \simeq H_0 + \sum_{k=1}^N H_k + \Delta E = H_0 + \sum_{k=1}^N \hbar\omega_k \hat{a}_k^\dagger a_k + \Delta E, \quad (1.56)$$

where H_0 is given by gN^2/L . The creation (annihilation operators $\hat{a}_k^{(\dagger)}$) fulfill the standard bosonic commutation relations and ΔE is an energy shift which is negative in 1D. As it will be shown in the following H_0 is the Gross-Pitaevskii mean field Hamiltonian and the uncoupled harmonic oscillators H_k correspond to the Bogoliubov Hamiltonian. In contrast to the derivation of the famous Bogoliubov theory for superfluids in 3D [45], special attention needs to be paid to the subtleties in lower dimension due to the absence of long-range order [46]: The Hamiltonian cannot be expanded in terms of $\hat{\Psi}(z)$ around $\langle \hat{\Psi}(z) \rangle$.

To overcome this problem we use the phase-density representation of $\hat{\Psi}$ in a coarse-grained approach where microscopic length scales are avoided. The field operator in the phase-density representation writes $\hat{\Psi} = \sqrt{n_0 + \delta\hat{n}}e^{i\hat{\theta}}$ with density fluctuations $\delta\hat{n} = \langle \hat{n} \rangle - \hat{n}$. This leading to the commutation relation⁷

$$[\hat{n}(z), \hat{\theta}(z')] = i\delta(z - z'), \quad (1.57)$$

$$[\hat{n}(z), \hat{n}(z')] = [\hat{\theta}(z), \hat{\theta}(z')] = 0. \quad (1.58)$$

⁷Here the delta function $\delta(z - z')$ should be understood as a notation for the discrete delta function $\delta_{z,z'}/l$ where l is the size of the grid.

In principle the phase operator in a homogeneous system is ill-defined. This problem is avoided by looking at the previously introduced coarse grained description with many atoms per cell.

The Lieb-Liniger Hamiltonian Eq. (1.8) in phase-density representation writes

$$\hat{H} = \frac{\hbar^2}{2m} \int dz \left[\left(\partial_z \sqrt{\hat{n}(z)} \right)^2 + \sqrt{\hat{n}(z)} (\partial_z \hat{\theta}(z))^2 \sqrt{\hat{n}(z)} \right] + \frac{g}{2} \int dz \hat{n}(z)^2 + \mu \int dz \hat{n}(z) + \Delta E \quad (1.59)$$

where the chemical potential μ in the grand canonical ensemble was added. Inside the quasi-condensate density fluctuations are small $|\delta \hat{n}| \ll n_0$. Additionally we can neglect very small wavelength excitations, such that the phase gradient is a second small parameter $|\partial_z \hat{\theta}| \ll n_0$. Note that latter is equivalent of having many particles per considered wavelength $N \gg L/\lambda$ which is typically very well fulfilled. We expand Eq. (1.59) with the two small parameters $|\delta \hat{n}|/n_0$ and $|\partial_z \hat{\theta}|/n_0$. At zeroth order this leads to the Gross-Pitaevskii (GP) pseudo-Hamiltonian

$$H_0 = \int \Psi^*(z) \left[-\frac{\hbar^2}{2m} \frac{\partial^2}{\partial z^2} + \frac{g}{2} |\Psi(z)|^2 - \mu \right] \Psi(z) dz, \quad (1.60)$$

where $\Psi(z)$ is chosen such that it satisfies

$$\left[-\frac{\hbar^2}{2m} \frac{\partial^2}{\partial z^2} + g |\Psi(z)|^2 - \mu \right] \Psi(z) = 0. \quad (1.61)$$

This choice of $\Psi(z)$ ensures that the first order terms in the expansion of \hat{H} vanish.

Second order — Bogoliubov Hamiltonian At second order one obtains

$$H_2 = \frac{\hbar^2}{m} \int dz \left[\frac{1}{8n_0} (\partial_z \delta \hat{n})^2 + \frac{n_0}{2} (\partial_z \hat{\theta})^2 \right] + \frac{g}{2} \int dz \delta \hat{n}^2. \quad (1.62)$$

Introducing the Fourier components

$$\delta \hat{n}(z) = \sqrt{\frac{2}{L}} \left[\sum_{q>0} \hat{n}_{c,q} \cos(qz) + \hat{n}_{s,q} \sin(qz) \right] \quad (1.63)$$

$$\hat{\theta}(z) = \sqrt{\frac{2}{L}} \left[\sum_{q>0} \hat{\theta}_{c,q} \cos(qz) + \hat{\theta}_{s,q} \sin(qz) \right] \quad (1.64)$$

where the subscript s/c stands for sine/cosine-component and L is the size of the system. The wavevector q takes discrete values $2\pi n/L$ where n is a positive integer. Introducing the Fourier components into Eq. (1.62) one obtains:

$$H_2 = \sum_{i=\{c,s\}} \sum_q \left[\left(\frac{g}{2} + \frac{\hbar^2 q^2}{8m n_0} \right) \hat{n}_{i,q}^2 + \frac{\hbar^2 q^2 n_0}{2m} \hat{\theta}_{i,q}^2 \right]. \quad (1.65)$$

This is the Bogoliubov Hamiltonian in density-phase representation, frequently used in this thesis [43, 46]. Its quadratic variables fulfill $[\hat{n}_{i,q}, \hat{\theta}_{i',q'}] = i\delta_{i,i'}\delta_{q,q'}$ and it represents N uncoupled harmonic oscillators. Frequently I will use the notation⁸

$$H_q = A_q \hat{n}_q^2 + B_q \hat{\theta}_q^2 \quad (1.66)$$

for the Bogoliubov Hamiltonian, where $A_q = \frac{g}{2} + \frac{\hbar^2 q^2}{8mn_0}$ and $B_q = \frac{\hbar^2 q^2 n_0}{2m}$. Each mode q describes a collective mode at a wavevector q and mode frequency

$$\hbar\omega_q = \sqrt{\frac{\hbar^2 q^2}{2m} \left(\frac{\hbar^2 q^2}{2m} + 2gn_0 \right)}. \quad (1.67)$$

One can distinguish two different types of excitations by introducing the healing length $\xi^{-1} = \sqrt{mg n_0}/\hbar$. For $q\xi \ll 1$ the excitations are sound waves which travel with the speed of sound $c = \sqrt{gn_0/m}$, also called hydrodynamic excitations. They are characterized by their phononic dispersion relation

$$\omega_q = cq. \quad (1.68)$$

For $q \gg \xi$ the excitations resemble massive free particle with an energy $\frac{\hbar^2 q^2}{2m} + gn_0$, with the "rest mass" term $gn_0 = c^2 m$.

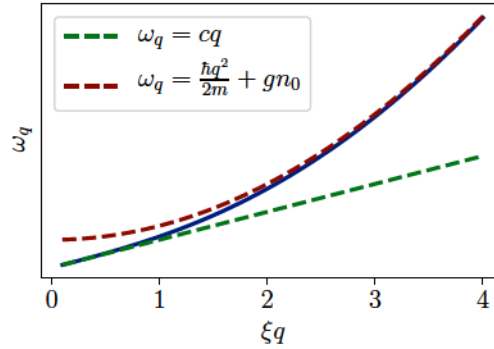


Figure 1.5 – Dispersion relation of the Bogoliubov collective excitations Eq. (1.67) (blue line). For small wave vectors $\xi q \ll 1$, the dispersion relation is linear (dashed green) and for large wave vectors $\xi q \gg 1$ the dispersion relation resembles massive free particles (dashed red).

Note that a rigorous calculation of the energy shift ΔE is needed for the calculation of the ground state energy of the system. In this thesis we do not make reference to the ground state and refer to [46] for a rigorous treatment of the problem.

⁸Here, the subscript for the sinus and cosinus modes has been dropped and it is left to the reader to add it when necessary.

The Bogoliubov Hamiltonian can be rewritten in the standard second quantized form by introducing the creation and annihilation operators with the standard transformation

$$\hat{a}_{q,r} = f_q \sqrt{n_0} \hat{\theta}_{q,r} - i f_q^{-1} \frac{1}{2\sqrt{n_0}} \hat{n}_{q,r} \quad (1.69)$$

where

$$f_q = \left(\frac{\frac{\hbar^2 q^2}{2m}}{\frac{\hbar^2 q^2}{2m} + 2g n_0} \right)^{\frac{1}{4}} \quad (1.70)$$

This finally leads to the form

$$H_q = \hbar \omega_q a_q^\dagger a_q \quad (1.71)$$

introduced in the beginning⁹.

1.3.1.1 Wigner representation

Let us consider a given Bogoliubov mode q . After tracing out all the other modes, the system is described by the reduced density matrix $\hat{\rho}$. Instead of $\hat{\rho}$ one can use the Wigner representation. The Wigner function of the mode q is given by

$$W(n_q, \theta_q) = \frac{1}{\pi} \int du \langle u + n_q | \hat{\rho} | u - n_q \rangle e^{-2iu\theta_q}, \quad (1.72)$$

The Wigner function is a quasiprobability function which can take values $W < 0$ for non-classical states. The Wigner function contains the full information of the system and expectation values of an observable $\hat{O}(n_q, \theta_q)$ are calculated according to

$$\langle \hat{O} \rangle = \iint dn_q d\theta_q W(n_q, \theta_q) O(n_q, \theta_q). \quad (1.73)$$

For classical states, the Wigner function can be interpreted as a probability function. It gives the probability that the given mode takes the values n_q and θ_q . For a harmonic oscillator, as the Bogoliubov Hamiltonian for a mode q in Eq. (1.66), the time evolution of the Wigner function is the same as the classical time evolution¹⁰. It is given by the Liouville equation

$$\frac{\partial W(n_q, \theta_q)}{\partial t} = - \frac{\partial W(n_q, \theta_q)}{\partial n_q} \frac{\partial H_q}{\partial \theta_q} + \frac{\partial W(n_q, \theta_q)}{\partial \theta_q} \frac{\partial H_q}{\partial n_q}. \quad (1.74)$$

⁹Note that Eq. (1.71) differs by the constant $\hbar\omega/2$ from Eq. (1.65) and which needs to be considered for the definition of ΔE .

¹⁰Since the evolution is classical, I will drop in the following the operator notation $\hat{\cdot}$ for n_q and θ_q .

At thermal equilibrium the Wigner function is a Gaussian distribution with the same energy in both quadratures

$$E_q/2 = A_q \langle n_q^2 \rangle = B_q \langle \theta_q^2 \rangle. \quad (1.75)$$

Experimentally we typically deal with excitations which are populated thermally $k_B T \gg \hbar\omega_q$. Such that we can write $E_q = k_B T$ for thermal states.

1.3.1.2 First order correlation function

The Bogoliubov approximation can be used to calculate the first order correlation function inside the quasi-condensate regime $g_1(z) = \langle \hat{\Psi}^\dagger(0)\Psi(z) \rangle$. Neglecting the density fluctuations, one writes

$$g_1(z) \approx n_0 \langle e^{i[\theta(0) - \theta(z)]} \rangle. \quad (1.76)$$

Using the Wick theorem $\langle e^{i\Delta\theta} \rangle = e^{-1/2\langle \Delta\theta^2 \rangle}$, valid since the Bogoliubov Hamiltonian is quadratic in θ , one obtains

$$g_1(z) \approx n_0 e^{-\frac{1}{2}\langle [\theta(0) - \theta(z)]^2 \rangle}, \quad (1.77)$$

which can be rewritten

$$\langle [\theta(0) - \theta(z)]^2 \rangle = \frac{2}{L} \sum_{q>0} \langle \theta_{q,c}^2 \rangle (\cos(qz) - 1)^2 + \frac{2}{L} \sum_{q>0} \langle \theta_{q,s}^2 \rangle (\sin(qz))^2. \quad (1.78)$$

At thermal equilibrium the partition theorem states that the energy of the two quadratures is

$$E_q/2 = A_q \langle \delta n_{q,j}^2 \rangle = B_q \langle \theta_{q,j}^2 \rangle. \quad (1.79)$$

At high enough temperatures such that $k_B T \gg \hbar\omega_q$, the energy is given by $k_B T = E_q$ which implies that $\langle \theta_{q,j}^2 \rangle = \frac{k_B T m}{\hbar^2 q^2 n_0}$ and one obtains

$$\begin{aligned} \langle [\theta(0) - \theta(z)]^2 \rangle &= 4 \int_0^\infty \frac{dq}{2\pi} \langle \theta_q^2 \rangle [1 - \cos(qz)] = \\ &= \frac{4mk_B T}{\hbar^2 n_0} \int_0^\infty \frac{dq}{2\pi} \frac{1 - \cos(qz)}{q^2} = \frac{mk_B T |z|}{\hbar^2 n_0}, \end{aligned} \quad (1.80)$$

where the sum was replaced by the integral over q . This implies that phase fluctuations stay small on distances much smaller than the phase coherence length $l_c = \frac{2\hbar^2 n_0}{mk_B T}$. We finally obtain

$$g_1(z) \approx n_0 e^{-\frac{|z|}{l_c}}. \quad (1.81)$$

1.3.2 Trapping potential

1.3.2.1 Local Density Approximation (LDA)

Until now, I considered homogeneous systems. Experimentally one typically uses systems trapped in some longitudinal trapping potential $V(z)$. At equilibrium the Local Density Approximation (LDA) can be used when the potential and the density vary slowly compared to the microscopic quantities, namely the phase coherence length l_c . In our experiment l_c is typically of the order of a few hundreds of nanometers¹¹. The LDA consists in a division of the system into small cells of size δz with $l_c \ll \delta z \ll n \left(\frac{dn}{dz}\right)^{-1}$. In each of the cells the density $n(z)$ is close to constant. Each cell can be approximated by a small homogeneous system with a local chemical potential given by $\mu(z) = \mu_p - V(z)$. Here, as for the whole thesis, we chose the convention that the potential vanishes at the peak density $V(0) = 0$, where $n(0) = n_p$.

Beyond the LDA approach the trapping potential $V_{\parallel}(z)$ needs to be added to Eq. (1.59) as

$$\hat{H}_V = \int dz V_{\parallel}(z) \hat{n}(z). \quad (1.82)$$

At zeroth order in the two small parameters the term $H_{V_{\parallel}} = \int dz V_{\parallel}(z) \Psi(z)^* \Psi(z)$ needs to be added to the Gross-Pitaevskii Hamiltonian (1.60). When neglecting the kinetic energy one obtains the Thomas-Fermi approximation, where the density profile is given by

$$n_0(z) = \begin{cases} \frac{(\mu_p - V(z))}{g} & |z| < R \\ 0 & \text{for } |z| > R, \end{cases}$$

where $\mu_p = gn_p$ is the peak chemical potential, with the peak density n_p and the Thomas Fermi radius such that $V(R) = \mu_p$. The neglect of the kinetic energy term in the GP-equation is equivalent to the previously introduced local density approximation.

1.3.2.2 Bogoliubov in a harmonic trap

In second order in the two small parameters the situation gets more complicated and in order to obtain analytic results, let us restrict to a harmonic longitudinal confinement $V(z) = 1/2 m \omega_{\parallel}^2 z^2$ and long wavelength excitations (hydrodynamic modes). The density and phase fluctuations can be developed on the normalized Legendre

¹¹In practice it is often sufficient to consider length-scales much larger than the interparticle distance.

polynomials [47, 48]

$$\theta(z) = \sum_{\nu} \theta_{\nu}(z) p_{\nu} \quad (1.83)$$

$$\delta n(z) = \sum_{\nu} n_{\nu}(z) x_{\nu}, \quad (1.84)$$

where

$$\theta_{\nu}(z) = \frac{1}{\sqrt{2}} \left(\frac{mg}{\hbar^2 n_p} \right)^{1/4} \frac{\sqrt{2\nu+1}}{(\nu(\nu+1))^{1/4}} P_{\nu}\left(\frac{z}{R}\right) \quad (1.85)$$

$$n_{\nu}(z) = \frac{\sqrt{2\nu+1}}{2R} (\nu(\nu+1))^{1/4} \left(\frac{\hbar^2 n_p}{mg} \right)^{1/4} P_{\nu}\left(\frac{z}{R}\right). \quad (1.86)$$

Here $P_{\nu}(z)$ are the Legendre polynomials of the first kind which can be approximated by

$$P_{\nu}(\cos \alpha) \simeq \left(\frac{2}{\pi(\nu + \frac{1}{2}) \sin \alpha} \right)^{1/2} \cos \phi_{\nu}, \quad (1.87)$$

for large ν and small $\cos(\alpha)$ where $\phi_{\nu} = (\nu + \frac{1}{2})\alpha - \frac{1}{4}$. In Fig. 1.6 a) the mode fluctuations n_{ν} are shown together with the approximation Eq. (1.87) which typically shows a very good agreement already for $\nu > 4$.

With the previously introduced canonically conjugated variables x_{ν} and p_{ν} the quadratic Bogoliubov Hamiltonian in a harmonic trap writes:

$$H_{\nu} = \hbar\omega_{\nu} \left(\frac{x_{\nu}^2}{2} + \frac{p_{\nu}^2}{2} \right). \quad (1.88)$$

The dispersion relation in the harmonic trap is given by

$$\omega_{\nu} = \sqrt{\frac{\nu(\nu+1)}{2}} \omega_{\parallel}. \quad (1.89)$$

Note that the dispersion relation in the harmonic trap is independent on the density. A description for other trapping potentials than harmonic ones, is given in our paper [23].

1.3.3 High density 3D effects

For high linear densities $n_0 a_{3D} \simeq 1$ interaction effects between atoms in the transverse direction become important which leads to a broadening of the transverse ground state. This effect can be experimentally important and is equivalent to the 1D condition $\mu \ll \hbar\omega_{\perp}$ not being fulfilled. For not too large $n a_{3D}$ it has been shown that a

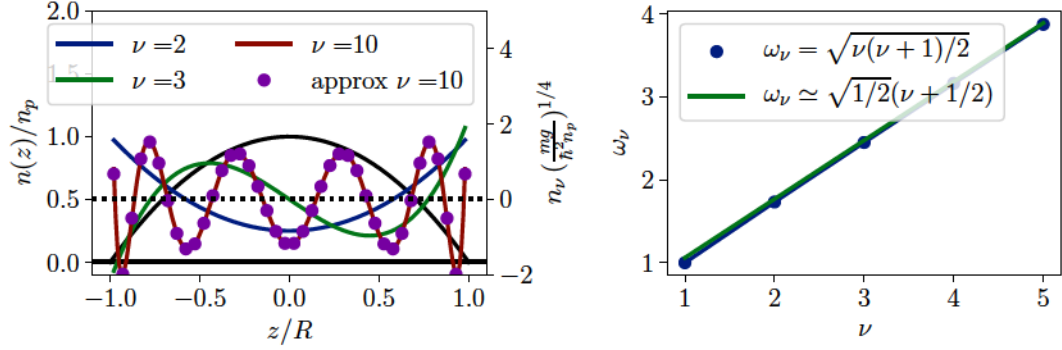


Figure 1.6 – a) The Thomas-Fermi profile in a harmonic trap in black with the density fluctuations n_ν for different mode indices ν . Already for $\nu = 10$, no difference between the exact and the approximate formula is visible. In the center the density fluctuations are close to sinusoidal modes, as in the homogeneous case. b) The dispersion relation ω_ν for a harmonic confinement, compared to the linear approximation, with a very fast convergence.

Gaussian ansatz for the transverse wave function is a good approximation. The width of the Gaussian is given by

$$\tilde{l}_\perp = l_\perp (1 + 2n_0 a_{3D})^{\frac{1}{4}} \quad (1.90)$$

and depends on the linear density and on the width of the single particle ground state $l_\perp = \sqrt{\hbar/(m\omega_\perp)}$ [49]. We have checked numerically with Gross-Pitaevskii calculations, that the width of the ground state follows Eq. (1.90) up to a maximal deviation of 20% for the experimentally relevant densities $na_{3D} < 1.3$.

Beyond the Gaussian ansatz a heuristic equation for the chemical potential inside the quasi-condensate regime can be found

$$\mu = \hbar\omega_\perp \left(\sqrt{1 + 4n_0 a_{3D}} - 1 \right) \xrightarrow{n_0 a_{3D} \ll 1} g n_0, \quad (1.91)$$

which shows the correct asymptotic behavior in both the low and large density limit [50, 51].

These high density effects can be taken into account in the LDA $\mu(z) = \mu_p - V(z)$ such that the mean density $n_0(z)$ in the Thomas-Fermi approximation is given by

$$n_0(z) = \frac{1}{4a_{3D}} \left\{ \left[\sqrt{1 + 4a_{3D}n_p} - \frac{V(z)}{\hbar\omega_\perp} \right]^2 - 1 \right\}. \quad (1.92)$$

Compare with Fig. 2.14 b) green curve, where the Thomas-Fermi profile is shown with the modified equation of state.

Although the previous parts suggest that even for $n_0 a_{3D} \sim 1$ an adapted 1D physics can be implemented, I want to stress out, that these effects are corrections arising from the 3D world and the physics at play cannot be considered as strictly 1D. Links to the Lieb-Liniger model and to integrability need to be taken with care in these situations.

1.3.3.1 Bogoliubov Hamiltonian with 3D effects

The Bogoliubov Hamiltonian for long wave-length modes $q \ll 1/\xi$ can be modified such that it takes into account these 3D effects. When rewriting the Bogoliubov Hamiltonian Eq. (1.65) for $q \ll 1/\xi$

$$H_q = \underbrace{\frac{mc^2}{2n_0} \delta n_q^2}_{E_{\text{int.}}} + \underbrace{\frac{\hbar^2 q^2 n_0}{2m} \theta_q^2}_{E_{\text{kin.}}}, \quad (1.93)$$

one realizes that the kinetic energy part $E_{\text{kin.}}$ is independent of the density fluctuations, since the phase fluctuations θ_q^2 are unaffected by the swelling of the transverse wavefunction. Let us expand the energy of the system $E(n_0 + \delta n)$. The second order term writes

$$E(\mathcal{O}(2)) = \frac{1}{2} \left. \frac{\partial \mu}{\partial n} \right|_{n_0} \delta n^2, \quad (1.94)$$

where $\mu = \frac{\partial E}{\partial n}$. This allows to rewrite the Hamiltonian at quadratic order in δn :

$$H_q = \frac{1}{2} \left. \frac{\partial \mu}{\partial n} \right|_{n_0} \delta n_q^2 + \frac{\hbar^2 q^2 n_0}{2m} \theta_q^2, \quad (1.95)$$

where now the chemical potential of Eq. (1.91) is used. This directly leads to the introduction of the modified speed of sound

$$c^2 = \frac{n_0}{m} \left. \frac{\partial \mu}{\partial n} \right|_{n_0} = \frac{c_{1D}^2}{\sqrt{1 + 4a_{3D}n_0}}, \quad (1.96)$$

where $c_{1D}^2 = gn_0/m$ is the expression in the purely 1D situation. Therefore we can use the expression Eq. (1.93) with the modified speed of sound to describe our system at high densities ($a_{3D}n \sim 1$). This Hamiltonian describes a situation, where the transverse shape follows adiabatically the density fluctuations arising from the sound waves of the Bogoliubov Hamiltonian. A more formal approach is given in the appendix of our paper [23] which also takes into account the longitudinal trapping potential. Furthermore, in [52] it has been proposed to heuristically extend the GP equation to take into account the broadening of the transverse ground state.

1.3.4 Classical field

The Gross-Pitaevskii Hamiltonian H_0 , introduced in Eq. 1.60, is a classical field equation where the quantum nature of the field has been neglected and the field is given by a complex number $\Psi(z, t)$. For very degenerate gases it can be generalized to finite temperatures where the probability for the field configuration Ψ is given by the Boltzmann factor $e^{-\beta H_0(\Psi)}/Z$. The partition function Z is given by the path integral

$$Z = \int e^{-\beta H_0(\Psi)} \mathcal{D}\Psi. \quad (1.97)$$

This classical problem can be mapped onto a quantum problem in zero dimensions, where it is equivalent of solving a particle in a 2D harmonic potential. This can be used for efficient numerical calculations. The classical field problem depends on a single parameter

$$\chi = \frac{\hbar^2 n^3 g}{m k_B^2 T^2} = l_c^2 / (4\xi^2). \quad (1.98)$$

The classical field approach is valid within the quasi-condensate regime, for which $\chi \ll 1$ and inside the degenerate ideal Bose gas regime, for which $\chi \gg 1$ [43]. This approach fails in the Maxwell-Boltzmann regime. The discrete nature of the atoms becomes important in the Maxwell-Boltzmann regime which is not captured by the classical field approach.

1.4 Dynamics of 1D Bose gases

1.4.1 Dynamics of the linearized theory in the quasi-condensate regime

After discussing the equilibrium properties of the 1D Bose gas, I will now turn to its dynamical properties — the main subject of my thesis. Many previously introduced concepts can be directly generalized to the dynamical situation. The dynamical version of Gross-Pitaevskii Hamiltonian Eq. (1.60) and the Bogoliubov Hamiltonian (1.65) can be directly obtained from the Heisenberg equation of motion:

$$i\hbar \frac{d\hat{\Psi}}{dt} = [\hat{\Psi}, \hat{H}]. \quad (1.99)$$

Gross-Pitaevskii Let us first ignore the quantum nature of $\hat{\Psi}$ and thus consider Ψ as a complex field. Then, Eq. (1.99) gives the Gross-Pitaevskii Equation (GPE)

$$i\hbar \frac{\partial \Psi(z, t)}{\partial t} = -\frac{\hbar^2}{2m} \frac{\partial^2 \Psi(z, t)}{\partial z^2} + g |\Psi(z, t)|^2 \Psi(z, t) + V_{\parallel}(z) \Psi(z, t). \quad (1.100)$$

The GPE (1.100) also gives the time evolution of the classical field approach of Sec. 1.3.4. It can be efficiently numerically implemented with the split-operator method [53].

Bogoliubov Hamiltonian In a homogeneous system the Bogoliubov Hamiltonian for each mode q is quadratic. The evolution of the Wigner function is classical (see Sec. 1.3.1.1) and the evolution of the quadratures n_q and θ_q is captured by the classical dynamics of:

$$\frac{\partial n_q}{\partial t} = -\frac{\partial H_q}{\partial \theta_q} = -2B_q \theta_q \quad (1.101)$$

$$\frac{\partial \theta_q}{\partial t} = \frac{\partial H_q}{\partial n_q} = 2A_q n_q. \quad (1.102)$$

For the unhomogeneous case, I refer the reader to [46].

1.4.2 Coarse grained description

In the following two sections (Sec. 1.4.4 and 1.4.3) we will consider the Lieb-Liniger system in a coarse-grained approach, also called the hydrodynamic picture, or the Euler scale. We consider length- and time scales that are large compared to the microscopic scales: The length scales are large compared to the healing length and times large compared to the local relaxation time t_{relax} . Therefore, we divide the system into small space-time boxes $dz \times dt$, such that the thermodynamic quantities varies slowly on those length scales¹². The system, inside such a small cell, is assumed to be in an equilibrium state and the following two Sections differ in the description of this state:

1. **The Conventional¹³ Hydrodynamics (CHD)** assumes that the system can be locally described after a short relaxation time t_{relax} by a Gibbs ensemble

$$\hat{\rho}_{\text{Gibbs}} = \frac{1}{Z} e^{-\beta(\hat{H}-\mu)}, \quad (1.103)$$

with $Z = \text{Tr} \left[e^{-\beta(\hat{H}-\mu)} \right]$ and the inverse temperature $1/\beta = k_B T$. The state inside the small cell is completely defined by μ and T and equivalently by the particle density n and the energy per particle e .

2. **The Generalized Hydrodynamics (GHD)** assumes that, after a short relaxation time t_{relax} , the system is locally described by the Generalized Gibbs Ensemble (GGE)¹⁴

$$\hat{\rho}_{\text{GGE}} = \frac{1}{Z} \exp \left(-\sum_i \beta_i \hat{Q}_i \right). \quad (1.104)$$

¹²For the space coordinate this is equivalent to the LDA (see Sec. 1.3.2.1).

¹³We use the word *conventional* hydrodynamics to highlight the difference to the Generalized Hydrodynamics (GHD) introduced in the next section.

¹⁴See Sec. 3.1 for further discussions of GGE.

GGE is determined by the complete set of conserved quantities Q_i that characterize the integrable system. The partition function is $Z = \text{Tr} [\exp(-\sum_i \beta_i Q_i)]$ and β_i are the Lagrange multipliers which maximize the entropy S . For the time evolution, GHD takes into account the conservation of all the charges of the Lieb-Linger model.

In an integrable system the CHD description represents, in most situations, an unjustified approximation. As will be discussed in Sec. 3.1, an integrable system is expected to relax towards a GGE.

1.4.3 Conventional Hydrodynamics (CHD)

The Conventional HydroDynamic (CHD) or simply the hydrodynamic equations are widely used to describe the dynamics of cold atom systems. They arise from the assumption that a system can be locally described by a Gibbs state, characterized by the energy per particle e and the particle density n . One writes the continuity relations associated to the conservation of total momentum, energy and atom number:

$$\frac{\partial}{\partial t} n + \frac{\partial}{\partial z} (nv) = 0, \quad (1.105)$$

$$\frac{\partial}{\partial t} np + \frac{\partial}{\partial z} (mnv^2 + P) = -n \frac{\partial V(z, t)}{\partial z} \quad (1.106)$$

$$\frac{\partial}{\partial t} \left(n \frac{mv^2}{2} + ne + nV \right) + \frac{\partial}{\partial z} \left[n \left(n \frac{mv^2}{2} + ne + nV \right) + nP \right] = 0, \quad (1.107)$$

where $v(z, t)$ is the hydrodynamic velocity of the fluid cell and $P(z, t)$ the pressure. In an external potential V_{\parallel} , the conservation of momentum is broken by the term $-n \frac{\partial V(z, t)}{\partial z}$. These equations can be solved together with the equation of state, relating P to n and e . This can be obtained from the Yang-Yang equation of state introduced in Sec. 1.2.3.1. The CHD results in Chap. 5 are all based on the numerical implementation of Eq. (1.105) - (1.107), together with the Yang-Yang equation of state.

1.4.4 Generalized Hydrodynamics (GHD)

The Generalized HydroDynamics (GHD) is a recent theoretical approach (2016) to describe the out-of-equilibrium dynamics of integrable systems [15, 16]. In contrast to CHD, GHD takes into account all the conserved charges of the Lieb-Liniger model. The operators of the conserved charges \hat{Q}_i , for which $[\hat{H}, \hat{Q}_i] = 0$, are complicated to construct and we focus on the expectation values of the conserved charges $Q_i = \langle \hat{Q}_i \rangle$. Additionally, we focus on a hydrodynamic description where the local charges $q_i(z) = Q_i/L$ depend on space. For the local charges $q_i(z)$ we can write the continuity

equation

$$\frac{\partial q_i(z)}{\partial t} + \frac{\partial j_i}{\partial z} = 0, \quad (1.108)$$

where $j_i(z)$ is the current associated to the charge q_i . In the Lieb-Liniger model the local conserved quantities are the quasi-particle densities $\{q_k\} = \{\rho_p(k)\}$ (see Eq. (1.32)). The quasi-particle densities $\{\rho_p(k)\}$, labeled by the quasi-momentum k , form a complete set in the space of conserved charges, such that we can replace the label i with k . In the hydrodynamics description, the quasi-particle density $\rho_p(k)$ becomes a space dependent function $\rho_p(z, k)$. In each cell the state is equivalent to a GGE state characterized by a quasi-particle density $\rho_p(k)$ [33].

The complexity lies in the calculation of the current j_k which was solved in [15]. In this thesis, I present a phenomenological approach to GHD, starting from the two-particle problem. In the following I refer explicitly to the Lieb-Liniger model, although GHD can be applied to integrable models in general.

1.4.4.1 Collision of two wave-packets

Let us reconsider the two-particle problem with contact interactions of Sec. 1.2.1 and study the collision of two wavepackets. The stationary solution of the two-particle problem $\Psi(z) = \sin[k|z| + \theta(k)]$ depends on the relative coordinate $z = z_1 - z_2$ and the scattering phase $\theta(k)$. Starting from the stationary solution, we construct a wavepacket with a function $A(k)$ peaked around k_0 :

$$|\phi(t)\rangle = \int dk A(k) \sin[k|z| + \theta(k)] e^{-i\frac{\hbar k^2}{m}t}. \quad (1.109)$$

The position of the particles is given within the stationary phase approximation by the condition

$$\left|z\right| + \frac{\partial\theta(k)}{\partial k} \Big|_{k_0} \pm \frac{2\hbar k_0 t}{m} = 0 \quad (1.110)$$

Eq. (1.110) describes the collision of two particles. The particle trajectory can be equivalently described by a free evolution and a jump in position by

$$\Delta z = - \frac{\partial\theta_k}{\partial k} \Big|_{k_0} = - \frac{2\hbar^2 m g}{m^2 g^2 + 4\hbar^4 k_0^2}. \quad (1.111)$$

as shown in Fig. 1.7.

1.4.4.2 The GHD equations

At each collision, the particle jumps by a distance Δz . For many collisions this jump affects the particle motion, as if the interaction slowed down the particle. This motivates the introduction, of an effective velocity.

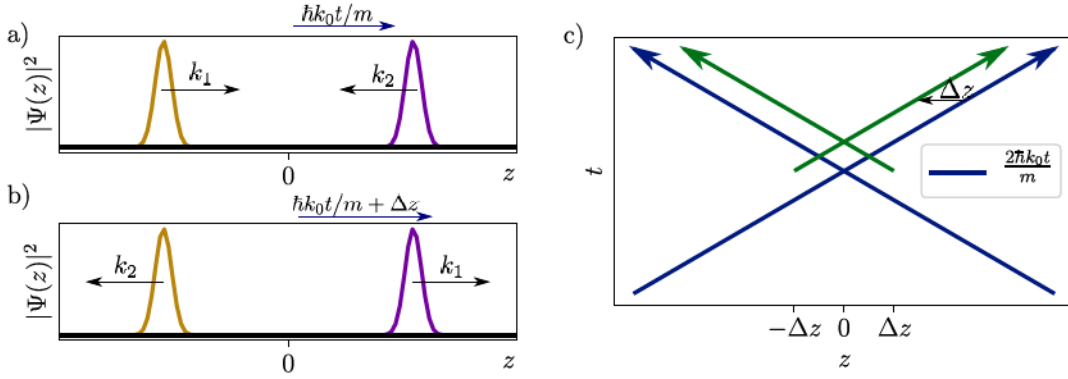


Figure 1.7 – a) Collision of two wave packets with rapidity $k_0 = k_1 - k_2$. b) After the collision the distance between the particles is shifted by Δz . c) Space-time diagram of the collision: The blue line shows the trajectory of non-interacting particles. Interacting particles are shifted backwards at the collision by Δz (green line). Note that there is no second collision happening. The discontinuity in the position is arising from the stationary phase approximation which cannot resolve distances smaller than the size of the wavepacket.

The effective velocity For many collisions between particles one introduces the effective velocity v_{eff} . It can be calculated by considering the correction to the bare velocity $\frac{\hbar k}{m}$. These corrections are given by the number of collisions and the shift in position at each collision:

$$v_{\text{eff}}(k) = \frac{\hbar k}{m} - \int dk' \underbrace{\rho_p(k') [v_{\text{eff}}(k) - v_{\text{eff}}(k')]}_{\text{Collisions per unit time}} \underbrace{\frac{2\hbar^2 mg}{m^2 g^2 + \hbar^4 (k - k')^2}}_{\text{Shift in position}}. \quad (1.112)$$

The effective velocity $v_{\text{eff}}(k)$ can thus be calculated with a similar implicit equation as already seen for the Yang-Yang equation of state (Eq. (1.38) & (1.39)). Eq. (1.112) can be rewritten in a more compact form

$$v_{\text{eff}}(z, k) = \frac{\hbar k}{m} - \int dk' \rho_p(z, k') (v_{\text{eff}}(z, k) - v_{\text{eff}}(z, k')) \Delta(k - k'), \quad (1.113)$$

with differential scattering phase $\Delta(k - k')$ introduced in Eq. (1.35). Additionally we explicitly noted the space dependence.

The authors in [15] showed that the current associated to $\rho_p(k)$ is given by $j(k) = v_{\text{eff}}(k)\rho_p(k)$. This leads to the GHD equation

$$\frac{\partial}{\partial t} \rho_p(z, k) + \frac{\partial}{\partial z} [v_{\text{eff}}(z, k)\rho_p(z, k)] = 0. \quad (1.114)$$

In a semiclassical interpretation the effective velocity v_{eff} can be seen as the velocity of the quasi-particle. Thus, Eq. (1.114) is simply the classically anticipated continuity equation. Note that although these heuristic arguments lead to a "simple" result, these results are non-trivial from the point of view of the quantum many-body problem. The full quantum problem contains additional correction terms to Eq. (1.114) which arise in the form of a diffusion between different cells and were calculated in [54].

External potential An external potential which varies slowly on the scale of a fluid cell, can be taken into account in the inhomogeneous GHD equations [55]:

$$\frac{\partial \rho_p(z, k)}{\partial t} + \frac{\partial}{\partial z} [v_{\text{eff}}(z, k) \rho_p(z, k)] = \frac{1}{\hbar} \frac{\partial V(z, t)}{\partial z} \frac{\partial \rho_p(z, k)}{\partial k}. \quad (1.115)$$

The numerical results in Chap. 5 are based on the calculation of v_{eff} in Eq. (1.113) and the GHD equation (1.115). Eq. (1.113) can be solved by numerically by iteration — similarly to the Yang-Yang equations — and (1.115) can be numerically integrated.

1.5 Losses

In ultra-cold atom systems losses are always present at various rates. Consider for example three-body losses due to three-body recombination or one-body losses by collisions with the background gas.

Losses in general cannot be described by the unitary evolution of the Schrödinger equation and a description by the density matrix $\hat{\rho}$ with the master equation is necessary

$$\frac{d}{dt} \hat{\rho} = \frac{1}{i\hbar} [H, \hat{\rho}] + \mathcal{L}[\hat{\rho}], \quad (1.116)$$

where $\mathcal{L}\{\hat{\rho}\}$ is the non-hermitian Lindblad-operator given by

$$\mathcal{L}\{\hat{\rho}\} = \int dz \left[\hat{L} \hat{\rho} \hat{L}^\dagger - \frac{1}{2} \hat{L}^\dagger \hat{L} \hat{\rho} - \frac{1}{2} \hat{\rho} \hat{L}^\dagger \hat{L} \right], \quad (1.117)$$

with the non-hermitian jump operator \hat{L} . This formalism is not restricted to losses. The Lindblad operator represents a coupling to an environment where the environment is the vacuum state in the case of losses. In Chap. 4 we treat the problem of j -body losses in more detail. j -body losses refer to a situation where the density $n = \hat{\Psi}^\dagger \hat{\Psi}$ evolves according to

$$\frac{d}{dt} \langle n \rangle = -\tilde{\kappa}_j \langle n \rangle^j g^{(j)}(0) \quad (1.118)$$

where $\tilde{\kappa}_j$ is the j -body loss rate constant and $g^{(j)}(0)$ the normalized j -body correlation function at zero distance. For j -body losses the jump operators \hat{L} takes the form

$$\hat{L} = \sqrt{\frac{\tilde{\kappa}_j}{j}} \hat{\Psi}^j(z), \quad (1.119)$$

which leads to the Lindblad operator

$$\mathcal{L}\{\hat{\rho}\} = \frac{\tilde{\kappa}_j}{j} \int dz \left[\hat{\Psi}^j(z) \hat{\rho} \hat{\Psi}^{\dagger j}(z) - \frac{1}{2} \hat{\Psi}^{\dagger j}(z) \hat{\Psi}^j(z) \hat{\rho} - \frac{1}{2} \hat{\rho} \hat{\Psi}^{\dagger j}(z) \hat{\Psi}^j(z) \right]. \quad (1.120)$$

It can be verified that this form of \hat{L} reproduces the correct time evolution of Eq. (1.118) as shown in Appendix Sec. A.4.

1.5.1 Quantum Monte-Carlo wave-function method

It can be shown that the time evolution given by the master equation Eq. (1.116) is equivalent to a stochastic description of different realizations of wavefunctions [56, 57]. The expectation values predicted by the Lindblad evolution are recovered by a sampling over many realizations. Considering the situation of losses within a short time interval dt ¹⁵. If a loss occurs within dt the initial wave-function $|\Psi(t)\rangle$ is propagated with

$$|\Psi(t+dt)\rangle = \hat{L}|\Psi(t)\rangle \quad (1.121)$$

and the probability that a loss occurs is given by

$$d\rho = \frac{\langle \Psi(t) | \hat{L}^\dagger \hat{L} | \Psi(t) \rangle}{\langle \Psi(t) | \Psi(t) \rangle} dt. \quad (1.122)$$

Note that here we choose unnormalized wavefunction which leads to the normalization in the expression of the probability.

At the same time there exists a probability $1 - d\rho$ that no loss occurs. In that case the wave function is propagated with

$$|\Psi(t+dt)\rangle = e^{-\frac{dt}{2} \hat{L}^\dagger \hat{L}} |\Psi(t)\rangle. \quad (1.123)$$

The last equation represent the fact that, even when no loss occurs, we gain information about the system. For example imagine that we observe a state with a non-zero variance in N . When we do not observe any loss for a very long period, we know that the system contains very few particles. The mean particle number is decreased by

¹⁵The time interval dt is chosen such that the probability $d\rho$ of a loss occurring within the time dt is small.

Eq. (1.123). The probability of no loss occurring can be rewritten in first order in dt as

$$1 - dp = \frac{\langle \Psi(t+dt) | \Psi(t+dt) \rangle}{\langle \Psi(t) | \Psi(t) \rangle}. \quad (1.124)$$

Eq. (1.121) - (1.123) represent the Wavefunction Quantum Monte-Carlo method, or in short Quantum Monte-Carlo (QMC). It can for example be implemented on a computer, where after each time step dt , one of the two possible evolution of the wavefunction is chosen with the corresponding probability. The repeated application of this procedure on the wave-function is called a quantum trajectory. This procedure is then repeated in order to obtain many quantum trajectories. The physical observable are obtained from averages over many trajectories.

Depending on the considered situation the QMC-method can have several advantageous over the Master equation: It allows to perform calculations for feedback on a quantum state. In Sec. 4.7 we use the QMC approach for a feedback scheme based on the atoms lost from a quasi-condensate. The stochastic approach of QMC can also lead to numerical advantage [58]. Instead of calculating the time evolution of a matrix with $N \times N$ entries, one calculates the time evolution of vectors with size N .

Summary:

- The Bethe-Ansatz is a powerful tool which solves the Lieb-Liniger model.
- Based on the Bethe-Ansatz an exact thermodynamics can be derived – the Yang-Yang thermodynamics. It allows to identify three equilibrium regimes of the Lieb-Linger model: the quasi-condensate, the ideal Bose gas and the Tonks regime.
- Inside the quasi-condensate regime the Bogoliubov approach in density-phase representation leads to a collection of uncoupled harmonic oscillators:

$$H_q = A_q n_q^2 + B_q \theta_q^2.$$

- The Generalized HydroDynamics (GHD) is a powerful new tool to describe the out-of-equilibrium dynamics based on the Bethe-Ansatz.

Chapter 2

The atomchip experiment

The atomchip experiment uses standard laser cooling and laser trapping techniques. In a first stage it creates a cold cloud of ^{87}Rb atoms which is magnetically trapped by micro-wires deposited on the atomchip. For a more detailed description about the experimental techniques I refer the reader to [36, 42, 59]. The working principles of these creation stages were not modified during my PhD and rather standard techniques for the cold atom community are used. The techniques which are particular to the experiment, as the modulated guide (Sec 2.3.1.2), or the double-well potential in the longitudinal direction (Sec 2.3.2.2), will be described in more details.

2.1 The experimental setup

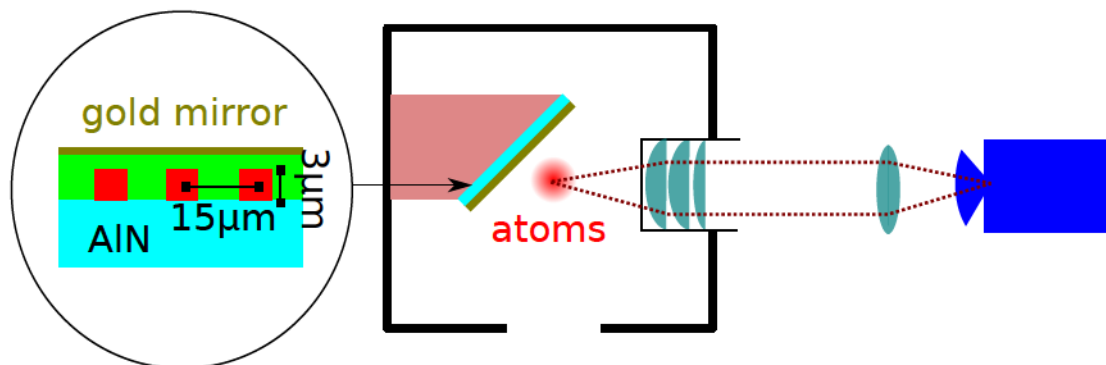


Figure 2.1 – Experimental setup with a zoom on its structure.

The experiment is built around its central piece, the atomchip inside a vacuum chamber at $\approx 10^{-11}$ mBar. The atomchip is produced by means of nanofabrication

techniques¹ and it consists of a principle layer of Aluminium-Nitride (AlN) which serves as an isolating layer and shows at the same time good heat-conducting properties [60]. The copper wires are deposited on the AlN substrate and covered by an insulating layer of benzocyclobutene (BCB). BCB is chosen for its properties to create flat surfaces after spin-coating. On top of this structure, there is a thin layer of gold, acting as a mirror for the MOT and the imaging system. The chip is mounted at an angle of 45° inside the vacuum chamber as shown in Fig. 2.1. Three pairs of Helmholtz coils outside of the vacuum chamber create homogeneous fields in the three spatial direction and one pair of anti-Helmholtz coils creates the magnetic quadrupole for the *external MOT* (see 2.2).

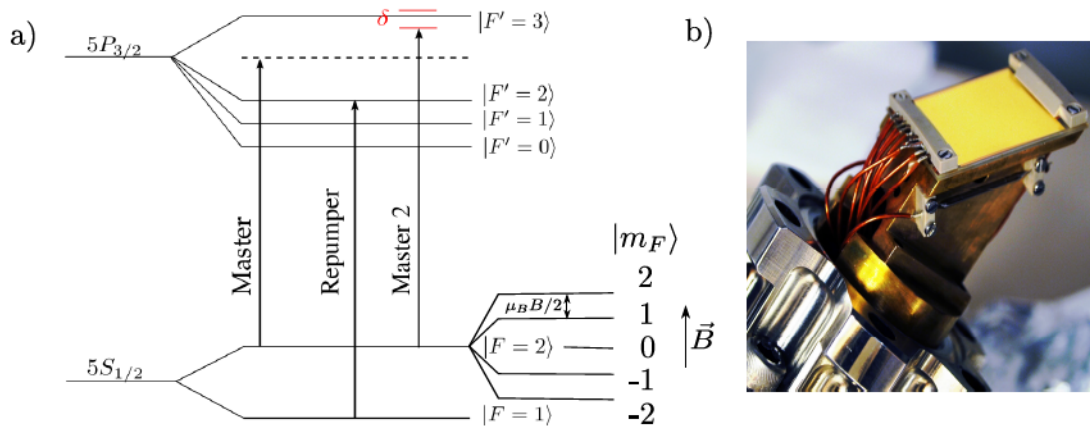


Figure 2.2 – a) Level structure of ^{87}Rb , with the different lasers used in the experiment. The atoms are magnetically trapped in the $|^5S_{1/2}, F=2, m_F=2\rangle$. The master laser is locked on the level crossing between $|F'=2\rangle$ and $|F'=3\rangle$ which serves as a frequency reference for the experiment. The Master 2 laser serves as the primary laser of the experiment; used for the MOT, molasses, optical pumping and imaging. Its frequency is locked using a beat-note with the Master laser, allowing to sweep its frequency of about 300 MHz. Adapted from [59].

b) Photo of the atomchip mounted on its copper mount.

2.2 Preparation scheme

The preparation scheme can be summarized by the following steps:

¹The production is led by Sophie Bouchoule at the Laboratoire Photonique et Nanostructures (LPN), CNRS / UPSUD in Marcoussis, now renamed in Centre de Nanosciences et Nanotechnologies (C2N).

1. **External MOT:** A mirror Magneto-Optical Trap (MOT) is created with the two beams reflecting on the chip surface. The magnetic quadrupole fields are provided by external coils outside the vacuum chamber. The use of the mirror MOT configuration reduces the number of beams to four (instead of six) and allows to create a MOT close (a few mm) to the chip surface.
2. **Chip MOT:** The atoms are loaded into a mirror MOT, whose magnetic quadrupole field is created by wires on the chip and the distance to the chip is reduced to 500 - 800 μm .
3. **Compressed MOT:** The compressed MOT is used to produce an elongated configuration closer to the chip surface; more adapted for the following very elongated trapping structures.
4. **Optical Molasses:** Optical Molasses are used to further cool and increase phase-space density.
5. **Optical Pumping:** As a preparation of magnetic trapping the atoms are optical pumped into the state $|^5S_{1/2}, F = 2, m_F = 2\rangle$ (see Figure 2.2).
6. **DC trap:** The atoms are transferred into an elongated magnetic trap created by a Z-shaped wire. This trap is initially at 500 μm distance from the chip surface and is then further compressed.
7. **Evaporative cooling:** Forced radio-frequency (RF) evaporative cooling is carried out to obtain about 2×10^5 atoms at $T \sim 1 \mu\text{K}$.
8. **Transfer to the science trap:** To obtain high magnetic gradients and therefore high trapping frequencies, the atoms are transferred into a position 6 μm from the chip surface on top of the three-wire guide which creates the final science trap. In comparison to previous chip designs, this transfer can be performed much easier due to the symmetric design of the chip: The new chip design places the center of the DC-trap and the science trap at the same longitudinal position, making the previously used longitudinal transfer obsolete. Catching schemes as mentioned in [59] turned out to be unnecessary.
9. **Science trap / Modulated guide:** The final trap consist of a very elongated trap geometry, whose principles are detailed in the following Sec. 2.3. We use a magnetic trap created by a fast modulated current where the atoms are sensitive to the time-average potential. Amongst other advantages, the modulation technique allows to circumvent the problem of potential roughness [61]. In the science trap, we initially trap about 8×10^4 atoms at $f_{\perp} \approx 1.5 - 15 \text{ kHz}$ and $f_{\parallel} = 8 \text{ Hz}$. Besides the harmonic longitudinal traps, quartic and double well potential can be realized (see Sec. 2.3.2.2).

10. **RF-cooling in the science trap:** In the science trap a RF-outcoupling is used to further cool down the gas into the 1D regime where we typically prepare some hundreds to a few ten thousand atoms inside the quasi-condensate regime. The cooling mechanism used in the science trap is discussed in more detail in Chap. 4.

2.3 Magnetic trapping

Neutral atoms with a magnetic moment $\vec{\mu}$ experience an energy shift in a magnetic field $\vec{B}(\mathbf{x})$ according to the Zeeman Hamiltonian

$$H_Z = -\vec{\mu} \cdot \vec{B} = \mu_B g_F \vec{F} \cdot \vec{B}, \quad (2.1)$$

with the Bohr magneton μ_B and g_F the Landé g-factor of the atomic hyperfine state. In the experiment we use the hyperfine state $F = 2$ where the Landé factor takes the value $g_F = 1/2$. The Zeeman effect can be used to create spatially varying potential $V(\mathbf{x})$, under the condition that the direction of the magnetic field changes much slower than the Larmor precession $|\mathrm{d}\vec{B}/\mathrm{d}t|/|\vec{B}| \ll \omega_L$, with $\omega_L = \mu_B B/\hbar^2$ [28]. Then m_F , the magnetic quantum number, is a constant of motion and the atom moves in the potential

$$V(\mathbf{x}) = g_F \mu_B m_F |B(\mathbf{x})|. \quad (2.2)$$

Depending on the sign of $g_F m_F$ ($-/+$) atoms get attracted towards the maximum/minimum of the magnetic field and are called *high field seekers/low field seekers* [63]. According to Maxwell's equation a magnetic field maximum in free space is forbidden in a static situation [64]. Therefore only low field seekers are of practical interest and we use the state $|F = 2; m_F = 2\rangle$ in this experiment.

2.3.1 Wire geometries for trapping neutral atoms

This section introduces different trapping geometries which are used on the experiment. Starting from the single wire, more complicated geometries are introduced.

2.3.1.1 Potential by a single wire

Let us consider a single, infinitely long, wire which carries the static current I . According to the Biot-Savart law, this wire creates a magnetic field $\vec{B}_\phi(r)$ as shown in Fig. 2.3

$$\vec{B}_\phi(r) = \frac{\mu_0 I}{2\pi r} \vec{e}_\phi, \quad (2.3)$$

²This adiabaticity condition can be typically critical at the bottom of the trap which induces losses, known as Majorana losses [62, 63].

with the magnetic vacuum permeability μ_0 , the radial distance to the wire r and \vec{e}_ϕ the unit vector in cylindrical coordinates. The single wire creates a $1/r$ potential in

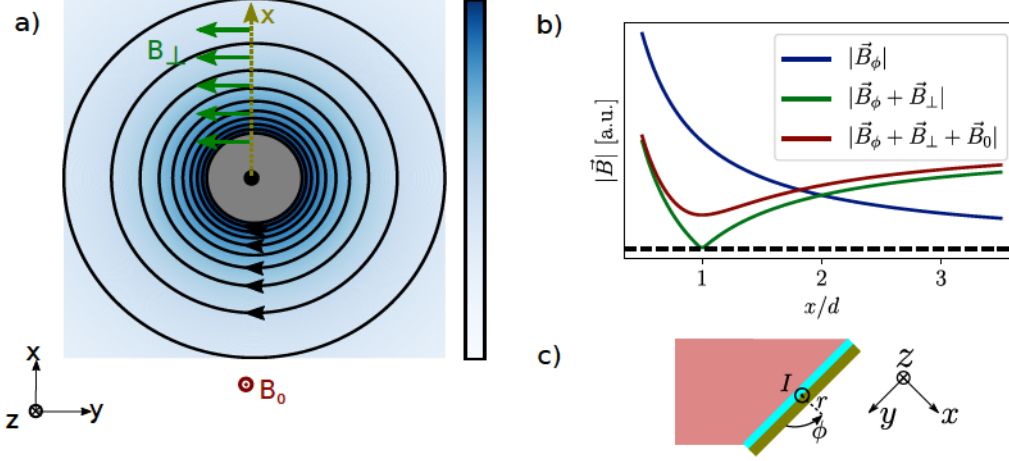


Figure 2.3 – Single wire configuration:

a) Cut through the wire plane with magnetic fields. b) Norm of the magnetic field along the x -axes. In blue magnetic field of the wire, in green with additional magnetic field B_\perp creating a potential minimum and in red together with magnetic field B_0 to lift the magnetic field and avoid a zero of the magnetic field. c) Orientation of the wire on the chip

the radial direction which does not allow a trapping potential on its own. An additional perpendicular magnetic field \vec{B}_\perp needs to be added in order to create a magnetic minimum (see Figure 2.3): There exists a point on the x -axis where \vec{B}_\perp cancels out the field created by the wire $\vec{B}_\phi(r)$. The total magnetic field $|\vec{B}_\perp + \vec{B}_\phi|$ obtains a minimum at the distance $d = \mu_0 I / (2\pi B_\perp)$ and the potential in the x -direction is given by

$$V(y=0) = \mu_B \sqrt{B_\perp^2 \left(\frac{d}{x} - 1 \right)^2}, \quad (2.4)$$

where $m_F g_F$ is dropped, since $m_F g_F = 1$ in the experimental implementation. However, since the magnetic field at the magnetic minimum at distance d is zero the adiabaticity condition cannot be fulfilled; the Larmor frequency $\omega_L = \mu_B B / \hbar$ becomes strictly zero. To avoid this problem an additional magnetic field \vec{B}_0 along the wire direction z is added. Then, the potential of a single wire, together with the two homogeneous magnetic fields³ create a useful trapping potential (see Figure 2.3 b)). The dominant field around the trapping minimum will always be given by B_0 , since at the

³The homogeneous magnetic fields \vec{B}_\perp and B_0 can be created by external coils in Helmholtz configuration. The creation of \vec{B}_\perp by wires on the chip is considered in the following section.

magnetic field minimum B_{\perp} cancels out the magnetic field of the wire \vec{B}_{ϕ} . We expand the magnetic fields in the potential in terms of $1/B_0$ around its minimum which leads to:

$$V = \mu_B \sqrt{B_x^2 + B_y^2 + B_0^2} \simeq \mu_B B_0 \left[1 + \frac{1}{2} \left(\frac{B_x}{B_0} \right)^2 + \frac{1}{2} \left(\frac{B_y}{B_0} \right)^2 \right], \quad (2.5)$$

where B_x, B_y are the x and y contributions of $\vec{B}_{\phi} + \vec{B}_{\perp}$. B_x and B_y can be expanded in terms of x/d and y/d from which we obtain the trapping frequency⁴ ω_{\perp}

$$\omega_{\perp} = \sqrt{\frac{\mu_B}{mB_0} \frac{\mu_0 I}{2\pi d^2}} = 2\pi \sqrt{\frac{\mu_B}{mB_0} \frac{B_{\perp}}{\mu_0 I}}. \quad (2.6)$$

The single wire configuration provides a trapping potential in two direction (x, y). A simple way to add a trapping potential in the remaining z -direction, can be obtained by bending the wire in "Z"-shape. This allows for trapping in 3D and slightly tilts the trap (for more details see [65]). The "Z"-shaped wire configuration is used in the atomchip for the first magnetic trap where we perform evaporative cooling. This trap is named DC-trap (see Sec. 2.2) and we typically use a current of $I = 3$ A, together with $B_{\perp} = 38$ G and a bias field $B_0 = 1.2$ G.

2.3.1.2 Three wire geometry and modulated guide

Three wire configuration The experiment uses in the perpendicular direction a three-wire configuration as the final science trapping potential⁵. First, consider a single wire as previously introduced with current I . In the three-wire geometry, the perpendicular magnetic field \vec{B}_{\perp} , previously created by the external coils, is now created by two parallel wires containing the same current in opposite direction (see Figure 2.4). The position of the potential minimum is located at the same distance d from the central wire. This renders the trap center insensitive to current fluctuations⁶. The trapping frequency is the same as in the single wire situation and given by

$$f_{\perp} = \frac{1}{2\pi} \sqrt{\frac{\mu_B}{mB_0} \frac{\mu_0 I}{2\pi d^2}}. \quad (2.7)$$

In order to obtain high transverse trapping frequencies, either high currents I or small distances d towards the wires, are necessary ($f_{\perp} \propto I/d^2$). The maximal current is fixed by the ohmic heat which the atomchip structure can absorb, leading to a technological barrier. When getting closer to the chip surface new physical problems arise. Close to the current carrying wires the effect of inhomogeneities in the

⁴Due to $\nabla \vec{B} = 0$ the trapping frequency in x and y -direction are the same for constant B_z .

⁵see Sec. 2.3.2 for the longitudinal confinement.

⁶Exactly the same current is flowing through the same wires due to inter-connections of the wires in loops.

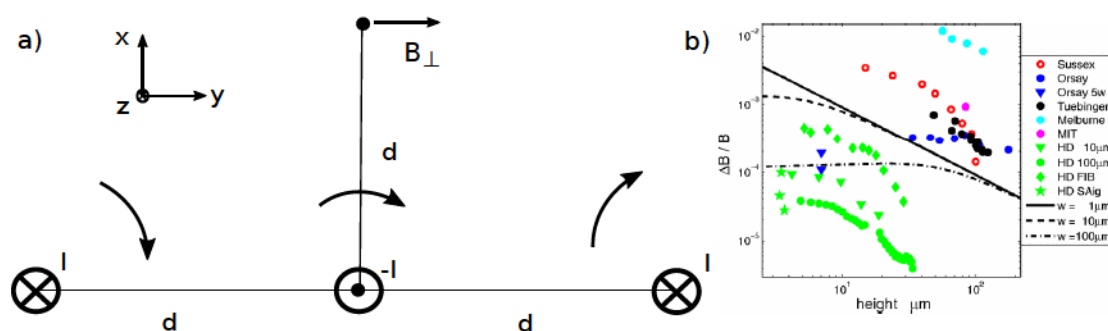


Figure 2.4 – a) The three wire configuration where \vec{B}_\perp is created by the two outer wires with currents in the opposite direction. b) Comparison of wire roughness of different chip designs. Note that although our chip, denoted "Orsay-Chip", does not show the best performance in terms of production quality, the problem of wire roughness does not effect our experiment, due to the modulated guide technique.

wires can become very important. Due to imperfections during the wire growing process, the wire cannot simply be described by perfect cuboids, with parallel planes (see Fig. 2.5). The current inside the wire locally starts to point away from the z -direction. This leads to a roughness of the potential induced by the current. In worst case this leads to a fragmentation of the condensate [66–68]. Two types of production defects were observed: wire edge imperfections and top surface imperfections. Both

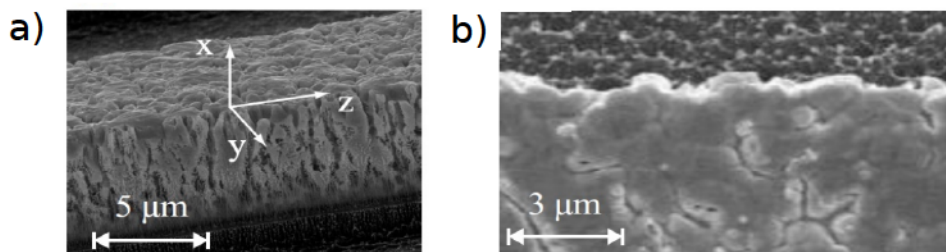


Figure 2.5 – a) Wire inhomogeneity with a zoom b). Taken from [69].

show an unfavorable scaling as $r^{-5/2}$ with the distance towards the wire r [67]. There exists two main directions to avoid this problem: Many groups focus on the quality of the production process which can be improved in order to reduce the imperfection of the wires [70] (see Fig. 2.4 b)). In our group we choose a different approach. It was observed that a reversed current creates a reversed potential [66] and as already pointed out in [66] a fast modulated current might overcome the potential roughness. Since 2007, our experiment uses this technique of a modulated guide to overcome the problem of wire roughness [61, 71]. Until today no potential roughness arising from wire defects was observed. The current implementation consists of the three-wire

geometry, as introduced above, and instead of a direct current (DC), an alternating current (AC) is used, modulated at a frequency $\omega_{\text{mod}}/(2\pi) = 400 \text{ kHz}$

$$I(t) = I_0 \cos(\omega_{\text{mod}} t). \quad (2.8)$$

The atoms cannot follow this fast current modulation and are sensitive to the time averaged potential

$$\langle V(\mathbf{r}, t) \rangle = \frac{1}{T} \int_0^T V(\mathbf{r}, t') dt'. \quad (2.9)$$

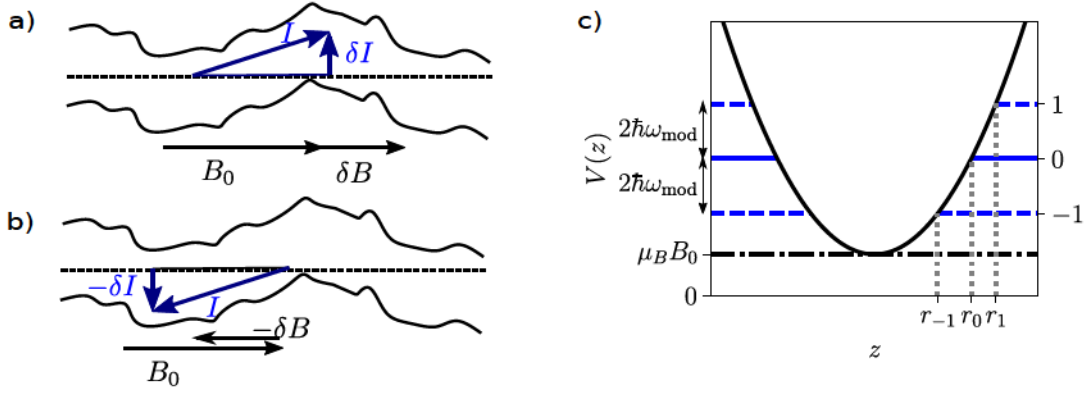


Figure 2.6 – a) Schematic representation of the effect of the wire roughness on the current deviation δI and the magnetic field δB for a current flowing to the right. b) The same current flowing to the left produces the opposite current deviation $-\delta I$ and consequently the opposite magnetic field distortion $-\delta B$. c) RF-evaporative cooling in the modulated guide with the principles knife of order 0 and the side bands of order ± 1 .

In the following I will calculate the time averaged potential $\langle V(\mathbf{r}, t) \rangle$ as in Eq. (2.5) where an inhomogeneity as depicted in Fig. 2.6 a) & b) is taken into account. The inhomogeneity creates a magnetic field distortion in the z -direction δB_z . Going back to Eq. (2.5) the potential writes

$$V(\mathbf{r}) = \mu_B \sqrt{(B_0 + \delta B_z)^2 + B_x^2 + B_y^2}. \quad (2.10)$$

Expanding this equation in quadratic order in B_i , leads to

$$V(\mathbf{r}, t) \simeq \mu_B B_0 \left[1 + \frac{\delta B_z}{B_0} + \frac{1}{2} \left(\frac{B_x}{B_0} \right)^2 + \frac{1}{2} \left(\frac{B_y}{B_0} \right)^2 \right]. \quad (2.11)$$

When modulating the current $I(t) = I_0 \cos(\omega_{\text{mod}} t)$, the term $\langle \delta B_z / B_0 \rangle$ averages out over a full period and the time averaged potential writes

$$\langle V(\mathbf{r}, t) \rangle = \mu_B B_0 \left[1 + \frac{1}{2} \frac{\langle B_x^2 \rangle}{B_0^2} + \frac{1}{2} \frac{\langle B_y^2 \rangle}{B_0^2} \right]. \quad (2.12)$$

With the use of $\langle B_{x/y}^2 \rangle = B_{x/y}^2/2$ where here $B_{x/y}$ stands for the static case, one recovers the expression in the static case of Eq. (2.5), differing by a factor $\frac{1}{\sqrt{2}}$. This leads to the trapping frequency f_{\perp}^{AC} in the modulated guide

$$f_{\perp}^{\text{AC}} = \frac{1}{\sqrt{2}} f_{\perp}. \quad (2.13)$$

Radio-frequency evaporative cooling inside the modulated guide In the DC trap, RF forced evaporative cooling is performed by spin flips to an untrapped state ($m_F = 0$). Consider a radio frequency (RF) field together with the previously introduced modulated guide. The resonance condition then depends on space and leads to spin-flips on the border of the trap. RF-induced spin flips in the modulated guide can be seen as a RF-field which is frequency modulated at $2\omega_{\text{mod}}$. This introduces side bands in the spectrum at $2\omega_{\text{mod}}$ [72]. The resonance condition writes

$$\hbar\omega_{\text{RF}} = \mu_B B_0 + \frac{\mu_B b'^2 r_n^2}{4B_0} - 2n\hbar\omega_{\text{mod}}, \quad (2.14)$$

with b' being the quadrupole gradient and r_n the position where the n -th sideband is resonant (see Fig. 2.6 c). Experimentally one is interested in working with a single RF-knife, for which we choose the order $n = 0$. This means that evaporative cooling inside the modulated guide is only possible inside a window of $\Delta V = 2\hbar\omega_{\text{mod}} = k_B 38 \mu\text{K}$. Therefore, the cloud has to be precooled in the DC trap, before it can be loaded into the modulated guide. This window has been increased at the beginning of my PhD by changing the modulation frequency from $\omega_{\text{mod}}/(2\pi) = 200 \text{ kHz}$ to $\omega_{\text{mod}}/(2\pi) = 400 \text{ kHz}$.

Stability of the trap In principle, one could be worried that the increase in ω_{mod} affects the stability of the trap. The modulated trap is stable under the condition that ω_{mod} is much greater than the transverse trapping frequency ω_{\perp} which is easily fulfilled. On the other hand, it must be much slower than the Larmor frequency ω_L ; assuring that adiabaticity condition, such that the atomic spin can follow the instantaneous magnetic field orientation:

$$\omega_{\perp} \ll \omega_{\text{mod}} \ll \omega_L. \quad (2.15)$$

In [72] a detailed study showed that at the new modulation frequency 400 kHz losses are still negligible.

2.3.2 Longitudinal trapping

The modulated guide only creates a transverse confinement and an additional confinement in the longitudinal direction is needed. As justified in the following, the

longitudinal potential is independent of the transverse confinement and the total confinement is given by the sum of the longitudinal and transverse confinement. For the longitudinal confinement we use wires perpendicular to the ones for the transverse confinement (see Fig. 2.7). These perpendicular wires are far from the atoms and we can develop the longitudinal potential in powers of z around its minimum

$$V(z) = \sum_{i=1} a_i z^i. \quad (2.16)$$

Close to the potential minimum where the atoms are located, higher orders lead in principle to smaller corrections. Each wire allows to control one current I_i . This directly fixes the maximal order in the powers series $V(z) = \sum_{i=1} a_i z^i$ which can be independently controlled. In the current chip design four wires for the longitudinal trapping geometry are implemented which we name D_1 , D_2 , δ_1 and δ_2 (see Appendix Fig. A.2). Those wires allow the creation of potentials up to order four (see Fig. 2.8).

To justify the decoupling between the longitudinal and transverse confinement let us calculate the full potential arising from the magnetic fields of modulated guide (three wire geometry) and the magnetic fields from the four wires for the longitudinal trapping. The modulated guide contributes with magnetic fields oscillating with $B_i^{\text{AC}} \cos(\omega_{\text{mod}} t)$ in x and y direction. The DC currents in the longitudinal wires lead to static magnetic fields B_z and B_x . In analogy to eq. (2.11) we expand the full potential up to second order in B_i/B_z^{tot} where $i = x, y$ and $B_z^{\text{tot}} = B_0 + B_z$:

$$V = \mu_B B_z^{\text{tot}} \left[1 + \frac{1}{2} \left(\frac{B_x + B_x^{\text{AC}} \cos(\omega_{\text{mod}} t)}{B_z^{\text{tot}}} \right)^2 + \frac{1}{2} \left(\frac{B_y^{\text{AC}} \cos(\omega_{\text{mod}} t)}{B_z^{\text{tot}}} \right)^2 \right]. \quad (2.17)$$

Taking the time average $\langle \dots \rangle$ over the fast modulation of the modulated guide, one obtains

$$\langle V \rangle = \mu_B B_z^{\text{tot}} \left[1 + \underbrace{\frac{1}{2} \frac{B_x^2}{(B_z^{\text{tot}})^2}}_{\text{longitudinal confinement } V_{\parallel}} + \underbrace{\frac{1}{4} \frac{\langle (B_x^{\text{AC}})^2 \rangle}{(B_z^{\text{tot}})^2} + \frac{1}{4} \frac{\langle (B_y^{\text{AC}})^2 \rangle}{(B_z^{\text{tot}})^2}}_{\text{transverse confinement } V_{\perp}} \right]. \quad (2.18)$$

The second part on the rhs., named transverse confinement V_{\perp} , corresponds to the expression already found for the transverse confinement in Eq. (2.12) where B_0 is replaced by B_z^{tot} . In most situations B_0 strongly dominates over B_z , where B_z is the contribution from the longitudinal DC wires, and we exactly recover Eq. (2.13). The small corrections arising from B_z and leading to $f_{\perp} \propto I/\sqrt{B_0 + B_z}$ are typically smaller than 1%, except for the quartic and double well potential which are discussed in Sec 5.1.3. When these corrections can be neglected, the transverse and the longitudinal confinement are independent and given by the sum of V_{\parallel} and V_{\perp} . The longitudinal confinement V_{\parallel} only varies with respect to z and the transverse confinement V_{\perp} with

respect to x and y . Note that the situation differs from the DC trapping schemes where the longitudinal and the transverse confinement are not independent of each other [42]. We make frequently use of this decoupling property in the modulated guide to control both parts independently and many parts, such as the interaction quench (Sec. 3.2) and GHD experiment (Chap. 5), heavily rely on his property.

Let us now calculate the longitudinal confinement V_{\parallel} which writes⁷ according to Eq. (2.18) in second order in B_i/B_0

$$V_{\parallel} = \mu_B B_0 \left[1 + \frac{B_z}{B_0} + \frac{1}{2} \left(\frac{B_x}{B_0} \right)^2 \right]. \quad (2.19)$$

We calculate V_{\parallel} starting from a single wire at distance $b = L/2 \simeq 0.945$ mm from the trap center (see Fig. 2.7). The single wire creates a magnetic field

$$B_x = \frac{\mu_0 I}{2\pi b^2} \frac{b+z}{1+2\frac{z}{b}+(\frac{z}{b})^2+(\frac{d}{b})^2} \simeq \frac{\mu_0 I}{2\pi b} \left[1 - \frac{z}{b} + \left(\frac{z}{b}\right)^2 - \left(\frac{z}{b}\right)^3 \right] \quad (2.20)$$

$$B_z = \frac{\mu_0 I}{2\pi} \frac{d}{b^2} \frac{1}{1+2\frac{z}{b}+(\frac{z}{b})^2+(\frac{d}{b})^2} \simeq \frac{\mu_0 I}{2\pi} \frac{d}{b^2} \left[1 - 2\frac{z}{b} + 3\left(\frac{z}{b}\right)^2 - 4\left(\frac{z}{b}\right)^3 + 5\left(\frac{z}{b}\right)^4 \right], \quad (2.21)$$

up to order $(z/b)^4$ in V_{\parallel} . Small correction of order $(d/b)^2 \approx 10^{-4}$ for $d = 15 \mu\text{m}$ are neglected.

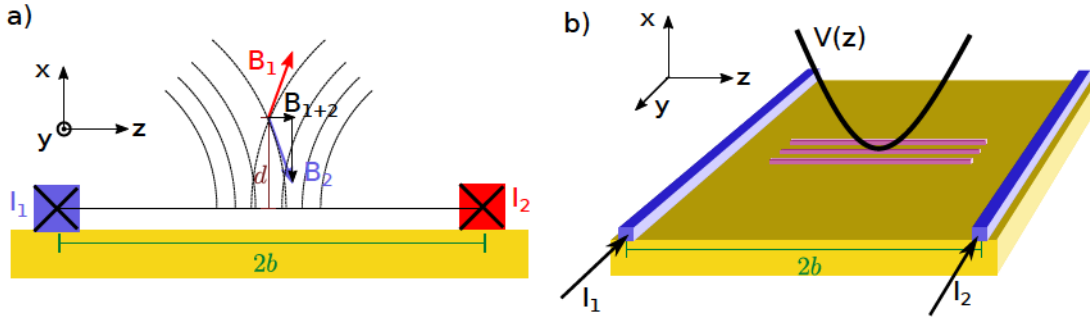


Figure 2.7 – a) Current configuration for the harmonic potential with both currents flowing in the same direction. The magnetic fields B_x from both wires cancel in the center at the potential minimum, while B_z adds up. b) View on the chip with the modulated guide in red and the wires responsible for the longitudinal confinement in purple.

⁷In the following the notation $\langle \dots \rangle$ for the time average is dropped.

2.3.2.1 Harmonic trapping potential

A harmonic trapping potential can be created by the use of two wires for which we use the two wires named D_1 and D_2 on the chip design (see Appendix Fig. A.2). For simplicity we assume a completely symmetric chip and the same currents $I_1 = I_2 = I$ in the wires D_1 & D_2 . Due to the symmetry of the problem, the magnetic field of the second wire can be obtained with Eq. (2.20) and $B_x \rightarrow -B_x$ with $z \rightarrow -z$. This leads to a total magnetic field of the wires in z -direction which only contains odd terms:

$$B_x = \frac{\mu_0 I}{2\pi b} \left[-2\frac{z}{b} - 2\left(\frac{z}{b}\right)^3 \right]. \quad (2.22)$$

For B_z the symmetry of the problem imposes $B_z \rightarrow B_z$ (and $z \rightarrow -z$), leaving only even terms in the expansion

$$B_z = \frac{\mu_0 I}{2\pi b} \frac{d}{b} \left[2 + 6\left(\frac{z}{b}\right)^2 + 10\left(\frac{z}{b}\right)^4 \right] \quad (2.23)$$

This leads to a two-wire potential

$$V_{\parallel} = \mu_B B_0 + \frac{\mu_B \mu_0 I}{2\pi b} \left[\underbrace{\frac{2d}{b} \left[1 + 3\left(\frac{z}{b}\right)^2 + 5\left(\frac{z}{b}\right)^4 \right]}_{\text{Contribution of } B_z} + \underbrace{\frac{\mu_0 I}{\pi b B_0} \left[\left(\frac{z}{b}\right)^2 + 2\left(\frac{z}{b}\right)^4 \right]}_{\text{Con. of } B_x} \right]. \quad (2.24)$$

In Eq. 2.24 two contributions can be identified: Arising from B_z a uniform term, a term in z^2 and a term in z^4 is created, while the potential arising from B_x does not contain any uniform contribution. Comparing the two contributions for our chip layout, one obtains that the B_x -contribution is dominant over the B_z -contribution ($2d \ll \mu_0 I / (\pi B_0)$). This is equivalent to the magnetic field created by the longitudinal trapping wires at the distance d is small compared to B_0 ($B_0 \ll \mu_0 I / (2\pi d)$) which holds for the typical values of $I = 1\text{A}$ and $d = 15\mu\text{m}$. The harmonic trapping frequency ω_{\parallel} within this approximation is then given by

$$\omega_{\parallel} = \sqrt{\frac{\mu_B \mu_0^2 I^2}{\pi^2 b^4 B_0 m}}. \quad (2.25)$$

This leads for the typical experimental parameters to a shallow confinement of $\omega_{\parallel} / (2\pi) = 0 - 150\text{Hz}$.

As discussed before, the term B_z introduces corrections to the transverse confinement $f_{\perp} \propto I / \sqrt{B_0 + B_z}$. The strongest contribution to B_z arises from the uniform term

$$B_z^{\text{uniform}} = \frac{\mu_0 I d}{\pi b^2}. \quad (2.26)$$

For the harmonic traps which are used in Chap. 3 & 4, the term B_z^{uniform} never exceeds 1% of B_0 which makes this effect negligible. Corrections which are non-uniform in z are even smaller. Depending on the direction of \vec{I}_1 & \vec{I}_2 with respect to \vec{B}_0 , this correction leads to a slightly increased or decreased transverse trapping frequency f_{\perp} . Note that additionally small corrections arise from higher terms in the $1/B_0$ expansion. Beyond second order in $1/B_0$ the decoupling between the longitudinal and the transverse direction is not valid anymore.

In this section we always assumed $I_1 = I_2$. In practice the wires on the chip are not completely symmetric which displaces the trap center and leads to z^3 terms. In practice we therefore chose slightly different values for I_1 and I_2 ($I_1 \approx I_2$). By controlling I_1 and I_2 independently, we can displace the center of the trap or correct for potential z^3 terms. Although, for detailed calculations the difference in I_1 and I_2 is important, the model with $I_1 = I_2$ still gives a good intuition of the creation of harmonic potentials.

Prior to my PhD the experimental potentials could be calculated numerically by taking into account the finite size of the wires and the full wire geometry⁸ [42]. Since the beginning of my PhD the calculated potentials did not match the experimental observations (center of the trap and ω_{\parallel}). An agreement with the calculations has been obtained by artificially adding an uniform⁹ magnetic field $B_x = 180$ mG. The origin of this hypothetical magnetic field is unclear and several reasons are under consideration: The unintended use of a magnetic piece inside the magnetic shielding or a leaky current.

2.3.2.2 Double well potential

To create a potential controlled up to order four we use a second pair of parallel wires carrying the current ι (see inner wires in Fig. 2.8 which correspond to the wire δ_1 & δ_2 in Fig. A.2). In contrast to the decoupling between the transverse confinement and the longitudinal confinement, the second pair of wires does not simply add a potential, due to the quadratic B_x^2 contribution of Eq. (2.17). The total potential is calculated using the same symmetry arguments used for Eq. (2.22) & (2.23) and ap-

⁸See Figure A.2: the wires are not simply given by straight lines and bend further in the current supply lines on the chip

⁹Adding a gradient ΔB_x did not significantly increase the model quality

proximating B_z^{tot} with B_0 which leads to

$$V_{\parallel} = \mu_B B_0 + \frac{\mu_B \mu_0}{2\pi} \left\{ \underbrace{2d \left(\frac{I}{b^2} + \frac{\iota}{\beta^2} \right) + 6d \left(\frac{I}{b^4} + \frac{\iota}{\beta^4} \right) z^2 + 10d \left(\frac{I}{b^6} + \frac{\iota}{\beta^6} \right) z^4}_{\text{Contribution of } B_z} + \underbrace{\frac{\mu_0}{B_0 \pi} \left[\left(\frac{I}{b^2} + \frac{\iota}{\beta^2} \right)^2 z^2 + 2 \left(\frac{I}{b^2} + \frac{\iota}{\beta^2} \right) \left(\frac{I}{b^4} + \frac{\iota}{\beta^4} \right) z^4 \right]}_{\text{Contribution of } B_x} \right\}. \quad (2.27)$$

In order to create a double well potential, an anti-confining term in z^2 and a confin-

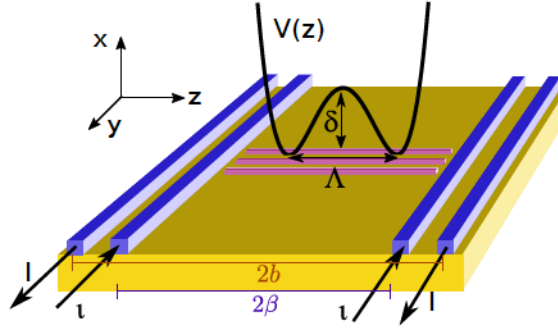


Figure 2.8 – Top view on the chip with a second pair of wires together (compare with Fig. 2.7) and a sketch of the double well potential $V(z)$ with well separation Λ a barrier height δ . The four green wires with the currents I and ι in opposite direction create the longitudinal confinement, while the transverse confinement is created by the three wires in red.

ing term in z^4 is needed. Concerning the z^2 part, the B_x contribution which strictly creates a confining z^2 potential, needs to be compensated by the B_z contribution. With $V(z) = a_2 z^2 + a_4 z^4$ we get

$$a_4 = \frac{\mu_B \mu_0}{2\pi} \left[10d \left(\frac{I}{b^6} + \frac{\iota}{\beta^6} \right) + \frac{2\mu_0}{B_0 \pi} \left(\frac{I}{b^2} + \frac{\iota}{\beta^2} \right) \left(\frac{I}{b^4} + \frac{\iota}{\beta^4} \right) \right] > 0 \quad (2.28)$$

$$a_2 = \frac{\mu_B \mu_0}{2\pi} \left[6d \left(\frac{I}{b^4} + \frac{\iota}{\beta^4} \right) + \frac{\mu_0}{B_0 \pi} \left(\frac{I}{b^2} + \frac{\iota}{\beta^2} \right)^2 \right] < 0. \quad (2.29)$$

Let us consider $I > 0$. Then $a_2(\iota)$ is a polynomial of order two with $a_2(\iota) \xrightarrow{\iota \rightarrow \pm\infty} +\infty$ and for $b > \beta$, there is always a negative part $a_2 < 0$ which occurs for $\iota < 0$ (see Fig. 2.9 a)). Therefore the currents for a double-well potential are chosen in opposite direction (see Fig. 2.8). For more details see Appendix A.3. For the experimental relevant

parameters $B_0 = 2.4\text{ G}$, $I = 5\text{ A}$, $d = 15\text{ }\mu\text{m}$, $b = 0.945\text{ }\mu\text{m}$ and $\beta = 0.722\text{ }\mu\text{m}$ the negative zone, is quite small. Additionally, a_4 needs to be positive (see Fig. 2.9 b)). Both conditions restrict the zone into a small interval $\iota = [-3.18\text{ A}; 2.98\text{ A}]$. Note however that in practice $a_4 < 0$ does not imply that the potential becomes anti-confining. For larger distances higher terms (a_6, \dots) will always ensure that the potential stays confining at larger distances. Again for a precise calculation the effects due to the finite

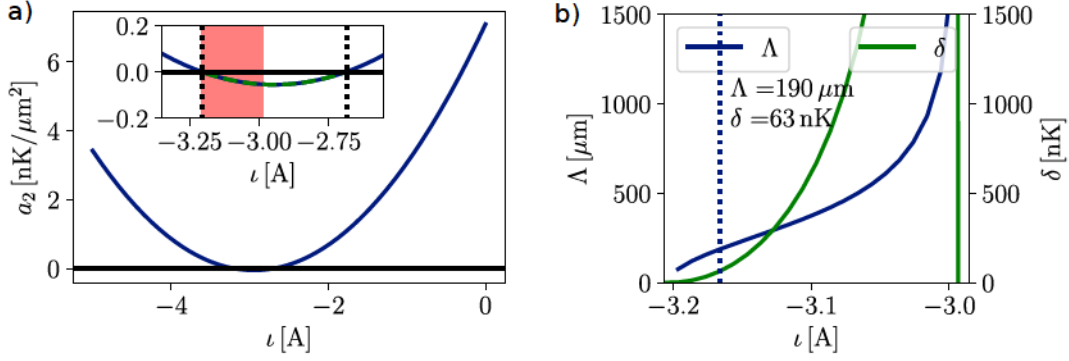


Figure 2.9 – a) The quadratic coefficient of the potential expansion a_2 as a function of ι for the experimentally relevant parameters $B_0 = 2.4\text{ G}$, $I = 5\text{ A}$, $d = 15\text{ }\mu\text{m}$, $b = 0.945\text{ }\mu\text{m}$ and $\beta = 0.722\text{ }\mu\text{m}$ with a zoom around the negative area. The red shaded area corresponds to the area where a double well potential is created with $a_4 > 0$. Note that the region for a double well potential is rather small. b) The width Λ and the depth δ of the double well potential (see Fig. 2.8) as a function of ι . The dashed line corresponds to a typical experimental realization, with $\Lambda = 200\text{ }\mu\text{m}$ corresponding to $\delta = 63\text{ nK}$.

size of the wires should be taken into account [42]. However, due to the problems previously explained it turned out that the calculations only gave a rough estimation of the created potential and an adaption on the experiment was necessary. The previously established corrections with $B_x = 180\text{ mG}$ failed to produce a precise model (also see discussion below about the sensitivity). Therefore, we developed the following rule of thumb technique, based on the previous discussion: We start from a hot cloud and create a harmonic trapping potential with the D_1 and D_2 wires, close to the maximal current in D_1 & D_2 which is about $I = 5\text{ A}$. Then, we decrease the currents $\iota_{1/2}$ in the wires $\delta_{1/2}$ from zero to negative values until we can observe the signature of a odd term (z^3) which manifests itself in an asymmetry in the cloud shape. By further decreasing the currents $\iota_{1/2}$, we counterbalance the asymmetry such that the cloud shape stays symmetric and in the center until a double well structure appears. In the typical parameter range a further decrease of the currents $\iota_{1/2}$ reduces the distance between the two minima (see Fig. 2.9 b)). By further cooling the cloud into the quasi-

condensate regime, we typically prepare double-well potentials with $\Lambda \simeq 200 \mu\text{m}$ and a barrier of $\delta \simeq 60 \text{ nK}$.

Quartic potentials With this procedure, we also reproduced quartic potentials with $a_2 = 0$

$$V_{\parallel} = a_4(x - x_0)^4. \quad (2.30)$$

By increasing the currents $\iota_{1/2}$ the coefficient a_2 approaches zero again and there exists a point where $a_2 = 0$ (see Fig.2.9 a). An experimental density profile of the quartic potential is shown in Fig 2.10 a). Quartic potentials have been previously produced on the experiment [42].

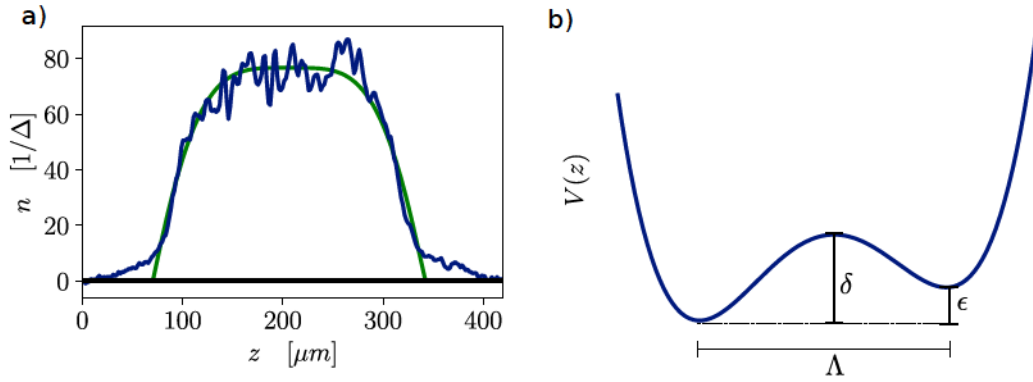


Figure 2.10 – a) In situ density profile in a quartic potential (blue line) inside the quasi-condensate regime. In green the Thomas-Fermi profile obtained from a fit with $a_4 = 3 \times 10^8 \frac{\text{K}}{\text{m}^4}$ where high density corrections due to the swelling of the wavefunction are taken into account. In the flat region of the cloud the potential roughness produced from adsorbed Rubidium atoms is visible. b) Sketch of the double well potential together with a small perturbation $V_{\delta I}^{x^1}$ lifting the degeneracy of the two minima and creating an offset ϵ .

Sensitivity of the double well potential The double well potential is experimentally rather delicate due to its sensitivity to the experimental parameters. Already in Fig. 2.9 b) one observes that a small change in ι directly leads to a very strong change in δ and Λ . In practice neither the chip layout is completely symmetric, nor the currents in the right and left wire can be perfectly controlled to be equal. Let us model the effect of an experimental defect as a fifth wire carrying a small current δI . For simplicity let us assume the fifth wire is at distance β . In order to estimate the largest contribution, let us compute at first order in z/b the contribution to the total potential from the fifth wire. The fifth wire introduces the linear perturbation $V_{\delta I}^{x^1} = a_1 z$.

This lifts the degeneracy of the two minima as shown in Fig. 2.10 b) and creates a potential which adds to Eq. (2.27):

$$V_{\delta I}^{x^1} = \frac{\mu_B \mu_0 \delta I}{\pi \beta} \left[\underbrace{\frac{d}{2\beta}}_{\text{from } B_z} + \underbrace{\frac{\mu_0}{\pi B_0} \left(\frac{I}{b^2} + \frac{\iota}{\beta^2} \right)}_{\text{from } B_x} \right] z. \quad (2.31)$$

Again the dominant contribution is given by B_x . For the experimentally relevant parameters (see caption of Fig. 2.9), a small current of $\delta I = 100 \mu\text{A}$ leads to a shift of the potential at the position of the minima of $\epsilon = 22 \text{ nK}$. This corresponds to one-third of the barrier depth $\delta = 60 \text{ nK}$. Note that $\delta I = 100 \mu\text{A}$ corresponds to 0.003% of $\iota = -3 \text{ A}$. We did not perform precision measurements of the current. Experimentally, however, a strong sensitivity was observed.

Before discussing the experimental observations, let me remind that the experiment works in a cycle of $\approx 20 \text{ s}$ and two effects can be distinguished: The long time stability of the trapping potential and the stability of the trapping potential within the cycle. Remarkably, when looking at the same time in the sequence over a several minutes to hours, no significant deviation was observable (see Fig. 2.11 b)). Taking the previous estimation into account, this is rather surprising. Still, when considering very long time scales of the order of several hours, a drift in the potential was observable. Between different data sets the balance between the two wells was corrected by small changes in ι_1 and ι_2 . The previous statement hold when the atoms were always observed at the same time within the experimental cycle. When observing the atoms for variable holding times in the trap, one observe a strong drift in the offset ϵ between the two wells (see Fig. 2.11 a)). This indicates that the experimental setup is well in a stationary situation. After each experimental cycle ($\approx 20 \text{ s}$) the experimental apparatus returns to its initial situation (heating, deformation, etc.). During a single cycle however, the experimental apparatus experiences changes which lead to strong reproducible drifts in the potential $V(z)$.

Additionally problems arise from using currents up to 5 A. This leads to considerable heating effects on the chip. The heating leads to a thermal expansion which can be observed via the imaging system. On the images the structure of the three wires, responsible for the transverse trapping (see Figure A.2 green wires), can clearly be distinguished. In order to maintain an image in focus of these wires, the position of the camera needs be adapted. From the change in focus one can deduce that the position of the chip surface changes by $\approx 60 \mu\text{m}^{10}$. This expansion of the chip can not be solely explained by an expansion of the BCB layer ($\approx 6 \mu\text{m}$ thick) and it is probably linked to a strong heating of the chip mount. The temperature expansion of the

¹⁰Here the conversion from the camera position to the focus position is obtained by a calibration from time-of-flight images.

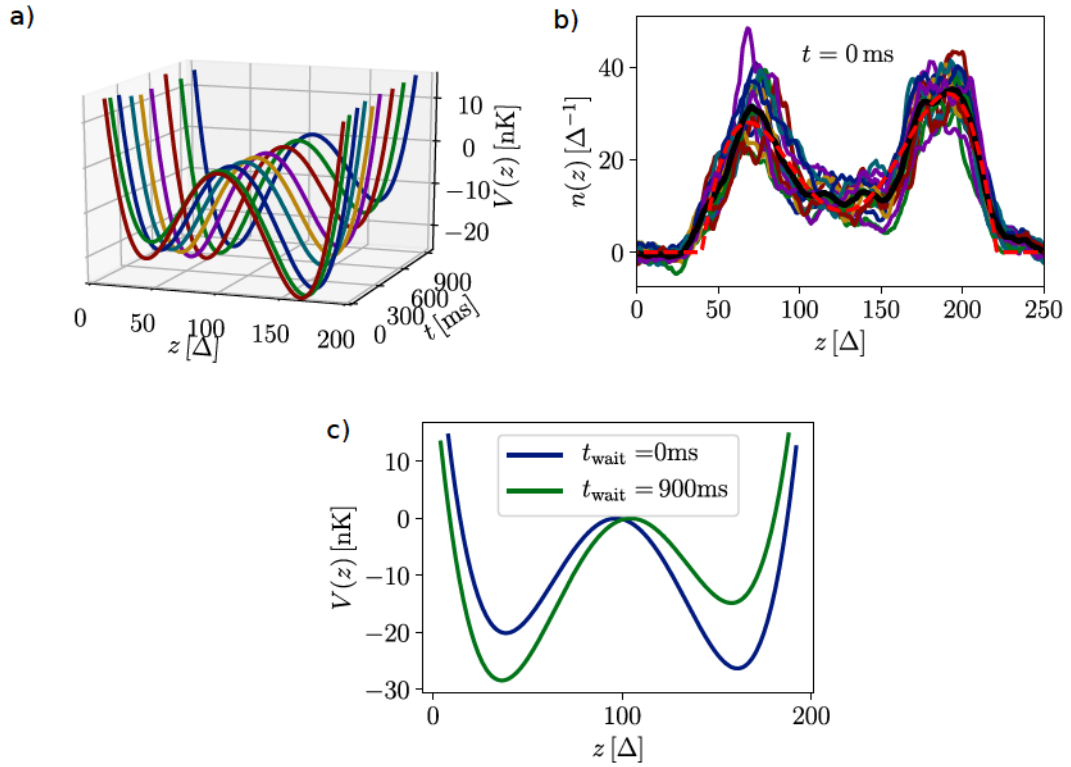


Figure 2.11 – a) The potential $V(z)$ obtained from the Thomas-Fermi approximation and a polynomial fit of the linear insitu density (see dashed red line in b)) for different waiting times t . The potential shows a significant deformation linked to the sensitivity of the double-well potential.

b) The single shot density $n(z)$ for the waiting time ($t = 0$ ms in b)) for 15 different realizations. For readability $n(z)$ was smoothed (mean value over 12 pixel). The black line is the average over the 15 realizations and the red line the polynomial fit used in a).

c) First and last potential of figure a)

cooper mount of a length of 3 cm, can be estimated at $\Delta T = 60$ K, to be of the same order ($30 \mu\text{m}$).

In summary: The heating of the chip and the sensitivity to small current deviations lead to very sensitive experimental situation. In practice the previous estimation of the offset between the right and the left well turned out to be too pessimistic. A rebalancing of the wells was experimentally manageable by controlling the currents up to 0.01 %. This discrepancy arises most probably from the simplification in the model, which neither takes into account the full geometry of the chip wires, nor higher order corrections. Nevertheless, the double-well potential pushes the experiment to its stability limits. A possible path to improve the situation could be the increase of B_0 . It leads to a smaller sensitivity to current imperfections (Eq. (2.31)) and at the same time the confining term of z^2 in Eq. (2.29) is reduced. This would be paid by the price of a reduced transverse confinement ($f_{\perp} \propto 1/\sqrt{B_0}$) which can be compensated with a stronger current in the transverse wires. At the same time this would also lead to a desired side effect of a reduced coupling between the transverse and the longitudinal confinement (see previous discussion in this section).

2.3.2.3 Potential roughness

The chip surface is coated with a thin layer of gold. It turns out that Rubidium is adsorbed by gold which leads to an accumulation of single Rubidium atoms on the chip surface. The adsorption induces a charge transfer and leaves electropositive rubidium atoms on the surface which creates an electrical stray field [73, 74]. The electric field influences the trapping potential via the Stark effect and leads to a potential roughness. The potential roughness is typically visible on the density profiles in the quasi-condensate regime as for example shown in Fig. 2.14 b) & Fig. 2.10. There exists different approaches to remove these stray electric fields: In [75] a monolayer of Rubidium on the chip surface in cryogenic environment was successfully used to circumvent the problem. Another approach at room temperature was used in [76] with a quartz surface on the chip together with a nearby electron source. It also seems that a silver mirror might bypass the problem by maintaining a high reflectivity and avoiding the adsorption [77]. Previous work in the group tried to implement a dielectric layer on top of the chip surface. Unfortunately, the dielectric layer cracked while inside the vacuum chamber.

2.4 Genetic algorithms

A typical work of a PhD student in experimental cold atom physics consists of many optimization tasks which do not always need a precise understanding of the underlying physics and equations. As a paradigmatic example consider the charging of a

magnetic trap from a MOT: Even though the underlying equations are well-known, in most practical situations theory does not predict the best choice of the parameter. Either because the problem is too complicated, the initial conditions are not precisely determined or the exact value of the magnetic fields etc. are not precisely enough known. In such situations one typically performs a manual optimization task of the final atom number. This corresponds to the optimization of a scalar function¹¹ $f(\vec{x})$ where f is the atom number and \vec{x} a vector containing the adjustable parameters. It is of strong practical interest to automatize such a task. In many situations this is not easily achievable, since the parameters of the problem are not controlled by a computer (e.g. adjustment screw of a mirror). For a atomchip experiment this situation is quite different compared with standard cold atom experiments. Most experimental parameters are currents on the chip which are directly computer controlled. On our experiment only the first stages from the *external MOT* to the molasses (see Sec. 2.2) are sensitive to such non-computer-controlled parameters. Therefore atomchip experiments are prime candidates for automatization.

Since there exists an immense variety of optimization algorithm, let me focus on some practical aspects. Many algorithms used in computer science rely on the deterministic nature of the function $f(\vec{x})$ which excludes them from use in experimental situations. There exists different approaches to deal with these noisy experimental situations. Some examples from the cold atom community are machine learning approaches [78, 79] or genetic algorithms [80, 81]. In this section I focus on an implementation of an elitist genetic algorithm. This approach is widely used, but until now has not been implemented on the atomchip experiment, nor in the atom optics group at the institute. The motivation behind the choice of the algorithm is based on simplicity of implication. We are well aware of much more involved and maybe more efficient methods [80]. The aim of this section is to demonstrate, how an efficient optimization method can be implemented with little effort.

2.4.1 The algorithm

Genetic algorithms are inspired by the Darwin principles of evolution of gene mixing by **reproduction**, **mutation** and **selection**. Here, an individual is a set of parameters $\vec{x} = \{x_1, x_2, \dots, x_n\}$. The selection takes places by the outcome of the experiment, namely the number of atoms of the set of parameters. The algorithm starts from M randomly chosen individuals (typically 10 on the experiment). The experiment then performs M runs where in each run a single individual is used (a different set of parameters) and the outcome (the number of atoms) is saved. Then, the algorithm

¹¹In some situation several parameters e.g. as the final temperature and the final atom number might be of interest. In such a situation a cost function can be created, mapping the problem back to an optimization problem of a scalar function.

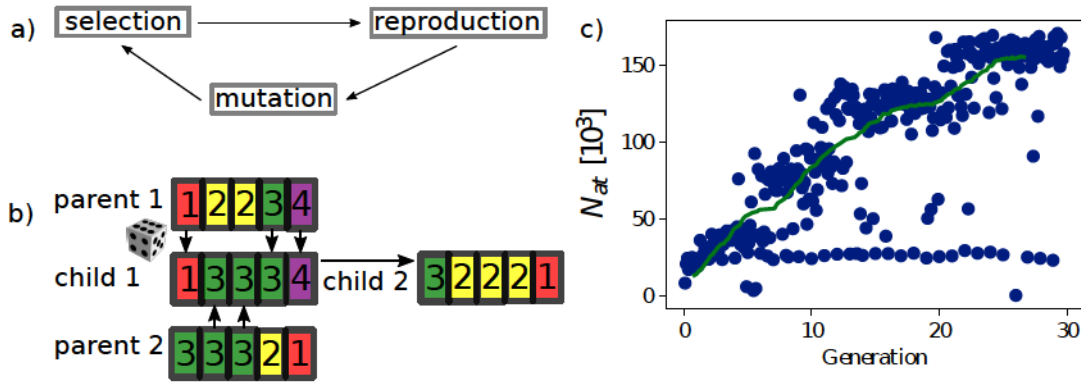


Figure 2.12 – a) Principles of the genetic algorithm.

b) Illustration of the reproduction process. Colors and numbers (genes) correspond to exemplary values of the parameter of the individuals. Child 1 is created by randomly choosing genes from the parents. Child 2 takes the previously unused genes.

c) Experimental implementation of the genetic algorithm. The atom number (blue points) as a function of the experimental cycle during the optimization process. One generation corresponds to 10 experimental cycles. For guidance, the individual data points are shown together with a smoothed green curve. After 20 generation the algorithm converges with about eight times more atoms than initially.

performs its task with its three principles. First it **selects** the two-third of the best performing individuals (highest atom number). It then **reproduces** the same amount of children, by randomly choosing two parents. The reproduction process can be performed as following (see Figure 2.12 b)): For each pair of parents two children are created. For each parameter it is randomly chosen, if child 1 obtains the *gene* (parameter value) from parent 1 or from parent 2. If child 1 obtains the gene from parent 1, child 2 will obtain the gene from the parent 2 and vice versa. This method ensures that no information is lost at this stage. One adds 1/3 of the best performing parents to the children created by this process. This stage can be skipped, but adds an *elitist* behavior to the algorithm which can speed up the optimization algorithm. At the final step **mutations** are added, by randomly changing one of the parameter on each individual. We perform mutations on a predefined interval around the original value x_k , such that the new value is given by

$$x'_k = x_k + sD2^{-uk}. \quad (2.32)$$

D defines the interval in which mutations are possible, s is the random sign of the mutation, k is the mutation precision and u a uniformly distributed number in the interval $[0, 1]$. This type of mutation is known as Mühlenbein's mutation [81, 82]. At the end of this three steps we end up with a new *generation* with the same number of

individuals M and the process starts again where this new generation is tested on the experiment. In our experimental implementation we did not predefine k and D and instead imposed for each parameter a maximal and minimal value together with a smallest step ϵ . The parameter ϵ was necessary to avoid infinitesimal small numbers which can cause problems with the our hardware control of the experiment. From the value of the maximal value, minimal value and ϵ , the parameter k and D can be calculated such that we obtain the same distribution as given in Eq. (2.32). We created the initial generation by performing random mutations on a single individual. The implementation of this algorithm has proven to be efficient in situations where not much physical intuition was available. An example is shown in Fig. 2.12 c) where the atom number is increased by a factor 8 after 300 experimental cycles. Still, human control was clearly outperforming the algorithm when a physical intuition was available.

2.5 Heating and losses

In this section I summarize the main sources of losses and heating in the experiment: Losses from the background gas and heating & losses from technical noise. Both heating and loss effects were observed during my PhD and the elimination of those processes was one of the most time consuming parts of my PhD work, at least on the technical side.

2.5.1 Background gas losses

Collisions with the background gas are a source of losses. Due to the high kinetic energy of the background gas atoms (room temperature) a collision with the background gas leads inevitably to a loss of the atom from the trap. The collision rate γ is then given by

$$\gamma \simeq n_{\text{back}} \bar{v}_{\text{back}} \sigma_{\text{back}}, \quad (2.33)$$

with n_{back} the density of the background gas, \bar{v}_{back} the mean velocity of the background gas and σ_{back} the cross section of the collisions. In the current experimental situation, if one assumes solely collisions with hydrogen molecules, one obtains $\Gamma = 1/\gamma = 100$ s for a pressure $P = 10^{-10}$ mBar¹² [63, 83]. Taking into account the measured lifetime of $\Gamma \simeq 7$ s, we conclude that collisions with the background gas should give a negligible contribution¹³. Heating due to collisions with the background gas,

¹²During the experimental cycle the pressure increases compared to the initial mentioned 10^{-11} mBar due to the rubidium vapour. We roughly estimate the increased pressure to be a factor 10 higher.

¹³Although collisions with different atomic species can contribute, the result for the tabled collisions as $Rb-Rb$ and $Rb-He$ in [83] do only differ by a few percent.

can be neglected due to the shallow traps.

2.5.2 Technical noise

In contrast to magnetic traps created by coils, atomchip setups do no benefit from the natural capacitive noise reduction of coils and thus may suffer from current noise. It is interesting to note that this problem can be reversed and atomchip setups can be used as very precise magnetic field sensors, combining high sensitivity with a high spatial resolution [84, 85].

Heating Let me focus on the three wire configuration where the atoms are at $d = 15\mu\text{m}$ from the wires and therefore potentially most sensitive to current noise. In the three-wire configuration the position of the trap center is fixed by the wire geometry (see Sec. 2.3.1.2) and it can be safely assumed that losses from a fluctuating trap center can be neglected¹⁴. Thus we assume that the dominant heating mechanism comes from fluctuations of the trapping frequency $\omega \rightarrow \omega(1 + \epsilon(t))$ where $\epsilon(t)$ are small fluctuations. The fluctuations can be characterized by a noise spectrum $J_\epsilon(\omega) = \int \langle \epsilon(0)\epsilon(t) \rangle e^{-i\omega t} dt$, whose spectral width is assumed to be large compared to ω . The trapping frequency oscillations lead to a parametric driving process where transitions from the quantum mechanical state $|n\rangle$ of the harmonic oscillator are driven towards $|n+2\rangle$ and $|n-2\rangle$. This leads to a heating process:

$$\frac{d\langle E \rangle}{dt} = \frac{\omega^2}{2} J_\epsilon(2\omega) \langle E \rangle. \quad (2.34)$$

Eq. (2.34) describes an exponential heating characterized with a time constant τ_{heat} . Since in the three-wire geometry $\omega \propto I$, we obtain

$$\tau_{\text{heat}}^{-1} = \frac{\omega^2}{2I^2} J_I(2\omega), \quad (2.35)$$

where $J_I(\omega) = \int \langle I(0)I(t) \rangle e^{-i\omega t} dt$. A characteristic heating time τ_{heat} which exceeds 10s under typical experimental situations with $I = 0.1\text{A}$ and $\omega/(2\pi) = 3\text{kHz}$ imposes that $J_I < 500\mu\text{A}^2/\text{Hz}$.

Losses For simplicity let us restrict this discussion to the DC trap- The strongest contribution of the magnetic field seen by the atoms comes from B_0 and polarizes

¹⁴Here it can be safely assumed that the current noise at each moment is the same in each of the three wires. The cables which interconnect the three wires are of lengths of some meters. Uncorrelated noise is therefore suppressed up to several gigahertz where the atoms cannot follow the fast movements.

the atoms along the z axes. However, the magnetic fields B_x and B_y couple the trap state to the remaining Zeeman levels. This loss rate is given by

$$\Gamma_{\text{noise}} \approx \frac{1}{2\hbar^2} \left(\frac{\mu_B \mu_0}{2\pi d} \right)^2 J_I(\omega_L), \quad (2.36)$$

where d is the distance to the wire and $\omega_L = \mu_B B / \hbar$ the Larmor frequency [63, 86]. In the DC-trap the atoms are at a distance $d \approx 150 \mu\text{m}$. Eq. (2.36) predicts that $J_I(\omega) < 15 \mu\text{A}^2/\text{Hz}$ in order to maintain a lifetime of $\tau_{\text{losses}} > 10 \text{ s}$.

The loss process is sensitive to the noise spectrum around the Larmor frequency which is typically on the order of $\omega_L / (2\pi) = 3 \text{ MHz}$. The heating process is sensitive to the noise spectrum around twice the trap frequency which is on the order of a few kHz. Experimentally both heating and losses were observed, with losses being in most situations the dominant effect. Experimentally both effects cannot be well separated in shallow traps, since spill-overs from heating eventually also leads to losses.

A precise characterization of the electronic noise on the chip is not straightforward. In principal the electronic noise on the experiment can be lower than the estimations of the limiting values in this sections. The best experimentally measured lifetime during my PhD was about $\Gamma \approx 7 \text{ s}$ which is probably still limited by electronic noise.

2.5.3 Switching-mode power devices

It is well known that switching-mode power devices can be an important source of electric noise. Their basic working principle consist in "cutting" the input voltage (typically $V_{\text{in}} = 220 \text{ V}$ modulated at 50 Hz) by a switching regulator into short time intervals and a subsequent filtering of the output voltage (typically V_{out} a few Volts). Noise created by the switching-mode power device does not only affect the electrical loop under consideration, but can propagate via the ground connections and affect different parts of the experiment. Due their low costs, switching-mode power devices became an industrial standard which in some practical cases make them almost impossible to avoid in laboratories. It is practically impossible to avoid switching-mode power devices in standard equipment, such as computers and screens. It is however worth to note, that good quality switching-mode power supplies can be of very low noise. However it can be difficult to link the noise quality of a certain switching-mode power device to its noise impact on the experimental setup from calculations. Experimental testing of the noise impact can be tricky, since some switching-mode power supplies only show a high noise level at certain moments. Even after a thorough testing of the impact of a certain switching-mode power supply on the experimental cycle, it is not exclude that after some time (even months later) the switching-power device becomes a major source of electric noise in the experiment. At the same time the noise of a switching-mode power device can also disappear for some while. The

electric noise finally leads to losses and heating on the experimental setup which was regularly observed on the experiment. During my PhD, problems due to switching-mode power devices significantly slowed down the scientific progress. All the above mentioned problems of noise appearing and disappearing randomly have been repeatedly observed. As a consequence almost all switching-mode power devices on the experiment have been steadily replaced by linear power supplies which led to a continuous improvement of the atom lifetime. Additionally, all the current carrying wires which are used for atom trapping purposes, have been shielded by special wires and connectors.

2.6 Technical instabilities

2.6.1 Mechanical instabilities

The scientific work of my PhD has been also significantly delayed due to technical instabilities which were all related to a newly installed movable lens system. These problems were all linked to the more general problem of maintaining a high mechanical stability of vertical moving massive object (some 200 g) over a large number of repetitions (some hundred of thousands repetitions).

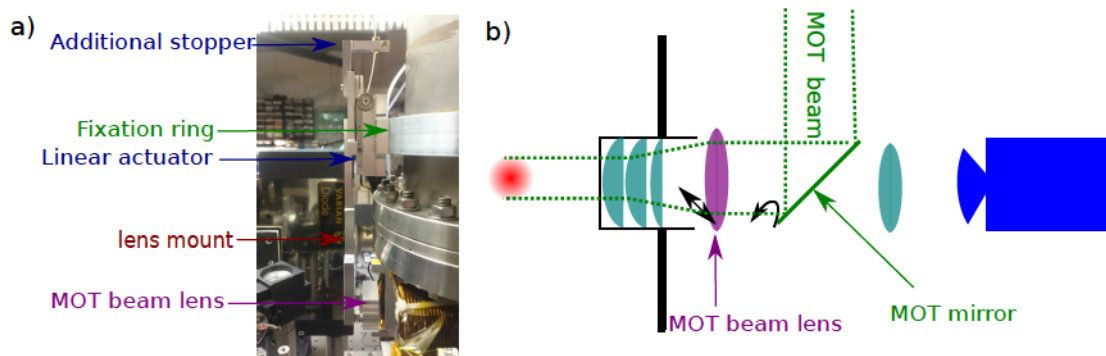


Figure 2.13 – The MOT beam with its movable parts. Left: Picture from the side. Right: Sketch from the top view. The MOT beam lens (the MOT beam mirror) are movable part which will be lifted up (sideways) during the DC trap phase (see 2.2).

The introduction of the vertical moving lens originates from major changes on the imaging system prior to my PhD¹⁵. The change of the objective of the imaging system required the use of an additional lens during the MOT-phase. This *MOT-lens* is needed to collimate the MOT beam passing through the new objective in reverse direction as shown in Fig. 2.13 b). Due to the high numerical aperture of the new

¹⁵For more details on the changes on the imaging system see [36, 59]).

objective, the MOT-lens needed to be placed a few centimeters beyond the objective to avoid a too large spreading of the MOT beam. Unfortunately, it is practically impossible to place the MOT-beam lens where the optical path of the imaging system is separated from the MOT beams (see Fig. 2.13 b)). The additional MOT-beam lens needs to be moved during the imaging, in order to not disturb the imaging part. Due to space constraints on the optical table, it was decided to mount the MOT-beam lens on a vertical moving platform (see Fig. 2.13 a)). This part of the experiment is inside the magnetic shielding which required the use of a special non-magnetic platform which strongly constrains the number of possible technical solutions. As a solution a linear actuator from SmarAct GmbH was chosen¹⁶ based on a stick-slip motor. Due to the operation in vertical position, an additional spring for gravity compensation was added, after consultation with the producer (see Fig. 2.13). The whole setup is fixed by a clamp ring (fixation ring) around a steel cylinder of diameter 30 cm (see Fig. 2.13 a)).

During my PhD the following parts showed significant degradation:

- **Spring:** The additional spring broke twice. Since the whole setup is hidden behind the magnetic shielding, this was not immediately realized. We do not know how long the linear actuator was running without gravity assistance of the spring.
- **The linear actuator:** Twice an early degradation was observed. Each time this resulted in a replacement of the stick-slip motor. After a detailed inspection with the producer, the cause of this early degradation remained unclear. According to the company these linear actuators are routinely used in similar conditions (number of repetitions/weight) without significant signs of degradation. It is unclear if this is linked to the broken spring mentioned above which might have lead to an excessive stress on the actuator. Each replacement was linked to several months of down-time of the experiment, due to the reparation by the producing company.
- **The clamp ring** The clamp ring changed several times its position. This effect was unexpected by several experienced technicians, although first observation signs were at hand. The clamp ring withstands at least the weight of 70 kg without any displacement and no displacement can be observed after several movements of the linear actuator with its load. However the situation can dramatically change when considering hundred of thousands of movement of the system¹⁷. Then, the lens together with its mount acts like a small hammer of about 200 g on the clamp ring. This led to a movement by several millimeters of

¹⁶The non-magnetic version of *SLC-2460-D-NM*: <http://www.smaract.com/products/linear-positioners/slc-series/slc-2460/>

¹⁷This is an estimation of the number of yearly movements of the linear actuator.

the clamp ring¹⁸. By adding metal spacers which are placed between the clamp ring and a fixed basis, this mechanical instability was removed.

In summary: the vertical displacement of a lens with a high precision and high reproducibility can be a more complicated task than anticipated and if possible a horizontal displacement is preferable. Although the system is functional at the moment, a replacement system was prepared which is based on the block and tackle technique with most of the parts outside of the magnetic shielding. It cannot be guaranteed that such a system does not show similar failures. However, all of its technical components can be easily replaced outside the magnetic shielding and the components are based on well known simple electric motors and "stone age" mechanics. With this replacement system we expect to avoid lengthy time delays in the future.

2.6.2 Magnetic stability

During my PhD, I observed increased fluctuations and long term drifts (on the order of hours), when working with low number of atoms ($n_p \simeq 5 \mu\text{m}^{-1}$). Its origin is not clear, however there are hints that it might be linked to fluctuations of the magnetic fields. The whole vacuum chamber is protected from external magnetic fields by a metallic shielding in two layers. The outer one out of mu-metal and the inner one out iron. In [71] it has been estimated that the stability provided by this shielding is better than $800 \mu\text{G}$. Since this measurement the inner layer of iron started to show signs of rust which changes the magnetic structure of the iron and probably its shielding capacity. Taking the upper bound of [71] as an estimation for a magnetic fluctuation $\delta B = 800 \mu\text{G}$ and assuming this field aligned to be with B_0 , this would result in a fluctuation of the potential offset of 7% compared to the chemical potential μ at $f_{\perp} = 3 \text{kHz}$ and $n_0 = 5 \mu\text{m}^{-1}$. In principle fluctuations of the potential offset are unimportant, unless working with RF-knives as used for the evaporative cooling.

2.7 Imaging system

We use standard absorption imaging techniques, whose key points will be introduced in the following. A more detailed description including the newly installed imaging system can be found in [36, 59]. Absorption imaging is based on the Beer-Lambert law

$$\frac{dI}{dx} = -n(x, y, z)\sigma(I), \quad (2.37)$$

where in this paragraph x is the direction of light propagation through the atomic cloud, I the imaging beam intensity, $\sigma(I)$ the absorption cross-section and $n(x, y, z)$

¹⁸This problem could be well summarized under the ancient Greek saying "Ραυι ενδελεχουσα κοιλαινει ετραν" — "constant dripping wears the stone" (Choerilus of Samos 5th century BC)

the 3D atomic density. In general $\sigma(I)$ in a multilevel atomic structure can not be easily obtained (see [42] for detailed analysis of the problem in presence of a multi-level structure). The situation changes drastically for a two-level system with light on resonance where the cross section is given by

$$\sigma(I) = \frac{\sigma_0}{1 + \frac{I}{I_{\text{sat}}}}, \quad (2.38)$$

with the low intensity cross section $\sigma_0 = 3\lambda^2/(2\pi)$, the saturation intensity $I_{\text{sat}} = \Gamma_{\text{im}}\hbar\pi c/(\lambda\sigma_0)$ and the natural linewidth Γ_{im} . A two-level system can be obtained by applying a strong magnetic field (10G) to split the hyperfine structure in its m_F states and addressing the atoms with an imaging beam of σ^+ polarization. We use the two-level system on the closed transition between $|F = 2, m_F = 2\rangle$ and $|F' = 3, m_F = 3\rangle$ which has natural linewidth $\Gamma_{\text{im}} = 2\pi 6.069 \text{ MHz}$ [87] for ^{87}Rb . We shine a resonant imaging beam at wavelength $\lambda = 780.24 \text{ nm}$ onto the atoms and an image is reconstructed from the absorbed light. The x integrated atom number n_{at} per pixel is then obtained by comparison with a reference image taken without atoms 60 ms after the first image:

$$n_{\text{at}}(y, z) = \frac{\Delta^2}{\sigma(I)} \ln \left(\frac{N_2^{\text{ph}}}{N_1^{\text{ph}}} \right). \quad (2.39)$$

N_i^{ph} is the number of photons in the i -th image where $i = 1$ is the image with atoms and $i = 2$ is the reference image. The size of the pixel in the object plane is $\Delta = 1.75 \mu\text{m}$. The imaging beam is shone on the atoms via the gold mirror on the surface of the chip at 45° (see Fig. 2.14). Without atoms this should lead to a flat image $n_{\text{at}} = 0$ everywhere. In practice, however, a small residual unevenness can be observed and a reference image without atoms is subtracted. Since we are interested in 1D physics, we use for almost all applications the integrated atomic density $n(z) = \int n_{\text{at}}(y, z) dy$; the atomic profile integrated over the transverse direction (see profile Figure 2.14 b)).

2.7.1 Time-of-flight images

We use a time-of-flight imaging technique in order to obtain a situation where the equation for the two-level system Eq. (2.38) is valid. We switch off the trapping potentials and the atoms fall under gravity during a short time-of-flight $t_f = 8 \text{ ms}$ ¹⁹. During the time-of-flight the imaging magnetic field $B^{\text{im}} = 10 \text{ G}$ is switched on. The imaging magnetic field B^{im} is orientated with respect to the imaging beam of polarization σ^+ , such that the only closed transition is given by $|F = 2, m_F = 2\rangle$ and $|F' = 3, m_F = 3\rangle$ (see Fig. 2.14). After the short time-of-flight the atoms are placed at a position where light

¹⁹For this whole manuscript t_f will be 8 ms, if not stated explicitly differently.

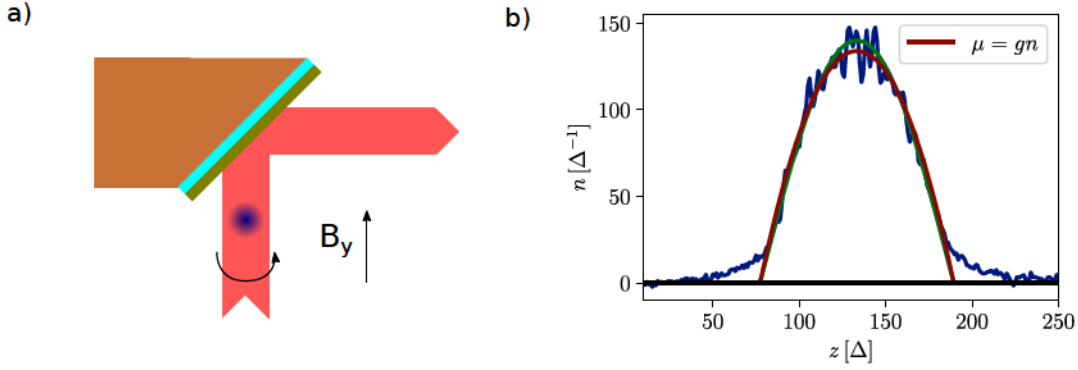


Figure 2.14 – a) The imaging laser beam is shone on the atoms. The laser beam is reflected from the chip surface into the imaging system b) Density profile $n(z)$ (blue) compared to Thomas-Fermi profile with the quasi-condensate equation of state $\mu = gn$ (red) and with corrections due to the swelling of ground state in the transverse direction $\mu = \hbar\omega_{\perp}(\sqrt{1+4na_{3D}}-1)$ (green). The bumps on the experimental profile are due to the potential roughness which arises from rubidium atoms adsorbed on the chip surface (see Sec. 2.3.2.3).

reflected from the chip surfaces does not recross the atomic cloud (see Fig. 2.14 a)). During the time-of-flight the cloud expands quickly in the transverse direction and a dilute cloud is imaged. This avoids problems of high densities as discussed below in Sec. 2.7.2. We use time-of-flight images to record the density ripples images (see Sec. 2.8.1) and to extract the momentum distribution (see Sec. 2.8.3). Additionally, they are used to calibrate the insitu number of atoms, as discussed in the following section.

2.7.2 In situ images

In contrast to time-of-flight images, in situ images do not directly contain the correct atom number, and always need to be calibrated with time-of-flight images. Still, in situ images can be very interesting for practical purposes when interested in the atomic profile. In situ images inside the quasi-condensate regime only contain small density fluctuations, in contrast to the large density ripples appearing after a time-of-flight (see below Sec.2.8.1). Therefore, the atomic profile can be obtained in a single shot with a relatively low level of noise and averaging over many realizations is unnecessary. This advantage is exploited in the GHD project (see Chap. 5).

We acquire insitu images after a very short time-flight of $100\mu s$, during which neither the density profile nor the density fluctuations are modified. In such a situation, the atoms absorb twice the imaging beam: The first absorption takes place

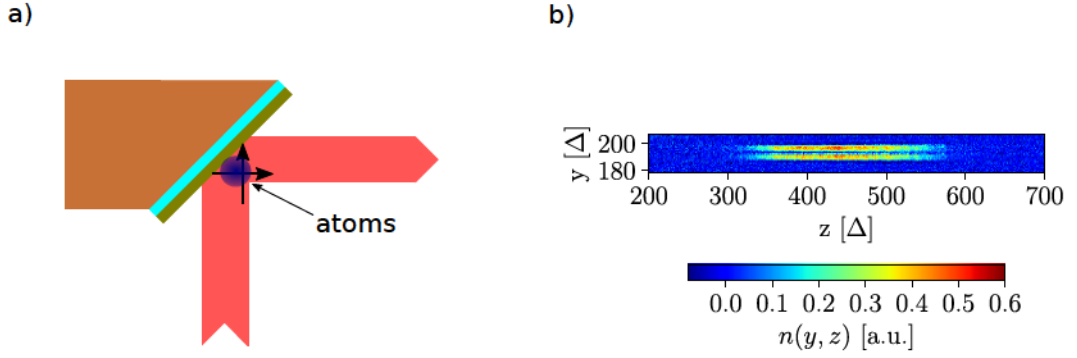


Figure 2.15 – In situ imaging. a) Position of the atoms with respect to the imaging beam and the chip. b) In situ absorption imaging of the atomic cloud and its mirror image. Note that the transverse ground state is smaller than the pixel size Δ . The atom number is calibrated with a time-of-flight image (see Fig. 2.14).

before the reflection on the chip surface and a second absorption after the reflection on the chip surface as shown in Fig. 2.15 a). This leads to two images of the atomic cloud: a real image and a mirror image of the atoms as shown in Fig. 2.15 b). A priori it is not directly possible to reconstruct $n(z)$, since without well-defined magnetic field the atoms cannot be described by a two level system (Eq. (2.38)). However, it turns out that for practical considerations Eq. (2.38) still holds [42, 88], with σ_0 replaced with $\alpha\sigma_0$. The correction coefficient is approximately $\alpha \simeq 0.8$ and the exact value depends on the detuning. The applicability is routinely verified by comparing the in situ profiles to the time-of-flight profiles and α is corrected for small variation in each data set. For high atomic densities the validity of the Beer-Lambert law can be lost and two effects can be distinguished: First, when the interparticle distance is smaller than the wavelength non-trivial reabsorption processes become important. Second, when the size of the cloud becomes much smaller than the size of the pixel Δ , the non-linearity of the logarithm leads to an under estimation of the atom number. Both effects can be observed on the experiment for high atomic densities in the center of the trap and in previous works [36, 42, 59] correction techniques were used. For the data presented in this thesis the atomic densities were chosen to be low enough such that these corrections were unnecessary. Additionally, the short time-of-flight of $100\mu\text{s}$ leads to a transverse expansion, such that the transverse size of the cloud becomes comparable to the pixel size. Note that it could be argued that only in situ images allow to extract the correct atomic profile in contrast to time-of-flight images. This, however, does not apply to the experimental situations considered in this thesis. Due to the shallow longitudinal trapping confinements and the short time-of-flights $t_f = 8\text{ms}$, no change in the longitudinal atomic profile was observed. Consid-

ering the data in this thesis the advantage of the insitu images over the time-of-flight images solely consists in a lower statistics: The large density fluctuations inside the quasi-condensate regime are removed and the signal to noise ratio is increased by avoiding the large spread in the transverse direction.

2.8 Analysis methods

2.8.1 Density ripple analysis

The method of the density ripple analysis was pioneered by [89] and later used in the Vienna group [19, 90, 91]. Inside the quasi-condensate regime density ripples appear after a short time-of-flight, during which initial phase-fluctuations are transformed into density fluctuations²⁰ $\delta\rho(z)$. This method has been proven to be a very useful tool for temperature measurements [19, 24]. Prior to my PhD the density ripple method was not used in our group²¹ and the temperature measurements mainly relied on in situ measurements of the atom number fluctuations [11, 92, 93]. Both measurements methods have their strengths and weakness. The advantage of the in situ atom number fluctuations method lies in its direct link to a thermodynamic quantity via the fluctuation-dissipation theorem. It can thus be used in all regimes of the phase diagram (Fig. 1.4). However, inside the quasi-condensate regime which we predominantly investigate, density fluctuations are suppressed which makes its observation technically difficult and requires a lot of statistics. In stark contrast, the density ripple method relies on the thermal phase-fluctuations which develop into large density fluctuations and which can be of the same order as the initial mean atomic density $n_0(z)$. These density ripples are therefore very easily visible on a single shot image as shown in Fig. 2.16 b) which drastically increases the signal to noise ratio. They are of stochastic nature and the average profile over several experimental realization gives the mean profile $\langle\rho(z)\rangle = \rho_0(z)$. Both methods are sensitive to excitation in the phononic regime. In the following I will show how the density ripple analysis can be used to extract information about individual Bogoliubov modes (see Sec 2.8.1.2) and how it can be used as a thermometry to extract the phononic temperature (see Sec 2.8.1.3).

2.8.1.1 Density ripples power spectrum

In this section I will rederive expressions for the density ripples spectrum $\langle|\tilde{\rho}(q)|^2\rangle$, first established in [90]. A more detailed derivation can be found in our paper [18], whose derivation is closely followed. Let us consider a gas initially trapped whose trapping potential is removed at $t = 0$. The atoms then fall under gravity during a time t_f . The power spectrum of the density ripples $\langle|\tilde{\rho}(q)|^2\rangle$ after time-of-flight writes as

$$\langle|\tilde{\rho}(q)|^2\rangle = \iint dz_1 dz_2 e^{iq(z_1-z_2)} \langle\delta\rho(z_1)\delta\rho(z_2)\rangle, \quad (2.40)$$

²⁰In the following the letter ρ is used for the atomic density after time-of-flight, while the letter n denotes the atomic density in the trap.

²¹One example measurement can be found in [36]

with $\delta\rho(z) = \rho(z) - \langle\rho(z)\rangle$ the density fluctuation after t_f . When expanding eq. (2.40) the term $|\int dz e^{iqz} \langle\rho(z)\rangle|^2$ appears. This term can be safely neglected, since we restrict ourselves to short time-of-flights, such that the cloud shape does not change ($\langle\rho(z)\rangle \simeq n_0(z)$ with $n_0(z)$ the insitu atomic density²² and at the same time we are only interested in wavevectors smaller than the inverse cloud length such that the term $-\int dz e^{iqz} \langle\rho(z)\rangle|^2$ gives negligible contributions to $\langle|\tilde{\rho}(q)|^2\rangle$. Then we obtain

$$\langle|\tilde{\rho}(q)|^2\rangle = \iint dz_1 dz_2 e^{iq(z_1 - z_2)} \langle\rho(z_1)\rho(z_2)\rangle. \quad (2.41)$$

Due to the strong transverse confinement, the gas expands fast in the transverse direction and interactions become almost immediately negligible (a more detailed discussion about the interactions follows in Sec. 2.8.1.7), such that one can calculate $\rho(z) = \hat{\Psi}^\dagger(z, t_f)\hat{\Psi}(z, t_f)$ with the free-particle propagator

$$\hat{\Psi}(z, t_f) = \frac{1}{\sqrt{2\pi t_f}} \int d\alpha \hat{\Psi}(\alpha, 0) e^{i\frac{(z-\alpha)^2}{2t_f}}. \quad (2.42)$$

For readability, I use in this paragraph $\hbar = m = 1$. This leads to

$$\langle\rho(z_1)\rho(z_2)\rangle = \frac{1}{(2\pi t_f)^2} \iiint d\alpha d\beta d\gamma d\delta \langle\hat{\Psi}_\alpha^+ \hat{\Psi}_\beta \hat{\Psi}_\gamma^+ \hat{\Psi}_\delta\rangle e^{-i\frac{(z_1-\alpha)^2}{2t_f} + i\frac{(z_1-\beta)^2}{2t_f} - i\frac{(z_2-\gamma)^2}{2t_f} + i\frac{(z_2-\delta)^2}{2t_f}}, \quad (2.43)$$

with the notation $\hat{\Psi}_\nu = \hat{\Psi}(\nu, 0)$. Expanding the exponential, we obtain

$$\langle\rho(z_1)\rho(z_2)\rangle = \frac{1}{(2\pi t_f)^2} \iiint d\alpha d\beta d\gamma d\delta \langle\hat{\Psi}_\alpha^+ \hat{\Psi}_\beta \hat{\Psi}_\gamma^+ \hat{\Psi}_\delta\rangle e^{i\frac{(\alpha-\beta)z_1}{t_f} + i\frac{\beta^2 - \alpha^2}{2t_f} + i\frac{(\gamma-\delta)z_2}{t_f} + i\frac{\delta^2 - \gamma^2}{2t_f}}. \quad (2.44)$$

Injecting into Eq. (2.41), and using $\int dz e^{ikz} = 2\pi\delta(k)$ and $\delta(x/\alpha) = |\alpha|\delta(x)$, we get

$$\langle|\tilde{\rho}(q)|^2\rangle = \iint d\alpha d\delta \langle\hat{\Psi}_\alpha^+ \hat{\Psi}_{\alpha+qt_f} \hat{\Psi}_{\delta+qt_f}^+ \hat{\Psi}_\delta\rangle e^{-i\frac{\alpha^2}{2t_f}} e^{i\frac{(\alpha+qt)^2}{2t_f}} e^{-i\frac{(\delta+qt)^2}{2t_f}} e^{i\frac{\delta^2}{2t_f}}. \quad (2.45)$$

Defining $\delta = \alpha + X$, we finally obtain

$$\langle|\tilde{\rho}(q)|^2\rangle = \iint d\alpha dX e^{iqX} \langle\hat{\Psi}_\alpha^+ \hat{\Psi}_{\alpha+qt_f} \hat{\Psi}_{\alpha+X+qt_f}^+ \hat{\Psi}_{\alpha+X}\rangle. \quad (2.46)$$

Up to now the derivation is general and did neither assume a specific regime nor a certain geometry of the cloud.

²²This property has been experimentally verified as discussed in Sec. 4.4.3.

Homogeneous gas in the quasi-condensate regime Let us consider a homogeneous system in order to obtain analytic results which can be helpful to obtain an intuition. We will later come back to different trapping potentials. We introduce the intensive quantity of a homogeneous system of length L which is given by $\langle |\rho(q)|^2 \rangle = \langle |\tilde{\rho}(q)|^2 \rangle / L$. Inside the quasi-condensate regime $\hat{\Psi}_z$ can be written as $\sqrt{n_0} e^{i\hat{\theta}(z)}$ (see Sec.1.3) where the density fluctuations $\hat{\delta}n(z)$ are neglected. Then Eq. 2.46 writes

$$\langle |\rho(q)|^2 \rangle \simeq n_0^2 \int_{-L/2}^{L/2} dX e^{iqX} \left\langle e^{i(\hat{\theta}_0 - \hat{\theta}_{qt_f} + \hat{\theta}_{X+qt_f} - \hat{\theta}_X)} \right\rangle, \quad (2.47)$$

where the translational invariance of the system was used to integrate out α and again we used the simplified notation $\hat{\theta}_z = \hat{\theta}(z)$.

2.8.1.2 Filter for Bogoliubov modes

In Eq. (2.47) only pairs of $\theta(z_1) - \theta(z_2)$ appear where $z_1 - z_2$ is separated by qt_f . When restricting to wavevectors such that $qt_f \ll l_c$, the difference $\theta(z_1) - \theta(z_2)$ stays small (see Sec.1.3) and we can expand the exponential in Eq. (2.47) which leads to

$$\langle |\rho(q)|^2 \rangle \simeq n_0^2 \int dX \left[1 - \frac{1}{2} \left\langle (\hat{\theta}_0 - \hat{\theta}_{qt_f} + \hat{\theta}_{X+qt_f} - \hat{\theta}_X)^2 \right\rangle \right] e^{iqX}. \quad (2.48)$$

In the whole section we are not interested in the contribution at $q = 0$, and for simplification of the calculation we drop all the terms which do not depend on X . Additionally $\langle \theta(z_1)\theta(z_2) \rangle$ only depends on the separation of $|z_1 - z_2|$ which leads to

$$\langle |\rho(q)|^2 \rangle = n_0^2 \left[2 - \left(e^{iq^2 t_f} + e^{-iq^2 t_f} \right) \right] \int dX \langle \theta(0)\theta(X) \rangle e^{iqX}, \quad (2.49)$$

where again the translation invariance was used. Let me now introduce the Fourier transform of $\theta(z)$

$$\bar{\theta}_q = \int e^{iqz} \theta(z) dz, \quad (2.50)$$

and we obtain

$$\langle |\rho(q)|^2 \rangle = 4n_0^2 \langle |\bar{\theta}_q|^2 \rangle \sin^2 \left(\frac{q^2 t_f}{2} \right), \quad (2.51)$$

The complex valued quantity $\bar{\theta}_q$ can be decomposed in its cosine and sine contribution with $\langle |\bar{\theta}_q|^2 \rangle = \frac{1}{2} \left(\langle \theta_{q,c}^2 \rangle + \langle \theta_{q,s}^2 \rangle \right)$. For a system which is invariant under translation both contributions are equal $\langle \theta_{q,c}^2 \rangle = \langle \theta_{q,s}^2 \rangle$ and we finally obtain

$$\langle |\rho(q)|^2 \rangle = 4n_0^2 \langle \theta_{q,r}^2 \rangle \sin^2 \left(\frac{\hbar q^2 t_f}{2m} \right), \quad (2.52)$$

where m and \hbar are reintroduced. The index r stands for $r = c, s$ and will be dropped in the following.

This implies that for low lying wavevectors $\hbar q t_f \ll l_c m$ the density ripple spectrum resolves individual Bogoliubov modes. On the data analysis side, Eq. (2.52) constitutes the central equation for the interaction quench which is introduced Chap. 3.

For a system at thermal equilibrium and thermally populated modes $k_B T \gg \hbar \omega_q$ where ω_q is the Bogoliubov mode frequency of Eq. (1.67), the equipartition theorem allows to write

$$\langle \theta_q^2 \rangle = m k_B T / (\hbar^2 n_0 q^2). \quad (2.53)$$

The prediction of Eq. (2.52) together with Eq. (2.53) is shown in Fig. 2.16.

2.8.1.3 Density ripple thermometry

Without the restriction to small wavevectors $\hbar q t_f \ll l_c m$ and in equilibrium situations in a homogeneous system an analytic formula can be obtained [90]. For higher q contribution different Bogoliubov wavevectors get mixed and the density ripple spectrum cannot resolve individual Bogoliubov modes. Starting from Eq. (2.47), we can use the fact that $\hat{\theta}$ is a Gaussian variable and apply the Wick theorem to rewrite the exponential:

$$\langle |\rho(q)|^2 \rangle = n_0^2 \int dX e^{iqX} e^{-\frac{1}{2} \langle (\hat{\theta}_0 - \hat{\theta}_{qt_f} + \hat{\theta}_{X+qt_f} - \hat{\theta}_X)^2 \rangle}. \quad (2.54)$$

The exponential can be further rewritten as

$$\frac{\langle |\rho(q)|^2 \rangle}{n_0^2} = \int dX e^{iqX} e^{-\frac{1}{2} \langle (\hat{\theta}_0 - \hat{\theta}_{qt_f})^2 + (\hat{\theta}_{X+qt_f} - \hat{\theta}_X)^2 + (\hat{\theta}_0 - \hat{\theta}_X)^2 + (\hat{\theta}_{qt_f} - \hat{\theta}_{X+qt_f})^2 - (\hat{\theta}_0 - \hat{\theta}_{X+qt_f})^2 - (\hat{\theta}_{qt_f} - \hat{\theta}_X)^2 \rangle}. \quad (2.55)$$

Using the first order correlation function

$$g_1(z) = \langle \hat{\Psi}^\dagger(0) \hat{\Psi}(z) \rangle \simeq n_0 e^{-\frac{1}{2} \langle [\hat{\theta}(z) - \hat{\theta}(0)]^2 \rangle} = n_0 e^{-|z|/l_c}, \quad (2.56)$$

with $l_c = \frac{2\hbar^2 n_0}{k_B T}$, one calculates

$$\frac{\langle |\rho(q)|^2 \rangle}{n_0^2} = \int_{-\infty}^{\infty} dX e^{iqX} e^{-2 \left(\frac{|qt_f| + |X|}{l_c} + \frac{|X+qt_f|}{l_c} + \frac{|X-qt_f|}{l_c} \right)}. \quad (2.57)$$

This Fourier transform of an even function on X can be rewritten

$$\frac{\langle |\rho(q)|^2 \rangle}{n_0^2} = 2 \int_0^{\infty} dX e^{-2 \left(\frac{|qt_f| + |X|}{l_c} + \frac{|X+qt_f|}{l_c} + \frac{|X-qt_f|}{l_c} \right)} \cos(qX). \quad (2.58)$$

As previously, let us restrict to $q > 0$ and we can distinguish the two cases $X > qt_f$ and $X < qt_f$. For $X > qt_f$ Eq. (2.58) only gives an irrelevant contribution to $q = 0$. For $X < qt_f$ Eq. (2.58) leads to

$$\frac{\langle |\rho(q)|^2 \rangle}{n_0^2} = 2 \int_0^{qt_f} dX e^{-2\frac{X}{l_c}} \cos(qX). \quad (2.59)$$

The integral of Eq. (2.59) can be solved analytically which leads to

$$\langle |\rho(q)|^2 \rangle = 2n_0^2 \frac{2ql_c - 2e^{-\frac{2\hbar qt_f}{ml_c}} \left(ql_c \cos\left(\frac{\hbar q^2 t_f}{m}\right) + 2 \sin\left(\frac{\hbar q^2 t_f}{m}\right) \right)}{q(4 + l_c^2 q^2)} \quad (2.60)$$

where \hbar and m are reintroduced. Eq. (2.60) represents the central results of this sec-

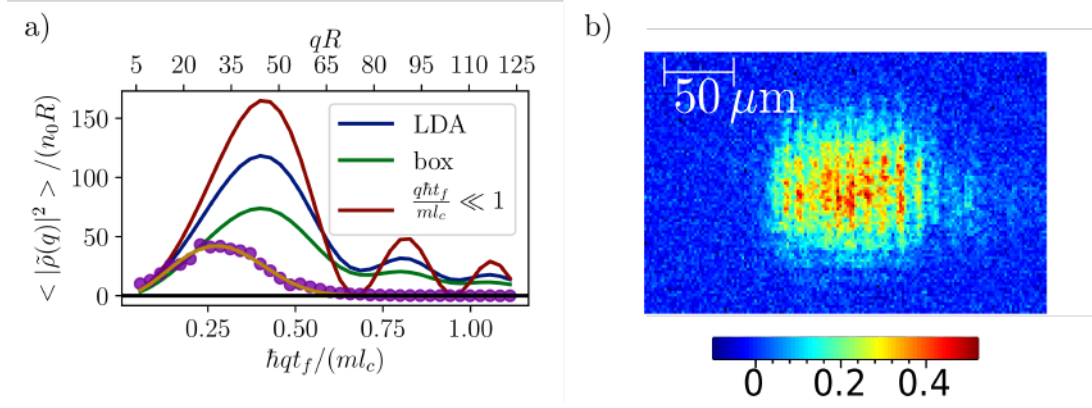


Figure 2.16 – a) Density ripple power spectrum. Green line corresponds to the prediction for a homogeneous gas $\langle |\tilde{\rho}(q)|^2 \rangle$ in a box of length $L = 2R$ and a the mean atomic density $n_0 = N/(2R)$ (Eq. 2.60). The blue line corresponds the local density prediction Eq. (2.64). The dots corresponds to a data set at $f_{\perp} = 3.1$ kHz and the yellow line to the corresponding fit which takes into account the LDA and the imaging resolution for which we obtain $\sigma = 1.97 \pm 0.04 \mu\text{m}$. All the plotted lines correspond to the same temperature $T = 53 \pm 4$ nK which is obtained from the fit. Note that the position of the first maximum of the density ripple is shifted to the left by the imaging resolution which prevents to observe the oscillatory behavior. The upper axis $j = qR$ corresponds to the wavevector which is dominated by the ν -th mode index for Bogoliubov modes in a a harmonic trap. The red line corresponds to the small q expansion (see Sec. 2.8.1.2) valid for $\hbar qt_f / (ml_c) \ll 1$.

b) Single shot 2D image of the density ripple. The longitudinal z -axis is horizontal.

tion. In Fig. 2.16 it is shown for experimentally relevant parameters. Eq. (2.60) shows

a damped oscillatory behavior where the height of the first maximum is approximately proportional to the temperature of the gas (see Eq. 2.52). The expression of Eq. (2.60) solely depends on the temperature T , apart from the experimentally well known density n_0 and the time-of-flight t_f . It can be therefore used to fit the experimental data to obtain the temperature.

2.8.1.4 Local density approximation

The expression for the filter of Bogoliubov modes Eq. (2.52) and for the thermometry Eq (2.60) only holds for a homogeneous gas, while the gas in our experimental realization is confined in an external potential. The conceptually most intuitive treatment of the trapped gas, can be obtained by the LDA. Later in this section, we show that corrections beyond the LDA approach can be neglected for the experimentally relevant situations.

In order to derive the density ripple power spectrum within the LDA, let us reintroduce the term $\mathcal{B} = |\int dz e^{iqz} \langle \rho(z) \rangle|^2$, neglected in Eq. 2.41. Applying the free particle propagator \mathcal{B} writes

$$\mathcal{B} = \iint d\alpha dX e^{iqX} \langle \hat{\Psi}_\alpha^+ \hat{\Psi}_{\alpha+qt_f} \rangle \langle \hat{\Psi}_{\alpha+X}^+ \hat{\Psi}_{\alpha+X+qt_f} \rangle. \quad (2.61)$$

Within the quasi-condensate where density fluctuations can be neglected, the field operators in Eq. (2.46) & Eq. (2.61) write

$$\hat{\Psi}_\alpha^+ \hat{\Psi}_{\alpha+qt_f} \hat{\Psi}_{\alpha+X+qt_f}^+ \hat{\Psi}_{\alpha+X} = \sqrt{n_\alpha n_{\alpha+qt_f} n_{\alpha+X+qt_f} n_{\alpha+X}} e^{i(\hat{\theta}_\alpha - \hat{\theta}_{\alpha+qt_f} + \hat{\theta}_{\alpha+X+qt_f} - \hat{\theta}_{\alpha+X})}. \quad (2.62)$$

The density is given by the Thomas-Fermi profile $n_\alpha = n_0(\alpha)$. Collecting Eq. (2.61) & (2.62) one writes:

$$\langle |\tilde{\rho}(q)|^2 \rangle = \iint d\alpha dX e^{iqX} \sqrt{n_\alpha n_{\alpha+qt_f} n_{\alpha+X+qt_f} n_{\alpha+X}} \times \left[\left\langle e^{i(\hat{\theta}_\alpha - \hat{\theta}_{\alpha+qt_f} + \hat{\theta}_{\alpha+X+qt_f} - \hat{\theta}_{\alpha+X})} \right\rangle - \left\langle e^{i(\hat{\theta}_\alpha - \hat{\theta}_{\alpha+qt_f})} \right\rangle \left\langle e^{i(\hat{\theta}_{\alpha+X+qt_f} - \hat{\theta}_{\alpha+X})} \right\rangle \right] \quad (2.63)$$

The LDA assumes that the size of the cloud L is much larger than l_c and additionally we can assume that $\hbar q t_f / m \ll l_c$. This implies that at constant α and for $X \gg l_c$ the second term in Eq. (2.63) vanishes. The density profile $n(z)$ varies only slowly on scales $z \ll L$. As long as we consider wavevectors for which holds $Lq \ll 1$ we can write

$$\langle |\tilde{\rho}(q)|^2 \rangle \simeq \int d\alpha \langle |\rho_{n_0(\alpha)}(q)|^2 \rangle. \quad (2.64)$$

The LDA result of Eq. (2.64) can be used to calculate the density ripple thermometry the power spectrum $\langle \tilde{\rho}(q) \rangle$ in a trap. The numerical result of Eq. (2.60) together

with Eq. (2.64) is shown in Fig. 2.17. The LDA results is also used to calculate the time evolution of $\langle \tilde{\rho}(q) \rangle$ after the interaction quench in the small wavevectors $\hbar q t_f / m \ll l_c$ approximation (see Sec. 3.4).

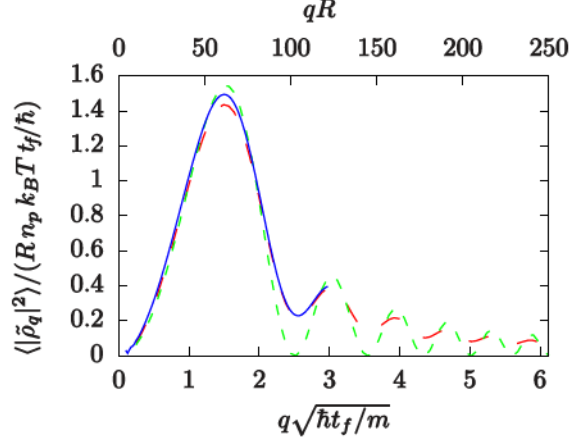


Figure 2.17 – Test of LDA: Density ripple power spectrum calculated for experimentally relevant parameters $l_c/R = 0.2$ and $t_f = 0.015 m l_c^2 / \hbar$, with $l_c = 2\hbar^2 n_p / (m k_B T)$ the correlation length at the center. The blue lines show calculation based on Bogoliubov calculations in trap which show excellent agreement with the LDA calculations in red dashed line. The green dotted line is the small q expansion for $\hbar q t_f \ll l_c m$ which shows similar to Fig. 2.16 a) good agreement up to $qR = 50$.

2.8.1.5 Bogoliubov in a trap

The validity of the LDA can be verified by the Bogoliubov treatment in a harmonic trap with the Legendre-polynomials which was introduced in Sec.1.3.2. Starting from Eq. (2.62) which holds in a trap, one can introduce the expansion of $\theta(z)$ in terms of the orthogonal Legendre polynomials which leads to

$$\langle |\tilde{\rho}(q)|^2 \rangle = \iint_R d\alpha dX \frac{e^{iqX} \sqrt{n_0(\alpha) n_0(\alpha + q t_f) n_0(\alpha + X + q t_f) n_0(\alpha + X)}}{e^{-\frac{1}{2} \sum_\nu \langle p_\nu^2 \rangle (\theta_\nu(\alpha) - \theta_\nu(\alpha + q t_f) + \theta_\nu(\alpha + X + q t_f) - \theta_\nu(\alpha + X))^2}} \quad (2.65)$$

For $\hbar q t_f / m \ll l_c$, the exponential can be expanded in analogy to Eq. (2.48).

For large ν one can use the approximation Eq. (1.87) for which the Legendre-polynomials behave approximately as $\cos((\nu + 1/2)z + \pi/4)$. Under this approximation the density ripple power spectrum $\langle |\tilde{\rho}(q)|^2 \rangle$ (Eq. (2.65)) for a single mode ν is peaked at approximately at $\nu = qR$. This justifies the use of the axis qR which directly indicates the mode $\nu = qR$ with the largest contribution at a given q .

As with the LDA, the Bogoliubov approach with its result Eq. (2.65) can be used to calculate the equilibrium density ripple profile. We use the equilibrium prediction

$\langle p_v^2 \rangle = k_B T / (\hbar \omega_v)$ and the result is shown in Fig. 2.17. For parameters close to the relevant values on the experiment, the Bogoliubov approximation in a trap is in very good agreement with the LDA calculations of Eq. (2.64). Since the integral of the LDA is numerically less demanding, than Bogoliubov calculations in a trap, we will use the LDA Eq. (2.64) together with Eq. (2.60).

2.8.1.6 Imaging system

Experimentally the finite imaging resolution needs to be taken into account. It can be modeled as a Gaussian response function in real space

$$\mathcal{A}(z) = \frac{1}{\sqrt{2\pi\sigma^2}} e^{-\frac{z^2}{2\sigma^2}}. \quad (2.66)$$

The measured density ρ^{meas} is given by the convolution of the real density $\rho^{\text{real}}(z)$ with $\mathcal{A}(z)$. This leads to a multiplication of the theoretical density ripple power spectrum $\langle |\rho(q)|^2 \rangle$ with $e^{-q^2\sigma^2}$.

In principle the imaging resolution was measured with pinholes before installation of the imaging system. We found an imaging response function close to a Gaussian with a resolution of $\sigma = 0.8 \mu\text{m}$. However, one can expect an increase of this value since the atomic cloud expands by a few hundreds microns in the transverse direction during time-of-flight. This is considerable compared to the depth-of-focus along the imaging beam which can be estimated to be on the order of $5 \mu\text{m}$. We thus expect that the effective imaging resolution is larger than the measured value $\sigma = 0.8 \mu\text{m}$. By fitting the experimental density ripple power spectrum with T and σ as free parameters we typically obtain $\sigma \simeq 2 \mu\text{m}$. This value depends on the transverse confinement and slightly larger values are observed for data sets at the highest experimental transverse confinements $\omega_{\perp} / (2\pi) > 6 \text{ kHz}$.

In practice, we also correct for the photon shot-noise which gives a small correction independent of q and which writes:

$$\langle \delta \rho_{\text{shot}}^2 \rangle = \left(\frac{\Delta^2}{\sigma(I)} \right)^2 \sum_y \left(\frac{1}{N_1^{\text{ph}}(y, z)} + \frac{1}{N_2^{\text{ph}}(y, z)} \right). \quad (2.67)$$

In summary: The density ripple thermometry is based on the analytic function in Eq. (2.60) together with the LDA of Eq. (2.64) and the imaging resolution which are used as a fit function with T and σ as free parameters. The density ripple analysis which resolves individual Bogoliubov modes is based on Eq. (2.52) together with the LDA of Eq. (2.64) and the effect of the imaging resolution can be taken into account which will be explained in Sec. 3.4.2.

2.8.1.7 Interactions during time-of-flight

In the previous derivations in this Sec. 2.8.1 it was always assumed that the interactions can be neglected during the time-of-flight. In [94] the effect of interactions during the time-of-flight were estimated. They consider a situation slightly different from the situation studied in this thesis and in the following I will argue that their results can still be used for our experimental data. Their derivation differs in two points our experimental situation: First, they consider the transverse Thomas-Fermi regime ($\mu \gg \hbar\omega_{\perp}$). Our data is in the harmonic oscillator regime $\mu < \hbar\omega_{\perp}$. It can be assumed that interaction effects in the harmonic oscillator regime are smaller than in the Thomas-Fermi regime, making the estimation in [94] an upper bound estimation. Second, they use a Bogoliubov approach (as introduced in 1.3) which assumes small density fluctuations and our clouds develop large density fluctuations during time-of-flight. If we restrict ourselves to small wave vectors, ($q \ll ml_c/(\hbar t_f)$) the density fluctuations stay small²³ and the Bogoliubov procedure still applies. Therefore for small wavevectors we can give the pessimistic correction factor \mathcal{C} which replaces $\langle |\rho(q)|^2 \rangle \rightarrow \langle |\rho(q)|^2 \rangle \mathcal{C}$

$$\mathcal{C} = (\omega_{\perp} t_f)^{-\left(\frac{cq}{\omega_{\perp}}\right)^2}. \quad (2.68)$$

In all experimental situations \mathcal{C} exceeds 0.95 where we used experimentally relevant wavevectors q of Chap. 3 and similar results hold for Chap. 4. This confirms that in the small q zone of $\langle |\rho(q)|^2 \rangle$ interactions are negligible. Taking into account that our calculations for $\langle |\rho(q)|^2 \rangle$ match well our experimental data over the whole q -range (see Fig. 2.16), it can be assumed that interactions during the time-of-flight can be neglected for all wave-vectors q .

2.8.2 Yang-Yang thermometry

As introduced in Sec. 1.2.3.1 the equation of state of the 1D Bose gas with contact interactions is exactly known and can be computed numerically. Using the equation of state, together with the local density approximation in a trap $\mu(z) = \mu_p - V(z)$, it can be used to extract the temperature of the gas [12, 92, 95]. If the potential is known, as it is typically the case for harmonic traps (see below Sec. 2.9), a given mean density profile $n(z)$ can be fitted with μ_p and T as free parameters. For this purpose it is advantageous to tabulate $\mu(n_{YY}, T)$ in the relevant parameter range²⁴ and extrapolate for the fitting purpose.

²³Here $q \ll ml_c/(\hbar t_f)$ should be understood in a stricter sense than in the previous derivation for quantitative results, such that we are in the linear part of the small q expansion in Sec. 2.8.1.2. This range of q is visible in Fig. 2.16 where $\langle |\tilde{\rho}(q)|^2 \rangle$ is linear in q and indeed density fluctuations stay small in this q range.

²⁴Courtesy to Karen Kheruntsyan and Giuseppe Carleo for numerical calculations.

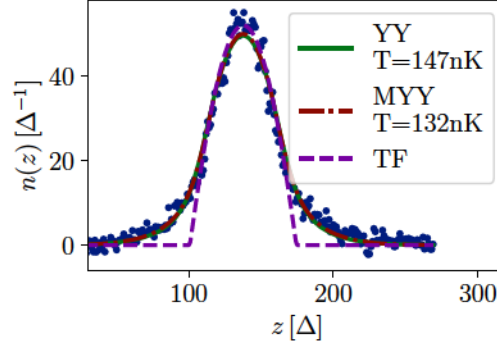


Figure 2.18 – The Yang-Yang thermometry in green compared with the modified Yang-Yang thermometry in red. Both theories fit well the experimental data but lead to different temperatures. For comparison the purple line is the Thomas-Fermi profile (TF).

In the experiment the 1D conditions $k_B T \ll \mu$ is not strictly fulfilled and corrections arising from the transverse excited states should²⁵ be taken into account. The few percent of atoms in the transverse excited states can be treated as ideal Bose gases, with the chemical potential $\mu(j_x, j_y) = \mu - (j_x + j_y)\hbar\omega_\perp$ for the excited states. Here j_x is the j -th excited state in the x direction and j_y respectively. The corresponding equation of state $n_{\text{TE}}(\mu(j), T)$ is given by

$$n_{\text{TE}}(\mu(j), T) = \frac{1}{\lambda_{\text{dB}}} g_{\frac{1}{2}} \left(e^{\frac{\mu(j)}{k_B T}} \right), \quad (2.69)$$

with the de Broglie wave length $\lambda_{\text{dB}} = \sqrt{\frac{2\pi\hbar^2}{mk_B T}}$ and the Bose-Einstein function $g_{\frac{1}{2}}(x) = \sum_{j=0}^{\infty} \frac{x^j}{j^{1/2}}$, also known as the polylogarithm $Li_{1/2}(x)$ [12, 93]. The total linear density is then given by

$$n(\mu, T) = n_{\text{YY}}(\mu, T) + \sum_{j=1}^{\infty} (j+1) n_{\text{TE}}(\mu(j), T), \quad (2.70)$$

with $j = j_x + j_y$. The prefactor $j+1$ takes into account the degeneracy of the excited states. For numerical purposes the sum is typically truncated at $j = 20$.

We typically apply the Yang-Yang thermometry to clouds which are in the quasi-condensate regime at center of the trap and confined in a harmonic trap as shown in Fig. 2.18. In such a situation the temperature obtained from the Yang-Yang thermometry is mainly due to the shape in the wings where the gas is in the ideal Bose gas

²⁵In Chap. 5 these corrections are not taken into account. The theory of Generalized HydroDynamics (GHD) cannot take into account the corrections from the transverse excited state. See Sec. 5.2 for more details.

regime. The central part the profil is dominated by the quasi-condensate equation of state $\mu = gn$ which does not depend on temperature.

The phononic excitation of the Bogoliubov Hamiltonian are mainly confined to the inverse parabola given by the Thomas-Fermi regime. Therefore, the Yang-Yang thermometry is not an adapted thermometry to measure the temperature of the phonons. Experimentally we typically observe different temperature between the Yang-Yang thermometry and the density ripple thermometry (or different thermometries which probe the temperature of the phonons) [22]. See Sec. 4.4.3 for more detail on this observation.

2.8.3 Momentum space distribution

For atomchip experiments with 1D gases it is practically impossible to reach the far field regime by standard time-of-flight techniques. Due to the very shallow confinements in the longitudinal direction of typically a few Hertz, the far field is reached for times and cloud sizes which exceed the typical apparatus parameter. To circumvent this problem pionnering work was performed in Amsterdam with the introduction of the magnetic lensing technique [96, 97]. This technique is now routinely used on our setup [40, 98, 99] with a more detailed description given in [42]. The process resembles the focusing of light with a lens where the lens is replaced by a tight harmonic *kick* potential characterized by ω_{kick} and applied during the a short time t_{kick} . Let us restrict the discussion to classical particles without interactions for the moment: We chose a kick time t_{kick} small enough such that atoms do not move inside the kick potential. This gives the condition $\omega_{\text{kick}} t_{\text{kick}} \ll 1$. The kick potential gives the atoms a velocity proportional to the distance from the center of the trap. Immediately afterwards the confining potentials are switched off and the atoms fall under gravity during a time t_f

$$t_f = \frac{1}{\omega_{\text{kick}}^2 t_{\text{kick}}}. \quad (2.71)$$

The time-of-flight is chosen such that all the atoms collapse at the central position when the initial velocity distribution is neglected. Taking into account the initial velocity distribution the atoms focus in the center of the trap and their spatial distribution is homothetic to the initial velocity distribution as illustrated in Fig. 2.19 a). Interactions during the time-of-flight can typically be neglected due to the fast expansion in the transverse direction which removes interactions almost immediately. In this thesis we typically use a kick potential with $\omega_{\text{kick}}/(2\pi) \simeq 51$ Hz together with a kick time $t_{\text{kick}} \simeq 0.4$ ms which leads to $t_f = 24$ ms. During this time the atoms fall 2.9 mm, for which the imaging system needs to correct its focus position in the horizontal direction (we use the mirror image). This distance is the maximal distance for which we are currently able to adapt the focus. The resolution of the measurement in

momentum space is given by $\Delta_v = \Delta/(t_f) \simeq 73 \mu\text{m/s}$, depending on the precise value of t_f .

The momentum focusing can be disturbed by several reasons, whose effects are discussed in detail in [42]. Experimentally the condition $\omega_{\text{kick}} t_{\text{kick}} \ll 1$ is not always well fulfilled and corrections to Eq. (2.71) need to be taken into account. Additionally interactions during the kick can play a role. It can be however shown with the scaling approach that for $\omega_{\parallel} t_{\text{kick}} \ll 1$ interactions are negligible. Additionally anharmonicities in the kick potential needs to be minimized.

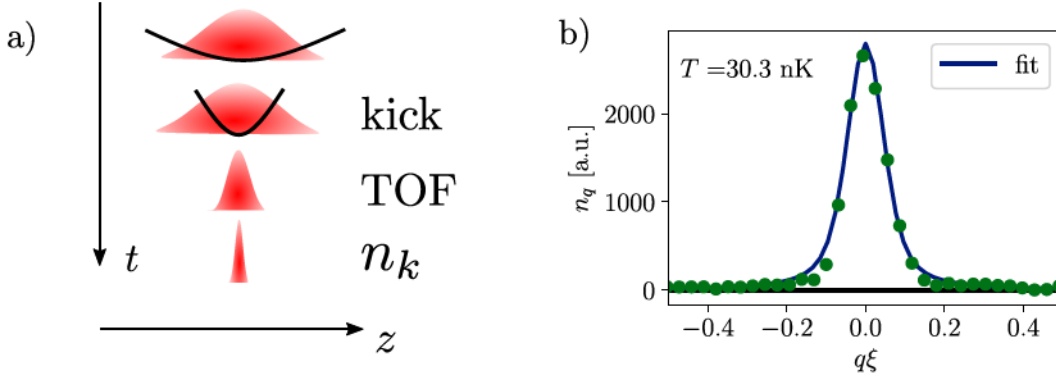


Figure 2.19 – a) Scheme of the momentum focus technique. b) Experimental momentum distribution together with a fit (green) taking into account the imaging response function and the LDA (see Eq. (2.73)). This leads to a temperature $T = 30.3 \text{ nK}$.

Comparison with theory The theoretical momentum distribution can be calculated by the Fourier transform of the one-body function correlation $g_1(z)$. Inside the quasi-condensate²⁶ at equilibrium and in a homogeneous system (see Eq. (1.81)) this corresponds to a Lorentzian of Full Width Half Maximum (FWHM) $2/l_c$.

$$n_q \propto \frac{1/l_c}{q^2 + 1/l_c^2}, \quad (2.72)$$

where $l_c = \frac{2\hbar^2 n_0}{mk_B T}$. Inside a trapping potential it can be calculated numerically with the LDA and we obtain:

$$n_q \propto \int_R^{-R} dz \frac{1/l_c(z)}{q^2 + 1/l_c^2(z)} n(z). \quad (2.73)$$

For comparison with the experiment, we convolute with a Gaussian of width σ_q , to mimic the imaging response function, as shown in Fig. 2.19 b) in blue. For very cold

²⁶For different regimes see [42]

clouds, for which l_c is large, the bulk of n_q is dominated by effects of the resolution and the fits gives a good estimation of σ_q . The values of σ_q corresponds to a width in real space $\sigma = 2\mu\text{m}$ (see Fig. 2.19 b)), in agreement with the value obtained from the density ripple analysis. The temperature can be compared with the temperature obtained from the density ripple analysis which agrees up to 20%, while both methods are sensitive to slightly different wave vectors. For comparison, the corresponding density ripple spectrum to Fig. 2.19 b) is peaked around $q\xi \approx 0.05$.

2.8.4 Comment about temperature measurements in the system

With our setup we are able to probe the temperature of the system with different methods (density ripples analysis, momentum focusing and Yang-Yang thermometry) and these methods not necessarily lead to the same values of the temperature [22, 36]. This is less surprising when considering that the 1D system is an integrable system. The equilibrium state of an integrable system is not described by a thermal equilibrium, but by a more general equilibrium (see Sec. 3.1 for a more detailed discussion). In our setup the fit of the profile with the Yang-Yang equation of state typically leads to higher values than the temperature obtained from the density ripple analysis or the momentum focusing technique. This is probably due to the preparation process [22, 59] but further investigation is needed. More details about this phenomenon are also discussed in Sec. 4.4.3.

2.9 Parameter calibration

Longitudinal trapping frequency In the case of a harmonic trapping potential its trapping frequency can be measured directly by a displacement of trap center and the recording of the subsequent oscillations of the center of mass around the potential minimum as shown in Fig. 2.20 a).

Transverse trapping frequency In the transverse direction the trap center cannot be easily displaced due to the three-wire geometry (see Sec. 2.3.1.2). To circumvent this problem we use a parametric heating process to measure the trap frequency f_{\perp} . The trap frequency can be modulated at a frequency f_{para} by modulating the amplitude of the AC-current with an additional signal generator

$$I = [I_0 + \Delta I \cos(2\pi f_{\text{para}} t)] \cos(\omega_{\text{mod}} t). \quad (2.74)$$

This leads to resonances at $f_{\text{para}} = 2nf_{\perp}$ where atoms are excited to higher motional states. The observable signal consists in a broadening of the atomic cloud in the transverse direction after a short time-of-flight. Equivalently, one can observe the

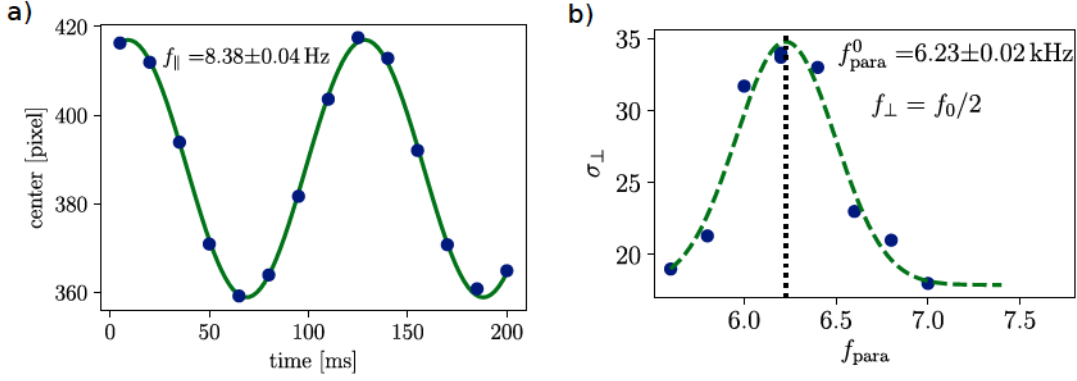


Figure 2.20 – a) Oscillation of the center of mass together with its sinusoidal fit. b) First resonance of the parametric heating. The transverse width σ_{\perp} after a short time of flight $t_f = 8$ ms is obtained from a Gaussian fit. The center frequency f_{para}^0 leads to $f_{\perp} = 3.1$ kHz where the dashed line corresponds to a Gaussian fit for guidance.

atom losses due to spill-overs. We typically used about 10 oscillations of the parametric heating signal with an amplitude $\delta I/I \simeq 10\%$. This method also allowed the verification of the $f_{\perp} \propto I$ dependence (see Eq. (2.7)) which was better than 1%.

Comment about uncertainties All the published scientific results in this thesis solely depend on the values $n(z)$, f_{\perp} , f_{\parallel} and the measured times. The uncertainties on the time is very small due to the technological standards of the clocks which are integrated in the hardware control. Its precision can be independently verified with a very high precision. The statistical error for f_{\perp} and f_{\parallel} is very low ($< 1\%$ see Figure 2.20). And the statistical uncertainty in $n(z)$ can easily be reduced by averaging over several runs. The estimation of the systematic error for $n(z)$, f_{\perp} and f_{\parallel} is much more tricky, since no independent measurement method is accessible within a reasonable amount of work and reasonable precision²⁷. At the same time we expect the systematic error to dominate over the statistic error. There exists however an indirect method to verify the consistency of our parameters. In the quasi-condensate regime, the shape of the cloud can be predicted by the Thomas-Fermi approximation (see Sec. 1.3.2), starting from the values of f_{\parallel} , f_{\perp} and the peak density n_p . In Fig. 2.14 b) the cloud shape and the Thomas-Fermi approximation is plotted with a high agreement. One could deduce error estimations from the atomic shapes which would lead to strong correlations between the uncertainties and we therefore decided to publish

²⁷ f_{\perp} can be calculated from Eq. (2.7), however at the current situation no precise knowledge of the exact parameters is available.

the values without error estimations²⁸. Further indication that the statistical error is not the dominant contribution can be recovered from the results in Chap. 3 and Chap. 4. If one assumes that the theoretical models are correct, the statistical uncertainty is much too small to explain the deviation from the theoretical results²⁹. This indicates that further systematic errors should come into play. In general it can be said that the systematic errors are expected to be of the order of a few percent.

Summary:

- We use an atomchip setup to create clouds of ^{87}Rb which are strongly confined in two dimensions. This allows to create 1D clouds inside the quasi-condensate regime.
- The modulated guide technique eliminates the problem of wire roughness and allows for an independent control of the longitudinal and transverse directions. In the longitudinal direction we can control the first terms of the Taylor expansion $V(z) = \sum_{i=1}^4 a_i z^i$.
- The density ripple analysis allows to access individual Bogoliubov modes and to obtain the phonon temperature

²⁸Another indirect verification method for the atomic density $n(z)$ can be obtained by verifying that the cross-section is independent of the atom number [71].

²⁹See for example the statistical error bars in Fig. 3.5 b) or in Fig. 4.10 where the errorbars for $\omega_{\perp}/(2\pi) = 1.6\text{kHz}$ would be too small to be visible.

Chapter 3

Interaction quench

This chapter first introduces the concept of quenches in isolated many-body quantum systems. It then focuses on an interaction quench in a 1D Bose gas and introduces its description in the quasi-condensate regime. I will present two experimental methods to study the dynamics generated by an interaction quench. The first one analyzes the evolution of momentum distribution which undergoes relaxation towards a thermal distribution. The second one uses the density ripple analysis which allows to access individual Bogoliubov modes. We show that the observed dynamics of the Bogoliubov modes continues for times longer than the thermalization time of the momentum distribution. These results are published in [18]. Finally, I will discuss the difficulties of observing recurrences in 1D Bose gases in a harmonic trap which indicates the presence of a damping of the Bogoliubov modes due to non-linear coupling between modes.

3.1 Quenches in integrable systems

Before introducing the work published in [18], I give a short motivation and overview of quenches in isolated quantum systems. It is a basic assumption in statistical physics that after some short time t_{relax} a macroscopic system can be described by a few thermodynamic quantities and two systems described by the same thermodynamic quantities differ only by microscopic fluctuations. In classical mechanics, this property arises from the ergodicity of the system which ensures that the system can explore the whole configuration space and remove the memory of the initial state. After t_{relax} the fundamental postulate of statistical mechanics becomes true: The system is with equal probability in any accessible microstate. For an isolated quantum system the situation is more complicated. For example consider an eigenstate $|\Psi_i\rangle$ of the Hamiltonian \hat{H} . Then, the system will stay under the unitary evolution of the \hat{H} in exactly the same state; up to an irrelevant phase factor $e^{-i\omega_i t}$. This situation clearly

differs from an evolution towards a statistical ensemble.

The thermalization of an isolated many-body-quantum system is one of the key questions in the field of out-of-equilibrium dynamics. Motivated by advances in recent years, mainly in the field of cold atom experiments [100–108], theoretical research was stimulated¹. The sudden quench is thereby one of the standard setups, on which we will focus in the following. The system is prepared in the initial density matrix $\hat{\rho}_0$ (or state $|\Psi_0\rangle$). At $t = 0$ the system is brought out-of-equilibrium by sudden change of a Hamiltonian parameter and time evolved with the new Hamiltonian \hat{H}'

$$\hat{\rho}(t) = e^{-i\frac{t}{\hbar}\hat{H}'}\hat{\rho}_0e^{i\frac{t}{\hbar}\hat{H}'}. \quad (3.1)$$

The thermalization of the system is typically defined by the expectation values of a physical² variable $\langle\hat{A}\rangle$. The system thermalizes if the expectation value tends in the long time limit towards

$$\langle\Psi(t)|\hat{A}|\Psi(t)\rangle \xrightarrow{t\rightarrow\infty} \text{Tr}(\hat{\rho}_{\text{Gibbs}}\hat{A}), \quad (3.2)$$

with $\hat{\rho}_{\text{Gibbs}} = \exp(-\beta\hat{H}')/\text{Tr}(\exp(-\beta\hat{H}'))$, the density matrix predicted from statistical mechanics.

Non-integrable systems For non-integrable systems it is widely assumed that the Eigenstate Thermalization Hypothesis (ETH) explains why the system can be described in the long-time limit by equilibrium statistical mechanics [109, 115]. The time evolution of Eq. (3.2) can be written explicitly in the energy eigenbasis $|i\rangle$ with eigenvalue $\hbar\omega_i$:

$$\langle\Psi(t)|\hat{A}|\Psi(t)\rangle = \sum_{i,j} \langle\Psi(0)|i\rangle\langle j|\Psi(0)\rangle\langle i|\hat{A}|j\rangle e^{i(\omega_i-\omega_j)t}. \quad (3.3)$$

In the long time limit the phase factor averages out for $i \neq j$ which leads to

$$\langle\Psi(t)|\hat{A}|\Psi(t)\rangle \underset{t\rightarrow\infty}{\simeq} \sum_i |\langle\Psi(0)|i\rangle|^2 \langle i|\hat{A}|i\rangle. \quad (3.4)$$

ETH predicts that the expectation value of \hat{A} in state $|i\rangle$ only depends on the energy $E_i = \hbar\omega_i$

$$\langle i|A|i\rangle = \langle A\rangle_{E_i} \quad (3.5)$$

where the microcanonical average $\langle A\rangle_E$ at energy E is the average over of all states inside a small shell $E, E + \Delta E$

$$\langle\hat{A}\rangle_E = \frac{1}{\mathcal{N}} \sum_{E' \in [E, E+\Delta E]} \langle E'|\hat{A}|E'\rangle. \quad (3.6)$$

¹There exists a large number of theoretical studies with some of the most prominent results [109–111] and the reviews [112–114] to cite a few.

² \hat{A} should be local or a few-body observable.

Eq. (3.5) can be interpreted as follows: The expectation value of an operator is almost independent of the details of the state and only depends on the energy of the state. This is the ETH statement. Note that no general proof of ETH exists, and mainly numerical evidence was found [111]. In the thermodynamic limit the microcanonical and canonical ensemble are equivalent and if the initial coefficients $\langle \Psi(0)|i \rangle$ are sufficiently narrow in energy the system evolves towards the thermal Gibbs state of Eq. (3.2).

Integrable systems and generalized eigenstate hypothesis In an integrable system ETH is not valid. This can be illustrated with the example of the trivial integrable model of a non-interacting gas and the observation of the momentum distribution $\hat{n}(p)$. Two momentum distributions can share the same energy $E = \int \hat{n}(p)p^2/(2m)$ and at the same time their expectation values $\langle \hat{n}(p) \rangle$ can be very different. In an integrable systems ETH can be naturally extended to the Generalized Eigenstate Thermalization Hypothesis (GETH). GETH assumes that the expectation value of $\langle \hat{A} \rangle$ not only depends on the energy, but on the expectation values of the conserved quantities³ $Q_i = \langle \hat{Q}_i \rangle$. The expectation value of Eq. (3.6) in the generalized microcanonical ensemble becomes

$$\langle i|A|i \rangle = \frac{1}{\mathcal{N}} \sum_{|s\rangle, \langle s|\hat{Q}_i|s\rangle \in \{Q_i + \delta Q_i\}} \langle s|\hat{A}|s \rangle. \quad (3.7)$$

The sum runs over all states $|s\rangle$ whose quantum numbers $\langle s|\hat{Q}_i|s \rangle$ fall in a narrow range around Q_i . All the states which share the same $\{Q_i\}$, within a narrow range, also share the same expectation values of \hat{A} . Each of those states can be described by some representative state $|s\rangle$. Equivalently this state can be characterized by the General Gibbs Ensemble (GGE) density matrix.

$$\hat{\rho}_{\text{GGE}} = \frac{1}{Z} \exp\left(-\sum_i \beta_i \hat{Q}_i\right), \quad (3.8)$$

with the Lagrange multipliers β_i imposed by the initial conditions and the partition function $Z = \text{Tr}[\exp(-\sum_i \beta_i \hat{Q}_i)]$. One typically chooses the first Lagrange multiplier to be the inverse temperature $\beta_0 = k_B T$ with the conserved quantity $\hat{Q}_0 = \hat{H}$ [116]. Experimentally a GGE was observed in [117].

Nearly integrable system A nearly integrable system is a system composed of a Hamiltonian $\hat{H} = \hat{H}_0 + \epsilon \hat{H}_1$ where \hat{H}_0 is integrable and $\epsilon \hat{H}_1$ a small non-integrable

³Note that the definition of the \hat{Q}_i is not trivial. All hermitian Hamiltonian posses a maximum set of independent commuting operators $\{\hat{Q}_i\}$. The choice of the meaningful set of $\{Q_i\}$ is very important [3].

perturbation with $\epsilon \ll 1$. In such a situation a prethermalized state is expected to occur [118–121]. The dynamics at the beginning is mainly governed by the almost conserved quantities and a non-thermal stationary state appears which is increasingly long-lived with ϵ approaching zero. At very long times the non-integrable part, can lead to a thermalization. Experimentally non-integrable perturbations are always present. Some examples are the excited states in the transverse direction, the coupling to the environment and the longitudinal trapping potential $V_{\parallel}(z)$.

Lieb-Liniger Within the class of integrable models the Lieb-Liniger model constitutes one of the paradigmatic models studied by theoreticians and the study of the quench dynamics in the Lieb-Liniger model attracts a lot of interest [122–132]. As previously stated, it is expected that the system relaxes towards a representative state which in the Lieb-Liniger model can be characterized by the quasi-momentum distribution $\rho_p(k)$.

On the experimental side, I specially want to highlight the result of the Vienna group [103] which observed a light-cone-like behavior in a similar system. This light-cone effect in the quasi-condensate regime will be described in detail in Sec. 3.2.1. Furthermore, quenches in integrable models have been studied in [133].

3.2 The Experiment

In this chapter we investigate the dynamics generated by an interaction quench. We prepare a few thousands to ten thousands of atoms in the quasi-condensate regime with $\omega_{\perp}/(2\pi) = 1.5\text{kHz}$ or 3.1kHz , depending on the data set and $\omega_{\parallel} = 8.5\text{Hz}$. We first increase the RF frequency by about 60kHz , to provide a shielding for three-body collisions residues and then let the system relax for about 150ms . Then, we perform a sudden quench of the interaction parameter g from its initial value g_i , to its final value $g_f = g_i(1 + \kappa)$, as depicted in Fig. 3.1 a) where κ is the so called *quench strength*. The interaction parameter g is directly proportional to the transverse trapping frequency ω_{\perp} , itself being proportional to the current I_0 in the modulated guide (see Eq. (2.7)). The interaction quench is performed by a linear current ramp during t_r , during which g changes from g_i to g_f (see Fig. 3.1a)) The change of g needs to be fast compared to the relevant longitudinal time scales $1/\omega_q \simeq 10\text{ms}$ and slow compared to the transverse time scales, such that no transverse excitation occur. Considering the transverse confinement, the process needs to be slower than $t_r \gg \Delta\omega_{\perp}/\omega_{\perp}^2$ to fulfill the adiabaticity condition for a linear ramp in ω_{\perp} . The Schrödinger equation for a linear ramp in g leads to an analytic solutions in term of the Airy functions. Numerical evaluation of these solutions show that the excitation to higher levels are less than a few percent in all the experimental situations ($t_r = 0.7\text{ms}$). Experimentally we could not observe any excitation to higher levels.

The longitudinal confinement The longitudinal trapping potential is always harmonic in this chapter. We created the longitudinal confinement $V_{\parallel} = \frac{1}{2}m\omega_{\parallel}^2 z^2$, by using the D_1 & D_2 chip wires (see Sec. 2.3.2.1 and Fig. A.2). The interaction quench modifies g which changes the equilibrium Thomas-Fermi profile. In order to maintain the same equilibrium profile, we modify the longitudinal trapping potential simultaneously to the interaction quench⁴. We adapt the longitudinal trapping frequency such that the Thomas-Fermi profile stays constant during the quench. This implies that the final trapping frequency ω_{\parallel} is given by:

$$\omega_{\parallel}^f = \sqrt{1 + \kappa} \omega_{\parallel}^i. \quad (3.9)$$

This is obtained by a linear current ramp in the longitudinal wires from the corresponding initial to the final currents. Since ω_{\parallel} is not proportional to $I_{1/2}$, in principal the profile is not at equilibrium during the ramp. For fast ramps ($t_r \ll 1/\omega_{\parallel}$) longitudinal excitation can be neglected which was experimentally verified.

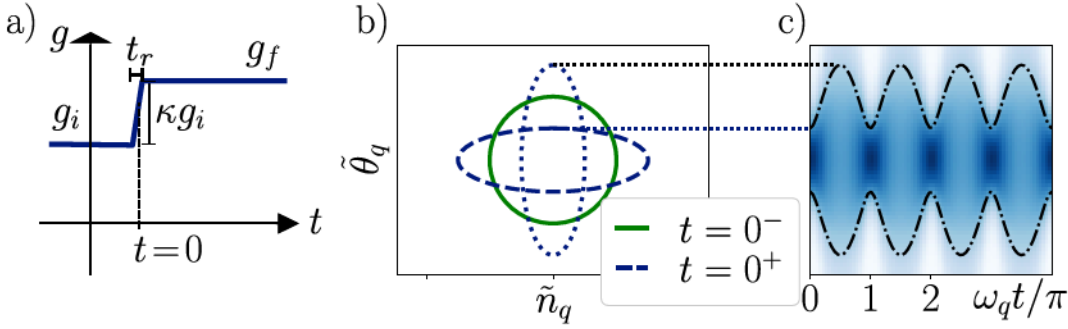


Figure 3.1 – The interaction quench: a) Scheme of the quench ramp for g for a ramp of amplitude κ and length t_r . b) The Gaussian phase space distribution before the quench ($t = 0^-$), immediately after the quench ($t = 0^+$) and after an evolution time $\omega_q t = \pi/2$. c) Probability distribution for $\kappa = 3$ with the subsequent breathing phenomena, the color represents the phase space distribution. The dashed line corresponds to a constant probability.

In Sec. 3.3.2 I present the observation after an interaction quench in momentum space and in Sec. 3.4 the observation by the density ripple analysis. Before discussing the experimental results I introduce the theoretical description of the evolution after an interaction quench inside the quasi-condensate regime.

⁴Without the modification of the longitudinal trap, we would strongly excite the breathing mode, whose physics has already been studied in detail in [98, 134].

3.2.1 Interaction quench in the quasi-condensate regime

For the theoretical description of the interaction quench I start with the conceptually simpler situation of a homogeneous system and an instantaneous quench $t_r = 0$. The Bogoliubov Hamiltonian for a given mode writes

$$H_q = A_q n_q^2 + B_q \theta_q^2 = \hbar \omega_q \left(\frac{\tilde{n}_q^2}{2} + \frac{\tilde{\theta}_q^2}{2} \right) \quad (3.10)$$

where we introduced a symmetric form with the reduced variables $\tilde{n}_q = n_q (A_q/B_q)^{1/4}$ and $\tilde{\theta}_q = \theta_q (B_q/A_q)^{1/4}$. For this chapter, we restrict ourselves to phononic excitations $q \ll \xi^{-1}$ and take into account high density effects, such that $A_q = mc^2/(2n_0)$ and $B_q = \hbar^2 q^2 n_0/(2m)$ as introduced in Sec. 1.3.3.

Wigner function For each mode q , the system can be described by a Wigner function as introduced in Sec. 1.3.1.1. Prior to the quench, the system is at thermal equilibrium. The Wigner function is an isotropic Gaussian in the $(\tilde{\theta}_q, \tilde{n}_q)$ -plane as depicted in Fig. 3.1 b) in green. The energy is equally distributed between the two quadratures such that the equipartition theorem holds. For the considered high energies $E_q \gg \hbar \omega_q$ we can relate the initial energy to the initial temperature T :

$$\frac{k_B T}{2} = A_q \langle n_q^2 \rangle = B_q \langle \theta_q^2 \rangle. \quad (3.11)$$

The instantaneous quench only effects A_q , while n_q and θ_q cannot follow. This leads to a squeezing of the Gaussian state⁵ in the $\tilde{\theta}_q$ direction and the variances become $\langle \tilde{\theta}_q^2 \rangle_{t=0^+} = \langle \tilde{\theta}_q^2 \rangle_{t=0^-} / (1 + \kappa)^{1/2}$ and $\langle \tilde{n}_q^2 \rangle_{t=0^+} = \langle \tilde{n}_q^2 \rangle_{t=0^-} (1 + \kappa)^{1/2}$. The anti-squeezing in the \tilde{n}_q direction is compensated by the squeezing in the $\tilde{\theta}_q$ direction. This ensures the preservation of the phase space density. The subsequent time evolution is a rotation in phase space with frequency $\omega_q = cq$. Looking at the θ_q component this leads to:

$$\langle \theta_q^2 \rangle = \langle \theta_q^2 \rangle_i [1 + \kappa \sin^2(cqt)]. \quad (3.12)$$

For a thermal state the initial value is given by $\langle \theta_q^2 \rangle_i = mk_B T / (\hbar^2 q^2 n_0)$. Eq. (3.12) is the main theoretical prediction of this chapter and I will describe its experimental observation in Sec. 3.4. Before discussing the observation of the squeezed Bogoliubov modes I introduce the effect on the one-body correlation function of the interaction quench. Thereby, I show that the one-body correlation function cannot be used to observe the squeezed Bogoliubov modes.

⁵The word *squeezing* should not be interpreted in the quantum sense where one of the quadrature obtains a width smaller than the ground state value. Although the presented equations apply for a quantum squeezing, we do not observe a quantum squeezing in these experiments.

3.3 Momentum space

The effect of the quench can be observed in momentum space. The momentum distribution is the Fourier transform of the one-body correlation function $g_1(z)$. The $g_1(z)$ function shows a characteristic light-cone phenomena which I derive in the following.

3.3.1 Light-cone like effect on the one-body correlation function

As introduced in Sec. 1.3, the one-body correlation at equilibrium writes

$$g_1(z) = n_0 e^{-\frac{1}{2}\langle[\theta(z)-\theta(0)]^2\rangle} = n_0 e^{-\frac{|z|}{l_c}}, \quad (3.13)$$

where $l_c = \frac{2\hbar^2 n_0}{mk_B T}$. In the derivation we used Wick's theorem. The use of Wick's theorem stays valid after the interaction quench, since the squeezing preserves the Gaussian nature of θ . The time evolution after the interaction quench can be calculated from $[\theta(z) - \theta(0)]^2$. In Eq. (1.80) we derived

$$\langle[\theta(z) - \theta(0)]^2\rangle = 4 \int_0^\infty \frac{dq}{2\pi} \langle\theta_q^2\rangle (1 - \cos(qz)). \quad (3.14)$$

Instead of using the equilibrium equation for $\langle\theta_q^2\rangle$, we inject the evolution of $\langle\theta_q^2\rangle$ according to Eq. (3.12) and obtain from integration

$$g_1(z, t) = \begin{cases} n_0 e^{-|z|\frac{\kappa+2}{2l_c}} & z < 2ct \\ n_0 e^{-|z|/l_c} & z > 2ct. \end{cases} \quad (3.15)$$

This behavior can be understood as a light-cone phenomena⁶ where quasi-particles travel with the speed of sound of the system and establish a new equilibrium situations for all distances $z < 2ct$. The new equilibrium situation is characterized by a new correlation length $l_c^f = 2l_c/(\kappa + 2)$. For distances larger than $2ct$ the system is still described by the initial equilibrium behavior with $g_1(z) = n_0 e^{-|z|/l_c}$. Fig. 3.2 a) shows the g_1 function for different times after the quench. At $z = 2ct$ a kink is visible. The kink travels in space with at the position $z = 2ct$. This light-cone phenomena reflects the ongoing out-of-equilibrium dynamics of the Bogoliubov modes. For practical purposes, the out-of-equilibrium dynamics becomes exponentially suppressed in

⁶Let me stress out, that the use of the word *light-cone*, does not refer to the Lieb-Robinson bound [135] which in principle only applies to finite dimensional Hilbert spaces, although extension to continuous systems exists [136]. Here, the word light-cone refers to the concept, borrowed from special relativity where particles travel with the speed of light and the speed of light is replaced by the speed of sound of the system.

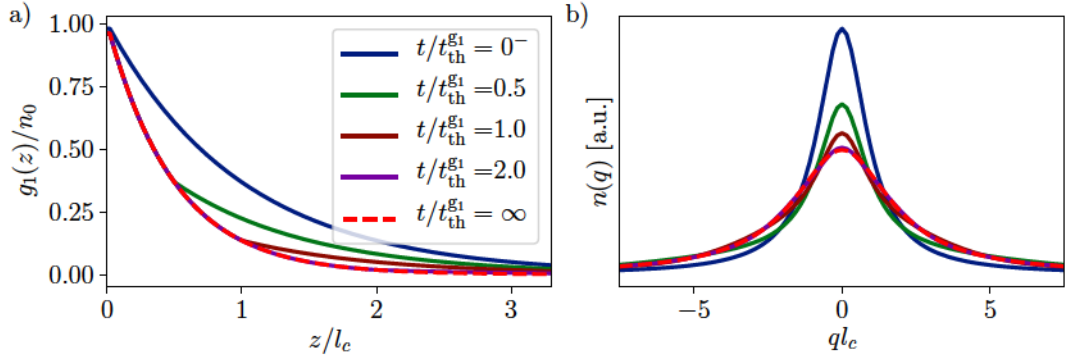


Figure 3.2 – The light-cone like effect in a homogeneous system for the $g_1(z)$ function shown in a) and its effect on the normalized momentum distribution shown in b). The color codes for different times are the same in a) and b). Prior to the quench the equilibrium $g_1(z)$ function, shows an exponential decay characterized by l_c . The subsequent time evolution after the quench leads to a new exponential decay characterized by $l_c^f = 2l_c/(\kappa + 2)$ for distance smaller than $2ct$, while the prequench characteristic decay survives for length exceeding $2ct$. For times larger than a few $t_{th}^{g_1}$, the g_1 function has essentially reached its new steady-state form. Already for $t/t_{th}^{g_1} = 2$ no difference with the long-time limit is visible.

time which is characterized by the thermalization time of the g_1 function $t_{th}^{g_1} = l_c^f/c$. For $t = \infty$ the g_1 function corresponds to an exponential decay. From the relation $l_c = 2\hbar^2 n_0/mk_B T$ one could associated a new temperature $T_f = T_i(\kappa + 2)/2$ to the exponentially decaying g_1 function where T_i is the initial temperature. This new thermal behavior of the one-body correlation function does not reflect a thermal equilibrium situation. The underlying Bogoliubov modes continue undamped oscillations as predicted by Eq. (3.12). As shown in Fig. 3.2 a) already for $t = 2t_{th}^{g_1}$ essentially no difference with the long-time limit is visible. The screening of the out-of-equilibrium dynamics mathematically arises from the sum over all modes q which is taken in Eq. (3.15) and which makes the oscillations of the Bogoliubov nontransparent in the g_1 function. When looking in momentum space – given by the Fourier transform of g_1 – the situation gets more complicated. The light-cone phenomena is not directly transparent as it is shown in Fig. 3.2 b).

This illustrates the fact that the observation of a non-equilibrium dynamics can strongly depend on the choice of the observable. In the following Sec. 3.3.2 I will present this thermalization-like behavior of the one-body-correlation function by experimentally accessing the momentum distribution.

3.3.1.1 Relation to the Vienna experiment

The light-cone like dynamics of the one-body correlation function was first observed in the Vienna group [103] in a similar system. The authors used a 1D quasi-condensate and split it into two uncoupled copies. By introducing the phase and the density fluctuation of the two condensates $\theta_{1/2}$, $\delta n_{1/2}(z)$, it can be shown that the dynamics of the relative variables

$$\theta(z) = \theta_1(z) - \theta_2(z) \quad \text{and} \quad \delta n(z) = \frac{1}{2} [\delta n_1(z) - \delta n_2(z)] \quad (3.16)$$

is governed in the linearized approximation by the Bogoliubov Hamiltonian for phononic excitations [137]:

$$H_q = g n_q^2 + \frac{\hbar^2 q^2 n_0}{4m} \theta_q^2. \quad (3.17)$$

This corresponds to the Bogoliubov Hamiltonian of Eq. (1.66) with a factor 2 difference in A_q . The definition of the Fourier coefficients follows the definition for the single 1D gas. At $t = 0$ the quasi-condensate is split into two identical copies. Initially, the phases of the two quasi-condensates are identical and the initial fluctuations of the relative phase is zero⁷. Density fluctuations are created by the Poissonian noise $\langle \delta N_1^2 \rangle = \langle N_1 \rangle$ associated to the splitting process. Thus the splitting corresponds to the creation of a squeezed state, as described in Sec. 3.2.1.

The authors of [103] access the phase correlation function of the relative phase

$$C(z, z') = \langle \cos(\theta(z) - \theta(z')) \rangle. \quad (3.18)$$

For small density fluctuations and Gaussian states $C(z, z')$ is equal to

$$C(z, z') = e^{-\frac{1}{2} \langle [\theta(z) - \theta(z')]^2 \rangle} \quad (3.19)$$

which corresponds to the normalized one-body correlation function. Eq. 3.19 can be calculated with the same arguments as in Sec. 3.3.1, resulting in the same light-cone phenomenon. The splitting can thus be interpreted as an interaction quench from $g_i = 0$ to the final value g_f of the 1D Bose gas. This light cone-phenomena was experimentally observed in [103].

3.3.2 Experimental observation in momentum space

In this Section I experimentally study the evolution of the momentum distribution after the interaction quench. This study is a complementary study which highlights

⁷Corrections from the Heisenberg uncertainty relation, as well as experimental imperfections are neglected.

the theoretical arguments which were presented in our article [18] and in the previous Sec. 3.3.1. We use the momentum focusing technique as introduced in Sec. 2.8.3 to measure the momentum distribution n_q . Fig. 3.3 shows the experimental momentum distribution prior the quench and its post-quench evolution. In order to compare with the theoretical predictions, we calculate the momentum distribution via the Fourier transform of the one-body correlation function. We use the prediction for light-cone phenomena on the g_1 function in Eq. (3.15) and apply the LDA together with the convolution of the imaging response function. We fit the initial equilibrium distribution to obtain the temperature of the cloud. We compare in Fig 3.3 a) the experimental data to the theoretical time evolution of the momentum distribution. The asymptotic limit is expected to correspond to a new equilibrium shape of the momentum distribution with $T_f/T_i = (\kappa + 2)/2$. We fit the steady state distribution with the equilibrium prediction and obtain the final temperatures T_f . The inset of Fig. 3.3 b) shows T_f for different κ .

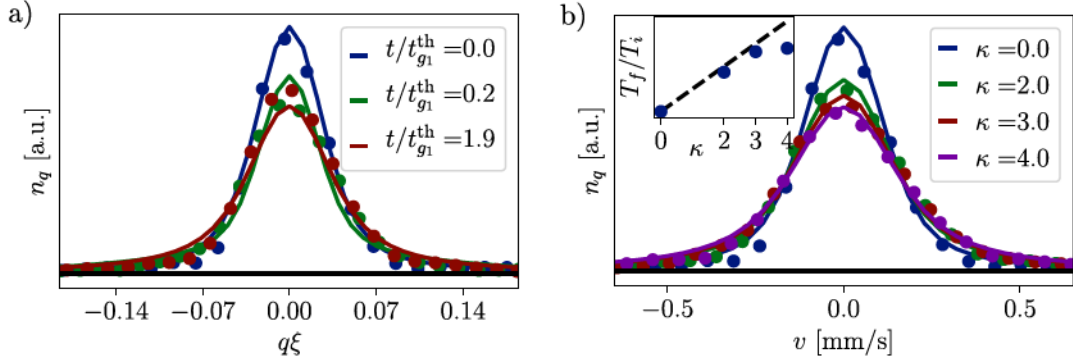


Figure 3.3 – The effect of the quench on the experimental normalized momentum distribution n_q . The equilibrium distribution in blue, is fitted with the temperature and the width of the imaging resolution as a free parameter. We obtain a temperature $T = 30$ nK, which corresponds to $k_B T / (g n_p) = 0.51$

a) The time evolution after a quench with $\kappa = 2$. As expected, the light-cone dynamics is difficult to observe. As shown in Fig. 3.2 for $t/t_{g_1}^{\text{th}} \simeq 2$, the long time limit is essentially reached. The theoretical prediction are the Fourier transform of Eq. (3.2) together with the LDA and a convolution of the imaging resolution.

b) The long time distribution ($t > 4.5 t_{\text{th}}^{g_1}$) for different quench strengths κ . The asymptotic limit is expected to correspond to a new equilibrium shape of the momentum distribution. The solid lines are fits of the equilibrium situation with the temperature T_f as a free parameter. The inset shows the fitting results T_f/T_i , compared with its theoretical prediction $T_f/T_i = (\kappa + 2)/2$.

As expected the momentum distribution n_q reaches a steady state, while the dy-

namics towards the steady state is barely resolved. This is related to a technical problem of the momentum focusing technique. The thermalization-like behavior of the g_1 -function is of the order of $t_{\text{th}}^{g_1} \simeq 1$ ms for typical samples. Such a fast dynamics cannot be followed by the momentum focusing technique. The momentum focusing technique contains the application of a short kick-potential which typically takes half a millisecond. The momentum focusing technique can still be used to access the asymptotic limit after the quench, as the experimental data in Fig. 3.3 b) shows.

3.4 Density ripple analysis

3.4.1 Squeezed Bogoliubov modes

The previous study of the post quench dynamics in momentum space, could not reveal the dynamics of the Bogoliubov modes. First, due to technical reasons the light-cone dynamics was not resolved. Second, even with an access to the light-cone phenomena – as obtained in [103] – the underlying dynamics becomes exponentially suppressed at long times. In order to reveal the ongoing dynamics of the Bogoliubov modes, we use the density ripple analysis and the results of this study can also be found in [18]. As introduced in Sec. 2.8.1.2 the density ripple analysis gives access to the phase quadrature $\langle \theta_q^2 \rangle$ of the Bogoliubov modes, from which we reveal the oscillatory behavior of $\langle \theta_q^2 \rangle$ as predicted in Eq. (3.12). For practical purposes we introduce the quantity $J(q, \tau) = \frac{\langle |\tilde{\rho}(q)|^2 \rangle}{\langle |\tilde{\rho}(q)|^2 \rangle_i}$ where $\langle |\tilde{\rho}(q)|^2 \rangle_i$ is the initial density ripple power spectrum at $t = 0$. The reduced time is given by $\tau = cq$ and the speed of sound c is calculated at the center of the trap. For a homogeneous system the quantity $J(q, \tau)$ oscillates as

$$J(q, \tau) = 1 + \kappa \sin^2(\tau), \quad (3.20)$$

which is independent of q .

Before introducing the experimental observation of the oscillatory behavior of Eq. 3.20 let me introduce two theoretical refinements to our model: the swelling of the transverse wavefunction due to high densities and the longitudinal trapping potential. Those effects are important for a quantitative comparison but do not change the overall picture of creation of squeezed collective excitations by the interaction quench.

Swelling of the transverse wavefunction Due to the high linear densities⁸ $na_{3D} \sim 1$, 3D correction arise from the swelling of the transverse ground state. In the Appendix of our paper [18] these corrections are calculated explicitly for a harmonic

⁸Sec. 3.4.4 justifies the use of such high densities.

trap. The speed of sound and the density is calculated with the modified equation of state $\mu(n) = \hbar\omega_{\perp}(\sqrt{1+4na_{3D}}-1)$. These corrections change the mode frequency $\omega_q = cq$ by approximately 30%, but have a small effect on the amplitude and the form of the oscillations.

The trapping potential In a harmonically confined trap Eq. (3.20) is modified as

$$J(q, \tau) = 1 + \kappa \mathcal{F}(\tau), \quad (3.21)$$

where the function $\mathcal{F}(\tau)$, calculated with (LDA), is

$$\mathcal{F} = \int dz n_0(z) \sin^2(c(z)qt) / N. \quad (3.22)$$

The local speed of sound is given by $c(z) = \sqrt{\frac{n_0(z)}{m} \frac{\partial \mu}{\partial n} \Big|_{n_0(z)}}$. For simplicity let me restrict this discussion to the pure 1D case. Detailed calculation of the effect of high densities in a trap are given in the Appendix or our article [18]. In the pure 1D case Eq. (3.22) is

$$\mathcal{F}_{1D} = \frac{3}{2} \int_0^1 d\tilde{z} (1 - \tilde{z}^2) \sin^2(\tau \sqrt{1 - \tilde{z}^2}). \quad (3.23)$$

In contrast to the homogeneous case, \mathcal{F}_{1D} shows damped oscillations which leads to a damping of the oscillations of the J . This damping is a pure dephasing effect, captured by the LDA argument below: In the LDA picture the system is described by local harmonic oscillators at each point in space which oscillate according to Eq. (3.12). The oscillators at different points in space oscillate with a local speed of sound $c(z)$ which leads to a dephasing of the oscillator collections. This translates into a damping of the quantity $J(q, \tau)$.

Beyond the LDA one can perform Bogoliubov calculations in a harmonic trap (Sec. 1.3.2). The quench modifies the canonical variables x_{ν} and p_{ν} according to

$$x_{\nu}(t=0^+) = \left(\frac{g_f}{g_i}\right)^{1/4} x_{\nu}(t=0^-), \quad (3.24)$$

$$p_{\nu}(t=0^+) = \left(\frac{g_i}{g_f}\right)^{1/4} p_{\nu}(t=0^-). \quad (3.25)$$

As in the homogeneous case, the initial Gaussian state is given by the equipartition theorem $\langle p_{\nu}^2 \rangle_i = \langle x_{\nu}^2 \rangle_i = \frac{k_B T}{\hbar\omega_{\nu}}$ for the phononic modes and for $k_B T \gg \hbar\omega_{\nu}$. The evolution of $\langle p_{\nu}^2 \rangle$ is given by

$$\langle p_{\nu}^2 \rangle(t) = \langle p_{\nu}^2 \rangle_i [1 + \kappa \sin(\omega_{\nu} t)]. \quad (3.26)$$

As in the LDA, the underlying modes perform undamped oscillations. In the Bogoliouov approach in a harmonic trap, the damping of J arises from the density ripple analysis. In contrast to the homogeneous case, the Legendre polynomials are not the good quantum number of the free evolution. Therefore, the free evolution of the density ripple analysis mixes different modes in the harmonic trap. The mixing of these modes leads to a damping effect in the density ripple power spectrum $\langle |\tilde{\rho}(q)| \rangle$. The effect can be calculated from Eq. (2.65) and it gives very similar predictions compared to the LDA. The LDA calculations are numerically less demanding and we will use the LDA predictions in the following.

In summary, a good understanding with a sufficient precision can be obtained from the physical picture of a quench in a homogeneous system, together with the dephasing effect predicted by the LDA, and a modification of the mode frequency by high density effects.

3.4.2 Experimental realization

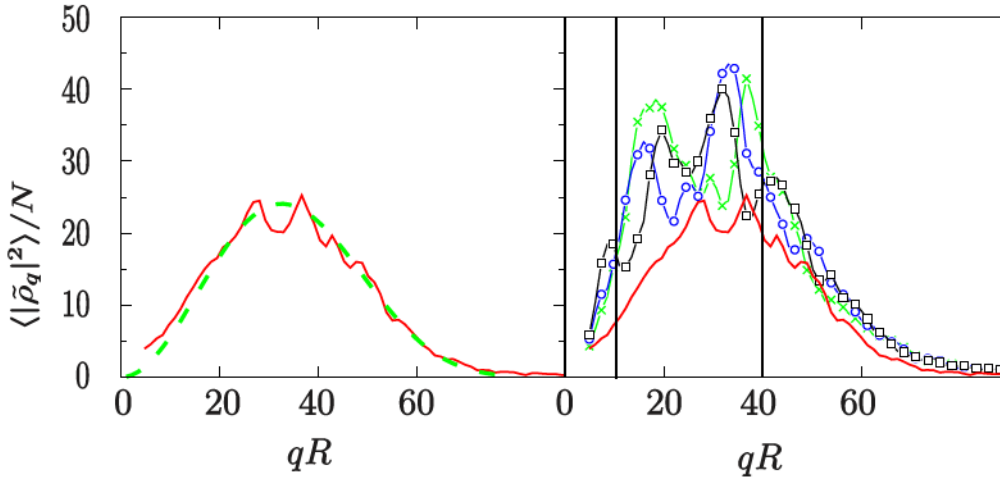


Figure 3.4 – Density power spectra: a) density power spectrum before the quench at thermal equilibrium with theoretical prediction in green (see Sec. 2.8.1.3), leading to a temperature $T = 55$ nK and $\sigma = 2$ μ m.

b) Density power spectra after the quench for a quench strength of $\kappa = 2$ at times $t = 2.1$ ms (green), $t = 2.6$ ms (blue) and $t = 4.6$ ms (black). For comparison the initial spectrum is shown in red line and the two black lines limit the range of q used for $J(q, \tau)$.

We typically record the density power spectrum before the quench at $t = 0$ and then every 0.5 ms over a total time of up to 10 ms. For each individual density ripple

power spectrum we use about 50 images and typical density ripple power spectra $\langle |\tilde{\rho}(q)|^2 \rangle$ are shown in Fig. 3.4. At first glance the post-quench spectra seem erratic. The oscillatory behavior of each Fourier component can be revealed by looking at the previously introduced quantity $J(q, \tau)$. Since we expect that $J(q, \tau)$ is independent of q we bin the data corresponding to different q values for a given interval in τ . The binning is implemented by a smooth binning on an irregular spaced grid. We use a numerical Gaussian convolution of a width $\bar{\Delta}$:

$$\bar{J}(\tau) = \frac{\sum_{\alpha} J(q_{\alpha}, \tau_{\alpha}) e^{-\frac{(\tau_{\alpha}-\tau)^2}{2\bar{\Delta}^2}}}{\sum_{\alpha} e^{-\frac{(\tau_{\alpha}-\tau)^2}{2\bar{\Delta}^2}}}, \quad (3.27)$$

where $\bar{\Delta} = 0.1\pi$. The sum over α is done over the data set where q is restricted to $10 < qR < 40$ in order to ensure both $q\hbar t_f/m \ll l_c$ and the validity of the LDA. The optical resolution depends on the transverse confinement which is not equal before and after the quench. We correct for this small effect by

$$\langle |\tilde{\rho}(q)|^2 \rangle \rightarrow \langle |\tilde{\rho}(q)|^2 \rangle e^{q^2(\sigma_i^2 - \sigma_f^2)}, \quad (3.28)$$

where the initial/final optical resolution $\sigma_{i/f}$ is obtained from fits of the equilibrium density ripples power spectra.

Fig. 3.5 a) shows the quantity $\bar{J}(\tau)$ where $\tau = cqt$ is evaluated at the trap center. It shows the expected oscillatory behavior. The frequency of \bar{J} is in good agreement with its predictions, when the 3D effects are taken into account. The oscillation shows the expected damping arising from the harmonic trap. The amplitude of the oscillation is smaller than expected. An artificial rescaling of the amplitude by $\kappa \rightarrow \kappa/2$ gave an approximate agreement between theory and data (black line in Fig 3.5 a)).

We repeat the experiment for different quench strengths $\kappa = -0.7, 2$ and 4 and different initial trapping frequencies $\omega_{\perp} = 1.5$ kHz and 3.1 kHz as shown in Fig. 3.5 b). In all the dataset the oscillator behavior can be observed. As in Fig. 3.5 a) the damping and the frequency are in agreement with its theoretical prediction. The amplitude depends on the dataset and is always smaller than the anticipated one. The origin of the discrepancy is not entirely understood and in Sec. 3.4.5 different effects which lead to a reduced amplitude are discussed. These oscillations of the Bogoliubov modes after an interaction quench have also been observed experimentally in [102] in 2D system.

3.4.3 Beyond the light-cone

As discussed in Sec. 3.3.1 one expects a light-cone behavior of the g_1 function which exponentially suppresses the prequench information on a typical time scale $t_{\text{th}}^{g_1} = l_c^f/c$. At $t = t_{\text{th}}^{g_1}$ the g_1 function has reached its final value for all distances $z < 2l_c^f$

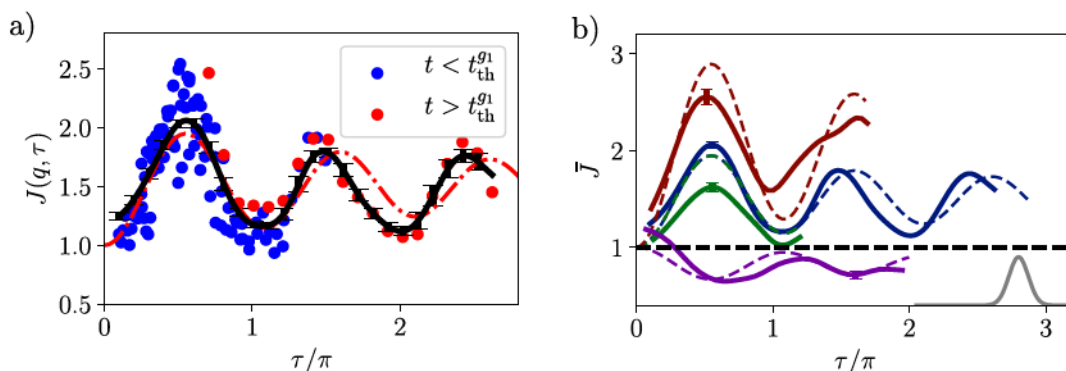


Figure 3.5 – Time evolution of the Bogoliubov modes after the interaction quench. The normalized density ripples power spectrum is plotted versus the reduced time $\tau = cq t$ where the speed of sound c is calculated for the central density. a) The data corresponds to an interaction quench with $\kappa = 2$ and an initial $f_{\perp} = 1.5$ kHz. Each data point corresponds to a measurement time t and a discrete q value. Blue points correspond to $t < t_{\text{th}}^{g_1}$ and red points to $t > t_{\text{th}}^{g_1}$. The black line corresponds to the resulting continuous averaged quantity \bar{J} , together with its error bars at an exemplary position. The red dashed-dotted line is the theoretical prediction for $\kappa = 1$. b) Time evolution of the experimental smoothed quantity \bar{J} for different data sets. The error bars show the typical statistical uncertainty on \bar{J} with 68% confidence interval. The initial transverse oscillation frequency is 1.5 kHz, except for the green curve for which it is 3 kHz. Quench strengths are $\kappa = 4$ (red), $\kappa = 2$ (blue and green) and $\kappa = -0.7$ (purple). Dashed lines are theoretical predictions for quench strengths reduced by a factor 0.5: (red: $\kappa = 2$, blue and green: $\kappa = 1$ and purple: $\kappa = -0.35$). The grey Gaussian curve corresponds to the smoothing function used for the data convolution. The blue line corresponds to the same data set as in a).

where the g_1 function has already dropped to $g_1 = n_0 e^{-2}$ and which corresponds to 14% of its value at $z = 0$ (see Fig. 3.2). In Fig. 3.5 a) we show the raw data points, each corresponding to a single pair of q and t . Red points correspond to $t > t_{\text{th}}^{g_1}$ and blue points to $t < t_{\text{th}}^{g_1}$. In Fig. 3.5 a) the oscillations continue for times $t > t_{\text{th}}^{g_1}$ which shows that the density ripple analysis gives access to information which is exponentially screened on the g_1 function.

3.4.4 Mode damping

The previous results are in agreement with the linearized approach of the Bogoliubov model. In the following I present unpublished results which indicate physics beyond the linearized approach.

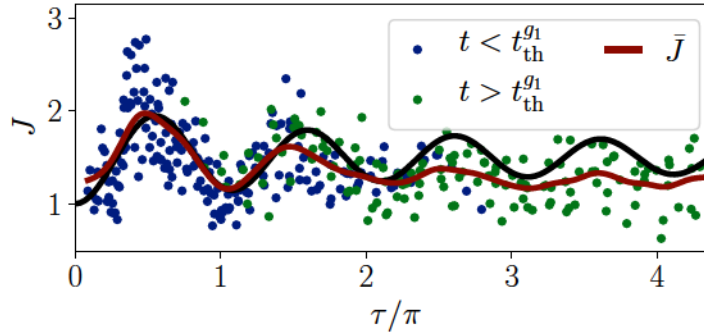


Figure 3.6 – Dataset containing data points up to $t = 16$ ms which exceeds more than three times $t_{\text{th}}^{g_1}$. Again the first oscillation is dominated by datapoints originating from $t < t_{\text{th}}^{g_1}$. The third and fourth periods are strongly damped and the oscillatory behavior finally vanishes. This damping is not captured by the rescaled theoretical prediction from the linearized model (black line).

In contrast to the previous result the following data set includes data points which exceed several times $t_{\text{th}}^{g_1}$. Fig. 3.6 contains data points up to three times $t_{\text{th}}^{g_1}$ and it clearly shows a damping which is not predicted by the linearized model of Sec. 3.2.1. It can be expected that theories beyond the linearized model predict further damping. Going beyond the Bogoliubov description with the full quantum treatment (Lieb-Liniger Hamiltonian) is tremendously difficult. A simpler approach can be obtained from the classical field equations (see Sec. 1.3.4). The classical field equations introduce an additional damping phenomena for the time evolution of a squeezed modes: They introduce coupling between different modes q and q' and coupling between the two quadratures θ_q and δn_q . The understanding of this damping is still work in progress. Let me finish this section with some preliminary remarks:

For simplicity let us restrict this discussion to a homogeneous systems. The classical field depends on a single parameter; the classical field parameter $\chi = l_c^2/(4\xi^2)$ (see Sec. 1.3.4). Fig. 3.7 shows two classical field simulations of the evolution of the density ripples spectrum after the quench. For higher χ , the damping becomes smaller. For larger χ the system is deeper into the quasi-condensate regime and the density fluctuations $\delta n/n_0$ are smaller. This leads to a smaller coupling between the modes.

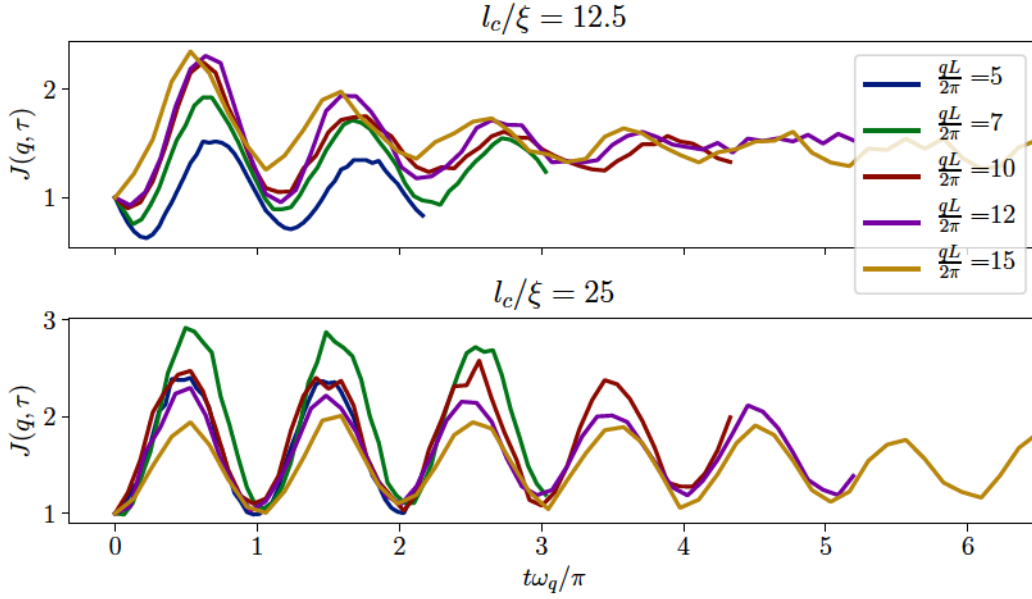


Figure 3.7 – Classical field simulation of time evolution of the quantity $J(q, \tau)$ after quench for different initial values of the classical field parameter $2\sqrt{\chi} = l_c/\xi$. Higher values of l_c/ξ lead to a weaker damping. The mode index is given by $j = qL/(2\pi)$. The colors codes are the same in both figures.

Justification for data with $a_{3D}n \simeq 1$. The mode damping is an interesting subject on its own. Still, the first aim of this study was to observe the oscillatory behavior of the Bogoliubov mode. Therefore, we are interested in situations where the mode damping is small, such that the oscillatory behavior can be observed.

In a typical situation we prepare quasi-condensate at temperatures $k_B T/(gn_0) \simeq y_\infty$ where y_∞ is some numerical factor very close to 1 (see Chap. 4 for a justification for this assumption). In such a situation χ can be rewritten as

$$\chi \simeq \frac{1}{\gamma}. \quad (3.29)$$

As shown in Fig. 3.7 the mode damping decreases with χ . Therefore we are interested in working with small γ . This can be obtained by high densities and small g . Due to practical restrictions the value of g cannot be varied in a large range. Its value needs to be large enough such that the system stays in the 1D regime and maintains a high aspect ratio. We therefore choose to work with high densities n . Unfortunately, the classical field simulations suggest that a low mode damping can only be obtained by working with densities such that corrections from the swelling of the transverse wavefunction become important. This was experimentally confirmed: When working with lower densities, compared to the previously presented results, we were unable to observe the oscillatory behavior of the Bogoliubov modes. We therefore raised the density such that na_{3D} did not stay very small. For example the corrections to the speed of sound accounts for up to 30% ($c/c_{1D} = 0.7$) in the data of Fig 3.5. A further increase of n_0 is unfeasible due to experimental constraints and also due to three-body losses which start become important.

3.4.5 Amplitude reduction

In the following, I briefly discuss different effects which lead to a reduction of the oscillations in $\bar{J}(\tau)$ which stands in discrepancy with our theoretical prediction (see Fig. 3.5). A more detailed discussion is given in the appendix of our paper [18].

Binning of the data The strongest effect comes from the smooth binning of our data. The raw density ripple data before smooth binning shows a large spread which requested a large $\bar{\Delta}$, in order to get rid of the noise in the data. The spread of the raw data shown in Fig. 3.5 b) is not representative and shows our best dataset. A more representative dataset is shown in Fig. 3.6. Assuming a pure sinusoidal behavior of $J = A \sin^2(\tau)$, the smoothing process of the Gaussian convolution Eq. (3.27) leads to an amplitude reduction of $A' = Ae^{-2\bar{\Delta}^2}$ which corresponds to 18% for $\bar{\Delta} = 0.1\pi$.

Finite ramp time In the previous analysis we assumed an instantaneous ramp with a ramp time $t_r = 0$. In the experiments we typically used $t_r = 0.7$ ms in order to ensure the adiabatic following of the transverse state. For large wavevectors t_r is not small compared to the oscillation period of the modes which reduces the mode squeezing produced by the quench. Assuming a linear ramp, one can calculate the squeezing factor S_q for each mode, with detailed calculations presented in the appendix of our paper [18]. The amplitude reduction can be calculated by solving the equation of motions of the Bogoliubov Hamiltonian (Eq. (1.101) & (1.102)) with a time dependent variable $A_q(t)$. The solution are given by the Airy-functions.

In Fig. 3.8 the experimentally observed amplitude reduction on the first oscillation is shown for different wavevectors q . The green line is the theoretical prediction

of the reduced squeezing due to the finite ramp time. As expected the squeezing of the mode decreases with q in agreement with the experimental data.

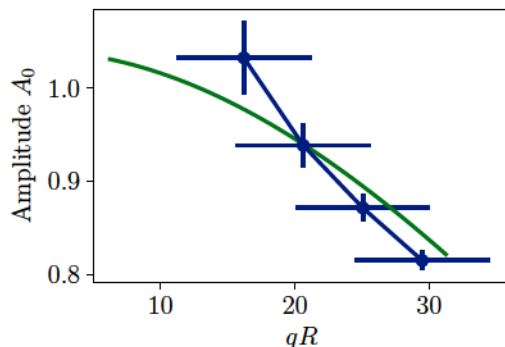


Figure 3.8 – The Amplitude of the first oscillation for different wavevectors q . The amplitude is obtained from calculating $J(\tau)$ for a narrow band of q , whose width is represented by the horizontal errorbars. We then fit the first oscillation of $J(\tau)$ with a sinusoidal $A_0 \sin^2(\tau) + 1$. The vertical errorbars correspond to 68% uncertainty obtained from the fit. The green line is the theoretical prediction rescaled by 0.5 as in for the previous theoretical predictions. The quench strength is $\kappa = 3$ and the ramp duration $t_r = 0.7$ ms.

In the previously presented data sets, a whole range of q contribute to $\bar{J}(q)$. In the experimental data, all the data points arise from a total observation time t_{\max} . Different modes q contribute up to a maximal time $\tau_{\max} = cq t_{\max}$. Small wavevectors q contribute to data points at smaller τ , while larger wavevectors q can contribute to higher τ . The quantity $\bar{J}(q, \tau)$ is dominated by smaller wavevectors q at small τ and by larger wavevectors q at larger⁹ q . Taking into account the weights of the different q , it can be estimated that this effect reduces the amplitude by typically 10% for the first oscillation.

In summary the two effects which arise from the finite ramp time and the data binning reduce the overall amplitude by approximately 75% while we observe an amplitude reduction by about 50%. The remaining 25% are not understood. It can be speculated that this discrepancy may arise from mode coupling or from effects due to atoms in the transversely excited states.

⁹Note that this effect cannot explain the additional damping observed in 3.6.

3.4.6 Recurrences in a harmonic trap

In [133] recurrence after the splitting process of a quasi-condensate into two were observed. During my PhD, we aimed to achieve similar results with a single quasi-condensate after an interaction quench. This section details why a recurrence in a single quasi-condensate was not observed and clarifies the difference to the observation in [133].

Homogeneous system For a linear dispersion relation after a time t_{rec} all the modes acquire the same phase. Let us start with box potential where the mode frequencies are given by $\omega_j = c\pi j/L$. The density ripple analysis is sensitive to the phase modulo¹⁰ π . After a time $t_{\text{rec}} = L/c$, all the modes acquire the same phase. The first mode performed half of a turn and acquires the phase π . The j -th mode acquires a phase $j\pi$. Consequently, the density ripple power spectrum at the recurrence time is identical to its initial distribution at $t = 0^+$.

Harmonic trap As already shown in Fig. 1.6 b) the dispersion relation in a harmonic trap is very close to linear, when excluding the first modes. This suggests that recurrence phenomena could also be expected in a harmonic trap. For large ν the dispersion relation in a trap can be expanded as

$$\omega_\nu = \sqrt{\frac{\nu(\nu+1)}{2}}\omega_{\parallel} \simeq \frac{1}{\sqrt{2}}\left(\nu + \frac{1}{2}\right)\omega_{\parallel}. \quad (3.30)$$

Again, the observable of interest $\langle |\tilde{\rho}(q)|^2 \rangle$ resolves the modes modulo π . The first recurrence occurs when the phase difference $\theta_{\nu+1} - \theta_\nu = (\omega_{\nu+1} - \omega_\nu)t$ is equal to π . With the linear approximation of Eq. (3.30) one obtains the recurrence time in a trap:

$$t_{\text{rec}} = \frac{\pi}{\omega_{\parallel}}\sqrt{2}. \quad (3.31)$$

At the first recurrence the first mode has approximately turned by $3\pi/2$ and the ν -th mode by $(\nu + 1/2)\pi$ as shown in Fig. 3.9 a). In contrast to a homogeneous system, the state at the recurrence time does not correspond to the initial situation at $t = 0^+$. All the modes acquire the same phase, but shifted by $\pi/2$ from the initial situation. For $\nu > 3$, this recurrence predicted from the large ν expansion turns out to be almost perfect. We therefore expect to observe an almost perfect recurrence when looking at the density ripple power spectrum $\langle |\tilde{\rho}(q)|^2 \rangle$ as shown in Fig. 3.9 b). The first modes, for which the recurrence is not perfect, can easily be excluded in the density power spectrum, as already performed in Sec 3.4.1.

¹⁰We are sensitive to $\langle \theta_q^2 \rangle$.

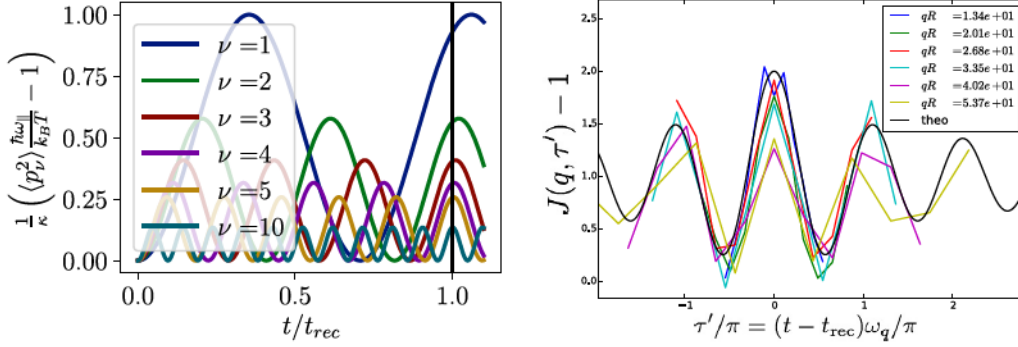


Figure 3.9 – a) The normalized expectations value of the Bogoliubov modes $\langle p_\nu^2 \rangle$ after the quench. At $t = t_{\text{rec}}$ first recurrence is visible, as predicted by the large ν approximation. Already for $\nu = 3$ the modes almost perfectly acquire the same phase where the agreement increases with the mode index ν .

b) The normalized density power spectrum vs. the dimensionless time $\tau' = \omega_q(t - t_{\text{rec}})$ around the recurrence time. The black line shows the theoretical prediction from the LDA. Note that in principle the LDA does not predict a recurrence. Still, it can be used predict the oscillation behavior around $t = t_{\text{rec}}$ which is the same as at $t = 0$ with a phase shift of $\pi/2$. Calculations are done for $l_c/R = 0.0033$ and $t_f/l_c = 0.2$.

3.4.6.1 Experimental realization

We experimentally investigated the recurrence phenomena after an interaction quench. One experimental challenge consists in a precise knowledge of the recurrence time t_{rec} . In order to apply the density ripple analysis and reveal how all the modes oscillate in phase around t_{rec} as seen in Fig. 3.9 b), the correct recurrence time needs to be chosen. Due to the high linear densities n_p the equation of state is modified which modifies the spectrum in the trap. From numerical calculation of the Bogoliubov modes with the modified equation of state, one can show that the new dispersion relation is given approximately by

$$\omega_\nu \approx \alpha(\eta) \sqrt{\frac{\nu(\nu+1)}{2}} \omega_\parallel, \quad (3.32)$$

where $\eta = \mu_p/\omega_\perp$ and $\alpha(\eta)$ can be calculated numerically as show in Fig. 3.11 a).

Unfortunately, it was impossible to produce a significant experimental observation of the recurrence phenomena in the harmonic trap. In Fig. 3.11 an exemplary dataset for the previously introduced quantity $J(\tau)$ is shown for different choices of t_{rec} . The reason why we could not observe the recurrence phenomena is most probably the damping of the Bogoliubov modes introduced in Sec. 3.4.4. The recurrence

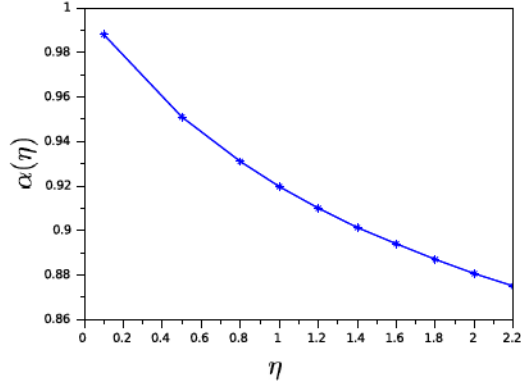


Figure 3.10 – 3D effects from the swelling of the transverse wavefunction at high densities. The figure shows the dependence of the coefficient $\alpha(\eta)$ on the density given by $\eta = \mu_p / \omega_{\perp} = \sqrt{1 + 4a_{3D}n_p} - 1$.

time is typically $t \simeq 60$ ms. As already visible in Fig. 3.6 the damping leads to a decreased oscillation amplitude at shorter times. The oscillations at the recurrence time are damped beyond the experimental resolution.

Comparison with recurrences after the splitting of a quasi-condensate In [133] recurrences were observed after the splitting of a quasi-condensate in two (see Sec. 3.3.1.1). For the observation a box potential was used. In [138] the same group showed that with their method the observation of recurrences in a harmonic potential was not possible. This is mainly due to the first mode $\nu = 1$ which smears out the signal on the phase correlation function (or on the g_1 function). This problem can be easily avoided with the density ripple analysis method where one can exclude the first modes. Still, we could not observe the recurrence signal. This is most probably due to the difference in temperature. The splitting of the initial quasi-condensate leads to an effective temperature of the anti-symmetric modes below the initial temperature of the quasi-condensate. The authors of [133] performed classical field simulation for the evolution of the two quasi-condensates in a box potential after the splitting. Their simulations indicate that the recurrence signal can only be observed for classical field parameters which are higher than the one of our system. Due to the splitting process their system obtains an effective temperature which is much lower than the one of a typical single quasi-condensate. The lower temperature leads to a higher classical field parameter which explains the reduced damping of the squeezed modes. We expect that the same qualitative arguments hold in a harmonic trap.

In summary: In principle the observation of a recurrence in a harmonic trap should be possible with the density ripple method. The method allows to exclude

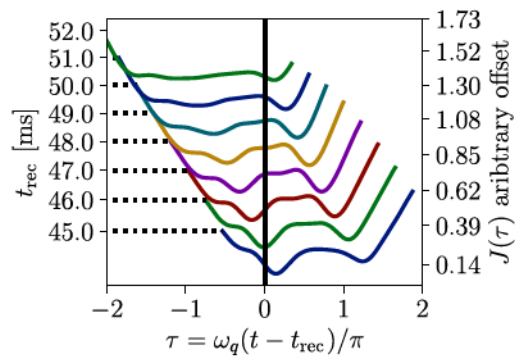


Figure 3.11 – The smooth quantity $J(\tau)$ around the expected recurrence shown at different offset which correspond to different t_{rec} . Note that the variation in $J(\tau)$ is significantly smaller than the previously observed oscillations at short times.

the non equally spaced first modes which hinder its observation on different observables, as the g_1 function. The damping of the squeezed Bogoliubov modes most probably prevented the observation of a recurrence with the density ripple method.

Summary:

- We realize an interaction quench by suddenly changing the transverse confinement.
- The observation in momentum space does not allow to resolve the subsequent dynamics.
- The density ripple analysis is a useful tool to study the out-of-equilibrium dynamics following the interaction quench.
- The published results are in good agreement with the linearized model (Bogoliubov Hamiltonian) and the out-of-equilibrium dynamics outlasts the dynamics observable on the first order correlation function $g^{(1)}(z)$.
- I present data sets that indicate effects which go beyond the Bogoliubov analysis: We observe an additional damping which is not in the Bogoliubov analysis. Such an effect is also seen in numerical classical field simulations.
- The observation of recurrences was not possible due to the mode damping.

Chapter 4

Losses in a Bose gas

The work presented in this chapter was originally triggered by the unexpected result that energy-independent losses can lead to the cooling of quasi-condensates. These results were first obtained by the Vienna group with a theoretical work [20] and an experimental verification [19]. These results led to several theoretical and an experimental work in our group [21–24]. In this chapter I will first introduce the theoretical tools to treat energy-independent losses (Sec. 4.1 - Sec. 4.3). The theoretical studies of our group [21–23] focus on different aspects and also use different approaches to describe the energy-independent losses. In Sec. 4.2 the losses are introduced with the wavefunction Monte-Carlo method, as used in [21]. In difference to [21] the method is extended from one-body losses to j -body losses. I advise a more experimental or an impatient reader to directly read Sec. 4.3 where the same theoretical results, as in Sec. 4.2, are obtained in a more intuitive way. It should be noted that the simplified approach of Sec. 4.3 cannot justify all of its approximation without referring to a more sophisticated approach as QMC.

The two different theoretical approaches suggest that a cooling should be expected from three-body losses. In Sec. 4.4 experimental results are presented which confirm the cooling by three-body losses and which are published in [24]. The end of the chapter collects different side aspects of the energy-independent cooling process. I present the three-body loss cooling observed by the Yang-Yang thermometry 4.4.3, for which theoretical predictions are difficult to obtain. Furthermore, I present a theoretical study based on the QMC approach which allows to cool a Bogoliubov mode to the ground state via a feedback loop. This work is published in [21].

The physical origin of the cooling At first hand a cooling introduced by energy-independent losses could seem contradictory. Especially when considering the well established evaporative cooling which specifically relies on the energy selectivity. A cooling induced by losses can be understood in the following way: Let us consider a

Bogoliubov mode q whose Hamiltonian is given by

$$H_q = \underbrace{A_q n_q^2}_{E_{\text{int}}} + \underbrace{B_q \theta_q^2}_{E_{\text{kin}}}, \quad (4.1)$$

as introduced in Sec. 1.3. When considering phonons, the first term on the r.h.s is the interaction energy E_{int} and the second term the kinetic energy E_{kin} . The losses reduce the amplitude of the density modulations $\langle n_q^2 \rangle$ and consequently remove interaction energy from the mode. This is an effect which can be understood from a mean field approach. It is important to note that the origin of this cooling effect is unrelated to the commonly used evaporative cooling, although its practical implementation might be very similar¹. The losses in the evaporative cooling process are selective in the kinetic energy and reduce the temperature by a thermalization process. Considering that the energy-independent losses decrease the interaction energy, it might be tempting to interpret the energy-independent loss process as the equivalent of the evaporative cooling where the kinetic energy is replaced by the interaction energy. This is however a strong oversimplification. The cooling induced by the energy-independent losses does not rely on thermalization, as I will show in this chapter.

The cooling by energy-independent losses also introduces a competing heating process. This second effect is due to the discrete nature of the atom losses. The loss of individual atoms is associated with a shot-noise which increases the density fluctuations. Thus it increases the energy per mode. This heating effect can not be captured by a mean-field approach.

In summary, a competition of these two processes leads to a stationary value of the ratio

$$k_B T / (g n_p) = y_\infty. \quad (4.2)$$

The parameter y_∞ is of the order of one and depends on the type of losses and the trapping geometry. This stationary value corresponds to the crossover between the quasi-condensate regime dominated by quantum fluctuations and the quasi-condensate regime dominated by thermal fluctuations (see Sec. 1.2.4).

4.1 j-body loss in a quasi-condensate

Let me first define the notion of j -body losses: It refers to a situation where the time evolution of the atomic density is given by

$$\frac{d}{dt} \langle n \rangle = -\tilde{\kappa}_j \langle n \rangle^j g^{(j)}(0), \quad (4.3)$$

¹More about this aspect in Sec. 4.5.

with the event rate constant $\tilde{\kappa}_j$ and the normalized j -body correlation function at zero distance

$$g^{(j)}(0) = \frac{\langle \Psi^{\dagger j}(0) \Psi^j(0) \rangle}{\langle n \rangle^j}. \quad (4.4)$$

The normalized j -body correlation function at zero distance gives the probability of having j particles at the same place, normalized to $\langle n \rangle^j$ – the value for uncorrelated atoms.

For the whole chapter, we will consider j -body losses in the quasi-condensate regime where $g^{(j)}(0)$ is close to one (also see Eq. (1.55))

$$g^{(j)}(0) \simeq 1. \quad (4.5)$$

This motivates the introduction of a new constant $\kappa_j = \tilde{\kappa}_j g^{(j)}(0)$ where the dependence on the temperature and the regime is recast into κ_j .

In the following two sections I will calculate the effects of j -body losses on the energy of a Bogoliubov mode q with two different methods. The first method in Sec. 4.2 uses the Quantum-Monte Carlo (QMC) method. The second method in Sec. 4.3 uses a simplified approach. Both sections are complementary and can be read independently of each other. The results of the QMC method give a deeper understanding of the process and form the basis of the feedback process of Sec. 4.7. The simplified approach of Sec. 4.3 gives a more intuitive access to the process.

4.2 Quantum Monte-Carlo

In this section we apply the wavefunction Quantum Monte-Carlo (QMC) method introduced in Sec. 1.5.1 to j -body losses.

In a small cell We discretize space into Q cells of length δz . These cells contain a large mean atom number N_0 with small fluctuations $\delta N = N - N_0$, since the gas lies in the quasi-condensate regime. Furthermore we assume that δz is large enough such that the fluctuations are large compared to unity $\delta N \gg 1$. Both can be fulfilled at length smaller than the healing length ξ . The small cell contains N atoms and its time evolution is given by

$$\frac{d}{dt} N = -K_j N^j, \quad (4.6)$$

where $K_j = \kappa_j \delta z^{1-j}$.

QMC method During the small time dt the QMC method of Sec. 1.5.1 is based on two possibilities: Either a loss event occurs or no loss event occurs.

1. **Loss event** If a loss event occurs the initial state $|\Psi(t)\rangle$ evolves as²

$$|\Psi(t+dt)\rangle = \hat{a}^j |\Psi(t)\rangle, \quad (4.7)$$

where \hat{a} annihilates a particle in the cell. The probability for this loss event is given by

$$dp = \langle \Psi(t) | L^\dagger L | \Psi(t) \rangle = \frac{K_j}{j} \langle \Psi(t+dt) | \Psi(t+dt) \rangle dt. \quad (4.8)$$

The factor $1/j$ arises from the fact that we look at the number of loss events and not at the number of lost atoms.

2. **No loss event** With the probability $1 - dp$ no loss events occurs and the state evolves according to

$$|\Psi(t+dt)\rangle = e^{\frac{K_j}{2j} \hat{a}^\dagger \hat{a} dt} |\Psi(t)\rangle. \quad (4.9)$$

The probability of for no loss event is given

$$1 - dp = \frac{\langle \Psi(t+dt) | \Psi(t+dt) \rangle}{\langle \Psi(t) | \Psi(t) \rangle}. \quad (4.10)$$

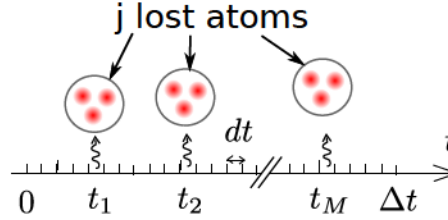


Figure 4.1 – A typical loss sequence during the time interval Δt . At each loss event, indicated by the arrows, j atoms are lost and the total number of lost atoms during the sequence is jM .

Loss sequence Let us look at a *loss sequence* during a small time interval Δt where atoms are lost from the cell at times $t_1 < t_2 < \dots < t_M$ as depicted in Fig. 4.1. The final state after this loss sequence is obtained by the successive application of Eq. (4.7) & (4.9) which leads to

$$|\Psi(t+\Delta t)\rangle = e^{\frac{K_j}{2j} \hat{a}^\dagger \hat{a} j(t+\Delta t-t_M)} \hat{a}^j e^{\frac{K_j}{2j} \hat{a}^\dagger \hat{a} j(t_M-t_{M-1})} \dots \hat{a}^j e^{\frac{K_j}{2j} \hat{a}^\dagger \hat{a} j(t_1-t)} |\Psi(t)\rangle. \quad (4.11)$$

²Note that we work with unnormalized states.

The probability of the loss sequence is given by

$$dp_{\{t_i\}} = \frac{\langle \Psi(t_1) | \Psi(t_1) \rangle}{\langle \Psi(t) | \Psi(t) \rangle} \frac{K_j dt}{j} \frac{\langle \Psi(t_1 + dt) | \Psi(t_1 + dt) \rangle}{\langle \Psi(t_1) | \Psi(t_1) \rangle} \cdots \frac{\langle \Psi(t + \Delta t) | \Psi(t + \Delta t) \rangle}{\langle \Psi(t_M + dt) | \Psi(t_M + dt) \rangle} \quad (4.12)$$

which leads to

$$dp_{\{t_i\}} = \left(\frac{K_j dt}{j} \right)^M \frac{\langle \Psi(t + \Delta t) | \Psi(t + \Delta t) \rangle}{\langle \Psi(t) | \Psi(t) \rangle}. \quad (4.13)$$

For the calculation of the loss sequence probability $dp_{\{t_i\}}$ we choose to work in the Fock state basis $|\Psi(t)\rangle = \sum_N c_N(t) |N\rangle$. The loss sequence changes the Fock state coefficients $c_N(t + \Delta t) = \langle N | \Psi(t + \Delta t) \rangle$. They are given by

$$c_N(t + \Delta t) = f_{\{t_i\}}(N + jM) c_{N+jM}(t) \quad (4.14)$$

where the function $f_{\{t_i\}}(N)$ depends on the loss sequence. The time interval Δt is chosen such that the number of lost atoms is much smaller than the total number of atoms N in the cell. Then, the function $f_{\{t_i\}}(N)$ becomes almost independent on the time sequence $\{t_i\}$ for a given number of loss events M . The function $f_{\{t_i\}}(N)$ can be approximated by

$$f_{\{t_i\}}(N) \simeq f_M(N) = N^{jM/2} e^{-\frac{K_j}{2j} N^j \Delta t}, \quad (4.15)$$

where we used $M \ll N$ and neglected the commutator $[\hat{a}, \hat{a}^\dagger] = 1$. The last approximation is valid as long as the atom number inside the considered cell is large $N \gg 1$. It is equivalent to Eq. (4.5). With the Fock state coefficients we can calculate the probability for the given sequence

$$dp_{\{t_i\}} = \sum_N |c_N|^2 \left(\frac{K_j}{j} N^j dt \right)^M e^{-\frac{K_j}{j} N^j \Delta t}. \quad (4.16)$$

Statistics of the trajectories A single loss sequence corresponds to a quantum trajectory. The probability of the quantum trajectory $dp_{\{t_i\}}$ only depends on the number of loss events M . The loss events are random events and one needs to take into account all possible quantum trajectories. Let us calculate the probability of having M events: We sum all the possible sequences by integrating over Eq. (4.16)

$$P(M) = \int \cdots \int_{0 < t_1 < t_2 \dots < \Delta t} dp_{\{t_i\}} = \frac{\sum_N |c_N|^2 \left(\frac{K_j}{j} N^j \Delta t \right)^M e^{-\frac{K_j}{j} N^j \Delta t}}{M!}. \quad (4.17)$$

For a given initial atom number N we recover the expected Poissonian distribution which can be approximated by a Gaussian with mean $\lambda = \frac{K_j}{j} N^j \Delta t$ and variance λ

$$P_N(M) = \frac{\lambda^M e^{-\lambda}}{M!} \underset{\lambda \gg 1}{\simeq} \frac{1}{\sqrt{2\pi\lambda}} \exp \left[-\frac{\left(M - \frac{K_j}{j} N^j \Delta t \right)^2}{2 \frac{K_j}{j} N^j} \right], \quad (4.18)$$

With the Gaussian approximation the mean number of loss events is

$$\langle M \rangle = \frac{K_j}{j} \langle N^j \rangle \Delta t \simeq \frac{K_j}{j} N_0^j \Delta t + K_j N_0^{j-1} \langle \delta N \rangle \Delta t. \quad (4.19)$$

In the second step we expanded $N = N_0 + \delta N$ in first order in δN . The variance of the Gaussian is given by:

$$\langle M^2 \rangle - \langle M \rangle^2 = \frac{K_j}{j} \langle N^j \rangle \Delta t \simeq \frac{K_j}{j} N_0^j \Delta t \quad (4.20)$$

where in the second step we expanded the expression in zeroth order in δN . As expected, for a fixed N , the number of events M obeys a Poissonian statistics, while the number of lost atoms jM only obeys a Poissonian statistics for $j = 1$.

Inside the quasi-condensate density fluctuations are small $\delta N \ll N_0$ and the number of events M is close to $\frac{K_j}{j} N_0^j \Delta t$ with small fluctuations $K_j N_0^{j-1} \langle \delta N \rangle \Delta t$ around this value. This motivates the introduction of a new random variable $M' = M - \frac{K_j}{j} N_0^j \Delta t$. Inside the quasi-condensate regime M' shows small fluctuations compared to $\frac{K_j}{j} N_0^j \Delta t$. Its mean and variance for different trajectories are given by

$$\langle M' \rangle = K_j N_0^{j-1} \langle \delta N \rangle \Delta t \quad \text{and} \quad \langle M'^2 \rangle - \langle M' \rangle^2 = \frac{K_j}{j} N_0^j \Delta t. \quad (4.21)$$

Calculation of the function $f_M(N)$: For a given M the function $f_M(N)$ in Eq. (4.15) is a sharply peaked function close to a Gaussian (see Fig. 4.2). We calculate the Gaussian function by expanding $\log(f_M(N))$ around its maximum \bar{N} :

$$\log(f_M(N)) \simeq \log(f_M(\bar{N})) + \frac{1}{2} \frac{\partial^2 \log(f_M(N))}{\partial N^2} \Big|_{\bar{N}} (N - \bar{N})^2. \quad (4.22)$$

The maximum is given by $\bar{N} = \left(\frac{jM}{K_j \Delta t} \right)^{1/j}$ and which leads to

$$f_M(N) \simeq A_M \exp \left[-\frac{1}{2} \frac{(N - \bar{N})^2}{\Sigma^2} \right] \quad (4.23)$$

with the normalization factor A_M and

$$\Sigma^2 = \frac{2(jM)^{2/j}}{j^2 M (K_j \Delta t)^{2/j}}. \quad (4.24)$$

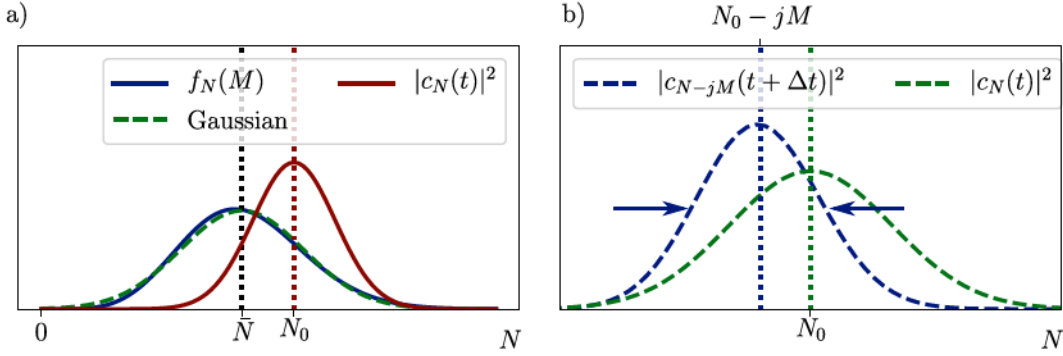


Figure 4.2 – a) The initial Fock state coefficients $c_N(t)$ are peaked around N_0 . The function $f_M(N)$ (blue line) is close to a Gaussian (dashed green line) and centered around \bar{N} .

b) The new Fock state coefficients $c_{N-jM}(t + \Delta t) = f_M(N)c_N(t)$ are shifted by jM . Its width is reduced due to the gain in knowledge on N .

Let us now introduce calculate \bar{N} by introducing M' : We use the fact that inside the quasi-condensate regime M' shows small fluctuations ($M' \ll \frac{K_j}{j} N_0^j \Delta t$). We approximate \bar{N} at first order in $jM'/(K_j N_0^j \Delta t)$ which leads to:

$$f_M(N) \simeq A_M \exp \left[-\frac{1}{2} \left(\delta N - \frac{M'}{K_j N_0^{j-1} \Delta t} \right)^2 \right]. \quad (4.25)$$

With the same arguments we can approximate the variance of the Gaussian Σ . The variable M at zeroth order in ΔN is typically close to $M \simeq \frac{K_j}{j} N_0^j \Delta t$ which leads to:

$$\Sigma^2 \simeq \frac{2N_0^{2-j}}{jK_j \Delta t}. \quad (4.26)$$

4.2.1 Generalization to all cells

The sole effect of losses does not introduce correlations between different cells and the result of Eq. (4.25) can directly be generalized to several cells. We introduce the variable M'_i in each cell and the Fock state $|N_1, N_2, \dots, N_Q\rangle$ in several cells. Then the

probability amplitude up to a global normalization factor writes:

$$c_{N_1, \dots, N_Q}(t + \Delta t) = c_{N_1 + jM_1, \dots, N_Q + jM_Q}(t) \prod_i A_{M_i} \exp \left[-\frac{1}{2} \left(\delta N_i - \frac{M'_i}{K_j N_0^{j-1} \Delta t} \right)^2 \frac{jK_j}{2} N_0^{j-2} \Delta t \right]. \quad (4.27)$$

Losses in different cells are uncorrelated which let us write

$$\langle M'_l M'_m \rangle - \langle M'_l \rangle \langle M'_m \rangle = \frac{K_j}{j} N_0^j \delta_{l,m} \Delta t \quad (4.28)$$

with the Kronecker Delta $\delta_{l,m}$.

Fourier decomposition In order to take into account the free evolution by the Bogoliubov Hamiltonian we introduce the Fourier decomposition of the atom number and the atom losses

$$n_{q,c} = \sqrt{\frac{Q}{2\delta z}} \sum_j \cos(qz_j) \delta N_j \quad \text{and} \quad n_{q,s} = \sqrt{\frac{Q}{2\delta z}} \sum_j \sin(qz_j) \delta N_j \quad (4.29)$$

$$M_{q,c} = \sqrt{\frac{Q}{2\delta z}} \sum_j \cos(qz_j) M'_j \quad \text{and} \quad M_{q,s} = \sqrt{\frac{Q}{2\delta z}} \sum_j \sin(qz_j) M'_j \quad (4.30)$$

where q takes the values $q = \frac{2\pi i}{L}$ with $i \in [1, \dots, (N-1)/2]$ and $L = Q\delta z$. The variable $M_{q,r}$ represents the Fourier-transform of the loss events in mode q, r . The previously introduced Fock state $|n_1, n_2, \dots, n_Q\rangle$ is also an eigenstate of the operator $\hat{n}_{q,r}$ where the subscript r stands for c or s :

$$|n_1, n_2, \dots, n_Q\rangle = |n_{2\pi/L,c}, n_{2\pi/L,s}, n_{4\pi/L,c}, n_{4\pi/L,s}, \dots, n_{(Q-1)\pi/L,c}, n_{(Q-1)\pi/L,s}\rangle = |\{n_{q,r}\}\rangle, \quad (4.31)$$

where we introduced the short notation $|\{n_{q,r}\}\rangle$. Equivalently, we write $\tilde{c}_{\{n_{q,r}\}} = c_{n_1, \dots, n_Q}$. With this notation and the introduction of the Fourier decomposition, we rewrite Eq. (4.27) as

$$\tilde{c}_{\{n_{q,r}\}}(t + \Delta t) = \tilde{c}_{\{n_{q,r} + M_{q,r}\}}(t) \prod_q A_{M_q} \exp \left[-\frac{1}{2} \left(n_{q,r} - \frac{M_{q,r}}{\kappa_j n_0^{j-1} \Delta t} \right)^2 \frac{jK_j}{2} n_0^{j-2} \Delta t \right]. \quad (4.32)$$

In Eq. (4.32) we used the orthogonality of the Fourier decomposition and the fact that the variances are independent of q and r . For readability let me rewrite this as

$$\tilde{c}_{\{n_{q,r}\}}(t + \Delta t) = \tilde{c}_{\{n_{q,r} + M_{q,r}\}}(t) \prod_q \frac{1}{\sqrt{2\pi\sigma^2}} e^{-\frac{(n_{q,r} - \bar{n}_{q,r})^2}{2\sigma^2}}, \quad (4.33)$$

where

$$\bar{n}_{q,r} = \frac{M_{q,r}}{\kappa_j n_0^{j-1} \Delta t} \quad (4.34)$$

$$\sigma^2 = \frac{2}{j \kappa_j n_0^{j-2} \Delta t}. \quad (4.35)$$

as given by Eq. (4.32). Using the definition of the Fourier transform Eq. (4.29) - (4.30) and the statistics of M'_i Eq. (4.21) and (4.28) we obtain the statistics of the different quantum trajectories for $M_{q,r}$:

$$\langle M_{q,r} \rangle = \kappa_j n_0^{j-1} \langle n_{q,r} \rangle \Delta t \quad (4.36)$$

$$\langle M_{q,r}^2 \rangle - \langle M_{q,r} \rangle^2 = j \kappa_j n_0^j \Delta t \quad (4.37)$$

Wigner function The effect of the losses can be conveniently described with the Wigner function. The effect of the losses does not introduce correlations between modes and we will focus on a given mode q where we will omit the subscript r . The Wigner function of the given mode q is:

$$W(n_q, \theta_q) = \frac{1}{\pi} \int du \langle u + n_q | \hat{\rho} | u - n_q \rangle e^{-2iu\theta_q}. \quad (4.38)$$

According to Eq. (4.33) the Wigner function after the loss sequence $W'(n_q, \theta_q)$ writes as

$$W'(n_q, \theta_q) = \frac{1}{2\pi^2 \sigma^2} \int du \langle u + n_q + M_q | \hat{\rho}(t) | u - n_q - M_q \rangle e^{-2iu\theta_q} e^{-\frac{(n_q - \bar{n}_q + u)^2}{2\sigma^2}} e^{-\frac{(n_q - \bar{n}_q - u)^2}{2\sigma^2}}. \quad (4.39)$$

Injecting $\langle u + n_q | \hat{\rho} | u - n_q \rangle = \int d\tilde{\theta}_q W(n_q, \tilde{\theta}_q) e^{2i\tilde{\theta}_q u}$ leads to

$$W'(n_q, \theta_q) = \frac{1}{2\pi^{3/2} \sigma} \int d\tilde{\theta}_q W(n_q + M_q, \tilde{\theta}) e^{-\sigma^2(\tilde{\theta}_q - \theta_q)} e^{-\frac{(n_q - \bar{n}_q)^2}{\sigma^2}}. \quad (4.40)$$

The losses introduces a shift in n_q . At the same time it changes the width in n_q and θ_q . The squeezing in n_q reflects the gain of knowledge acquired on n_q by the losses. The associated anti-squeezing in θ_q ensures the preservation of the Heisenberg uncertainty-relation (see Fig. 4.3 for a Gaussian Wigner function).

Gaussian Wigner function Let us consider a situation where initially the distribution is given by a Gaussian state:

$$W(n_q, \theta_q) = \frac{1}{2\pi \sqrt{\det(C)}} e^{-\frac{1}{2}[(\vec{X} - \vec{R})^T B (\vec{X} - \vec{R})]} \quad (4.41)$$

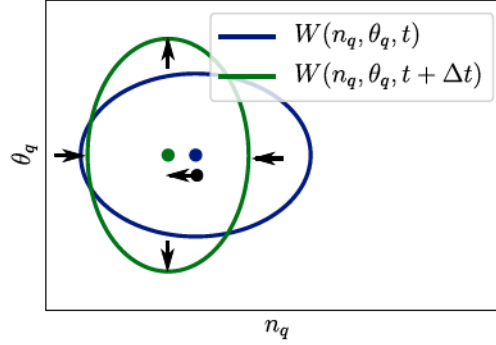


Figure 4.3 – The Wigner function under the effect of losses: The ellipses represent the RMS of the Gaussian Wigner functions at time t (blue) and $t + \Delta t$ (green). The corresponding dots are the center of the Gaussian Wigner functions. The losses effect both the center and the shape of the Gaussian: The center is shifted towards smaller n_q . At the same time the width in n_q is decreased and the width in θ_q increased, such that the uncertainty relation is respected.

where $\vec{X} = \begin{pmatrix} n_q \\ \theta_k \end{pmatrix}$, \vec{R} is the center of the distribution and C is the covariance matrix with $B = C^{-1}$. The transformation in Eq. (4.40) transforms the initial Gaussian state into a new Gaussian state centered on R' with a new covariance matrix C' . The details of the calculation for this new Gaussian state are given in Appendix Sec. A.4.2. The calculation of the new covariance matrix C' in first order in Δt gives

$$C' = C - j\kappa_j \Delta t n_0^{j-2} \begin{pmatrix} C_{11}^2 & C_{11}C_{12} \\ C_{11}C_{12} & C_{12}^2 - \frac{1}{4} \end{pmatrix}. \quad (4.42)$$

For the new center \vec{R}' we obtain in first order in Δt :

$$\vec{R}' = \vec{R} + \left[\frac{jM_q}{n_0} - j\kappa_j n_0^{j-2} \Delta t \langle n_q \rangle \right] \begin{pmatrix} C_{11} \\ C_{12} \end{pmatrix} - \begin{pmatrix} M_q \\ 0 \end{pmatrix}. \quad (4.43)$$

For practical purposes let us replace the variable M_q with a new random variable $d\xi$ centered around 0:

$$d\xi = M_q - \kappa_j n_0^{j-1} \langle n_q \rangle \Delta t \quad (4.44)$$

with

$$\langle d\xi^2 \rangle = j\kappa_j n_0^j \Delta t, \quad (4.45)$$

which leads to

$$\vec{R}' = \vec{R} - \kappa_j n_0^{j-1} \Delta t \begin{pmatrix} \langle n_q \rangle \\ 0 \end{pmatrix} - d\xi \begin{pmatrix} 1 - \frac{C_{11}}{n_0} \\ -\frac{C_{12}}{n_0} \end{pmatrix}. \quad (4.46)$$

The two equation Eq. (4.42) & (4.46) are the main results so far. They described how the initial Gaussian state evolve under the effect of losses.

4.2.2 Effect of the Bogoliubov Hamiltonian

A single trajectory of a Gaussian Wigner function evolves under the sole effect of losses according to Eq. (4.42) and Eq. (4.46). Additionally, the intrinsic dynamics of the system needs to be taken into account with the Bogoliubov Hamiltonian (see Sec. 1.3.1). Its evolution corresponds to a rotation in phase space with the matrix

$$\mathfrak{R}(\omega_q t) = \begin{pmatrix} \cos(\omega_q t) & \sqrt{B/A} \sin(\omega_q t) \\ -\sqrt{A/B} \sin(\omega_q t) & \cos(\omega_q t) \end{pmatrix}. \quad (4.47)$$

Evolution of the covariance matrix C Let us first focus on the evolution of the covariance matrix under the combined effect of losses and the intrinsic evolution under the Bogoliubov Hamiltonian: The evolution of the covariance matrix C is independent of the trajectory. For an initial thermal state, the energy associated to the covariance matrix E_C is equally distributed between the two quadratures and given by

$$\frac{E_C}{2} = A_q C_{11} = B_q C_{22}. \quad (4.48)$$

Additionally, let us focus on a situation where the free evolution for the considered mode q is fast compared to the losses $\kappa_j n^{j-1} \ll \omega_q$. Then, C stays isotropic at each moment. Eq. (4.48) stays valid, together with $C_{12} \simeq 0$ at all times.

A single trajectory The evolution of R depends on the trajectory. The center \vec{R} performs a random motion depending on $d\xi$. The effect on the center R and on the covariance matrix are shown in Fig. 4.4 with numerical simulations. The losses lead to a random motion of the center in the $(\bar{n}_q, \bar{\theta}_q)$ -plane and, as expected, the Gaussian stays isotropic³

4.2.3 Average over different trajectories

If one does not record losses, only averages over different trajectories are meaningful. Let us first investigate the evolution of a a given single quantum trajectory, i.e. a given value of $d\xi$. If the Wigner distribution is initially centered around zero, it will stay

³Note that the reason, that the Gaussian stays in a thermal state, namely the same width in both quadratures, is not due to a thermalization progress. It is due to the fast rotation of the Bogoliubov modes which avoids the creation of a squeezing in n_q .

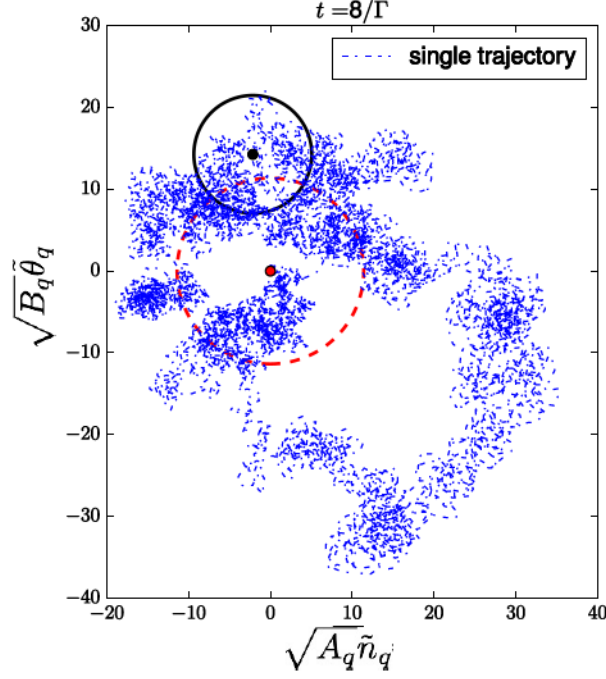


Figure 4.4 – The figure shows the evolution of the phase-space distribution for a single trajectory and $j = 1$. The time evolution goes from $t = 0$ to $t = 8/\kappa_1$. We consider a phononic mode with $\xi q = 0.1$ and an initial temperature $T_i = 1.1 g n_0$. The loss rate is $\kappa_1 = \omega_q/400$. Scattered blue points give the evolution of the center \vec{R} . The evolution is given by the numerical implementation of Eq. (4.46), (4.42) & (4.47). We verified that C_{12} stays small while, at any time with $A_k C_{11} \simeq B_q C_{22} \simeq E_c/2$, as expected for $\omega_q \gg \kappa_1$. The black solid-circle, of radius $\sqrt{E_c}$, represents the final RMS width of the Wigner function. For comparison, the red dashed-circle, of radius \sqrt{E} where E is the final energy obtained after averaging over 100 trajectories, gives the rms width of the averaged phase space distribution. The coordinates are given in the frame rotating according to the free evolution: namely, the plotted quantity is $\vec{\tilde{R}} = (\tilde{n}_q, \tilde{\theta}_q) = \mathfrak{R}^{-1}(\omega_q t) \vec{R}$.

centered around zero. For a given trajectory, initially centered at $R(0) = 0$, the center acquires a random displacement according to Eq. (4.46):

$$\bar{R}' = \bar{R} - \begin{pmatrix} 1 - \frac{C_{11}}{n_0} \\ -\frac{C_{12}}{n_0} \end{pmatrix} d\xi. \quad (4.49)$$

Considering the two contribution of a random shift of the center and the modification of the covariance matrix according to Eq. (4.42) one obtains

$$\langle n_q^2(t + \Delta t) \rangle_{st} = \langle n_q^2(t) \rangle - j\kappa_j n_0^{j-2} C_{11}^2 + d\xi^2 \left(1 - \frac{C_{11}}{n_0}\right)^2 \quad (4.50)$$

$$\langle \theta_q^2(t + \Delta t) \rangle_{st} = \langle \theta_q^2(t) \rangle - j\kappa_j n_0^{j-2} \left(C_{12}^2 - \frac{1}{4}\right) + d\xi^2 \left(\frac{C_{12}}{n_0}\right)^2, \quad (4.51)$$

where the subscript st stands for single trajectory. Then, we compute the average over the different trajectories with the use of $\langle d\xi^2 \rangle_{tr} = j\kappa_j n_0^j \Delta$ and $C_{12} \simeq 0$ for a fast free evolution. From Eq. (4.50) & (4.51) we obtain

$$\langle n_q^2(t + \Delta t) \rangle_{tr} - \langle n_q^2(t) \rangle = -2j\kappa_j n_0^{j-1} \langle n_q^2 \rangle \Delta t + j\kappa_j n_0^j \Delta t \quad (4.52)$$

$$\langle \theta_q^2(t + \Delta t) \rangle_{st} - \langle \theta_q^2(t) \rangle = \frac{j\kappa_j n_0^{j-2} \Delta t}{4}. \quad (4.53)$$

The subscript tr stands for trajectories. As expected Eq. (4.52) & (4.53) are identical to the ones obtained from the master equation and found in [20, 22]. The derivation in this Sec. 4.2 corresponds to the one we described in [21] for $j = 1$.

Evolution of the mode energy Let us now calculate the time evolution of the mode energy $E_q = A_q \langle n_q^2 \rangle + B_q \langle \theta_q^2 \rangle$. Again we assume slow losses, such that the equipartition of energy holds for all time. The losses changes the Hamiltonian parameters A_q and B_q according to

$$\frac{dA_q}{dt} = \frac{\hbar^2 q^2}{8mn_0} \kappa_j n_0^{j-1} \quad (4.54)$$

$$\frac{dB_q}{dt} = -\kappa_j B_q n_0^{j-1}. \quad (4.55)$$

The quadratures evolve according to Eq. (4.52) & (4.53) which write in differential notation:

$$\frac{d\langle n_q^2 \rangle}{dt} = -2j\kappa_j n_0^{j-1} \langle n_q^2 \rangle + j\kappa_j n_0^j \quad (4.56)$$

$$\frac{d\langle \theta_q^2 \rangle}{dt} = \frac{j\kappa_j n_0^{j-2}}{4}. \quad (4.57)$$

Using the equipartition of energy, one obtains

$$\frac{dE_q}{dt} = \kappa_j n_0^{j-2} \left[E_q n_0 \left(\frac{\hbar^2 q^2}{8mn_0} \frac{1}{2A_q} - j - \frac{1}{2} \right) + j n_0^2 A_q + \frac{j B_q}{4} \right]. \quad (4.58)$$

Eq. (4.58) could have been equivalently derived from the master equation and the Lindbladian in Eq. (1.120). Nevertheless, the Lindblad approach can not be used for the feedback scheme which will be introduced in Sec. 4.7. The feedback scheme relies on the results for the individual trajectories obtained in Eq. (4.42) & (4.46). Furthermore, compared to the master equation approach, the QMC approach provides interesting physical insights into the loss process.

In the phononic limit $\xi q \ll 1$ of Eq. (4.58) the phase diffusion term can be neglected and Eq. (4.58) turns into Eq. (4.71) which will be derived independently in the following Sec. 4.3. The following Sec. 4.3 gives detailed discussion about Eq. (4.58) for phonons.

4.3 Simplified approach

In this section I introduce a complementary approach which leads to the same result as the Quantum Monte-Carlo (QMC) approach for phonons. This derivation is independent from the QMC approach and it follows the derivations in [23, 24]. As in the previous section, we consider j -body losses in a quasi-condensate. The evolution of the linear density n is given by:

$$\frac{dn}{dt} = -\kappa_j n^j. \quad (4.59)$$

The atom number in a small cell of size δz evolves according to $\frac{dN}{dt} = -K_j N^j$ where $K_j = \kappa_j \delta z^{1-j}$. The atom number inside the small cell is $N = N_0 + \delta N$, with δN small compared to N_0 (quasi-condensate regime). During a small time interval⁴ dt the losses are stochastic and the number of events M is close to a Poissonian distribution

$$p(M) = \frac{\lambda^M e^{-\lambda}}{M!} \quad (4.60)$$

with variance and mean $\lambda = \frac{K_j}{j} N^j \Delta t$. The mean number of lost atoms $\tilde{M} = jM$ is

$$\langle \tilde{M} \rangle = K_j N^j dt \quad (4.61)$$

and its variance

$$\langle \tilde{M}^2 \rangle - \langle \tilde{M} \rangle^2 = j K_j N^j dt. \quad (4.62)$$

⁴The small time interval dt in this section would correspond to Δt in the quantum Monte-Carlo approach of Sec. 4.2.

The prefactor j represents the fact that at each loss event j atoms are lost.

Let us now calculate the evolution of the density during dt which is given by:

$$dN = N - \tilde{M} = -K_j N^j dt + d\eta. \quad (4.63)$$

In the last step, we replaced the random variable \tilde{M} by the shifted random variable $d\eta$ of vanishing mean and the same variance $\langle d\eta^2 \rangle = jK_j N^j dt$. The mean density up to first order in δN evolves as

$$dN_0 = -K_j N_0^j dt. \quad (4.64)$$

The density fluctuations up to first order in δN evolve according to

$$d\delta N = -jK_j N_0^{j-1} \delta N dt + d\eta. \quad (4.65)$$

The first term corresponds to a decrease of density fluctuations by losses. This contribution can be obtained from a mean field approach which ignores the quantification of atoms, i.e. their discrete nature. The second term increases density fluctuations due to the shot noise of the losses. The shot noise of the losses can not be captured in a mean field approach.

In the next step let us approximate the variance by $\langle d\eta^2 \rangle = jK_j N^j dt \simeq jK_j N_0^j dt$ and assume that losses in different cells are uncorrelated. Going to the continuous limit this leads to:

$$\langle d\eta(z)d\eta(z') \rangle = jK_j N_0^j \delta(z - z') dt. \quad (4.66)$$

Introducing the Fourier components $n_{q,r}$ according to Eq. (1.63), one obtains in first order in dt the following time evolution:

$$\frac{d\langle n_{q,r}^2 \rangle}{dt} = -2j\kappa_j n_0^{j-1} \langle n_{q,r}^2 \rangle + j\kappa_j n_0^j. \quad (4.67)$$

Here again $r = c, s$ stands for the cosine and sine modes. Since the sine and cosine modes obey the same equations and share the same initial value, I will drop the index r in the following.

Evolution of the Hamiltonian Let us consider the time evolution of the energy for a given mode $E_q = \langle H_q \rangle$ that lies in the phononic regime, i.e. $q\xi \ll 1$. The Bogoliubov Hamiltonian of this mode is

$$H_q = A_q n_q^2 + B_q \theta_q^2 = \frac{mc^2}{2n_0} n_q^2 + \frac{\hbar^2 q^2 n_0}{2m} \theta_q^2. \quad (4.68)$$

The system is initially at thermal equilibrium. At thermal equilibrium the energy is equally distributed between the quadratures, such that

$$\langle H_q \rangle / 2 = A_q \langle n_q^2 \rangle = B_q \langle \theta_q^2 \rangle. \quad (4.69)$$

Let us compute the evolution of $\langle H_q \rangle$ under the effect of losses⁵. The Hamiltonian parameter $A_q = g/2$ stays unmodified by the losses and B_q changes according to

$$\frac{dB_q}{dt} = -\kappa_j B_q n_0^{j-1}. \quad (4.70)$$

Moreover, the density fluctuations $\langle n_q^2 \rangle$ are modified according to Eq. (4.67). In principle one should also consider the effect of losses on the phase quadrature $\langle \theta_q^2 \rangle$. In Sec. 4.2.3 it was shown that this effect is negligible for the phononic modes which we consider in this approach. Furthermore, we assume that the losses rate $\kappa_j n^{j-1}$ is slow compared to the mode frequency $\omega_q = 2\sqrt{A_q B_q}/\hbar$. Then, the equipartition in Eq. (4.69) holds for all times. Summing up the two contributions of Eq. (4.67) & (4.70) and using the equipartition one obtains:

$$\frac{d\langle H_q \rangle}{dt} = -\kappa_j n_0^{j-1} \left[\langle H_q \rangle \left(j + \frac{1}{2} \right) \right] - \frac{g}{2} j \kappa_j n_0^j. \quad (4.71)$$

The mode energy in (4.71) tends to zero in the long time limit. Instead of considering the mode energy, let us focus on the ratio $y = \langle H_q \rangle / (g n_0)$. This ratio obeys the differential equation

$$\frac{dy}{dt} = \kappa_j n_0^{j-1} \left[-y \left(j - \frac{1}{2} \right) + \frac{j}{2} \right], \quad (4.72)$$

which is independent of g . From Eq. (4.72) one deduces that y converges in the long time limit to

$$y_\infty = \frac{1}{2 - 1/j}. \quad (4.73)$$

In the long time limit, the mode energy H_q decreases in the same way as the density decreases and the quantity $y = \langle H_q \rangle / (g n_0)$ becomes a constant. Assuming that we initially start from $y(t=0) > y_\infty$, we have that $y(t) \geq y_\infty \forall t$, which implies that $\langle H_q \rangle > g n_0$. For phononic modes we have $g n_0 \gg \hbar \omega_q$. Those two conditions imply that the phonon occupation number stays large at any time. We can thus introduce the phononic temperature⁶ as $k_B T = \langle H_q \rangle$.

In summary, we obtain that in the long term limit a homogeneous quasi-condensate under the influence of one-body losses tends towards the temperature $k_B T = g n_0$. For three-body losses, it tends to $k_B T = 0.6 g n_0$. For any j it tends to $k_B T = y_\infty g n_0$ where $y_\infty \in [1/2, 1]$.

For further use it is advantageous to rewrite Eq. (4.72) as

$$\frac{dy}{dn_0} = \frac{1}{n_0} \left[y \left(j - \frac{1}{2} \right) - \frac{j}{2} \right], \quad (4.74)$$

⁵For the moment we neglect 3D correction due to the transverse swelling of the transverse ground state such that $c = c_{1D}$.

⁶Eq. (4.72) does not depend on q . Thus the definition of the temperature does not depend on q . Note that this does not hold anymore, when considering particle excitation [22].

which is independent of κ_j . A numerical integration of Eq.(4.74) is shown in Fig. 4.5 for $j = 1, 2, 3$.

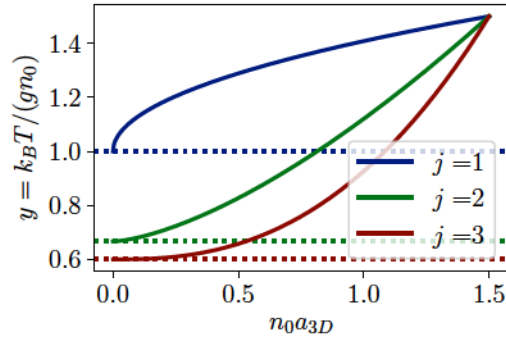


Figure 4.5 – The time evolution of the ratio $y = k_B T / g n_0$ for different j , together with its long time limit (dashed lines). The x-axis $n_0 a_{3D}$ decreases as time increases.

4.4 Cooling by three body losses

In the previous sections (Sec. 4.2 & Sec. 4.3), it was shown that that j -body losses are expected to cool a 1D Bose gas in the quasi-condensate regime. This results is important, since it contradicts "common believe" in our domain. This is particularly true for the case $j = 3$. Within the community of cold atom physicist three-body losses have been generally considered as "bad" losses. They are considered to be linked to undesired heating effects. For thermal gases, they predominantly occur in regions of high atomic densities and lead to an "anti-evaporation" process. In BECs confined in deep traps, it was predicted that three-body collisions produce a heating through secondary collisions with high energy excitations formed by the loss process [139]. Apart from its conceptional interest, the case $j = 3$ is experimentally relevant. As I will describe later, our cold atomic gases can be dominated by three-body losses.

In this Section I present the experimental data which shows that three-body losses indeed cool a 1D Bose gas in the quasi-condensate regime. The experimental data is in agreement with the previously presented theory of Sec. 4.2 & Sec. 4.3. Before describing those results, I will introduce the concept of three-body losses.

Three-body losses Ultracold atom gases are metastable systems. Their ground state is typically a solid. They are thus plagued with intrinsic recombination processes, that limit their lifetime. The main process is the three-body recombination. In a three-body recombination, a molecule (a dimer) is formed and its binding energy is released in the form of kinetic energy of the molecule and the remaining atom. After the three-body recombination process both final constituents are typically lost from the trap. Their energy is typically much larger than the trap depth which we intentionally limit by a radio-frequency field. Additionally, it can be assumed that they do not cause any secondary collisions: The considered process is a 3D process. There is only a very low chance that the leaving constituents collide again with a trapped atom. These arguments justify that the three-body recombination process should lead to the loss of all the three initial atoms involved in the collision. In the following step, we verify this assumption experimentally.

4.4.1 The evolution of the peak density n_p under three-body losses

The aim of this section is to experimentally demonstrate that three-body losses can cool clouds that lie in the quasi-condensate regime. For this purpose, let me argue that in absence of RF-outcoupling, our system should be dominated by three-body losses: Two-body losses are negligible for spin-polarized ^{87}Rb [7, 140]. One-body losses from the background gas and from technical noise are small on our ex-

periment (see Sec. 2.5.1 & Sec. 2.5.2) and they have been measured to be smaller than 0.14s^{-1} . In order to observe clouds dominated by three-body losses⁷, we prepare quasi-condensates by RF-evaporative cooling in a harmonic trapping potential $V(z) = 1/2m\omega_{\parallel}z^2$. We then increase the RF-field by several kHz and verify that after a long waiting time the number of atoms is independent of the frequency of the RF-field. We then investigate the evolution during the time t . We present five different data set with different transverse trapping frequencies ω_{\perp} , initial temperatures T and peak densities n_p . The peak density n_p as a function of the waiting time t is shown in Fig. 4.6. To verify that these clouds are dominated by three-body losses, we calculate the evolution of n_p under the sole effect of three-body losses. Three-body losses decrease the 3D density ρ_{3D} according to

$$\frac{d\rho_{3D}}{dt} = -\kappa^{3D} g^{(3)}(0) \rho_{3D}^3, \quad (4.75)$$

with the 3D three-body loss constant κ^{3D} which is known from literature: $\kappa^{3D} = (1.8 \pm 0.5) \times 10^{-41} \text{ m}^6/\text{s}$ for ^{87}Rb [140]. Inside the quasi-condensate $g^{(3)}(0) \simeq 1$ (see Sec. 4.1). The 3D density factorizes into (see Sec. 1.1)

$$\rho_{3D}^3(x, y, z) = n_0(z) \rho_{2D}(x, y), \quad (4.76)$$

where $\rho_{2D}(x, y) = |\phi_0(x, y)|^2$ is the transverse density with a Gaussian shape as introduced in Eq. (1.2). The 1D three-body rate κ_3 is given by $\frac{dn_0}{dt} = -\kappa_3 n_0^3$, and it is obtained by integrating $\frac{d\rho_{3D}}{dt}$ over the transverse shape of the cloud:

$$\kappa_3 = \kappa_{3D} \iint dx dy \rho_{2D}(x, y)^3 = \frac{\kappa_{3D}}{(\pi l_{\perp}^2)^3} \iint dx dy e^{-\frac{3(x^2+y^2)}{l_{\perp}^2}} = \frac{\kappa_{3D} m^2 \omega_{\perp}^2}{3\pi^2 \hbar^2}, \quad (4.77)$$

In the last step we used the fact that the atoms are in the harmonic oscillator ground state. Since we are interested in having strong three-body losses, we typically work with high densities where 3D effects lead to the swelling of the transverse ground state. As discussed in Sec. 1.3.3 these effects can be taken into account by modifying the width of the Gaussian by $\tilde{l}_{\perp}^2 = l_{\perp}^2 \sqrt{1 + 2n_0 a_{3D}}$. This leads to $\kappa'_3(z) = \kappa_3 / (1 + 2n_0 a_{3D})$. The change of the total atom number N_{at} is then given by

$$\frac{dN_{\text{at}}}{dt} = - \int_{-\infty}^{\infty} \kappa'_3(z) n_0(z)^3 dz. \quad (4.78)$$

In these experiments, we use loss rates which are small enough, such that the cloud profiles follow the equilibrium profiles. Inside the quasi-condensate regime the equilibrium profiles can be approximated by the Thomas-Fermi profile

$$n_0(z) = n_p - \frac{1}{2g} m \omega_{\parallel}^2 z^2 \left(1 - \frac{m \omega_{\parallel}^2 z^2}{4 \hbar \omega_{\perp}} \right), \quad (4.79)$$

⁷To my knowledge, j -body losses with $j > 3$ have never been observed.

which extends over $2R = 2\sqrt{\frac{2\mu_p}{m\omega_{\perp}^2}}$ and 3D effects are taken into account by the modified equation of state (see Sec. 1.3.3). The total atom number N_{at} and the profile $n_0(z)$ are completely determined by n_p and Eq. (4.78) can be rewritten as a differential equation on n_p . We use for this Eq. (4.79) & Eq. (4.78) which we integrate numerically. The result of this numerical integration is shown in Fig. 4.6. The evolution of n_p is in good agreement with the sole effect of three-body losses. Note that these calculations do not contain any fitting parameter.

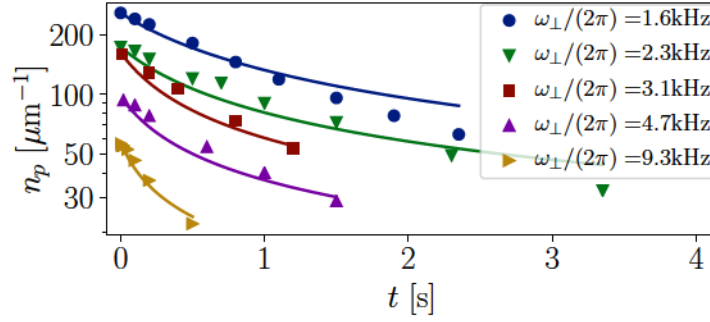


Figure 4.6 – The peak density n_p in log scale versus the waiting time t . Solid lines are ab-initio calculations of the effect of three-body losses for initial peak densities equal to the of the experiment.

Limitations of the model It should be noted that the calculation for n_p assume that the cloud lies completely inside the quasi-condensate regime. This approximation fails in the wings of the cloud where the cloud enters the ideal Bose gas regime. The calculation of this section cannot take into account the atoms which are in the wings. This is the reason why we plot n_p instead of N_{at} . The total atom number N_{at} is more sensitive to those effects in the wings. Another limitation is the value of $g^{(3)}(0)$ which changes from 1 in the quasi-condensate to 6 in the ideal Bose gas regime. The exact dependence is complicated to evaluate. Again, this effect is less important when looking at n_p instead of N_{at} . Finally, it should be noted that the value of κ_{3D} is only known by a precision of 27% [140].

4.4.2 The phonon temperature

The temperature of the gas is obtained by the density ripple thermometry as introduced in Sec. 2.8.1.3 and a typical spectrum is shown in the inset of Fig. 4.7. The main graph of Fig. 4.7 shows the time evolution of the temperature T for the same data sets

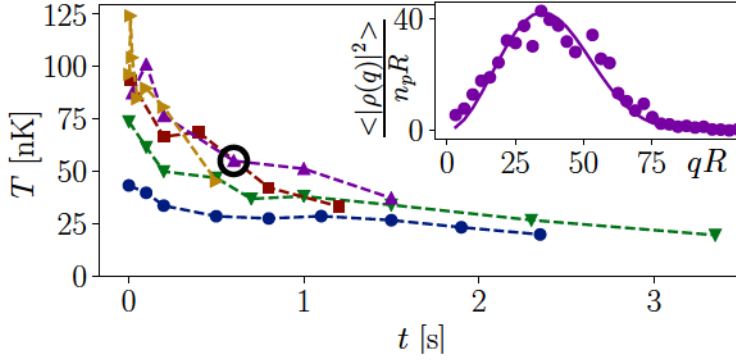


Figure 4.7 – Evolution of the temperature for the five data sets with the same color code as in a). The inset shows a typical density ripple power spectrum which corresponds to the encircled point. The solid line is the fit from which we obtain the temperature T .

as shown in Fig. 4.6. For all data sets the temperature drops and for $\omega_{\perp}/(2\pi) = 2.3$ kHz the temperature drops by a factor as large as 4. Note that the density ripple thermometry is sensitive to phononic excitations. The temperature obtained from the density ripple thermometry can be compared to the predictions of the QMC approach of Sec. 4.3 for phononic modes or equivalently to the simplified approach of Sec. 4.2.

Comment about the fitting procedure The density ripple thermometry is based on a fit with the temperature T and the imaging resolution σ as a free parameter. The imaging resolution σ is a parameter of the the optical imaging system. For the data sets in this chapter it only depends on the transverse width of the cloud and thus on the transverse trapping frequency ω_{\perp} . For each data set (same ω_{\perp}) we fit at $t = 0$ the density ripple spectrum with T and σ as a free parameter. For all the other data points we fit the density ripple spectrum with T as a free parameter and use the value for σ obtained at $t = 0$. The assumption of this procedure can be experimentally verified by fitting every data point with T and σ as a free parameter. The imaging resolution σ shows a very small dispersion for the same ω_{\perp} , except for data at low densities where the signal to noise ratio is low.

The statistical uncertainty on the temperature T , obtained from the fit, is typically very low (a few percent) and hardly visible in Fig. 4.7. As discussed in Sec. 2.9, we do not expect the statistical error to be dominant and we do not show error bars.

4.4.2.1 Comparison to theory

Before comparing the experimental data to theoretical predictions, let me introduce two theoretical refinements of the theoretical model introduced in Sec. 4.2 and equiv-

alently in Sec. 4.3. Those refinements are important for a quantitative comparison with the experimental results. The two refinements correspond to the effect of the trapping potential and the effect of the swelling of the transverse wavefunction due to high densities. These corrections modify the equations, but do not modify the overall picture of the cooling induced by three-body losses, as presented up to now.

High density effects We explicitly choose experimental situations where the three-body losses rate is large enough to be the dominant process. At low ω_{\perp} this directly imposes to use high densities and 3D corrections due to the transverse swelling of the transverse ground state cannot be neglected. As detailed in Sec. 1.3.3 in a linearized approach, the Bogoliubov Hamiltonian can be written as in Eq. (4.68) where the speed of sound is given by $c^2 = \frac{c_{1D}^2}{\sqrt{1+4a_{3D}n_0}}$. The time evolution of B_q stays unmodified (Eq. (4.70)), and the modification of A_q is given by:

$$\frac{dA_q}{dt} = A_q \kappa_{1D} n_0^2 \frac{2n_0 a_{3D}}{1+4a_{3D}n_0}. \quad (4.80)$$

Following the same arguments as in Sec. 4.3, we obtain

$$\frac{d\tilde{y}}{dt} = \kappa_{1D} n_0^2 \left[-\tilde{y} \left(3 - \frac{1+2a_{3D}n_0}{2(1+4a_{3D}n_0)} \right) + \frac{3}{2} \right] \quad (4.81)$$

where we introduced the quantity $\tilde{y} = \frac{k_B T}{mc^2}$. The quantity \tilde{y} is the natural generalization of $y = \frac{k_B T}{gn_0}$ and as we will see later, it is the most relevant quantity. In the asymptotic limit n_0 tends to zero and we recover the same expression as in Eq. (4.73) & (4.72). This leads to $\tilde{y}_{\infty} = 0.6$ for three-body losses. The effect of the transverse broadening allows the system to reach transiently slightly lower scaled temperatures than the final $\tilde{y}_{\infty} = 0.6$, even for $\tilde{y}(t=0) > 0.6$. The minimal value that $\tilde{y}(t)$ can reach for $y(0) > y_{\infty}$ is

$$\tilde{y}_{\min}(a_{3D}n_0) = \frac{3(1+4a_{3D}n_0)}{5+22a_{3D}n_0}. \quad (4.82)$$

This value stays in the interval $[0.6, 0.54]$. The coldest temperatures thus never deviates by more than 10% from the asymptotic value 0.6 as shown in Fig. 4.8. This situation is different when considering the scaled temperature T/μ or $k_B T/(gn_0)$ where much larger deviations would appear. This justifies the previous introduction of the quantity \tilde{y} . Detailed calculations for any j , can be found in [23].

Trapping potential For the treatment of the trapping potential let us come back to a pure 1D situations ($na_{3D} \ll 1$) and let us restrict the discussion to a harmonic potential. Then, the wave functions of the Bogoliubov modes are the Legendre polynomials as introduced in Sec. 1.3.2. In a trap, the additional condition that the loss

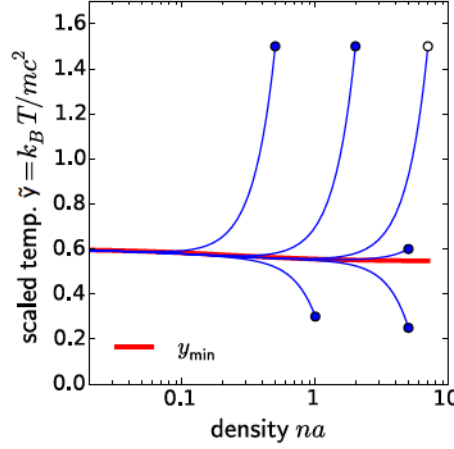


Figure 4.8 – Three-body cooling of a homogeneous quasi-condensate. The initial densities are high, such that the transverse broadening is relevant. The blue curves correspond to different initial values. The red line shows the function \tilde{y}_{min} which gives the values of \tilde{y}_{min} during the cooling process.

rate is small compared to the mode frequency difference $\Delta\omega_v \simeq \frac{1}{2}\sqrt{2}\omega_{||}$ needs to hold, such that the losses do not introduce coupling between different modes⁸. The system follows adiabatically the effect of the losses such that equipartition of the energy holds at all times and the ratio $A_v = \langle H_v \rangle / (\omega_v)$ is unaffected by the modification of n_0 . The dynamics of A_v is then given by the modifications of $\delta n(z)$ and $\theta(z)$ induced by the losses and we have

$$\frac{dA_v}{dt} = \frac{1}{2} \left(\frac{d\langle x_v^2 \rangle}{dt} + \frac{d\langle p_v^2 \rangle}{dt} \right). \quad (4.83)$$

Here x_v and p_v are the canonically conjugated variables introduced in Sec. 1.3.2. The time evolution of $\frac{d\langle x_v^2 \rangle}{dt}$ and $\frac{d\langle p_v^2 \rangle}{dt}$ is calculated in [23]. For a harmonic trap, we replaced the ratio \tilde{y} by $\tilde{y} = k_B T / (mc_p^2)$ where c_p is the speed of sound at the center of the trap. When using the asymptotic expansion of the Legendre polynomials of Eq. (1.87) one can show that the asymptotic value is given by

$$y_{\infty} \simeq \frac{\frac{3}{\pi} \int_0^{\pi/2} d\alpha \sin^6 \alpha}{\frac{6}{\pi} \int_0^{\pi/2} d\alpha \sin^4 \alpha - \int_0^{\pi/2} d\alpha \sin^7 \alpha} \simeq 0.701. \quad (4.84)$$

⁸This condition was already imposed by the calculation for the peak density n_p in Sec. 4.4.1. Since in Fig 4.6 the experimental data is in good agreement with those calculations, one can assume that this condition is verified.

Thus the asymptotic value evaluated at the trap center only differs by 15% from the one in the homogeneous case. Detailed calculation in a trap are given in our paper [23] which also considers correction due the transverse swelling in a trap.

Comparison with the two theoretical refinements In order to compare the observed drop in temperature due to three-body losses of Fig. 4.7, we show the same data in Fig. 4.9. The temperature is replaced by the quantity $\tilde{y} = k_B T / (m c_p^2)$ for which all data sets should reach the same asymptotic value. Additionally, the data is shown as a function of n_p , such that the underlying differential equation (Eq. (4.74)) is independent⁹ of κ_3 . While n_p explores more than one order of magnitude, $k_B T / (m c_p^2)$ shows a small dispersion and stays close to the predicted asymptotic value \tilde{y}_∞ . The data qualitatively agrees with numerical calculations that take into account the transverse swelling and the trapping potential (shown in grey lines) for typical initial situations.

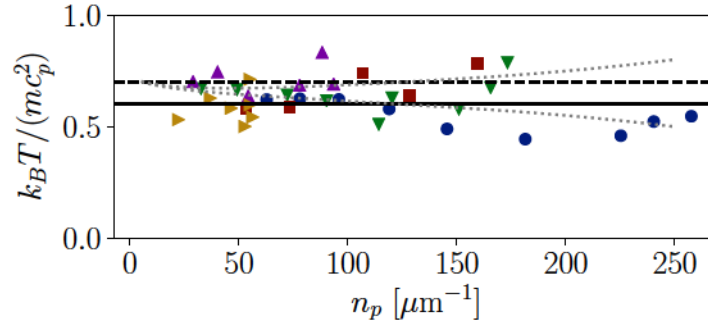


Figure 4.9 – a) Evolution of the ratio $k_B T / (m c_p^2)$ during the three-body loss process for the five data sets (same color codes and data sets as in Fig. 4.6). The solid line corresponds to the asymptotic ratio for a 1D homogeneous gas. The dashed line corresponds to the asymptotic ratio for a 1D gas confined in a harmonic trap. The dotted lines are numerical calculations that take into account the transverse swelling and the trapping potential for two different initial situations.

4.4.2.2 Evolution towards the asymptotic ratio

Already at the beginning of the observed time-evolution the ratio $k_B T / (m c_p^2)$ is close to its asymptotic one. In principle, one could expect that initially the cloud would be hotter ($\tilde{y} > \tilde{y}_\infty$), as shown in the theoretical predictions of Fig. 4.8. We do not

⁹The same holds in a trap, as shown in Eq. (32) in [23].

attribute a fundamental reason to the lack of values of \tilde{y} much larger than \tilde{y}_∞ . We interpret this situation as a technical artifact. Data was only taken for gases which were already sufficiently cooled by evaporative cooling so that the gas lies in the quasi-condensate regime, where both the thermometry and theoretical description apply. It occurs that, in our experiment, when the gas enters the quasi-condensate regime, the ratio $k_B T / (mc_p^2)$ is already close to \tilde{y}_∞ .

Quenching towards different values of \tilde{y} We did not take any data with the intention to study this effect of the evolution towards \tilde{y}_∞ . However, a reanalysis of old data sets, taken with the purpose to study the recurrence phenomena, turned out to show the expected behavior.

A gas with a value of \tilde{y} different than \tilde{y}_∞ can be realized after an interaction quench (see Chap. 3). A short time (some milliseconds) after the quench the system evolves towards a new equilibrium situation. This was observed on the density ripple spectrum as discussed in (see Sec. 3.4.4). The new equilibrium temperature after the quench with quench strength κ is given by $T' = (\kappa + 2) T_i / 2$. The new ratio¹⁰ $y' = \frac{k_B T'}{g' n_0} = \frac{k_B T}{g n_0} \frac{\kappa + 2}{2(\kappa + 1)}$ decreases for a quench to higher g' ($\kappa > 0$).

Even though it does not corresponds to the paradigmatic situation of cooling from high \tilde{y} towards its final value \tilde{y}_∞ , let us consider the situation of a quench with $\kappa = 4$ where we expect \tilde{y} to increase to its asymptotic value \tilde{y}_∞ . The increased value of g' accelerates the three-body losses and Fig. 4.10 shows how the gas evolves from an initial value $\tilde{y} < \tilde{y}_\infty$ to its final value not far from $\tilde{y}_\infty = 0.7$. Since this data set was not taken with the purpose of studying this phenomena, the uncertainty is quite high and we show the statistical uncertainty in Fig. 4.10. The initial value \tilde{y} , prior to quench, is already below its asymptotic value for three-body losses. This is due to the preparation scheme with RF-outcoupling (see Sec. 4.5)¹¹.

In principle one could observe the cooling towards \tilde{y}_∞ from higher values of \tilde{y} by a quench to lower g' ($\kappa < 0$). This method is however not very practical. A decrease of g' leads to a reduced three body-losses rate which makes it difficult to create situations which are dominated by three body-losses.

4.4.2.3 The phase diagram

In Fig. 4.9 the data was presented as a function of the linear density n_p which is not the most relevant quantity. Pure 1D gases are described by the Lieb-Liniger model which is parameterized by the dimensionless quantities t_{YY} and γ (see Sec. 1.2.4).

¹⁰The same arguments hold for \tilde{y} when corrections due the swelling of the transverse wave function are taken into account.

¹¹In principle it could be argued that it is sufficient to observe the ratio starting from the preparation $\tilde{y} \approx 0.3$. In practice it turned out, that in such a situation the density was already too low and not dominated by three-body losses.

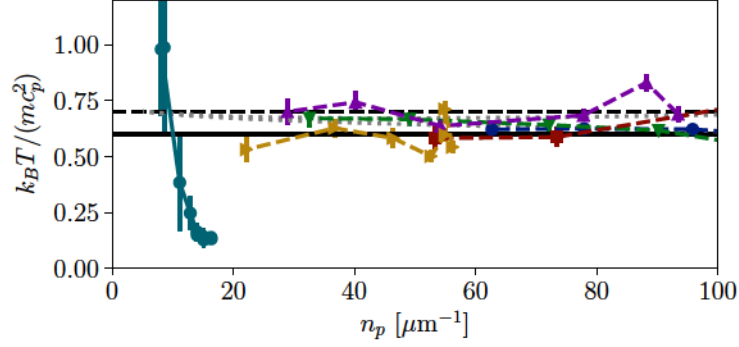


Figure 4.10 – The evolution of the ratio $k_B T / (m c_p^2)$ during the three-body losses after an interaction quench of $\kappa = 4$ shown in pale blue dots. The other data points are the previously presented data presented in Fig. 4.9 (same color codes). After the quench we wait for $t = 60$ ms to let the system thermalize. The quench reduces the initial parameter \tilde{y} and the temperature evolves towards a value close to its expected final value $\tilde{y}_\infty = 0.7$. Note that this set of data was not taken on purpose for this task which explains the large error bars for the last points. The error bars represent 68% confidence interval are fitting errors which are shown in order to highlight the uncertainty on the last data points.

Here, we generalize those quantities to situations where the swelling of the transverse wavefunction is important. This leads to

$$\tilde{t}_{YY} = \frac{\hbar^2 k_B T n^2}{m^3 c^4} \quad \text{and} \quad \tilde{\gamma} = \frac{m^2 c^2}{\hbar^2 n^2}. \quad (4.85)$$

In the case of the harmonically confined gas, we evaluate those quantities at the center of the trap. The asymptotic limit then corresponds to $k_B T / (m c_p^2) = \tilde{\gamma} \tilde{t}_{YY} \simeq 0.7$. The evolution of the gas in the phase diagram is shown in Fig. 4.11. All the data collapse on the line $\tilde{\gamma} \tilde{t}_{YY} \simeq 0.7$, with a maximum deviation of 36%, while \tilde{t}_{YY} explores more than 2 orders of magnitude. Fig. 4.11 suggests that the system would enter the Tonks regime, as the density further decreases by three-body losses. This is not guaranteed. Close to the Tonks regime the three-body loss coefficient drops to zero and the dynamic starts to take place on very long time scales. Additionally, the theory presented in Sec. 4.2 (or equivalently Sec. 4.3) is valid inside the quasi-condensate regime. The effect of losses in the crossover towards the Tonks regime remains an open questions and is worth further investigation.

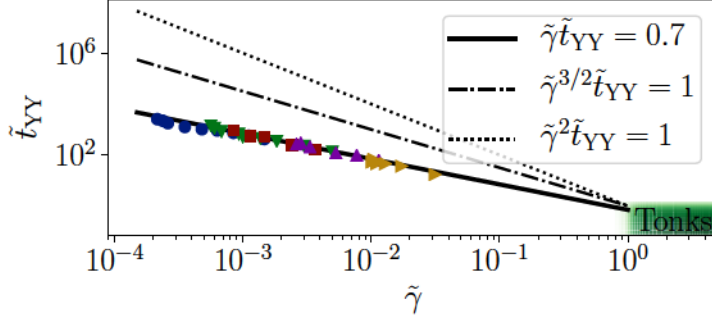


Figure 4.11 – The experimental data in the Lieb-Liniger phase diagram (see Sec. 1.2.4). The data collapses on the line $\tilde{\gamma} \tilde{t}_{YY} = 0.7$ which corresponds to the crossover between the thermal and quantum quasi-condensate (and which corresponds at the same time to the asymptotic limit in a harmonic trap). The data sets and colors codes are the same as in Fig. 4.6.

4.4.3 Yang-Yang thermometry

The previous part of this chapter focused on the phonon temperature deduced by the density ripple analysis. As observed in [22, 36] the phonon temperature, deduced by the insitu density fluctuations, can significantly differ from the temperature deduced by the fit of the density profile with the Yang-Yang equation of state (see Sec. 2.8.2). One can expect a similar difference in the temperature deduced from the density ripple analysis and the temperature deduced from the density profile. In this section I apply, in a preliminary study, the Yang-Yang thermometry on the profile of the clouds and study the effect of the fitted temperature under the effect of three-body losses.

It turns out that for this study no new data is necessary and we apply the analysis on the data sets studied in this section: Indeed, we verified that the longitudinal profile does not change for the short time-of-flight of $t = 8$ ms which was used for the density ripple analysis. We thus fit the mean density profile of the data sets used for the density ripple analysis with the Yang-Yang thermometry. More precisely, we use the modified Yang-Yang equation of state which takes into account the transverse excited states and we apply the LDA. The fitting algorithm with two free parameters: the temperature T_{YY} and the peak chemical potential μ_p . Since we are interested in a high atomic density, such that the three-body loss rate is large, 3D corrections due to the transverse swelling of the quasi-condensate in the center of the trap can be important in these data sets. The Yang-Yang thermometry cannot take into account these corrections and the fits are applied in a zone where $a_{3D}n(z) \ll 1$ and transverse swelling is negligible. In practice we chose the condition $a_{3D}n(z) < 0.3$ (see Fig. 4.12). This procedure excludes a zone of the central part of the cloud for the

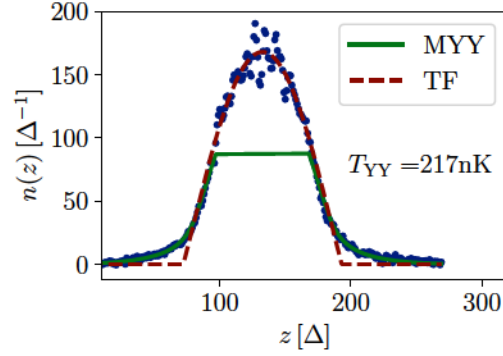


Figure 4.12 – A typical density profile together with the modified Yang-Yang (MYY) (see Sec. 1.2.3.1). In comparison the Thomas Fermi (TF) profile obtained from the modified equation of state Eq. (1.91). The Yang-Yang fits are restricted to zones of low atomic density ($a_{3D}n < 0.3$), such that correction due the swelling of the transverse wavefunction are small.

fitting routine (see Fig. 4.12). The width of the this zone depends on the peak density. For very high peak densities the part of the cloud which is used for the fit can completely lie in the ideal Bose gas regime. This leads to unstable fit results: The information for μ_p is mainly contained in the zone which lies in the quasi-condensate regime (see Thomas-Fermi (TF) profile in Fig. 4.12). When the quasi-condensate region is not contained in the fitting data, the result for μ_p started to deviate from the expected value $\mu_p = \hbar\omega_{\perp} (\sqrt{1 + 4n_p a_{3D}} - 1)$ and showed strong dependence on the initial value. Therefore, we restrict our analysis to data sets where, at least, a part of the cloud followed the Thomas-Fermi in the zone $na_{3D} < 0.3$. This effectively restricted the analysis to the previous data sets with $\omega_{\perp}/(2\pi) \geq 4.7$ kHz. The result of the Yang-Yang thermometry is presented in Fig. 4.13. For all data sets the temperature drops during the three-body losses. The ratio between the phonon temperature, measured with the density ripple analysis method and the temperature measured by the modified Yang-Yang fits, T_{YY}/T_{phonon} increases up to a factor of 5.

As expected from the results of [22, 36] the temperature deduced from density fluctuations and the temperature deduced from a fit of the profile (Yang-Yang thermometry) are different. The authors of [22, 36] observed that T_{YY} is typically a factor two higher than the phonon temperature. In 4.13 the initial ratio T_{YY}/T_{phonon} is also close to 2. Subsequently, the three-body losses even increase the ratio T_{YY}/T_{phonon} to a maximal value of 5. This clearly indicates that we observe an out-of-equilibrium situation.

In contrast to the density ripple thermometry the Yang-Yang thermometry does not measure the phonon temperature. It is typically sensitive to the part of the cloud

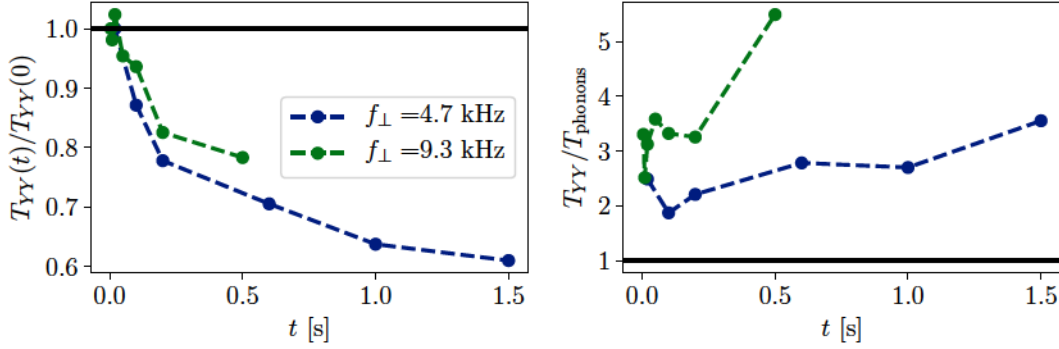


Figure 4.13 – a) The modified Yang-Yang temperature T_{YY} obtained from fitting the density profile (see Fig. 4.12) under the influence of three-body losses. In both cases the temperature drops. b) The ratio between the phonon temperature and the modified Yang-Yang temperature T_{YY} which increases during the three-body losses.

which is in the ideal Bose gas regime. The theoretical considerations introduced in the beginning of this chapter (Sec. 4.2 & 4.3) are only valid in the quasi-condensate regime and cannot be directly compared to T_{YY} .

4.5 Cooling by one-body losses

The results of Sec. 4.2 (or equivalently Sec. 4.3) show that one-body losses should cool a 1D Bose gas in the quasi-condensate regime. One-body losses can be implemented by RF-outcoupling scheme (see Sec. 2.3.1.2). In the following section 4.5.1 I give an overall description how the RF-outcoupling is thought to cool a single cloud on the atomchip experiment. In the next section 4.5.2 I discuss where this simplified picture stands in contradiction to the current experimental observations.

4.5.1 Cooling a single cloud into the 1D regime

On the atomchip experiment we start with a hot 3D cloud on which we apply forced evaporative cooling with RF-outcoupling (see Sec. 2.3.1.2). The RF-outcoupling steadily removes the most energetic atoms of the cloud and the subsequent thermalization leads to a reduction of the temperature, as sketched in Fig.4.14. This outcoupling therefore relies on an energy-selective process.

Failure of evaporative cooling in 1D Once the cloud enters the 1D regime, the evaporative cooling is expected to drop drastically in efficiency. This is due to the

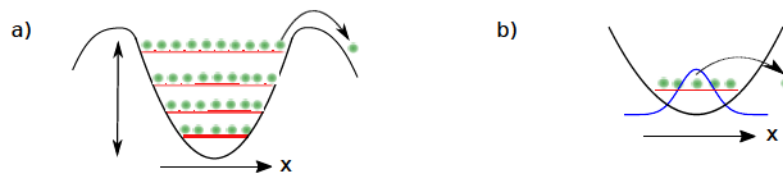


Figure 4.14 – The transverse direction during evaporative cooling into the ground state. a) At the beginning the most energetic atoms are removed. The loss occurs by an adiabatic following of the states dressed by RF-field: the low field seeking state is adiabatically transformed into the high field seeking state as the resonance is crossed. b) Once all the atoms are in the ground state, the loss process is not selective in energy in the transverse direction. A small RF-amplitude leads to a coupling of the trapped state to the untrapped state.

following effects:

- **No energy selectivity in the transverse direction:** Let us for the moment restrict ourselves to the transverse directions: Once the atoms enter the 1D regime, almost all the atoms populate the transverse ground state and the losses cannot be selective in energy anymore (see sketch of Fig. 4.14).
- **Suppressed cooling rate in shallow traps:** Concerning the longitudinal direction the efficiency of the evaporative cooling is expected to be strongly reduced. In the experiment we use shallow traps whose oscillation frequency is of the order of a few Hertz. Cooling due to evaporative cooling is expected to occur on time scales larger than a $1/\omega_{\parallel}$. Observed cooling rates are much faster. Additionally, thermalization in an integrable system is not guaranteed, while it is required for evaporative cooling.

One therefore expects that the evaporative cooling scheme gradually stops working once the cloud approaches the 1D regime.

Energy-independent cooling by one-body losses When the cloud enters the 1D regime in the quasi-condensate regime the cooling scheme induced by energy-independent losses becomes important. The RF-outcoupling produces approximately homogeneous one-body losses ($j = 1$). Note that this is a simplification. The atoms are trapped in a longitudinal magnetic potential which makes the loss process a priori space dependent, since the resonance condition for spin-flips depends on z . In [19, 138] it is argued that in typical situations the losses are almost homogeneous in the longitudinal direction. For homogeneous losses one can use the theoretical prediction of this chapter (see Sec. 4.3 or Sec. 4.2 equivalently) which leads to further cool-

ing. The temperature is expected to decrease¹² with the peak density n_p

$$k_B T \propto mc_p^2 \underbrace{\approx gn_p}_{\text{1D-limit}}. \quad (4.86)$$

In the view of the experimental implementation the difference between evaporative cooling due to RF-outcoupling and cooling by energy-independent RF-outcoupling might appear very technical. The physical concepts of both cooling mechanisms are, however, very different.

4.5.2 Experimental results for $j = 1$

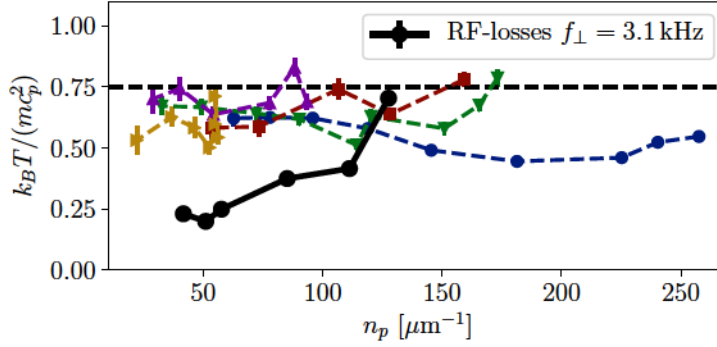


Figure 4.15 – Cooling with one-body losses induced by RF-outcoupling (black points) in comparison with the previously presented data from three-body losses (same data as in Fig. 4.9). The observed temperatures are clearly below the expected limiting temperature $k_B T = 0.75 m c_p^2$ inside a harmonic trap (black dashed line).

As in Sec. 4.4 for three-body losses the theoretical predictions for one-body losses can be tested experimentally. Again, we use the density ripple analysis to observe the temperature evolution of a cloud dominated by one-body losses. A cloud dominated by one-body losses is produced by lowering the RF-frequency, such that a strong out-coupling of atoms occur. This ensure that the losses by RF-outcoupling occur on timescales much faster than the three-body losses. The result for a cloud dominated by one-body losses is shown in Fig. 4.15. In a harmonic trap one expects that for $j = 1$ the limiting temperature is $k_B T = 0.75 m c_p^2$ [23]. The experimental data (black points) clearly differs from this expectation and drops to much lower temperatures. In [19]

¹²Three-body losses may also play a role in the current experimental setup. This does not change the picture of the cooling process. The system follows $k_B T = \gamma_\infty m c_p^2$ where γ_∞ is close to 1 and depends on j and the trapping geometry. See also Sec. 4.6 for a different trapping geometry.

the cooling by RF-outcoupling was also observed. Similarly to the results in Fig. 4.15, the temperature dropped to values as low as $k_B T = 0.25 g n_0$.

In summary, the experimental results for $j = 1$ do not correspond to the theoretical expectation and the limiting temperature for one-body losses ($k_B T = 0.75 m c_p^2$) is not observed. This differs from the situation for $j = 3$ where precisely this limiting temperature was observed. This discrepancy is not understood: A non-homogeneous outcoupling might be behind this observation, but further investigation is needed. Still, we observe a cooling which cannot be explained by evaporative cooling. Note that three-body losses rely on the intrinsic atomic properties where such technical problems are not present.

4.6 Quartic potentials

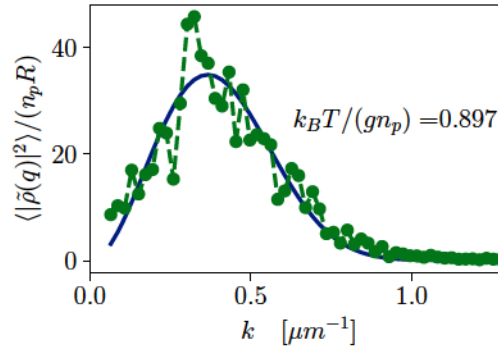


Figure 4.16 – Density ripple spectrum for a quartic longitudinal trapping potential, together with a fit of the temperature

The density ripple thermometry can also be performed in different longitudinal trapping geometries, as the double well potential and the quartic trapping potential. In Fig. 4.16 a density spectrum inside the quartic trapping potential is shown. Its structure resembles the ones obtained in the harmonic confinement. The density ripple thermometry inside the quartic potential and inside the double-well potential always led to temperatures close to $k_B T / (m c_p^2) = \tilde{y}_\infty$ where \tilde{y}_∞ was always close and smaller than 1. This corresponds to the anticipation from¹³ [23]. A detailed study of the effect of losses on the temperature in the quartic trap was not possible. The

¹³Although no explicit calculation for a quartic potential are performed in [23], the introduced theory applies to any smooth potential. The results differs only on the numerical factor \tilde{y}_∞ .

quartic potential is not stable in time¹⁴ due to drift in the potentials as detailed in Sec. 2.3.2.2.

4.7 Quantum Feedback

This section is based on our paper [21] which extends the previously introduced cooling by losses. It contains a proposal to cool one collective mode of a 1D Bose gas to its ground state via a feedback loop. For this task, we imagine position resolved detectors together with a 1D lattice whose amplitude is controlled by the feedback loop as shown in Fig. 4.17. Depending on the losses in the 1D Bose gas, the amplitude is adapted and a cooling of the phononic mode of wavevector equal to the one of the lattice can be achieved, as I will detail in the following. Its theoretical description relies on the Quantum Monte-Carlo approach introduced in Sec. 4.2 and cannot be understood by the simplified approach introduced in Sec. 4.3. In principle this section could be generalized to j -body losses. For simplicity I will restrict myself to the case $j = 1$ and to a homogeneous system.

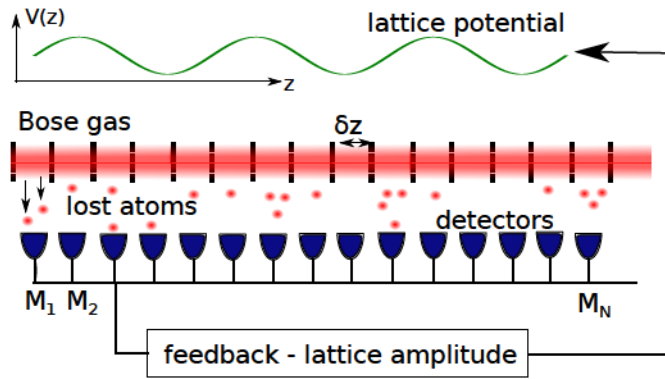


Figure 4.17 – The 1D Bose gas with atom losses and a spatially resolved single atom detector system. The information on the losses can be used to create a feedback loop on the atoms via a lattice potential. The amplitude of the lattice potential is controlled by a processing unit which uses the information gained from the atom losses.

As previously shown the phononic excitations reach an asymptotic temperature $k_B T = gn_0$. This asymptotic temperature is the result of the competition of a heating and a cooling process, mentioned in the introduction. The idea of this section is to overcome this limit by compensating the heating process via the feedback loop.

¹⁴The stability arguments presented in Sec. 2.3.2.2 for the double-well, directly apply to the quartic trap.

If the number of lost atoms¹⁵ M_i inside a small cell during the time interval Δt are recorded, the trajectory followed of the center the Wigner distribution \vec{R} can be followed exactly. The feedback process then forces \vec{R} to stay in the center of the phase-space (n_q, θ_q) .

Modification of g It turns out that the cooling of the phonons to the ground state can only be achieved, when g is adapted in time as

$$g(t) = g(t=0)e^{\Gamma t}, \quad (4.87)$$

where $\Gamma = \kappa_1$ is the one-body loss rate. As detailed in [21], without this modification of g an initial phononic excitation is already promoted to the particle regime before approaching the ground state $\hbar\omega_q/2$. When considering the modification of Eq. (4.87) the dispersion relation is unmodified by the losses. The change in g also modifies the long time limit into $k_B T = gn_0/2$.

The feedback hamiltonian Let us now follow a given phononic mode q, c and consider the effect of the feedback lattice given by the periodic potential

$$V(z) = A(t) \cos(qz). \quad (4.88)$$

This potential could be implemented by an optical lattice or a spatial light modulator. The Hamiltonian of this lattice is given by $H_{\text{fb}} = A(t)\sqrt{L/2}\hat{n}_{q,c}$. In order to counteract the diffusion process of the center of the Gaussian R , one could adjust $A(t)$ such that the feedback Hamiltonian is given by

$$H_{\text{fb}} = -\hbar\nu\langle\theta_{q,c}\rangle\hat{n}_{q,c}. \quad (4.89)$$

At each time interval $\langle\theta_{q,c}\rangle$ is computed by integrating the equation of motion including the effect of losses, the free evolution and the feedback process. The feedback Hamiltonian then acts as an active damping which prevents $\langle\theta_{q,c}\rangle$ to drift from the phase space center. The free evolution of the Bogoliubov Hamiltonian ensure that neither θ_q , nor n_q drift away from the center. For a large enough damping rate ν the contribution of \vec{R} to the energy of the mode is expected to be negligible compared to the contribution of the covariance matrix C . It can be shown that the covariance matrix reaches the ground state (for details of calculation see [21]). Fig. 4.18 shows numerical calculations of the energy evolution averaged over quantum trajectories. Without feedback ($\nu = 0$) the system evolves towards the asymptotic limit¹⁶ $k_B T = gn_0/2$. For a strong enough feedback strengths ν , the system evolves towards

¹⁵For $j = 1$, we have $M'_i = M_i$.

¹⁶The factor two arises from the modification in $g(t)$.

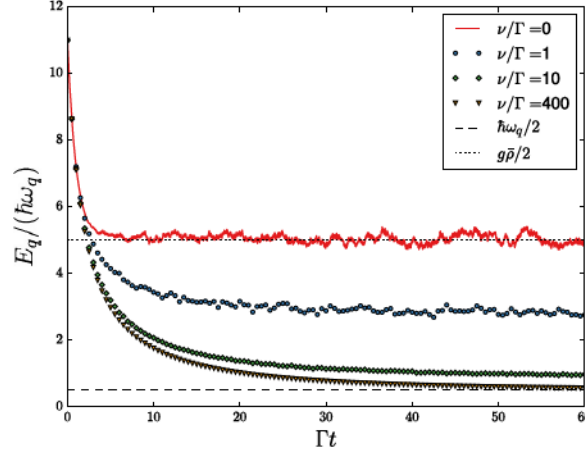


Figure 4.18 – Simulation of the loss process for different feedback strengths ν : The energy in the mode q is obtained from 550 quantum trajectories and the parameters are the same as in Fig. 4.4. Without feedback the mode energy evolves to $gn_0/2$ (dotted line). With a sufficiently large feedback strength, the system evolves into its ground state $\hbar\omega_q/2$ (dashed line).

its ground state $E = \hbar\omega_q$. The drift of the center is almost completely prohibited and the mode is cooled to its ground state. The feedback does not represent a Maxwell's demon. Close to the ground state effects as the spontaneous emission in the lattice laser becomes important, such that the second law of thermodynamics is not violated.

Note that this proposal is not brought to full maturity. Its practical implementation is not straightforward. For a cooling of the whole system, as many lattices as modes would be necessary. Furthermore, we did not perform any calculations on the sensitivity of the parameters. Probably a very precise knowledge of the mode frequency would be necessary.

A theoretical generalization to j -body losses should be straightforward. Since the practical interest is not very strong, we leave the generalization to j -body losses to further work.

4.8 Outlook

Higher dimensions As long as one considers the linear Bogoliubov approach, the theoretical arguments for the cooling by energy independent-losses also hold in higher dimensions ($d = 2, 3$) [23]. Taking into account that three-body losses are a common phenomenon in ultra-cold atom physics and until now, no observation of a cooling by

three-body losses was observed¹⁷, these theoretical arguments should be taken with caution. Let me finish this aspect with some more speculative arguments: One possible explanation to this puzzle might be the role of integrability. As shown in [22] the one-body outcoupling process creates an out-of-equilibrium situation where all the Bogoliubov modes are cooled and the particle excitations ($q\xi \gg 1$) obtain higher temperatures than the phonons. This situation is stable in time and we expect the same to hold for three-body losses. Again in [22] we show that this out-of-equilibrium situations vanishes by a coupling to a second 1D system with a different mass¹⁸. The energy of the phononic modes starts to increase due to a coupling to the hotter particle like excitations. Note that this coupling breaks the integrability of the system. The same arguments could be expected to hold in higher dimensions, since in higher dimensions the system is not integrable anymore. The coupling to the particle-like excitation reduce the cooling effect.

An additional effect which could screen the cooling effect in higher dimensions is due the difference in the density of states. The density of states $D_d(E)$ in d dimensions for particle like excitations scales like

$$D_d(E) \propto E^{\frac{d}{2}-1}. \quad (4.90)$$

For $d > 1$ there exists more states for higher energies than for $d = 1$. This might make the effect of an "heating" of the phonons by the particles more pronounced than in higher dimensions. Note that we expect that the loss process still cools the particle like excitations, however less than the phonons. It can therefore be speculated that the cooling still exists in higher dimensions, but it is strongly suppressed. Its effect might be too small for observation.

Out-of-equilibrium state The observation of Sec. 4.4.3 shows that the three-body losses create an equilibrium situation with $T_{YY} \neq T_{\text{phonon}}$. Similar results were also obtained in [22, 36] for one-body losses. This observation challenges the description of the clouds on the atomchip setup. Both the Yang-Yang thermometry and the density ripple thermometry are based on the assumption of a thermal equilibrium. It is unclear how these two temperature (T_{YY} and T_{phonon}) should be related to an underlying quasi-momentum distribution $\rho_p(k)$. Losses are central to the creation of 1D clouds in the quasi-condensate regime. We cool the cloud with one-body and/or three-body losses into the 1D regime where at least one of the two loss-types are always present. Therefore, it has to be assumed that this out-of-equilibrium states exists in all the realizations of a quasi-condensate.

¹⁷The observation of the phonon temperature in higher dimensions is experimentally challenging. For a system which thermalizes, one could still expect to observe a cooling of the temperature of the system.

¹⁸The coupled system consists of two homogeneous 1D Bose gases with contact interactions and different masses m and m' . The system is simulated by classical field simulations.

GHD with losses The theoretical approach in this chapter is based on the Bogoliubov description inside the quasi-condensate regime. It would be interesting to study the effect of losses in different regimes. Ideally, such a theory is based on the Bethe-Ansatz such that it can be applied to all 1D regimes. In the next chapter we study the theory of Generalized Hydrodynamics (GHD) which is based on the Bethe-Ansatz solution. GHD faithfully predicts the dynamics of the density profile, but cannot take into account particle losses. In collaboration with Benjamin Doyon and Jérôme Dubail we are working on a Quantum-Monte Carlo approach (Sec. 4.2) applied to GHD. Such an approach could predict the evolution of the density profile due to losses and a comparison to the results in Sec. 4.4.3 could be interesting.

Summary:

- We compute the cooling of collective modes produced by j -body losses inside the quasi-condensate regime. For phonons we find that at large times T is proportionally to mc^2 where c is the speed of sound of the system which decreases in time and we compute the stationary ratio of $k_B T / (mc^2)$.
- We experimentally verify this prediction for $j = 3$ and observed the expected cooling which is in agreement with the expected stationary value.
- Based on a Quantum-Monte Carlo approach we propose a feedback scheme to cool a Bogoliubov mode to its ground state.

Chapter 5

Generalized Hydrodynamics (GHD)

This chapter presents the first experimental study of the recent theory of Generalized HydroDynamics (GHD) [15, 16]. The aim of the chapter is to show that GHD predicts the correct out-of-equilibrium dynamics of 1D Bose gases. Moreover, we are able to show that the "standard" theories fail to describe the experimental results. For those standard theories we take into account:

- Ideal Bose Gas (IBG)
- Gross-Pitaevskii (GP)
- Classical Field (CF)
- Conventional HydroDynamics (CHD).

Of course such a list is never complete and we restrict ourselves to theories which are widely used to model cold atom experiments. Special emphasize is put on the comparison with CHD which is the counterpart of GHD in a non-integrable system.

We created three different experimental setups with increasing experimental complexity. In each setup we start from an equilibrium situations and follow the evolution of the density profile after a quench of the longitudinal potential. In the first setup, we show that GHD gives a very accurate descriptions of the experimental results. At the same time we show that, already at equilibrium, most previously mentioned standard theories fail to reproduce the density profile. In the second one, we show that the prediction of CHD fails, while GHD gives the correct description. In the last setup CHD does not produce a meaningful result, since it develops a shock on the experimental timescale. At the same time GHD shows reasonable good agreement with the experimental data . The work in this chapter can be found in [25].

5.1 GHD experiment

The GHD equations can be seen as a dynamical extension of the Yang-Yang equation of state. As shown in [12] the Yang-Yang equations have proven to be a very power-

ful and elegant tool to describe the equilibrium profiles of the Lieb-Liniger model in atomchip experiments. The Yang-Yang equations are exact and apply to the whole Lieb-Liniger phase diagram. In the same way GHD applies to the whole phase diagram and offers an elegant description of the out-of-equilibrium dynamics based on the Bethe-ansatz.

GHD and the Yang-Yang equations are based on the quasi-particle density $\rho_p(k)$. As introduced in Sec. 1.4.4 the quasi-particle distribution $\rho_p(k)$ evolves according to the GHD dynamics by

$$\frac{\partial}{\partial t} \rho_p(z, k) + \frac{\partial}{\partial z} [v_{\text{eff}}(z, k) \rho_p(z, k)] = \frac{1}{\hbar} \frac{\partial V(z, t)}{\partial z} \frac{\partial \rho_p(z, k)}{\partial k}, \quad (5.1)$$

where the effective velocity is given by:

$$v_{\text{eff}}(z, k) = \frac{\hbar k}{m} - \int dk' \rho_p(z, k') [v_{\text{eff}}(z, k) - v_{\text{eff}}(z, k')] \Delta(k - k'). \quad (5.2)$$

In absence of an external potential Eq. 5.1 is a conservation equation and expresses the fact that the Lieb-Liniger possesses an infinity of conserved charges. In the following sections we use the GHD equation to model the dynamics of a 1D Bose gas. We compare the GHD results to the experimental in situ linear density by calculating

$$n(z) = \int dk \rho_p(z, k). \quad (5.3)$$

Phase-space occupation The phase-space occupation is a practical quantity for this study:

$$v(z, k) = \frac{\rho_p(z, k)}{\rho_s(z, k)}, \quad (5.4)$$

where $\rho_s(z, k)$ is the density of states (see Eq.(1.34)). At $T = 0$ the phase-space occupation $v(z, k)$ resembles a Fermi distribution with $v(z, k) = 1$ inside a certain range of k and outside $v(z, k) = 0$. Inside the quasi-condensate regime and at $T = 0$, the rectangular function $v(z, k)$ extends up to $[-2\xi^{-1}, 2\xi^{-1}]$ in k . At finite temperature the two sides of the rectangle are rounded off (see Fig. 5.5).

It can be shown that the GHD evolution of $\rho_s(z, k)$ is the same as Eq. (5.1), where $\rho_p(z, k)$ is replaced by $\rho_s(z, k)$. From the GHD equations for $\rho_s(z, k)$ and $\rho_p(z, k)$ one obtains directly the GHD equation for the phase-space occupation:

$$\frac{\partial}{\partial t} v(z, v) + v_{\text{eff}}(z, v) \frac{\partial}{\partial z} v(z, v) = \frac{1}{m} \frac{\partial V(z, t)}{\partial z} \frac{\partial v(z, v)}{\partial v} \quad (5.5)$$

where the bare velocity $v = \hbar k / m$ was introduced.

5.1.1 The experiments

The aim of this project is to verify that GHD provides a good description of the dynamics of 1D cold atom experiments. For this purpose we compare the GHD predictions to the out-of-equilibrium dynamics of the atomic density. We start with a cloud at thermal equilibrium which is longitudinally confined in harmonic trapping potential. We initiate the dynamics by suddenly switching off the longitudinal potential. Further experiments use more involved protocols that permit to exclude CHD. The CHD calculations are based on Eq. (1.105) - (1.107) together with the Yang-Yang equation of state (see Eq. 1.41).

5.1.2 Expansion from harmonic trap

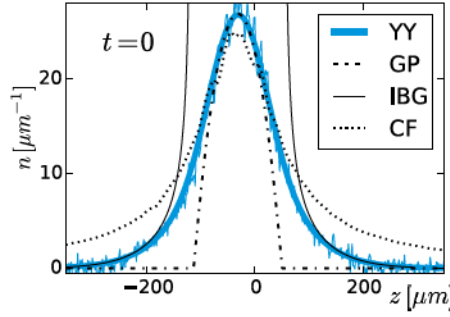


Figure 5.1 – Initial cloud before the expansion. The experimental data is the blue noisy line. The blue solid line is obtained from the Yang-Yang (YY) fit which gives $T = 0.043 \mu\text{K}$ and $\mu_p = 0.307 \hbar \omega_{\perp}$. The following theoretical predictions are based on those values of μ_p and T : The dashed-dotted line is the Gross-Pitaevskii (GP) prediction which corresponds to the Thomas-Fermi profile. The dashed line is the Ideal Bose Gas (IBG) prediction and the solid the classical field prediction (CF).

The initial profile We prepare a cloud with $N_{\text{at}} = 4600$ atoms whose central region lies in the quasi-condensate regime. The longitudinal potential $V(z) = \frac{1}{2} m \omega_{\parallel} z^2$ is harmonic with $\omega_{\parallel} = 2\pi \times 8.8 \text{ Hz}$ and the transverse confinement is given by $\omega_{\perp} = 2\pi \times 7.75 \text{ kHz}$. The initial density profile is shown in Fig. 5.1 (blue noisy line). The density profile is fitted with the Yang-Yang thermometry¹ (solid blue line), from which we obtain $T = 0.43 \mu\text{K}$

¹In this chapter we use the Yang-Yang thermometry without the corrections from the excited states (modified Yang-Yang). GHD is not able to take those effects into account. A discussion follows in Sec. 5.2.

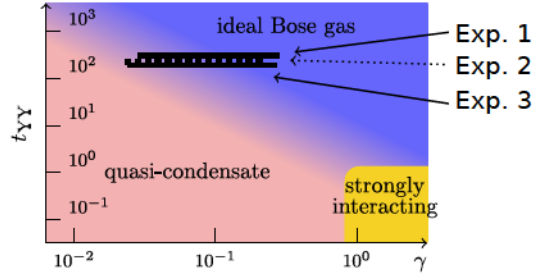


Figure 5.2 – The three different data sets in the Lieb-Liniger phase diagram (see Sec.1.2.4 for a discussion of the phase diagram). The horizontal lines reflect the change in density throughout the trap. The lines extend up to the point which corresponds to $n_p/10$. In all data sets the peak density lies in the quasi-condensate. In the wings the data sets extend into the ideal Bose gas regime. Exp. 1 is the experimental setup of Sec. 5.1.2 (expansion from harmonic trap), Exp. 2 is the experimental setup of Sec. 5.1.3 (expansion from double-well) and Exp. 3 the experimental setup of Sec. 5.1.4 (the Newton’s cradle experiment).

Failure of most approximate theories at equilibrium The density of the trapped cloud changes throughout the trapping potential (see Fig. 5.1). Consequently, the interaction parameter $\gamma = mg/(\hbar^2 n)$ changes throughout the cloud which corresponds to a horizontal line in Fig. 5.2. Typically, the center of the cloud lies inside the quasi-condensate regime, while the wings explore the ideal Bose gas. Let us turn to the standard theories mentioned at the beginning of this chapter and whose predictions are shown in Fig. 5.1. The prediction of the equation of state of the IBG Eq. (1.46), together with the LDA, is shown by the solid line, with T and μ_p obtained from the Yang-Yang fit. As expected the IBG prediction gives the correct description of the wings and fails in the central part. As μ approaches zero the density n diverges (see Sec. 1.2.4.1). The dashed-dotted line shows the Thomas-Fermi profile² which approximately corresponds to the experimental data in the central part of the cloud (same μ_p as Yang-Yang). The classical field theory is capable to describe the quasi-condensate regime and degenerate ideal Bose gas regime. The prediction from the equation of state of the classical field theory together with the LDA is shown by the solid line (same T and μ_p as the Yang-Yang fit). As expected, the prediction of the classical field agrees with the experimental data in the central region and in a larger region of the wings than the Thomas-Fermi profile. When the gas starts to enter the Maxwell-Boltzmann regime, the classical field equation fails to predict the density profile due to the quantized nature of the atoms.

In summary: Neither the ideal Bose gas equation of state, nor the equation of

²The Thomas-Fermi profile is the equilibrium prediction of the Gross-Pitaevskii equation.

state of the quasi-condensate regime, nor the classical field prediction can describe the equilibrium profile in our system³. This result was expected. Compared to the atomic clouds typically studied in Chap. 3 and Chap. 4, we use a cloud with larger wings to increase the effects. This is obtained by a lower peak density n_p and a higher transverse confinement. Both changes lead to an increased γ . The gas in the harmonic trap extends in the phase diagram from its peak value on a horizontal line as shown in Fig. 5.2. At increased γ , the region inside the quasi-condensate becomes more narrow. Therefore a substantial part of the cloud lies in the cross-over regime to the ideal Bose gas, and even in the Maxwell-Boltzmann regime (also see in Fig. 1.4).

Expansion In the first setup, we study the expansion from the harmonic trap. At $t = 0$ we suddenly switch off the longitudinal trapping potentials and let the cloud freely expand in 1D for $t = 40$ ms. We compare the GHD prediction with the experimental

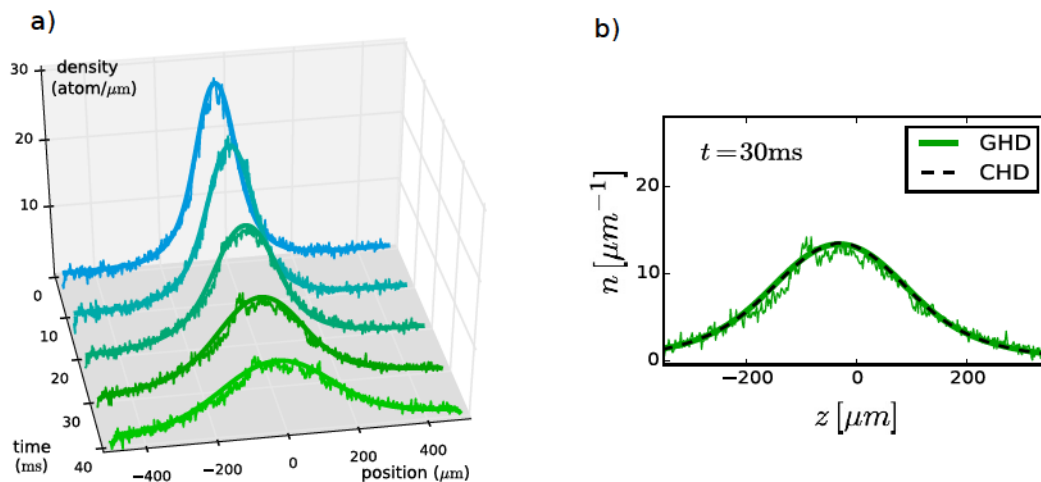


Figure 5.3 – a) Expansion from the a harmonic potential. Initial profile is shown in Fig. 5.1. The data is the noisy line and the solid line are the calculation from GHD. b) Situation at $t = 30$ ms. The data is shown together with GHD and CHD.

data as shown in Fig. 5.3 a). The GHD predictions are shown in solid lines and show a very good agreement with the experimental data.

³We are aware of refined theories, based on classical field which include a cut-off above which the excitation are treated as a quantum gas [141, 142]. We decided to exclude those theories from the discussion. Already in the equilibrium situation the Yang-Yang thermodynamics offers a much more powerful, elegant and reliable description. Their dynamical extension is not trivial. In the dynamical situation, we expect that GHD supersede those refined theories in the same way as Yang-Yang in the equilibrium situation.

Comparison with Conventional HydroDynamics (CHD) The standard theories, mentioned in the beginning of this chapter, all failed to describe the experimental data, except the Conventional HydroDynamics (CHD). CHD is based on the Yang-Yang equation of state (see Sec. 1.4.3 for an introduction). Therefore the initial equilibrium state does not differ from the Yang-Yang prediction. In Fig. 5.3 b) the evolution of the cloud after the release from the harmonic potential is compared to both GHD and CHD. There is no visible difference between the prediction of CHD and GHD. At the same time both theories are in very good agreement with the experimental data.

We attribute this coincidence of GHD and CHD to the initial harmonic trapping potential. It can be argued that in the asymptotic regime (Gross-Pitaevskii regime at $T = 0$ and ideal Bose gas at $T = \infty$) GHD and CHD coincide for the release from a harmonic trap. In the intermediate regime it can be shown that both theories give very similar results. It turns out that both theories start to clearly differ for a release from a trapping potential with significant contribution from terms in z^4 or higher. A more detailed discussion of this coincidence is given in the Supplementary Material of our paper [25].

5.1.3 Expansion from double well

In order to discriminate between GHD and CHD, we chose to work with a double-well potential $V(z) = a_2 z^2 + a_4 z^4$ with $a_2 < 0$. At $t = 0$ we switch off the longitudinal trapping potentials. The evolution of the density profile is shown in Fig. 5.4 a). Again we obtain a very good agreement between the GHD prediction and the experimental data (noisy line).

Creation of the double-well potential on the atomchip experiment For the double-well potential we use the four longitudinal wires D_1, D_2, δ_1 and δ_2 (see Fig. A.2). The double-well potential is implemented according to the considerations of Sec. 2.3.2.2. The creation of the double-well potential demands high currents which create a small, but non-negligible B_z contribution. This changes the transverse confinement according to $\omega_{\perp} \propto I_0 / \sqrt{B_0 + B_z}$. To maintain the same transverse confinement before and after the release from the longitudinal confinement, we adapt the current I_0 , such that ω_{\perp} stays constant.

GHD vs. CHD In Fig. 5.4 b) we show the prediction of GHD and CHD for the same initial state. At $t = 40$ ms both theories clearly differ. GHD shows a very good agreement with the experimental data, while CHD differs from the experimental profile by several standard deviations. The CHD simulation develops a large density wave which is a precursor of the shock which develops at later times.

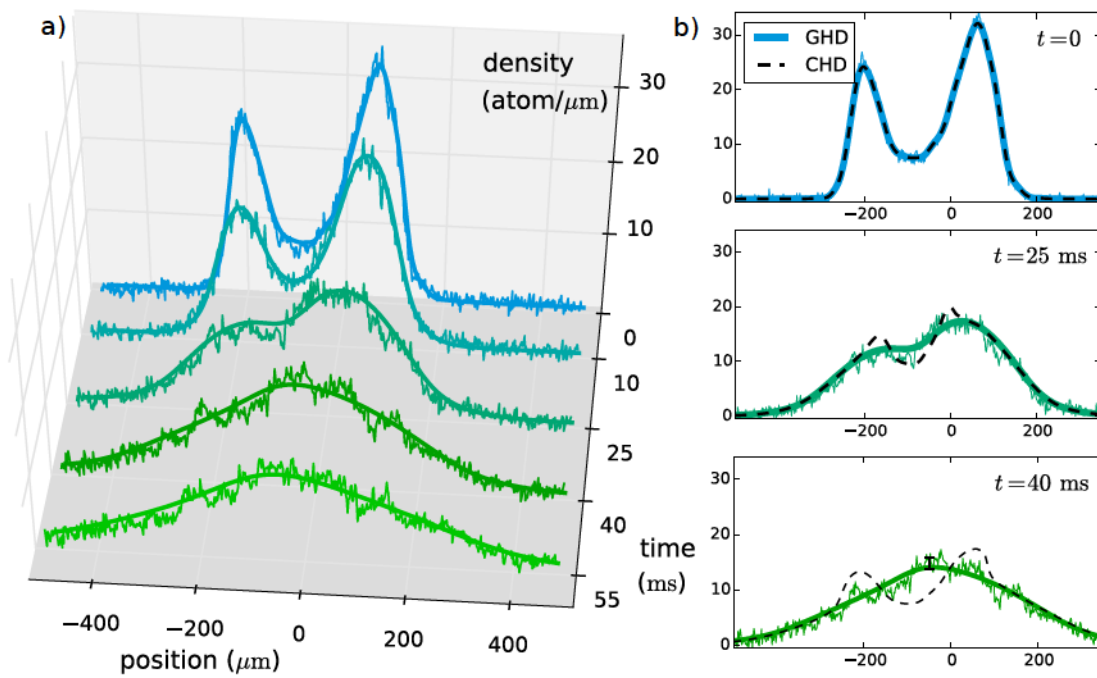


Figure 5.4 – a) Expansion from the double-well potential compared to GHD (smooth line). b) Comparison between GHD and CHD. The error bar shown in the inset for $t = 40$ ms corresponds to 68% confidence interval and is representative for all the data sets.

More insights can be obtained from the phase-space occupation $\nu(z, v)$ (see Eq. 5.4). Fig. 5.5 a) shows the evolution of $\nu(z, v, t)$ obtained from the GHD calculations. Initially, at each slice in z , the distribution is close to a rectangle with smoothed edges due to temperature effects. This results in a peanut like structure in the (z, v) -plane. The time evolution distorts the initial structure. At $t = 25$ ms the phase-space occupation is far from an equilibrium distribution with the appearance of two maxima for the central slices in z . Such a distribution with several maxima is clearly far from a thermal equilibrium situation which could be described by CHD. In comparison Fig. 5.5 b) shows the phase-space occupation obtained from the CHD calculations. The CHD calculations are based on the Yang-Yang equation of state and Fig. 5.5 shows the phase-space occupation which corresponds to the Yang-Yang state in CHD. At each moment CHD enforces a thermal equilibrium situation. At $t = 25$ ms the central part of the cloud clearly differs from the GHD distribution. The difference between GHD and CHD continues to increase for larger times.

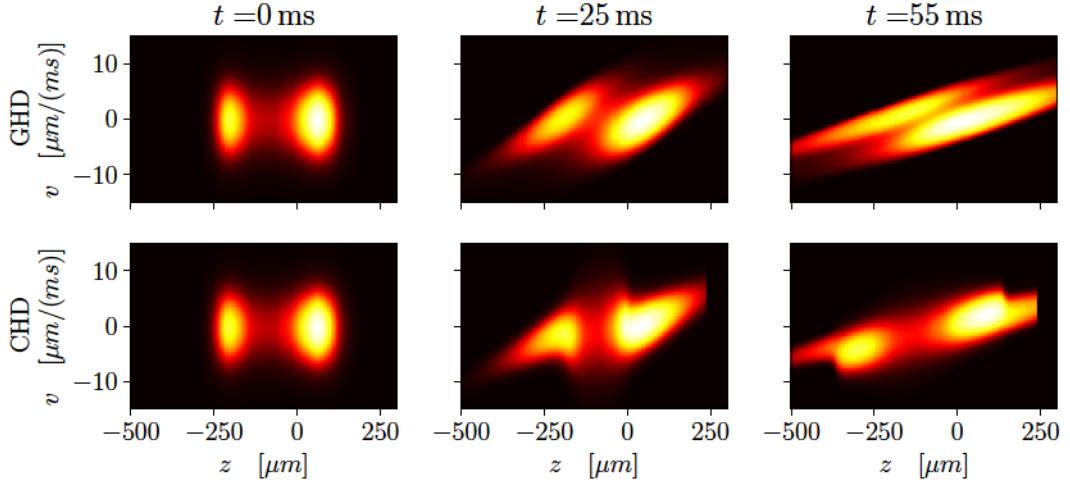


Figure 5.5 – Phase space occupation $\nu(z, v, t)$ for the expansion from the double well. The first line shows the phase space occupation $\nu(z, v, t)$ obtained from GHD and the second line shows the phase space occupation $\nu(z, v, t)$ obtained from CHD.

The initial temperature In the previous setup (Sec. 5.1.2) we fitted the initial profile with the Yang-Yang equation of state together with the LDA. The use of the LDA depends on a precise knowledge of the trapping potential. In the harmonic trap we use the precise values obtained from the measurement of the oscillations of the center-of-mass (see Sec. 2.9). For the double-well potential we cannot use this method and rely on more indirect methods. For example, one could fit the profile using the Yang-

Yang equation of state with 6 fitting parameters: T , μ_p and four parameters of the Taylor expansion⁴ of $V(z)$. However, such a high number of fitting parameters gave unreliable results for the temperature. To circumvent this problem, we decided to proceed as follows:

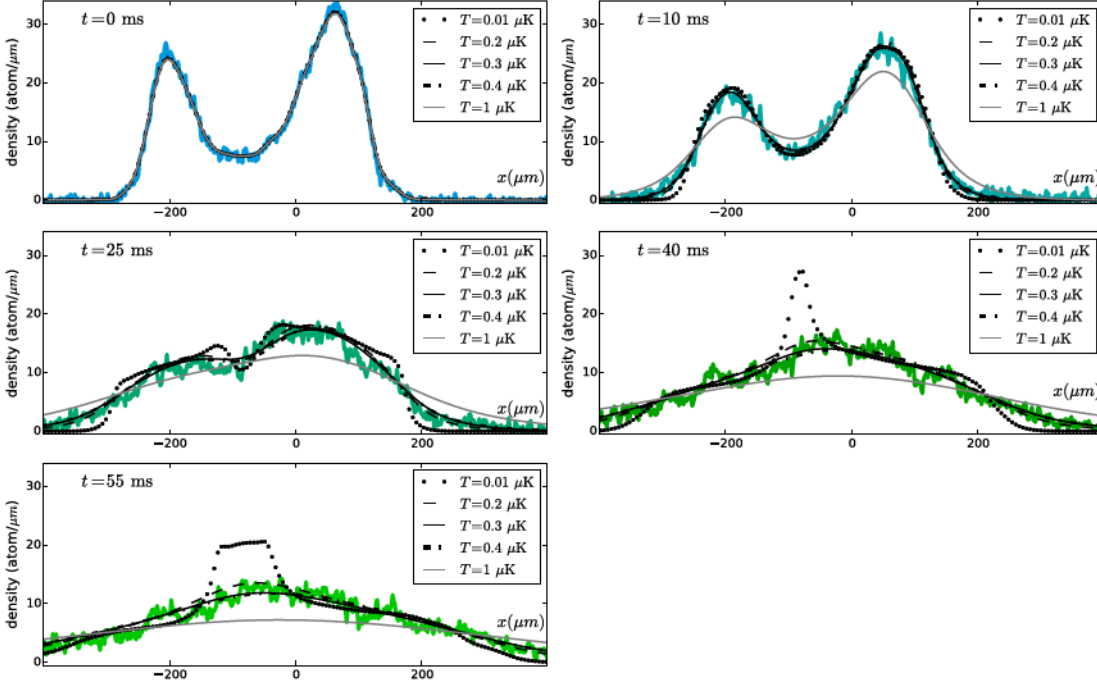


Figure 5.6 – Comparison of experimental data with GHD simulations for different temperatures T . Around $T = 0.3 \mu\text{K}$ the GHD results are almost independent on T . For very high ($T = 1 \mu\text{K}$) and very low ($T = 0.01 \mu\text{K}$) temperatures the GHD results clearly differ from the experimental observation.

First, we postulate an initial temperature T and construct the initial quasi-momentum distribution $\rho_p^T(z, v)$, such that $\rho_p^T(z, v)$ is the thermal equilibrium quasi-momentum distribution at temperature T and density $n(z, t = 0)$. We then calculate the time evolution $n_{\text{GHD}}(z, t)$ with GHD which we compare with the experimental data. We perform these calculations for different initial temperatures T and calculate the distance h to the experimental data

$$h = \sqrt{\frac{1}{N_{\text{data}}} \sum_{z,t} [n_{\text{data}}(z, t) - n_{\text{GHD}}(z, t)]^2}, \quad (5.6)$$

⁴Although, we intend to create a potential $V(z) = a_2 z^2 + a_4 z^4$, in practice an asymmetry is always present and all the four terms needs to be taken into account.

with the total number of data points N_{data} . Simulating the time evolution from $t = 0 - 50$ ms takes about 10 hours on a laptop with our code. Thus the GHD code is not suited for a fitting algorithm. We calculated n_{GHD} for a few temperatures between $T = 10$ nK and $t = 1 \mu\text{K}$. The minimum value of h is found for $T = 0.3 \mu\text{K}$. The uncertainty for this value is large. The GHD results for $T = 0.2 \mu\text{K}$ and $T = 0.4 \mu\text{K}$ do not differ much (see Fig. 5.6). However, for temperatures very different ($T = 10$ nK and $T = 10 \mu\text{K}$) the GHD prediction clearly differ from the observed data (see Fig. 5.6). We verified that the potential which corresponds to this quasi-momentum distribution $\rho_p^T(x, v)$, is close to the anticipated double-well potential.

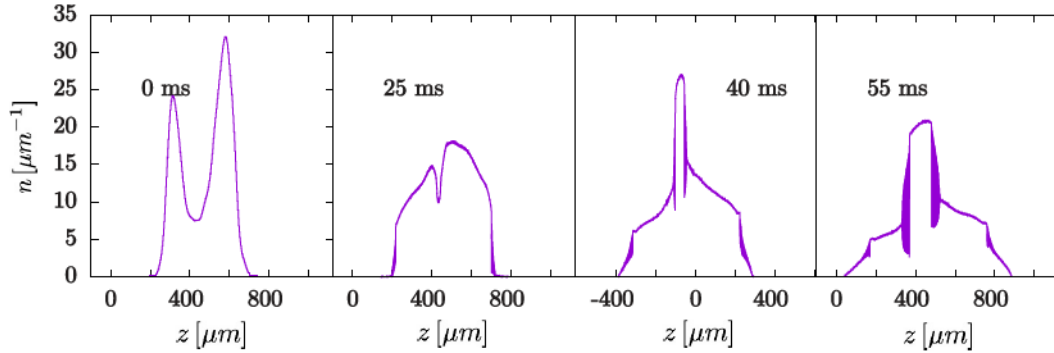


Figure 5.7 – GP simulation for the expansion from the double-well potential. The initial density distribution is equal to the experimental one. The appearance of the central peak strongly differs from the experimental profile.

Gross-Pitaevskii Although it was shown in Fig. 5.1 that the Gross-Pitaevskii (GP) theory cannot predict the equilibrium profile, a comparison with the GP dynamics (Eq. (1.100)) can still be interesting. We simulated the GP equation with the split-operator method [53] and the results are shown in Fig. 5.7. The results clearly differ from the experimental situation (see Fig. 5.4). At the same time, the GP results are close to the GHD results at low⁵ T , when the fast oscillations are averaged out (see Fig. 5.6). GHD is a classical description of the system. Thus, it does not predict interference phenomena.

5.1.4 Release from double-well into harmonic potential

In the third experimental realization we mimic the famous quantum Newton's cradle [26, 143, 144]. In contrast to these previous realizations, our cloud is in the weakly interacting regime.

⁵Compare to $T = 0.01 \mu\text{K}$

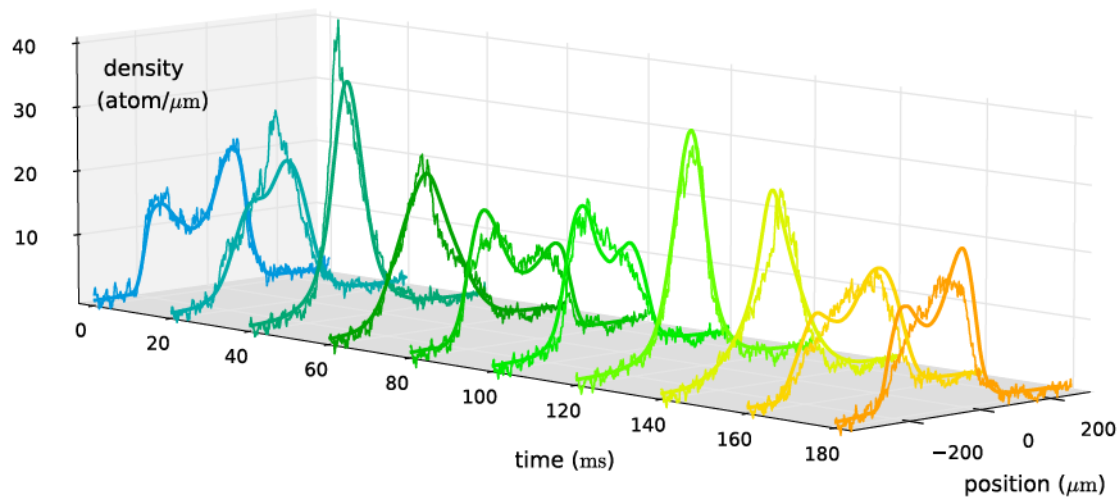


Figure 5.8 – Quench from double-well to harmonic potential compared to the GHD prediction. The noisy lines are the experimental data.

We prepare a cloud in a double-well potential and at $t = 0$ we replace the double well potential with a harmonic potential with frequency $\omega_{\parallel} = 2\pi \times 6.5\text{Hz}$. We obtain the temperature with the same method as used for the expansion from the double-well potential (see Sec. 5.1.3), and which leads to $T = 0.15\ \mu\text{K}$. For the Newton’s cradle experiment, CHD develops shocks at earlier times ($t \simeq 30\text{ms}$) and can not give useful predictions for the time evolution of Fig. 5.8. The experimental data in Fig. 5.8 is shown together with the GHD prediction. For this setup, the agreement between GHD and the experimental data is less striking.

Periodicity The motion in Fig. 5.8 is approximately periodic, with a period slightly longer than $2\pi/\omega_{\parallel}$. At a quarter of a period, and at three quarters of a period, the density distribution shows a single thin peak⁶. This approximate period is not an experimental artifact. The phase-space distribution calculated by GHD does not show a strict periodic behavior (see Fig. A.3 in Appendix for more details). The distribution does not exactly come back to its initial distribution and only shows an approximate periodicity. The interactions between the atoms distort the phase-space distribution during the evolution. This is in contrast to the IBG regime and the strongly interacting regime where the motion is periodic with the frequency of the trapping potential.

⁶If the initial cloud was completely symmetric under $z \rightarrow -z$, the period would be divided by two.

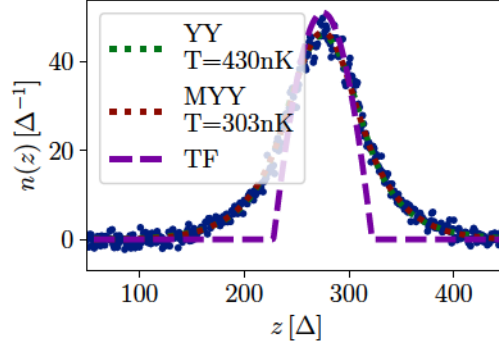


Figure 5.9 – Modified Yang-Yang thermometry for the same data set as in Fig. 5.1. In red the fitting results from the modified Yang-Yang equations (MYY) compared to the Yang-Yang equations in red (YY). While both theories agree well with the experimental data, the temperature differs by 30%.

5.2 Summary and Outlook

The presented study revealed that GHD is the only theory which can faithfully predict the out-of-equilibrium dynamics of the density profile in the experiment. The standard approximate theories (IBG, GP and CF) already fail to describe the equilibrium situation. The failure of the "older" theory (CHD) is directly related to the integrability of the system. We therefore demonstrated that these experimental observations are directly linked to the integrability of the underlying system.

At longer times (see Fig. 5.8) the experimental data shows small deviations from the GHD prediction. We attribute this deviations to experimental effects beyond the GHD description and identified two main effects:

1. **Atom losses:** During the 180ms shown in Fig. 5.8, 15% of the atoms are lost, mainly due to three-body losses.
2. **Transverse excited states:** If the initial profile in Fig. 5.1 is fitted with the modified Yang-Yang equation of state (see Sec. 2.8.2), we obtain a temperature which is 30% lower than the temperature we obtained from the pure Yang-Yang fit (see Fig. 5.9). This indicates that the transverse excite states might play a non-negligible role.

These two effects can in principle be overcome in future experiments. As shown in Sec. 4.4.3 the temperature decreases with fewer atoms. At lower temperatures effects from atom the transverse excited states become smaller and at the same time three-body losses are reduced due to the decreases linear density. Nevertheless, working with low atomic densities is experimentally challenging (see Sec. 2.6.2). Additionally, we collaborate with Benjamin Doyon and Jérôme Dubail, on a theoretical ap-

proach which combines the Quantum-Monte Carlo approach introduced in Sec. 4.2 and GHD.

Summary:

- This chapter presents the first experimental comparison with the Generalized HydroDynamics (GHD) approach. GHD is a new theory (2016) based on the conserved quantities of the integrable Lieb-Liniger system.
- We create three different experimental setups where we initiate an out-of-equilibrium dynamics by suddenly changing the longitudinal trapping potential at $t = 0$. We follow the evolution of the density of the cloud which we compare to different theoretical approaches.
- A similar and older theory, the Conventional Hydrodynamics (CHD), fail to describe the experimental observation. CHD only takes into account the conservation of energy, particles and momentum in contrast to GHD which takes into account all the conserved quantities of the integrable model.
- Moreover, GHD is the only "simple" theoretical approach which can faithfully describe the evolution of the density in all setups.

Conclusion

This thesis contains three main studies on the dynamics of 1D Bose gases. Those studies are the realization of an interaction quench in Chap. 3, the cooling by three-body losses in Chap. 4 and an experimental study of the theory of Generalized Hydrodynamics (GHD) in Chap. 5. Each of these studies calls for further investigations on its own. Let me summarize in the following some of the most important aspects and perspectives:

This thesis focuses on the out-of-equilibrium dynamics of integrable systems. An important and widely accepted assumption for the out-of-equilibrium dynamics of integrable systems is the appearance of a new equilibrium situation after some short relaxation time t_{relax} . This new equilibrium state is characterized by a Generalized Gibbs Ensemble (GGE). The appearance of a GGE state is far from trivial and no proof of its appearance exists. In the Lieb-Liniger model the set of mean values of the conserved quantities entering GGE completely defines the quasi-momentum distribution $\rho_p(k)$. The concept of GGE, derived from the generalized eigenstate hypothesis, states that all microstates of some $\rho_p(k)$ are identical. Thus, the system is completely defined by the distribution $\rho_p(k)$. In Chap. 3 we investigated the dynamics which occurs before the appearance of a new equilibrium situation. For the published data [18] presented in Sec. 3.4.2 this dynamics is in good agreement with the linearized approach given by the Bogoliubov description. The Bogoliubov model is a "trivially" integrable model. However, its conserved charges are not the conserved quantities of the underlying Lieb-Liniger model. One therefore expects that the dynamics of the Bogoliubov modes should relax at some point and not persist for long times. In Sec. 3.4.4 I presented data which shows indication of this relaxation phenomena with the observation of a mode damping. Further indication of this phenomena is given in Sec. 3.4.6 where the recurrence phenomenon could not be observed due to the damping of the modes. For further studies a characterization of the relaxation time t_{relax} and the new equilibrium state would be very interesting. In general, it can be expected that in an integrable system such a state is not a Gibbs ensemble. Most ideally such a state should be characterized by its quasi-momentum distribution $\rho_p(k)$ to which I will come back later.

In Chap. 5 we leave out this question of how, and on which timescale, the system

relaxes towards the new equilibrium situations. GHD assumes the validity of the generalized eigenstate hypothesis and the appearance of a GGE on timescales short compared to the experimental timescales. The GHD results showed a very good agreement with the experimental data which indirectly justifies the assumption of the relaxation phenomena. Chap. 5 showed that GHD is a very important tool to faithfully describe the out-of-equilibrium dynamics of 1D gases in cold atom setups. It opens many directions of new research: For example, it could be interesting to study experimentally transport phenomena between two reservoirs in 1D and compare those to the GHD prediction. Furthermore, it would be interesting to extend GHD such that it can predict the evolution of the quasi-momentum distribution $\rho_p(k)$ under the effect of losses. In Sec. 4.4.3 I presented experimental indications that the effect of losses probably has a non-trivial effect on the quasi-momentum distribution. The effect of three-body losses on the phonon temperature is in good agreement with a linearized description by the Bogoliubov modes (see Sec. 4.4). When analyzing the density profile by using the Yang-Yang equation of state, we obtained temperatures which differed by up to a factor of 5 from the phonon temperature. This indicates that we observe an out-of-equilibrium state which should be described by a non-thermal distribution of the quasi-momentum distribution $\rho_p(k)$.

In general, a tool which could access the quasi-momentum distribution $\rho_p(k)$ would be very helpful for the investigation of the out-of-equilibrium situations. Theoretically, $\rho_p(k)$ could be obtained in the far field from an expansion in 1D [145]. In practice, the far field cannot be attained due to the limited size of the atomchip. GHD might be able to circumvent this problem and reconstruct the initial $\rho_p(k)$ from the density at different times during the expansion. This method could be used to characterize the out-of-equilibrium state due to atom losses. The same approach could be used, to characterize $\rho_p(k)$ after an interaction quench.

Another natural extension of studies in integrable systems is the controlled breaking of integrability, as for example realized in [143] to study the Newton's cradle experiment. The breaking of integrability could be achieved in several different ways: One could couple a second gas, as realized in [10], or add an optical lattice which creates a periodic potential varying on distance short to the microscopical quantities. Another possibility is to add a new internal state. By controlling the interactions between different species, the system can be tuned to the integrable point of symmetric interactions [146].

For future experiments it would be interesting to perform studies in a regime of higher interaction parameters $\gamma = mg/(\hbar^2 n)$. Most preferable in the strongly interaction regime, characterized by $\gamma \gg 1$ and $t \ll 1$. This would allow to study interaction quenches in a new regime and show the universality of GHD in all regimes. Additionally, it would allow to study how the loss cooling process extends towards the strongly interacting regime. Is it even possible to enter the strongly interacting regime with

this energy-independent cooling process?

Higher values of γ are in principle achievable and $\gamma = 3$ was already achieved on the experimental apparatus in [42]. Even higher values of γ could be expected with an optimized chip design which allows to increase the current I_0 for the transverse confinement.

Finally, the cooling process of Chap. 4 leaves two main open questions: Why was the cooling limit for one-body losses not observed? Can we expect a cooling by losses in 3D (2D)?

Appendix A

Appendix

A.1 Values of ^{87}Rb

Name	Symbol	Value
3D scattering length in $ F = 2, m_F = 2\rangle$	a_{3D}	$5.311 \pm 0.005 \text{ nm}$ [147]
Mass of rubidium 87	m	$1.44316 \times 10^{-25} \text{ kg}$
Three-body loss coefficient	κ_3^{3D}	$(1.8 \pm 0.5) \times 10^{-41} \text{ m}^6/\text{s}$ [140]
Bohr magnetic moment	μ_B	$9.274 \times 10^{-24} \text{ J/T}$
magnetic vacuum permeability	μ_0	$4\pi 10^{-7} \text{ H/m}$

Table A.1 – Physical values used in this thesis (for ^{87}Rb).

A.2 Chip layout

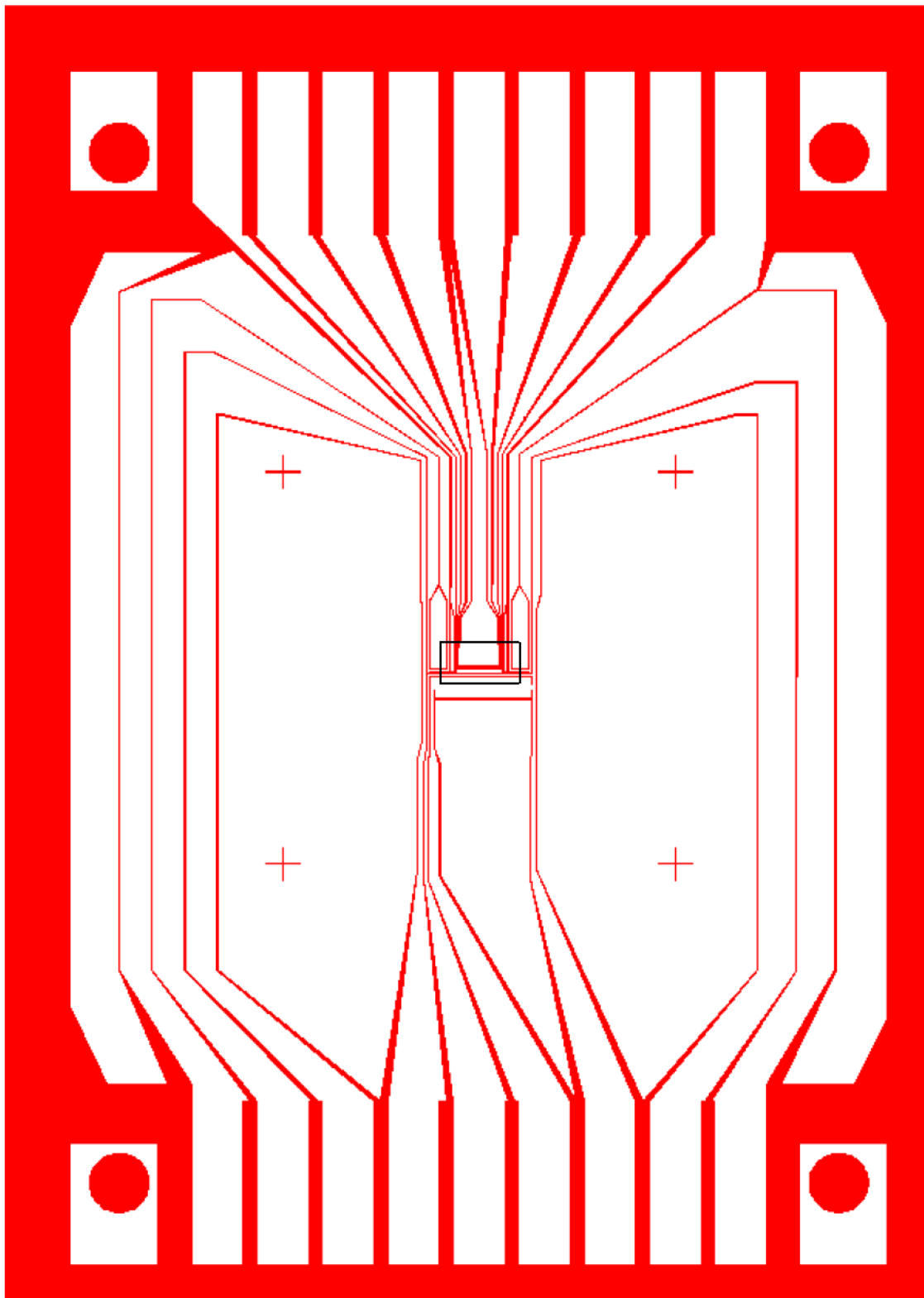


Figure A.1 – Chip layout. Black box shows zoomed region of Fig. A.2.
166

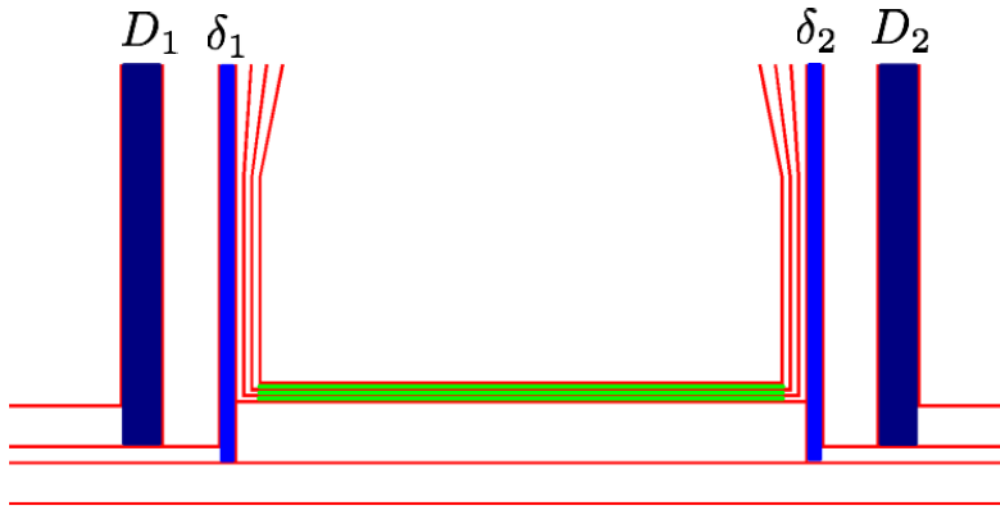


Figure A.2 – Zoom of on the center region of fig. A.1 with the parts of the wires colored, which are used in the model description of the trapping potentials introduced in this thesis (see Section 2.3). In the model description, wires are infinitely long and the *supply part*, which connects the pin of the chip to the considered wire (see Figure A.1 on the top and lower end of the chip) is neglected. The transverse confinement is obtained by the three small green wires with the modulated guide technique (see Section 2.3.1.2). The four blue wires are used to create the longitudinal confinement. The outer dark blue wires D_1 & D_2 are used to create a harmonic confinement. With the use of the D_1 & D_2 together with the δ_1 and δ_2 wires, polynomial potentials are created which can be controlled up to order four (see Section 2.3.2).

A.3 Longitudinal anti-confining term

a_2 is a polynomial of degree two in ι

$$a_2 = \frac{\mu_B \mu_0}{2\pi} \left\{ \iota^2 \frac{\mu_0}{\beta^4 B_0 \pi} + \iota \left(\frac{6d}{\beta^4} + \frac{\mu_0 2I}{B_0 \pi b^2 \beta^2} \right) + \frac{6dI}{b^4} + \frac{\mu_0 I^2}{B_0 \pi b^4} \right\}, \quad (\text{A.1})$$

whose discriminant is given

$$\Delta_{\text{discr}} = \frac{36d^2}{\beta^8} + \frac{24\mu_0 d I}{B_0 \pi b^2 \beta^4} \left(\frac{1}{\beta^2} - \frac{1}{b^2} \right). \quad (\text{A.2})$$

For $I > 0$, this leads to the condition $b > \beta$ in order to assure two roots and therefore $a_2 < 0$. For $I < 0$ the situations gets more complicated and $a_2 < 0$ can practically not be attained with the geometry of our chip experiment ($b > \beta$).

A.4 Atom losses

A.4.1 The Lindblad operators

While the choice of the Lindblad jump operators \hat{L} is not unique, let me justify the choice of the operators. Therefore, I will show that this choice reproduces the expected time evolution of the density operator for j -body losses [148]. Let us consider a coarse grained description as in 4.2, in which case we write:

$$\hat{L} = \sqrt{\frac{\tilde{K}_j}{j}} \hat{a}^j, \quad (\text{A.3})$$

where \hat{a} destroys a particle in the small cell and $\tilde{K}_j = \tilde{\kappa}_j \delta z^{1-j}$. Let us calculate the time evolution of the mean atom number $\hat{N} = \hat{a}^\dagger \hat{a}$

$$\frac{d}{dt} \langle \hat{N} \rangle = \text{Tr} \left(\hat{N} \frac{d}{dt} \hat{\rho} \right) = \text{Tr} (\mathfrak{L}\{\hat{\rho}\} \hat{N}) \quad (\text{A.4})$$

with the density matrix $\hat{\rho}$. The Lindblad operator $\mathfrak{L}\{\hat{\rho}\}$ given by Eq. 1.120 rewritten for losses in a small cell is given by:

$$\mathfrak{L}\{\hat{\rho}\} = \frac{\tilde{K}_j}{j} \left[\hat{a}^j \hat{\rho} \hat{a}^{\dagger j} - \frac{1}{2} \hat{a}^{\dagger j} \hat{a}^j \hat{\rho} - \frac{1}{2} \hat{\rho} \hat{a}^{\dagger j} \hat{a}^j \right]. \quad (\text{A.5})$$

The Hamiltonian commutes with the total atom number, which leads to

$$\frac{d}{dt} \langle \hat{N} \rangle = \frac{\tilde{K}_j}{j} \left[\text{Tr} \left(\hat{a}^j \hat{\rho} \hat{a}^{\dagger j} \hat{N} \right) - \frac{1}{2} \text{Tr} \left(\hat{a}^{\dagger j} \hat{a}^j \hat{\rho} \hat{N} \right) - \frac{1}{2} \text{Tr} \left(\hat{\rho} \hat{a}^{\dagger j} \hat{a}^j \hat{N} \right) \right]. \quad (\text{A.6})$$

Using the commutation relation $[\hat{N}, \hat{a}^j] = -j \hat{a}^j$, the cyclic property of the trace and $\text{Tr}(\hat{A}^\dagger) = \text{Tr}(\hat{A})$ one obtains

$$\frac{d}{dt} \langle \hat{N} \rangle = -\tilde{K}_j \text{Tr} \left(\hat{\rho} \hat{a}^{\dagger j} \hat{a}^j \right). \quad (\text{A.7})$$

Going back to the continuous limit, this leads to

$$\frac{d}{dt} \langle \hat{n} \rangle = -\tilde{\kappa}_j \langle \hat{n} \rangle^j g^{(1)}(0), \quad (\text{A.8})$$

with the normalized j -body correlation function at zero distance

$$g^{(j)}(0) = \langle \hat{\Psi}^{\dagger j}(0) \hat{\Psi}^j(0) \rangle / \langle \hat{n} \rangle^j. \quad (\text{A.9})$$

This confirms that this choice of \hat{L} leads to the anticipated evolution of the atom number for j -body losses as predicted by Eq. (4.3).

A.4.2 New Gaussian state

Let us compute this new Gaussian state: First, the convolution on the axis θ does not change R and only changes C in \tilde{C} according to

$$\tilde{C} = C + \begin{pmatrix} 0 & 0 \\ 0 & \frac{1}{2\sigma^2} \end{pmatrix}. \quad (\text{A.10})$$

Second, the multiplication by a Gaussian centered around $\vec{n} = \begin{pmatrix} \bar{n} \\ 0 \end{pmatrix}$ gives the following condition:

$$(\vec{X} - \vec{R})^T \tilde{B} (\vec{X} - \vec{R}) + (\vec{X} - \vec{n})^T \begin{pmatrix} \frac{2}{\sigma^2} & 0 \\ 0 & 0 \end{pmatrix} (\vec{X} - \vec{n}) = [\vec{X} - (\vec{R}' - \vec{M}_q)]^T B' [\vec{X} - (\vec{R}' - \vec{M}_q)], \quad (\text{A.11})$$

with the notation $\vec{M}_q = \begin{pmatrix} M_q \\ 0 \end{pmatrix}$. Eq. (A.11) needs to hold for $\forall \vec{X}$, implying

$$\tilde{B} + \begin{pmatrix} \frac{2}{\sigma^2} & 0 \\ 0 & 0 \end{pmatrix} = B', \quad (\text{A.12})$$

which leads in first order in Δt to

$$C' = B'^{-1} = \left[\mathbb{1} + \tilde{C} \begin{pmatrix} \frac{2}{\sigma^2} & 0 \\ 0 & 0 \end{pmatrix} \right]^{-1} \tilde{C} \simeq \left[\mathbb{1} - j\kappa_j n_0^{j-2} \Delta t \begin{pmatrix} C_{11} & 0 \\ C_{12} & 0 \end{pmatrix} \right] \tilde{C}, \quad (\text{A.13})$$

where we used $C_{11} = \tilde{C}_{11}$ and $C_{12} = \tilde{C}_{12}$ and which let us write

$$C' = C - j\kappa_j \Delta t n_0^{j-2} \begin{pmatrix} C_{11}^2 & C_{11}C_{12} \\ C_{11}C_{12} & C_{12}^2 - \frac{1}{4} \end{pmatrix}. \quad (\text{A.14})$$

From eq. (A.11) we get a second condition on \vec{R}' :

$$\tilde{B}\vec{R} + \begin{pmatrix} \frac{2}{\sigma^2} & 0 \\ 0 & 0 \end{pmatrix} \vec{n} = B' \left[\vec{R}' + \begin{pmatrix} M_q \\ 0 \end{pmatrix} \right]. \quad (\text{A.15})$$

Using Eq. (4.42) we can write

$$\vec{R}' = \left[\mathbb{1} - j\kappa_j \Delta t n_0^{j-2} \begin{pmatrix} C_{11} & 0 \\ C_{12} & 0 \end{pmatrix} \right] \left[\vec{R} + \tilde{C} \begin{pmatrix} \frac{2}{\sigma^2} & 0 \\ 0 & 0 \end{pmatrix} \vec{n} \right] - \begin{pmatrix} M_q \\ 0 \end{pmatrix}. \quad (\text{A.16})$$

Expanding in first order in Δt we finally obtain

$$\vec{R}' = \vec{R} + \left[\frac{jM_q}{n_0} - j\kappa_j n_0^{j-2} \Delta t \langle n_q \rangle \right] \begin{pmatrix} C_{11} \\ C_{12} \end{pmatrix} - \begin{pmatrix} M_q \\ 0 \end{pmatrix}. \quad (\text{A.17})$$

A.5 Phase space occupation

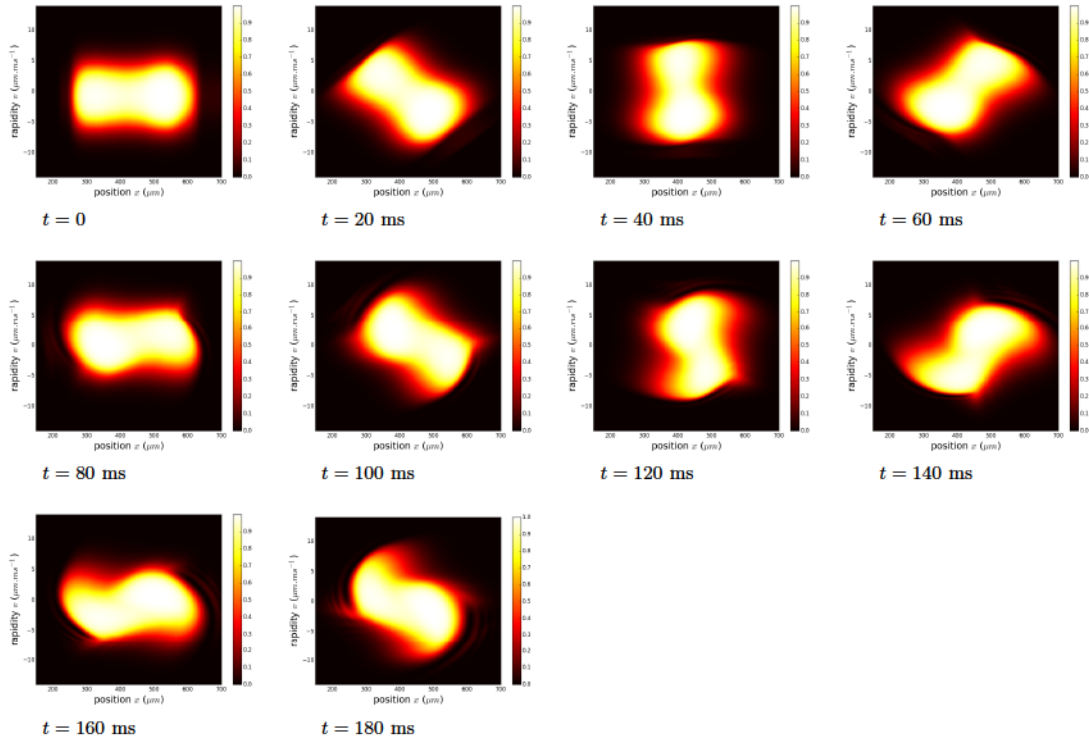


Figure A.3 – Phase space occupation $\nu(z, v, t)$ for the Newton's Cradle experiment obtained from GHD (see Sec. 5.1.4). The motion is approximately periodic. The period of the harmonic trap is 154 ms and the approximate period is 165 ms.

Annexe B

Résumé en français

Ce manuscrit présente les résultats de ma thèse, effectués dans l'équipe Puce Atomique. Nous utilisons un système de type « puce atomique » pour créer des pièges magnétique très allongés dans lesquels nous chargeons des atomes bosoniques (^{87}Rb). Nous gelons les degrés de liberté transverses et créons un gaz 1D avec des interactions de contact. Le modèle qui décrit ce système est connu sous le nom « modèle de Lieb-Liniger » et il a la particularité d'être un modèle intégrable. Ce manuscrit contient trois études expérimentales sur la dynamique dans ce système Lieb-Liniger.

Le premier chapitre introduit les outils théoriques qui ont été utilisés pour décrire les expériences. Premièrement, j'introduis le modèle qui décrit le gaz qui a été étudié. Il s'agit des bosons avec des interaction de contact en 1D ; le modèle de Lieb-Liniger. Il peut être résolu par la technique de l'ansatz de Bethe qui permet de calculer les états propres d'une manière exacte. Basé sur cette technique j'introduis une thermodynamique exacte, dite « thermodynamique de Yang-Yang ». La thermodynamique de Yang-Yang permet de distinguer différents régimes du modèle de Lieb-Liniger notamment le régime quasi-condensat. La plupart des expériences de cette thèse ont été effectuées dans ce régime et j'introduis des méthodes approximatives qui s'appliquent à l'intérieur du régime quasi-condensat. La méthode Bogoliubov retient particulièrement notre attention. Dans l'approximation de Bogoliubov le système est décrit par un ensemble d'oscillateurs harmoniques indépendants. Dans la suite j'introduis des théories qui décrivent la dynamique hors-équilibre des gaz 1D. Notamment une nouvelle théorie de 2016, baptisé hydrodynamique généralisée (en anglais *generalized hydrodynamics*). A l'inverse de l'hydrodynamique conventionnelle qui se base sur la conservation de l'énergie, de l'impulsion et du nombre de particule, cette théorie prend en compte un nombre infini de charges conservées du système intégrable. Je motive cette nouvelle théorie avec un approche simple qui considère des collisions à deux particules.

Le deuxième chapitre contient la description de notre expérience de type puce atomique. Les parties principales de refroidissement n'ont pas été modifiées pendant

ma thèse et un résumé des étapes les plus importantes est donné. Le piégeage magnétique est décrit avec plus de détails. Notamment la création d'un piège en forme de double puits dans la direction 1D. Dans la suite j'introduis l'utilisation des algorithmes génétiques comme méthode d'optimisation de l'expérience et je discute les problèmes techniques observés pendant la thèse. Ensuite, les méthodes d'analyse des données de l'expérience sont décrites et je me concentre sur l'analyse des franges de densité (en anglais *density ripples*). Je présente une formule centrale qui permet de déterminer la température des phonons, qui sont les modes de Bogoliubov de basse fréquence. Ensuite, je montre que cette analyse des franges de densité permet de résoudre les modes de Bogoliubov et d'accéder à la variance de la quadrature « phase » des premiers modes.

Le troisième chapitre contient des études sur la dynamique suite à une trempe (modification rapide) des interactions. Une première étude non-publiée mesure la distribution d'impulsion ce qui permet d'accéder à la fonction de corrélation d'un corps g_1 . On s'attend à un phénomène du type « cône de lumière » sur la fonction g_1 , en revanche la méthode expérimentale n'est pas adaptée pour mesurer ce phénomène dynamique. Seul le comportement à temps long pouvait être mesuré. Ensuite, j'introduis une méthode plus adaptée pour observer la dynamique suite à la trempe des interaction qui est basée sur l'analyse des franges de densité. Cette analyse permet d'observer expérimentalement la dynamique du gaz avec un phénomène de respiration des modes collectifs. Nous montrons que cette dynamique se poursuit sur des échelles de temps qui ne pourraient pas être observés par des observables basées sur la fonction g_1 . La fin du chapitre détaille les raisons qui rendent difficile, avec ce dispositif expérimental, l'observation des phénomènes de récurrence. À cause du couplage entre les modes collectifs, la dynamique est déjà trop amortie avant le temps de récurrence. Le quatrième chapitre contient les résultats sur le refroidissement par des pertes. Ce processus initialement inattendu a été découvert par le groupe de Vienne *Rauer, et al. Cooling of a one-dimensional Bose gas. PRL, 116.3 (2016) : 030402* [19]. Il permet de refroidir un gaz unidimensionnel en régime quasi-condensat par des pertes homogènes qui ne dépendent pas de l'énergie. Premièrement, je présente deux approches théoriques différentes qui décrivent l'effet des ces pertes. La première approche utilise une méthode de type Monte-Carlo quantique et qui consiste en une généralisation de la dérivation de notre papier *Schemmer, et al. Monte Carlo wave-function description of losses in a one-dimensional Bose gas and cooling to the ground state by quantum feedback PRA, 95.4 (2017) : 043641* [21]. La deuxième approche est une approche simplifiée permettant d'expliquer l'effet sur les phonons. Dans la suite je teste expérimentalement ces prédictions pour le cas des pertes à trois corps et la température des phonons. Ce cas est particulièrement intéressant car les pertes à trois-corps étaient généralement associées à un effet de chauffage. Les résultats expérimentaux reproduisent bien la limite de ce refroidisse-

ment qui consiste en un équilibre entre le refroidissement introduit par les pertes et le chauffage introduit par l'effet de bruit de grenaille due aux pertes d'atomes discrets *Schemmer, and Bouchoule. Cooling a Bose gas by three-body losses. PRL 121.20 (2018) : 200401 [24]*.

Le quatrième chapitre contient un test expérimental de la théorie hydrodynamique généralisée. Pour ce test nous créons différentes situations expérimentales qui montrent que l'hydrodynamique généralisée est la seule théorie capable d'expliquer l'ensemble des données expérimentales. La première situation consiste au relâchement d'un gaz piégé à l'équilibre dans un potentiel harmonique et l'observation de l'expansion dans la direction 1D. Déjà à l'équilibre les théories approximées ne parviennent pas à décrire le profil de densité et seule une théorie basée sur la thermodynamique de Yang-Yang décrit correctement le profil. La dynamique prédite par l'hydrodynamique généralisée décrit très bien nos résultats expérimentaux. Cependant, pour cette expérience, la prédiction de l'hydrodynamique généralisée coïncide avec la prédiction de l'hydrodynamique conventionnelle. Pour différencier ces deux théories nous préparons un nuage doublement piqué (réalisé dans un double puits de potentiel) et nous observons l'expansion dans la direction 1D suite au relâchement du piège. Dans ce cas, la prédiction de l'hydrodynamique conventionnelle dévie des données expérimentales et des prédictions de l'hydrodynamique généralisée, toutes les deux en très bon accord. Cette déviation s'accroît avec le temps d'évolution et la théorie hydrodynamique conventionnelle développe des divergences à un temps fini (un choc). La dernière expérience est l'expérience dite du pendule de Newton. Il s'agit d'un relâchement d'un nuage doublement piqué dans un piège harmonique. Dans ce cas l'hydrodynamique conventionnelle développe des chocs à temps courts et est donc incapable de fournir des prédictions à temps longs et l'hydrodynamique généralisée est la seule théorie capable d'expliquer les résultats expérimentaux.

Annexe C

Publications

Monte Carlo wave-function description of losses in a one-dimensional Bose gas and cooling to the ground state by quantum feedback

M. Schemmer, A. Johnson, R. Photopoulos, and I. Bouchole

*Laboratoire Charles Fabry, Institut d'Optique, Centre National de la Recherche Scientifique, Université Paris Sud 11,
2 Avenue Augustin Fresnel, F-91127 Palaiseau Cedex, France*

(Received 13 February 2017; published 28 April 2017)

The effect of atom losses on a homogeneous one-dimensional Bose gas lying within the quasicondensate regime is investigated using a Monte Carlo wave-function approach. The evolution of the system is calculated, conditioned by the loss sequence, namely, the times of individual losses and the position of the removed atoms. We describe the gas within the linearized Bogoliubov approach. For each mode, we find that, for a given quantum trajectory, the state of the system converges towards a coherent state, i.e., the ground state, displaced in phase space. We show that, provided losses are recorded with a temporal and spatially resolved detector, quantum feedback can be implemented and cooling to the ground state of one or several modes can be realized.

DOI: [10.1103/PhysRevA.95.043641](https://doi.org/10.1103/PhysRevA.95.043641)

In [1], the effect of atom losses on a one-dimensional quasicondensate was investigated. The authors have shown that, within a linearized approach and for a large enough initial temperature, one expects the temperature of the low-lying modes to decrease in time, in agreement with recent experimental results [2]. The fluctuation induced by the loss process due to the discrete nature of atoms is, however, responsible for a heating, limiting the temperature which can be achieved. More precisely, one expects that the temperature asymptotically converges towards $g\rho(t)$ where g is the coupling constant and ρ is the linear atomic density [1,3]. In particular, excitations in the phononic regime, i.e., of frequency much smaller than $g\rho(t)/\hbar$, never enter the quantum regime: their mean occupation number stays very large such that they lie in the Rayleigh-Jeans regime. This heating only occurs if one ignores the results of the losses or, equivalently, if one takes the partial trace on the state of the reservoir in which losses occur, ending up with the master equation for the system's density matrix. If, on the other hand, one records the losses, more information is gained on the system and the analysis made in [1] is no longer sufficient.

In this paper, we assume the losses are monitored with a spatially and temporally resolved detector and we describe the evolution of the system using a Monte Carlo wave-function analysis. The measurement back action leads to an evolution of the system conditioned by the result of the loss process, namely, a given history of losses. Averaging over the different possible histories, the results of [1] are recovered. The analysis proposed in this paper, however, not only presents an alternative picture conveying more physical insight but also opens the road to the realization of measurement based quantum feedback: controlled dynamics, conditioned on the monitored losses, allows one to reach lower temperatures. In this paper, we show that feedback on a given mode of the system could in principle allow one to cool this mode to the ground state. In particular we show that phononic excitations can be brought to the quantum regime. State preparation using information inferred from losses has already been used to prepare a well-defined phase between two condensates [4], with a Monte Carlo wave-function approach providing a very clear understanding of the mechanism [5]. Manipulation of

cold atomic clouds by quantum feedback has been proposed in many theoretical papers using dispersive light-atom interaction [6,7], while feedback has been implemented for internal degrees of freedom [8–10].

I. DISCRETIZATION OF THE PROBLEM

We consider a one-dimensional Bose gas with contact repulsive interactions of coupling constant g , such that the Hamiltonian writes, in second quantization,

$$H = -\frac{\hbar^2}{2m} \int dx \psi^\dagger \partial^2 \psi / \partial x^2 + \frac{g}{2} \int dx \psi^\dagger(x) \psi^\dagger(x) \psi(x) \psi(x).$$

We assume the gas is submitted to atom losses, the loss mechanism being a single atom process described by a loss rate Γ . For instance, magnetically trapped atoms could be submitted to a radio-frequency field that would transfer atoms to an untrapped state, as realized experimentally in [2]. Atoms could also be ionized by laser fields [11], or expelled by collision with fast electrons [12]. We moreover assume the lost atoms are detected one by one with position-resolved detectors, as sketched in Fig. 1. We denote $\bar{\rho}$ the mean linear density and we assume the gas lies within the quasicondensate regime such that the atomic density fluctuations are small and their characteristic length scale, equal to the healing length $l_h = \hbar/\sqrt{mg\bar{\rho}}$, is much larger than the mean interparticle distance [13]. We discretize space in N cells of length δx , containing a large mean atom number $\bar{n} = \delta x \bar{\rho}$ and with small relative fluctuations. We furthermore assume that δx is large enough such that the fluctuations are large compared to unity [14]. The state of the gas may be expanded (as long as one is not interested in length scales smaller than δx) on the Fock basis of each cell:

$$|\psi\rangle = \sum_{n_1, n_2, \dots, n_N} c_{n_1, n_2, \dots, n_N} |n_1, n_2, \dots, n_N\rangle. \quad (1)$$

Time is also discretized in intervals Δt small compared to the time scales involved in the longitudinal dynamics of the gas. This allows one to consider, during Δt , the sole effect of

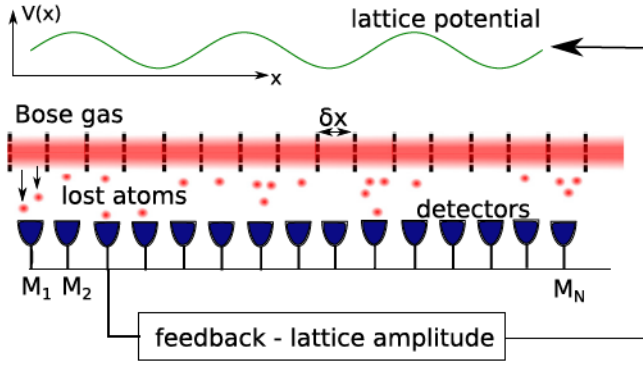


FIG. 1. A one-dimensional Bose gas with atom losses and a spatially resolved single atom detectors system. The information on the atom loss can be used to create a feedback loop on the atoms via a lattice potential. The amplitude of the lattice potential is controlled by a processing unit which uses the information gained from the atom losses.

losses first and then the effect of the free evolution. We will first concentrate on the effect of losses. Since losses do not introduce correlations between different cells, it is relevant to consider the case of a single cell first.

II. MONTE CARLO DESCRIPTION OF LOSSES IN A SINGLE CELL

Considering a single cell, the initial state writes $|\psi(t)\rangle = \sum_n c_n |n\rangle$. Let us split Δt in elementary time steps of length dt , small enough so that the probability to have an atom lost during dt is small. According to the Monte Carlo wavefunction procedure [15], if no atoms are detected during a time step dt , then the state of the system evolves according to the non-Hermitian Hamiltonian $H_{\text{eff}} = -i\hbar\Gamma a^\dagger a/2$, which ensures the decrease of the probability of highly occupied states. If on the other hand a lost atom has been detected, the new state is obtained by the application of the jump operator \hat{a} , which annihilates an atom in the cell. Let us now assume M atoms have been lost from the cell between time t and time $t + \Delta t$, at times $t_1 < t_2 < \dots < t_M$, as sketched in Fig. 2. By successively applying the procedure described above, we construct the quantum trajectory followed by the system and we find

$$|\psi(t + \Delta t)\rangle = e^{-iH_{\text{eff}}(t+\Delta t-t_M)/\hbar} \hat{a} e^{-iH_{\text{eff}}(t_M-t_{M-1})/\hbar} \dots \hat{a} e^{-iH_{\text{eff}}(t_1-t)/\hbar} |\psi(t)\rangle. \quad (2)$$

With the normalization chosen here, the probability of the loss sequence is $(dt\Gamma)^M \langle \psi(t + \Delta t) | \psi(t + \Delta t) \rangle / \langle \psi(t) | \psi(t) \rangle$. From Eq. (2), we find that the Fock state coefficients

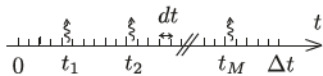


FIG. 2. A typical loss sequence during a time interval Δt , for a single cell. The associated quantum trajectory followed by the system's wave function is given by Eq. (2).

$c_n(t + \Delta t) = \langle n | \psi(t + \Delta t) \rangle$ write

$$c_n(t + \Delta t) = f_{\{t_i\}}(n + M) c_{n+M}(t), \quad (3)$$

where the function $f_{\{t_i\}}(n)$ depends on the loss sequence. Assuming Δt is small enough so that M is much smaller than the mean atom number in the cell, itself much larger than 1, $f_{\{t_i\}}(n)$, for a given M , becomes almost independent on the time sequence $\{t_i\}$ and can be approximated by

$$f_{\{t_i\}}(n) \simeq f_M(n) = n^{M/2} e^{-\Gamma n \Delta t}. \quad (4)$$

Within this approximation, the probability of the sequence is $\sum_n |c_n|^2 (\Gamma n \Delta t)^M e^{-\Gamma n \Delta t}$. Summing over all possible sequences with M lost atoms, we find that the probability to have M lost atoms is $P(M) = \sum_n |c_n|^2 (\Gamma n \Delta t)^M e^{-\Gamma n \Delta t} / M!$. For a given initial atom number n , we recover the expected Poissonian distribution. In the limit $\bar{n}\Gamma\Delta t \gg 1$, the typical number of losses is much larger than 1 and the function $f_M(n)$ can be approximated by the Gaussian

$$f_M(n) \simeq \mathcal{A}_M e^{-\frac{[n - M/(\Gamma\Delta t)]^2 (\Gamma\Delta t)^2}{4M}}, \quad (5)$$

where \mathcal{A}_M is the normalization factor. Using the fact that the number of lost atoms M is typically equal to $\bar{n}\Gamma\Delta t$ and presents small relative fluctuations, Eq. (5) further approximates to

$$f_M(n) \simeq \mathcal{A}_M e^{-\frac{[n - M/(\Gamma\Delta t)]^2 \Gamma \Delta t}{4n}}. \quad (6)$$

The same approximations lead to a mean number of lost atoms $\langle M \rangle_{\text{tr}} = \langle n \rangle \Gamma \Delta t$, with a variance $\langle M^2 \rangle_{\text{tr}} - \langle M \rangle_{\text{tr}}^2 = \Gamma \Delta t \bar{n}$, where the symbol tr indicates that averaging is done here over many different quantum trajectories.

III. GENERALIZATION TO ALL CELLS AND BOGOLIUBOV DECOMPOSITION

The results above can immediately be generalized to the case of several cells. If M_i denotes the number of lost atoms in the cell i , the probability amplitude of the Fock state $|n_1, n_2, \dots, n_N\rangle$ is, up to a global normalization factor,

$$c_{n_1, n_2, \dots, n_N}(t + \Delta t) = c_{n_1 + M_1, n_2 + M_2, \dots, n_N + M_N}(t) \prod_i e^{-\frac{[n_i - M_i/(\Gamma\Delta t)]^2 \Gamma \Delta t}{4n_i}}. \quad (7)$$

Since the atom number per cell is typically very large and presents fluctuations large compared to unity, one can approximate discrete sums on n_i by continuous integrals and treat the n_i as continuous variables.

Since the gas lies in the quasicondensate regime, its Hamiltonian is well approximated by the Bogoliubov Hamiltonian [13]. For a homogeneous system, the Bogoliubov modes are obtained from the Fourier decomposition. More precisely, let us introduce the Fourier quantities

$$n_{k_i, c} = \sqrt{\frac{2}{N}} \sum_j \cos(k_i j \delta x) n_j$$

$$n_{k_i, s} = \sqrt{\frac{2}{N}} \sum_j \sin(k_i j \delta x) n_j. \quad (8)$$

Here $k_i = i2\pi/L$, where i is an integer taking values between 1 and $(N - 1)/2$. We introduce in the same way the operator $\hat{n}_{k_i, c}$ and $\hat{n}_{k_i, s}$. The Bogoliubov Hamiltonian acts independently on

each Fourier mode and, for a given mode (k, r) , where r stands for c or s , it writes, up to a constant term,

$$\hat{H}_{k,r} = A_k \hat{n}_{k,r}^2 + B_k \hat{\theta}_{k,r}^2, \quad (9)$$

where the phase operator $\hat{\theta}_{k,r}$ is the operator conjugated to \hat{n}_k [16], $A_k = [g/2 + \hbar^2 k^2 / (8m\bar{\rho})] / \delta x$, $B_k = \hbar k^2 \bar{\rho} \delta x / (2m)$, and the mean particle density $\bar{\rho} = \bar{n} / \delta x$. The frequency of the mode is $\omega_k = 2\sqrt{A_k B_k} / \hbar$.

Let us now investigate the effect of losses in the Bogoliubov basis. The state $|n_1, n_2, \dots, n_N\rangle$ is also an eigenstate of each operator $\hat{n}_{k_i,r}$, where r stands for c or s , with eigenvalue $n_{k_i,r}$. We thus use the notation $|n_1, n_2, \dots, n_N\rangle = |\{n_{k_i,r}\}\rangle$, where $\{n_{k_i,r}\}$ is a short notation for $n_{k_1,c}, n_{k_1,s}, n_{k_2,c}, n_{k_2,s}, \dots, n_{k_N,c}, n_{k_N,s}$. The state of the system then writes

$$|\psi\rangle = \int \prod_{i,r} dn_{k_i,r} \tilde{c}_{\{n_{k_i,r}\}} |\{n_{k_i,r}\}\rangle, \quad (10)$$

where $\tilde{c}_{\{n_{k_i,r}\}} = c_{n_1, n_2, \dots, n_N}$. The modification of the state of the system after a time Δt due to atom losses is then, according to Eq. (7),

$$\tilde{c}_{\{n_{k_i,r}\}}(t + \Delta t) = \tilde{c}_{\{n_{k_i,r} + M_{k_i,r}\}}(t) \prod_i e^{-\frac{[n_{k_i} - M_{k_i,r} / (\Gamma \Delta t)]^2 \Gamma \Delta t}{4n}}, \quad (11)$$

where $M_{k_i,c} = \sqrt{2/N} \sum_j M_j \cos(k_i x_j)$ and $M_{k_i,s} = \sqrt{2/N} \sum_j M_j \sin(k_i x_j)$. We used the facts that, here, on one hand the variances of each Gaussian in Eq. (7) are all equal and on the other hand the density profiles of Bogoliubov modes are orthogonal, namely, the transformation between the basis n_i and $n_{k,r}$ is orthogonal. The statistics of the different quantum trajectories gives a Gaussian distribution for $M_{k_i,r}$ with $\langle M_{k_i,r} \rangle_{\text{tr}} = \Gamma \Delta t \langle n_{k,r} \rangle$ and $\langle M_{k_i,r}^2 \rangle_{\text{tr}} - \langle M_{k_i,r} \rangle_{\text{tr}}^2 = \Gamma \Delta t \bar{n}$. Equation (11) shows that the losses affect each Fourier component, i.e., each Bogoliubov mode, independently.

If the initial state is at thermal equilibrium, different Bogoliubov modes are uncorrelated. The free evolution, under the Bogoliubov Hamiltonian, as well as the effect of losses, do not introduce correlations between modes and one can consider each mode independently. In the following, we consider a given mode of momentum k and we will omit the subscript c or s , since the upcoming considerations apply for both.

IV. EVOLUTION OF A GIVEN BOGOLIUBOV MODE: WIGNER REPRESENTATION

Here we consider a given mode, described by the two conjugate variables n_k and θ_k . A convenient representation of the state of the system is its Wigner function W , a two-dimensional real function, the expression of which, as a function of the density matrix D of the state, is

$$W(n_k, \theta_k) = \frac{1}{2\pi^2} \int dadbe^{i(an_k - b\theta_k)} \text{Tr}(D e^{(-ia\hat{n}_k + ib\hat{\theta}_k)}). \quad (12)$$

The effect of losses during Δt , in the n_k representation, is given by Eq. (11), and this effect transforms W into the new

Wigner function W' according to

$$W'(n_k, \theta_k) = \frac{\Gamma \Delta t}{2\pi^{3/2} \bar{n}} \int d\tilde{\theta} W(n_k + M_k, \tilde{\theta}) \times e^{-\frac{\Gamma \Delta t}{2\bar{n}} [n_k - M_k / (\Gamma \Delta t)]^2} e^{-\frac{2\bar{n}}{\Gamma \Delta t} (\tilde{\theta} - \theta)^2}. \quad (13)$$

The multiplication by a Gaussian function along the n_k axis shifts the distribution towards $M_k / (\Gamma \Delta t)$, the value for which $\langle M_k \rangle_{\text{tr}}$ is equal to the recorder value M_k . It also decreases the width in n_k , which reflects the gain of knowledge acquired on n_k by the detection of the number of lost atoms. The associated convolution along the axis θ_k increases the width in θ_k , and ensures preservation of uncertainty relations.

The thermal state of the Bogoliubov Hamiltonian has a Gaussian Wigner function. Since the Gaussian character is preserved by Eq. (13) and by the free evolution, the state of the system stays Gaussian. W is then completely determined by its center $R = (\langle n_k \rangle, \langle \theta_k \rangle)$ and its covariance matrix:

$$C = \begin{pmatrix} \langle n_k^2 \rangle - \langle n_k \rangle^2 & \langle n_k \theta_k \rangle - \langle n_k \rangle \langle \theta_k \rangle \\ \langle n_k \theta_k \rangle - \langle n_k \rangle \langle \theta_k \rangle & \langle \theta_k^2 \rangle - \langle \theta_k \rangle^2 \end{pmatrix}. \quad (14)$$

As shown in Appendix A, to first order in Δt , the transformation in Eq. (13) changes R and C to R' and C' with

$$C' = C + \frac{\Gamma \Delta t}{\bar{n}} \begin{pmatrix} -C_{11}^2 & -C_{11} C_{12} \\ -C_{11} C_{12} & -C_{12}^2 + \frac{1}{4} \end{pmatrix} \quad (15)$$

and

$$R' = R - \begin{pmatrix} \Gamma \Delta t \langle n_k \rangle \\ 0 \end{pmatrix} - d\xi \begin{pmatrix} 1 - C_{11}/\bar{n} \\ -C_{12}/\bar{n} \end{pmatrix}. \quad (16)$$

Here we introduced $d\xi = M_k - \Gamma \Delta t \langle n_k \rangle$. According to the statistic of trajectories, $d\xi$ is a Gaussian variable centered on zero and of variance $\langle d\xi^2 \rangle_{\text{tr}} = \Gamma \Delta t \bar{n}$. The above equations account for the evolution of the state under the sole effect of atom losses. One should then implement the evolution under the Hamiltonian (9), which amounts to a simple rotation of the Wigner function in phase space and acts independently on C and R [17]. Finally, one can compute the long term evolution iteratively following the procedure above, knowing, at each time interval Δt , the number of atoms lost in each cell, M_i , from which $d\xi$ is computed.

V. EVOLUTION OF THE CORRELATION MATRIX

Equation (15) shows that the evolution of the correlation matrix is the same for all possible quantum trajectories, and general statements can be made. Let us first consider a very slow mode such that one can ignore the free evolution. Then C_{12} stays at zero during the evolution and time integration of Eq. (15) on long times gives

$$C_{11} \simeq \bar{n}(t) / (1 - e^{-\Gamma t}), \quad C_{22} \simeq (1 - e^{-\Gamma t}) / [4\bar{n}(t)] \quad (17)$$

where $\bar{n}(t) = \bar{n}(t=0)e^{-\Gamma t}$ is the time-dependent mean atom number per cell. The system thus goes towards a state of minimal uncertainty, as expected, since more and more information is acquired on the system. Let us now consider the other limit of a mode of very high frequency. Then the free evolution of the system ensures, at any time, $C_{12} \simeq 0$ and the equipartition of the energy between the two degrees

of freedom. Thus $A_k C_{11} \simeq B_k C_{22} \simeq \langle E_c \rangle / 2$ where $\langle E_c \rangle = A_k C_{11} + B_k C_{22}$ is the contribution of the correlation matrix to the energy. We then find

$$\frac{d[\langle E_c \rangle / (\hbar \omega_k)]}{dt} = \Gamma_{\text{eff}} \{-[\langle E_c \rangle / (\hbar \omega_k)]^2 + 1/4\}, \quad (18)$$

where $\Gamma_{\text{eff}} = \Gamma / \sqrt{1 + 4mg\bar{\rho}/(\hbar^2 k^2)}$. Γ_{eff} depends on time via the exponential decrease of $\bar{\rho}$ due to losses. At long times, $\langle E_c \rangle / (\hbar \omega_k)$ goes to $1/2$, such that the state of the system, as long as only the matrix C is concerned, evolves towards the ground state. If one assumes the excitation is initially in the phononic regime, however, we show in Appendix B that $\langle E_c \rangle$ approaches $\hbar \omega_k$ only once the decrease of $\bar{\rho}$ has already promoted the excitation to the particle regime. Thus phononic excitations cannot reach the quantum regime. The situation is different if the decrease of $\bar{\rho}$ is compensated by the following time dependence of g :

$$g(t) = g(t=0)e^{\Gamma t}. \quad (19)$$

Then Γ_{eff} and ω_k are constant and an excitation lying in the phononic regime stays in the phononic regime during the whole loss process and, as long as the C matrix is concerned, is cooled to the ground state. In the following, we will assume g is modified according to Eq. (19).

VI. AVERAGING OVER TRAJECTORIES

If the loss events are not recorded, then only the quantities averaged over all possible trajectories are meaningful. If the Wigner distribution is initially centered around zero, it will stay centered at zero. Let us investigate its evolution over a time Δt . For a given quantum trajectory, i.e., a given value $d\xi$, the losses modify the correlation matrix according to Eq. (15) as well as the center R , which acquires the nonzero value $R = -d\xi(1 - C_{11}/\bar{n}; -C_{12}/\bar{n})$. One then has

$$\langle n_k^2 \rangle_{\text{st}}(t + \Delta t) = \langle n_k^2 \rangle(t) - \Gamma \Delta t / \bar{n} C_{11}^2 + d\xi^2 \left(1 - \frac{\langle n_k^2 \rangle}{\bar{n}} \right)^2 \quad (20)$$

and

$$\langle \theta_k^2 \rangle_{\text{st}}(t + \Delta t) = \langle \theta_k^2 \rangle(t) + \Gamma \Delta t / \bar{n} (1/4 - C_{12}^2) + (d\xi C_{12} / \bar{n})^2, \quad (21)$$

where the subscript st specifies that this holds for a single trajectory. Averaging over all possible trajectories, we then find, using $\langle d\xi^2 \rangle_{\text{tr}} = \Gamma \Delta t \bar{n}$, that losses modify the variances according to

$$\langle n_k^2 \rangle(t + \Delta t) - \langle n_k^2 \rangle(t) = -2\Gamma \Delta t \langle n_k^2 \rangle(t) + \Gamma \Delta t \bar{n}(t) \quad (22)$$

and

$$\langle \theta_k^2 \rangle(t + \Delta t) - \langle \theta_k^2 \rangle(t) = \Gamma \Delta t / (4\bar{n}). \quad (23)$$

As expected, Eqs. (22) and (23) are equal to those obtained using a master equation description of the loss process [1,18]. Due to the diffusive process experienced by R , an increased rate in both equations limits the decrease of the mode energy. For phonons, and assuming the loss rate is small compared to the mode frequency, we show in Appendix C that the temperature asymptotically goes towards $g\bar{\rho}(t)/2$.

This value of the asymptotic temperature T_∞ is particular to the case of a homogeneous gas with a coupling constant evolving according to Eq. (19). For constant g the asymptotic temperature is $T_\infty = g\bar{\rho}$ [1,18]. For a gas trapped in a harmonic potential we expect T_∞ to scale as $g\rho_p$, where ρ_p is the peak density. The proportionality factor has not been derived yet, but since the averaged density is smaller than ρ_p , one naively expects that T_∞ is smaller than $g\rho_p$. Experimentally T_∞ has not been identified, while temperatures as low as $0.25 g\rho_p$ have been reported for a harmonically confined gas [2].

VII. USING INFORMATION RETRIEVED FROM LOSSES DETECTION: QUANTUM FEEDBACK

If the losses are recorded, such that at each time interval Δt the values M_j are recorded, the trajectory followed by the center of the Wigner distribution, R , can be computed exactly, and the heating associated to the diffusion process seen in Eqs. (23) and (22) can be compensated for. One strategy is to perform, during the whole time evolution, a quantum feedback on the system, based on the knowledge acquired via the atom losses, in order to prevent the center of the Wigner distribution from drifting away from the phase-space center. Let us here, as an illustration, assume one is interested in a given mode k, c . The most simple back action is to submit the atomic cloud to a potential $V(x) = A(t) \cos(kx)$, where the computed amplitude $A(t)$ depends on the recorded history of the losses. Such a potential could be realized, for instance, using the dipole potential experienced by atoms in a laser field. The cosine modulation of the laser intensity can be realized using an optical lattice, or using a spatial light modulator. The contribution to the Hamiltonian of this potential is $\hat{H}_{\text{fb}} = A(t) \sqrt{N/2} \hat{n}_{k,c}$. In order to counteract the diffusion process of R due to the loss process, one could adjust $A(t)$ such that the feedback Hamiltonian is

$$\hat{H}_{\text{fb}} = -\hbar \nu \langle \theta_{k,c} \rangle \hat{n}_{k,c} \quad (24)$$

where, at each time interval, $\langle \theta_{k,c} \rangle$ is computed by integrating the equations of motion including the effect of losses, the free evolution, and the feedback process. This Hamiltonian acts as an active damping, the damping rate ν preventing θ_k from drifting far from the phase-space center. The free-evolution Hamiltonian, by coupling the two degrees of freedom, will ensure that neither θ_k nor n_k drifts away. For a large enough damping rate ν , the contribution of R to the energy of the mode is expected to be negligible compared to the contribution of the covariance matrix C and, according to Eq. (18), one expects to reach the ground state. We present numerical results illustrating such a scenario below.

Before presenting numerical results, let us identify the relevant quantities governing the dynamics. Introducing the reduced variable $\tilde{n}_k = \bar{n}^{-1/2} n_k$ and $\tilde{\theta}_k = \bar{n}^{1/2} \theta_k$, as shown in Appendix D, we find as expected that the cell size δx drops out of the problem and, provided time is rescaled by $1/\Gamma$, the dynamics of the mode of wave vector k is solely governed by the dimensionless parameters ω_k/Γ , $\hbar^2 k^2 / (mg\bar{\rho})$ and ν/Γ . The relevant measurement signal, for the time interval Δt , is then $\tilde{M}_k = \sqrt{2/N_{\text{at}}} \int dx m(x) \cos(kx)$, where N_{at} is the total atom number and $m(x)$ is the number of lost atoms per unit length. Figure 3 shows the phase-space evolution of a

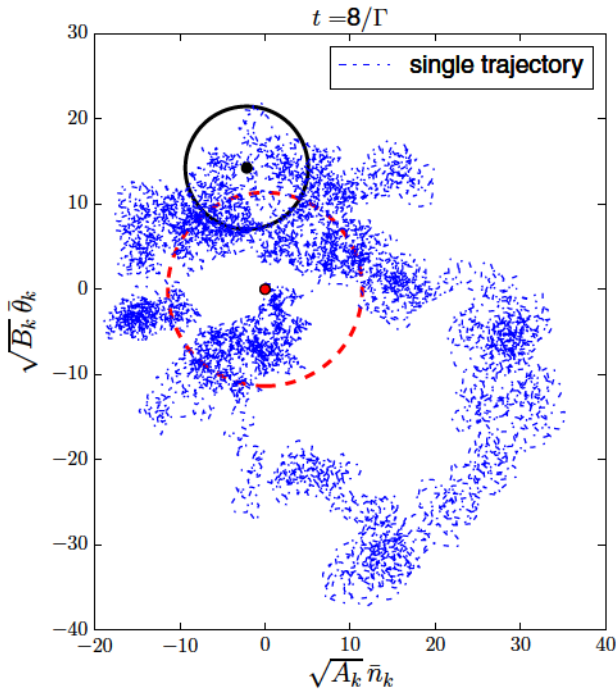


FIG. 3. Evolution of the phase-space distribution for a single trajectory from time $t = 0$ to $8/\Gamma$ in the absence of feedback. The mode $k = 0.1\sqrt{mg\bar{\rho}}/\hbar$ is considered, with the initial temperature $T_i = 1.1g\bar{\rho}$ and a loss rate $\Gamma = \omega_k/400$. Scattered blue points give the evolution of the center R . We verified that C_{12} stays small while, at any time, $A_k C_{11} \simeq B_k C_{22} \simeq E_c/2$, as expected for such a large ω_k . The black solid circle, of radius $\sqrt{E_c}$, represents the final rms width of the Wigner function. For comparison, the red dashed circle, of radius \sqrt{E} , where E is the energy obtained after averaging over 100 trajectories, gives the rms width of the averaged phase-space distribution. The coordinates are given in the frame rotating according to the free evolution: namely, the plotted quantity is $\bar{R} = (\bar{n}_k, \bar{\theta}_k) = \mathfrak{R}^{-1}(\omega_k t)R$ [17].

single quantum trajectory, for a mode lying in the phononic regime, in the absence of quantum feedback. Figure 4 shows the time evolution of the energy in this mode, averaged over quantum trajectories, both in the absence and in the presence of feedback. In the absence of feedback, the energy converges towards the expected value $g\bar{\rho}/2$. If the feedback scheme is implemented, we observe that the energy in the mode reaches much smaller values. For a large feedback strength ν , the drift of the center is almost completely prohibited and the mode is cooled to its ground state.

VIII. DISCUSSION

In conclusion, we proposed a description of the effect of losses in a many-body system through a Monte Carlo wave-function approach, and we showed that quantum feedback by monitoring losses could be used to cool down selected modes of a quasicondensate to vanishing temperatures. This work could be extended in many directions. In view of practical implementation, the sensitivity of the feedback mechanism on the exact knowledge of the system parameters should be investigated. Assuming, as is done in this paper, the system

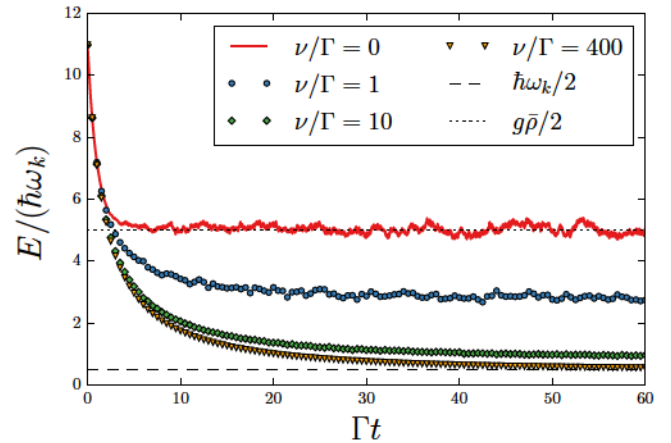


FIG. 4. Simulation of the loss process for different feedback strengths ν . Plotted is the time evolution of the energy in the mode k , averaged over 500 quantum trajectories, the parameters being those of Fig. 3. Without feedback the energy converges to $g\bar{\rho}/2$ (horizontal dotted line); lower energies are obtained with feedback, and the ground state, of energy $\hbar\omega_k/2$ (horizontal dashed line), is reached for large enough ν .

parameters are known exactly, the larger the feedback strength the better the cooling. In the presence of uncertainties, a too large feedback strength will induce heating as it will not match the exact dynamics. Additionally, in most experimental situations the quasicondensates, trapped in a shallow longitudinal potential, are nonhomogeneous. Then, the linearized description should use, instead of the sinusoidal modes, the spatial density profiles of the Bogoliubov modes, which are not necessarily orthogonal. These issues complicate the picture. Losses might then induce correlations between modes [7]. Another concern is the coupling between modes, which exists beyond the linearized approach considered here. Such coupling is present, for instance, in the Gross-Pitaevskii equation, which is a classical field approximation of the Lieb-Liniger model. However, long-lived nonthermal states with different Bogoliubov modes experiencing long lifetimes [19] have been reported, which indicates small coupling between modes and the possibility to cool down a particular Bogoliubov mode. Finally, note that this cooling process is not limited to one-dimensional systems.

ACKNOWLEDGMENTS

The authors thank K. Mølmer for inspiring discussions. M.S. gratefully acknowledges support by the Studienstiftung des Deutschen Volkes.

APPENDIX A: EFFECT OF LOSSES ON THE WIGNER REPRESENTATION

Here we consider a given mode and we will omit the subscripts k, r to make our notations lighter. We also introduce $\sigma^2 = \bar{n}/(\Gamma\Delta t)$ and $q_0 = M_k/(\Gamma t)$. Equation (12) writes, in

representation n ,

$$W(n, \theta) = \frac{1}{\pi} \int du \langle u + n | D | u - n \rangle e^{-2iu\theta}. \quad (\text{A1})$$

The effect of losses given by Eq. (11) transforms the Wigner function of the mode to

$$W'(n + M_k, \theta) = \frac{1}{2\pi^2\sigma^2} \int du \langle u + n | D | u - n \rangle e^{-2iu\theta} \times e^{-(n-q_0+u)^2/(4\sigma^2)} e^{-(n-q_0-u)^2/(4\sigma^2)}. \quad (\text{A2})$$

Injecting $\langle u + n | D | u - n \rangle = \int d\tilde{\theta} W(n, \tilde{\theta}) e^{i2\tilde{\theta}u}$, we then find Eq. (13).

Let us now consider a Gaussian state. Its Wigner function writes

$$W(n, \theta) = \frac{1}{2\pi\sqrt{\det(C)}} e^{-\frac{1}{2}[(X-R)^\dagger B(X-R)]} \quad (\text{A3})$$

where $X = \begin{pmatrix} n \\ \theta \end{pmatrix}$, R is the center of the distribution, C is the covariant matrix, and $B = C^{-1}$. The transformation in Eq. (13) transforms the Gaussian state into a new Gaussian state centered on R' and of covariance C' . The convolution on the axis θ does not change R and changes C in \tilde{C} according to

$$\tilde{C} = C + \begin{pmatrix} 0 & 0 \\ 0 & \frac{1}{4\sigma^2} \end{pmatrix}. \quad (\text{A4})$$

Let us now consider the effect of the multiplication of W by $e^{-\frac{1}{2\sigma^2}(n-q_0)^2}$, as well as the shift along n by M_k . From Eq. (A3), we find

$$B' = \begin{pmatrix} 1/\sigma^2 & 0 \\ 0 & 0 \end{pmatrix} + \tilde{B} \quad (\text{A5})$$

and

$$\tilde{B}R + \frac{q_0}{\sigma^2} \begin{pmatrix} 1 \\ 0 \end{pmatrix} = B' \left[R' + \begin{pmatrix} M_k \\ 0 \end{pmatrix} \right] \quad (\text{A6})$$

where $\tilde{B} = \tilde{C}^{-1}$ and $B' = C'^{-1}$. From Eq. (A5), we obtain

$$C' = \left[Id + \tilde{C} \begin{pmatrix} 1/\sigma^2 & 0 \\ 0 & 0 \end{pmatrix} \right]^{-1} C_2. \quad (\text{A7})$$

Injecting $\sigma = \sqrt{\tilde{n}/(\Gamma\Delta t)}$ and expanding to first order in Δt , one gets

$$C' \simeq \left[Id - \frac{\Gamma\Delta t}{\tilde{n}} \begin{pmatrix} C_{11} & 0 \\ C_{12} & 0 \end{pmatrix} \right] \tilde{C}. \quad (\text{A8})$$

Here we used the fact that $\tilde{C}_{11} = C_{11}$ and $\tilde{C}_{12} = C_{12}$. This equation also takes the form of Eq. (15). Let us now consider the center of the distribution. Multiplying the left- and

right-hand parts of Eq. (A6) by C' and injecting Eq. (A8), we deduce

$$R' = \left[Id - \frac{\Gamma\Delta t}{\tilde{n}} \begin{pmatrix} C_{11} & 0 \\ C_{12} & 0 \end{pmatrix} \right] \left[R + \frac{M_k}{\tilde{n}} \begin{pmatrix} C_{11} \\ C_{12} \end{pmatrix} \right] - \begin{pmatrix} M_k \\ 0 \end{pmatrix}. \quad (\text{A9})$$

Neglecting terms beyond first order in Δt , we obtain

$$R' = R + \left(\frac{M_k}{\tilde{n}} - \frac{\Gamma\Delta t}{\tilde{n}} \langle n_k \rangle \right) \begin{pmatrix} C_{11} \\ C_{12} \end{pmatrix} - \begin{pmatrix} M_k \\ 0 \end{pmatrix}. \quad (\text{A10})$$

Injecting $M_k = \Gamma\Delta\langle n_k \rangle + d\xi$, we recover Eq. (16).

APPENDIX B: EVOLUTION OF E_C FOR CONSTANT g

We assume $\omega_k \gg \Gamma$ such that Eq. (18) is valid. Note that the condition $\omega_k \gg \Gamma$ also ensures adiabatic following, namely, the time evolution of the Hamiltonian parameters A_k and B_k preserves the ratio $E_C/(\hbar\omega_k)$, such that Eq. (18) holds both for a constant g and a time-varying g . Let us introduce the variable $y = \frac{(E_C)}{g\bar{\rho}}$ and rewrite Eq. (18) in the form

$$y'(t) = y\Gamma \left\{ 1 - \frac{g\rho}{2g\bar{\rho} + \hbar^2 k^2/(2m)} (1+y) \right\} + \frac{\Gamma\hbar^2 k^2}{8mg\bar{\rho}}. \quad (\text{B1})$$

For $y = 1$ we see that $y'(t) \geq 0$ and therefore $y(t)$ has to be an increasing function at $y = 1$. It follows that for all initial conditions $y(0) \geq 1$ the energy E_C stays greater than $g\bar{\rho}$. This implies in particular that, as long as an excitation stays in the phononic regime (i.e., its frequency stays much smaller than $g\bar{\rho}/\hbar$), it stays in the high-temperature regime, namely, $E_C/(\hbar\omega_k) \gg 1$.

APPENDIX C: ASYMPTOTIC TEMPERATURE FOR NONRECORDED LOSSES

We consider a mode k (we omit the index r for simplicity) and we assume averaging is done over trajectories. Then evolution of the variances of n_k and θ_k due to the loss process is given in Eqs. (22) and (23). Let us consider the quantity $\tilde{E} = \langle H_k \rangle / (\hbar\omega_k)$. We assume the loss rate is small enough so that the free evolution under the Hamiltonian (9) ensures equipartition of the energy between the two quadratures, namely, at each time $A_k \langle n_k^2 \rangle = B_k \langle \theta_k^2 \rangle = E/2$. Note that this is equivalent to the condition of adiabatic following. Then the modification of \tilde{E} under the loss process is

$$\frac{1}{\Gamma} \frac{d\tilde{E}}{dt} = -\tilde{E} + (K + 1/K)/4 \quad (\text{C1})$$

where $K = 4\tilde{n}A_k/\omega_k = 2\tilde{n}\sqrt{A_k/B_k}$. The evolution under the Hamiltonian (9), provided the adiabatic following condition is satisfied, does not modify \tilde{E} . Thus Eq. (C1) gives the total time evolution of \tilde{E} , and it is valid both when A_k and B_k depend on time and when they do not depend on time. In this paper, we consider the situation given by Eq. (19), where the exponential decrease of $\bar{\rho}$ is compensated by a time dependence of g such that K is time independent. Then Eq. (C1) evolves at long

times to

$$\tilde{E} \xrightarrow{t \rightarrow \infty} (K + 1/K)/4. \quad (\text{C2})$$

For phononic modes, for which $k^2 \ll g\rho$, one has $K \simeq 2\sqrt{g\rho}/k$. Then \tilde{E} goes to $\sqrt{g\rho}/(2k)$ at long times, which gives

$$E \xrightarrow{t \rightarrow \infty} \frac{1}{2}g\rho. \quad (\text{C3})$$

This energy is very large compared to ω_k . Thus the excitation lies in the high-temperature limit and its temperature is $T \simeq E \simeq g\rho/2$. Note that, in the case g is constant, then K depends on time and solving Eq. (C1) with the time-dependant value of K gives that E converges to $g\bar{\rho} = g\rho_0 e^{-\Gamma t}$, as derived in [1].

APPENDIX D: EQUATIONS IN REDUCED VARIABLES

Here we derive the evolution equations for the reduced variables $\tilde{n}_k = n_0^{-1/2}n_k$ and $\tilde{\theta}_k = n_0^{1/2}\theta_k$. We denote \tilde{R} and \tilde{C} the associated mean vector and covariant matrix. Taking into account the exponential decrease of n_0 , Eqs. (15) and (16) give

$$\tilde{C}' = \tilde{C} + \Gamma \Delta t \begin{pmatrix} -\tilde{C}_{11}^2 + \tilde{C}_{11} & -\tilde{C}_{11}\tilde{C}_{12} \\ -\tilde{C}_{11}\tilde{C}_{12} & -\tilde{C}_{12}^2 + \frac{1}{4} - \tilde{C}_{22} \end{pmatrix} \quad (\text{D1})$$

and

$$\tilde{R}' = \tilde{R} + d\tilde{\xi} \begin{pmatrix} \tilde{C}_{11} - 1 \\ \tilde{C}_{12} \end{pmatrix} - \frac{1}{2} \begin{pmatrix} 3\Gamma \Delta t \langle \tilde{n}_k \rangle \\ -\Gamma \Delta t \langle \tilde{\theta}_k \rangle \end{pmatrix}. \quad (\text{D2})$$

Here $d\tilde{\xi} = \tilde{M}_k - \Gamma \Delta t \langle \tilde{n}_k \rangle$ where $\tilde{M}_k = M_k/\sqrt{n_0}$. The statistic of trajectory implies that \tilde{M}_k follows a Gaussian statistic with $\langle \tilde{M}_k \rangle = \Gamma \Delta t \langle \tilde{n}_k \rangle$ and $\text{Var}\tilde{M}_k = \Gamma \delta t$.

-
- [1] P. Grišins, B. Rauer, T. Langen, J. Schmiedmayer, and I. E. Mazets, *Phys. Rev. A* **93**, 033634 (2016).
- [2] B. Rauer, P. Grišins, I. E. Mazets, T. Schweigler, W. Rohringer, R. Geiger, T. Langen, and J. Schmiedmayer, *Phys. Rev. Lett.* **116**, 030402 (2016).
- [3] We express temperature in energy (effectively taking $k_B = 1$).
- [4] M. Saba, T. A. Pasquini, C. Sanner, Y. Shin, W. Ketterle, and D. E. Pritchard, *Science* **307**, 1945 (2005).
- [5] Y. Castin and J. Dalibard, *Phys. Rev. A* **55**, 4330 (1997).
- [6] S. S. Szigeti, M. R. Hush, A. R. R. Carvalho, and J. J. Hope, *Phys. Rev. A* **80**, 013614 (2009).
- [7] A. C. J. Wade, J. F. Sherson, and K. Mølmer, *Phys. Rev. Lett.* **115**, 060401 (2015).
- [8] T. Vanderbruggen, R. Kohlhaas, A. Bertoldi, S. Bernon, A. Aspect, A. Landragin, and P. Bouyer, *Phys. Rev. Lett.* **110**, 210503 (2013).
- [9] G. Vasilakis, H. Shen, K. Jensen, M. Balabas, D. Salart, B. Chen, and E. S. Polzik, *Nat. Phys.* **11**, 389 (2015).
- [10] A. Kuzmich, L. Mandel, and N. P. Bigelow, *Phys. Rev. Lett.* **85**, 1594 (2000).
- [11] S. Kraft, A. Günther, J. Fortágh, and C. Zimmermann, *Phys. Rev. A* **75**, 063605 (2007).
- [12] T. Gericke, P. Würtz, D. Reitz, T. Langen, and H. Ott, *Nat. Phys.* **4**, 949 (2008).
- [13] C. Mora and Y. Castin, *Phys. Rev. A* **67**, 053615 (2003).
- [14] Note that these criteria can be fulfilled within the quasicondensate regime, for a pixel size δx smaller than the healing length.
- [15] K. Mølmer and Y. Castin, *Quantum Semiclass. Opt.* **8**, 49 (1996).
- [16] $[n_k, \theta_k] = i$.
- [17] The free evolution during a time t amounts to a rotation in phase space according to the matrix $\mathfrak{R}(\omega_k t) = \begin{pmatrix} \cos \omega_k t & \sqrt{B/A} \sin \omega_k t \\ -\sqrt{A/B} \sin \omega_k t & \cos \omega_k t \end{pmatrix}$ with $\omega_k = 2\sqrt{AB}$.
- [18] A. Johnson, S. Szigeti, M. Schemmer, and I. Bouchoule, [arXiv:1703.00322](https://arxiv.org/abs/1703.00322).
- [19] T. Langen, S. Erne, R. Geiger, B. Rauer, T. Schweigler, M. Kuhnert, W. Rohringer, I. E. Mazets, T. Gasenzer, and J. Schmiedmayer, *Science* **348**, 207 (2015).

Long-lived nonthermal states realized by atom losses in one-dimensional quasicondensates

A. Johnson,¹ S. S. Szigeti,^{2,3} M. Schemmer,¹ and I. Bouchoule¹

¹Laboratoire Charles Fabry, Institut d'Optique, CNRS, Université Paris Sud 11, 2 Avenue Augustin Fresnel, F-91127 Palaiseau Cedex, France

²School of Mathematics and Physics, University of Queensland, Brisbane, QLD 4072, Australia

³ARC Centre of Excellence for Engineered Quantum Systems, University of Queensland, Brisbane, QLD 4072, Australia

(Received 6 March 2017; published 24 July 2017)

We investigate the cooling produced by a loss process nonselective in energy on a one-dimensional (1D) Bose gas with repulsive contact interactions in the quasicondensate regime. By performing nonlinear classical-field calculations for a homogeneous system, we show that the gas reaches a nonthermal state where different modes have acquired different temperatures. After losses have been turned off, this state is robust with respect to the nonlinear dynamics, described by the Gross-Pitaevskii equation. We argue that the integrability of the Gross-Pitaevskii equation is linked to the existence of such long-lived nonthermal states and illustrate this by showing that such states are not supported within a nonintegrable model of two coupled 1D gases of different masses. We go beyond a classical-field analysis, taking into account the quantum noise introduced by the discreteness of losses, and show that the nonthermal state is still produced and its nonthermal character is even enhanced. Finally, we extend the discussion to gases trapped in a harmonic potential and present experimental observations of a long-lived nonthermal state within a trapped 1D quasicondensate following an atom-loss process.

DOI: [10.1103/PhysRevA.96.013623](https://doi.org/10.1103/PhysRevA.96.013623)

I. INTRODUCTION

Ultracold temperatures are routinely obtained in dilute atomic gas experiments using evaporative cooling. Here, an energy-selective loss process removes the most energetic atoms; provided these atoms have a high enough energy, rethermalization of the remaining atoms leads to a lower temperature [1]. Naively, one expects evaporative cooling to be highly inefficient in (quasi-)one-dimensional (1D) geometries where the transverse degrees of freedom are suppressed and the atoms mainly populate the transverse ground state. Evaporative cooling then only relies on longitudinal dynamics, and we expect its efficiency to be poor, particularly for the very shallow longitudinal confinements realized experimentally. Despite this issue, cooling deep in the 1D regime to temperatures as low as one-tenth of the transverse energy gap has been reached experimentally in Bose gas experiments [2,3]. This has allowed the realization of 1D quasicondensates, where the repulsive interactions between atoms strongly suppress the density fluctuations and low excitations of the gas are collective density waves, also called phonons [4]. The nature of the cooling mechanism in such 1D geometries is still not well understood. However, its investigation is essential in order to properly characterize both the equilibrium and out-of-equilibrium properties of these atomic clouds, especially with a view towards their application in quantum simulation experiments [5].

Recently, Ref. [6] theoretically considered a 1D quasicondensate subject to a simple energy-independent loss process and showed, within a linearized approach where excitations are treated independently, that cooling was possible. More precisely, for a given mode, losses amount to a decrease of the mode's energy due to the decrease of both the mean density and the amplitude of density fluctuations. Free evolution, if fast enough, ensures equipartition of energy between the mode's two quadratures, such that one can assign an effective temperature to the mode, so losses consequently amount to a reduction of the mode's temperature. The temperature

decrease predicted by this linearized theory was observed in an experiment probing the low-energy modes of a quasicondensate undergoing a continuous and homogeneous outcoupling process [7]. However, studies for homogeneous systems show that the cooling rate is expected to depend on the mode energy, with higher-energy modes cooled at a slower rate than low-energy excitations. Thus, as long as the linearized approach is trusted, losses should produce a nonthermal state (i.e., a state that is not described by the Gibbs ensemble). Typically, this state is not guaranteed to be long lived, since coupling between modes *a priori* redistributes energy, leading to global thermal equilibrium. However, 1D Bose gases with repulsive contact interactions are peculiar since they are described by the Lieb-Liniger Hamiltonian, which belongs to the class of integrable models. Relaxation of observables towards their values predicted by the Gibbs ensemble is not granted in such systems [8,9]. Consequently, the nonthermal nature of the state produced by the loss process could be robust against coupling between modes. This might be the origin of the nonthermal nature of the long-lived 1D quasicondensates produced by evaporative cooling and reported in [10,11].

In this article, we go beyond the linearized approach and show that a simple uniform loss process realizes long-lived nonthermal states of 1D quasicondensates. We numerically investigate the simple case of homogeneous gases and describe the quasicondensate within a classical-field approach, its dynamics being governed by a nonlinear partial differential equation: the Gross-Pitaevskii equation with an additional term taking losses into account. We believe the realization of long-lived nonthermal states is related to the integrability of the system, supported by numerical simulations showing that the system thermalizes towards the Gibbs ensemble when integrability is violently broken. We then present numerical studies showing that long-lived nonthermal states are also produced if one incorporates the shot noise associated with the loss process, due to the discreteness of losses, namely the quantum nature of the atomic field operator.

Finally, we discuss the case of a gas trapped in a harmonic potential. Both the excitation spectrum and the form of the excitations differ from that of a homogeneous system, and hence one cannot directly extend the results for the homogeneous system to the trapped case. We nevertheless argue that we still expect a nonthermal state to be produced by the loss process. We present recent observations of long-lived out-of-equilibrium states on our experimental atom-chip setup that could be related to the conclusions of our theoretical study.

II. LINEARIZED APPROACH FOR HOMOGENEOUS SYSTEMS WITHIN THE CLASSICAL-FIELD APPROACH

We first recall results obtained within the linearized approach in the classical-field framework. For this purpose, consider the simple case of a 1D Bose gas confined in a box of length L that is initially at thermal equilibrium at temperature T_i and mean density ρ_i . We use the density-phase representation of the atomic field $\psi = \sqrt{\rho} e^{i\theta}$ and denote ρ_0 the (time-dependent) mean density. Density fluctuations $\delta\rho = \rho - \rho_0$ are small in the quasicondensate regime and phase fluctuations occur on long wavelengths; therefore, as a first approximation one can linearize the equations of motion. Expanding θ and $\delta\rho$ on sinusoidal modes, $\theta = \sum_{k>0} \sqrt{2/L} [\theta_{ck} \cos(kz) + \theta_{sk} \sin(kz)]$ and $\delta\rho = \sum_{k>0} \sqrt{2/L} [\delta\rho_{ck} \cos(kz) + \delta\rho_{sk} \sin(kz)]$, we find that θ_{jk} and $\delta\rho_{jk}$ are conjugate variables (i.e., $[\delta\rho_{jk}, \theta_{j'k'}] = i\delta_{jj'}\delta_{kk'}$) and that each mode is governed by its own Hamiltonian

$$H_{jk} = A_k \delta\rho_{jk}^2 + B_k \theta_{jk}^2, \quad (1)$$

where the coefficients $A_k = g/2 + \hbar^2 k^2 / (8m\rho_0)$ and $B_k = \hbar^2 k^2 \rho_0 / (2m)$ depend on ρ_0 . Here $j = c$ or s and k takes discrete values $2n\pi/L$, where n is a positive integer. Within the classical-field approach, the thermal state of the mode jk corresponds to a Gaussian distribution of θ_{jk} and ρ_{jk} satisfying the equipartition relation $A_k \langle \delta\rho_{jk}^2 \rangle = B_k \langle \theta_{jk}^2 \rangle = k_B T / 2$.

Now consider the uniform loss of atoms at rate Γ and its effect on a given mode jk . Losses decrease ρ_0 at the rate Γ and, ignoring at first evolution under the Hamiltonian (1), $\delta\rho_{jk}$ is decreased at the same rate—i.e., $d\delta\rho_{jk}/dt|_L = -\Gamma\delta\rho_{jk}$, where the symbol L indicates that we are only considering the effect of losses. Thus the losses decrease the energy in each quadrature, due both to the decrease of $\delta\rho_{jk}$ and the modification of A_k and B_k . If the loss rate is small compared to the mode frequency $\omega_k = 2\sqrt{A_k B_k}$, one expects adiabatic following under the modification of A_k and B_k . In particular, equipartition of energy between the two conjugate variables holds at all times. Then, the quantity $\tilde{E} = E / (\hbar\omega_k)$ is unaffected by the modification of A_k and B_k due to the decrease of ρ_0 , and its modification comes solely from the decrease of $\delta\rho_{jk}$ due to losses. We finally find

$$\frac{d\tilde{E}}{dt} = -\Gamma\tilde{E}. \quad (2)$$

Our assumption of energy equipartition allows us to associate a temperature $k_B T_k = E_k$ to the mode, and so Eq. (2) can be rewritten as

$$\frac{T_k(t)}{T_i} = e^{-\Gamma t} \frac{\omega_k(t)}{\omega_k(0)}. \quad (3)$$

Note that the form of Hamiltonian (1) is not particular to the case of a homogeneous gas, provided $\delta\rho_{k,j}$ and $\theta_{k,j}$ are replaced by the proper quadratures of the Bogoliubov mode, corresponding to density and phase fluctuations, respectively, and A_k and B_k take values which depend on the Bogoliubov wave functions [12]. Thus Eqs. (2) and (3) are general, provided the adiabatic following condition is fulfilled. Note that, in Eq. (3), changes of the parameters A_k and B_k only contribute to the temperature evolution via the ratio $\frac{\omega_k(t)}{\omega_k(0)}$, while the exponential prefactor amounts to the extra cooling due to the loss-induced squeezing of the density-fluctuation quadrature. For the particular case of a homogeneous gas, Eq. (3) gives

$$\frac{dT_k}{dt} = -\Gamma T_k \frac{3 + \hbar^2 k^2 / (2\rho_0 m g)}{2 + \hbar^2 k^2 / (2\rho_0 m g)}. \quad (4)$$

Losses thus lead to the cooling of each mode, but at different rates explicitly dependent on k . In the phononic regime $k \ll \sqrt{mg\rho_0}/\hbar$, the cooling rate is $3\Gamma/2$, compared to Γ in the particle regime $k \gg \sqrt{mg\rho_0}/\hbar$. Therefore, within the linearized approximation, a uniform loss process produces a nonthermal state, where different modes correspond to different temperatures. Such a state can be viewed as a generalized Gibbs ensemble [13], where the different conserved quantities are the energies in each linearized mode.

III. NONLINEAR CLASSICAL-FIELD APPROACH

Beyond the linearized approximation, but still within the classical-field approach, the system's evolution in the absence of loss is given by the Gross-Pitaevskii equation for the atomic field ψ

$$i\hbar \frac{\partial\psi}{\partial t} = -\frac{\hbar^2}{2m} \frac{\partial^2\psi}{\partial z^2} + g|\psi|^2\psi. \quad (5)$$

This equation contains coupling between the linearized modes studied above, which acquire a finite lifetime [14,15]. In a generic system, such coupling redistributes the energy between the modes such that the system reaches the Gibbs ensemble where all modes share the same temperature. However, the Gross-Pitaevskii equation for a 1D homogeneous gas leads to integrable dynamics and relaxation towards thermal equilibrium is not granted. Consequently, the out-of-equilibrium state produced by the atom-loss process might be robust against this nonlinear mode coupling.

To check whether the nonthermal state survives coupling between modes, we numerically evolved stochastic samples of $\{\psi(z)\}$ from an initial thermal state at temperature T_i and density ρ_i according to the dissipative Gross-Pitaevskii equation [Eq. (5) with the additional loss term $\partial\psi/\partial t = -i\Gamma\psi/2$]. Each sample [i.e., each single stochastic realization of the initial field $\{\psi(z)\}$] was constructed using the linearized approach above and the associated thermal Gaussian distribution of the conjugate variables θ_{jk} and $\delta\rho_{jk}$. Normalizing ψ by $\sqrt{\rho_i}$ and lengths by $\xi_i = \hbar/\sqrt{mg\rho_i}$, the initial statistical properties of ψ depend on the single parameter $\chi = T_i/T_{co}$, where $T_{co} = \hbar\rho_i\sqrt{\rho_i g/m}$ [16,17], while the subsequent time evolution only depends on $\Gamma/(\rho_i g)$, provided time is normalized to $\hbar/(\rho_i g)$. After a certain time t , the quantities $\delta\rho_{jk}$ and θ_{jk} are extracted, from

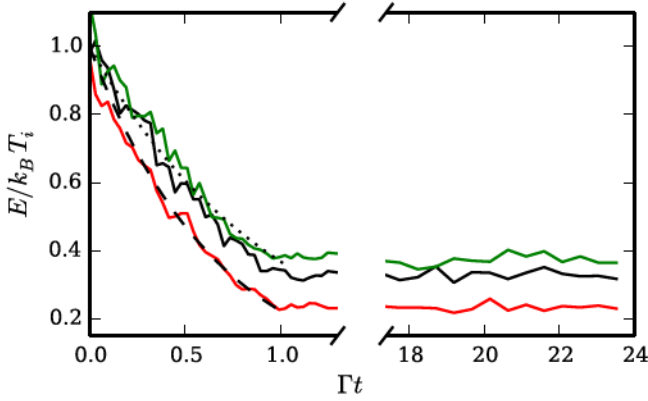


FIG. 1. Time evolution of the mode energy during the loss process ($\Gamma t < 1$), and subsequent dynamics after the loss rate is set to zero, for modes of wave vectors $k\xi_i = 0.5$ (red, lowest curve), 2.5 (black), and 6 (green, highest curve). The dashed and dotted lines are the expected behavior for phonons ($e^{-3\Gamma t/2}$) and high-energy excitations ($e^{-\Gamma t}$), respectively. Here $\chi = T_i/(\rho_i\sqrt{\hbar\rho_i g/m}) = 0.05$ and the loss rate is $\Gamma = 2 \times 10^{-3} \rho_i g/\hbar$.

which we compute the energy in each mode. Figure 1 shows the time evolution of the mean energy, using an ensemble of 10 stochastic samples, in three different Bogoliubov modes of wave vectors $k = 0.5/\xi_i$, $6/\xi_i$, and $2.5/\xi_i$, lying respectively in the phononic regime, the particle regime, and an intermediate regime. Here $\chi = 0.05$ and the loss rate $\Gamma = 2 \times 10^{-3} \rho_i g$ is small compared to the frequencies of the modes analyzed. We verified that equipartition between the two quadratures is fulfilled within a few percent during the whole time evolution, confirming that the energy in each mode can be associated with a temperature. We find that, for modes lying in the phononic regime and in the particle regime, the results are in good agreement with the linearized prediction given by Eq. (4) and the different modes reach different temperatures. This nonthermal situation produced by atom loss is stable over long times; after the loss process has stopped, the temperature of each mode is stationary over times as large as $10^3 \hbar/\rho_i g$.

Such long-lived nonthermal states are probably only possible due to the integrability of the 1D Gross-Pitaevskii equation. Nevertheless, the long-lived nature of the state is not obvious, since the energies in the linearized modes are not conserved quantities. Lifetimes of the linearized modes are finite [14] and nonthermal distributions inside the phononic regime show good thermalization [18]. The long lifetime of the nonthermal state generated here is probably due to the poor coupling between modes lying in the phononic and particle regimes, respectively. The quantum counterpart might be viewed as a form of many-body localization in momentum space.

IV. EFFECT OF INTEGRABILITY ON NONTHERMAL STATE LIFETIME

We investigated the role integrability plays in supporting these long-lived nonthermal states by considering a closely related nonintegrable system. Specifically, we coupled a second atomic field φ , consisting of particles with mass

$m' \neq m$, to the first field via coupling constant \tilde{g} , which is described by the evolution equations

$$i\hbar \frac{\partial \psi}{\partial t} = -\frac{\hbar^2}{2m} \frac{\partial^2 \psi}{\partial z^2} + (\tilde{g}|\varphi|^2 + g|\psi|^2)\psi, \quad (6a)$$

$$i\hbar \frac{\partial \varphi}{\partial t} = -\frac{\hbar^2}{2m'} \frac{\partial^2 \varphi}{\partial z^2} + (g|\varphi|^2 + \tilde{g}|\psi|^2)\varphi. \quad (6b)$$

As before, we constructed samples of an initial thermal state by identifying the two Bogoliubov modes for each wave vector k , and stochastically sampling Gaussian distributions of these modes (for details, see Appendix A). We then evolved the system in the presence of losses at the same rate Γ for both species until a substantial fraction of atoms was lost, and subsequently evolved the system further without the loss term. The energy in each mode was then extracted via the linearized approach. As illustrated in Fig. 1, when the two fields are coupled ($\tilde{g} \neq 0$) the modes evolve towards an equipartition of energy over a long propagation time scale. In contrast, within the uncoupled system ($\tilde{g} = 0$) the energies of the modes remain distinct.

There are many ways to break the integrability of the system. In the model of two gases with different masses, the integrability is violently broken since a two particle collisional event does not preserve the set of momenta. A gentler way to break the integrability would be to consider two gases with atoms of the same mass, but with an interspecies

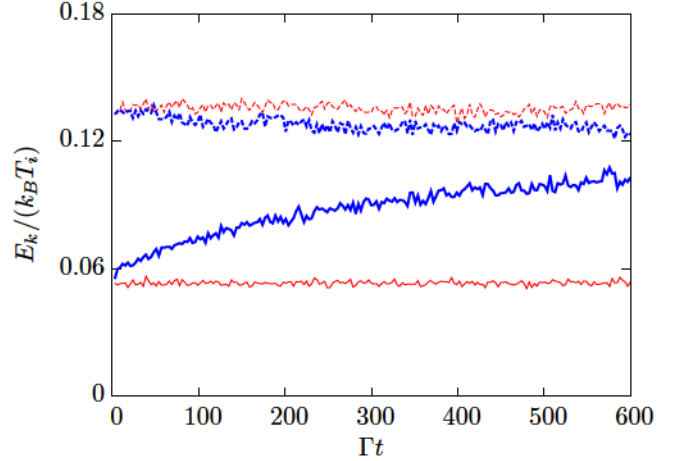


FIG. 2. Time evolution of the mean energy of modes of wave vectors $k = 0.3\sqrt{mg\rho_i}/\hbar$ (solid lines) and $k = 6.0\sqrt{mg\rho_i}/\hbar$ (dashed lines), where ρ_i is the initial density of each species, in the coupled (fat blue lines, $\tilde{g} = 0.4g$) and uncoupled (thin red lines, $\tilde{g} = 0$) cases. The loss process is turned off at time $t = 2/\Gamma$ and shown is the subsequent evolution of the isolated system. The modes in the two uncoupled gases retain their respective energies after dissipation has been turned off to form a long-lived nonthermal state as above, while the modes in the coupled system relax towards an equipartition of energy. This highlights the role of integrability in the establishment of the long-lived nonthermal configuration. Here results are obtained by averaging over 10 samples, and for each sample we average the mode energy over a k interval of $0.2\sqrt{mg\rho_i}/\hbar$. The parameters of the simulation are $T_i/(\rho_i\sqrt{\hbar g\rho_i/m}) = 0.04$, $m'/m = 3$, and $\hbar\Gamma/(\rho_i g) = 4 \times 10^{-3}$.

coupling \tilde{g} different from the intraspecies coupling g . Here, any two-particle collision does preserve the set of momenta. This system is nevertheless nonintegrable. However, our simulations of the classical-field version of this system did not show any relaxation on the time scales shown in Fig. 2.

V. EFFECT OF QUANTUM FLUCTUATIONS ASSOCIATED WITH THE ATOM-LOSS PROCESS

The above treatment does not take into account the quantized nature of the atomic field, i.e., the discreteness of the atoms. In particular, it ignores the shot noise in the loss process, which introduces additional heating and therefore limits the lowest attainable temperature. A description that accounts for the discreteness of the losses is provided by the stochastic Gross-Pitaevskii equation

$$i\hbar d\psi = \left(-\frac{\hbar^2}{2m} \frac{\partial^2}{\partial z^2} \psi + g|\psi|^2\psi - i\frac{\Gamma}{2}\psi \right) dt + d\xi, \quad (7)$$

where $\langle d\xi^*(z)d\xi(z') \rangle = \Gamma dt \delta(z - z')/2$. This equation can be derived by converting the master equation for the system density operator to a partial differential equation for the Wigner quasiprobability distribution. After the third- and higher-order derivatives associated with the nonlinear atomic interaction term are truncated (an uncontrolled approximation, but one that is typically valid for weakly interacting Bose gases, provided the occupation per mode is not too small over the simulation time scale), evolution of the Wigner distribution takes the form of a Fokker-Planck equation, which can be efficiently simulated via Eq. (7). There exists a formal correspondence between the quantum field $\hat{\psi}(z)$ and $\psi(z)$: averaging over solutions to Eq. (7) correspond to symmetrically ordered expectations (for more details, see Appendix B; an alternative derivation is provided in [6]).

As shown in Appendix B, linearizing Eq. (7) in density fluctuations and phase gradient gives an independent evolution of each mode. Modes with frequencies much larger than the loss rate remain thermal; however, their temperatures depend on the mode energy and have the following long-time behavior: $T_{\text{phonon}} \xrightarrow{t \rightarrow \infty} \rho_0(t)g/k_B$ for phononic modes and

$T_{\text{part}} \xrightarrow{t \rightarrow \infty} \frac{\hbar^2 k^2}{2m} \frac{1}{k_B \Gamma t}$ for particle modes. Note that, in contrast to pure classical-field predictions, the temperature within the particle regime depends on k . Moreover, the ratio between T_{part} and T_{phonon} ,

$$\frac{T_{\text{part}}}{T_{\text{phonon}}} \xrightarrow{t \rightarrow \infty} \frac{k^2}{2g\rho_i} \frac{e^{\Gamma t}}{\Gamma t}, \quad (8)$$

is much larger than the one predicted by a pure classical-field theory. Thus the effect of the shot noise associated with the discreteness of lost atoms amplifies the nonthermal nature of the state.

In order to test whether the above predictions including quantum noise are robust beyond the linearized approach, we numerically simulated the evolution given by Eq. (7). The initial thermal state, deep in the quasicondensate regime, was sampled stochastically by using the linearized approach and taking into account quantum fluctuations (which is equivalent to sampling the Wigner function for a thermal state [19,20]). These samples were then evolved according to

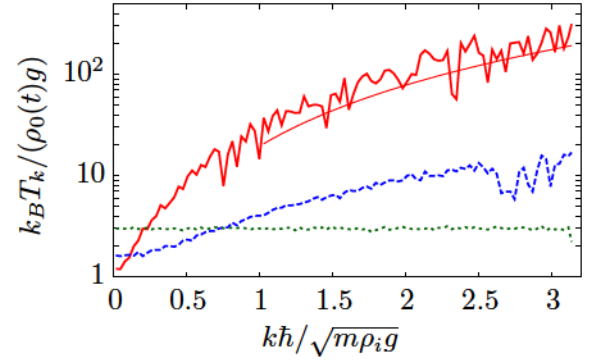


FIG. 3. Temperature of each mode, obtained from the stochastic Gross-Pitaevskii equation, as a function of the wave vector k of the mode, for different evolution times: $\Gamma t = 0$ (dotted green line), $\Gamma t = 2.5$ (dashed blue line), and $\Gamma t = 5.3$ (solid fat red line). The initial temperature is $k_B T_i / (\rho_i g) = 3$. As atoms are lost, the gas is driven out of equilibrium and T_k acquire a k dependence. For phononic particles, we observe that T_k tends towards $g\rho_0(t)$, as expected from the linearized approach. The smooth red solid line is the asymptotic result of Eq. (8), valid at long times for excitations in the particle regime, computed for $\Gamma t = 5.3$. Parameters of the simulation are $k_B T_i / (\hbar \rho_i \sqrt{g \rho_i / m}) = 3 \times 10^{-3}$, $\hbar \Gamma / (g \rho_i) = 2 \times 10^{-3}$, and $m g / (\hbar^2 \rho_i) = 10^{-6}$.

Eq. (7) and the energy E_k of each Bogoliubov mode computed at each time (with averages over trajectories yielding $\langle E_k \rangle$ and the corresponding temperature $T_k = \hbar \omega_k / \{k_B \ln[(E_k + \hbar \omega_k / 2) / (E_k - \hbar \omega_k / 2)]\}$). Figure 3 shows T_k as a function of k at three distinct times and reveals that a nonthermal state is realized with a k -dependent temperature. At small k we find, in agreement with the linearized approach, that the temperature converges towards $\rho_0(t)g$ at long times. At long times and large k , predictions from Eq. (8) are recovered.

VI. LONG-LIVED NONTHERMAL STATES IN HARMONICALLY CONFINED 1D GASES

The generation of a state which is out of equilibrium raises concerns about experiments probing one-dimensional Bose gases, where this nonselective cooling scheme is expected to occur. In standard experiments, atoms are confined in a harmonic potential, which complicates the picture. To zeroth order in fluctuations, the density profile of the gas is given by the Thomas-Fermi inverted parabolic shape [21,22]. At finite temperature, excitation modes above this Thomas-Fermi profile get populated. If the loss rate is sufficiently small, one expects that each mode adiabatically follows the changes of the Thomas-Fermi shape, such that each mode can be treated independently and, within the pure classical-field approximation, Eq. (3) is still valid, where k is now a positive integer that indexes the mode. The frequency of phononic modes, i.e., modes of energy much smaller than the chemical potential μ , are well approximated by $\omega_k = \nu \sqrt{k(k+1)}/2$, where ν is the harmonic trapping frequency [23]. Thus, for modes which stay within the phonon regime during the entire loss process, Eq. (3) predicts that their temperature decreases as $e^{-\Gamma t}$.

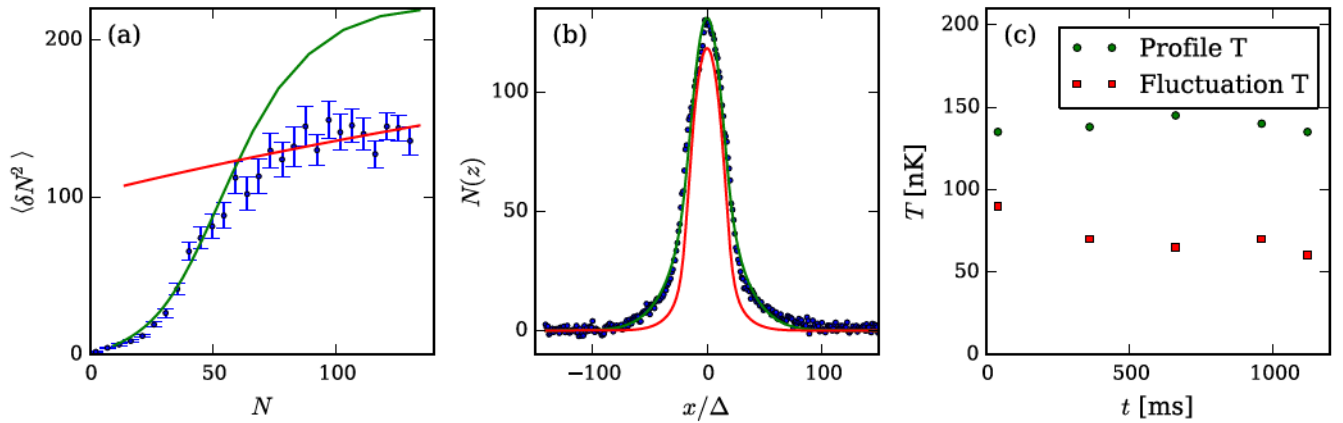


FIG. 4. Results of the two thermometries we performed on the experiment. (a) Atom number fluctuations. Fitting the central region of the cloud, i.e., the high atom-number part, (red line) gives a first temperature $T_{fl} = 80$ nK. However, the expected profile from this temperature [also the red curve on (b)] lies well below the experimental data. A second temperature $T_{pr} = 140$ nK is found by fitting the profile with the equation of state (solid green line). By plotting the expected atom number fluctuations from T_{pr} on (a), the prediction is in good agreement with the small atom number region. That is, the center of the cloud appears to be at a different temperature than the edges. The close to 50% discrepancy is well beyond the uncertainty we have on the temperature measurements, which is around 10%. (c) Data showing that this temperature difference is stationary over time: we observed a long-lived nonthermal state.

The description of higher-energy modes, called particle modes, is not simple since they explore regions where the Thomas-Fermi density vanishes and the quasicondensate approximation fails. It is reasonable, however, to believe that the energy spectrum at energies much larger than μ is close to the energy spectrum of free particles, so that frequencies of these modes are equally spaced, separated by ν . Since the chemical potential decreases during the loss process, many excitations initially in the phononic regime are transferred to the particle regime. Let us consider such an excitation. Its frequency goes from $\omega_k \simeq kv/\sqrt{2}$ before the loss process [24] to about kv at the end of the loss process when it lies in the particle regime. The ratio $\omega_k(t_f)/\omega_k(0)$ is thus larger than one. According to the classical-field prediction of Eq. (3), one therefore expects these excitations to attain a higher temperature than those lower excitations staying within the phonon regime.

The effect of shot noise on the loss process is not easy to treat for a trapped gas. However, we expect that, as in the case of a homogeneous gas, the quantum noise will amplify the nonthermal behavior of the system, so the temperature differences between modes could be even larger.

VII. EXPERIMENTAL OBSERVATION OF A LONG-LIVED NONTHERMAL STATE

Observing the nonthermal nature of the gas experimentally requires the ability to address modes of different energies independently. This is *a priori* not an easy task for gases confined in a box since all modes overlap spatially. However, since the atomic clouds in typical experiments are confined longitudinally in a slowly varying harmonic potential, there is some spatial separation of modes of different energy. At very low temperatures, thermal excitations of energy larger than $\rho_p g$ give the density profile “wings” that extend beyond the Thomas-Fermi inverted parabola of peak density ρ_p . In contrast, low-energy excitations lying in the phononic regime

do not extend beyond the Thomas-Fermi profile, but are responsible for long-wavelength density fluctuations in the central region of the cloud. The density profile of the gas is thus most sensitive to high-energy excitations. Low-energy excitations, on the other hand, can be probed by investigating, within the Thomas-Fermi profile, atom-number fluctuations $\langle \delta N^2 \rangle$, in pixels of length Δ much larger than the healing length ξ_0 [25].

Experimentally, we prepare clouds of ^{87}Rb atoms by radio-frequency evaporation in our atom-chip experiment, as described in [26], and we record a set of density profiles taken under the same experimental conditions. The longitudinal trapping frequency is 6.2 Hz, while the transverse confinement is 1.9 kHz. Atoms are polarized in the $|F=2, m=2\rangle$ hyperfine ground state, where the interactions are characterized by the *s*-wave scattering length $a = 5.2$ nm. Since the local density approximation is well fulfilled longitudinally, the equilibrium profile can be computed using the equation of state for longitudinally homogeneous gases, $\rho(\mu, T)$, where μ is the chemical potential. Using the well-established modified Yang-Yang equation of state [26,27], where the effective 1D coupling constant is $g = 2\hbar\omega_{\perp}a$, the experimental density profile is fitted for a temperature $T_{pr} = 140$ nK (see Fig. 4). We also extract atom-number fluctuations $\langle \delta N^2 \rangle$ in each pixel from the same data set, giving an independent temperature measurement. Since Δ is both much smaller than the cloud size and much larger than the healing length, the physics of homogeneous gases is locally probed and thermodynamics predicts $\langle \delta N^2 \rangle = k_B T \Delta \partial \rho / \partial \mu$ [26]. In Fig. 4, we plot $\langle \delta N^2 \rangle$ versus the mean atom number in the pixel. Fitting the large atom-number region, corresponding to pixels lying inside the Thomas-Fermi profile, with the fluctuation-dissipation relation and the quasicondensate equation of state, we extract a temperature $T_{fl} = 80$ nK (as summarized in Fig. 4). The difference between T_{pr} and T_{fl} is a signature that the cloud is out of equilibrium. We also confirmed that, after the radio-frequency loss mechanism has been removed, this situation

is stable over the cloud lifetime of about 1 s (Fig. 4). Since the profile is more sensitive to high-energy excitations while the density fluctuations are more sensitive to low-energy excitations, the fact that $T_{\text{pr}} > T_{\text{fl}}$ could be related to the above quantitative study of homogeneous gases and the qualitative arguments given for the trapped system. In the experiments presented in [7], only low-energy excitations were probed and consequently this nonthermal character was not revealed.

To conclude, we theoretically investigated the long-lived nonthermal state produced by the nonselective removal of atoms in order to cool a uniform one-dimensional Bose gas. This dissipation drives the system out of equilibrium, with different excitation modes losing energies at different rates. This out-of-equilibrium character is robust against coupling between modes introduced in the Gross-Pitaevskii equation and is related to the integrable nature of the considered system. We performed simulations of a two-species Bose mixture with different masses, a nonintegrable system, and confirmed a slow relaxation towards an equipartition of energy between excitations. Truncated Wigner simulations that go beyond the pure classical-field description and include the shot-noise associated to the loss process due to the quantized nature of the atomic field further confirmed the nonthermal nature of the state produced by dissipation. Finally, we discussed the relevance of our findings for experimental realizations of 1D Bose gases trapped in a harmonic potential. From a theoretical point of view, in the linearized classical-field approach, a small temperature difference between modes of different energies is indeed expected, and this effect could be amplified by the presence of quantum noise. In our quasicondensate experiments, we indeed have signatures of a nonthermal character since different thermometries that probe different parts of the excitation spectrum give substantially different temperatures. However, a more careful and quantitative description in the trap, perhaps via finite-temperature classical-field simulations [28], is still required in order to draw firm conclusions on the relation between these experimental long-lived nonthermal states and our theoretical findings.

The study performed in this paper is particularly important for experiments that use 1D gases for quantum simulations and the investigation of out-of-equilibrium gases, which both require a high degree of control over the initial system state. The nonthermal character of the gas may not be visible if observables do not access the high-energy part of the energy spectrum, and so an experimenter may incorrectly believe the gas to be in thermal equilibrium. Nevertheless, the nonthermal nature of the gas may impact the subsequently observed physics, and therefore must be accounted for in order to derive correct conclusions from such experiments.

ACKNOWLEDGMENTS

We acknowledge fruitful discussions with M. J. Davis, K. V. Kheruntsyan, and M. Olshanii. This work has been supported by Cnano IdF. S.S.S. acknowledges support from the Australian Research Council (ARC) Centre of Excellence for Engineered Quantum Systems (Grant No. CE110001013) and the ARC Discovery Project Grant No. DP160103311. M.S. acknowledges support by the Studienstiftung des Deutschen Volkes.

APPENDIX A: BREAKING INTEGRABILITY: TWO COUPLED 1D BOSE GASES

An example of a nonintegrable system is two quasicondensates of different masses m and m' coupled via an interaction term of coupling constant \tilde{g} . Here integrability is broken by two-body collisions involving an atom of each species, which does not preserve the set of two initial momenta. Within the classical-field approximation, this system is described by the Hamiltonian

$$H = \int dz \frac{\hbar^2}{2m} \left| \frac{\partial \psi}{\partial z} \right|^2 + \int dz \frac{\hbar^2}{2m'} \left| \frac{\partial \varphi}{\partial z} \right|^2 + \frac{g}{2} \int dz |\psi(z)|^4 + \frac{g}{2} \int dz |\varphi(z)|^4 + \tilde{g} \int dz |\psi(z)|^2 |\varphi(z)|^2, \quad (\text{A1})$$

which yields the equations of motion (6). Within the density-phase representation, we can write $\psi = \sqrt{\rho} e^{i\theta}$ and $\varphi = \sqrt{\rho'} e^{i\theta'}$. For sufficiently low temperatures, the repulsive interactions result in very small density fluctuations and long-wavelength phase fluctuations, such that one can linearize the equations of motion in $\delta\rho$, $\delta\tilde{\rho}$, $\partial\theta/\partial z$, and $\partial\theta'/\partial z$, or equivalently retain only second-order terms in the Hamiltonian, which can then be diagonalized using a standard Bogoliubov procedure. We give more details on this approach below.

Since Eqs. (6) do not explicitly depend on z , different Fourier components evolve independently of each other. Let us consider the Fourier components of wave vector $k = 2n\pi/L$, where n is a positive integer and L is the length of the box that confines the gases. As for the single component case, we introduce Fourier coefficients $\delta\rho_{ck} = \sqrt{2/L} \int dz \delta\rho(z) \cos(kz)$ and $\delta\rho_{sk} = \sqrt{2/L} \int dz \delta\rho(z) \sin(kz)$, and similarly for $\delta\tilde{\rho}$, θ , and θ' . Each mode jk evolves independently according to the quadratic Hamiltonian

$$H_{jk} = \left(\frac{g}{2} + \frac{\hbar^2 k^2}{8m\rho_0} \right) \delta\rho_{jk}^2 + \frac{\hbar^2 k^2 \rho_0}{2m} \theta_{jk}^2 + \left(\frac{g}{2} + \frac{\hbar^2 k^2}{8m'\rho_0} \right) \delta\tilde{\rho}_{jk}^2 + \frac{\hbar^2 k^2 \rho_0}{2m'} \tilde{\theta}_{jk}^2 + \tilde{g} \delta\rho_{jk} \delta\tilde{\rho}_{jk}, \quad (\text{A2})$$

where $j = c$ or s . This gives the following linearized equation of motion:

$$i\hbar \frac{\partial}{\partial t} \begin{pmatrix} 2\sqrt{\rho_0}\theta_{jk} \\ \delta\rho_{jk}/\sqrt{\rho_0} \\ 2\sqrt{\rho_0}\tilde{\theta}_{jk} \\ \delta\tilde{\rho}_{jk}/\sqrt{\rho_0} \end{pmatrix} = \mathcal{L} \begin{pmatrix} 2\sqrt{\rho_0}\theta_{jk} \\ \delta\rho_{jk}/\sqrt{\rho_0} \\ 2\sqrt{\rho_0}\tilde{\theta}_{jk} \\ \delta\tilde{\rho}_{jk}/\sqrt{\rho_0} \end{pmatrix}, \quad (\text{A3})$$

where

$$\mathcal{L} = i \begin{pmatrix} 0 & 2\rho_0 g + \frac{\hbar^2 k^2}{2m} & 0 & 2\tilde{g}\rho_0 \\ -\frac{\hbar^2 k^2}{2m} & 0 & 0 & 0 \\ 0 & 2\tilde{g}\rho_0 & 0 & 2\rho_0 g + \frac{\hbar^2 k^2}{2m'} \\ 0 & 0 & -\frac{\hbar^2 k^2}{2m'} & 0 \end{pmatrix}. \quad (\text{A4})$$

Symmetry properties of \mathcal{L} show that this operator has two eigenvectors,

$$\mathcal{L} \begin{pmatrix} F_1^+ \\ iF_1^- \\ F_2^+ \\ iF_2^- \end{pmatrix} = \omega_a \begin{pmatrix} F_1^+ \\ iF_1^- \\ F_2^+ \\ iF_2^- \end{pmatrix} \quad (\text{A5})$$

and

$$\mathcal{L} \begin{pmatrix} G_1^+ \\ iG_1^- \\ G_2^+ \\ iG_2^- \end{pmatrix} = \omega_b \begin{pmatrix} G_1^+ \\ iG_1^- \\ G_2^+ \\ iG_2^- \end{pmatrix}, \quad (\text{A6})$$

where $F_1^+, F_1^-, F_2^+, F_2^-, G_1^+, G_1^-, G_2^+, G_2^-$ are real and satisfy the normalization condition:

$$G_1^- G_1^+ + G_2^- G_2^+ = 1, \quad (\text{A7a})$$

$$F_1^- F_1^+ + F_2^- F_2^+ = 1. \quad (\text{A7b})$$

The vectors $(F_1^+, -iF_1^-, F_2^+, -iF_2^-)^T$ and $(G_1^+, -iG_1^-, G_2^+, -iG_2^-)^T$ are eigenvectors of \mathcal{L} of eigenenergies $-\omega_a$ and $-\omega_b$, respectively, which complete the basis. Expanding the state $(2\sqrt{\rho_0}\theta_{jk}, \delta\rho_{jk}/\sqrt{\rho_0}, 2\sqrt{\rho_0}\tilde{\theta}_{jk}, \delta\tilde{\rho}_{jk}/\sqrt{\rho_0})^T$ on these the eigenbasis of \mathcal{L} gives

$$2\sqrt{\rho_0}\theta_{jk} = -F_1^+ i(a - a^*) - G_1^+ i(b - b^*), \quad (\text{A8a})$$

$$\delta\rho_{jk}/\sqrt{\rho_0} = F_1^- (a + a^*) + G_1^- (b + b^*), \quad (\text{A8b})$$

$$2\sqrt{\rho_0}\tilde{\theta}_{jk} = -F_2^+ i(a - a^*) - G_2^+ i(b - b^*), \quad (\text{A8c})$$

$$\delta\tilde{\rho}_{jk}/\sqrt{\rho_0} = F_2^- (a + a^*) + G_2^- (b + b^*), \quad (\text{A8d})$$

where a and b are complex numbers satisfying

$$i\hbar\partial a/\partial t = \hbar\omega_a a, \quad (\text{A9a})$$

$$i\hbar\partial b/\partial t = \hbar\omega_b b. \quad (\text{A9b})$$

Inserting into Eq. (A2), we find that the Hamiltonian H_{jk} can be written as

$$H_{jk} = \hbar\omega_a |a|^2 + \hbar\omega_b |b|^2. \quad (\text{A10})$$

Although the above procedure utilizes the classical-field approach, a quantum version yields similar results, with a and b replaced by bosonic operators and $\hat{H}_{jk} = E_k^0 + \hbar\omega_a \hat{a}^\dagger \hat{a} + \hbar\omega_b \hat{b}^\dagger \hat{b}$, where E_k^0 is the contribution of the modes a and b to the vacuum energy.

We use the linearization above to sample the initial state according to a thermal distribution. For this purpose, for each jk Fourier component, we diagonalize \mathcal{L} and we then sample the complex numbers a and b according to the thermal Gaussian law $k_B T = \hbar\omega_a \langle |a|^2 \rangle$ and $k_B T = \hbar\omega_b \langle |b|^2 \rangle$. From this, we can compute the fields ψ and φ , subsequently evolve according to Eqs. (6), and extract the energy H_{jk} of each Fourier component at each time point.

APPENDIX B: STOCHASTIC GROSS-PITAEVSKII EQUATION

1. Derivation via truncated Wigner

Here we present a derivation of Eq. (7) from a Wigner distribution formalism and the truncated Wigner approximation. This methodology has had great success in the numerical modeling of weakly interacting Bose gases in regimes where quantum fluctuations are important [29–32], and furthermore underpins the classical-field methodology used for both zero and finite temperature simulations [28]. Since the Bose gas is described by a quantum field, the derivation should strictly rely upon functional calculus (for details see, for example, Ref. [33]). However, since we are primarily concerned with numerical simulation on discrete grids with a finite number of points, for simplicity of presentation we will discretize the problem. That is, we divide space into cells of length δx , and discretize the field operator such that $\hat{\psi}_r$ annihilates an atom in the cell r , and satisfies $[\hat{\psi}_r^\dagger, \hat{\psi}_{r'}] = \delta_{r,r'}$. Furthermore, we introduce the per-cell interaction energy $\tilde{g} = g/\delta x$ and the operator $\partial_r^2 \equiv \partial^2/\partial r^2$, which must be interpreted as $\partial_r^2\{f\}|_r = (f_{r+1} + f_{r-1} - 2f_r)/\delta x^2$ when applied to a discrete function f_r , where integer r indexes the cell.

A homogeneous 1D Bose gas undergoing a nonselective loss process can be described by the master equation

$$\frac{\partial \rho}{\partial t} = -\frac{i}{\hbar}[\hat{H}, \rho] + \Gamma \sum_r \mathcal{D}[\hat{\psi}_r] \rho, \quad (\text{B1})$$

where ρ is the system density operator, $\mathcal{D}[\hat{L}]\rho \equiv \hat{L}\rho\hat{L}^\dagger - \frac{1}{2}\hat{L}^\dagger\hat{L}\rho - \frac{1}{2}\rho\hat{L}^\dagger\hat{L}$, and \hat{H} is the Lieb-Liniger Hamiltonian

$$\hat{H} = \sum_r \left(-\hat{\psi}_r^\dagger \frac{\hbar^2}{2m} \partial_r^2 \hat{\psi}_r + \frac{\tilde{g}}{2} \hat{\psi}_r^\dagger \hat{\psi}_r^\dagger \hat{\psi}_r \hat{\psi}_r \right). \quad (\text{B2})$$

The system density operator can be equivalently described by the Wigner quasiprobability distribution, W , which is a real function of a complex field $\psi(z)$:

$$W(\{\psi_r, \psi_r^*\}) = \int \prod_r d^2\lambda_r \frac{e^{-(\lambda_r \psi_r^* + \lambda_r^* \psi_r)}}{\pi^2} \chi(\{\lambda_r, \lambda_r^*\}), \quad (\text{B3})$$

where $\chi(\{\lambda_r, \lambda_r^*\})$ is the characteristic function

$$\chi(\{\lambda_r, \lambda_r^*\}) = \text{Tr} \left\{ \rho \exp \left[\sum_r (\lambda_r \hat{\psi}_r^\dagger - \lambda_r^* \hat{\psi}_r) \right] \right\}. \quad (\text{B4})$$

Averages of functions of ψ_r, ψ_r^* over W correspond to expectations of the corresponding symmetrically ordered operators. Using the operator correspondences [28,33]

$$\hat{\psi}_r \rho \rightarrow \left(\psi_r + \frac{1}{2} \frac{\partial}{\partial \psi_r^*} \right) W(\{\psi_r, \psi_r^*\}), \quad (\text{B5a})$$

$$\hat{\psi}_r^\dagger \rho \rightarrow \left(\psi_r^* - \frac{1}{2} \frac{\partial}{\partial \psi_r} \right) W(\{\psi_r, \psi_r^*\}), \quad (\text{B5b})$$

$$\rho \hat{\psi}_r \rightarrow \left(\psi_r - \frac{1}{2} \frac{\partial}{\partial \psi_r^*} \right) W(\{\psi_r, \psi_r^*\}), \quad (\text{B5c})$$

$$\rho \hat{\psi}_r^\dagger \rightarrow \left(\psi_r^* + \frac{1}{2} \frac{\partial}{\partial \psi_r} \right) W(\{\psi_r, \psi_r^*\}), \quad (\text{B5d})$$

we can map the master equation (B1) to the following partial differential equation for the Wigner function:

$$\frac{\partial W}{\partial t} = \frac{\partial W}{\partial t} \Big|_{\text{kin}} + \frac{\partial W}{\partial t} \Big|_{\text{nonlin}} + \frac{\partial W}{\partial t} \Big|_{\text{loss}}, \quad (\text{B6})$$

where

$$\frac{\partial W}{\partial t} \Big|_{\text{kin}} = \frac{i\hbar}{2m} \sum_r \left\{ \frac{\partial}{\partial \psi_r} \partial_r^2 \psi_r - \frac{\partial}{\partial \psi_r^*} \partial_r^2 \psi_r^* \right\} W \quad (\text{B7})$$

corresponds to the kinetic-energy term,

$$\begin{aligned} \frac{\partial W}{\partial t} \Big|_{\text{nonlin}} = & \frac{i\tilde{g}}{\hbar} \sum_r \left\{ \frac{1}{4} \left(\frac{\partial^3}{\partial^2 \psi_r \partial \psi_r^*} \psi_r - \frac{\partial^3}{\partial^2 \psi_r^* \partial \psi_r} \psi_r^* \right) \right. \\ & \left. + \left(\frac{\partial}{\partial \psi_r} \psi_r - \frac{\partial}{\partial \psi_r^*} \psi_r^* \right) (|\psi_r|^2 - 1) \right\} W, \quad (\text{B8}) \end{aligned}$$

corresponds to the nonlinear atom-atom collisional term, and

$$\frac{\partial W}{\partial t} \Big|_{\text{loss}} = \frac{\Gamma}{2} \sum_r \left\{ -\frac{\partial}{\partial \psi_r} \psi_r + \frac{\partial}{\partial \psi_r^*} \psi_r^* + \frac{\partial^2}{\partial \psi_r \partial \psi_r^*} \right\} W \quad (\text{B9})$$

corresponds to the loss term. This is currently no easier to simulate than the master equation (B1). However, if we truncate the third-order derivatives in term Eq. (B8) that arise due to the nonlinearity, then Eq. (B6) takes the form of a Fokker-Planck equation with positive definite diffusion. It can therefore be efficiently simulated via a set of stochastic differential equations. We also replace $(|\psi|^2 - 1)$ in Eq. (B8) with $|\psi|^2$ since this corresponds to a simple shift in energy and is thus irrelevant. We then find that the differential equations are just the stochastic Gross-Pitaevskii equation, Eq. (7). The truncation of these third-order derivatives is an uncontrolled approximation, but is typically valid for weakly interacting Bose gases, provided the occupation per mode is not too small over the simulation time scale. Note that the truncated Wigner approximation applied here concerns the treatment of interactions between atoms in the quasicondensate. The sole effect of losses is captured in a exact way by this procedure at the quantum level.

2. Linearized approach

In the quasicondensate regime density fluctuations and phase gradients are small. A linearized approach can therefore be used to identify independent modes, following the procedure below. Separating the real and imaginary parts of Eq. (7) and linearizing in density fluctuations and the phase gradient gives the stochastic equations

$$d\delta\rho_r = -\frac{\hbar^2\rho_0}{m} \partial_r^2 \theta_r dt - \Gamma \delta\rho_r dt + \sqrt{\rho_0} d\eta_r, \quad (\text{B10a})$$

$$d\theta_r = -\left(\tilde{g} - \frac{\hbar^2}{4m\rho_0} \partial_r^2 \right) \delta\rho_r dt + \frac{1}{2\sqrt{\rho_0}} dv_r, \quad (\text{B10b})$$

where dv_r and $d\eta_r$ are random Gaussian variables with zero mean and variances $\langle d\eta_r d\eta_{r'} \rangle = \langle dv_r dv_{r'} \rangle = \delta_{r,r'} \Gamma dt$. Expanding θ_r and $\delta\rho_r$ on sinusoidal modes, $\theta = \sum_{k>0} \sqrt{2/L} [\theta_{ck} \cos(kz) + \theta_{sk} \sin(kz)]$ and

$\delta\rho = \sum_{k>0} \sqrt{2/L} [\delta\rho_{ck} \cos(kz) + \delta\rho_{sk} \sin(kz)]$ gives

$$d\delta\rho_{jk} = \frac{\hbar^2 k^2 \rho_0}{m} \theta_{jk} dt - \Gamma \delta\rho_{jk} dt + \sqrt{\rho_0} d\eta_{jk}, \quad (\text{B11a})$$

$$d\theta_{jk} = -\left(\tilde{g} - \frac{\hbar^2 k^2}{4m\rho_0} \right) \delta\rho_{jk} dt + \frac{1}{2\sqrt{\rho_0}} dv_{jk}, \quad (\text{B11b})$$

where dv_{jk} and $d\eta_{jk}$ are random Gaussian variables of vanishing mean and variances $\langle d\eta_{jk}^2 \rangle = \langle dv_{jk}^2 \rangle = \Gamma dt$. An initial centered Gaussian Wigner distribution (such as a thermal state) remains Gaussian under the above linearized stochastic evolution. Moreover, after averaging over stochastic trajectories, it remains centered on $\langle \delta\rho_{jk} \rangle = \langle \theta_{jk} \rangle = 0$. Consequently the Wigner distribution for each mode is entirely determined by variances and covariances of the variables—explicitly, entirely determined by the following coupled differential equations:

$$\frac{d}{dt} \langle \delta\rho_{jk}^2 \rangle = 2 \frac{\hbar^2 k^2 \rho_0}{m} \langle \theta_{jk} \delta\rho_{jk} \rangle - 2\Gamma \langle \delta\rho_{jk}^2 \rangle + \rho_0 \Gamma, \quad (\text{B12a})$$

$$\frac{d}{dt} \langle \theta_{jk}^2 \rangle = -2 \left(\tilde{g} - \frac{\hbar^2 k^2}{4m\rho_0} \right) \langle \theta_{k,j} \delta\rho_{jk} \rangle + \frac{\Gamma}{4\rho_0}, \quad (\text{B12b})$$

$$\frac{d}{dt} \langle \delta\rho_{jk} \theta_{jk} \rangle = \frac{\hbar^2 k^2 \rho_0}{m} \langle \theta_{jk}^2 \rangle - \left(\tilde{g} - \frac{\hbar^2 k^2}{4m\rho_0} \right) \langle \theta_{jk}^2 \rangle. \quad (\text{B12c})$$

The link between these *classical* averages over $\delta\rho_{jk}$ and $\delta\theta_{jk}$ and the expectations over the corresponding *quantum* operators is not immediate. Strictly, averages over various combinations of the *c*-number fields ψ_r and ψ_r^* correspond to expectations of symmetric orderings of the corresponding quantum operators—for example,

$$\langle (\hat{\psi}_r^\dagger \hat{\psi}_r + \hat{\psi}_r \hat{\psi}_r^\dagger) / 2 \rangle = \overline{\psi_r^* \psi_r}.$$

However, since in the quasicondensate regime correlation lengths are much larger than the mean interparticle distance and density fluctuations are small, one can use a coarse-grained approximation where the atom number in each cell is large, yielding small relative fluctuations. Then the atomic density $\langle \hat{\psi}_r^\dagger \hat{\psi}_r \rangle$ and its higher-order moments are well approximated simply by classical averages over $\psi^* \psi$ and its powers. Put another way, those corrections that arise due to the noncommutativity of the operators are small and can be neglected. A similar argument holds for the phase operator. Consequently, we are justified in interpreting those classical averages within Eqs. (B12) as quantum expectations.

Let us focus on the evolution of a given mode of wave vector k and assume the loss rate is very small compared to the mode frequency $\omega_k = \sqrt{\hbar^2 k^2 / (2m) [\hbar^2 k^2 / (2m) + 2\tilde{g}\rho_0]}$. Then, the free evolution ensures equipartition of the energy between the two conjugate variables $\delta\rho_{jk}$ and θ_{jk} at any time, which corresponds to thermal equilibrium. The Wigner function is then solely determined by the mean energy in the mode E_k and one finds, from Eq. (B12),

$$\frac{d}{dt} \bar{E} = \Gamma (-\bar{E} + (\bar{A}_k^2 + 1/\bar{A}_k^2)/4), \quad (\text{B13})$$

where $\bar{A}_k = \{[\hbar^2 k^2 / (2m) + 2\tilde{g}\rho_0] / [\hbar^2 k^2 / (2m)]\}^{1/4}$ and $\bar{E} = E_k / \omega_k$. For phonons, $\bar{A}_k \approx [4mg\rho_0 / (\hbar^2 k^2)]^{1/4}$ and is much larger than 1. Using this time-dependant approximation of A_k

to solve Eq. (B13), we find that E_k asymptotically goes towards $g\rho_0(t)$. Since $g\rho_0(t)$ is much larger than the ground-state energy for phonons, the Rayleigh-Jeans limit is attained, and this corresponds to a thermal equilibrium at temperature

$$k_B T_{\text{phonon}} \underset{t \rightarrow \infty}{\simeq} \rho_0(t)g. \quad (\text{B14})$$

In contrast, for modes with $k \gg \sqrt{m\rho_0 g}/\hbar$, an expansion of \bar{A}_k in powers of $g\rho_0/(\hbar^2 k^2/m)$ gives

$$\bar{\epsilon} \simeq \left(\frac{mg\rho_0}{\hbar^2 k^2} \right)^2 e^{-\Gamma t} (1 - e^{-\Gamma t}) + \bar{\epsilon}_0 e^{-\Gamma t}, \quad (\text{B15})$$

where $\bar{\epsilon} = (\bar{E} - 1/2)/\omega_k$ is the mean quantum occupation number of the mode. At large times, $\bar{\epsilon}$ becomes much smaller than one. This corresponds to a temperature $k_B T \simeq$

$-\left[\hbar^2 k^2/(2m)\right] \ln(\bar{\epsilon})$, much smaller than ω_k . At large times, we find

$$k_B T_{\text{part}} \underset{t \rightarrow \infty}{\simeq} \frac{\hbar^2 k^2}{2m} \frac{1}{\Gamma t}. \quad (\text{B16})$$

The temperature of those modes depends on k and takes much larger values than T_{phonon} .

Finally, note that, while in this appendix we start from the truncated Wigner stochastic equation to derive the above linearized approach, an alternative approach is to linearize the Lieb-Liniger Hamiltonian and then consider, for a given mode, the effect of losses. Thus the validity of the linearized approach does not require that the mode occupation number be large. It is valid even in the quantum regime, the approximation here being that the gas lies deeply enough in the quasicondensate regime.

-
- [1] O. J. Luiten, M. W. Reynolds, and J. T. M. Walraven, *Phys. Rev. A* **53**, 381 (1996).
- [2] S. Hofferberth, I. Lesanovsky, T. Schumm, A. Imambekov, V. Gritsev, E. Demler, and J. Schmiedmayer, *Nat. Phys.* **4**, 489 (2008).
- [3] T. Jacqmin, J. Armijo, T. Berrada, K. V. Kheruntsyan, and I. Bouchoule, *Phys. Rev. Lett.* **106**, 230405 (2011).
- [4] K. V. Kheruntsyan, D. M. Gangardt, P. D. Drummond, and G. V. Shlyapnikov, *Phys. Rev. Lett.* **91**, 040403 (2003).
- [5] I. Bloch, J. Dalibard, and W. Zwerger, *Rev. Mod. Phys.* **80**, 885 (2006).
- [6] P. Grišins, B. Rauer, T. Langen, J. Schmiedmayer, and I. E. Mazets, *Phys. Rev. A* **93**, 033634 (2016).
- [7] B. Rauer, P. Grišins, I. E. Mazets, T. Schweigler, W. Rohringer, R. Geiger, T. Langen, and J. Schmiedmayer, *Phys. Rev. Lett.* **116**, 030402 (2016).
- [8] J. M. Deutsch, *Phys. Rev. A* **43**, 2046 (1991).
- [9] M. Rigol, V. Dunjko, and M. Olshanii, *Nature (London)* **452**, 854 (2008).
- [10] B. Fang, G. Carleo, A. Johnson, and I. Bouchoule, *Phys. Rev. Lett.* **113**, 035301 (2014).
- [11] B. Fang, A. Johnson, T. Roscilde, and I. Bouchoule, *Phys. Rev. Lett.* **116**, 050402 (2016).
- [12] A. C. J. Wade, J. F. Sherson, and K. Mølmer, *Phys. Rev. A* **93**, 023610 (2016).
- [13] T. Langen, S. Erne, R. Geiger, B. Rauer, T. Schweigler, M. Kuhnert, W. Rohringer, I. E. Mazets, T. Gasenzer, and J. Schmiedmayer, *Science* **348**, 207 (2015).
- [14] M. Kulkarni and A. Lamacraft, *Phys. Rev. A* **88**, 021603 (2013).
- [15] I. E. Mazets and J. Schmiedmayer, *Eur. Phys. J. B* **68**, 335 (2009).
- [16] Y. Castin, R. Dum, E. Mandonnet, A. Minguzzi, and I. Carusotto, *J. Mod. Opt.* **47**, 2671 (2000).
- [17] I. Bouchoule, S. S. Szigeti, M. J. Davis, and K. V. Kheruntsyan, *Phys. Rev. A* **94**, 051602 (2016).
- [18] P. Grisins and I. E. Mazets, *Phys. Rev. A* **84**, 053635 (2011).
- [19] A. Sinatra, C. Lobo, and Y. Castin, *J. Phys. B* **35**, 3599 (2002).
- [20] M. Olsen and A. Bradley, *Opt. Commun.* **282**, 3924 (2009).
- [21] C. J. Pethick and H. Smith, *Bose Einstein Condensation in Dilute Gases*, 2nd ed. (Cambridge University Press, Cambridge, UK, 2008).
- [22] We assume here the trapping frequency is much smaller than $g\rho_p$, where ρ_p is the central atomic density.
- [23] T.-L. Ho and M. Ma, *J. Low Temp. Phys.* **115**, 61 (1999).
- [24] We assume here $k \gg 1$.
- [25] J. Esteve, J.-B. Trebbia, T. Schumm, A. Aspect, C. I. Westbrook, and I. Bouchoule, *Phys. Rev. Lett.* **96**, 130403 (2006).
- [26] J. Armijo, T. Jacqmin, K. Kheruntsyan, and I. Bouchoule, *Phys. Rev. A* **83**, 021605 (2011).
- [27] A. H. van Amerongen, J. J. P. van Es, P. Wicke, K. V. Kheruntsyan, and N. J. van Druten, *Phys. Rev. Lett.* **100**, 090402 (2008).
- [28] P. B. Blakie, A. S. Bradley, M. J. Davis, R. J. Ballagh, and C. W. Gardiner, *Adv. Phys.* **57**, 363 (2008).
- [29] P. D. Drummond and A. D. Hardman, *Europhys. Lett.* **21**, 279 (1993).
- [30] S. J. Carter, *Phys. Rev. A* **51**, 3274 (1995).
- [31] M. J. Steel, M. K. Olsen, L. I. Plimak, P. D. Drummond, S. M. Tan, M. J. Collett, D. F. Walls, and R. Graham, *Phys. Rev. A* **58**, 4824 (1998).
- [32] A. Polkovnikov, *Ann. Phys. (NY)* **325**, 1790 (2010).
- [33] B. Opanchuk and P. D. Drummond, *J. Math. Phys.* **54**, 042107 (2013).

Monitoring squeezed collective modes of a one-dimensional Bose gas after an interaction quench using density-ripple analysis

Max Schemmer, Aisling Johnson,^{*} and Isabelle Bouchoule[†]

Laboratoire Charles Fabry, Institut d'Optique, CNRS, Université Paris Sud 11, 2 Avenue Augustin Fresnel, F-91127 Palaiseau Cedex, France



(Received 13 December 2017; published 3 October 2018)

We investigate the out-of-equilibrium dynamics following a sudden quench of the interaction strength in a one-dimensional quasicondensate trapped at the surface of an atom chip. Within a linearized approximation, the system is described by independent collective modes and the quench squeezes the phase-space distribution of each mode, leading to a subsequent breathing of each quadrature. We show that the collective modes are resolved by the power spectrum of density ripples which appear after a short time of flight. This allows us to experimentally probe the expected breathing phenomenon. Our results are in good agreement with theoretical predictions which take the longitudinal harmonic confinement into account.

DOI: [10.1103/PhysRevA.98.043604](https://doi.org/10.1103/PhysRevA.98.043604)

I. INTRODUCTION

The out-of-equilibrium dynamics of isolated quantum many-body systems is a field attracting a lot of interest [1], triggered in part by progress in cold atom experiments. A particular focus has been devoted to the case of sudden quenches where the system is brought out of equilibrium by a sudden change of a Hamiltonian parameter, and in particular the case of an interaction quench, both theoretically [2] and experimentally [3–7]. Whether and how the system relaxes towards an equilibrium state is the subject of intense theoretical work. The role of integrability, not completely elucidated, is the focus of many studies. Within this context, the case of a one-dimensional (1D) Bose gas with contact repulsive interactions, described by the integrable Lieb-Liniger model, is a prime theoretical candidate to uncover the underlying physics, studied in, e.g., [8–11].

This paper constitutes an experimental study of the out-of-equilibrium dynamics following a sudden quench of the interaction strength in a 1D Bose gas with repulsive interactions. Within a linearized approximation, the evolution following a splitting of a 1D Bose gas in two copies, studied in [6], can be interpreted as an interaction quench in an effective 1D Bose gas. Investigating the first-order correlation function, the authors observed an apparent thermalization, taking the form of a light cone effect. This observation may however conceal underlying nonequilibrium dynamics, as revealed recently by the observation of recurrences in a similar experiment [12]. Finding appropriate observables revealing these dynamics is thus a key point for investigating out-of-equilibrium phenomena. In this paper, by investigating the density ripples appearing after short time of flight, the behavior of collective modes is probed, rather than a global quantity such as the first-order correlation function, allowing for a better understanding of

the physics at play after an interaction quench. The dynamics is revealed by the oscillatory behavior of each component of the density-ripple power spectrum, observed for times that go beyond the apparent thermalization time seen on the first-order correlation function. We show that these oscillatory dynamics are the signature of squeezed collective modes: for each collective mode, the quench produces a squeezed phase-space distribution, leading to a subsequent oscillation of the width of its quadratures—a *breathing behavior*. As well as improving the understanding of the effect of an interaction quench, this work constitutes an observation of squeezed collective modes, a result interesting on its own.

II. INTERACTION QUENCH WITHIN THE LINEARIZED APPROACH

The physics at play can be understood by considering a 1D homogeneous Bose gas, of length L , temperature T , and density n_0 , with particles of mass m interacting with a two-body repulsive contact interaction $g\delta(z)$, where z is the distance between the two particles. At $t = 0$, g is suddenly changed from g_i to $g_f = (1 + \kappa)g_i$, where κ is the quench strength. While the complete treatment of an interaction quench is tremendously difficult the problem is greatly simplified if

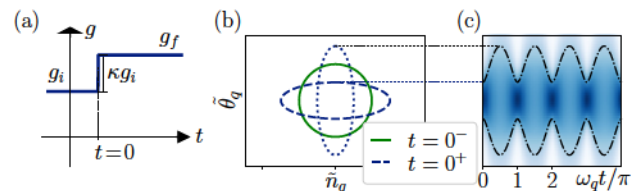


FIG. 1. Squeezing of each collective mode after an interaction strength quench from g_i to g_f . The Gaussian phase-space distributions before the quench ($t = 0^-$), just after the quench ($t = 0^+$), and after an evolution time $\pi/(2\omega_q)$ (dashed ellipse) are represented in (b), where lines correspond to a given probability density (here we chose $\kappa = 3$). The subsequent breathing is seen in (c), where the time evolution of the phase distribution is shown in color plot.

^{*}Present address: Vienna Center for Quantum Science and Technology, TU Wien-Atominstut, Stadionallee 2, 1020 Vienna, Austria.

[†]isabelle.bouchoule@institutoptique.fr

one can rely on a linearized approach, as presented below. Within the quasicondensate regime, density fluctuations are strongly reduced ($|\delta n(z)| \ll n_0$) and phase fluctuations occur on large length scales, such that the Hamiltonian of the system can be diagonalized using the phase-density representation of the field operator $\Psi(z) = \sqrt{n_0 + \delta n(z)} \exp[i\theta(z)]$ and the Bogoliubov procedure [13]. The obtained linearized modes correspond to Fourier modes. For each wave vector q , the dynamics is governed by the harmonic oscillator Hamiltonian [14]

$$H_q = A_q n_q^2 + B_q \theta_q^2 = \hbar \omega_q (\tilde{n}_q^2/2 + \tilde{\theta}_q^2/2), \quad (1)$$

where the canonically conjugated Hermitian operators n_q and θ_q are the Fourier components [15] of δn and θ and where the reduced variables are defined by $\tilde{n}_q = n_q (A_q/B_q)^{1/4}$ and $\tilde{\theta}_q = \theta_q (B_q/A_q)^{1/4}$. For wave vectors q much smaller than the inverse healing length $\xi^{-1} = \sqrt{mgn_0}/\hbar$, the excitations are of hydrodynamic nature [16]. Their frequency is $\omega_q = cq$, where the speed of sound is $c = \sqrt{n_0 \partial_n \mu/m}$, and the Hamiltonian's coefficients are $B_q = \hbar^2 q^2 n_0 / (2m)$ and $A_q = mc^2 / (2n_0)$. Here $\mu(n)$ is the equation of state of the gas relating the chemical potential μ to the linear density, which reduces to $\mu = gn$ for pure 1D quasicondensate. For a given q , the dynamics of the quenched harmonic oscillator is represented in Fig. 1. Before the quench the phase-space distribution is the one of a thermal state: an isotropic Gaussian in the $(\tilde{\theta}_q, \tilde{n}_q)$ plane. The quench affects A_q while θ_q and n_q do not have time to change. The variances thus become $\langle \tilde{\theta}_q^2 \rangle_{t=0^+} = \langle \tilde{\theta}_q^2 \rangle_{t=0^-} / (1 + \kappa)^{1/2}$ and $\langle \tilde{n}_q^2 \rangle_{t=0^+} = \langle \tilde{n}_q^2 \rangle_{t=0^-} (1 + \kappa)^{1/2}$ [17]. The subsequent evolution is a rotation in phase space at a frequency ω_q leading to a breathing of each quadrature. In particular

$$\langle \theta_q^2 \rangle = \langle \theta_q^2 \rangle_i [1 + \kappa \sin^2(cqt)], \quad (2)$$

where the initial value $\langle \theta_q^2 \rangle_i$ is the thermal prediction $\langle \theta_q^2 \rangle = mk_B T / (\hbar^2 n_0 q^2)$ [18].

Probing the nonequilibrium dynamics following a quench is not straightforward, especially concerning the choice of the observable. Since density fluctuations are very small within the quasicondensate regime, it is more advantageous to probe the phase fluctuations [19]. One way is to investigate the one-body correlation function $g_1(z) = \langle \hat{\Psi}^\dagger(z) \hat{\Psi}(0) \rangle$, which, for $z \gg \xi$ and in the quasicondensate regime, writes $g_1(z) \simeq n_0 e^{-i(\theta(z) - \theta(0))^2/2}$ [13]. However since phase fluctuations are large in a quasicondensate, the exponential cannot be linearized and $g_1(z)$ mixes contributions from all Bogoliubov modes [20], preventing the observation of the squeezed dynamics. In fact, the linearized model above predicts the light-cone effect on the g_1 function: $g_1(z)$ changes from its initial exponential decay $\exp(-|z|/l_c^i)$, where $l_c^i = 2\hbar^2 n_0 / (mk_B T)$, to an exponential decay with a new correlation length $l_c^f = 2l_c^i / (\kappa + 2)$ for $z < 2ct$. The breathing of each squeezed Bogoliubov mode is not transparent here. Moreover, for times larger than a few $t_{\text{th}}^{g_1} = l_c^f / c$, the g_1 function essentially reaches the form expected for a thermal state at a temperature $T_f = T(\kappa + 2)/2$, and the ongoing dynamics is hidden. In this paper we use the density-ripple analysis to reveal the nonequilibrium dynamics of the gas by probing the breathing of each mode.

III. RESOLVING BOGOLIUBOV MODES WITH DENSITY RIPPLES

Density ripples appear after switching the interactions off and waiting for a free evolution time t_f (time of flight), during which phase fluctuations transform into density fluctuations [21–24]. Consider the power spectrum of density ripples $\langle |\rho(q)|^2 \rangle$, where $\rho(q) = (1/\sqrt{L}) \int dz [n(z, t_f) - n_0] e^{iqz}$. Propagating the field operator during the time of flight and assuming translational invariance we obtain [25]

$$\langle |\rho_{n_0}(q)|^2 \rangle = \int dx e^{-iqx} [f(q, x) - n_0^2], \quad (3)$$

where

$$f(q, x) \simeq n_0^2 \langle e^{i[\theta(0) - \theta(-\hbar qt/m) + \theta(x - \hbar qt/m) - \theta(x)]} \rangle; \quad (4)$$

averages in Eq. (4) are taken before the time of flight. The function f involves only pairs of points separated by $\hbar qt_f/m$. For small wave vectors $q\hbar t_f/m \ll l_c$, the phase difference between those points is small and one can expand the exponential. To lowest order, assuming uncorrelated distributions for each mode q and vanishing mean values, we then find

$$\langle |\rho_{n_0}(q)|^2 \rangle = 4n_0^2 \langle \theta_q^2 \rangle \sin^2[\hbar q^2 t_f / (2m)], \quad (5)$$

showing that, for low-lying q , the density-ripple spectrum directly resolves the phase quadrature $\langle \theta_q^2 \rangle$ of individual Bogoliubov modes [26]. The proportionality between $\langle |\rho_{n_0}(q)|^2 \rangle$ and $\langle \theta_q^2 \rangle$ implies that $\langle |\rho_{n_0}(q)|^2 \rangle$ oscillates according to Eq. (2) when varying the time t after the quench. Density ripples are thus an ideal tool to investigate the quench dynamics. Note that in the following we are interested, for each wave vector q , in the evolution of $\langle |\rho_{n_0}(q)|^2 \rangle$ with the evolution time t , such that the proportionality factor $4n_0^2 \sin^2[\hbar q^2 t_f / (2m)]$ is irrelevant for our data analysis.

In typical experiments, atoms are confined by a smooth potential $V(z)$. For weak enough confinement and for wavelengths much smaller than the system's size, one can however use the above results for homogeneous systems within a local-density approximation (LDA) [27]. Then $\tilde{\rho}(q) = \int dz \delta n(z, t_f) e^{iqz}$ fulfills $\tilde{\rho}(q) \simeq \int dz \langle |\rho_{n_0(z)}(q)|^2 \rangle$ where $n_0(z)$ is the density profile, which can itself be evaluated within the LDA using the gas equation of state and the local chemical potential $\mu(z) = \mu_0 - V(z)$. Injecting Eq. (2) and Eq. (5) into the LDA integral, we find

$$\langle |\tilde{\rho}(q)|^2 \rangle / \langle |\tilde{\rho}(q)|^2 \rangle_i = 1 + \kappa \mathcal{F}(cqt), \quad (6)$$

where c is the speed of sound after the quench evaluated at the trap center and \mathcal{F} only depends on the shape of $V(z)$. For a boxlike potential, one recovers previous results and $\mathcal{F}(\tau) = \sin^2(\tau)$. The expression of \mathcal{F} is given in Appendix D in the case of a harmonic potential: The oscillatory behavior is preserved, although the spread in frequencies originating from the inhomogeneity in n_0 introduces damping, which is a pure dephasing effect.

IV. EXPERIMENTAL REALIZATION

The experiment uses an atom-chip setup [28] where ^{87}Rb atoms are magnetically confined using current-carrying microwires. The transverse confinement, acting in a vertical

plane, is provided by three parallel wires carrying ac current modulated at 400 kHz, which renders the magnetic potential insensitive to wire imperfections and allows for independent control of the transverse and longitudinal confinements. We perform radio frequency (rf) forced evaporative cooling until we reach the desired temperature. We then increase the rf frequency by 60 kHz, providing a shield for energetic three-body collision residues and wait during 150 ms relaxation time. The clouds contain a few thousand atoms, in a trap with a transverse frequency $\omega_{\perp}/2\pi = 1.5$ or 3.1 kHz, depending on the data set, and a longitudinal frequency $\omega_{\parallel}/2\pi = 8.5$ Hz. The samples are quasi-1D, the temperature and chemical potential satisfying $\mu, k_B T < \hbar\omega_{\perp}$. The temperature is low enough so that the gas typically lies well within the quasicondensate regime [29]. The equation of state is well described by $\mu = \hbar\omega_{\perp}(\sqrt{1+4na} - 1)$, where $a = 5.3$ nm is the 3D scattering length [30]. While, for $na \ll 1$, one recovers the pure 1D expression $\mu = gn$, where $g = 2\hbar\omega_{\perp}a$, this equation of state takes the broadening of the transverse size at larger na into account. The longitudinal density profile, well described by the LDA, extends over twice the Thomas-Fermi radius $R_{TF} = \sqrt{2\mu_0/m}/\omega_{\parallel}$. The speed of sound derived from the equation of state is $c = c_{1D}/(1+4na)^{1/4}$ where $c_{1D} = \sqrt{2\hbar\omega_{\perp}na/m}$ is the pure 1D expression. For data presented in this paper, c/c_{1D} is close to 0.7. Since the effective interaction strength is proportional to c^2 , it is proportional to ω_{\perp} .

The interaction strength quench is performed by ramping the transverse trapping frequency ω_{\perp} from its initial value $\omega_{\perp,i}$ to its final value $\omega_{\perp,f} = (1+\kappa)\omega_{\perp,i}$ within a time t_r , typically of the order of 1 ms. This time is long enough for the transverse motion of the atoms to follow adiabatically but short enough so that the quench can be considered as almost instantaneous with respect to the probed longitudinal excitations (see Appendix H 1). We simultaneously multiply ω_{\parallel} by $\sqrt{1+\kappa}$, to avoid modification of the mean profile and of the Bogoliubov wave functions (see Appendix E).

In order to probe density ripples, we release the atoms from the trap and let them fall under gravity for a time $t_f = 8$ ms before taking an absorption image. The transverse expansion, occurring on a time scale of $1/\omega_{\perp}$, ensures the effective instantaneous switching off of the interactions with respect to the probed longitudinal excitations. The density ripples produced by the phase fluctuations present before the free fall are visible in each individual image, as seen in Fig. 2(a). From the image, we record the longitudinal density profile $\rho(z, t_f)$ and its discrete Fourier transform [31] $\tilde{\rho}(q)$. We acquire about 40 images taken in the same conditions with atom number fluctuations smaller than 10%. From this data set, we then extract the power spectrum $\langle |\tilde{\rho}(q)|^2 \rangle$. The power spectrum obtained before the quench is noted $\langle |\tilde{\rho}(q)|^2 \rangle_i$, and a typical spectrum is shown in Fig. 2(b). We chose to normalize the momenta by R_{TF}^{-1} : since the Fourier distribution of the i th Bogoliubov mode of a 1D quasicondensate is peaked at $k_i \simeq i/R_{TF}$ (see Appendix E), the x axis roughly corresponds to the mode index. The predicted power spectrum $\langle |\tilde{\rho}(q)|^2 \rangle_{th}$ is computed using the LDA and analytical solution of Eq. (3) for thermal equilibrium (see Appendixes B and C). This expression is peaked around $kR_{TF} \simeq \sqrt{\pi m/(\hbar t_f)} R_{TF} \simeq 50$. For comparison with experimental data, we take the imaging resolution into account by multiplying $\langle |\tilde{\rho}(q)|^2 \rangle_{th}$ with $e^{-k^2\sigma^2/2}$

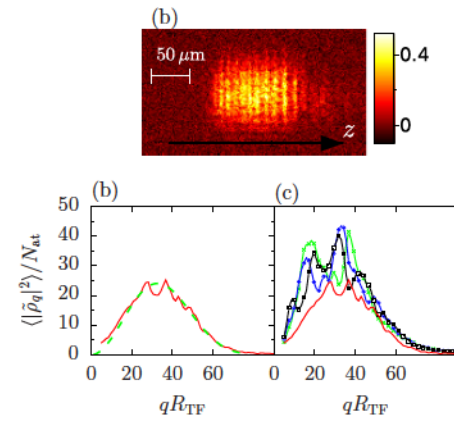


FIG. 2. Density ripples analysis. (a) Typical absorption image (optical density shown) taken after a time of flight $t_f = 8$ ms. (b) Power spectrum of density ripples, obtained by averaging over about 50 images, for a cloud at thermal equilibrium containing 16000 atoms confined in a trap with frequencies $\omega_z/(2\pi) = 8.5$ Hz and $\omega_{\perp}/(2\pi) = 1.5$ kHz, yielding a Thomas-Fermi radius $R_{TF} = 75$ μm. The dashed (green) line is a theoretical fit (see text), yielding a temperature $T = 55$ nK and an optical resolution $\sigma = 2.9$ μm. (c) Power spectra after a quench of strength $\kappa = 2$, at times $t = 2.1$ ms (crosses, green), $t = 2.6$ ms (circles, blue) and $t = 4.6$ ms (squares, black), the solid (red) curve being the initial power spectrum.

where σ is the rms width of the impulse imaging response function, assumed to be Gaussian (Appendix F discusses the effect of this finite optical resolution). The experimental data ultimately compared well with the theoretical predictions, as shown in Fig. 2(b), where T and σ are obtained by fitting the data [32,33]. Finally we obtain $k_B T/\mu_0 = 0.4$, close to the lowest value obtained in similar setups [24,34].

We investigate the dynamics following the quench of the interaction strength by acquiring power spectra of density ripples at different evolution times t after the quench. We typically acquire power spectra every 0.5 ms, over a total time of 5 ms. A few raw spectra are shown in Fig. 2(b), for a quench strength $\kappa = 2.0$. At first sight the power spectra seem erratic. In order to reveal the expected oscillatory behavior of each Fourier component we introduce, for each wave vector q of the discrete Fourier transform, and each measurement time t , the reduced time $\tau = cqt$, where c is evaluated for the central density, and compute $J(q, \tau) = \langle |\tilde{\rho}(q)|^2 \rangle(t) / \langle |\tilde{\rho}(q)|^2 \rangle_i$. We restrict the range of q values to $10 < qR_{TF} < 40$, to ensure both the condition $q\hbar t_f/m \ll l_c$ and the validity of the LDA. On the resulting set of sparse data, shown in the inset of Fig. 3, an oscillatory behavior appears, despite noise on the data. To combine all the data in a single graph, we perform a “smooth” binning in τ , i.e., we compute, for any given reduced time τ , the weighted averaged of the data with a Gaussian weight function in τ of width $\Delta = 0.31$: namely we compute $\bar{J}(\tau) = \sum_{\alpha} J(q_{\alpha}, \tau_{\alpha}) e^{-(\tau_{\alpha}-\tau)^2/(2\Delta^2)} / \sum_{\alpha} e^{-(\tau_{\alpha}-\tau)^2/(2\Delta^2)}$, where the sum is done on the data set. The function $\bar{J}(\tau)$, shown in Fig. 3, shows a clear oscillatory behavior.

We repeat the experiment for different quench strengths $\kappa = (\omega_{\perp,f}/\omega_{\perp,i} - 1) = \{0.3, 3, 5\}$, and initial trapping oscillation frequencies $\omega_{\perp} = \{3, 1.5\}$ kHz. The oscillatory behavior is present in all cases as shown in Fig. 3. We compared

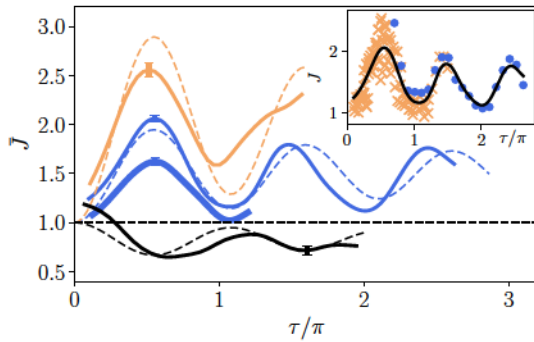


FIG. 3. Time evolution of squeezed collective modes produced by an interaction quench. The normalized density-ripple power spectrum is plotted vs the reduced time $\tau = cqt$, where the speed of sound c is calculated for the central density. Inset shows the data corresponding to each measurement time and discrete q values, for a data set corresponding to $\kappa = 2$ and $\omega_{\perp,i} = 2\pi \times 1.5$ kHz, together with the resulting continuous averaged quantity \bar{J} (see text). Orange crosses correspond to $t < t_{\text{th}}^{g_1}$ and blue circles to $t > t_{\text{th}}^{g_1}$. The main graph shows the evolution of the experimental smoothed quantity \bar{J} for different data sets. The error bars show the typical statistical uncertainty on \bar{J} . The initial transverse oscillation frequency is 1.5 kHz, except for the thick dark grey (blue) curve for which it is 3 kHz. Quench strengths are $\kappa = 4$ [light gray (orange)], $\kappa = 2$ [dark gray (blue)] data, and $\kappa = -0.7$ (black). Dashed lines are theoretical predictions for quench strengths $\kappa = 2$ [light gray (orange)], 1 (light gray), and -0.35 (black).

the observed oscillations with the theoretical predictions from the linearized model, Eq. (6). The temporal behavior of the data is in good agreement with the predicted one: both the frequency and the observed damping are in agreement with the predictions. The amplitude of the experimental oscillations on the other hand are significantly smaller than the predictions, and in Fig. 3 we plot the theoretical predictions for quench strengths twice as small as the experimental ones. Moreover, for a given quench strength, the observed amplitude depends on the initial transverse frequency, in contradiction with the theoretical model. Several effects leading to a decrease of the oscillation amplitude are discussed in Appendix H. However, they only partially account for the observed amplitude reduction.

V. DISCUSSION

In conclusion, analyzing density ripples, we revealed the physics at play after a sudden quench of the interaction strength in a quasi-1D Bose gas, namely the breathing associated to the squeezing of each collective mode. The observed out-of-equilibrium dynamics continues for times larger than $t_{\text{th}}^{g_1}$, for which the g_1 function essentially reached its asymptotic thermal behavior [35]. This can be seen in the inset of Fig. 3 where data corresponding to $t > t_{\text{th}}^{g_1}$, shown as blue circles, still present an oscillatory behavior. This clearly underlines the power of the density-ripple analysis to unveil out-of-equilibrium physics. The observed damping is compatible with the sole dephasing effect due to the longitudinal harmonic confinement. At later times, the discreteness of the spectrum and its almost constant level spacing is expected to

produce a revival phenomenon. Its observation might however be hindered by a damping of each collective mode due to non-linear couplings. Such a damping occurs, despite the integrability of the 1D Bose gas with contact repulsive interactions, because the Bogoliubov collective modes do not correspond to the conserved quantities. A long-lived nonthermal nature of the state produced by the interaction strength might be revealed either by observing excitations in both the phononic regime and the particle regime of the Bogoliubov spectrum [36], or, ideally, in finding a way to access the distribution of the Bethe-ansatz rapidities.

ACKNOWLEDGMENTS

This work was supported by Région Île de France (DIM NanoK, Atocirc project). The authors thank Dr. S. Bouchoule of C2N (Centre Nanosciences et Nanotechnologies, CNRS/UPSUD, Marcoussis, France) for the development and microfabrication of the atom chip. A. Durnez and A. Harouri of C2N are acknowledged for their technical support. C2N laboratory is a member of RENATECH, the French national network of large facilities for micronanotechnology. M.S. acknowledges support by the Studienstiftung des Deutschen Volkes.

APPENDIXES

These appendixes gives technical information and details of calculations. In Appendix A we give a general derivation of the density-ripple power spectrum, which does not *a priori* assume a homogeneous system. Appendix B gives the result for a homogeneous system and the analytical prediction for thermal equilibrium [37]. Appendix C details the derivation of the density-ripple power spectrum for a trapped gas, computed using the results for homogeneous gases and the local-density approximation. Appendix D provides the explicit calculation of the postquench evolution of the power spectrum for a harmonically trapped gas, namely the calculation of the function \mathcal{F} of the main text. In Appendix E we verify the validity of the local-density approximation for the parameters of the data presented in the main text. For this purpose, we compute the density-ripple power spectrum using the Bogoliubov modes of the trapped gas. In Appendix F, we investigate the effect of finite resolution on the measured density-ripple power spectrum. We also make the link between the power spectrum and the autocorrelation function, which permits us to compare our data at thermal equilibrium with previously published work. In Appendix G, we justify that interactions play a negligible role during time of flight, so that the calculations of the density-ripple power spectrum, which assume instantaneous switch-off of the interactions, are valid. In Appendix H, we investigate two effects responsible for a reduction of the oscillation amplitude of the quantity $\bar{J}(\tau)$, extracted from the data, as compared to the simple theoretical predictions Eq. (6) of the main text: First the finite ramp time of the interaction strength decreases the squeezing of the collective modes, and second the finite resolution in τ resulting from data binning is responsible for a decrease of the expected oscillation amplitude on the processed data.

APPENDIX A: DERIVATION OF THE DENSITY-RIPPLE POWER SPECTRUM

The power spectrum of density ripples has been first investigated in the limit of small density ripples and for a gas initially in the 3D Thomas-Fermi regime (i.e., $\mu \gg \hbar\omega_{\perp}$) [22,38]. It was then computed assuming instantaneous switching off of the interactions in [21]. Here, for consistency, we rederive Eqs. (4) and (5) of the main text. Since we will later consider trapped gases, let us first assume a general scenario where we do not restrict ourselves to the homogeneous case. We let the gas evolve freely for a time t_f after interactions have been switched off. The power spectrum of the density fluctuations after t_f writes

$$\langle |\tilde{\rho}(q)|^2 \rangle = \iint dz_1 dz_2 e^{iq(z_1 - z_2)} \langle \delta n(z_1, t_f) \delta n(z_2, t_f) \rangle. \quad (\text{A1})$$

Writing $\delta n(z) = n(z) - \langle n(z) \rangle$ and expanding the above equation, the term $|\int dz e^{iqz} \langle n(z, t_f) \rangle|^2$ appears. Here we

consider times of flight short enough so that the shape of the cloud barely changes during time of flight, so that $\langle n(z, t_f) \rangle \simeq \langle n(z, 0) \rangle$. We moreover consider wave vectors q much larger than the inverse of the cloud length, such that $|\int dz e^{iqz} \langle n(z, 0) \rangle|^2$ is a negligible quantity. We then have

$$\langle |\tilde{\rho}(q)|^2 \rangle \simeq \iint dz_1 dz_2 e^{iq(z_1 - z_2)} \langle n(z_1, t_f) n(z_2, t_f) \rangle. \quad (\text{A2})$$

To compute $n(z, t_f) = \Psi^\dagger(z, t_f) \Psi(z, t_f)$ we evolve the atomic field with the free-particle propagator, which leads to

$$\psi(z, t_f) = \frac{1}{\sqrt{2\pi t_f}} \int d\alpha \psi(\alpha, 0) e^{i[(z-\alpha)^2/2t_f]}, \quad (\text{A3})$$

where for simplicity we use a unit system in which $m = \hbar = 1$. We then have

$$\langle n(z_1, t_f) n(z_2, t_f) \rangle = \frac{1}{(2\pi t_f)^2} \iiint d\alpha d\beta d\gamma d\delta \langle \psi_\alpha^\dagger \psi_\beta \psi_\gamma^\dagger \psi_\delta \rangle e^{-i[(z_1-\alpha)^2/2t_f]} e^{i[(z_1-\beta)^2/2t_f]} e^{-i[(z_2-\gamma)^2/2t_f]} e^{i[(z_2-\delta)^2/2t_f]}, \quad (\text{A4})$$

where we use the simplified notation $\psi_v = \psi(v, 0)$. Expanding the exponentials, the above expression writes

$$\langle n(z_1, t_f) n(z_2, t_f) \rangle = \frac{1}{(2\pi t_f)^2} \iiint d\alpha d\beta d\gamma d\delta \langle \psi_\alpha^\dagger \psi_\beta \psi_\gamma^\dagger \psi_\delta \rangle e^{i[(\alpha-\beta)z_1/t_f]} e^{i[(\beta^2-\alpha^2)/2t_f]} e^{i[(\gamma-\delta)z_2/t_f]} e^{i[(\delta^2-\gamma^2)/2t_f]}. \quad (\text{A5})$$

Injecting into Eq. (A2), and using $\int dz e^{ikz} = 2\pi \delta(k)$ and $\delta(x/\alpha) = \alpha \delta(x)$, we get

$$\langle |\tilde{\rho}(q)|^2 \rangle = \iint d\alpha d\delta \langle \psi_\alpha^\dagger \psi_{\alpha+qt_f} \psi_{\delta+qt_f}^\dagger \psi_\delta \rangle e^{-i[\alpha^2/2t_f]} e^{i[(\alpha+qt_f)^2/2t_f]} e^{-i[(\delta+qt_f)^2/2t_f]} e^{i[\delta^2/2t_f]}. \quad (\text{A6})$$

Defining $\delta = \alpha + X$, we obtain

$$\langle |\tilde{\rho}(q)|^2 \rangle = \iint d\alpha dX e^{iqX} \langle \psi_\alpha^\dagger \psi_{\alpha+qt_f} \psi_{\alpha+X+qt_f}^\dagger \psi_{\alpha+X} \rangle. \quad (\text{A7})$$

For gases lying deep in the quasicondensate regime, one can neglect density fluctuations when estimating the expectation value in the above equation, such that

$$\langle |\tilde{\rho}(q)|^2 \rangle \simeq \iint d\alpha dX e^{iqX} \sqrt{n(\alpha) n(\alpha + qt_f) n(\alpha + X + qt_f) n(\alpha + X)} \langle e^{i(\theta(\alpha) - \theta(\alpha + qt_f) + \theta(\alpha + X + qt_f) - \theta(\alpha + X))} \rangle. \quad (\text{A8})$$

The following section applies this result to homogeneous systems. This equation is however not restricted to homogeneous systems and we will use it to treat the effect of the trap beyond the local-density approximation.

APPENDIX B: POWER SPECTRUM OF THE DENSITY RIPPLES FOR A HOMOGENEOUS GAS

For a homogeneous gas, the relevant quantity is an intensive variable which relates to the expression $\langle |\tilde{\rho}(q)|^2 \rangle$ of the previous section by

$$\langle |\rho(q)|^2 \rangle = \frac{1}{L} \langle |\tilde{\rho}(q)|^2 \rangle, \quad (\text{B1})$$

where L is the length of the box. Injecting Eq. (A8) into Eq. (B1), we recover Eqs. (3) and (4) of the main text, up to an irrelevant term in $\delta(q)$ [39]. In fact, Wick's theorem is applicable since θ is a Gaussian variable [40], which leads to

$$\frac{\langle |\rho(q)|^2 \rangle}{n_0^2} = \int dX e^{iqX - (1/2)[(\theta(0) - \theta(qt_f) + \theta(X + qt_f) - \theta(X))^2]}. \quad (\text{B2})$$

To compute the power spectrum of density ripples for a thermal equilibrium state, we follow the calculation made in [21] and expand the exponential term in Eq. (B2) as a function of the first-order correlation function $g^{(1)}(z) = n_0 e^{-(1/2)[(\theta(0) - \theta(z))^2]}$, which fulfils $g^{(1)}(z) = n_0 e^{-|z|/l_c}$ where $l_c = 2\hbar^2 n_0 / (k_B T)$ [21]. Calculation of the integral in Eq. (B2) then leads to

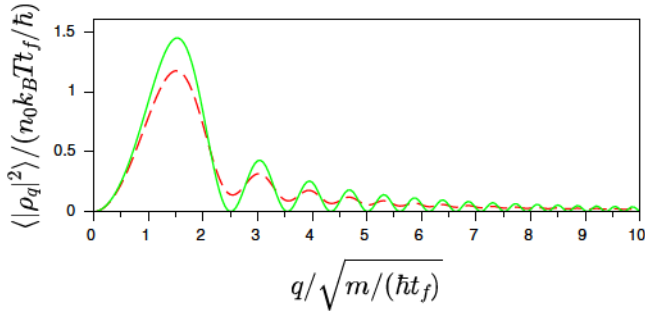


FIG. 4. Density ripples power spectrum for a homogeneous gas. The exact formula Eq. (B3) (dashed curve) is compared to the small q approximation given Eq. (5) of the main text, where $\langle |\rho(q)|^2 \rangle$ is proportional to $\langle \theta_q^2 \rangle$ (solid curve). The only relevant parameter is $\hbar t_f / (m l_c^2)$. Results are shown for $\hbar t_f / (m l_c^2) = 0.05$, a value corresponding to the data depicted in Fig. 2(b) of the main text, the correlation length $l_c = 2\hbar^2 n_0 / (m k_B T)$ being computed for the central density. The effect of the imaging resolution is to multiply this theoretical power spectrum with $e^{-\sigma^2 q^2}$, where σ is the rms width of the imaging pulse response function, assumed to be Gaussian. For our data, $\sigma \sqrt{m / (\hbar t_f)} = 0.85$ and only the first maximum of $\langle |\rho(q)|^2 \rangle$ remains visible.

$$\frac{\langle |\rho(q)|^2 \rangle}{n_0^2} = \frac{4q l_c}{q(4 + l_c^2 q^2)} - \frac{4e^{-2\hbar q t_f / m l_c} (q l_c \cos(\frac{\hbar q^2 t_f}{m}) + 2 \sin(\frac{\hbar q^2 t_f}{m}))}{q(4 + l_c^2 q^2)}. \quad (\text{B3})$$

Note that we corrected the formula given in [21]. The power spectrum computed with this equation is compared in Fig. 4 to the approximated formula valid for small q , namely Eq. (5) of the main text.

APPENDIX C: DENSITY RIPPLE POWER SPECTRUM FOR A HARMONICALLY CONFINED GAS UNDER THE LDA

Let us investigate the density-ripple power spectrum in the case of a gas trapped in a longitudinal potential smooth enough so that the cloud size L is much larger than the typical phase correlation length l_c and much larger than $\hbar q t_f / m$: $L \gg l_c, \hbar q t_f / m$. As in Appendix A, we moreover consider the power spectrum for wave vectors $q \gg 1/L$. Let us start with the general expression Eq. (A1) that we write

$$\langle |\bar{\rho}(q)|^2 \rangle = \int dz \int du \langle \delta\rho(z, t_f) \delta\rho(z + u, t_f) \rangle e^{iqu}. \quad (\text{C1})$$

Consider $\langle \delta\rho(z, t_f) \delta\rho(z + u, t_f) \rangle$ for a given z . This expression vanishes over a length much smaller than L , so values of u significantly contributing to the integral are much smaller than L . Moreover the region of the initial cloud contributing most to $\langle \delta\rho(z, t_f) \delta\rho(z + u, t_f) \rangle$ is much smaller than L for sufficiently large L . Then, to compute $\langle \delta\rho(z, t_f) \delta\rho(z + u, t_f) \rangle$ one can perform a local density approximation and use the result of a homogeneous gas at a density $n_0(z)$. We then obtain

$$\langle |\bar{\rho}(q)|^2 \rangle = \int dz \langle |\rho_{n_0(z)}(q)|^2 \rangle, \quad (\text{C2})$$

where the subscript $n_0(z)$ specifies that one considers the result for a homogeneous gas of density $n_0(z)$. This expression is referred to as the local-density approximation expression (LDA) of the power spectrum. We have tested this approximation, for conditions close to the experimental data presented in the main text, by comparing it with calculations based on the Bogoliubov excitations of the trapped system (see Appendix E).

APPENDIX D: TIME EVOLUTION OF THE DENSITY-RIPPLE POWER SPECTRUM FOR A HARMONICALLY CONFINED GAS

Here we give an explicit derivation of Eq. (6) of the main text, for a gas harmonically confined in a longitudinal trap of frequency ω_{\parallel} . Injecting Eqs. (5) and (2) of the main text into Eq. (C2), and using the local initial power spectrum of θ which writes $\langle \theta_q^2 \rangle = m k_B T / (\hbar^2 n_0 q^2)$, we derive Eq. (6) of the main text with

$$\mathcal{F} = \int dz n_0(z) \sin^2[c(z)qt] / N, \quad (\text{D1})$$

where N is the total atom number. The density profile $n_0(z)$ is estimated itself within the LDA, using the local chemical potential

$$\mu(z) = \mu_p [1 - (z/R_{\text{TF}})^2], \quad (\text{D2})$$

where R_{TF} is the Thomas-Fermi radius of the density profile and μ_p is the chemical potential at the trap center. For a transverse harmonic confinement of frequency ω_{\perp} , it has been checked, by comparing with predictions of the 3D Gross-Pitaevskii equation, that the equation of state of the gas is very well described by the heuristic formula [30]

$$\mu(n) = \hbar\omega_{\perp} (\sqrt{1 + 4na} - 1), \quad (\text{D3})$$

where a is the 3D scattering length between atoms. For small linear densities, we recover the 1D expression $\mu = 2\hbar\omega_{\perp} a n$, valid far from the confinement-induced resonance [41]. Using Eqs. (D3) and (D2), we obtain the density profile

$$n_0(z) = [(\eta(1 - \bar{z}^2) + 1)^2 - 1] / (4a), \quad (\text{D4})$$

where we introduced $\bar{z} = z/R_{\text{TF}}$ and $\eta = \mu_p / (\hbar\omega_{\perp})$. This yields $N = (4/3\eta + 8\eta^2/15)R_{\text{TF}}/(2a)$. The local speed of sound on the other hand, obtained from the thermodynamic relation $c = \sqrt{n(\partial\mu/\partial n)/m}$, writes

$$c(z) = c_p \sqrt{\frac{(1 + \eta)\{[1 + \eta(1 - \bar{z}^2)]^2 - 1\}}{[1 + \eta(1 - \bar{z}^2)][(1 + \eta)^2 - 1]}}, \quad (\text{D5})$$

where c_p is the speed of sound computed for the central density. Injecting into Eq. (D1), we then find

$$\mathcal{F} = \frac{1}{4\eta/3 + 8\eta^2/15} \int_0^1 d\bar{z} \{ [1 + \eta(1 - \bar{z}^2)]^2 - 1 \} \times \sin^2 \left(\tau \sqrt{\frac{(1 + \eta)\{[1 + \eta(1 - \bar{z}^2)]^2 - 1\}}{[1 + \eta(1 - \bar{z}^2)][(1 + \eta)^2 - 1]}} \right). \quad (\text{D6})$$

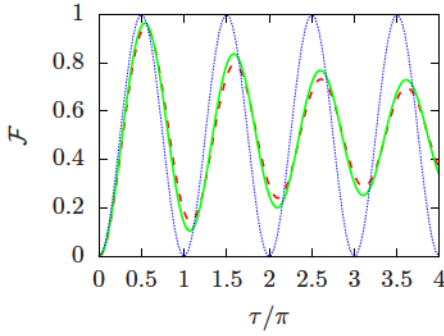


FIG. 5. Oscillation of each spectral component of the power spectrum for a harmonically confined gas in the LDA. The function \mathcal{F} is shown as thick solid lines (green), for $\eta = \mu_p/(\hbar\omega_\perp) = 1.0$. The pure 1D limit, corresponding to $\eta \ll 1$ is shown as dashed (red) lines. The undamped oscillations expected for a homogeneous gas are shown as dotted (blue) line. In all the cases, $\tau = cqt$ where c is the central sound velocity.

When the gas is deeply 1D, namely for $\eta \ll 1$, this expression reduces to

$$\mathcal{F}_{1D} = \frac{3}{2} \int_0^1 d\tilde{z} (1 - \tilde{z}^2) \sin^2(\tau\sqrt{1 - \tilde{z}^2}). \quad (\text{D7})$$

Experimentally, values of η are in the range [0.6; 1.3]. Figure 5 shows the function \mathcal{F} , computed for $\eta = 1$. We compare it to \mathcal{F}_{1D} and to the expression expected for a homogeneous gas, namely $\sin^2(\tau)$.

APPENDIX E: BEYOND THE LDA: CALCULATION USING BOGOLIUBOV MODES OF A HARMONICALLY CONFINED 1D GAS

Here we consider a 1D gas confined longitudinally in a harmonic trap of frequency ω_\parallel . In opposition to the calculations done in the previous appendix we do not rely on the local-density approximation but use the Bogoliubov modes of the trapped gas to compute the postquench evolution and the density-ripple power spectrum. The relevant collective modes lie deep in the phononic regime. The Bogoliubov modes, indexed by an integer ν , then acquire an analytical dispersion relation and analytical wave functions that one can use for calculations. For each mode, the dynamics are accounted for

by the harmonic oscillator Hamiltonian

$$H_\nu = \hbar\omega_\nu \left(\frac{x_\nu^2}{2} + \frac{p_\nu^2}{2} \right), \quad (\text{E1})$$

where $\omega_\nu = \omega_\parallel \sqrt{\nu(\nu+1)}/2$ and x_ν and p_ν are canonically conjugate variables. The phase and density fluctuation operators write

$$\begin{cases} \theta(z) = \sum_\nu \theta_\nu(z) p_\nu \\ \delta n(z) = \sum_\nu n_\nu(z) x_\nu \end{cases}, \quad (\text{E2})$$

where

$$\begin{cases} \theta_\nu(z) = \frac{1}{\sqrt{2}} \left(\frac{mg}{\hbar^2 n_p} \right)^{1/4} \frac{\sqrt{2\nu+1}}{[\nu(\nu+1)]^{1/4}} P_\nu \left(\frac{z}{R_{\text{TF}}} \right) \\ n_\nu(z) = \frac{\sqrt{2\nu+1}}{2R_{\text{TF}}} [\nu(\nu+1)]^{1/4} \left(\frac{\hbar^2 n_p}{mg} \right)^{1/4} P_\nu \left(\frac{z}{R_{\text{TF}}} \right) \end{cases}. \quad (\text{E3})$$

Here n_p and R_{TF} are the central density and radius of the Thomas-Fermi profile $n_0(z) = n_p [1 - (z/R_{\text{TF}})^2]$ and P_ν are the Legendre polynomials. The interaction quench consists of a sudden change of the interaction parameter g from g_i to $g_f = (1 + \kappa)g_i$ at $t = 0$, while changing the longitudinal oscillation frequency by a factor $\sqrt{1 + \kappa}$ so that R_{TF} stays constant. Then the interaction quench preserves the shapes of the wave functions θ_ν and n_ν , and it simply changes the canonical variables x_ν and p_ν according to

$$\begin{cases} x_\nu(t = 0^+) = (g_f/g_i)^{1/4} x_\nu(t = 0^-) \\ p_\nu(t = 0^+) = (g_i/g_f)^{1/4} p_\nu(t = 0^-) \end{cases}. \quad (\text{E4})$$

Under such a transformation, the initial thermal state, an isotropic Gaussian, becomes a squeezed state and its subsequent evolution under the Hamiltonian Eq. (E1) leads to a breathing of each quadrature. In particular

$$\langle p_\nu^2 \rangle = \langle p_\nu^2 \rangle_i [1 + \kappa \sin^2(\omega_\nu t)]. \quad (\text{E5})$$

The initial value $\langle p_\nu^2 \rangle_i$ is given by the thermal expectation value, which reduces to

$$\langle p_\nu^2 \rangle_i = k_B T / (\hbar\omega_\nu) \quad (\text{E6})$$

for the low-lying modes for which $k_B T \gg \hbar\omega_\nu$.

Injecting Eq. (E2) into Eq. (A8), using Wick's theorem and the fact that different modes are uncorrelated, we get

$$\langle |\tilde{\rho}(q)|^2 \rangle = \iint d\alpha dX e^{iqX} \sqrt{n_0(\alpha)n_0(\alpha + qt_f)n_0(\alpha + X + qt_f)n_0(\alpha + X)} e^{-(1/2) \sum_\nu \langle p_\nu^2 \rangle_i [\theta_\nu(\alpha) - \theta_\nu(\alpha + qt_f) + \theta_\nu(\alpha + X + qt_f) - \theta_\nu(\alpha + X)]^2}. \quad (\text{E7})$$

For $\hbar qt_f/m \ll l_c$, where l_c is the phase correlation length, one can expand the exponential and $\langle |\tilde{\rho}(q)|^2 \rangle$ is obtained by summing the contribution of each mode. Since the Legendre polynomials behave as $\cos[(\nu + 1/2)x + \pi/4]$ at small x , the contribution of the mode ν is peaked at $q \simeq \nu/R_{\text{TF}}$.

The predictions of Eq. (E7) may be compared to the one obtained within the local-density approximation.

Here we focus on the case of thermal equilibrium. We compute the density-ripple spectrum injecting the thermal equilibrium value Eq. (E6) and the mode wave function Eq. (E3) into Eq. (E7). Figure 6 shows the result for a cloud whose Thomas-Fermi radius fulfills $l_c/R_{\text{TF}} = 0.2$, where $l_c = 2\hbar^2 n_p / (mk_B T)$ is the correlation length of the first-order correlation function at the center of the cloud, and for a time of flight $t_f = 6 \times 10^{-4} m R_{\text{TF}}^2 / \hbar$. These parameters are close

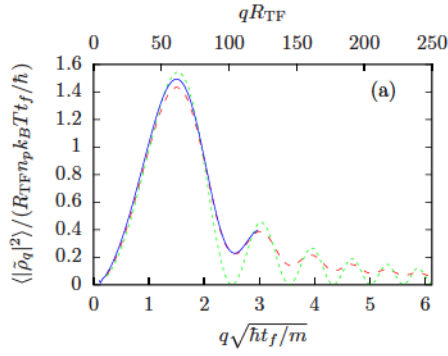


FIG. 6. Test of the local-density approximation (LDA). The plot shows the density-ripple spectrum of a gas at thermal equilibrium confined in a harmonic potential. The complete calculation, based on the expansion on the Bogoliubov modes, whose wave functions are given by the Legendre polynomial, is shown as solid line (blue). It is in excellent agreement with the spectrum computed within the local-density approximation (LDA) shown as dashed line (red). The further approximation of small wave vectors, Eq. (5) of the main text, injected into the LDA, shown as dotted line (green), is also in good agreement, for wave vectors fulfilling $qR_{\text{TF}} < 50$. Calculations are done for a Thomas-Fermi radius $l_c/R_{\text{TF}} = 0.2$ and time-of-flight $t_f = 0.015m_l^2/\hbar$, where $l_c = 2\hbar^2 n_p / (mk_B T)$ is the correlation length at the center of the cloud. These parameters are close to those of the experimental data.

to the experimental ones. We compared the results with the LDA together with the analytical formula for homogeneous gases Eq. (B3) and we find excellent agreement. We also compare with the LDA but using, instead of Eq. (B3), the approximation Eq. (5) of the main text. We find very good agreement as long as $qR_{\text{TF}} < 50$.

APPENDIX F: EFFECT OF A FINITE OPTICAL RESOLUTION AND AUTOCORRELATION FUNCTION

The effect of the imaging resolution is to multiply the theoretical power spectrum of density ripples with $e^{-\sigma^2 q^2}$, where σ is the rms width of the imaging pulse response function, assumed to be Gaussian. The resulting power spectrum, for a harmonically confined cloud at thermal equilibrium, is shown in Fig. 7 for $\sigma\sqrt{m/(\hbar t_f)} = 0.85$, a value typical for our experiments. The large q behavior of the power spectrum is highly dominated by the effect of resolution and only the first maximum of $\langle |\rho(q)|^2 \rangle$ remains visible. Fitting the experimental power spectrums for clouds at thermal equilibrium, we extract both the temperature and the imaging resolution (see Fig. 2 of the main text). The obtained rms widths σ , close to $3\ \mu\text{m}$, are compatible with the expected values if one takes into account the depth of focus of our imaging system ($\simeq 5\ \mu\text{m}$) and the fact that after the expansion time t_f the cloud explores several tens of μm along the imaging axis. Note finally that the imaging resolution is irrelevant for the investigation of the dynamics following an interaction quench, since, for each Fourier component q , we investigate the time behavior of the normalized quantity $\langle |\tilde{\rho}(q)|^2 \rangle(t) / \langle |\tilde{\rho}(q)|^2 \rangle_i$ (see main text): the imaging resolution has no effect on this normalized quantity.

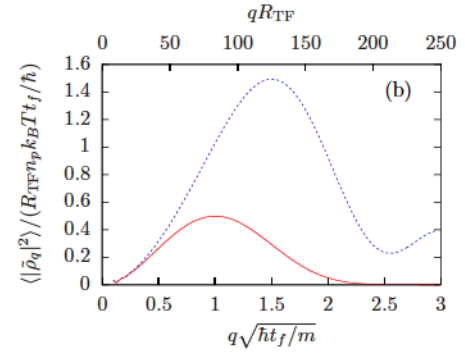


FIG. 7. Effect of the finite resolution. We consider a cloud at thermal equilibrium in a harmonic potential with the same parameters as in Fig. 6. The power spectrum for infinite resolution (blue dashed curve) is compared to the power spectrum expected for a finite imaging resolution (red solid curve). The effect of the imaging resolution is to multiply the power spectrum with $e^{-\sigma^2 q^2}$, where σ is the rms width of the imaging pulse response function, assumed to be Gaussian. Here we took $\sigma\sqrt{m/(\hbar t_f)} = 0.85$, a value close to that of experimental data.

In our paper, we extract from the data the density-ripple power spectrum since it is the relevant quantity that enables us to resolve the collective Bogoliubov modes. Alternatively, one could consider the autocorrelation function of the density ripples $C(u) = \int dz \langle \delta n(z) \delta n(z+u) \rangle dz$, which is the Fourier transform of the density-ripple power spectrum: $C(u) = 1/(2\pi) \int dq \langle |\tilde{\rho}(q)|^2 \rangle e^{-iqu}$. In [23], the authors introduced the normalized autocorrelation function $g_2(u) = 1 + C(u) / \int du \langle n(z) \rangle \langle n(z+u) \rangle$. Figure 8 shows $g_2(u)$ for the data at thermal equilibrium (before the quench) shown in Fig. 2 of the main text. A behavior very similar to that observed in [23] is recovered.

APPENDIX G: BEYOND INSTANTANEOUS INTERACTION SWITCH OFF: FINITE TRANSVERSE EXPANSION TIME

In the data presented in the main text, the frequency of the probed longitudinal modes, of the order of cq , is no more than

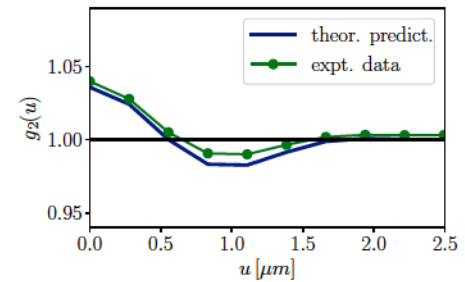


FIG. 8. Normalized autocorrelation function of the density ripples. The data set used is the same as that of Fig. 2(b) of the main text. Experimental data are shown in green and the theoretical prediction for a cloud at a temperature $T = 55\ \text{nK}$ and an optical resolution $\sigma = 2.9\ \mu\text{m}$ is shown in blue.

$0.15 \times \omega_{\perp}$. Then, due to the rapid transverse expansion, interactions during time of flight become almost instantaneously negligible and are expected to give only minor corrections to the density-ripple spectrum computed for an instantaneous switching off of the interactions. It is nevertheless interesting to estimate their effect. This has already been computed in [38], in the limit $\mu \gg \hbar\omega_{\perp}$ and using time-dependent Bogoliubov equations, i.e., equations of motion linearized in density fluctuations and phase gradient. The linearized calculations *a priori* require that density fluctuations stay small. Although in our case density ripples at the end of the time of flight have large amplitudes, the Bogoliubov calculations hold for the small q components, which fulfill $q \ll ml_c/(\hbar t_f)$ and which are considered in our paper. The condition $\mu \gg \hbar\omega_{\perp}$ on the other hand is not verified for the data shown in the main text. We nevertheless believe that the calculations of [38] give a relevant estimation of the effect of interactions during the time of flight for our data. From results of [38], we find that the density-ripple power spectrum for the small q wave vectors, given by Eq. (5) of the main text, should be corrected by the factor

$$C = (\omega_{\perp} t_f)^{-(ck/\omega_{\perp})^2}. \quad (\text{G1})$$

In all experimental situations $C > 0.95$, which confirm that the effect of interactions during the time of flight is small.

APPENDIX H: EFFECTS WHICH MAY REDUCE THE OSCILLATION AMPLITUDE

In this section we investigate two effects responsible for a reduction of the amplitude of the oscillations of \bar{J} (see main text), as compared to the theoretical prediction given by Eq. (6) of the main text. We first consider the effect of the finite ramp time of the interaction strength, which reduces the squeezing of the Bogoliubov modes, as compared to an instantaneous quench. This effect contributes to the reduction of the amplitude on the order of 10%. We then investigate the reduction of the amplitude induced by the binning of the data with a finite resolution in τ . This effect amounts to an additional reduction of the amplitude by 18%.

1. Beyond the instantaneous quench: Finite ramp time

In the experiment, the change of the effective interaction strength is not instantaneous: to ensure the adiabatic following of the transverse motion, we perform a ramp of the transverse oscillation frequency during a time t_r . The finite value of t_r is responsible for a decrease of the induced squeezing of each mode. In the asymptotic limit of very large t_r , the squeezing vanishes since then the modes follow adiabatically the modification of the interaction strength. In the following we compute the effect of the ramp on the squeezing of each mode and we use this result to compute the resulting decrease of the oscillation amplitude of \bar{J} .

In order to estimate the effect of the finite ramp time, we will consider a homogeneous gas for simplicity. The Bogoliubov modes are then described by the Hamiltonian of

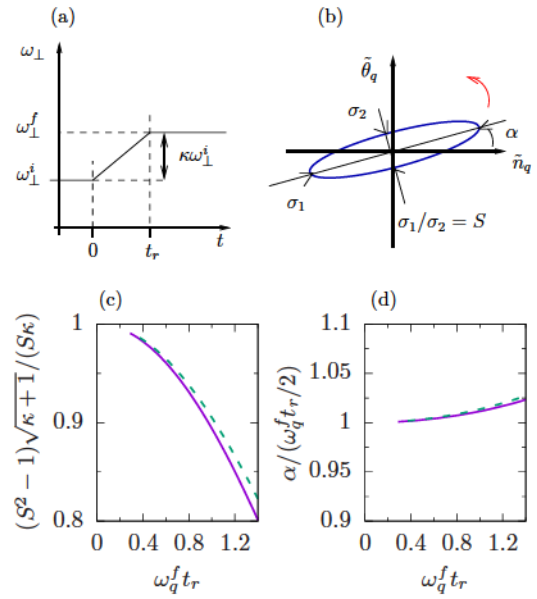


FIG. 9. Effect of the interaction strength ramp on the squeezing of longitudinal modes. The time sequence is shown in (a). An example of the phase-space distribution at the end of the ramp is shown in (b): the $1/\sqrt{e}$ line of the Gaussian distribution is plotted. The squeezing factor S is the ratio between the rms widths along the antisqueezed and the squeezed directions. The curved arrow shows the direction of rotation under free evolution. Quantitative results are shown in (c) and (d) for a quench strength $\kappa = \omega_{\perp}^f/\omega_{\perp}^i - 1 = 2$ (solid lines) and $\kappa = 4$ (dashed lines). (c) shows $\sqrt{\kappa+1}(S^2 - 1)/(S\kappa)$, which gives the amplitude of the resulting breathing oscillations normalized to the amplitude for an instantaneous quench (see text), vs $\omega_q^f t_r$, where ω_q^f is the final frequency of the mode. The squeezing angle is shown in (d), normalized by $\omega_q^f t_r/2$.

Eq. (1) of the main text, namely

$$H_q = A_q n_q^2 + B_q \theta_q^2. \quad (\text{H1})$$

We regard the effect of a ramp of ω_{\perp} between the time $t = 0$ and the time t_r : ω_{\perp} goes from ω_{\perp}^i to $\omega_{\perp}^f = (\kappa + 1)\omega_{\perp}^i$, as depicted in Fig. 9. The coefficient $B_q = n_0 \hbar^2 q^2 / (2m)$ is time independent, while the coefficient A_q evolves linearly during the ramp (i.e., during time interval $0 < t < t_r$), since it is proportional to c^2 , itself proportional to ω_{\perp} . Then, the solution of the second-order equations describing the evolution of θ_q and n_q during the ramp is given in terms of the Airy functions. In order to investigate the squeezing, it is natural to introduce the reduced variables

$$\begin{cases} \tilde{\theta}_q = \theta_q / \bar{\theta}_q \\ \tilde{n}_q = n_q / \bar{n}_q \end{cases}, \quad (\text{H2})$$

where $\bar{\theta}_q = [A_q(t)/B_q]^{1/4}$ and $\bar{n}_q = [B_q/A_q(t)]^{1/4}$ are the time-dependent widths of the ground state. For given initial values, the values of $\tilde{\theta}_q$ and \tilde{n}_q at the end of the ramp are

$$\begin{pmatrix} \tilde{\theta}_q(t_r) \\ \tilde{n}_q(t_r) \end{pmatrix} = M \begin{pmatrix} \tilde{\theta}_q(0) \\ \tilde{n}_q(0) \end{pmatrix}, \quad (\text{H3})$$

where the matrix M has the following components:

$$\begin{cases} M_{11} = (\kappa + 1)^{-1/4} \pi \{-B_i(-\delta^{-2/3})A'_i[-(\kappa + 1)\delta^{-2/3}] + A_i(-\delta^{-2/3})B'_i[-(\kappa + 1)\delta^{-2/3}]\} \\ M_{22} = (\kappa + 1)^{1/4} \pi \{B'_i(-\delta^{-2/3})A_i[-(\kappa + 1)\delta^{-2/3}] - A'_i(-\delta^{-2/3})B_i[-\delta^{-2/3}(\kappa + 1)]\} \\ M_{21} = [\delta^{-4/3}(\kappa + 1)]^{1/4} \pi \{-B_i(-\delta^{-2/3})A_i[-\delta^{-2/3}(\kappa + 1)] + A_i(-\delta^{-2/3})B_i[-\delta^{-2/3}(\kappa + 1)]\} \\ M_{12} = [\delta^{-4/3}(\kappa + 1)]^{-1/4} \pi \{B'_i(-\delta^{-2/3})A'_i[-\delta^{-2/3}(\kappa + 1)] - A'_i(-\delta^{-2/3})B'_i[-\delta^{-2/3}(\kappa + 1)]\} \end{cases} \quad (\text{H4})$$

Here A_i, B_i are the first and second kind Airy functions and A'_i, B'_i , their derivatives and $\delta = \kappa/(t_r \omega_q^i)$ the quench speed normalized to the initial mode frequency (we recall that the quench strength is $\kappa = \omega_\perp^f/\omega_\perp^i - 1$). Under this transformation, the initial isotropic Gaussian distribution transforms into a squeezed distribution, i.e., a Gaussian elliptical distribution with a squeezing angle α and ratio between the rms width of the two eigenaxes equal to the squeezing factor S . In order to find α and S , let us compute, for any angle β , the width along the quadrature $\tilde{x}_\beta = \cos(\beta)\tilde{\theta}_q + \sin(\beta)\tilde{n}_q$. Using the fact that the initial state is a thermal equilibrium state fulfilling $\langle \tilde{\theta}_q^2 \rangle_i = \langle \tilde{n}_q^2 \rangle_i \equiv V$ and $\langle \tilde{\theta}_q \tilde{n}_q \rangle_i = 0$, and using the transformation above, we find

$$\langle \tilde{x}_\beta^2 \rangle = V \{ \cos^2(\beta)(M_{11}^2 + M_{22}^2) + \sin^2(\beta)(M_{21}^2 + M_{12}^2) + 2 \cos(\alpha) \sin(\alpha)(M_{11}M_{21} + M_{22}M_{12}) \}. \quad (\text{H5})$$

The squeezing angle α is found by imposing $d\langle \tilde{x}_\beta^2 \rangle/d\beta|_{\beta=\alpha} = 0$, which leads to

$$\tan(2\alpha) = -2 \frac{M_{11}M_{21} + M_{22}M_{12}}{M_{21}^2 + M_{22}^2 - M_{11}^2 - M_{12}^2}. \quad (\text{H6})$$

The most squeezed quadrature is \tilde{x}_α while $\tilde{x}_{\alpha+\pi/2}$ is the most antisqueezed quadrature. The squeezing factor is $S = \sqrt{\langle \tilde{x}_\alpha^2 \rangle} / \sqrt{\langle \tilde{x}_{\alpha+\pi/2}^2 \rangle}$. It also writes $S = \langle \tilde{x}_\alpha^2 \rangle / V$ since the conservation of the phase-space area ensures $\sqrt{\langle \tilde{x}_\alpha^2 \rangle} \sqrt{\langle \tilde{x}_{\alpha+\pi/2}^2 \rangle} = V$, and it is evaluated injecting $\beta = \alpha$ in Eq. (H5). Results are shown in Fig. 9 for quench amplitudes $\kappa = 2$ and $\kappa = 4$ as a function of $\omega_q^f t_r$ where ω_q^f is the final frequency of the mode. For very slow modes $\omega_q^f t_r \ll 1$, one recovers the results expected for an instantaneous quench: $\alpha \simeq 0$ and $(S^2 - 1) \simeq \kappa$. For modes of larger frequency, the effect of the ramp is to reduce the squeezing and also to rotate its axis.

The postquench dynamics results in a breathing of the $\tilde{\theta}_q$ quadrature: $\langle \tilde{\theta}_q^2 \rangle$ oscillates with an amplitude $V(S^2 - 1)/S$. Coming back to the variable θ_q , the evolution at times $t > t_r$ writes

$$\langle \theta_q^2 \rangle(t) = \langle \theta_q^2 \rangle_i \frac{\sqrt{\kappa + 1}}{S_q} \{ 1 + (S_q^2 - 1) \sin^2 [\omega_q^f(t - t_r) + \alpha_q] \}, \quad (\text{H7})$$

where the indice q in S and α indicates these quantities depend on q . As seen in Fig. 9, the angle α_q is very close to $\omega_q^f t_r/2$, for moderate values of $\omega_q^f t_r$. Injecting this value into Eq. (H7), we find that it amounts to shifting the time reference to $t_r/2$. We perform this shift when analyzing the data; in other terms the reduced variable τ is $\tau = c q(t - t_r/2)$.

Let us now consider the evolution of the density-ripple power spectrum $\langle |\tilde{\rho}_q|^2 \rangle(t)$. For small q , $\langle |\tilde{\rho}_q|^2 \rangle(t)$ is

proportional to $\langle \theta_q^2 \rangle(t)$ such that the evolution of $\langle |\tilde{\rho}_q|^2 \rangle(t)$ is given by Eq. (H7). This leads to

$$J(q, \tau) = \frac{\sqrt{\kappa + 1}}{S_q} [1 + (S_q^2 - 1) \sin^2(\tau)]. \quad (\text{H8})$$

Let us now investigate the quantity $\bar{J}(\tau)$, defined in the main text for experimental data. Here we will assume that the measurement times are spread over $[t_m, t_M]$ and we denote $h(t)dt$ the number of points in the time interval $[t, t + dt]$. The q values are assumed to be equally spaced, as in the case of a fast Fourier transform, and only q values in the interval $[q_m, q_M]$ are considered. We assume that $\bar{J}(\tau)$ is obtained by binning in τ the collection of data with a bin size Δ small enough so that, for all measurement times t , $J(q, \tau)$ is about constant in the interval $q \in [\tau/(ct), (\tau + \Delta)/(ct)]$. Then, one has

$$\bar{J}(\tau) = \frac{1}{\int h(t)dt \Delta/(ct)} \int h(t)dt J[q = \tau/(ct), \tau] \Delta/(ct), \quad (\text{H9})$$

where the integrals are evaluated between t_1 and t_2 , where $t_1 = \text{Max}[t_m, \tau/(cq_M)]$ and $t_2 = \text{Min}[t_M, \tau/(cq_m)]$. Typically, in the experiment small times are sampled more densely than large times. Taking h proportional to $1/t$, we obtain

$$\bar{J}(\tau) = \frac{1}{\int dt/t^2} \int dt \frac{J[q = \tau/(ct), \tau]}{t^2} = \frac{\int dq J(q, \tau)}{q_2(\tau) - q_1(\tau)}, \quad (\text{H10})$$

where $q_1 = \max[\tau/(c)t_M, q_m]$ and $q_2 = \min[\tau/(c)t_m, q_M]$.

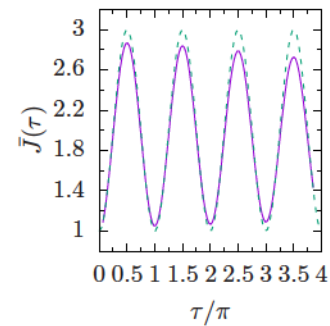


FIG. 10. Effect of the finite ramp time of the interaction strength for a homogeneous gas. The expected behavior of \bar{J} (solid line) is compared to the case of an instantaneous ramp (dashed line). Here we consider a gas of rubidium atoms at conditions close to the experimental ones. More precisely, the linear density is $n_0 = 630$ atoms per μm , the initial transverse oscillation frequency is $\omega_\perp = 2\pi \times 1.5$ kHz, the quench strength is $\kappa = 2$, and the ramp time is $t_r = 0.7$ ms. The range of q values used to compute \bar{J} is $q \in [0.1, 0.5] \mu\text{m}^{-1}$ and the range of measurement times is $t \in [t_r/2, 6$ ms].

The predicted time evolution of \bar{J} is shown in Fig. 10 for parameters close to that of the experimental data shown in the main text. The amplitude of the first oscillation is decreased by about 10%.

2. Finite width of the convolution function used in data processing

The data shown in the inset of Fig. 3 of the main text correspond to a data set with an exceptionally good signal over noise. In general, the spread of the data points corresponding to a given value of τ (and thus corresponding to different times t and wave vectors q) is as large as about 50%. In such conditions, a binning of the data as a function of the reduced time $\tau = cqt$ with a bin size sufficiently large to accommodate many data points is required in order to increase

the signal over noise. As describe in the main text, we use a “smooth” binning: we compute the weighted average of the data, \bar{J} , with a Gaussian cost function of rms width Δ . For a very dense data set, we can define the local average value $\bar{J}(\tau) = \sum_{i, \tau_i \in [\tau, \tau+d\tau]} J_i/d\tau$, where the sum is done on the data set and $d\tau$ is much smaller than Δ . Then \bar{J} corresponds to the convolution of \bar{J} with a convolution width Δ . This convolution reduces the amplitude of the oscillations. To estimate this amplitude reduction, let us disregard the small damping of the oscillations coming from the cloud inhomogeneity (see Sec. III) and thus consider data which would follow the oscillatory behavior $\bar{J} = A \sin^2(\tau)$. The smoothing $\bar{J}(\tau) = \int_{-\infty}^{\infty} d\tau' \bar{J}(\tau') e^{-(\tau'-\tau)^2/(2\Delta^2)} / (\sqrt{2\pi}\Delta^2)$ reduces the amplitude to $A' = A e^{-2\Delta^2}$. For $\Delta = 0.1\pi$, as used for the data analysis shown in the main text, the amplitude is reduced by 18%.


-
- [1] A. Polkovnikov, K. Sengupta, A. Silva, and M. Vengalattore, Colloquium: Nonequilibrium dynamics of closed interacting quantum systems, *Rev. Mod. Phys.* **83**, 863 (2011).
- [2] See [42] and references therein.
- [3] S. Trotzky, Y.-A. Chen, A. Flesch, I. P. McCulloch, U. Schollwöck, J. Eisert, and I. Bloch, Probing the relaxation towards equilibrium in an isolated strongly correlated one-dimensional Bose gas, *Nat. Phys.* **8**, 325 (2012).
- [4] M. Cheneau, P. Barmettler, D. Poletti, M. Endres, P. Schauß, T. Fukuhara, C. Gross, I. Bloch, C. Kollath, and S. Kuhr, Light-cone-like spreading of correlations in a quantum many-body system, *Nature (London)* **481**, 484 (2012).
- [5] C.-L. Hung, V. Gurarie, and C. Chin, From cosmology to cold atoms: Observation of sakharov oscillations in a quenched atomic superfluid, *Science* **341**, 1213 (2013).
- [6] T. Langen, T. Schweigler, E. Demler, and J. Schmiedmayer, Double light-cone dynamics establish thermal states in integrable 1d Bose gases, *New J. Phys.* **20**, 023034 (2018).
- [7] J.-C. Jaskula, G. B. Partridge, M. Bonneau, R. Lopes, J. Ruauudel, D. Boiron, and C. I. Westbrook, Acoustic Analog to the Dynamical Casimir Effect in a Bose-Einstein Condensate, *Phys. Rev. Lett.* **109**, 220401 (2012).
- [8] J. De Nardis, B. Wouters, M. Brockmann, and J.-S. Caux, Solution for an interaction quench in the Lieb-Liniger Bose gas, *Phys. Rev. A* **89**, 033601 (2014).
- [9] P. Calabrese and P. Le Doussal, Interaction quench in a Lieb-Liniger model and the KPZ equation with flat initial conditions, *J. Stat. Mech.* (2014) P05004.
- [10] M. A. Cazalilla and M.-C. Chung, Quantum quenches in the Luttinger model and its close relatives, *J. Stat. Mech.* (2016) 064004.
- [11] T. Świsłocki and P. Deuar, Quantum fluctuation effects on the quench dynamics of thermal quasicondensates, *J. Phys. B* **49**, 145303 (2016).
- [12] B. Rauer, S. Erne, T. Schweigler, F. Cataldini, M. Tajik, and J. Schmiedmayer, Recurrences in an isolated quantum many-body system, *Science* **360**, 307 (2018).
- [13] C. Mora and Y. Castin, Extension of Bogoliubov theory to quasicondensates, *Phys. Rev. A* **67**, 053615 (2003).
- [14] M. Schemmer, A. Johnson, R. Photopoulos, and I. Bouchoule, Monte Carlo wave-function description of losses in a one-dimensional Bose gas and cooling to the ground state by quantum feedback, *Phys. Rev. A* **95**, 043641 (2017).
- [15] For each positive q value, one has two Fourier components: $\hat{n}_{q,c} = \sqrt{2/L} \int dz n(z) \cos(qz)$ and $\hat{n}_{q,s} = \sqrt{2/L} \int dz n(z) \sin(qz)$, with similar expressions for θ . We omit the subscript c or s in the text for simplicity.
- [16] For quasi-1D gases the hydrodynamic condition is replaced by $\omega_q \ll \omega_{\perp}$.
- [17] The phase-space area is preserved, one quadrature being squeezed while the other is antisqueezed.
- [18] For the q values considered, $\omega_q \ll k_B T$ and the Raighley-Jeans approximation holds.
- [19] In Ref. [5], the evolution of density fluctuations has however been investigated for a 2D gas.
- [20] Isolating the contribution of individual modes to the function $g_1(z)$ requires looking at the Fourier transform of $\ln[g_1(z)]$, which requires large detection dynamics.
- [21] A. Imambekov, I. E. Mazets, D. S. Petrov, V. Gritsev, S. Manz, S. Hofferberth, T. Schumm, E. Demler, and J. Schmiedmayer, Density ripples in expanding low-dimensional gases as a probe of correlations, *Phys. Rev. A* **80**, 033604 (2009).
- [22] S. Dettmer, D. Hellweg, P. Ryytty, J. J. Arlt, W. Ertmer, K. Sengstock, D. S. Petrov, G. V. Shlyapnikov, H. Kreutzmann, L. Santos, and M. Lewenstein, Observation of Phase Fluctuations in Elongated Bose-Einstein Condensates, *Phys. Rev. Lett.* **87**, 160406 (2001).
- [23] S. Manz, R. Bucker, T. Betz, Ch. Koller, S. Hofferberth, I. E. Mazets, A. Imambekov, E. Demler, A. Perrin, J. Schmiedmayer, and T. Schumm, Two-point density correlations of quasicondensates in free expansion, *Phys. Rev. A* **81**, 031610 (2010).
- [24] B. Rauer, P. Grišins, I. E. Mazets, T. Schweigler, W. Rohringer, R. Geiger, T. Langen, and J. Schmiedmayer, Cooling of a One-Dimensional Bose Gas, *Phys. Rev. Lett.* **116**, 030402 (2016).
- [25] For consistency we rederive this expression (established in [21]) see Appendixes B and C.
- [26] In Eq. (5), $\langle \theta_q^2 \rangle = (\langle \theta_{q,c}^2 \rangle + \langle \theta_{q,s}^2 \rangle)/2$ where $\theta_{q,c}$ and $\theta_{q,s}$ are the cosine and sine Fourier components, which fulfill $\langle \theta_{q,c}^2 \rangle = \langle \theta_{q,s}^2 \rangle$ for translationally invariant systems.

- [27] Validity of LDA is established in Appendix E.
- [28] The experiment is described in more detail in [43].
- [29] K. V. Kheruntsyan, D. M. Gangardt, P. D. Drummond, and G. V. Shlyapnikov, Pair Correlations in a Finite-Temperature 1d Bose Gas, *Phys. Rev. Lett.* **91**, 040403 (2003).
- [30] J. N. Fuchs, X. Leyronas, and R. Combescot, Hydrodynamic modes of a one-dimensional trapped Bose gas, *Phys. Rev. A* **68**, 043610 (2003).
- [31] The box L is chosen to be about twice the size of the cloud.
- [32] The transverse size of the cloud after the time of flight is comparable to the depth of focus of the imaging system and depends on the transverse confinement. We thus expect slightly different optical resolutions, σ_i and σ_f for data taken before and after the quench respectively. We correct for this effect to make quantitative comparison of data taken before and after the quench.
- [33] The values of resolution obtained by such fits are close to the expected values if one takes into account the depth of field of our imaging system and the fact that, after the expansion time t_f the cloud explores about $50 \mu\text{m}$ along the imaging direction.
- [34] T. Jacqmin, J. Armijo, T. Berrada, K. V. Kheruntsyan, and I. Bouchoule, Sub-Poissonian Fluctuations in a 1d Bose Gas: From the Quantum Quasicondensate to the Strongly Interacting Regime, *Phys. Rev. Lett.* **106**, 230405 (2011).
- [35] At a time $t = t_{\text{th}}^{g_1}$ the g_1 function has reached the thermal value $e^{-|z|/l_c^f}$ for all $z < 2l_c^f$, the deviation from this thermal state being restricted to long distances where $g_1(z) < e^{-2} \approx 10\%$.
- [36] A. Johnson, S. S. Szigeti, M. Schemmer, and I. Bouchoule, Long-lived nonthermal states realized by atom losses in one-dimensional quasicondensates, *Phys. Rev. A* **96**, 013623 (2017).
- [37] We corrected the formula published in [21].
- [38] D. Hellweg, S. Dettmer, P. Ryytty, J. J. Arlt, W. Ertmer, K. Sengstock, D. S. Petrov, G. V. Shlyapnikov, H. Kreutzmann, L. Santos, and M. Lewenstein, Phase fluctuations in Bose-Einstein condensates, *Appl. Phys. B* **73**, 781 (2001).
- [39] This term is due to the approximation made when going from Eq. (A1) to Eq. (A2), which is valid only for q values larger than the inverse of the cloud size.
- [40] Since the Hamiltonian of interest is quadratic in θ , the distribution of θ is Gaussian at thermal equilibrium. The squeezing of each collective mode produced by the interaction quench preserves the Gaussian nature of θ .
- [41] M. Olshani, Atomic Scattering in the Presence of an External Confinement and a Gas of Impenetrable Bosons, *Phys. Rev. Lett.* **81**, 938 (1998).
- [42] A. Mitra, Quantum quench dynamics, *Annu. Rev. Condens. Matter Phys.* **9**, 245 (2018).
- [43] T. Jacqmin, B. Fang, T. Berrada, T. Roscilde, and I. Bouchoule, Momentum distribution of one-dimensional Bose gases at the quasicondensation crossover: Theoretical and experimental investigation, *Phys. Rev. A* **86**, 043626 (2012).

Cooling a Bose Gas by Three-Body Losses

Max Schemmer and Isabelle Bouchoule*

*Laboratoire Charles Fabry, Institut d'Optique, CNRS, Université Paris Saclay,
2 Avenue Augustin Fresnel, F-91127 Palaiseau Cedex, France*

 (Received 26 June 2018; published 16 November 2018)

We report the demonstration of cooling by three-body losses in a Bose gas. We use a harmonically confined one-dimensional (1D) Bose gas in the quasicondensate regime and, as the atom number decreases under the effect of three-body losses, the temperature T drops up to a factor of 4. The ratio $k_B T/(mc^2)$ stays close to 0.64, where m is the atomic mass and c the speed of sound in the trap center. The dimensionless 1D interaction parameter γ , evaluated at the trap center, spans more than 2 orders of magnitudes over the different sets of data. We present a theoretical analysis for a homogeneous 1D gas in the quasicondensate regime, which predicts that the ratio $k_B T/(mc^2)$ converges towards 0.6 under the effect of three-body losses. More sophisticated theoretical predictions that take into account the longitudinal harmonic confinement and transverse effects are in agreement within 30% with experimental data.

DOI: 10.1103/PhysRevLett.121.200401

The identification and understanding of cooling processes, both on the theoretical and the experimental side, is crucial to the development of cold atom physics [1,2]. It can help to elaborate strategies to enter new regimes and it can also improve the control over state preparation in experiments where cold atoms are used as quantum simulators of many body systems. Ultracold atom gases are metastable systems, their ground state being a solid phase. They are thus plagued with intrinsic recombination processes, that in practice limit their lifetime. Such processes are mainly three-body collisions during which a strongly bound dimer is formed. It amounts to three-body losses because the dimer is typically no longer trapped and the remaining atom escapes because of its large kinetic energy. These losses are known to produce an undesired heating in cold gases. In the case of a thermal gas, since they occur predominantly in the regions of high atomic density, where the potential energy is low, these losses increase the energy per remaining particle, leading to an antievaporation process [3]. In Bose-Einstein condensates (BEC) confined in deep traps, it was predicted that three-body collisions produce a heating of the BEC through secondary collisions with high energy excitations formed by the loss process [4]. This Letter constitutes a breakthrough since we identify a cooling associated with three-body losses in a cold Bose gas.

A similar counterintuitive cooling was recently investigated in [5–8] where the effect of one-body losses in quasicondensate regime [9] is considered. Although one-body losses are also central for evaporative cooling, here the losses are energy independent and the cooling originates from a very different physics. Those works were recently extended [11] to any j -body loss process, for Bose gases in the BEC or quasicondensate regime, in any dimension d , and for homogeneous gases as well as gases

confined in a smooth potential. These studies focus on the effect of losses on low energy excitations in the gas, the phononic modes, which correspond to density waves propagating in the condensate. On the one hand, the energy in these modes is reduced by losses since the amplitude of density modulations is decreased, removing interaction energy from the mode. On the other hand, the discrete nature of the loss process comes with accompanying shot noise which induces density fluctuations, increasing the energy per mode. It has been shown that the competition between these processes leads to a stationary value of the ratio $k_B T/(mc^2)$ where m is the atom mass and c the speed of sound. This value, of the order of one, depends on j , d , and on the confining potential [11]. For three-body losses in a 1D quasicondensates ($j=3$, $d=1$) confined in a harmonic potential one expects $k_B T/(mc_p^2)$ to converge to 0.70 [11], where c_p is evaluated at the peak density. In contrast to evaporative cooling, this loss-induced cooling does not rely on a thermalization mechanism in the gas [12].

In this Letter, we show experimentally that three-body losses induce a cooling and we identify the stationary value of $k_B T/(mc_p^2)$ associated with the three-body process. More precisely, investigating the time evolution of a 1D quasicondensate, we observe a decrease of the temperature as the atom number decreases under the effect of three-body losses. Moreover, on the whole observed time interval, the ratio $k_B T/(mc_p^2)$ stays about constant, at a value close to 0.64, which indicates that the stationary value of $k_B T/(mc_p^2)$ imposed by the loss process is reached. We took several data sets for different parameters. In terms of the 1D dimensionless parameter γ [13] characterizing the strength of the interactions [14], our data span more than 2

orders of magnitude. We compare the experimental data with numerical calculations based on the results of [11], which take into account the harmonic longitudinal confinement of the gas and the swelling of the transverse wave function under the effect of interactions. The experimental results are close to those predictions. In order to present the underlying physics, we derive in this Letter the evolution of the temperature under three-body losses, in the more simple case of a homogeneous purely 1D quasicondensate.

The experiment uses an atom-chip setup [15] where ^{87}Rb atoms are magnetically confined using current-carrying microwires. An elongated atomic cloud is prepared using radio frequency forced evaporative cooling in a trap of transverse frequency ω_{\perp} . Depending on the data set, $\omega_{\perp}/(2\pi)$ varies between 1.5 and 9.2 kHz and the atomic peak linear densities n vary between 22 and $257 \mu\text{m}^{-1}$. The temperature fulfills $k_B T < \hbar\omega_{\perp}$ and the gas mostly behaves as a 1D Bose gas [17]. It, moreover, lies in the quasicondensate regime [18], characterized by weak correlations between atoms, as in Bose-Einstein condensates [19], and in particular small density fluctuations [20]. As long as the atoms are in the ground state of the transverse potential, interactions between atoms are well described by a 1D effective coupling constant $g = 2\hbar\omega_{\perp}a$, where $a = 5.3 \text{ nm}$ is the 3D scattering length [21], and the chemical potential is given by $\mu = gn$. This is valid only as long as $\mu \ll \hbar\omega_{\perp}$, which requires $na \ll 1$. In the presented data na takes values as large as 1.3 and the broadening of the transverse wave function due to interactions has to be taken into account for quantitative analysis. In particular, the equation of state becomes $\mu = \hbar\omega_{\perp}(\sqrt{1 + 4na} - 1)$ [23]. The quasicondensates are confined in the longitudinal direction with a harmonic potential $V(z)$ of trapping frequency $\omega_z/(2\pi) = 8.5 \text{ Hz}$, weak enough so that the longitudinal profile $n_0(z)$ is well described by the local density approximation (LDA), with a local chemical potential $\mu(z) = \mu_p - V(z)$, where μ_p is the peak chemical potential. It extends over $2R$ where the Thomas-Fermi radius R fulfills $V(R) = \mu_p$. Once the quasicondensate is prepared, we increase the frequency of the radio-frequency field, by several kHz, a value sufficient so that it no longer induces losses. We then investigate the evolution during the waiting time t . Five different data set are investigated, differing in the value of the transverse confinement and the initial temperature and peak density.

Using absorption images we record the density profile of the gas, from which we extract the peak density n_p . Figure 1 shows the evolution of n_p with the waiting time t for the different data sets. The observed nonexponential decrease of n_p is neither due to one-body losses (whose rate is smaller than about 0.14 s^{-1} in our experiment), nor to inelastic two-body collisions, negligible for spin polarized ^{87}Rb [24,25]. Its origin is three-body recombinations, as justified by calculations presented below. In a three-body recombination, a molecule (a dimer) is formed and its

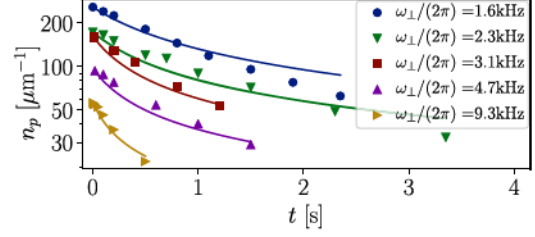


FIG. 1. Peak density, in log scale, versus the waiting time t , for the five different data sets. Solid lines are *ab initio* calculations of the effect of three-body losses, for initial peak densities equal to that of the experimental data.

binding energy is released in the form of kinetic energy of the molecule and the remaining atom. They both leave the trap since their energy is typically much larger than the trap depth, limited by the radio-frequency field. Thus, the effect of the three-body process is to decrease the gas density according to $d\rho/dt = -\rho^3 g^{(3)}(0)\kappa$, where ρ is the three dimensional atomic density, $g^{(3)}(0)$ is the normalized three-body correlation function at zero distance, and $\kappa = (1.8 \pm 0.5) \times 10^{-41} \text{ m}^6/\text{s}$ is the three-body loss rate for ^{87}Rb [24]. In a quasicondensate, correlations between atoms are small and $g^{(3)}(0) \simeq 1$ [26]. Moreover, integrating $d\rho/dt$ over the transverse shape of the cloud, we obtain a one-dimensional rate of density decrease $dn_0(t)/dt = -Kn_0(t)^3$, where $K = (\kappa/n_0^3) \iint dx dy \rho(x,y)^3$. Taking into account the transverse broadening of the wave function using the Gaussian ansatz results of [27], we obtain $K = K^0/(1 + 2n_0a)$, where $K^0 = \kappa m^2 \omega_{\perp}^2 / (3\pi^2 \hbar^2)$ [28]. Finally, the rate of variation of the total atom number N is

$$\frac{dN}{dt} = - \int_{-R}^R dz K(z) n_0(z)^3. \quad (1)$$

At any time, the measured profile is very close to an equilibrium profile, which indicates the loss rate is small enough to ensure adiabatic following of $n_0(z)$. Then N and $n_0(z)$ are completely determined by n_p and Eq. (1) can be transformed into a differential equation for n_p . We solve it numerically for the parameters of the experimental data, namely the frequency ω_{\perp} and the initial peak density, using the LDA to relate N and $n_0(z)$ to n_p . Calculations, shown in Fig. 1, are in good agreement with the experimental data, which confirms that losses are largely dominated by three-body losses. In contrast to [5], where losses are dominated by engineered large one-body losses, we rely here on intrinsic collisional properties of the gas.

The temperature of the gas is determined analyzing the large density ripples that appear after a time of flight t_f [5,29–32]. Interactions are effectively quickly turned off by the transverse expansion of the gas and the subsequent free evolution transforms longitudinal phase fluctuations into density fluctuations. Using an ensemble of images taken in

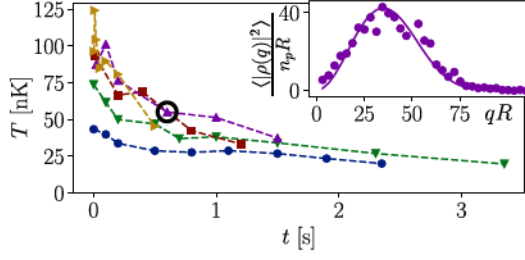


FIG. 2. Evolution of the temperature for the five data sets (same color code and symbols as in Fig. 1). Inset: density ripples power spectrum corresponding to the encircled point, with the fit in solid line yielding the temperature.

the same experimental condition, we extract the density ripple power spectrum

$$\langle |\rho(q)|^2 \rangle = \left\langle \left| \int dz [n(z, t_f) - \langle n(z, t_f) \rangle] e^{iqz} \right|^2 \right\rangle. \quad (2)$$

We choose t_f small enough so that the density ripples occurring near the position z are produced by atoms which were initially in a small portion of the cloud, located near z . We can thus use, within a LDA, the analytic predictions for homogeneous gases to compute the expected power spectrum of the trapped gas [32]. We take into account the finite resolution of the imaging system modeling its impulse response function by a Gaussian of rms width σ_{res} . For a given data set the density ripple power spectrum recorded at $t = 0$ is fitted with the temperature T and σ_{res} , the latter depending on the transverse width of the cloud and thus on ω_{\perp} . We then fit $\langle |\rho_q|^2 \rangle$ at larger values of t with T as a single parameter (see inset Fig. 2). The time evolution of T is shown in Fig. 2 for the five different data sets investigated in this Letter. The temperature decreases with t , which indicates a cooling mechanism associated with the three-body losses. Note that this thermometry probes phononic collective modes since the experimentally accessible wave vectors are much smaller than the inverse healing length $\xi^{-1} = \sqrt{mgn_0}/\hbar$.

Figure 3 shows the same data, with the temperature normalized to mc_p^2 , where $c_p = \sqrt{n_p \partial_n \mu|_{n_p}/m}$ is the sound velocity at the center of the cloud, shown versus the peak density n_p . While n_p explores more than one order of magnitude, remarkably $k_B T / (mc_p^2)$ shows small dispersion and is close to its mean value 0.64, the standard deviation being 0.02 [33].

The absolute linear density is, however, not the most relevant quantity. A 1D gas at thermal equilibrium is characterized by the dimensionless quantities $\gamma = mg/(\hbar^2 n)$ and $t_{YY} = \hbar^2 k_B T / (mg^2)$ [18]. In particular, the quantum degeneracy condition corresponds to the line $\gamma^2 t_{YY} \simeq 1$. Moreover, the crossover between the ideal Bose gas regime and the quasicondensate regime occurs, within

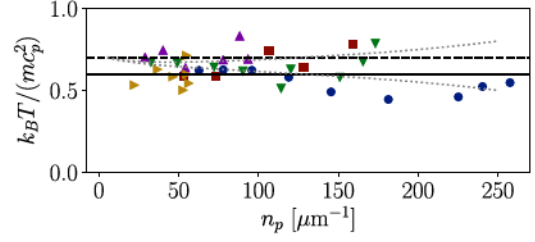


FIG. 3. Evolution of the ratio $k_B T / (mc_p^2)$, in the course of the three-body loss process, for the five data sets (same color code and symbols as in Fig. 1). The temperature decreases with c_p^2 , which is approximately proportional to n_p . Solid (respectively, dashed) lines: asymptotic ratio for a 1D homogeneous (respectively, harmonically confined) gas. Dotted lines: numerical calculation, that takes into account the transverse swelling, for two different initial situations close to that of experimental data.

the region $\gamma \ll 1$, along the line $\gamma^{3/2} t_{YY} \simeq 1$. Finally, within the quasicondensate regime, the line $\gamma t_{YY} \simeq 1$ separates the high temperature regime, where the zero distance two- and three-body correlations functions $g^{(2)}(0)$ and $g^{(3)}(0)$ are dominated by thermal fluctuations and are larger than 1 from the low temperature regime, where $g^{(2)}(0)$ and $g^{(3)}(0)$ are dominated by quantum fluctuations and are smaller than 1 [34]. Here, we generalize these 1D parameters to quasi-1D gases introducing $\tilde{t}_{YY} = \hbar^2 k_B T n^2 / (m^3 c^4)$ and $\tilde{\gamma} = m^2 c^2 / (\hbar^2 n^2)$. For a harmonically confined gas, we refer in the following to the values of \tilde{t}_{YY} and $\tilde{\gamma}$ evaluated at the trap center. The evolution of the state of the gas during the three-body loss process is shown in Fig. 4 in the $(\tilde{t}_{YY}, \tilde{\gamma})$ space. All data collapse on the line $\tilde{\gamma} \tilde{t}_{YY} = k_B T / (mc_p^2) = 0.7$, with a maximum deviation of 36%, while \tilde{t}_{YY} explore more than 2 orders of magnitude.

The physics at the origin of the observed behavior can be understood by considering the simple case of a pure 1D homogeneous quasicondensate. We give here a simplified analysis and refer the reader to [11] for a more complete study. At first, let us solely consider the effect of three-body losses, during a time interval dt , in a small cell of the gas of length Δ . The density is $n = n_0 + \delta n$, where n_0 is the mean density and $\delta n \ll n_0$ since we consider a quasicondensate.

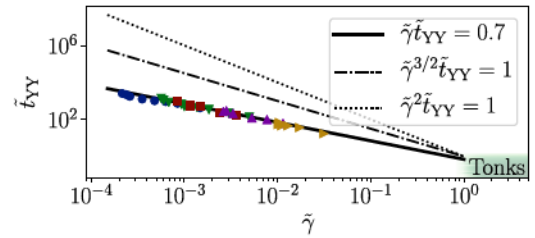


FIG. 4. The data collapse on the line $\tilde{\gamma} \tilde{t}_{YY} = 0.7$. The lower right corner corresponds to the strongly interacting Tonks-Girardeau regime. The data sets and color (symbols) codes are the same as in all other figures.

The density evolves according to $dn = -Kn^3 dt + d\eta$, where $d\eta$ is a random variable of vanishing mean value reflecting the stochastic nature of the loss process. During dt the loss process is close to Poissonian and $\langle d\eta^2 \rangle = 3Kn^3 dt/\Delta \simeq 3Kn_0^3 dt/\Delta$, where the factor 3 comes from the fact that each loss event amounts to the loss of 3 atoms. To first order in δn , the mean density evolves according to $dn_0 = -Kn_0^3 dt$, and the expansion of dn yields

$$d\delta n = -3Kn_0^2 \delta n dt + d\eta. \quad (3)$$

The two terms of the right-hand side correspond to the two competing effects of losses. The first term, a drift term, reduces the density fluctuations: it thus decreases the interaction energy, leading to a cooling. The second term, a stochastic term due to the discrete nature of the atom losses, increases the density fluctuations and thus induces a heating. Going to the continuous limit, one has $\langle d\eta(z)d\eta(z') \rangle = 3Kn_0^3 dt \delta(z - z')$.

Let us now consider the intrinsic dynamics of the gas. Within the Bogoliubov approximation, valid in the quasicondensate regime, one identifies independent collective modes and, up to a constant term, the Hamiltonian of the gas writes $H = \sum_k H_k$, where

$$H_k = A_k \delta n_k^2 + B_k \theta_k^2 \quad (4)$$

is the Hamiltonian of the collective mode of wave vector k [8]. Here, the conjugate quadratures δn_k and θ_k are the Fourier components of δn and θ , $B_k = \hbar^2 k^2 n_0 / (2m)$, and, as long as phononic modes are considered, $A_k = g/2$. At thermal equilibrium the energy is equally distributed between the quadratures so that $\langle H_k \rangle / 2 = A_k \langle \delta n_k^2 \rangle = B_k \langle \theta_k^2 \rangle$. Let us compute the evolution of $\langle H_k \rangle$ under the effect of losses, assuming the loss rate is small compared to the mode frequency ω_k such that the equipartition holds for all times. First, the Hamiltonian parameter B_k changes according to $dB_k = -Kn_0^2 B_k dt$. Second, according to Eq. (3), the losses modify the distribution on the quadrature δn_k and we obtain $d\langle \delta n_k^2 \rangle / dt = -6Kn_0^2 \langle \delta n_k^2 \rangle + 3Kn_0^3$ [35]. Summing this two contributions leads to

$$\frac{d\langle H_k \rangle}{dt} = -\frac{7}{2} Kn_0^2 \langle H_k \rangle + \frac{3}{2} Kn_0^3 g. \quad (5)$$

From this equation, and using $dn_0/dt = -Kn_0^3$, we derive the evolution of the ratio $y = \langle H_k \rangle / (mc^2)$, where $c = \sqrt{gn_0/m}$ is the speed of sound. We find that y converges at long times towards the stationary value $y_\infty = 0.6$. Phononic modes typically have large occupation numbers for values of y of the order of or larger than 1 so that $\langle H_k \rangle \simeq k_B T$, where T is the mode temperature, and $y = k_B T / (mc^2)$.

In the presence of a harmonic longitudinal potential, calculations which assume that the loss rate is small enough

to neglect nonadiabatic coupling between modes, predict a stationary value of the ratio $k_B T / (mc_p^2)$ equal to $y_\infty = 0.70(1)$ [11], a value close to experimental data. For a more precise comparison of data with theory, we compute the time evolution of y according to the formula derived in [11], that takes into account the transverse swelling of the wave function which occurs in our data at large na . The results, shown in Fig. 3 for two different initial situations, is close to experimental data. Even at the beginning of the observed time evolution, the ratio $k_B T / (mc_p^2)$ in our gases is close to its asymptotic value. Data are taken only for gases that were sufficiently cooled by evaporative cooling to be in the quasicondensate regime, where both our thermometry and the theoretical description of the effect of losses are applicable. It occurs that, in our experiment, when the gas enters the quasicondensate regime the ratio $k_B T / (mc_p^2)$ is already close to 0.7.

In conclusion, we showed in this Letter that, under a three-body losses process, the temperature of a quasicondensate in the quasi-1D regime decreases in time. The ratio $k_B T / (mc_p^2)$ stays close to the predicted stationary value, which results from the competition between the cooling effect of losses and the heating due to the stochastic nature of losses. This work raises many different questions. First, the cooling mechanism presented in this Letter is not restricted to 1D quasicondensates and it would be interesting to investigate it in other regimes and dimensions, in particular as one approaches the Tonks regime of 1D gases. Second, while results presented in this Letter concern only the phononic modes, it would be interesting to study the effect of losses on higher energy modes. They might reach higher temperatures than phononic modes, as predicted for one-body losses [7], and the stability of such a nonthermal situation might be particular to the case of 1D gases. Finally, it is interesting to compare the three-body losses cooling to the commonly used evaporative cooling mechanism, which occurs via the removal of atoms whose energy is larger than the trap depth. Its efficiency drops drastically for temperatures lower than mc_p^2/k_B : the relevant excitations are then phonons, which do not extend beyond the condensate, and are thus very difficult to “evaporate.” Thus, obtaining, by means of evaporative cooling, temperatures lower than the asymptotic temperature imposed by three-body losses is not guaranteed.

This work was supported by Région Île de France (DIM NanoK, Atocirc project). The authors thank Dr. Sophie Bouchoule of C2N (centre nanosciences et nanotechnologies, CNRS/UPSUD, Marcoussis, France) for the development and microfabrication of the atom chip. Alan Durnez and Abdelmounaim Harouri of C2N are acknowledged for their technical support. The C2N laboratory is a member of RENATECH, the French national network of large facilities for micronanotechnology. M. Schemmer acknowledges support by the Studienstiftung des Deutschen Volkes.

- *isabelle.bouchoule@institutoptique.fr
- [1] J. Dalibard and C. Cohen-Tannoudji, *J. Opt. Soc. Am. B* **6**, 2023 (1989).
- [2] M.H. Anderson, J.R. Ensher, M.R. Matthews, C.E. Wieman, and E.A. Cornell, *Science* **269**, 198 (1995).
- [3] T. Weber, J. Herbig, M. Mark, H.-C. Nägerl, and R. Grimm, *Phys. Rev. Lett.* **91**, 123201 (2003).
- [4] D. Guéry-Odelin and G. V. Shlyapnikov, *Phys. Rev. A* **61**, 013605 (1999).
- [5] B. Rauer, P. Grišins, I.E. Mazets, T. Schweigler, W. Rohringer, R. Geiger, T. Langen, and J. Schmiedmayer, *Phys. Rev. Lett.* **116**, 030402 (2016).
- [6] P. Grišins, B. Rauer, T. Langen, J. Schmiedmayer, and I.E. Mazets, *Phys. Rev. A* **93**, 033634 (2016).
- [7] A. Johnson, S.S. Szigeti, M. Schemmer, and I. Bouchoule, *Phys. Rev. A* **96**, 013623 (2017).
- [8] M. Schemmer, A. Johnson, R. Photopoulos, and I. Bouchoule, *Phys. Rev. A* **95**, 043641 (2017).
- [9] Quasicondensates are characteristic of weakly interacting 1D Bose gases at low enough temperature: repulsive interactions prevent large density fluctuations such that the gas resembles locally a BEC, although it does not sustain true long range order [10].
- [10] D.S. Petrov, G.V. Shlyapnikov, and J.T.M. Walraven, *Phys. Rev. Lett.* **85**, 3745 (2000).
- [11] I. Bouchoule, M. Schemmer, and C. Henkel, *SciPost Phys.* **5**, 043 (2018).
- [12] 1D gases in cold atom experiment are well described by the Lieb-Liniger model. Since this model is integrable, thermalization of the gas is in fact not guaranteed.
- [13] E. H. Lieb and W. Liniger, *Phys. Rev.* **130**, 1605 (1963).
- [14] $\gamma = mg/(\hbar^2 n)$, where g is the interaction coupling constant, n is the linear density, m is the atomic mass, and \hbar is the Planck constant. We evaluate it using the linear density at the trap center.
- [15] The experiment is described in more details in [16].
- [16] T. Jacqmin, B. Fang, T. Berrada, T. Roscilde, and I. Bouchoule, *Phys. Rev. A* **86**, 043626 (2012).
- [17] J. Armijo, T. Jacqmin, K. Kheruntsyan, and I. Bouchoule, *Phys. Rev. A* **83**, 021605 (2011).
- [18] K. V. Kheruntsyan, D. M. Gangardt, P. D. Drummond, and G. V. Shlyapnikov, *Phys. Rev. Lett.* **91**, 040403 (2003).
- [19] Thermally activated phonons, however, prevent the establishment of a well-defined phase.
- [20] Density fluctuations are considered only in a coarse grained approximation, valid for lengths much larger than the interparticle distance.
- [21] We are far from confinement-induced resonances predicted in [22].
- [22] M. Olshanii, *Phys. Rev. Lett.* **81**, 938 (1998).
- [23] J. N. Fuchs, X. Leyronas, and R. Combescot, *Phys. Rev. A* **68**, 043610 (2003).
- [24] J. Söding, D. Guéry-Odelin, P. Desbiolles, F. Chevy, H. Inamori, and J. Dalibard, *Appl. Phys. B* **69**, 257 (1999).
- [25] B. L. Tolra, K. M. O'Hara, J. H. Huckans, W. D. Phillips, S. L. Rolston, and J. V. Porto, *Phys. Rev. Lett.* **92**, 190401 (2004).
- [26] According to 1D Bogoliubov calculations, $g^{(3)}(0) - 1 = 3[g^{(2)}(0) - 1] = \sqrt{\gamma}f[k_B T/(gn)]$, where f is a dimensionless function which takes the value $f(0.64) \simeq -1.5$. We then find *a posteriori* that $|g^{(3)}(0) - 1|$ spans the interval [0.02, 0.25] for our data.
- [27] L. Salasnich, A. Parola, and L. Reatto, *Phys. Rev. A* **65**, 043614 (2002).
- [28] We check the Gaussian ansatz gives correct results up to 20% for our parameters by comparing with numerical solution of the Gross-Pitaevskii equation.
- [29] A. Imambekov, I.E. Mazets, D. S. Petrov, V. Gritsev, S. Manz, S. Hofferberth, T. Schumm, E. Demler, and J. Schmiedmayer, *Phys. Rev. A* **80**, 033604 (2009).
- [30] S. Dettmer, D. Hellweg, P. Ryytty, J. J. Arlt, W. Ertmer, K. Sengstock, D. S. Petrov, G. V. Shlyapnikov, H. Kreutzmann, L. Santos, and M. Lewenstein, *Phys. Rev. Lett.* **87**, 160406 (2001).
- [31] S. Manz, R. Bücker, T. Betz, C. Koller, S. Hofferberth, I.E. Mazets, A. Imambekov, E. Demler, A. Perrin, J. Schmiedmayer, and T. Schumm, *Phys. Rev. A* **81**, 031610 (2010).
- [32] M. Schemmer, A. Johnson, and I. Bouchoule, *Phys. Rev. A* **98**, 043604 (2018).
- [33] These values have been obtained on the data points satisfying $n_p a < 0.2$ such that the effect of transverse swelling is small.
- [34] $g^{(2)}(0) = 1$ for $\gamma t_{\gamma\gamma} = 1.5(1)$ and, within Bogoliubov approximation $g^{(3)}(0)$ is linked to $g^{(2)}(0)$ (see Ref. [26]).
- [35] Losses are also responsible for an increase of the spread along the quadrature θ_k . However, the associated heating is negligible for phononic modes [11].

Cooling phonon modes of a Bose condensate with uniform few body losses

Isabelle Bouchoule^{1*}, Max Schemmer¹ and Carsten Henkel²

¹ Laboratoire Charles Fabry, Institut d'Optique, CNRS, Université Paris Saclay,

2 Avenue Augustin Fresnel, 91127 Palaiseau Cedex, France

² Institute of Physics and Astronomy, University of Potsdam,
Karl-Liebknecht-Str. 24/25, 14476 Potsdam, Germany

* isabelle.bouchoule@institutoptique.fr

Abstract

We present a general analysis of the cooling produced by losses on condensates or quasi-condensates. We study how the occupations of the collective phonon modes evolve in time, assuming that the loss process is slow enough so that each mode adiabatically follows the decrease of the mean density. The theory is valid for any loss process whose rate is proportional to the j th power of the density, but otherwise spatially uniform. We cover both homogeneous gases and systems confined in a smooth potential. For a low-dimensional gas, we can take into account the modified equation of state due to the broadening of the cloud width along the tightly confined directions, which occurs for large interactions. We find that at large times, the temperature decreases proportionally to the energy scale mc^2 , where m is the mass of the particles and c the sound velocity. We compute the asymptotic ratio of these two quantities for different limiting cases: a homogeneous gas in any dimension and a one-dimensional gas in a harmonic trap.



Copyright I. Bouchoule *et al.*

This work is licensed under the Creative Commons

[Attribution 4.0 International License](https://creativecommons.org/licenses/by/4.0/).

Published by the SciPost Foundation.

Received 04-07-2018

Accepted 26-10-2018

Published 02-11-2018

doi:[10.21468/SciPostPhys.5.5.043](https://doi.org/10.21468/SciPostPhys.5.5.043)



Check for updates

Contents

1	Introduction	2
2	Model	3
2.1	Stochastic dynamics of the particle density	3
2.2	Shot noise and phase broadening	4
2.3	Collective excitations	5
3	Cooling dynamics	6
3.1	Evolution of the excitations	6
3.2	Example: homogeneous gas	8
3.3	Example: 1D harmonic trap	10
4	Conclusion	12

A Reduction to low-dimensional hydrodynamics	13
B Hydrodynamic Bogoliubov modes	15
C Numerical calculation	16
References	16

1 Introduction

Despite their extensive use as quantum simulators or for quantum sensing, the temperatures reached in ultracold gases are not fully understood. Careful analyses of the cooling mechanisms have a long tradition in the cold atoms community, and the corresponding temperature limits constitute important benchmarks. The role of atom losses, however, is not yet elucidated, although such processes often play a role in quantum gas experiments. Different loss processes may occur. One-body processes are always present, their origin could be for instance a collision with a hot atom from the residual vapour. The familiar method of evaporative cooling involves losses that depend on the particle energy, a case we exclude in this paper. For clouds trapped in an internal state which is not the lowest energy state, such as low-field seekers in a magnetic trap, two-body (spin flip) collisions may provide significant loss. Finally, three-body processes where atoms recombine into strongly bound dimers are always present and are often the dominant loss mechanism. The effect of one-body losses for an ideal Bose gas was investigated in [1]. Loss processes involving more than one body are a source of heating for trapped thermal clouds, since they remove preferentially atoms in dense regions where the potential energy is low [2]. Here we are interested in the effect of losses in Bose condensates or quasi-condensates, and we focus on low energy collective modes, whose physics is governed by interactions between atoms.

One-body losses have recently been investigated for one-dimensional (1D) quasi-condensates [3–6]. Quasi-condensates characterise weakly interacting 1D Bose gases at low enough temperature: repulsive interactions prevent large density fluctuations such that the gas resembles locally a Bose Einstein condensate (BEC), although it does not sustain true long-range order [7, 8]. The above studies have focussed on low-energy excitations in the gas, the phonon modes. These correspond to hydrodynamic waves propagating in the condensate, where long-wavelength phase (or velocity) modulations are coupled to density modulations. On the one hand, losses reduce density fluctuations and thus remove interaction energy from each phonon mode. This decrease in energy, and thus of quasiparticle occupation, amounts to a cooling of the modes. On the other hand, the shot noise due to the discrete nature of losses feeds additional density fluctuations into the gas. This increases the energy per mode and amounts to heating. Theoretical studies [4–6], valid for one-body losses in 1D homogeneous gases, predict that as a net result of these competing processes, the system is cooling down in such a way that the ratio between temperature $k_B T$ and the chemical potential μ becomes asymptotically a constant (equal to 1). Many questions remain open. For instance, the role of longitudinal confinement has not been elucidated. Moreover, theoretical predictions for higher-body loss processes are lacking, although cooling by three-body losses was recently demonstrated experimentally [9].

In this paper, we generalise the theoretical results for one-body losses in homogeneous 1D gases and extend the analysis to a BEC or a quasicondensate in any dimension, for any

j -body loss process, and for homogeneous gases as well as clouds confined in a smoothly varying trapping potential. We concentrate on phonon modes and the loss rate is assumed small enough to ensure adiabatic following of each mode. Low-dimensional systems are realised experimentally by freezing the transverse degrees of freedom with a strong transverse confinement. However, in many experiments the interaction energy is not negligible compared to the transverse excitation frequencies such that the freezing is not perfect. The interactions then broaden the wave function in the transverse directions, and phonon modes in the weakly confined directions are associated with transverse breathing [10–12]. Our theory can take this into account with a modified equation of state: the quantities μ and mc^2 , where m is the atomic mass and c the sound velocity, equal for a strong transverse confinement, no longer coincide. We find that the evolution produced by losses is better described by a constant ratio $k_B T/(mc^2)$ instead of $k_B T/\mu$. The asymptotic ratio $k_B T/(mc^2)$ is computed for a few examples. Predictions from this paper have been tested successfully against recent experimental results obtained at Laboratoire Charles Fabry on the effect of three-body losses in a harmonically confined 1D Bose gas [9].

2 Model

We consider a condensate, or quasi-condensate, in dimension $d = 1, 2$ or 3 . The gas is either homogeneous or trapped in a smoothly varying potential $V(\mathbf{r})$. We assume it is subject to a j -body loss process of rate constant κ_j : the number of atoms lost per unit time and unit volume is $\kappa_j n^j$ where n is the density. This density includes fluctuations of quantum and thermal nature, and its average profile is denoted $n_0(\mathbf{r}, t)$. Instead of using involved powerful theoretical techniques such as the truncated Wigner approach [13, 14], we compute the effect of losses in this paper with a spatially coarse-grained approach that does not rely on involved theory and in which the approximations are made transparent. For the same pedagogical reason, we explicitly construct the phase-density representation of the collective excitations of the gas, in a similar way as is done for instance in [15].

2.1 Stochastic dynamics of the particle density

Let us first consider the sole effect of losses and fix a cell of the gas of volume Δ , small enough so that the density of the (quasi)condensate is about homogeneous in this volume, but large enough to accommodate many atoms. The atom number in the cell is $N = N_0 + \delta N$ where $N_0 = n_0 \Delta$ and $\delta N \ll N_0$ since the gas lies in the (quasi)condensate regime. (We drop the position dependence $n_0 = n_0(\mathbf{r})$ for the moment.) Since typical values of δN are much smaller than N_0 , one can assume without consequence that δN is a variable that takes discrete values between $-\infty$ and ∞ . Hence, one can define a phase operator θ , whose eigenvalues span the interval $[0, 2\pi[$ and that is canonically conjugate to δN . Losses will affect both the density fluctuations and the phase fluctuations.

We first concentrate on the effect of losses on density fluctuations. Consider a time step dt , small enough that the change dN in atom number is much smaller than N , but large enough such that dN is much larger than 1. After the time step, we have

$$dN = -K_j N^j dt + d\xi, \tag{1}$$

where $K_j = \kappa_j / \Delta^{j-1}$. Here, $d\xi$ is a random number with vanishing mean value that translates the shot noise associated with the statistical nature of losses. The number of loss events during the small step dt is Poisson distributed so that the variance of $d\xi$ relates to the mean number of lost atoms by

$$\langle d\xi^2 \rangle = j K_j N^j dt \simeq j K_j N_0^j dt, \tag{2}$$

the factor j coming from the fact that at each event, j atoms are lost. The evolution of fluctuations in the atom number is obtained from $d\delta N = dN - dN_0$, where dN_0 is the change of the mean number, equal to $dN_0 = -K_j N_0^j dt$ in the lowest order in δN . Expanding N^j in Eq.(1) to first order in δN , we obtain the following evolution for the density fluctuation $\delta n = \delta N/\Delta$:

$$d\delta n = -j\kappa_j n_0^{j-1} \delta n dt + d\eta, \tag{3}$$

where $d\eta = d\xi/\Delta$ is a random variable of variance $\langle d\eta^2 \rangle = j\kappa_j n_0^j dt/\Delta$. The first term in the r.h.s, the drift term, decreases the density fluctuations. It will thus reduce the interaction energy associated to fluctuations in the gas and produce cooling. The second term on the other hand increases the density fluctuations in the gas which leads to heating.

2.2 Shot noise and phase broadening

We now compute the effect of losses on the phase fluctuations, following an approach similar to Ref. [16]. For this purpose, one imagines that one records the number of lost atoms during dt . This measurement increases the knowledge about N , and thus δN . To quantify this increase of knowledge, we use the Bayes formula

$$P(\delta N|N_l) = \frac{P(\delta N)}{\int d(\delta N') P(N_l|\delta N')} P(N_l|\delta N), \tag{4}$$

where $P(\delta N)$ is the initial probability of having an atom number $N = N_0 + \delta N$, and $P(N_l|\delta N)$ is the probability that a number N_l of atoms will be lost, given that the initial atom number was $N_0 + \delta N$. Finally, $P(\delta N|N_l)$ is the probability that the final number is $N_0 - N_l + \delta N$, knowing the fact that N_l atom have been lost. As argued above, the Poissonian nature of the loss process and the assumption that the number of lost atoms is large compare to one, imply the Gaussian distribution

$$P(N_l|\delta N) \simeq \frac{1}{\sqrt{2\pi}\sigma_l} e^{-(N_l - K_j N^j dt)^2 / (2\sigma_l^2)}, \tag{5}$$

where $N = N_0 + \delta N$ and $\sigma_l^2 = jK_j N_0^j dt$. Expanding N^j around N_0^j and introducing $\overline{\delta N} = N_l / (jK_j N_0^{j-1} dt) - N_0/j$, one has

$$\frac{(N_l - K_j N^j dt)^2}{\sigma_l^2} \simeq \frac{(\overline{\delta N} - \delta N)^2}{\sigma_{\delta N}^2}, \tag{6}$$

where

$$\sigma_{\delta N}^2 = \frac{N_0}{jK_j N_0^{j-1} dt}. \tag{7}$$

Thus, according to Eq.(4), the width of the distribution in δN is multiplied by a function of rms width $\sigma_{\delta N}$ after recording the number of lost atoms. This narrows the number distribution and must be associated with a broadening in the conjugate variable, θ , lest the uncertainty relations are violated. The phase broadening must be equal to

$$\langle d\theta^2 \rangle = \frac{1}{4\sigma_{\delta N}^2} = \frac{j\kappa_j n_0^{j-1}}{4n_0\Delta} dt. \tag{8}$$

This spreading of the phase results from the shot noise in the loss process.

In the following, keeping in mind that only length scales larger than the interparticle distance have to be considered, we go to the continuous limit. The factors $1/\Delta$ in the variance

for $d\eta$ in Eq.(3) and in the phase diffusion of Eq.(8) then turn into

$$\langle d\eta(\mathbf{r})d\eta(\mathbf{r}') \rangle = j\kappa_j n_0^j \delta(\mathbf{r}-\mathbf{r}')dt, \quad (9)$$

$$\langle d\theta(\mathbf{r})d\theta(\mathbf{r}') \rangle = \frac{j}{4}\kappa_j n_0^{j-2} \delta(\mathbf{r}-\mathbf{r}')dt. \quad (10)$$

Both diffusion terms are due to the quantised nature of the bosonic field, namely the discreteness of atoms. Their effects become negligible compared to the drift term in Eq. (3) in the classical field limit, i.e. $n_0 \rightarrow \infty$ at fixed typical density fluctuations $\delta n/n_0$. Note finally that these results could also have been obtained using a truncated Wigner approach [13,14], using approximations based on the relation $\delta n \ll n_0$.

Before going on, let us make a remark concerning gases in reduced dimension. An effective 1D (resp. 2D) gas is obtained using a strong transverse confinement in order to freeze the transverse degree of freedom: the atoms are in the transverse ground state of the confining potential, of wave function $\psi(x_\perp)$. In the case of j -body losses with $j > 1$, the loss process a priori modifies the transverse shape of the cloud since it occurs preferentially at the center, where the density is the highest. In other words, it introduces couplings towards transverse excitations. We assume here the loss rate to be much smaller than the frequency gap ω_\perp between the transverse ground and first excited states. Then the coupling to transverse excitations has negligible effects, and the above analysis of the effect of losses also holds for the effective 1D (resp. 2D) gas, provided $\kappa_j = \kappa_j^{3D} \int d^2x_\perp |\psi(x_\perp)|^{2j}$ (resp. $\kappa_j = \kappa_j^{3D} \int dx_\perp |\psi(x_\perp)|^{2j}$), where κ_j^{3D} is the rate constant coefficient for the 3D gas.

2.3 Collective excitations

Let us now take into account the dynamics of the gas. Under the effect of losses the profile $n_0(\mathbf{r}, t)$ evolves in time and, except for a homogeneous system, a mean velocity field appears, generated by a spatially dependent phase $\theta_0(\mathbf{r}, t)$. Here we assume the loss rate is small enough so that, at any time, $n_0(\mathbf{r})$ is close to the equilibrium profile. We moreover assume the potential varies sufficiently smoothly such that the equilibrium profile is obtained with the local density approximation. Then, at any time, $n_0(\mathbf{r})$ fulfills

$$\mu(n_0(\mathbf{r})) = \mu_p - V(\mathbf{r}), \quad (11)$$

where $\mu(n)$ is the chemical potential of a homogeneous gas of density n and μ_p is the peak chemical potential, which fixes the total atom number¹. In most cases $\mu = gn$ where g is the coupling constant. In 3D condensates, $g = 4\pi\hbar^2 a/m$ where a is the scattering length describing low-energy collisions. In situations where two (resp. one) degrees of freedom are strongly confined by a transverse potential of frequency ω_\perp , μ depends on a , on the linear (resp. surface) density n , and on ω_\perp . As long as $\hbar\omega_\perp \gg \mu$, the transverse cloud shape is close to that of the transverse ground state², and one recovers the expression $\mu = gn$ where the effective 1D (resp. 2D) coupling constant g depends only on a and on ω_\perp [17, 18]. At large densities, $\hbar\omega_\perp \sim \mu$, the transverse degrees of freedom are no longer completely frozen: interactions broaden the transverse wave function, and μ is no longer linear in n [11, 12]. We discuss one example in Sec.3.2.

To treat the dynamics around the average density $n_0(\mathbf{r}, t)$, a Bogoliubov approximation is valid since the gas is in the (quasi)condensate regime: one can linearise the equations of motion in the density and phase fluctuations $\delta n(\mathbf{r})$ and $\varphi(\mathbf{r}) = \theta - \theta_0$ [15, 19]. These equations

¹The peak density is reached at the position \mathbf{r}_p where V reaches its minimum value. We impose $V(\mathbf{r}_p) = 0$.

²We assume here that the transverse width of the cloud fulfills $l_\perp \gg a$ such that the effect of interactions is well captured treating the gas as a 3D gas.

involve the mean velocity field $\hbar\nabla\theta_0/m$. Here we assume the loss rate is small enough so that such terms are negligible. We moreover consider only length scales much larger than the healing length. Then, as detailed in Appendix A, the dynamics of $\delta n(\mathbf{r})$ and $\varphi(\mathbf{r})$ is governed by the hydrodynamic Hamiltonian

$$H_{\text{hdyn}} = \frac{\hbar^2}{2m} \int d^d\mathbf{r} n_0 (\nabla\varphi)^2 + \frac{m}{2} \int d^d\mathbf{r} \frac{c^2}{n_0} \delta n^2. \quad (12)$$

Here the speed of sound $c = c(\mathbf{r})$ is related to the local compressibility, $mc^2 = n_0\partial_n\mu$, evaluated at $n_0(\mathbf{r})$. At a given time, H_{hdyn} can be recast as a collection of independent collective modes. The collective modes are described by the eigenfrequencies ω_ν and the real functions g_ν [details in Appendix B]. They obey

$$\nabla \cdot (n_0 \nabla (\frac{c^2}{n_0} g_\nu)) = -\omega_\nu^2 g_\nu, \quad (13)$$

and are normalised according to

$$\delta_{\nu,\nu'} = \frac{m}{\hbar\omega_\nu} \int d^d\mathbf{r} \frac{c^2}{n_0} g_\nu(\mathbf{r}) g_{\nu'}(\mathbf{r}). \quad (14)$$

Then $H_{\text{hdyn}} = \sum_\nu H_\nu$, where

$$H_\nu = \frac{\hbar\omega_\nu}{2} (x_\nu^2 + p_\nu^2). \quad (15)$$

The dimensionless canonically conjugate quadratures x_ν and p_ν are related to δn and φ respectively. More precisely,

$$\begin{cases} \delta n(\mathbf{r}) = \sum_\nu x_\nu g_\nu(\mathbf{r}) \\ \varphi(\mathbf{r}) = \frac{mc^2}{n_0} \sum_\nu p_\nu \frac{g_\nu(\mathbf{r})}{\hbar\omega_\nu}, \end{cases} \quad (16)$$

which inverts into

$$\begin{cases} x_\nu = \frac{m}{\hbar\omega_\nu} \int d^d\mathbf{r} \frac{c^2}{n_0} \delta n(\mathbf{r}) g_\nu(\mathbf{r}) \\ p_\nu = \int d^d\mathbf{r} \varphi(\mathbf{r}) g_\nu(\mathbf{r}). \end{cases} \quad (17)$$

At thermal equilibrium, the energy in the mode ν is equally shared between both quadratures and, for temperatures $T \gg \hbar\omega_\nu$, one has $\langle H_\nu \rangle = T$.

3 Cooling dynamics

3.1 Evolution of the excitations

Let us consider the effect of losses on the collective modes. The loss process modifies in time the mean density profile and thus the two functions of \mathbf{r} , n_0 and c , that enter into the Hamiltonian Eq. (12). We however assume the loss rate is very low compared to the mode frequency and their differences $\omega_\nu - \omega_{\nu'}$, so that the system follows adiabatically the effect of these modifications. As a consequence, equipartition of the energy holds at all times for any collective mode ν , and the adiabatic invariant $A_\nu = \langle H_\nu \rangle / (\hbar\omega_\nu)$ is unaffected by the slow evolution of n_0 . The dynamics of A_ν is then only due to the modifications of $\delta n(\mathbf{r})$ and $\varphi(\mathbf{r})$ induced by the loss process (subscript l), namely

$$\frac{dA_\nu}{dt} = \frac{1}{2} \left(\frac{d\langle x_\nu^2 \rangle_l}{dt} + \frac{d\langle p_\nu^2 \rangle_l}{dt} \right). \quad (18)$$

Injecting Eq. (3) into Eq. (17), we obtain for the ‘density quadrature’

$$(dx_\nu)_l = \frac{m}{\hbar\omega_\nu} \int d^d\mathbf{r} \frac{c^2}{n_0} g_\nu(\mathbf{r}) \left(-j\kappa_j n_0^{j-1} \delta n(\mathbf{r}) dt + d\eta(\mathbf{r}) \right). \quad (19)$$

Using the mode expansion (16) for $\delta n(\mathbf{r})$ in the first term, we observe the appearance of couplings between modes. In the adiabatic limit (loss rate small compared to mode spacing), the effect of these couplings is however negligible. Then, Eq. (19) leads to

$$\frac{d\langle x_\nu^2 \rangle_l}{dt} = -\frac{2j\kappa_j m}{\hbar\omega_\nu} \langle x_\nu^2 \rangle \int d^d\mathbf{r} c^2 n_0^{j-2} g_\nu^2 + \frac{j\kappa_j m^2}{(\hbar\omega_\nu)^2} \int d^d\mathbf{r} c^4 n_0^{j-2} g_\nu^2. \quad (20)$$

Let us now turn to the phase diffusion associated with losses. It modifies the width of the conjugate quadrature p_ν , according to

$$\frac{d\langle p_\nu^2 \rangle_l}{dt} = \frac{j\kappa_j}{4} \int d^d\mathbf{r} n_0^{j-2} g_\nu^2. \quad (21)$$

The hydrodynamic modes are characterised by low energies, $\hbar\omega_\nu \ll mc^2$, when the speed of sound is evaluated in the bulk of the (quasi)condensate. Then $d\langle p_\nu^2 \rangle_l/dt$ gives a contribution that scales with the small factor $(\hbar\omega_\nu/mc^2)^2$ compared to the second term of Eq. (20). In other words one expects that the phase diffusion associated to the loss process gives a negligible contribution to the evolution of A_ν [Eq.(18)] for phonon modes³.

We see from Eq.(20) that the adiabatic invariant A_ν is actually changed by j -body losses. We now show that the decrease in the energy per mode $\langle H_\nu \rangle$ is better captured by the energy scale associated with the speed of sound, as their ratio will converge towards a constant during the loss process. More precisely, we introduce

$$y_\nu = \frac{\langle H_\nu \rangle}{mc^2} \simeq \frac{k_B T_\nu}{mc_p^2}, \quad (22)$$

where c_p is the speed of sound evaluated at the peak density n_p . The second expression is valid as long as the phonon modes stay in the classical regime, $\langle H_\nu \rangle \gg \hbar\omega_\nu$. From Eq. (18) and (20), neglecting the contribution of Eq.(21), we immediately obtain

$$\frac{d}{dt} y_\nu = \kappa_j n_p^{j-1} [-(j\mathcal{A} - \mathcal{C})y_\nu + j\mathcal{B}], \quad (23)$$

where the dimensionless parameters \mathcal{A} , \mathcal{B} and \mathcal{C} are

$$\mathcal{A} = \frac{m}{\hbar\omega_\nu} \int d^d\mathbf{r} \frac{c^2 n_0^{j-2}}{n_p^{j-1}} g_\nu^2(\mathbf{r}), \quad (24)$$

$$\mathcal{B} = \frac{m}{2\hbar\omega_\nu} \int d^d\mathbf{r} \frac{c^4 n_0^{j-2}}{c_p^2 n_p^{j-1}} g_\nu^2(\mathbf{r}), \quad (25)$$

$$\mathcal{C} = \frac{d \ln(mc_p^2/\hbar\omega_\nu)}{dN_{\text{tot}}} \int d^d\mathbf{r} \frac{n_0^j}{n_p^{j-1}}. \quad (26)$$

In general, all of them depend on ν but we omit the index ν for compactness. The term \mathcal{A} is the rate of decrease of y_ν , induced by the reduction of the density fluctuations under the loss

³At the border of the (quasi)condensate, where the density becomes small, the condition $\hbar\omega_\nu \ll mc^2$ breaks down, however. The effect of phase diffusion is more carefully evaluated in Sec.3.3.

process, normalised to $\kappa_j n_p^{j-1}$. The term \mathcal{B} originates from the additional density fluctuations induced by the stochastic nature of the losses. The term \mathcal{C} arises from the time dependence of the ratio $mc_p^2/\hbar\omega_\nu$. It is computed using the dependence of $mc_p^2/\hbar\omega_\nu$ on the total atom number, the latter evolving according to

$$\frac{dN_{\text{tot}}}{dt} = - \int d^d \mathbf{r} \kappa_j n_0^j. \quad (27)$$

Eqs. (23–26) constitute the main results of this paper. They have been solved numerically for the experimental parameters corresponding to the data of [9] ($j = 3$ and anisotropic harmonic confinement) and their predictions compare very well with experimental results.

We would like at this stage to make a few comments about these equations. First, the factor \hbar , although it appears explicitly in the equations, is not relevant since it is canceled by the \hbar contained in the normalisation (14) of the mode functions g_ν . Second, we note that \mathcal{A} , \mathcal{B} and \mathcal{C} are intensive parameters: they are invariant by a scaling transformation $V(\mathbf{r}) \rightarrow V(\lambda\mathbf{r})$ and depend only on the peak density n_p and on the shape of the potential. Finally, Eqs. (23–26) depend on ν and it is possible that the lossy (quasi-)condensate evolves into a non-thermal state where different modes acquire different temperatures. Such a non-thermal state of the gas is permitted within the linearised approach where modes are decoupled. In the examples studied below, however, it turns out that all hydrodynamic modes share about the same temperature⁴. In the following, we investigate the consequences of Eq. (23-26), considering different situations.

3.2 Example: homogeneous gas

In this case, density n_0 and speed of sound c are spatially constant. The collective modes are sinusoidal functions, labelled by ν and of wave vector \mathbf{k}_ν ⁵. The frequencies are given by the acoustic dispersion relation $\omega_\nu = c|\mathbf{k}_\nu|$ and the mode functions $g_{\nu c,s}(\mathbf{r})$ are normalised to

$$\int d^d \mathbf{r} g_\nu^2(\mathbf{r}) = \frac{\hbar\omega_\nu}{mc^2} n_0. \quad (28)$$

Then Eqs.(23-26) reduce to

$$\frac{d}{dt} y = \kappa_j n_0^{j-1} \left[-y \left(j - \frac{\partial \log c}{\partial \log n_0} \right) + j/2 \right], \quad (29)$$

which is the same for all modes ν . Let us consider the limit $\mu = gn_0$, valid in 3D gases, or in low-dimensional gases with strong transverse confinement (negligible broadening of the transverse wave function). Then $c \propto n_0^{1/2}$ and Eq. (29) shows that y tends at long times towards the asymptotic value

$$y_\infty = \frac{1}{2 - 1/j}, \quad (30)$$

independent of the mode energy⁴. For one-body losses, one recovers the result $y_\infty = 1$ [4, 5]. In the case of 3-body losses, one finds $y_\infty = 3/5$.

Let us now consider a quasi-low-dimensional gas, where transverse broadening of the wave function cannot be neglected. The logarithmic derivative in Eq.(29) is then no longer constant.

⁴ In the case of one-body losses, theories that go beyond the hydrodynamic approximation predict non-thermal states to appear, where the high-frequency modes reach higher temperatures than the phonon modes [4, 5].

⁵ For 1D gases, $\nu = (p, \sigma)$ where p is a positive integer and $\sigma = c$ or s depending whether we consider cosine or sine modes. The wave-vector is $k_\nu = 2p\pi/L$ where L is the length of the box, assuming periodic boundary conditions. This generalises to higher dimensions with $\nu = (p_1, \sigma_1, p_2, \sigma_2, p_3, \sigma_3)$ in 3D for instance.

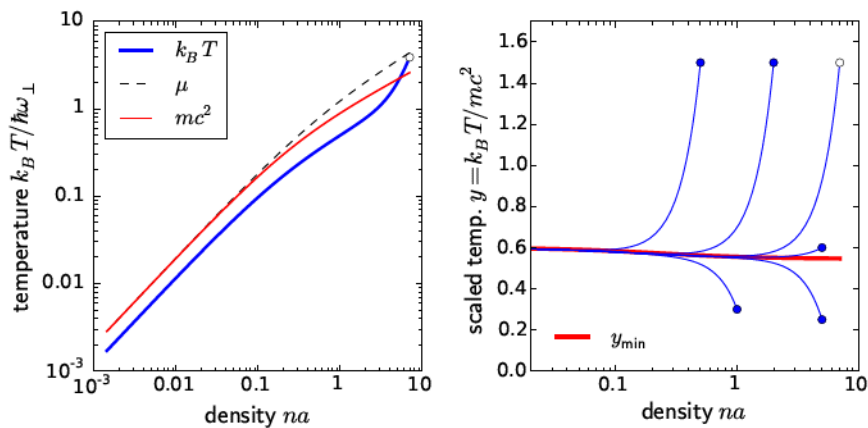


Figure 1: Cooling a quasi-1D gas, homogeneous along the axial direction, by three-body losses. The density is initially so high that transverse broadening is relevant [the chemical potential does not fulfill $\mu \ll \hbar\omega_{\perp}$]. Left: time evolution of the temperature (thick blue), shown versus the time decreasing density. Black dashed and thin red lines show the intrinsic energy scales μ and mc^2 . The system rapidly evolves into a dynamical state where the temperature follows the energy scale mc^2 , rather than the chemical potential. Right: evolution of the ratio $y = k_B T / mc^2$ vs. the density. The curves correspond to different initial values (marked with dots, the white dot corresponding to the parameters on the left). The thick red line shows the function y_{\min} that gives the positions of lowest values taken by y in the course of cooling. In this system (homogeneous along the axial direction), all hydrodynamic modes evolve with the same temperature.

We will focus on the case of a quasi-1D gas, as realised experimentally for instance in [9]. The effect of the transverse broadening is well captured by the heuristic equation of state [11, 12]

$$\mu = \hbar\omega_{\perp} (\sqrt{1 + 4n_0 a} - 1), \tag{31}$$

where ω_{\perp} is the frequency of the transverse confinement and a the 3D scattering length. Inserting into Eq. (29), one can compute the evolution of y . The transverse broadening also modifies the rate coefficient κ_j , making it density-dependent. However, re-scaling the time according to $u = \int_0^t \kappa_j(\tau) n_p^{j-1} d\tau = \ln(n_0(0)/n_0(t))$, Eq. (29) transforms into

$$\frac{dy}{du} = -y \left(j - 1/2 + \frac{n_0(0)a e^{-u}}{1 + 4n_0(0)a e^{-u}} \right) + j/2 \tag{32}$$

and no longer depends on κ_j . Fig.1 shows the solution of this differential equation in the case of 3-body losses, and for a few initial situations, namely different values of y and $n_0 a$ (right plot). The asymptotic value $y = y_{\infty}$ is always reached at long times since the transverse broadening then becomes negligible. Note that in distinction to pure 1D gases, the effect of transverse broadening allows the system to reach transiently lower scaled temperatures $y < y_{\infty}$, even when starting at values of y larger than y_{∞} . More precisely, let us denote $y_{\min}(n_0) = j/2 / (j - 1/2 + an_0 / (1 + 4an_0))$. When starting with $y > y_{\min}$, the lowest value of y is reached for some (non-vanishing) density, and it falls on the curve y_{\min} . For $j = 3$, one find that y_{\min} varies between $y_{\infty} = 0.6$ and $6/11 \simeq 0.55$. Thus, the coldest temperatures in the course of the loss process never deviate by more than 10% from the asymptotic value 0.6: the impact of transverse swelling is relatively small. Note that, if one considered the scaled temperature T/μ rather than y , much larger deviations would appear.

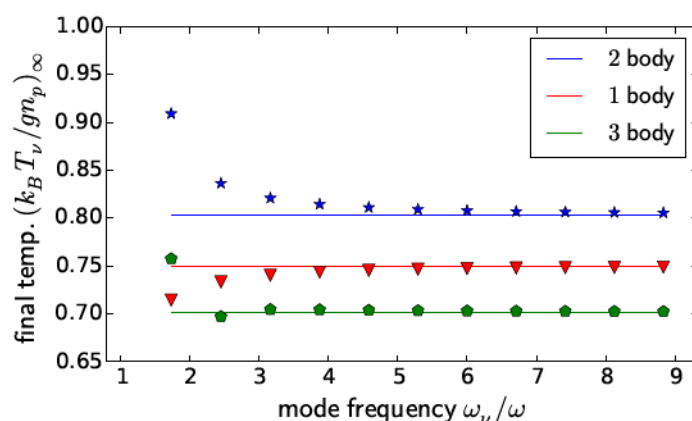


Figure 2: Asymptotic ratio $y_\infty = k_B T_\nu / mc^2$ for hydrodynamic collective modes of a 1D quasi-condensate confined in a harmonic trap, for 1-body (red), 2-body (blue) and 3-body (green) losses. The modes are labeled by their eigenfrequencies $\omega_\nu = \omega \sqrt{\nu(\nu+1)}/2$ and we only consider $\nu \geq 2$. Symbols: calculation based on the Legendre polynomials of Eq.(34), inserted into Eqs. (24, 25). Solid lines: large- ν approximation given by Eq. (36) with values $y_\infty = 3/4, 45/56, 525/748$ for $j = 1, 2, 3$.

3.3 Example: 1D harmonic trap

We consider a 1D gas confined in a harmonic potential of trapping frequency ω . We assume for simplicity a pure 1D situation with $\mu = gn = mc^2$. In the Thomas-Fermi approximation, the mean density profile is

$$n_0(z) = n_p(1 - (z/R)^2), \quad |z| \leq R, \quad (33)$$

where n_p is the peak density and $R = \sqrt{2gn_p/(m\omega^2)}$ is the axial radius of the quasicondensate. From Eq.(13), we recover the known result that the hydrodynamic modes are described by the Legendre polynomials P_ν , and the eigenfrequencies are $\omega_\nu = \omega \sqrt{\nu(\nu+1)}/2$ [7, 20]. A trivial calculation using $N_{\text{tot}} = \frac{4}{3}n_p R \propto c_p^3$ and the substitution $z = R \cos \alpha$ gives $\mathcal{C} = \int_0^{\pi/2} d\alpha \sin^{2j+1} \alpha = 2/3, 8/15, 16/35$ for $j = 1, 2, 3$. To compute \mathcal{A} and \mathcal{B} , one needs the exact expression of g_ν , which according to the normalisation (14) can be written

$$g_\nu(z) = \sqrt{\frac{\hbar\omega_\nu}{2gR}} \sqrt{2\nu+1} P_\nu(z/R). \quad (34)$$

Inserting this expression, together with Eq. (33), into the integrals (24) and (25), we find that \mathcal{A} , \mathcal{B} , and \mathcal{C} are time-independent. Thus y tends at long times towards the asymptotic value $y_\infty = j\mathcal{B}/(j\mathcal{A} - \mathcal{C})$. For large ν , one can use the asymptotic expansion [21]

$$P_\nu(\cos \alpha) \simeq \left(\frac{2}{\pi(\nu + \frac{1}{2}) \sin \alpha} \right)^{1/2} \cos \phi_\nu, \quad (35)$$

with $\phi_\nu = (\nu + \frac{1}{2})\alpha - \frac{1}{4}\pi$. Moreover the fast oscillations of $P_\nu(\cos \alpha)$ can be averaged out in the calculation of the coefficients \mathcal{A} and \mathcal{B} . Then \mathcal{A} and \mathcal{B} no longer depend on ν , so that y_∞ is identical for all modes, and we find

$$y_\infty \simeq \frac{\frac{j}{\pi} \int_0^{\pi/2} d\alpha \sin^{2j} \alpha}{\frac{2j}{\pi} \int_0^{\pi/2} d\alpha \sin^{2j-2} \alpha - \int_0^{\pi/2} d\alpha \sin^{2j+1} \alpha}. \quad (36)$$

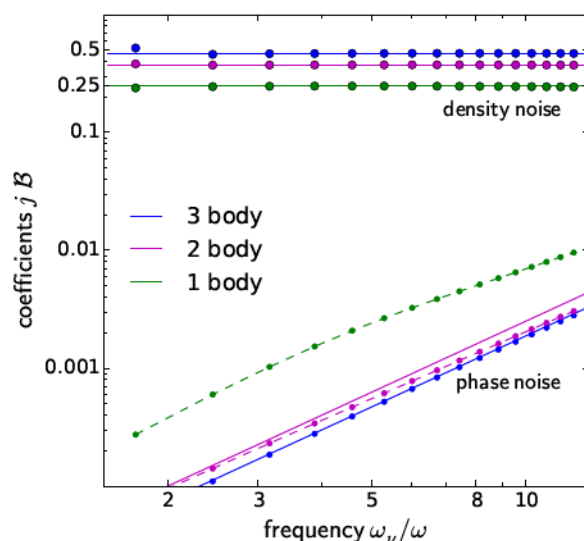


Figure 3: Diffusion of density and phase quadratures associated with many-body loss in a one-dimensional gas trapped in a harmonic potential. We plot the dimensionless coefficients $j\mathcal{B}$ [Eq.(25)] and $j\mathcal{B}_\varphi$ [Eq.(37)] that are proportional to the shot noise projected onto the corresponding quadratures. Symbols: numerically computed mode functions, improving upon the hydrodynamic approximation. Solid lines: approximate results based on the Legendre modes (34). Dashed lines: guide to the eye. Parameters: strictly 1D equation of state $\mu = gn$, peak chemical potential $\mu_p \approx gn_p = 100 \hbar\omega$.

For one- and three-body losses, this gives $y_\infty = 3/4 = 0.75$ and $y_\infty = 525/748 \simeq 0.701$, respectively. This asymptotic result is compared to calculations using the expression Eq. (34) in Fig. 2. We find very good agreement as soon as the mode index is larger than 5.

To conclude this example, we come back to the diffusive dynamics of the ‘phase quadratures’ p_ν we neglected so far. In the case of one-body losses, however, it happens that the integral (21) does not converge: while the mode function $g_\nu(z)$ [Eq.(34)] remains finite at the condensate border $z \rightarrow \pm R$, the integrand $n_0^{j-2}(z)g_\nu^2(z)$ is not integrable for $j = 1$. This is actually an artefact of the hydrodynamic approximation, which breaks down at the border of the condensate.

We have performed numerical calculations of the collective excitations by solving the Bogoliubov equations⁶. The mode functions $g_\nu(z)$ are defined according to Eq.(61): they extend smoothly beyond the Thomas-Fermi radius and match well with the Legendre polynomials (34) within the bulk of the gas. The resulting values for the parameter \mathcal{B} [Eq.(25)] are shown in Fig.3: they depend very weakly on the mode index ν and are well described by the approximate calculation based on the Legendre modes mentioned after Eq.(35) (solid lines). In the lower part of the figure, the corresponding values for the diffusion coefficient originating from phase noise are shown, namely the parameter

$$\mathcal{B}_\varphi = \frac{\hbar\omega_\nu}{8mc_p^2} \int d^d\mathbf{r} \frac{n_0^{j-2}}{n_p^{j-1}} g_\nu^2(\mathbf{r}). \quad (37)$$

They remain at least one order of magnitude below. For losses involving more than one particle, the approximation, under which the functions g_ν are given by the Legendre polynomials,

⁶For the condensate wave-function, we also went beyond the Thomas-Fermi approximation by allowing for a ‘spill-over’ of the condensate density beyond the inverted parabola.

gives a convergent integral in Eq.(37). The result is shown as solid lines for two- and three-body losses, where we made the additional approximation Eq. (35) on the Legendre functions and we averaged out the oscillating part. We find that the Legendre approximation performs better for three-body losses than for 2-body losses, which is expected since a stronger weight is given to the bulk rather than the edge of the condensate. In conclusion of this numerical study, we verified the validity of the assumption that, for phonon modes, the phase diffusion term gives negligible contribution to the evolution of y . This term becomes noticeable when one leaves the phonon regime $\hbar\omega_\nu \ll mc^2$. Then, one should go beyond the hydrodynamic Hamiltonian Eq.(12) to properly compute the mode dynamics.⁷

4 Conclusion

In this paper, we construct a stochastic model to describe the effect of losses on the hydrodynamic collective modes of condensates or quasicondensates. Explicit formulas for cooling and diffusion of the density and phase quadratures are derived. They provide the behaviour of the mode temperature T with time. We show that T becomes proportional to the energy scale mc^2 where c is the hydrodynamic speed of sound. The asymptotic ratio $k_B T/(mc^2)$ is computed explicitly in different situations and for different j -body processes. These results are in good agreement with recent experiments performed in Laboratoire Charles Fabry [9] where three-body losses provided the dominant loss channel.

This work raises many different questions and remarks. First, it is instructive to investigate the evolution of the ratio $D = \hbar^2 n^{2/d}/(mk_B T)$, where d is the gas dimension, since D quantifies the quantum degeneracy of the gas.⁸ Let us focus for simplicity on a homogeneous system and use $mc^2 = gn$. Once the ratio $k_B T/(mc^2)$ has become stationary, we find that D increases in time for 3-dimensional gases, while it decreases for one-dimensional gases. Starting with a 1D Bose gas in the quasi-condensate regime, losses let the quantity $D\gamma$ reach a stationary value of order one, but increase the dimensionless interaction parameter $\gamma = mg/(\hbar^2 n)$. When γ , from values much smaller, approaches 1, the gas lies at the crossover between four regimes: the quasi-condensate ($\gamma \ll 1, D\sqrt{\gamma} \gg 1$), the quantum-degenerate ideal Bose gas ($D\sqrt{\gamma} \ll 1, D \gg 1$), the non-degenerate ideal Bose gas ($D\gamma^2 \ll 1, D \ll 1$) and the Tonks-Girardeau regime ($\gamma \gg 1, D\gamma^2 \gg 1$). At later times, one expects the cloud to leave the quasi-condensate regime and we believe it becomes a non-degenerate ideal Bose gas. Second, the effect of losses on high-frequency modes, not described by our hydrodynamic model, leads a priori to higher temperatures; this was investigated for 1D gases subject to one-body losses [5]. The gas is then described by a generalised Gibbs ensemble where different collective modes experience different temperatures. This non-thermal state is even long lived in 1D quasicondensates [5]. While the calculations presented here are formally valid for higher dimensions, efficient coupling between modes may reduce their relevance, since such coupling favours a common temperature. It is an open question whether our methods could be extended to the case of evaporative cooling where the one-body loss rate is energy- or position-dependent. This mechanism may play a role in experiments where temperatures as low as $k_B T \approx 0.3 mc^2$ have been observed, lower than the predicted temperatures for uniform losses [3]. Finally, it would be interesting to extend this work to different regimes of the gas. For instance, one may ask how the effect of losses transforms as one goes from a quasi-condensate to the ideal gas regime. The approximation of weak density fluctuations then clearly becomes invalid. One could also investigate losses at even lower densities, where the 1D gas enters the fermionised (or Tonks-Girardeau)

⁷A full treatment going beyond the hydrodynamic approximation has been performed for one-body losses in homogeneous 1D quasi-condensates [4, 5].

⁸Note however that the temperature used in the definition of D refers to the phononic modes only.

regime. Here, one expects that the losses act in a similar way as in a non-interacting Fermi gas. One-body losses, for example, should then produce heating, since the temperature increases as the degeneracy of an ideal Fermi gas decreases. Finally, it would be interesting to investigate whether the results presented here may also cover interacting Fermi gases in the superfluid regime.

Acknowledgements

M. S. gratefully acknowledges support by the *Studienstiftung des deutschen Volkes*. This work was supported by Région Île de France (DIM NanoK, Atocirc project). The work of C. H. is supported by the *Deutsche Forschungsgemeinschaft* (grant nos. Schm 1049/7-1 and Fo 703/2-1).

A Reduction to low-dimensional hydrodynamics

As mentioned in the main text, we assume the loss process is slow enough so that, first, the mean profile at each time is very close to the equilibrium profile with the same atom number, and second, we can safely neglect any mean velocity field when computing the time evolution of the fluctuating fields δn , φ . The evolution equations $\partial \delta n / \partial t$ and $\partial \varphi / \partial t$ are thus, at a given time, equal to those for a time-independent quasi-condensate. In the purely 3D, 2D and 1D cases, for contact interactions, we can use the well known results based on Bogoliubov theory. We then find that the equation of state takes the form $\mu = gn$ and $\partial \delta n / \partial t$ and $\partial \varphi / \partial t$ derive from Eq. (12) for the long-wavelength modes.

Let us now consider the case where the gas is confined strongly enough in 1 or 2 dimensions, such that the relevant low-lying excitations are of planar or axial nature. We allow, however, for a transverse broadening of the wave function under the effect of interactions. We show below that the equations of motion for the slow phononic modes, for which the transverse shape adiabatically follows the density oscillations, also derive from Eq. (12). The proof given here is complementary to Refs. [10, 11] because it does not need an explicit model about the shape of the transverse wave function. In order to simplify the notations, we restrict ourselves to the quasi-1D situation. The derivation can be easily translated to quasi-2D situations.

We thus consider a gas confined in a separable potential consisting of a strong transverse confinement and a smooth longitudinal confinement. The equilibrium density distribution of the quasi-condensate is $|\phi_0(x, y, z)|^2$ where the real function $\phi_0(x, y, z)$ obeys the stationary Gross-Pitaevskii equation

$$\left(-\frac{\hbar^2}{2m} \partial_z^2 - \frac{\hbar^2}{2m} \Delta_{\perp} + V_{\perp}(x, y) + V(z) + g|\phi_0|^2 - \mu_p \right) \phi_0 = 0. \quad (38)$$

Here $g = 4\pi\hbar^2 a/m$ is the 3D coupling constant with a the zero-energy scattering length. Within the Bogoliubov theory, the evolution of excitations is governed by the equations [19]

$$\begin{cases} i\hbar \partial_t \tilde{f}^+ &= \left(-\frac{\hbar^2}{2m} \partial_z^2 - \frac{\hbar^2}{2m} \Delta_{\perp} + V_{\perp}(x, y) + V(z) + g|\phi_0|^2 - \mu_p \right) \tilde{f}^- \\ i\hbar \partial_t \tilde{f}^- &= \left(-\frac{\hbar^2}{2m} \partial_z^2 - \frac{\hbar^2}{2m} \Delta_{\perp} + V_{\perp}(x, y) + V(z) + 3g|\phi_0|^2 - \mu_p \right) \tilde{f}^+. \end{cases} \quad (39)$$

The field operators are half sum and difference of the fluctuating field operators $\delta\psi$ and $\delta\psi^\dagger$. \tilde{f}^+ is linked to density fluctuations and \tilde{f}^- to phase fluctuations.

Since we assume that the axial variation is slow compared to the transverse one, the solution ϕ_0 can be approximated by a function ψ that depends on the axial coordinate z only via a local chemical potential

$$\phi_0(x, y, z) \simeq \psi(x, y; \mu), \quad \mu = \mu_p - V(z). \quad (40)$$

Here, ψ solves the Gross-Pitaevskii equation for an axially homogeneous system:

$$\left(-\frac{\hbar^2}{2m} \Delta_{\perp} + V_{\perp}(x, y) + g|\psi|^2 - \mu \right) \psi = 0. \quad (41)$$

This procedure is consistent, e.g., with making the Thomas-Fermi approximation in the axial direction. Solving this equation yields the local chemical potential as a function of the axial (average) density $\mu = \mu(n_0)$ with

$$n_0(z) = \int dx dy |\phi_0(x, y, z)|^2 \simeq \int dx dy |\psi(x, y; \mu)|^2. \quad (42)$$

This motivates the following separation *Ansatz* for the Bogoliubov functions in Eq.(39):

$$\begin{cases} \tilde{f}^+ = \partial_{\mu} \psi \partial_n \mu F^+ \\ \tilde{f}^- = i \phi_0 F^- \end{cases} \quad (43)$$

where the functions F^+ and F^- depend only on z and the derivative $\partial_n \mu$ is evaluated at the local density n_0 . Inserting this into the second line of Eq.(39), we find

$$-\phi_0 \hbar \partial_t F^- = \left(-\frac{\hbar^2}{2m} \partial_z^2 - \frac{\hbar^2}{2m} \Delta_{\perp} + V_{\perp}(x, y) + V(z) + 3g|\phi_0|^2 - \mu_p \right) (\partial_{\mu} \psi \partial_n \mu F^+). \quad (44)$$

The action of this operator on $\partial_{\mu} \psi$ can be worked out by differentiating Eq. (41) versus μ : this gives

$$\left(-\frac{\hbar^2}{2m} \Delta_{\perp} + V_{\perp}(x, y) + 3g|\psi|^2 - \mu \right) \partial_{\mu} \psi = \psi \simeq \phi_0. \quad (45)$$

Eq.(44) thus simplifies into

$$-\phi_0 \hbar \partial_t F^- = -\frac{\hbar^2}{2m} \partial_z^2 (\partial_{\mu} \psi \partial_n \mu F^+) + \phi_0 \partial_n \mu F^+. \quad (46)$$

To find a closed equation for the axial dynamics, we multiply with $\psi(x, y; \mu)$ and integrate over the transverse coordinates. Using Eq.(42) and its derivatives with respect to μ and z , we find the identities

$$\int dx dy \phi_0 \partial_{\mu} \psi = \frac{1}{2} \partial_{\mu} n_0 = \frac{1}{2 \partial_n \mu}, \quad \int dx dy \phi_0 \partial_z \phi_0 = \frac{1}{2} \partial_z n_0. \quad (47)$$

Using the first one, Eq.(46) becomes:

$$-\hbar \partial_t F^- = -\frac{\hbar^2}{4mn_0} \partial_z^2 F^+ + \partial_n \mu F^+ \simeq -\partial_n \mu F^+, \quad (48)$$

where in the second step, we took the long-wavelength limit.

Let us now insert the *Ansatz* (43) into the first line of Eq.(39):

$$\hbar \partial_{\mu} \psi \partial_n \mu \partial_t F^+ = \left(-\frac{\hbar^2}{2m} \partial_z^2 - \frac{\hbar^2}{2m} \Delta_{\perp} + V_{\perp}(x, y) + V(z) + g|\phi_0|^2 - \mu_p \right) (\phi_0 F^-). \quad (49)$$

The action of the operator in parentheses on ϕ_0 simply vanishes because this is the Gross-Pitaevskii equation (38). Since F^- does only depend on the axial coordinate, we are left with:

$$\partial_\mu \psi \partial_n \mu \partial_t F^+ = -\frac{\hbar}{m} (\partial_z \phi_0) \partial_z F^- - \frac{\hbar}{2m} \phi_0 \partial_z^2 F^-. \quad (50)$$

We again project out the transverse coordinates and use the identities (47). Combining the axial derivatives, we then have

$$\partial_t F^+ = -\frac{\hbar}{m} \partial_z (n_0 \partial_z F^-). \quad (51)$$

These calculations illustrate that the *Ansatz* of Eq.(43) captures well the axial and transverse dependence of the collective excitations in the low-dimensional gas. Note in particular how the density fluctuations (\tilde{f}^+) are accompanied by density-dependent changes in the transverse wave function.

To make contact with the hydrodynamic Hamiltonian (12), we need to relate F^+ and F^- to the low-dimensional density and phase fields, δn and φ . Bogoliubov theory tells us that three-dimensional density fluctuations are linked to \tilde{f}^+ via $\delta \rho = 2\phi_0 \tilde{f}^+$. Integrating $\delta \rho$ over the transverse plane, replacing \tilde{f}^+ by its *Ansatz* (43) and using Eq. (47), we obtain

$$F^+ = \delta n = n - n_0. \quad (52)$$

Phase fluctuations on the other hand are linked to \tilde{f}^- according to $\tilde{f}^- = i\phi_0 \varphi$. [Recall that the *ansatz* (43) assumes a uniform phase in the x, y plane.] Comparison with Eq. (43) gives immediately

$$F^- = \varphi. \quad (53)$$

Then Eq.(48) and Eq.(51) are precisely the evolution equations derived from the Hamiltonian (12).

B Hydrodynamic Bogoliubov modes

Here we consider low-energy modes of either a three-dimensional gas or low-dimensional gas, whose dynamics is described by the hydrodynamic approximation. More precisely, we diagonalize the Hamiltonian (12), for a given, time-independent, equilibrium profile $n_0(\mathbf{r})$. From Eq.(12) we derive the evolution equations

$$\frac{\partial}{\partial t} \begin{pmatrix} \delta n / \sqrt{n_0} \\ \sqrt{n_0} \varphi \end{pmatrix} = \mathcal{L} \begin{pmatrix} \delta n / \sqrt{n_0} \\ \sqrt{n_0} \varphi \end{pmatrix}, \quad (54)$$

where

$$\mathcal{L} = \begin{pmatrix} 0 & -\frac{\hbar}{m\sqrt{n_0}} \nabla \cdot \left(n_0 \nabla \left(\frac{1}{\sqrt{n_0}} \cdot \right) \right) \\ -mc^2/\hbar & 0 \end{pmatrix}. \quad (55)$$

The factors $\sqrt{n_0}$ are convenient to give the two components the same dimension and to symmetrize the differential operator that appears in \mathcal{L} . The two equations derived from Eq.(54) correspond to the hydrodynamic equations provided we identify $\hbar \nabla \varphi / m$ with the velocity: the first one is the continuity equation, the second one gives the Euler equation.

We build the mode expansion on pairs of real functions that form right eigenvectors of \mathcal{L} :

$$\mathcal{L} \begin{pmatrix} f_\nu^+ \\ if_\nu^- \end{pmatrix} = i\omega_\nu \begin{pmatrix} f_\nu^+ \\ if_\nu^- \end{pmatrix}. \quad (56)$$

Due to symmetry properties of \mathcal{L} , Eq.(56) entails the following properties: (a) $(f_v^+, -if_v^-)$ is a right eigenvector of \mathcal{L} of eigenvalue $-i\omega_v$; (b) (if_v^-, f_v^+) is a left eigenvector of same eigenvalue; and (c) different right eigenvectors of \mathcal{L} verify $\int d^d\mathbf{r} f_v^- f_{v'}^+ = 0$. It is convenient to consider those eigenvectors of \mathcal{L} which are normalized according to $\int d^d\mathbf{r} f_v^- f_v^+ = 1$. This yields the expansions

$$\begin{pmatrix} \delta n / \sqrt{n_0} \\ \sqrt{n_0} \varphi \end{pmatrix} = \frac{1}{\sqrt{2}} \sum_v \left\{ a_v \begin{pmatrix} f_v^+ \\ -if_v^- \end{pmatrix} + a_v^\dagger \begin{pmatrix} f_v^+ \\ if_v^- \end{pmatrix} \right\}, \quad (57)$$

which invert into

$$a_v = \frac{1}{\sqrt{2}} \int d^d\mathbf{r} \left(\frac{\delta n(\mathbf{r})}{\sqrt{n_0}} f_v^-(\mathbf{r}) + i\sqrt{n_0} \varphi(\mathbf{r}) f_v^+(\mathbf{r}) \right). \quad (58)$$

The normalisation of the eigenvectors and the relation $[\delta n(z), \varphi(z')] = i\delta(z - z')$ ensure $[a_{v'}, a_v^\dagger] = \delta_{v', v}$.

We introduce the function

$$g_v = \sqrt{n_0} f_v^+, \quad (59)$$

and use the relation $f_v^- = mc^2 f_v^+ / (\hbar\omega_v)$ that follows from the eigenvalue problem (56). Then the normalisation of g_v [Eq.(14)] follows from that of (f_v^+, if_v^-) . Defining the quadratures $x_v = (a_v + a_v^\dagger) / \sqrt{2}$ and $p_v = -i(a_v - a_v^\dagger) / \sqrt{2}$, the expansions (57) give Eqs.(16) of the main text.

C Numerical calculation

For the numerical results shown in Fig.3, we have solved the Gross-Pitaevskii equation in a 1D harmonic trap by minimising the corresponding energy functional: this gives a smooth density profile $n_0(z)$. The Bogoliubov equations are solved with a finite-difference scheme on a non-uniform grid. We get a frequency spectrum that coincides to better than one percent with the Legendre spectrum for all modes with $\hbar\omega_v \lesssim 0.1 gn_p$ (n_p is the peak density). The traditional Bogoliubov modes u_v and v_v are related to the eigenfunctions of Eq.(56) by

$$f_v^+ = \sqrt{2}(u_v + v_v), \quad (60)$$

$$f_v^- = (u_v - v_v) / \sqrt{2}. \quad (61)$$

Inserting this into Eq.(59) gives the modes g_v . We have checked for phonon excitations with frequencies $\hbar\omega_v \ll gn_p$, that the proportionality between f^+ and f^- [see after Eq.(59)] is an excellent approximation in the bulk of the condensate.


References

- [1] T. F. Schmidutz, I. Gotlibovych, A. L. Gaunt, R. P. Smith, N. Navon and Z. Hadzibabic, *Quantum Joule-Thomson effect in a saturated homogeneous Bose gas*, Phys. Rev. Lett. **112**, 040403 (2014), doi:[10.1103/PhysRevLett.112.040403](https://doi.org/10.1103/PhysRevLett.112.040403).
- [2] T. Weber, J. Herbig, M. Mark, H.-C. Nägerl and R. Grimm, *Three-body recombination at large scattering lengths in an ultracold atomic gas*, Phys. Rev. Lett. **91**, 123201 (2003), doi:[10.1103/PhysRevLett.91.123201](https://doi.org/10.1103/PhysRevLett.91.123201).

- [3] B. Rauer, P. Grišins, I. E. Mazets, T. Schweigler, W. Rohringer, R. Geiger, T. Langen and J. Schmiedmayer, *Cooling of a one-dimensional Bose gas*, Phys. Rev. Lett. **116**, 030402 (2016), doi:[10.1103/PhysRevLett.116.030402](https://doi.org/10.1103/PhysRevLett.116.030402).
- [4] P. Grišins, B. Rauer, T. Langen, J. Schmiedmayer and I. E. Mazets, *Degenerate Bose gases with uniform loss*, Phys. Rev. A **93**, 033634 (2016), doi:[10.1103/PhysRevA.93.033634](https://doi.org/10.1103/PhysRevA.93.033634) [[arXiv:1411.4946](https://arxiv.org/abs/1411.4946)].
- [5] A. Johnson, S. Szigeti, M. Schemmer and I. Bouchoule, *Long-lived non-thermal states realized by atom losses in one-dimensional quasi-condensates*, Phys. Rev. A **96**, 013623 (2017), doi:[10.1103/PhysRevA.96.013623](https://doi.org/10.1103/PhysRevA.96.013623) [[arXiv:1703.00322](https://arxiv.org/abs/1703.00322)].
- [6] M. Schemmer, A. Johnson, R. Photopoulos and I. Bouchoule, *Monte Carlo wavefunction description of losses in a 1D Bose gas and cooling to the ground state by quantum feedback*, Phys. Rev. A **95**, 043641 (2017), doi:[10.1103/PhysRevA.95.043641](https://doi.org/10.1103/PhysRevA.95.043641) [[arXiv:1702.01020](https://arxiv.org/abs/1702.01020)].
- [7] D. S. Petrov, G. V. Shlyapnikov and J. T. M. Walraven, *Regimes of quantum degeneracy in trapped 1D gases*, Phys. Rev. Lett. **85**, 3745 (2000), doi:[10.1103/PhysRevLett.85.3745](https://doi.org/10.1103/PhysRevLett.85.3745).
- [8] U. Al Khawaja, N. P. Proukakis, J. O. Andersen, M. W. J. Romans and H. T. C. Stoof, *Dimensional and temperature crossover in trapped Bose gases*, Phys. Rev. A **68**, 043603 (2003), doi:[10.1103/PhysRevA.68.043603](https://doi.org/10.1103/PhysRevA.68.043603).
- [9] M. Schemmer and I. Bouchoule, *Cooling a Bose gas by three-body losses* (2018), [arXiv:1806.09940](https://arxiv.org/abs/1806.09940).
- [10] S. Stringari, *Dynamics of Bose-Einstein condensed gases in highly deformed traps*, Phys. Rev. A **58**, 2385 (1998), doi:[10.1103/PhysRevA.58.2385](https://doi.org/10.1103/PhysRevA.58.2385).
- [11] L. Salasnich, A. Parola and L. Reatto, *Effective wave equations for the dynamics of cigar-shaped and disk-shaped Bose condensates*, Phys. Rev. A **65**, 043614 (2002), doi:[10.1103/PhysRevA.65.043614](https://doi.org/10.1103/PhysRevA.65.043614).
- [12] J. N. Fuchs, X. Leyronas and R. Combescot, *Hydrodynamic modes of a one-dimensional trapped Bose gas*, Phys. Rev. A **68**, 043610 (2003), doi:[10.1103/PhysRevA.68.043610](https://doi.org/10.1103/PhysRevA.68.043610).
- [13] A. A. Norrie, R. J. Ballagh, C. W. Gardiner and A. S. Bradley, *Three-body recombination of ultracold Bose gases using the truncated Wigner method*, Phys. Rev. A **73**, 043618 (2006), doi:[10.1103/PhysRevA.73.043618](https://doi.org/10.1103/PhysRevA.73.043618).
- [14] B. Opanchuk and P. D. Drummond, *Functional Wigner representation of quantum dynamics of Bose-Einstein condensate*, J. Math. Phys. **54**, 042107 (2013), doi:[10.1063/1.4801781](https://doi.org/10.1063/1.4801781).
- [15] C. Mora and Y. Castin, *Extension of Bogoliubov theory to quasicondensates*, Phys. Rev. A **67**, 053615 (2003), doi:[10.1103/PhysRevA.67.053615](https://doi.org/10.1103/PhysRevA.67.053615).
- [16] A. N. Korotkov, *Continuous quantum measurement of a double dot*, Phys. Rev. B **60**, 5737 (1999), doi:[10.1103/PhysRevB.60.5737](https://doi.org/10.1103/PhysRevB.60.5737).
- [17] D. S. Petrov, M. Holzmann and G. V. Shlyapnikov, *Bose-Einstein condensation in quasi-2D trapped gases*, Phys. Rev. Lett. **84**, 2551 (2000), doi:[10.1103/PhysRevLett.84.2551](https://doi.org/10.1103/PhysRevLett.84.2551).
- [18] M. Olshanii, *Atomic scattering in the presence of an external confinement and a gas of impenetrable bosons*, Phys. Rev. Lett. **81**, 938 (1998), doi:[10.1103/PhysRevLett.81.938](https://doi.org/10.1103/PhysRevLett.81.938).

- [19] L. P. Pitaevskii and S. Stringari, *Bose-Einstein condensation*, vol. 116 of *International Series of Monographs on Physics*, Oxford University Press, Oxford New York (2003).
- [20] T.-L. Ho and M. Ma, *Quasi 1 and 2d dilute Bose gas in magnetic traps: existence of off-diagonal order and anomalous quantum fluctuations*, *J. Low. Temp. Phys.* **115**, 61 (1999), doi:[10.1023/A:1021894713105](https://doi.org/10.1023/A:1021894713105)
- [21] Formula (18.15.E12) in Digital Library of Mathematical Functions, <http://dlmf.nist.gov>. We adjusted the prefactor to give the normalisation (14) when \cos^2 is averaged over.

Generalized Hydrodynamics on an Atom Chip

M. Schemmer,¹ I. Bouchoule,¹ B. Doyon,² and J. Dubail³¹Laboratoire Charles Fabry, Institut d'Optique, CNRS, Université Paris-Saclay, 91127 Palaiseau cedex, France²Department of Mathematics, King's College London, Strand, London WC2R 2LS, United Kingdom³Laboratoire de Physique et Chimie Théoriques, CNRS, Université de Lorraine, UMR 7019, F-54506 Vandoeuvre-les-Nancy, France (Received 24 October 2018; revised manuscript received 12 December 2018; published 5 March 2019)

The emergence of a special type of fluidlike behavior at large scales in one-dimensional (1D) quantum integrable systems, theoretically predicted in O. A. Castro-Alvaredo *et al.*, Emergent Hydrodynamics in Integrable Quantum Systems Out of Equilibrium, *Phys. Rev. X* **6**, 041065 (2016) and B. Bertini *et al.*, Transport in Out-of-Equilibrium XXZ Chains: Exact Profiles of Charges and Currents, *Phys. Rev. Lett.* **117**, 207201 (2016), is established experimentally, by monitoring the time evolution of the *in situ* density profile of a single 1D cloud of ⁸⁷Rb atoms trapped on an atom chip after a quench of the longitudinal trapping potential. The theory can be viewed as a dynamical extension of the thermodynamics of Yang and Yang, and applies to the whole range of repulsive interaction strength and temperature of the gas. The measurements, performed on weakly interacting atomic clouds that lie at the crossover between the quasicondensate and the ideal Bose gas regimes, are in very good agreement with the theory. This contrasts with the previously existing “conventional” hydrodynamic approach—that relies on the assumption of local thermal equilibrium—which is unable to reproduce the experimental data.

DOI: 10.1103/PhysRevLett.122.090601

The emergent hydrodynamic behavior of many interacting particles is a fascinating phenomenon: at the atomic level, all quantum (classical) systems are described by the Schrödinger (Newton) equation, yet these unique microscopic descriptions give rise to a wealth of different liquid and gas phases at larger scales, from the ideal gas to liquid water to plasmas to superfluid helium to Bose-Einstein condensates, to name but a few. Inferring the correct hydrodynamic behavior directly from the microscopic constituents of a many-body system is, in general, a very ambitious task that typically involves extensive numerical simulations and a hierarchy of different modelings on intermediate scales [1,2].

However, there exist a few simpler systems where the emergence of a special kind of hydrodynamics can be linked directly to the underlying microscopic rules [3]. One such system is the one-dimensional (1D) classical billiard, or hard-rod gas [3–5], whose hydrodynamic behavior, as seen below, is similar to that of the quantum system studied in this Letter. The hard-rod gas consists of N identical impenetrable rods of fixed diameter Δ that move along a line, and exchange their momenta upon colliding elastically. At large N , the 1D billiard admits a hydrodynamic description: in the limit of density variations of very long wavelength, the billiard can be described by a continuous distribution $\rho(x, v)$ of rods moving at velocity v around a position x and this distribution satisfies an exact evolution equation which resembles the Liouville equation for phase space densities, up to a renormalization of the bare velocity

v [see Eq. (2)]. The latter renormalization encodes the following microscopic mechanism: when one rod with velocity v hits another one with velocity $w < v$ from the left, they exchange their momenta. Equivalently, because all the rods are identical, one can think of the collision as an instantaneous exchange of their positions, as if the rod with bare velocity v jumped instantaneously by a distance Δ to the right. Thus, the time needed by that rod to travel a distance ℓ is not ℓ/v , but rather $(\ell - \Delta)/v$. For a finite density of rods, this results in each rod with bare velocity v moving at an effective velocity $v^{\text{eff}}(v)$, that depends on the distribution $\rho(x, v)$ [3–5]. In distributions of long wavelengths, the evolution equation for $\rho(x, v)$ becomes a hydrodynamic flow controlled by the local effective velocity v^{eff} . The 1D billiard thus exhibits an interesting hydrodynamic behavior that is straightforwardly related to its microscopics. Slight generalizations of that model exist, where the jumping distance Δ depends on the relative velocity $v - w$, which possess a similar hydrodynamic description [6].

Remarkably, the *same* emergent hydrodynamics was rediscovered in 2016 in the context of 1D quantum integrable models [7,8]—the resulting theoretical framework is now dubbed generalized hydrodynamics (GHD). Cold atom experiments offer a unique platform to test the validity of this theoretical breakthrough. Indeed 1D clouds are well described by the 1D Bose gas with contact repulsion [9–11], a paradigmatic integrable system known as the Lieb-Liniger model [12] whose large-scale dynamics

is argued to be given by GHD [7,13–22]. Many other integrable models are argued to be described by GHD, leading to intense research activity in the past two years [8,23–32].

The goal of this Letter is to establish *experimentally* GHD as the correct hydrodynamic description of the 1D Bose gas. To do so, we measure the *in situ* density profiles of a time-evolving 1D atomic cloud trapped on an atom chip, and compare the data with predictions from GHD. We contrast those predictions with the ones of the conventional hydrodynamic (CHD) approach—based on the assumption of local thermal equilibrium [33]—that has been frequently used [34–39]. Starting from a cloud at thermal equilibrium in a longitudinal potential $V(x)$, dynamics is triggered by suddenly quenching $V(x)$. We consider three types of quenches. The first is a 1D expansion of the cloud from an initial harmonic potential (Fig. 1); the second is a 1D expansion from a double-well potential (Fig. 3); the third is a quench from double-well to harmonic potential (Fig. 4). We find that only GHD is able to accurately describe the time evolution of the cloud beyond the harmonic case.

Generalized hydrodynamics.—The Hamiltonian that describes our atomic gas of N bosons of mass m confined in a potential $V(x)$ with contact repulsion is

$$H = -\frac{\hbar^2}{2m} \sum_{i=1}^N \partial_{x_i}^2 + g \sum_{i<j} \delta(x_i - x_j) + \sum_{i=1}^N V(x_i), \quad (1)$$

which reduces to the model solved by Lieb and Liniger [12] when $V(x) = 0$. As in any hydrodynamic approach, the idea is to trade that microscopic model for a simpler, long-wavelength, description in terms of continuous densities.

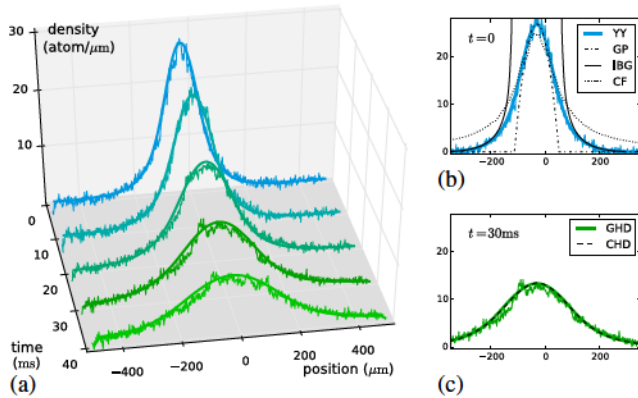


FIG. 1. (i) *In situ* density profile after longitudinal expansion from a harmonic trap of a 1D cloud of $N = 4600 \pm 100$ ^{87}Rb atoms; the smooth curve is the theoretical prediction of GHD and the noisy one is the experimental data. (ii) Initial profile obtained from the Yang-Yang equation of state (YY), Gross-Pitaevskii, ideal Bose gas, and classical field [40], with the same temperature and chemical potential as for YY. (iii) Evolution from the YY initial profile with GHD and conventional hydrodynamics.

The fluid consists of local “fluid cells” of size δx , with δx very short compared to the wavelength of density variations, but very long compared to microscopic lengths in the gas. The state inside each local fluid cell $[x, x + \delta x]$ is a macrostate of the Lieb-Liniger model that is entirely characterized by its distribution $\rho(x, v)$ of rapidities v , similarly to the celebrated thermodynamic Bethe ansatz of Yang and Yang [46,47] (as explained in Refs. [7,8], that these are the correct local macrostates can be seen as a consequence of recent results on “generalized thermalization” [48,49]). Semiclassically, one may view the rapidity v as the bare velocity of a *quasiparticle*. As in the 1D billiard, the velocity v gets renormalized in the presence of other quasiparticles, resulting in an effective velocity that is the solution of an integral equation [3,5,7,8],

$$v^{\text{eff}}(v) = v + \int dw \rho(w) \Delta(v-w) [v^{\text{eff}}(v) - v^{\text{eff}}(w)]. \quad (2a)$$

However, while in the classical billiard the jumping distance $\Delta(v-w)$ at each collision is a constant—the length of the rods—in the Bose gas it corresponds to the time delay resulting from the two-body scattering phase $\phi(v-w)$ through differentiation [12], $\Delta(v-w) = -(\hbar/m) \times \{[d\phi(v-w)]/[d(v-w)]\}$. This gives $\Delta(v-w) = -\{(2g/m)/[(g/\hbar)^2 + (v-w)^2]\}$ for the Dirac delta potential (see Ref. [6] for an extended discussion). The effective velocity enters the evolution equation for the distribution $\rho(x, v)$ as follows [7,8,13]:

$$\partial_t \rho + \partial_x [v^{\text{eff}} \rho] = \left(\frac{\partial_x V}{m} \right) \partial_v \rho. \quad (2b)$$

This resembles a Liouville equation for phase space densities of quasi-particles, although it is to be stressed that it is a Euler hydrodynamic equation, determining the evolution of the degrees of freedom emerging at large wavelengths. GHD consists of Eqs. (2a) and (2b). In practice, for a given initial distribution $\rho(x, v)$, the GHD equations can be efficiently solved numerically [6,14,17,19]; in this Letter we rely on a finite-difference method similar to the one discussed in Ref. [19]. Importantly, for our purposes, the atomic density $n(x)$ is obtained from the distribution $\rho(x, v)$ by integrating locally over all rapidities, $n(x) = \int dv \rho(x, v)$.

The atom chip.—Our experimental setup is described in detail in Ref. [50]. ^{87}Rb atoms are confined in a magnetic trap produced by microwires deposited on the surface of a chip. The transverse confinement is provided by three 1.3 mm long parallel wires (red wires in Fig. 2), which carry ac currents modulated at 400 kHz: atoms are guided along x , at a distance of $12\mu\text{m}$ above the central wire, with a transverse frequency ω_{\perp} which lies between 5 and 8 kHz. The modulation technique permits an independent control of the longitudinal potential $V(x)$, which is realized by two

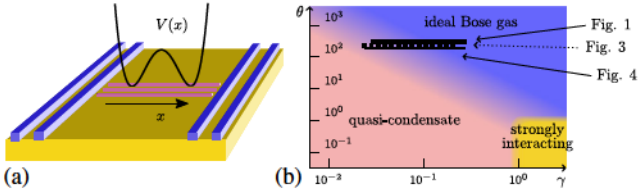


FIG. 2. (a) The atom chip setup with the four wires (blue) creating the longitudinal potential and the three wires (red) creating the strong transverse confinement. (b) Position of our three data sets in the thermal equilibrium phase diagram of the Lieb-Liniger gas with $\gamma = mg/(\hbar^2 n)$ and $\theta = 2\hbar^2 k_B T/(mg^2)$ [51]. At the center of the cloud γ is of order 10^{-2} , but it increases in the wings as the density decreases; we display the segments $[\gamma_{\min}, \gamma_{\min}/10]$ corresponding to a local density $n(x)$ not smaller than a tenth of the maximal density in the cloud. The asymptotic regimes of the Lieb-Liniger gas, separated by smooth crossovers, are shown in colors. Our data sets lie at the crossover between the quasicondensate and the ideal Bose gas regimes.

pairs of wires perpendicular to x , running dc current (blue wires in Fig. 2). The atomic cloud is far from those wires, in a region where $V(x)$ is well approximated by its Taylor expansion at small x . By tuning the currents in the four wires, we effectively control the coefficients of the x , x^2 , x^3 , and x^4 terms in that expansion: we can thus produce harmonic potentials, but also double-well potentials.

Using radio-frequency evaporative cooling we produce cold atomic clouds in the 1D regime, with a typical energy per atom smaller than the transverse energy gap: the temperature and chemical potential fulfill $k_B T, \mu < \hbar\omega_{\perp}$. The gas is then well described by the 1D model (1), with the effective 1D repulsion strength $g = 2\hbar a\omega_{\perp}$ [52], where the 3d scattering length of ^{87}Rb is $a = 5.3$ nm, and the mass is $m = 1.43 \times 10^{-25}$ kg. Moreover the length scale on which $n(x)$ varies is much larger than microscopic lengths—the phase correlation length at thermal equilibrium, which is the largest microscopic length in the quasicondensate regime, is of order $n\hbar^2/(mk_B T)$ [53,54], typically $0.1 \mu\text{m}$ for our clouds—so the hydrodynamic description applies. At equilibrium, the latter is equivalent to the local density approximation (LDA), and the local properties of the gas are parametrized by the dimensionless repulsion strength $\gamma = mg/(\hbar^2 n)$ and the dimensionless temperature $\theta = 2\hbar^2 k_B T/(mg^2)$ [51]. The range (γ, θ) explored by our data sets is displayed in Fig. 2(b). In this Letter we analyze the density profiles $n(x)$, which we measure using absorption images [50], averaging over typically ten images, with a pixel size of $1.74 \mu\text{m}$ in the atomic plane.

The Yang-Yang initial profile.—We start by trapping a cloud of $N = 4600 \pm 100$ atoms, with $\omega_{\perp} = 2\pi \times (7.75 \pm 0.02)$ kHz, in a harmonic potential $V(x) = m\omega_{\perp}^2 x^2/2$ with $\omega_{\parallel} = 2\pi \times (8.8 \pm 0.04)$ Hz, and measure its density profile [Fig. 1(b)]. To evaluate the temperature of the cloud, we fit the experimental profile with the one predicted by the Yang-Yang equation of state [9–11,46], relying on LDA

and on the assumption that the cloud is at thermal equilibrium; we find $T = (0.43 \pm 0.013) \mu\text{K}$. This gives $\theta = (3.5 \pm 0.1) \times 10^2$, while the interaction parameter is $\gamma = (2.8 \pm 0.1) \times 10^{-2}$ at the center.

As the density varies from the center of the cloud to the wings, the gas locally explores several regimes [51], from quasicondensate to highly degenerate ideal Bose gas (IBG) to nondegenerate IBG; see Fig. 2(b). The Yang-Yang equation of state [46] is exact in the entire phase diagram of the Lieb-Liniger model, and thus faithfully describes the density profile within LDA. We stress that this is the most natural and powerful method to describe the initial state of the gas [9–11], and that no simpler approximate theory [40] can account for the whole initial density profile; see Fig. 1(b). The Gross-Pitaevskii (GP) theory works in the central part—because it is close to the quasicondensate regime, but not in the wings. The opposite is true for the IBG model: it correctly describes the wings, but not the center of the cloud—the chemical potential is positive in the center, so the density diverges in the IBG. The classical field theory captures the quasicondensation transition for gases deep in the weakly interacting regime but it fails to reproduce faithfully the wings of our cloud since the latter are not highly degenerate.

Expansion from harmonic trap: Agreement with both GHD and CHD.—At $t = 0$, we suddenly switch off the longitudinal harmonic potential $V(x)$, and let the cloud expand freely in one dimension. We measure the *in situ* profiles at times $t = 10, 20, 30$ and 40 ms; see Fig. 1(a).

Two theories are able to give predictions for the expansion starting from the locally thermal initial state. One is GHD, presented above, where the full distribution of quasiparticles $\rho(x, v)$ is evolved in time [55]. The other is the *conventional* hydrodynamics (CHD) of the gas which, contrary to GHD, assumes that all local fluid cells are at thermal equilibrium, and keeps track only of three quantities that entirely describe the local state of the gas: the density $n(x)$, the fluid velocity $u(x)$, and the internal energy $e(x)$ [40]. We calculate the evolution of the density profile with both theories, and find that both of them are in excellent agreement with the experimental data, see Fig. 1(c) for the result at $t = 30$ ms.

GHD and CHD thus appear to be indistinguishable in that situation, at least for the expansion times that we probe here. We attribute this coincidence to the initial *harmonic* potential, which is very special. In this case it is simple to see that the GHD and CHD predictions coincide in the ideal Bose gas regime, and they can be shown to stay relatively near even beyond that regime [56].

Discussion: GHD vs CHD.—We wish to identify a setup where the theoretical predictions of both theories clearly differ, in order to experimentally discriminate between them. This will be the case if GHD predicts, for some time t and at some position x , that the distribution of rapidities $\rho(x, v)$ will differ strongly from a thermal equilibrium one.

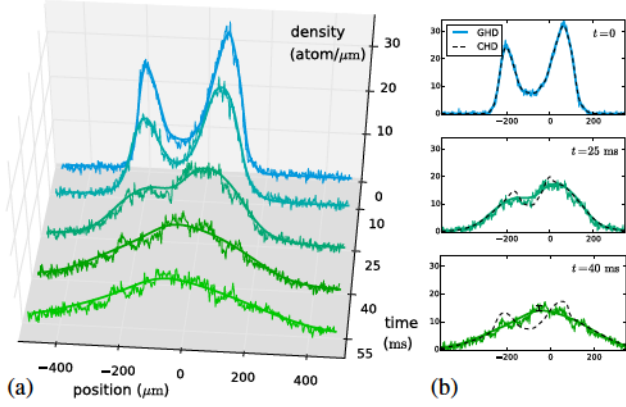


FIG. 3. (i) Longitudinal expansion of a cloud of $N = 6300 \pm 200$ atoms initially trapped in a double-well potential, compared with GHD. (ii) Even though the initial state is the same for GHD and CHD, both theories clearly differ at later times. CHD wrongly predicts the formation of two large density waves. The error bar shown at the center at $t = 40$ ms corresponds to a 68% confidence interval, and is representative for all data sets.

Such a situation occurs during the expansion of a cloud that initially has two well separated density peaks (Fig. 3). The reason can be captured by the following argument. The fluid cells $[x, x + \delta x]$ that are around either of the two peaks contain more quasiparticles, including quasiparticles of large rapidities, than the fluid cells near the center at $x = 0$. Under time evolution, the quasiparticles from the left peak that have a large positive rapidity $+u$ soon meet the ones coming from the right peak that have a large negative rapidity $-u$, around $x = 0$. Then, the distribution of rapidities near $x = 0$ is double peaked, with maxima at $v \simeq \pm u$, so it is clearly very far from a thermal equilibrium distribution, which would be single peaked. This phenomenon is obvious for noninteracting particles, Eq. (2) reducing to the standard Liouville equation, and GHD calculations indicate that this is true also for interacting particles [17,57].

Expansion from a double well.—To realize the above scenario, we prepare a cloud of $N = 6300 \pm 200$ atoms, with $\omega_{\perp} = 2\pi \times (8.1 \pm 0.03)$ kHz, at thermal equilibrium in a longitudinal double-well potential $V(x)$, such that the atomic density presents two well separated peaks, the peak density corresponding to $\gamma = (2.45 \pm 0.07) \times 10^{-2}$. Then at $t = 0$ we suddenly switch off the potential $V(x)$ and measure the *in situ* profiles at time $t = 10, 25, 40, 55$ ms (Fig. 3).

To compare with theoretical predictions, we need to know the initial temperature T of the cloud. However, we cannot estimate T from fitting the initial density profile $n_0(x)$ with the Yang-Yang equation of state and LDA because we do not have a good knowledge of the initial potential $V(x)$ that we create on the chip. Instead, we proceed as follows. First we postulate an initial temperature T and construct the initial rapidity distribution $\rho_T(x, v)$ such that, for a given x , $\rho_T(x, v)$ is the Yang-Yang thermal equilibrium rapidity distribution [46] at temperature T and density $n_0(x)$. We

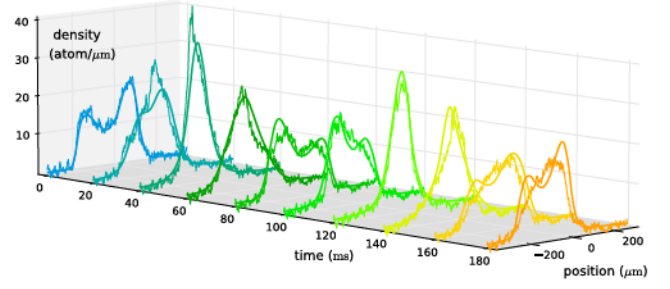


FIG. 4. Quench from double-well to harmonic potential, compared to the GHD prediction, with an atomic cloud that contains $N = 3500 \pm 140$ atoms initially. The main features of the experimental data are well reproduced by GHD. One experimental effect, not modeled in GHD, that appears to be particularly important, are the three-body losses: after 180 ms, the number of atoms drops by approximately 15%.

then evolve $\rho_T(x, v)$ using GHD and compute $n_T(x, t)$. While, by construction, $n_T(x, 0) = n_0(x)$, $n_T(x, t)$ may differ from the data at later times. We repeat this procedure for several initial temperatures and we select the value of T whose time evolution is in best agreement with the data [58]. We obtain $T \simeq 0.3 \mu\text{K}$, corresponding to $\theta \simeq 2 \times 10^2$, see Fig. 2(b).

The comparison between the expansion data and GHD is shown in Fig. 3(a); the agreement is excellent. We also simulate the time evolution of the cloud with CHD, for the exact same initial state. As we expected, expanding from a double-well potential reveals a clear difference between CHD and GHD, see Fig. 3(b). Two large density waves emerge in CHD and large gradients develop, eventually leading to shocks [14], features which are not seen in GHD [57].

Quench from double-well to harmonic potential.—Finally, we trap $N = 3500 \pm 140$ atoms, with $\omega_{\perp} = 2\pi \times (5.4 \pm 0.02)$ kHz, in a double-well potential, and we study the evolution of the cloud after suddenly switching off the double well and replacing it by a harmonic potential of frequency $\omega_{\parallel} = 2\pi \times (6.5 \pm 0.03)$ Hz. We measure the *in situ* profiles at time $t = 0, 20, 40, \dots, 180$ ms; see Fig. 4. The initial peak density corresponds to $\gamma = (2.13 \pm 0.07) \times 10^{-2}$. To estimate the temperature of the cloud, we proceed as in the previous case [58]; we find $T \simeq 0.15 \mu\text{K}$, corresponding to $\theta \simeq 2.2 \times 10^2$ [Fig. 2(b)].

This quench protocol mimics the famous quantum Newton's Cradle experiment [59]—see also Refs. [60,61] for recent realizations—which is realized here in a weakly interacting gas. Exactly like in the previous paragraph, this is a situation where GHD predicts the appearance of non-thermal rapidity distributions [17,62], and must therefore differ strongly from CHD. In fact, we have observed that CHD develops a shock at short times (around $t \simeq 30$ ms), so it is simply unable to give any prediction for the whole evolution time investigated experimentally [63].

Importantly, the motion is not periodic, contrary to what would be seen purely in the IBG or in the strongly interacting fermionized regime. Nevertheless, the motion of the cloud preserves an *approximate* periodicity, with a period close to, but slightly longer than, $2\pi/\omega_{\parallel}$ [62] (of course, if the cloud was symmetric under $x \rightarrow -x$, the period would be divided by two). At a quarter of the period—and three quarters of the period—the density distribution shows a single thin peak located near $x = 0$. We find good agreement with the GHD predictions, with the initial temperature T as the only free parameter [58]. However, experimental effects not taken into account by the GHD equations (2) appear to be more important in this setup than in the previous ones of Figs. 1–3, where shorter times were probed. For instance, the number of atoms N is not constant in our experimental setup: it decreases with time and drops by approximately 15% after 180 ms, probably because of three-body losses that occur at large density. This might partially explain the difference between the experimental density profile and the GHD one. We also suspect the small residual roughness of the potential $V(x)$ of affecting the experimental profiles.

Conclusion.—The results presented in this Letter are the first experimental check of the validity of GHD for 1D integrable quantum systems. We have shown that GHD—which predicts the time evolution of the distribution of rapidities—accurately captures the motion of 1D cold bosonic clouds made of $N \sim 10^3$ atoms, on timescales of up to ~ 0.2 s. We probed situations where the GHD predictions significantly differ from the ones of the conventional hydrodynamic approach, even at short times. We stress that GHD is applicable to all regimes of the 1D Bose gas, and it would therefore be particularly interesting to probe the strongly interacting regime. More generally, GHD is applicable to all Bethe ansatz solvable models, including multicomponent mixtures of fermions and bosons with symmetric interactions [64–67], so it would be very exciting to use it to describe the dynamics of more complex gases that can be realized in experimental setups different from ours [68,69].

We thank R. Dubessy for very stimulating discussions, and M. Cheneau for his careful reading of the manuscript. B. D. and J. D. thank J.-S. Caux, R. Konik, and T. Yoshimura for joint work on closely related projects. M. S. and I. B. thank S. Bouchoule of C2N (Centre Nanosciences et Nanotechnologies, CNRS/UPSUD, Marcoussis, France) for the development and microfabrication of the atom chip. A. Durnez and A. Harouri of C2N are acknowledged for their technical support. C2N laboratory is a member of RENATECH, the French national network of large facilities for micronanotechnology. M. S. acknowledges support by the Studienstiftung des Deutschen Volkes. This work was supported by Région Île de France (DIM NanoK, Atocirc project), and by the CNRS Mission Interdisciplinaire “Défi Infini” (J. D.).

B. D. thanks the Centre for Non-Equilibrium Sciences (CNES) and the Thomas Young Centre (TYC), as well as the Perimeter Institute (Waterloo, Canada) for hospitality while some of this work was done; J. D. also thanks SISSA in Trieste for hospitality. B. D. and J. D. thank the Galileo Galilei Institute for Theoretical Physics (Florence, Italy) for hospitality during the workshop “Entanglement in Quantum Systems,” and the Erwin Schrödinger Institute (Vienna, Austria) for hospitality during the programme “Quantum Paths.”

-
- [1] J.-P. Hansen and I. R. McDonald, *Theory of Simple Liquids*, 2nd ed. (Academic Press, San Diego, CA, 1990).
 - [2] M. P. Allen and D. J. Tildesley, *Computer Simulation of Liquids*, 2nd ed. (Oxford University Press, Oxford, UK, 2017).
 - [3] H. Spohn, *Large Scale Dynamics of Interacting Particles* (Springer, Berlin, 1991).
 - [4] J. K. Percus, Exact solution of kinetics of a model classical fluid, *Phys. Fluids* **12**, 1560 (1969).
 - [5] C. Boldrighini, R. L. Dobrushin, and Yu. M. Sukhov, One-dimensional hard rod caricature of hydrodynamics, *J. Stat. Phys.* **31**, 577 (1983).
 - [6] B. Doyon, T. Yoshimura, and J.-S. Caux, Soliton Gases and Generalized Hydrodynamics, *Phys. Rev. Lett.* **120**, 045301 (2018).
 - [7] O. A. Castro-Alvaredo, B. Doyon, and T. Yoshimura, Emergent Hydrodynamics in Integrable Quantum Systems Out of Equilibrium, *Phys. Rev. X* **6**, 041065 (2016).
 - [8] B. Bertini, M. Collura, J. De Nardis, and M. Fagotti, Transport in Out-of-Equilibrium XXZ Chains: Exact Profiles of Charges and Currents, *Phys. Rev. Lett.* **117**, 207201 (2016).
 - [9] A. H. van Amerongen, J. J. P. van Es, P. Wicke, K. V. Kheruntsyan, and N. J. van Druten, Yang-Yang Thermodynamics on an Atom Chip, *Phys. Rev. Lett.* **100**, 090402 (2008).
 - [10] T. Jacqmin, J. Armijo, T. Berrada, K. V. Kheruntsyan, and I. Bouchoule, Sub-Poissonian Fluctuations in a 1D Bose Gas: From the Quantum Quasicondensate to the Strongly Interacting Regime, *Phys. Rev. Lett.* **106**, 230405 (2011).
 - [11] A. Vogler, R. Labouvie, F. Stubenrauch, G. Barontini, V. Guarrera, and H. Ott, Thermodynamics of strongly correlated one-dimensional Bose gases, *Phys. Rev. A* **88**, 031603(R) (2013).
 - [12] E. H. Lieb and W. Liniger, Exact analysis of an interacting Bose gas. I. The general solution and the ground state, *Phys. Rev.* **130**, 1605 (1963); F. Berezin, G. Pokhil, and V. Finkelberg, Schrödinger equation for a system of 1D particles with point interaction, *Vestn. MGU* **1**, 21 (1964).
 - [13] B. Doyon and T. Yoshimura, A note on generalized hydrodynamics: Inhomogeneous fields and other concepts, *SciPost Phys.* **2**, 014 (2017).
 - [14] B. Doyon, J. Dubail, R. Konik, and T. Yoshimura, Large-Scale Description of Interacting One-Dimensional Bose Gases: Generalized Hydrodynamics Supersedes Conventional Hydrodynamics, *Phys. Rev. Lett.* **119**, 195301 (2017).

- [15] B. Doyon and H. Spohn, Drude weight for the Lieb-Liniger Bose gas, *SciPost Phys.* **3**, 039 (2017).
- [16] V. B. Bulchandani, R. Vasseur, C. Karrasch, and J. E. Moore, Solvable Hydrodynamics of Quantum Integrable Systems, *Phys. Rev. Lett.* **119**, 220604 (2017).
- [17] J.-S. Caux, B. Doyon, J. Dubail, R. Konik, and T. Yoshimura, Hydrodynamics of the interacting Bose gas in the Quantum Newton Cradle setup, [arXiv:1711.0873](https://arxiv.org/abs/1711.0873).
- [18] J. Dubail, A more efficient way to describe interacting quantum particles in 1D, *Viewpoint on Refs. [7,8] in Physics* **9**, 153 (2016).
- [19] V. B. Bulchandani, R. Vasseur, C. Karrasch, and J. E. Moore, Bethe-Boltzmann hydrodynamics and spin transport in the XXZ chain, *Phys. Rev. B* **97**, 045407 (2018).
- [20] J. De Nardis, D. Bernard, and B. Doyon, Hydrodynamic Diffusion in Integrable Systems, *Phys. Rev. Lett.* **121**, 160603 (2018).
- [21] D.-L. Vu and T. Yoshimura, Equations of state in generalized hydrodynamics, [arXiv:1809.03197](https://arxiv.org/abs/1809.03197).
- [22] A. Bastianello and L. Piroli, From the sinh-Gordon field theory to the one-dimensional Bose gas: Exact local correlations and full counting statistics, *J. Stat. Mech.* (2018) 113104.
- [23] A. De Luca, M. Collura, and J. De Nardis, Non-equilibrium spin transport in integrable spin chains: Persistent currents and emergence of magnetic domains, *Phys. Rev. B* **96**, 020403 (2017).
- [24] B. Doyon and H. Spohn, Dynamics of hard rods with initial domain wall state, *J. Stat. Mech.* (2017) 073210.
- [25] E. Ilievski and J. De Nardis, Microscopic Origin of Ideal Conductivity in Integrable Quantum Models, *Phys. Rev. Lett.* **119**, 020602 (2017).
- [26] L. Piroli, J. De Nardis, M. Collura, B. Bertini, and M. Fagotti, Transport in out-of-equilibrium XXZ chains: Nonballistic behavior and correlation functions, *Phys. Rev. B* **96**, 115124 (2017).
- [27] E. Ilievski and J. De Nardis, Ballistic transport in the one-dimensional Hubbard model: The hydrodynamic approach, *Phys. Rev. B* **96**, 081118 (2017).
- [28] M. Fagotti, Higher-order generalized hydrodynamics in one dimension: The noninteracting test, *Phys. Rev. B* **96**, 220302 (2017).
- [29] V. B. Bulchandani, On classical integrability of the hydrodynamics of quantum integrable systems, *J. Phys. A* **50**, 435203 (2017).
- [30] B. Doyon, H. Spohn, and T. Yoshimura, A geometric viewpoint on generalized hydrodynamics, *Nucl. Phys. B* **926**, 570 (2018).
- [31] M. Collura, A. De Luca, and J. Viti, Analytic solution of the domain wall non-equilibrium stationary state, *Phys. Rev. B* **97**, 081111 (2018).
- [32] A. Bastianello, B. Doyon, G. Watts, and T. Yoshimura, Generalized hydrodynamics of classical integrable field theory: The sinh-Gordon model, *SciPost Phys.* **4**, 045 (2018).
- [33] By thermal equilibrium we mean a state represented by the Gibbs ensemble at a given temperature and chemical potential.
- [34] S. Stringari, Dynamics of Bose-Einstein condensed gases in highly deformed traps, *Phys. Rev. A* **58**, 2385 (1998).
- [35] C. Menotti and S. Stringari, Collective oscillations of one-dimensional Bose-Einstein gas in a time-varying trap potential and atomic scattering length, *Phys. Rev. A* **66**, 043610 (2002).
- [36] S. Peotta and M. Di Ventra, Quantum shock waves and population inversion in collisions of ultracold atomic clouds, *Phys. Rev. A* **89**, 013621 (2014).
- [37] I. Bouchoule, S. S. Szigeti, M. J. Davis, and K. V. Kheruntsyan, Finite-temperature hydrodynamics for one-dimensional Bose gases: Breathing-mode oscillations as a case study, *Phys. Rev. A* **94**, 051602(R) (2016).
- [38] G. De Rosi and S. Stringari, Hydrodynamic versus collisionless dynamics of a one-dimensional harmonically trapped Bose gas, *Phys. Rev. A* **94**, 063605 (2016).
- [39] Y. Y. Atas, D. M. Gangardt, I. Bouchoule, and K. V. Kheruntsyan, Exact nonequilibrium dynamics of finite-temperature Tonks-Girardeau gases, *Phys. Rev. A* **95**, 043622 (2017).
- [40] See Supplemental Material at <http://link.aps.org/supplemental/10.1103/PhysRevLett.122.090601> for a brief introduction of the Gross-Pitaevskii and the classical field models, which includes Refs. [41–45].
- [41] Y. Castin, R. Dum, E. Mandonnet, A. Minguzzi, and I. Carusotto, Coherence properties of a continuous atom laser, *J. Mod. Opt.* **47**, 2671 (2000).
- [42] I. Bouchoule, M. Arzamasovs, K. V. Kheruntsyan, and D. M. Gangardt, Two-body momentum correlations in a weakly interacting one-dimensional Bose gas, *Phys. Rev. A* **86**, 033626 (2012).
- [43] T. Jacqmin, B. Fang, T. Berrada, T. Roscilde, and I. Bouchoule, Momentum distribution of one-dimensional Bose gases at the quasicondensation crossover: Theoretical and experimental investigation, *Phys. Rev. A* **86**, 043626 (2012).
- [44] P. B. Blakie, A. S. Bradley, M. J. Davis, R. J. Ballagh, and C. W. Gardiner, Dynamics and statistical mechanics of ultracold Bose gases using c-field techniques, *Adv. Phys.* **57**, 363 (2008).
- [45] S. P. Cockburn, A. Negretti, N. P. Proukakis, and C. Henkel, A comparison between microscopic methods for finite temperature Bose gases, *Phys. Rev. A* **83**, 043619 (2011).
- [46] C. N. Yang and C. P. Yang, Thermodynamics of a one-dimensional system of bosons with repulsive delta-function interaction, *J. Math. Phys.* **10**, 1115 (1969).
- [47] A. Zamolodchikov, Thermodynamic Bethe ansatz in relativistic models. Scaling three state Potts and Lee-Yang models, *Nucl. Phys. B* **342**, 695 (1990).
- [48] J. Mossel and J.-S. Caux, Generalized TBA and generalized Gibbs, *J. Phys. A* **45**, 255001 (2012).
- [49] E. Ilievski, M. Medenjak, T. Prosen, and L. Zadnik, Quasilocal charges in integrable lattice systems, *J. Stat. Mech.* (2016) 064008.
- [50] A. Johnson, Ph.D. thesis, 2016, <https://tel.archives-ouvertes.fr/tel-01432392v1>.
- [51] K. V. Kheruntsyan, D. M. Gangardt, P. D. Drummond, and G. V. Shlyapnikov, Pair Correlations in a Finite-Temperature 1D Bose Gas, *Phys. Rev. Lett.* **91**, 040403 (2003).
- [52] M. Olshanii, Atomic Scattering in the Presence of an External Confinement and a Gas of Impenetrable Bosons, *Phys. Rev. Lett.* **81**, 938 (1998).
- [53] C. Mora and Y. Castin, Extension of Bogoliubov theory to quasicondensates, *Phys. Rev. A* **67**, 053615 (2003).

- [54] M. Cazalilla, Bosonizing one-dimensional cold atomic gases, *J. Phys. B* **37**, S1 (2004).
- [55] For each x , the initial distribution $\rho(x, v)$ is given by the thermodynamic Bethe ansatz [46].
- [56] See Supplemental Material at <http://link.aps.org/supplemental/10.1103/PhysRevLett.122.090601> for a detailed discussion of why the GHD prediction is close to the CHD one for the release from a harmonic trap.
- [57] See Supplemental Material at <http://link.aps.org/supplemental/10.1103/PhysRevLett.122.090601> for plots of the distribution of quasiparticles in phase space and more details on why the double-well potential allows to discriminate between GHD and CHD.
- [58] See Supplemental Material at <http://link.aps.org/supplemental/10.1103/PhysRevLett.122.090601> for full details on our selection procedure for the GHD profiles in the case where we do not have good knowledge of the initial potential.
- [59] T. Kinoshita, T. Wenger, and D. S. Weiss, A Quantum Newton's Cradle, *Nature (London)* **440**, 900 (2006).
- [60] Y. Tang, W. Kao, K.-Y. Li, S. Seo, K. Mallayya, M. Rigol, S. Gopalakrishnan, and B. L. Lev, Thermalization near Integrability in a Dipolar Quantum Newton's Cradle, *Phys. Rev. X* **8**, 021030 (2018).
- [61] C. Li, T. Zhou, I. Mazets, H.-P. Stimming, Z. Zhu, Y. Zhai, W. Xiong, X. Zhou, X. Chen, and J. Schmiedmayer, Dephasing and relaxation of bosons in 1D: Newton's cradle revisited, [arXiv:1804.01969](https://arxiv.org/abs/1804.01969).
- [62] See Supplemental Material at <http://link.aps.org/supplemental/10.1103/PhysRevLett.122.090601> for plots of the distribution of quasiparticles in phase space that show that the behavior predicted by GHD is only approximately periodic.
- [63] To go beyond the shock time, one would need to properly regularize the solution, for instance, by considering entropy-producing diffusive terms.
- [64] C. N. Yang, Some Exact Results for the Many-Body Problem in one Dimension with Repulsive Delta-Function Interaction, *Phys. Rev. Lett.* **19**, 1312 (1967).
- [65] B. Sutherland, Further Results for the Many-Body Problem in One Dimension, *Phys. Rev. Lett.* **20**, 98 (1968).
- [66] M. Gaudin, Un système a une dimension de fermions en interaction, *Phys. Lett.* **24A**, 55 (1967).
- [67] X.-W. Guan, M. Batchelor, and C. Lee, Fermi gases in one dimension: From Bethe ansatz to experiments, *Rev. Mod. Phys.* **85**, 1633 (2013).
- [68] P. Wicke, S. Whitlock, and N. van Druten, Controlling spin motion and interactions in a one-dimensional Bose gas, [arXiv:1010.4545](https://arxiv.org/abs/1010.4545).
- [69] G. Papagano *et al.*, A one-dimensional liquid of fermions with tunable spin, *Nat. Phys.* **10**, 198 (2014).

Supplemental Material for “Generalized Hydrodynamics on an Atom Chip”

M. Schemmer,¹ I. Bouchoule,¹ B. Doyon,² and J. Dubail³

¹*Laboratoire Charles Fabry, Institut d’Optique, CNRS, Université Paris Sud 11,
2 Avenue Augustin Fresnel, F-91127 Palaiseau Cedex, France*

²*Department of Mathematics, King’s College London, Strand, London WC2R 2LS, UK*

³*Laboratoire de Physique et Chimie Théoriques, CNRS,
Université de Lorraine, UMR 7019, F-54506 Vandoeuvre-les-Nancy, France*

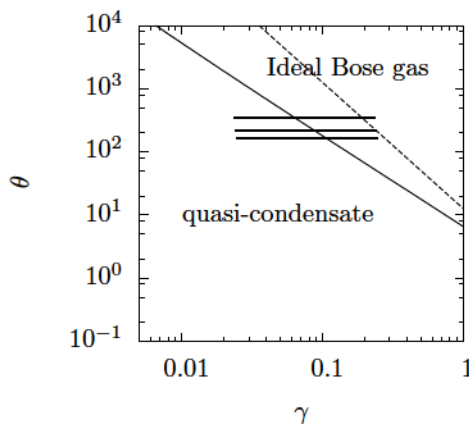


FIG. 1. Position of the three sets of data shown in the text in the (γ, θ) space. The thin solid line is the line corresponding to a vanishing chemical potential, computed using Yang-Yang equation of state, which indicates the crossover from the Ideal Bose gas to the quasi-condensate. The dashed line is the line $n\lambda_{dB} = 1$ which indicates the crossover from a non-degenerate to a highly degenerate gas. The horizontal fat lines correspond to the experimental data investigated in the main text (from top to bottom data of Fig.1, data of Fig.3 and data of Fig. 4).

I. REGIMES OF THE LIEB-LINIGER GAS AT THERMAL EQUILIBRIUM

Properties of the Lieb-Liniger gas at thermal equilibrium have been studied extensively. The gas at thermal equilibrium is entirely parametrized by the dimensionless parameters γ and θ . Three main regimes have been identified, which correspond to different asymptotic value of the normalized zero-distance two-body correlation function $g^{(2)}(0)$ [50]. The region in the (γ, θ) plane corresponding to $\gamma \ll 1$ and $\theta \ll \gamma^{-3/2}$ is that of the quasicondensate regime. In this regime, correlations between particles are small and $g^{(2)}(0) \simeq 1$. Thus locally, the gas resembles a Bose-Einstein condensate, although quantum and thermal fluctuations associated to long wavelength phonons prevent true long range order. The region $\theta \gg \max(1, \gamma^{-3/2})$ is that of the ideal Bose gas regime, characterized by $g^{(2)}(0) \simeq 2$. In this regime repulsive interactions are not strong enough to prevent the thermally activated large density fluctuations associated to the bosonic bunching phenomenon. Finally, the region $\theta \ll 1$ and $\gamma \gg 1$ is that of the strongly interacting regime, also called Tonks-Girardeau or fermionized regime. There, interactions are strong enough to almost prevent two atoms to sit at the same position so that $g^{(2)}(0) \ll 1$.

The above-mentioned regimes are all separated by smooth crossovers. Quantitative values for the position of these transitions depend on the quantity that is considered and on the criteria used. One possible criterion to locate the transition from the IBG to qBEC regime is the condition $\mu = 0$, where μ is the chemical potential: in the IBG regime, $\mu < 0$ while $\mu > 0$ in the qBEC regime ($\mu \simeq gn$ in the qBEC regime). In Fig. 1, we plot the line $\mu = 0$, found using the Yang-Yang equation of state. This line follows the expected scaling $\theta \propto \gamma^{-3/2}$ of the crossover between the IBG and the qBEC regime. It lies however substantially above the line $\theta = \gamma^{-3/2}$ [50].

The IBG regime can be divided into two subregimes: the highly non-degenerate regime corresponding to $\theta \gg \gamma^{-1/2}$ and the highly degenerate regime corresponding to $\gamma^{-3/2} \ll \theta \ll \gamma^{-1/2}$. The crossover between these two subregimes is very wide and in fig. 1, we signal this transition with the line corresponding to $n\lambda_{dB} = 1$, where $\lambda_{dB} = \hbar/\sqrt{2\pi mk_B T}$ is the de Broglie wavelength.

II. APPROXIMATE THEORIES THAT WE COMPARE TO GHD

A. Conventional hydrodynamics based on Yang-Yang thermodynamics (or Thermodynamic Bethe Ansatz)

What we call ‘conventional’ hydrodynamics (CHD) in the main text is simply the Euler equations that hold in normal fluids that are locally at thermal equilibrium, that govern the variation of the particle density $n(x, t)$, the fluid velocity $u(x, t)$, and the internal energy per particle $e(x, t)$:

$$\begin{cases} \partial_t n + \partial_x (un) = 0 \\ \partial_t u + u\partial_x u + \frac{1}{m} \partial_x P = -\frac{1}{m} \partial_x V \\ \partial_t e + u\partial_x e + \frac{e}{n} \partial_x n = 0. \end{cases} \quad (1)$$

Here $P(n, e)$ is the pressure, which is given by the equation of state of the fluid. One can put these three equations in a form that expresses conservation of mass, momentum—broken by the external potential $V(x)$ —, and energy,

$$\begin{cases} \partial_t n + \partial_x(un) = 0 \\ \partial_t(mnu) + \partial_x(u(mnu) + P) = -n\partial_x V \\ \partial_t(n\frac{mu^2}{2} + ne + nV) + \partial_x(u(n\frac{mu^2}{2} + ne + nV) + uP) = 0. \end{cases} \quad (2)$$

These are the evolution equations we solve to obtain the Conventional HydroDynamics (CHD) curves in the main text. The pressure $P(n, e)$ is obtained from the thermodynamic Bethe Ansatz, also known as the Yang-Yang equation of state [40].

One convenient way to calculate the pressure is to observe that it is the momentum current, and then to use the formula from [7] for the latter,

$$P = \frac{m^2}{\hbar} \int \frac{dv}{2\pi} v \nu(v) v^{\text{dr}}. \quad (3)$$

Here $\nu(v) \in [0, 1]$ is the occupation function, which, for the thermal Gibbs state at inverse temperature $\beta = 1/(\kappa_B T)$, satisfies the integral equation of Yang and Yang [40],

$$\beta \frac{mv^2}{2} = \log \left[\frac{1 - \nu(v)}{\nu(v)} \right] - \int \frac{dw}{2\pi} K(v - w) \log [1 - \nu(w)], \quad (4)$$

where $K(v - w) = \frac{2(v-w)/\hbar}{(g/\hbar)^2 + (v-w)^2}$ is the differential scattering phase, or Lieb-Liniger kernel. The superscript 'dr' in (3) stands for 'dressing', and is defined as follows for a function $f(v)$,

$$f^{\text{dr}}(v) = f(v) + \int \frac{dw}{2\pi} K(v - w) \nu(w) f^{\text{dr}}(w) \quad (5)$$

(and by a slight abuse of notation, we write v^{dr} for $\text{id}^{\text{dr}}(v)$ where $\text{id}(v) = v$ is the identity function). The occupation function $\nu(v)$ and the distribution $\rho(v)$ used in the main text are related by

$$\rho(v) = \frac{m}{2\pi\hbar} \nu(v) 1^{\text{dr}}(v) \quad (6)$$

where $1(v) = 1$. The function $\nu(v)$ gives the occupation fraction of the rapidities, which are the fermionic quantities defining a Bethe-Anstaz eigenstate [40].

B. Gross-Pitaevskii approach

The Gross-Pitaevskii description (GP) assumes that the gas is Bose-condensed : all the atoms are in the same single-particle wave function $\psi(x)$. It describes a Bose gas at zero temperature in the limit of weak repulsion $\gamma \rightarrow 0$, as long as their extension is much smaller than $\xi e^{\pi/\sqrt{\gamma}}$, where $\xi = \hbar/\sqrt{m\rho}$ is the healing length. The latter condition, usually fulfilled in experiment with weakly interacting gases, ensures that quantum fluctuations do not break long-range order. At equilibrium the wavefunction ψ obeys

$$\mu\psi = \left(-\frac{\hbar^2}{2m} \partial_x^2 + g|\psi|^2 + V(x) \right) \psi \quad (7)$$

where μ is the chemical potential. After modification of the potential, the time evolution of ψ is given by the Gross-Pitaevskii equation

$$i\hbar\partial_t\psi = \left(-\frac{\hbar^2}{2m} \partial_x^2 + g|\psi|^2 + V(x) \right) \psi. \quad (8)$$

Here $\psi(x, t)$ is the wavefunction of the condensate at time t , normalized such that

$$\int dx |\psi(x, t)|^2 = N. \quad (9)$$

Separating the phase and the amplitude of the wavefunction of the condensate,

$$\psi(x, t) = \sqrt{n(x, t)}e^{i\varphi(x, t)}, \quad (10)$$

and introducing the velocity field $u = \frac{\hbar}{m}\partial_x\varphi$, one gets GP in Madelung form,

$$\begin{aligned} \partial_t n + \partial_x(un) &= 0 \\ \partial_t u + u\partial_x u &= -\frac{1}{m}\partial_x \left[gn + V(x) - \frac{\hbar^2}{2m} \frac{\partial_x^2 \sqrt{n}}{\sqrt{n}} \right]. \end{aligned} \quad (11)$$

The first equation expresses conservation of mass, the second is the Euler equation for a fluid with the equation of state $\mu = gn$ in an external potential $V(x)$, with an additional *quantum pressure* term $\frac{\hbar^2}{2m} \frac{\partial_x^2 \sqrt{n}}{\sqrt{n}}$. In the *Euler limit* of long wavelengths for density variations, the quantum pressure term can be neglected. Then Eq. (11) reduces to the Euler equation with a pressure term $P = gn^2/2$, which is indeed the pressure of a condensate or a quasicondensate. Note however that the GP equation goes beyond this *Euler limit* of long wavelength variation of ψ . For instance, it would capture correctly the “quantum Newton cradle” experiment presented in the main text, for a weakly interacting cloud at $T = 0$. At the “collision-time” where the two initial clouds are on top of each other, GP predicts fast oscillations of the density reflecting interference phenomena. Of course such fast oscillations, which, in terms of Bethe-Ansatz states, would imply interference between different states (of very similar quasi-momentum distribution), is not accounted for by GHD. However we expect that predictions of GHD (for a weakly interacting gas at $T = 0$) would coincide with the GP ones, if one perform a spatial coarse-grained approximation of the GP solution, smearing out the interference fringes. It is an open question under which precise conditions and coarse-graining procedure the predictions of GHD coincide with the coarse-grained GP predictions.

C. The classical field approximation

In the domain characterized by $\gamma^{-1} \ll \theta \ll \gamma^{-2}$, the typical occupation number of the relevant modes (either the one-particle states for $\theta \gg \gamma^{-3/2}$, or the Bogolioubov collective modes for $\theta \ll \gamma^{-3/2}$) is much larger than one: in particular the correlation functions are mainly dominated by the contribution of highly populated modes. In such a condition, a theory that neglects the quantification of the atomic field $\hat{\psi}$ and treat it as a complex classical field—or equivalently, that considers statistical fluctuation of the condensate’s single-particle wave function—is expected to provide the relevant physics. This is the so-called classical field approximation [67]. At thermal equilibrium the complex field $\psi(x)$ obeys the probability distribution

$$P(\{\psi(x)\}) = Z^{-1} e^{-\beta \int dx (\hbar^2/(2m)|\partial_x \psi|^2 + g/2|\psi|^4 + (V(x) - \mu)|\psi|^2)}, \quad (12)$$

where $\beta = 1/(k_B T)$, μ is the chemical potential, and the partition function Z ensures the correct normalization. At sufficiently shallow confining potential, a local density approximation is valid and the external potential $V(x)$ is not very relevant. Note that while two parameters are required to describe a Lieb-Liniger gas, only one parameter, which can be taken as $\eta = \mu(\hbar^2/(mg^2 k_B^2 T^2))^{1/3}$ in terms of the temperature and chemical potential, is sufficient to characterize the classical field, providing lengths and densities are correctly rescaled [67, 68]. One way of sampling the field ψ according to Eq. (12) is to numerically evolve ψ under a stochastic differential equation.

In contrast to the GP approach above, the classical field takes into account thermal fluctuations in the system. In particular it captures the quasicondensation crossover, which occurs, for $\gamma \ll 1$, around the line $\theta = \gamma^{-3/2}$, although very large values of θ are required for an accurate description of the gas [69]. On the other hand, it ignores the quantification of atoms. This leads to an overestimation of the population in high energy modes: within CF theory the mode population is $k_B T/\epsilon_\nu$, regardless of the mode energy ϵ_ν , a value much larger, for modes of energy $\epsilon_k \gg k_B T$, than the expected exponential behavior $e^{-\epsilon_k/(k_B T)}$ (this is a similar phenomenon as that of the well-known UV catastrophe of thermal ensembles of electromagnetic fields). This explains why the equilibrium profile predicted by the classical field model strongly overestimate the wings of the atomic clouds, see Fig. 1(ii) in the main text. We are aware of refined theories, based on classical field, that include a well-chosen cutoff above which the excitations are treated as a quantum gas, see [? ?] and references therein. They permit to reproduce the equilibrium density profiles of trapped weakly interacting gases [?]. However, expanding such theories to time-dependent problems is a priori not trivial. We also think that, in the same way as Yang-Yang thermodynamics offers a much more powerful, reliable and elegant way of describing the equilibrium profiles [9–11], GHD would supersede complicated and ad-hoc theories based on the classical field approximation.

III. RELATION BETWEEN GHD AND CHD FOR AN EXPANSION FROM A HARMONIC POTENTIAL

As we observed in the main text, the one-dimensional expansion of the gas starting from a state where it is confined by harmonic potential is well described both by GHD and CHD. This is surprising, as GHD takes into account infinitely many conservation laws, while CHD only takes into account three: mass, momentum and energy. Of course, the initial state is, in both cases, obtained by a Gibbs local density approximation, according to which in every mesoscopic cell the gas is a Gibbs state, thermalized with respect to the energy and number of particles (with zero average momentum). Nevertheless, one generically expects that under the GHD evolution, other conservation laws become involved, the fluid being, after some time, locally a generalized Gibbs ensemble – involving higher conserved charges – instead of a Gibbs ensemble.

There are two limits where one can show that the GHD evolution is, in fact, the same as the CHD evolution.

The first is the zero-temperature limit. It was shown in Ref. [14] that if the initial state is at zero temperature, where, in every cell x , the quasi-particle occupation function $\nu(x, v)$ takes the value 1 on an interval $v \in [v_l(x), v_r(x)]$ and 0 elsewhere, then, at least for small enough times, a GHD evolution is completely equivalent to a CHD evolution, and the state stays at zero temperature. This holds from any initial potential, harmonic or not. The equivalence between the evolutions breaks down when in CHD shocks develop; in GHD, large gradients are temporary, and the fluid passes to a higher-dimensional space of states afforded by the higher conservation laws.

The other limit is that of the free gases - either the ideal Fermi gas (at strong coupling) or the ideal Bose gas (IBG) (at large temperatures). Let us consider the latter, as it is more relevant to the present experiment. In the free limit, the effective velocity becomes equal to the velocity, and the initial fluid's Bosonic occupation function $\tilde{\nu}(x, v)$ (note that this is related to, but not the same as, the quasi-particle – or fermionic – occupation function $\nu(x, v)$) is of the form

$$\tilde{\nu}(x, v) = \frac{1}{e^{(mv^2/2 + m\omega_{\parallel}^2 x^2/2 - \mu)/T} - 1}. \quad (13)$$

The GHD evolution during the expansion is very simple,

$$\partial_t \tilde{\nu} + v \partial_x \tilde{\nu} = 0, \quad (14)$$

and thus the solution is obtained as

$$\tilde{\nu}(x, t, v) = \frac{1}{e^{(mv^2/2 + m\omega_{\parallel}^2 (x-vt)^2/2 - \mu)/T} - 1} = \frac{1}{e^{(m(v-u(x,t))^2/2)(1+\omega_{\parallel}^2 t^2)/T} e^{(m\omega_{\parallel}^2/(1+\omega_{\parallel}^2 t^2) x^2/2 - \mu)/T} - 1}, \quad (15)$$

where $u(x, t) = \omega_{\parallel}^2/(1 + \omega_{\parallel}^2 t^2) xt$. Eq. (15) shows that the distribution of v at a given x is that of a Gibbs ensemble for a gas whose center of mass moves at velocity $u(x, t)$. Hence, all currents obtained after GHD evolution are evaluated within Gibbs states, completely determined by the first three conserved densities. Therefore, it is sufficient to restrict to the evolution described by the first three conservation laws, and we recover CHD.

These two limits, however, only partially explain the observation we have made: the parameters of the experiment, the full range of regimes covered by the gas (see Fig. 2b in the main text), imply that there are regions where the occupation function is both relatively far from the zero-temperature form (see typical initial quasi-particle occupation functions in section IV) and from the IBG form.

We provide below a calculation that shows that, more generally, one may expect the GHD solution to stay relatively near to CHD solution in an expansion from a harmonic potential, even away from the two limits described above. The main result is that under GHD evolution from a harmonic potential, the occupation function has *the same asymptotics at large v* , of the form $e^{-P(v)}$ with $P(v)$ a polynomial of degree 2, as that obtained from a CHD evolution. That is, the “wings” in quasi-momentum space are not drastically affected by the presence of higher conservation laws. Further, at finite v , the discrepancies must stay bounded. If the occupation function is near enough to the zero-temperature form, with a region relatively near to 1 at small velocities, surrounded by wings where it tends towards 0, then a combination of the zero-temperature result recalled above, and the asymptotic results derived below, suggests that indeed the GHD and CHD solutions should stay near. Typical initial occupation functions shown in section IV indeed have this form, and thus these arguments explain our observation.

In terms of the quasi-particle occupation function $\nu(v)$, related to the quasi-particle density $\rho(x, v)$ via (6), it turns out that Eq. (2b) in the main text becomes

$$\partial_t \nu + v^{\text{eff}} \partial_x \nu = 0. \quad (16)$$

The pseudoenergy ϵ , defined via $\nu = 1/(1 + e^{\epsilon})$, hence satisfies the same equation,

$$\partial_t \epsilon + v^{\text{eff}} \partial_x \epsilon = 0. \quad (17)$$

In order to describe the macrostate, it is convenient to use the energy function $e(v)$, in terms of which the pseudoenergy can be expressed as the solution to the non-linear integral equation [40]

$$\epsilon(v) = e(v) - \int \frac{dw}{2\pi} K(v-w) \log(1 + e^{-\epsilon(w)}). \quad (18)$$

Like the quasi-particle density, the energy function $e(v)$, in GHD, becomes space-time dependent, and we can re-write (17) using (18). One can show that [13]

$$(\partial_t e)^{\text{dr}} + v^{\text{eff}} (\partial_x e)^{\text{dr}} = 0 \quad (19)$$

where the dressing operation is defined in (5). Note that the effective velocity (Eq. 2a in the main text) can be written as

$$v^{\text{eff}} = v^{\text{dr}} / 1^{\text{dr}} \quad (20)$$

where v^{dr} is the dressed of the function v (the identity function), and 1^{dr} is the dressed of the constant function 1 (1^{dr} and all dressed quantities are functions of v , as well as, of course, the space-time position x, t). Therefore, we have

$$(\partial_t e)^{\text{dr}} + \frac{v^{\text{dr}}}{1^{\text{dr}}} (\partial_x e)^{\text{dr}} = 0 \quad (21)$$

In the initial state, at $t = 0$, for each position x the state of the gas is given by the Gibbs ensemble, with a chemical potential $\mu - m\omega_{\parallel}^2 x^2$ and a temperature T , and the energy function reduces to [40]

$$e(x, 0, v) = \frac{1}{T} \left(\frac{mv^2}{2} + \frac{m\omega_{\parallel}^2 x^2}{2} - \mu \right). \quad (22)$$

We propose that an *approximate* solution to the evolution equation from a harmonic potential is of the form

$$e(x, t, v) \approx f(t)v^2 + g(t)vx + h(t)x^2 - \mu. \quad (23)$$

This approximate solution holds if the following condition is approximately satisfied,

$$(v^{\text{dr}})^2 \approx (v^2)^{\text{dr}} 1^{\text{dr}}. \quad (24)$$

Indeed inserting (23) in (19) gives

$$f'(t)(v^2)^{\text{dr}} + g'(t)v^{\text{dr}}x + h'(t)x^2 1^{\text{dr}} + g(t)(v^{\text{dr}})^2 / 1^{\text{dr}} + h(t)xv^{\text{dr}} \approx 0 \quad (25)$$

And so we have

$$h'(t) = 0, \quad g'(t) = -h(t), \quad f'(t)(v^2)^{\text{dr}} \approx -g(t)(v^{\text{dr}})^2 / 1^{\text{dr}}. \quad (26)$$

If the approximation (24) holds, then the last (approximate) equation becomes

$$f'(t) \approx -g(t) \quad (27)$$

and we find

$$h(t) = a, \quad g(t) = b - at, \quad f(t) = c - bt + at^2/2. \quad (28)$$

The initial condition is satisfied, with $a = m\omega_{\parallel}^2/(2T)$, $b = 0$ and $c = m/(2T)$.

We now note that the approximate solution (23) with (28) is *exactly* the form we would obtain (under (24)) from CHD: in all cells it is a boosted Gibbs state, completely determined by the mass, momentum and energy densities, hence we can restrict to these conservation laws. The validity of CHD thus reduced to the investigation of the validity of the approximation (24).

From (18), we see that $\epsilon(v)$ has the same leading large- $|v|$ asymptotics as $e(v)$. Hence, in states with power-law growing $e(v)$, the occupation function decays as an exponential of a power at large $|v|$. From the dressing operation (5), it is then clear that, in any such state, the dressed $f^{\text{dr}}(v)$ of any function $f(v)$ has exactly the same asymptotic expansion in powers of $1/v$ up to powers $1/v^2$: the corrections coming from the occupation function are exponentially decaying, hence the main corrections come from integrating the differential scattering kernel around finite regions of

the integration variable w (the size of the finite region being controlled by the exponential decay of the occupation function). These give the power law $1/v^2$. That is, assuming $f^{\text{dr}}(v)$ stays finite for finite values of v , we have

$$f^{\text{dr}}(v) = f(v) + O(1/v^2). \quad (29)$$

Therefore

$$(v^{\text{dr}})^2 = (v^2)^{\text{dr}} + O(1/v) \quad (30)$$

and the condition (24) is satisfied up to vanishing terms at large v . This fully justifies that the approximate solution (23) indeed holds as written, up to vanishing terms, and shows that CHD reproduces the correct non-vanishing large- v asymptotics of $e(v)$, and thus (by a similar asymptotic analysis as above) of $\epsilon(v)$.

At small velocities, the effective velocity v^{eff} is different from v due to transport within its local environment: for instance, a quasi-particle of bare velocity $v = 0$ acquires a nonzero effective velocity $v^{\text{eff}} \neq 0$ if its surrounding environment carries nonzero currents. However, these differences are bounded, and tend to be relatively small. Similar effects occur for the dressing of any function, and therefore the approximation (24) has an error that stays bounded at finite v .

Finally, we note from the above calculations and especially from (29) that the *free evolution* (with trivial dressing) generically (that is, in all situations where the occupation function decays at least exponentially) describes correctly the first three leading powers of the large- v asymptotics of the source term $e(v)$ under the one-dimensional expansion (recall that in the case of the initial harmonic potential, the free evolution agrees with CHD, but that in general it does not). One could for instance consider an initial potential with higher powers, say up to x^4 . Then we see that an approximate solution of similar type, valid at large v , would have powers of v up to v^4 , with the coefficients of the powers v^2 , v^3 and v^4 correctly described by a free evolution equation. This is definitely very far from a CHD solution, as powers of v^3 and v^4 are forbidden in CHD. That is, when starting from non-harmonic potentials, CHD does not describe the correct large- v asymptotics of the distribution, hence is quite far for all v – the maximal deviation for the function $e(v)$ is in fact unbounded. It is these effects that are seen in section IV.

IV. GHD VS. CHD: COMPARISON OF THE PHASE-SPACE OCCUPATION FUNCTIONS $\nu(x, v)$

Here we display the phase-space occupation $\nu(x, v)$ for the expansion from a double-well potential shown in Fig. 3 in the main text. At each x , the occupation function $\nu(v)$ is related to the density $\rho(v)$ used in the main text by Eq. (6). At thermal equilibrium, one can think of it as a Fermi distribution: at zero temperature, it is exactly a rectangular function, with support $[-2\sqrt{\frac{q\eta}{m}}, 2\sqrt{\frac{q\eta}{m}}]$ in the limit of weak repulsion. At finite temperature the two sides of the rectangle are rounded off. The GHD evolution equation can be written directly in terms of the occupation function $\nu(v)$, see Eq. (16).

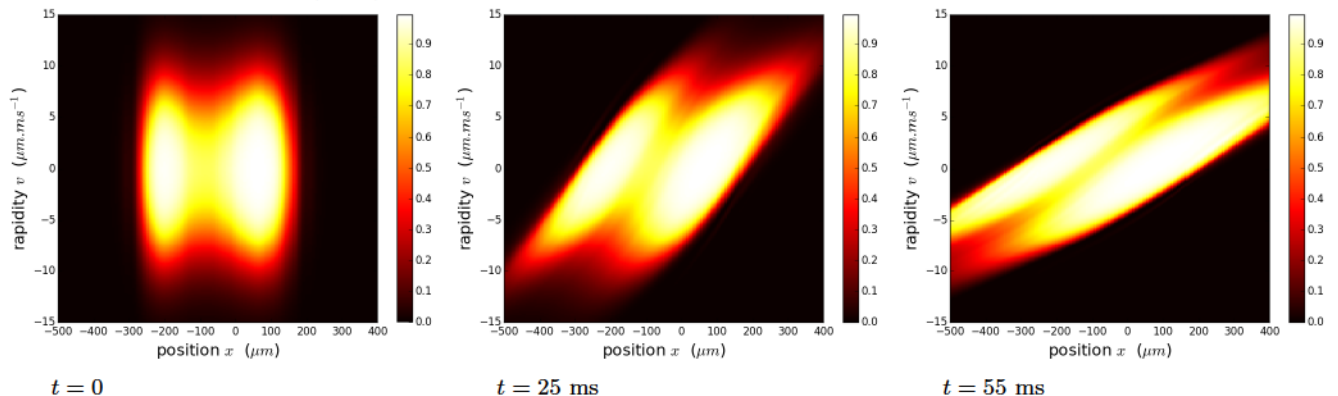
On the phase-space pictures in Fig. 2, one clearly sees why CHD must differ from GHD. Indeed, initially the phase-space occupation is the equilibrium one at temperature $T = 0.3 \mu\text{K}$, obtained from LDA in the double-well potential $V(x)$, see the main text. Because the atomic density increases near the two minima of the potential $V(x)$, the interval $[v_1, v_2]$ in which the occupation function is close to 1 is larger near these points. This results in the support of $\nu(x, t)$ looking like a peanut at $t = 0$. By definition, the initial distribution is the same for GHD and CHD.

At later times, the distribution gets distorted. GHD predicts that the top of the support of $\nu(x, v)$ moves to the right, while the bottom of the support moves to the left. At $t \simeq 25$ ms we already see that, for a fixed x in the central region around $x = 0$, the occupation function $\nu(v)$ does not look like a thermal equilibrium distribution anymore: instead of being a rounded rectangular function, it is now a function that has two maxima. This gets worse as time increases: the distribution $\nu(v)$, for fixed position x , differs more and more from an equilibrium one.

CHD, on the contrary, enforces an equilibrium occupation function at all positions and all times. Therefore, it must differ significantly from GHD. Indeed, this is what we see in the phase-space occupation at $t = 25$ ms, where the occupation function of CHD is distorted in the central region, compared to the GHD one, in order to maintain a thermal state. The discrepancy between GHD and CHD then keeps increasing at later times.

The density profiles of Fig. 3 in the main text are obtained from these phase-space occupation function $\nu(x, \theta)$ by Eq. (6) and then integrating over all rapidities at fixed position x , $n(x) = \int \rho(x, v) dv$.

Generalized Hydrodynamics (GHD):



Conventional hydrodynamics (CHD):

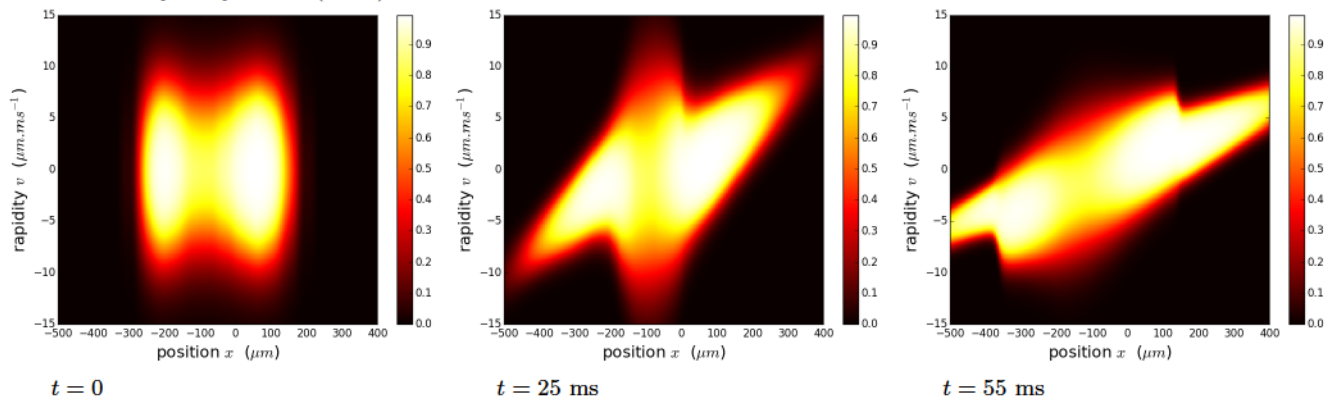


FIG. 2. Phase-space occupation $\nu(x, v)$ at time t for the parameters of Fig. 3 in the main text, simulated with GHD and CHD. Since CHD does not allow non-thermal local distributions of rapidities, we see that the distribution gets quickly distorted, compared to the GHD one. This results in the two in situ density profiles being clearly different, see Fig. 3 in the main text.

V. GROSS PITAEVSKII PREDICTIONS FOR EXPANSION FROM A DOUBLE WELL

We performed a Gross Pitaevskii calculation for the situation considered in Fig.3. In this calculation, the initial wavefunction is $\psi(x) = \sqrt{n_0(x)}$, where $n_0(x)$ is the initial experimental profile. We then evolve this initial profile according to the time-dependant Gross-Pitaevskii equation Eq. (8). The resulting time evolution, shown in Fig.(3), is very different from that observed experimentally. This indicates that thermal excitations initially present in the cloud play an important role in the time-evolution shown in Fig.3. Note that GHD calculations performed at a very low temperature are in agreement with these Gross-Pitaevskii calculations, provided fast oscillations shown in the Gross-Pitaevskii profiles are averaged out (see section VI).

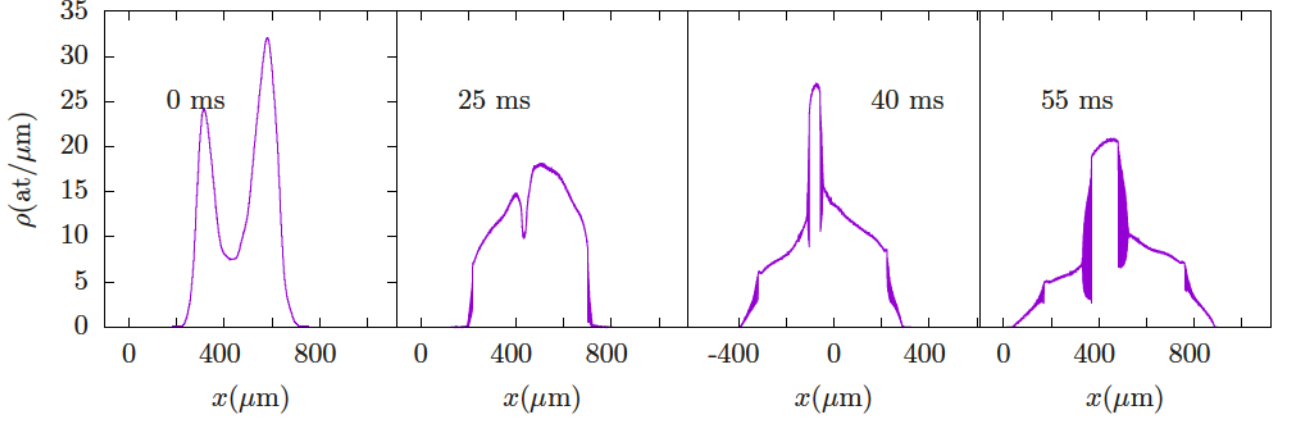


FIG. 3. Expansion of a cloud whose initial density distribution is equal to that of the experimental data of Fig. 3 in the main text, according to the Gross-Pitaevskii equation. The evolution is very different from that observed experimentally, with the appearance of a central peak, not seen experimentally.

VI. RUNNING THE GHD SIMULATION WITHOUT GOOD KNOWLEDGE OF THE INITIAL POTENTIAL $V(x)$

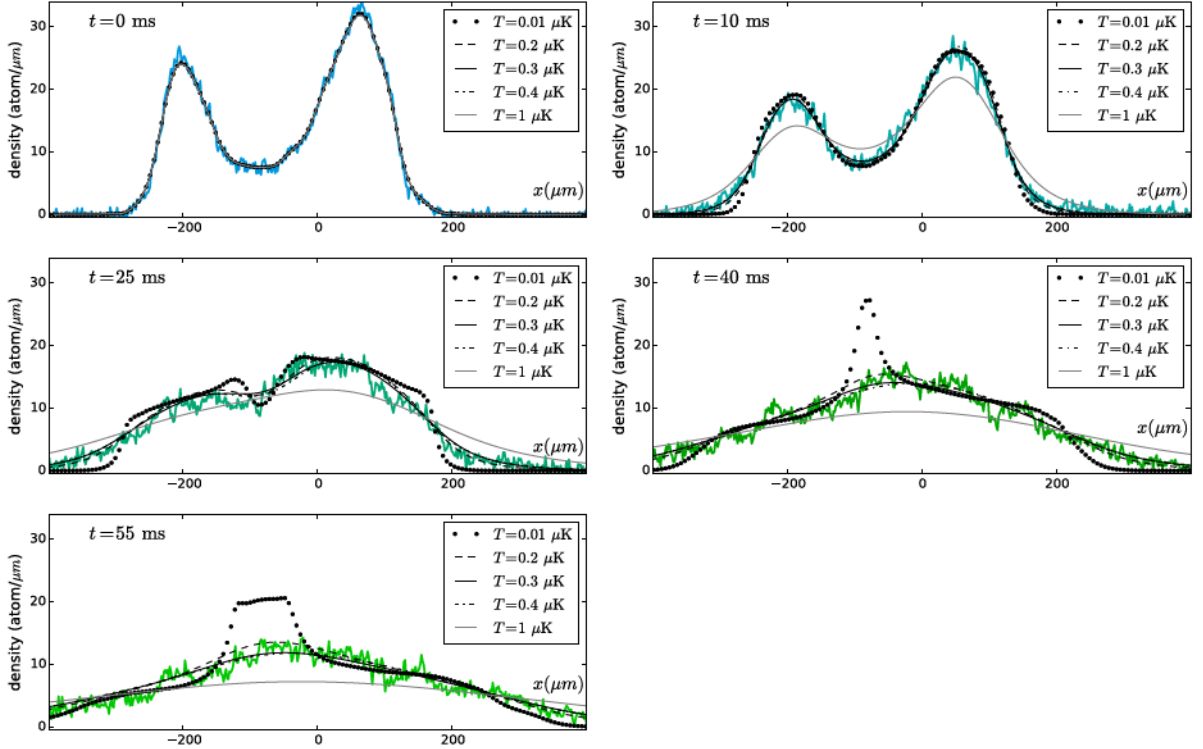


FIG. 4. Comparison between the experimental data of Fig. 3 in the main text, and the GHD simulation assuming three different temperatures of the initial state. For Fig. 3 in the main text, we selected the results corresponding to $T = 0.3 \mu\text{K}$.

The creation of a double-well potential on the chip is experimentally tricky, and, as a result, we do not have a very good knowledge of this potential. It should be close to a polynomial potential of fourth degree, $V(x) \simeq \sum_{p=0}^4 a_p x^p$,

but we do not know the coefficients a_p . One could extract them from a fit, but then we would have 6 adjustable parameters in total: the five coefficients a_p , and the temperature of the initial state.

On the other hand, the initial potential $V(x)$ is needed only to reconstruct the initial distribution $\rho(x, v)$. So, instead of trying to reconstruct first the potential $V(x)$ and then the initial distribution $\rho(x, v)$, we find it more satisfying to construct directly that distribution, assuming that it is given by a thermal Gibbs state in every fluid cell at position x . When we do that, there is a single adjustable parameter: the initial temperature, assumed to be initially homogeneous throughout the cloud.

We proceed as follows. First, we take a convolution of the experimental density at time $t = 0$ with a gaussian, in order to get a smooth initial density profile $n(x)$. Then we fix arbitrarily a temperature T , and, assuming that the gas is locally at equilibrium at temperature T , we reconstruct the occupation function $\nu(x, \theta)$ —or equivalently the distribution $\rho(x, \theta)$ —using the Yang-Yang equation of state (4). Let us emphasize that, at this point, we have reconstructed a density profile, which corresponds to some potential $V_T(x)$, and the latter potential is not independent of the choice of the temperature T . What we then want, of course, is to identify the correct T corresponding to the correct experimental $V(x)$ which, unfortunately, we do not know a priori. We then run the GHD simulation, which allows us to compute the density profiles at later times t . Those density profiles at later times depend on the initial state, therefore they depend on T .

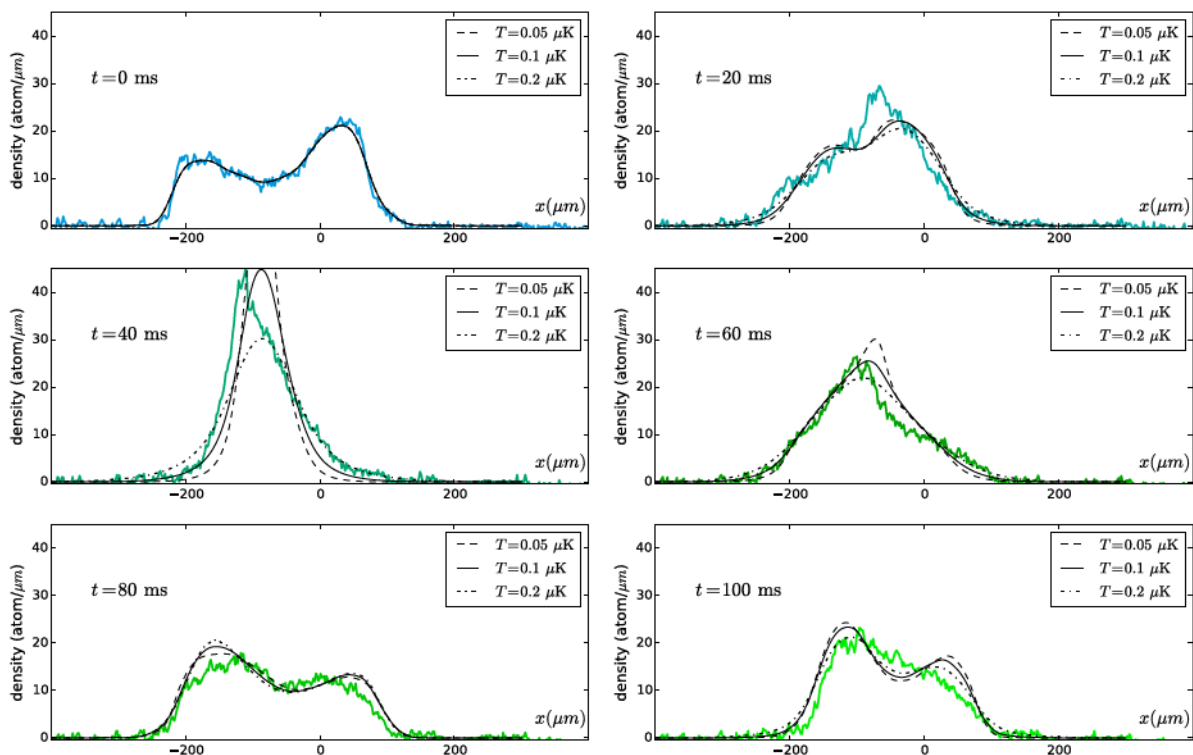


FIG. 5. Comparison between the experimental data of Fig. 4 in the main text, and the GHD simulation assuming three different temperatures of the initial state. For Fig. 4 in the main text, we selected the results corresponding to $T = 0.1 \mu\text{K}$.

We do this for several values of the initial temperature T . In Fig. 4 we display the results for the data set shown in Fig. 3 in the main text, for initial temperatures $0.2 \mu\text{K}$, $0.3 \mu\text{K}$ and $0.4 \mu\text{K}$. We see that the results do not strongly depend on the temperature. More quantitatively, for each T we measure the mean distance between the experimental data and the GHD prediction defined as $\sqrt{\frac{1}{N_{\text{data}}} \sum_{x,t} [n_{\text{data}}(x, t) - n_{\text{GHD}}(x, t)]^2}$, where the sum is done over all the data points for different positions x and times t and N_{data} is the total number of data points. For temperatures $T = 0.01, 0.2, 0.25, 0.3, 0.35, 0.4, 1 \mu\text{K}$, we find that the distance is respectively 1.21, 0.66, 0.62, 0.61, 0.64, 0.63, 1.26 (atom/ μm). In the main text, we have selected the GHD results with $T = 0.3 \mu\text{K}$, corresponding to the minimum of that distance for the set of temperatures simulated.

We have proceeded in the same way for the quench from a double-well to harmonic potential, corresponding to the data set shown in Fig. 4 in the main text. In Fig. 5 we display the GHD curves for initial temperatures $0.05 \mu\text{K}$, $0.1 \mu\text{K}$ and $0.2 \mu\text{K}$, up to time $t = 100$ ms after the quench. We have performed the GHD simulation for temperatures $T = 0.05, 0.75, 0.1, 0.125, 0.15, 0.2, 0.3 \mu\text{K}$, we find that the mean distance is respectively 2.69, 2.19, 1.88, 1.71, 1.64, 1.72, 2.08 (atom/ μm). In the main text, we have selected the GHD results with $T = 0.15 \mu\text{K}$, corresponding to the minimum of that distance for the set of temperatures simulated.

VII. APPROXIMATE PERIODICITY OF THE GHD SOLUTION FOR THE QUENCH FROM DOUBLE-WELL TO HARMONIC POTENTIAL

In Fig. 6 we display the phase-space occupation $\nu(x, v)$ for the quench from double-well to harmonic potential, corresponding to the GHD data shown in Fig. 4 in the main text. We recall that $\nu(x, v)$ is the phase-space occupation, and that it is related to the phase-space density used in the main text by Eq. (6). One can roughly think of $\nu(x, v)$ as a Fermi distribution, see App. III above. The GHD evolution equation can be written directly in terms of the occupation function $\nu(v)$, see Eq. (16).

It is clear from these plots that, after one period of the harmonic trap (the period is 154 ms), the distribution is only approximately similar to the initial one. So, even though our atomic clouds are weakly interacting, the behavior that is predicted by GHD is clearly different from the one of non-interacting particles, since the latter would be exactly periodic.

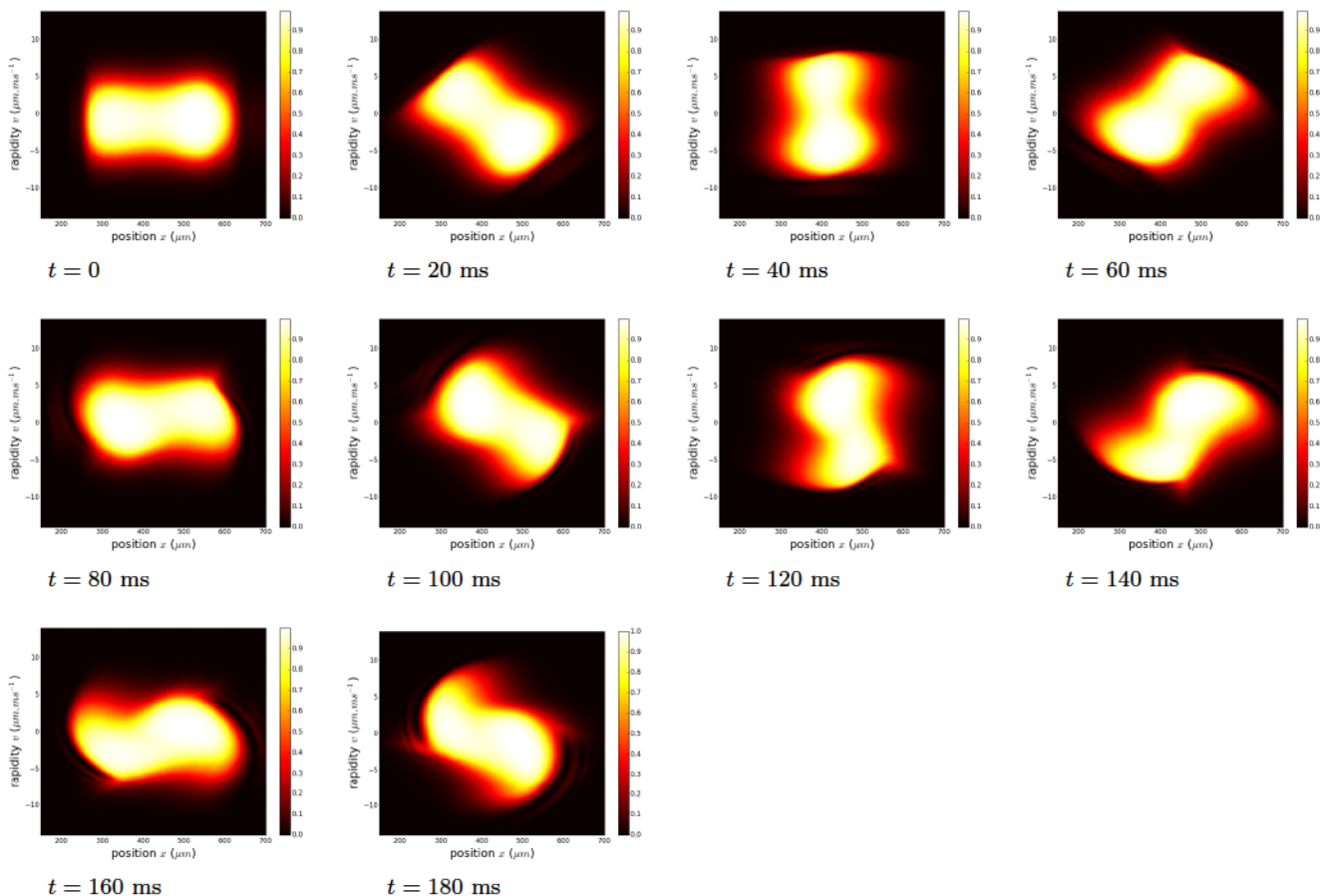


FIG. 6. Phase-space occupation $\nu(x, v)$ obtained from GHD for the quench from double-well to harmonic potential shown in Fig. 4 in the main text. The motion is *approximately* periodic, although one clearly sees that the distribution does not come back exactly to its initial shape after one period; instead, it gets slightly distorted by the interactions between the atoms. The period of the harmonic trap is 154 ms, and we see that the approximate period is roughly 165 ms.

-
- [1] J.-P. Hansen and I.R. McDonald, “Theory of simple liquids”, Second Edition. Academic Press, San Diego CA, 1990.
- [2] M.P. Allen and D.J. Tildesley, “Computer simulation of liquids”, Second Edition. Oxford University Press, Oxford UK, 2017.
- [3] H. Spohn, “Large Scale Dynamics of Interacting Particles”, Springer, Berlin, 1991.
- [4] J.K. Percus, “Exact solution of kinetics of a model classical fluid”, *The Physics of Fluids*, 12(8), 1560-1563 (1969).
- [5] C. Boldrighini, R. L. Dobrushin and Yu. M. Sukhov, “One-dimensional hard rod caricature of hydrodynamics”, *J. Stat. Phys.* **31**, 577 (1983).
- [6] B. Doyon, T. Yoshimura and J.-S. Caux, “Soliton gases and generalized hydrodynamics”, *Phys. Rev. Lett.* **120**, 045301 (2018).
- [7] O. A. Castro-Alvaredo, B. Doyon, and T. Yoshimura, “Emergent Hydrodynamics in Integrable Quantum Systems Out of Equilibrium”, *Phys. Rev. X* **6**, 041065 (2016).
- [8] B. Bertini, M. Collura, J. De Nardis, and M. Fagotti, “Transport in Out-of-Equilibrium XXZ Chains: Exact Profiles of Charges and Currents”, *Phys. Rev. Lett.* **117**, 207201 (2016).
- [9] A.H. van Amerongen, J.J.P. van Es, P. Wicke, K.V. Kheruntsyan, and N.J. van Druten, “Yang-Yang Thermodynamics on an Atom Chip”, *Phys. Rev. Lett.* **100**, 090402 (2008).
- [10] T. Jacqmin, J. Armijo, T. Berrada, K.V. Kheruntsyan, I. Bouchoule, “Sub-poissonian fluctuations in a 1d bose gas: From the quantum quasicondensate to the strongly interacting regime”, *Phys. Rev. Lett.* **106**, 230405 (2011).
- [11] A. Vogler, R. Labouvie, F. Stubenrauch, G. Barontini, V. Guarrera, and H. Ott, “Thermodynamics of strongly correlated one-dimensional Bose gases”, *Phys. Rev. A* **88**, 031603(R) (2013).
- [12] E.H. Lieb, W. Liniger, “Exact analysis of an interacting Bose gas. I. The general solution and the ground state”, *Phys. Rev.* **130**(4), 1605 (1963); F. Berezin, G. Pokhil, V. Finkelberg, “Schrödinger equation for a system of 1d particles with point interaction”, *Vestnik MGU* **1**, 21 (1964).
- [13] B. Doyon, T. Yoshimura, “A note on generalized hydrodynamics: inhomogeneous fields and other concepts”, *SciPost Phys.* **2**, 014 (2017).
- [14] B. Doyon, J. Dubail, R. Konik and T. Yoshimura, “Large-scale description of interacting one-dimensional Bose gases: generalized hydrodynamics supersedes conventional hydrodynamics”, *Phys. Rev. Lett.* **119**, 195301 (2017).
- [15] B. Doyon and H. Spohn, “Drude weight for the Lieb-Liniger Bose gas”, *SciPost Physics*, **3**(6), 039 (2017).
- [16] V.B. Bulchandani, R. Vasseur, C. Karrasch, J.E. Moore, “Solvable Hydrodynamics of Quantum Integrable Systems”, *Phys. Rev. Lett.* **119**, 220604 (2017).
- [17] J.-S. Caux, B. Doyon, J. Dubail, R. Konik and T. Yoshimura, “Hydrodynamics of the interacting Bose gas in the Quantum Newton Cradle setup”, arXiv:1711.0873.
- [18] J. Dubail, “A More Efficient Way to Describe Interacting Quantum Particles in 1D”, *Viewpoint on Refs. [7, 8] in Physics* **9**, 153 (2016).
- [19] V.B. Bulchandani, R. Vasseur, C. Karrasch, J.E. Moore, “Bethe-Boltzmann Hydrodynamics and Spin Transport in the XXZ Chain”, *Phys. Rev. B* **97**, 045407 (2018).
- [20] J. De Nardis, D. Bernard, B. Doyon, “Hydrodynamic Diffusion in Integrable Systems”, arXiv:1807.02414.
- [21] D.-L. Vu, T. Yoshimura, “Equations of state in generalized hydrodynamics”, arXiv:1809.03197.
- [22] A. Bastianello, L. Piroli, “From the sinh-Gordon field theory to the one-dimensional Bose gas: exact local correlations and full counting statistics”, arXiv:1807.06869.
- [23] A. De Luca, M. Collura, J. De Nardis, “Non-equilibrium spin transport in integrable spin chains: persistent currents and emergence of magnetic domains”, *Phys. Rev. B* **96**, 020403 (2017).
- [24] B. Doyon and H. Spohn, “Dynamics of hard rods with initial domain wall state”, *J. Stat. Mech.* 073210 (2017).
- [25] E. Ilievski, J. De Nardis, “Microscopic Origin of Ideal Conductivity in Integrable Quantum Models”, *Phys. Rev. Lett.* **119**, 020602 (2017).
- [26] L. Piroli, J. De Nardis, M. Collura, B. Bertini, M. Fagotti, “Transport in out-of-equilibrium XXZ chains: Nonballistic behavior and correlation functions”, *Phys. Rev. B* **96**, 115124 (2017).
- [27] E. Ilievski, J. De Nardis, “Ballistic transport in the one-dimensional Hubbard model: the hydrodynamic approach”, *Phys. Rev. B* **96**, 081118 (2017).
- [28] M. Fagotti, “Higher-order generalized hydrodynamics in one dimension: The noninteracting test”, *Phys. Rev. B* **96**, 220302 (2017).
- [29] V. B. Bulchandani, “On classical integrability of the hydrodynamics of quantum integrable systems”, *J. Phys. A: Math. Theor.* **50** 435203 (2017).
- [30] B. Doyon, H. Spohn, T. Yoshimura, “A geometric viewpoint on generalized hydrodynamics”, *Nucl. Phys. B* **926**, 570 (2018).
- [31] M. Collura, A. De Luca, J. Viti, “Analytic solution of the domain wall non-equilibrium stationary state”, *Phys. Rev. B* **97**, 081111 (2018).
- [32] A. Bastianello, B. Doyon, G. Watts, T. Yoshimura, “Generalized hydrodynamics of classical integrable field theory: the sinh-Gordon model”, *SciPost Phys.* **4**, 045 (2018).
- [33] By thermal equilibrium we mean a state represented by the Gibbs ensemble at a given temperature and chemical potential.
- [34] S. Stringari, “Dynamics of Bose-Einstein Condensed Gases in Highly Deformed Traps”, *Phys. Rev. A* **58**, 2385 (1998).
- [35] C. Menotti, S. Stringari, “Collective oscillations of one-dimensional Bose-Einstein gas in a time-varying trap potential and

- atomic scattering length”, *Phys. Rev. A* **66**, 043610 (2002).
- [36] S. Peotta, M. Di Ventra, “Quantum shock waves and population inversion in collisions of ultracold atomic clouds”, *Phys. Rev. A* **89**, 013621 (2014).
- [37] I. Bouchoule, S. Szigeti, M. Davis, K. Kheruntsyan, “Finite-temperature Hydrodynamics for One-dimensional Bose gases: Breathing-mode Oscillations as a Case Study”, *Phys. Rev. A* **94**, 051602(R) (2016).
- [38] G. De Rosi and S. Stringari, “Hydrodynamic versus collisionless dynamics of a one-dimensional harmonically trapped Bose gas”, *Phys. Rev. A* **94**, 063605 (2016).
- [39] Y. Atas, D. Gangardt, I. Bouchoule, K. Kheruntsyan, “Exact nonequilibrium dynamics of finite-temperature Tonks-Girardeau gases”, *Phys. Rev. A* **95**, 043622 (2017).
- [40] C.N. Yang and C.P. Yang, “Thermodynamics of a one-dimensional system of bosons with repulsive delta-function interaction”, *Journal of Mathematical Physics* **10**, 1115 (1969).
- [41] A. Zamolodchikov, “Thermodynamic Bethe Ansatz in Relativistic Models. Scaling Three State Potts and Lee- Yang Models”, *Nucl. Phys. B* **342**, 695 (1990).
- [42] J. Mossel, J.-S. Caux, “Generalized TBA and generalized Gibbs”, *J. Phys. A* **45**, 255001 (2012).
- [43] E. Ilievski, M. Medenjak, T. Prosen, L. Zadnik, “Quasilocal Charges in Integrable Lattice Systems”, *J. Stat. Mech.* **2016**, 064008 (2016).
- [44] M. Schemmer and I. Bouchoule, “Cooling a Bose gas by three-body losses”, arXiv:1712.04642.
- [45] M. Schemmer, A. Johnson, I. Bouchoule, “Monitoring squeezed collective modes of a one-dimensional Bose gas after an interaction quench using density-ripple analysis”, *Phys. Rev. A* **98**, 043604 (2018).
- [46] A. Johnson, PhD thesis (2016), <https://tel.archives-ouvertes.fr/tel-01432392v1>
- [47] M. Olshanii, “Atomic Scattering in the Presence of an External Confinement and a Gas of Impenetrable Bosons”, *Phys. Rev. Lett.* **81**, 938 (1998).
- [48] C. Mora and Y. Castin, “Extension of Bogoliubov theory to quasicondensates”, *Phys. Rev. A* **67**, 053615 (2003).
- [49] M. Cazalilla, “Bosonizing one-dimensional cold atomic gases”, *Journal of Physics B: Atomic, Molecular and Optical Physics*, **37**, S1 (2004).
- [50] K. Kheruntsyan, D. Gangardt, P. Drummond and G. Shlyapnikov, “Pair Correlations in a Finite-Temperature 1D Bose Gas”, *Phys. Rev. Lett.* **91**, 040403 (2003).
- [51] For a brief introduction of the Gross-Pitaevskii and the classical field models, see the Supplemental Material, which contains Refs. [67? ? -69].
- [52] For each x , the initial distribution $\rho(x, v)$ is given by the thermodynamic Bethe Ansatz [40].
- [53] See the Supplemental material for a detailed discussion of why the GHD prediction is close to the CHD one for the release from a harmonic trap.
- [54] See the Supplemental Material for plots of the distribution of quasi-particles in phase space and more details on why the double-well potential allows to discriminate between GHD and CHD.
- [55] See the Supplemental Material for full details on our selection procedure for the GHD profiles in the case where we do not have good knowledge of the initial potential.
- [56] T. Kinoshita, T. Wenger, and D. S. Weiss, “A Quantum Newton’s Cradle”, *Nature* **440**, 900-903 (2006).
- [57] Y. Tang, W. Kao, K.-Y. Li, S. Seo, K. Mallayya, M. Rigol, S. Gopalakrishnan and B. Lev, “Thermalization near Integrability in a Dipolar Quantum Newton’s Cradle”, *Phys. Rev. X* **8**, 021030 (2018).
- [58] C. Li, T. Zhou, I. Mazets, H.-P. Stimming, Z. Zhu, Y. Zhai, W. Xiong, X. Zhou, X. Chen and J. Schmiedmayer, “Dephasing and Relaxation of Bosons in 1D: Newton’s Cradle Revisited”, arXiv:1804.01969.
- [59] See the Supplemental Material for plots of the distribution of quasi-particles in phase space that show that the behavior predicted by GHD is only approximately periodic.
- [60] To go beyond the shock time, one would need to properly regularize the solution, for instance by considering entropy-producing diffusive terms.
- [61] C.N. Yang, “Some Exact Results for the Many-Body Problem in one Dimension with Repulsive Delta-Function Interaction”, *Phys. Rev. Lett.* **19**, 1312 (1967).
- [62] B. Sutherland, “Further Results for the Many-Body Problem in One Dimension”, *Phys. Rev. Lett.* **20**, 98 (1968).
- [63] M. Gaudin, “Un système a une dimension de fermions en interaction”, *Physics Letters A* **24**, 55 (1967).
- [64] X.-W. Guan, M. Batchelor, C. Lee, “Fermi gases in one dimension: From Bethe ansatz to experiments”, *Rev. Mod. Phys.* **85**, 1633 (2013).
- [65] P.Wicke, S.Whitlock, N. van Druten, “Controlling spin motion and interactions in a one-dimensional Bose gas”, arXiv:1010.4545.
- [66] G. Papagano et al., “A one-dimensional liquid of fermions with tunable spin”, *Nature Physics* **10** (3), 198 (2014).
- [67] Y. Castin, R. Dum, E. Mandonnet, A. Minguzzi, I. Carusotto, “Coherence properties of a continuous atom laser”, *J. Mod. Opt.* **47**, 2671 (2000).
- [68] I. Bouchoule, M. Arzamasovs, K. V. Kheruntsyan, and D. M. Gangardt, “Two-body momentum correlations in a weakly interacting one-dimensional Bose gas”, *Phys. Rev. A* **86**, 033626 (2012).
- [69] T. Jacqmin, B. Fang, T. Berrada, T. Roscilde and I. Bouchoule, “Momentum distribution of one-dimensional Bose gases at the quasicondensation crossover: Theoretical and experimental investigation”, *Phys. Rev. A*, **86**, 043626 (2012).

Bibliographie

- [1] S. I. Newton and E. Halley, *Philosophiae naturalis principia mathematica*. Jussu Societatis Regiae ac typis Josephi Streater, prostant venales apud Sam. Smith, 1687. [p. 3]
- [2] B. Sutherland, *Beautiful Models : 70 Years of Exactly Solved Quantum Many-Body Problems*. World Scientific Publishing Company, June 2004. [p. 3, 11, 16]
- [3] J.-S. Caux and J. Mossel, “Remarks on the notion of quantum integrability,” *Journal of Statistical Mechanics : Theory and Experiment*, vol. 2011, no. 02, p. P02023, 2011. [p. 3, 87]
- [4] H. Bethe, “Zur Theorie der Metalle,” *Zeitschrift für Physik*, vol. 71, pp. 205–226, Mar. 1931. [p. 3]
- [5] E. H. Lieb and W. Liniger, “Exact Analysis of an Interacting Bose Gas. I. The General Solution and the Ground State,” *Physical Review*, vol. 130, pp. 1605–1616, May 1963. [p. 3, 9, 11]
- [6] T. Kinoshita, T. Wenger, and D. S. Weiss, “Observation of a One-Dimensional Tonks-Girardeau Gas,” *Science*, vol. 305, pp. 1125–1128, Aug. 2004. [p. 3]
- [7] B. L. Tolra, K. M. O’Hara, J. H. Huckans, W. D. Phillips, S. L. Rolston, and J. V. Porto, “Observation of Reduced Three-Body Recombination in a Correlated 1D Degenerate Bose Gas,” *Physical Review Letters*, vol. 92, p. 190401, May 2004. [p. 21, 126]
- [8] B. Paredes, A. Widera, V. Murg, O. Mandel, S. Fölling, I. Cirac, G. V. Shlyapnikov, T. W. Hänsch, and I. Bloch, “Tonks–Girardeau gas of ultracold atoms in an optical lattice,” *Nature*, vol. 429, pp. 277–281, May 2004.
- [9] T. Kinoshita, T. Wenger, and D. S. Weiss, “Local Pair Correlations in One-Dimensional Bose Gases,” *Physical Review Letters*, vol. 95, p. 190406, Nov. 2005.

- [10] T. Schumm, S. Hofferberth, L. M. Andersson, S. Wildermuth, S. Groth, I. Bar-Joseph, J. Schmiedmayer, and P. Krüger, “Matter-wave interferometry in a double well on an atom chip,” *Nature Physics*, vol. 1, pp. 57–62, Oct. 2005. [p. 162]
- [11] J. Esteve, J.-B. Trebbia, T. Schumm, A. Aspect, C. I. Westbrook, and I. Bouchoule, “Observations of Density Fluctuations in an Elongated Bose Gas : Ideal Gas and Quasicondensate Regimes,” *Physical Review Letters*, vol. 96, p. 130403, Apr. 2006. [p. 70]
- [12] A. H. van Amerongen, J. J. P. van Es, P. Wicke, K. V. Kheruntsyan, and N. J. van Druten, “Yang-Yang Thermodynamics on an Atom Chip,” *Physical Review Letters*, vol. 100, p. 090402, Mar. 2008. [p. 78, 79, 147]
- [13] E. Haller, M. Gustavsson, M. J. Mark, J. G. Danzl, R. Hart, G. Pupillo, and H.-C. Nägerl, “Realization of an Excited, Strongly Correlated Quantum Gas Phase,” *Science*, vol. 325, pp. 1224–1227, Sept. 2009. [p. 3]
- [14] F. Salces-Carcoba, C. J. Billington, A. Putra, Y. Yue, S. Sugawa, and I. B. Spielman, “Equations of state from individual one-dimensional Bose gases,” *New Journal of Physics*, vol. 20, no. 11, p. 113032, 2018. [p. 3, 16]
- [15] O. A. Castro-Alvaredo, B. Doyon, and T. Yoshimura, “Emergent Hydrodynamics in Integrable Quantum Systems Out of Equilibrium,” *Physical Review X*, vol. 6, p. 041065, Dec. 2016. [p. 3, 32, 33, 34, 147]
- [16] B. Bertini, M. Collura, J. De Nardis, and M. Fagotti, “Transport in Out-of-Equilibrium XXZ Chains : Exact Profiles of Charges and Currents,” *Physical Review Letters*, vol. 117, p. 207201, Nov. 2016. [p. 32, 147]
- [17] J. Dubail, “Viewpoint : A More Efficient Way to Describe Interacting Quantum Particles in 1D,” *Physics*, vol. 9, Dec. 2016. [p. 3]
- [18] M. Schemmer, A. Johnson, and I. Bouchoule, “Monitoring squeezed collective modes of a one-dimensional Bose gas after an interaction quench using density-ripple analysis,” *Physical Review A*, vol. 98, p. 043604, Oct. 2018. [p. 4, 70, 85, 94, 95, 96, 102, 161]
- [19] B. Rauer, P. Grišins, I. E. Mazets, T. Schweigler, W. Rohringer, R. Geiger, T. Langen, and J. Schmiedmayer, “Cooling of a One-Dimensional Bose Gas,” *Physical Review Letters*, vol. 116, p. 030402, Jan. 2016. [p. 4, 70, 109, 138, 139, 174]
- [20] P. Grišins, B. Rauer, T. Langen, J. Schmiedmayer, and I. E. Mazets, “Degenerate Bose gases with uniform loss,” *Physical Review A*, vol. 93, p. 033634, Mar. 2016. [p. 4, 109, 121]

- [21] M. Schemmer, A. Johnson, R. Photopoulos, and I. Bouchoule, “Monte Carlo wave-function description of losses in a one-dimensional Bose gas and cooling to the ground state by quantum feedback,” *Physical Review A*, vol. 95, p. 043641, Apr. 2017. [p. 5, 109, 121, 141, 142, 174]
- [22] A. Johnson, S. S. Szigeti, M. Schemmer, and I. Bouchoule, “Long-lived nonthermal states realized by atom losses in one-dimensional quasicondensates,” *Physical Review A*, vol. 96, p. 013623, July 2017. [p. 80, 82, 121, 124, 135, 136, 144]
- [23] I. Bouchoule, M. Schemmer, and C. Henkel, “Cooling phonon modes of a Bose condensate with uniform few body losses,” *SciPost Physics*, vol. 5, p. 043, Nov. 2018. [p. 27, 29, 109, 122, 130, 131, 132, 139, 140, 143]
- [24] M. Schemmer and I. Bouchoule, “Cooling a Bose Gas by Three-Body Losses,” *Physical Review Letters*, vol. 121, p. 200401, Nov. 2018. [p. 5, 70, 109, 122, 175]
- [25] M. Schemmer, I. Bouchoule, B. Doyon, and J. Dubail, “Generalized Hydrodynamics on an Atom Chip,” *Physical Review Letters*, vol. 122, p. 090601, Mar. 2019. [p. 5, 147, 152]
- [26] T. Kinoshita, T. Wenger, and D. S. Weiss, “A quantum Newton’s cradle,” *Nature*, vol. 440, pp. 900–903, Apr. 2006. [p. 5, 156]
- [27] H. Ouerdane and M. J. Jamieson, “S-wave and p-wave scattering in a cold gas of Na and Rb atoms,” *The European Physical Journal D*, vol. 53, pp. 27–32, May 2009. [p. 8]
- [28] C. J. Pethick and H. Smith, *Bose-Einstein Condensation in Dilute Gases*. Sept. 2008. [p. 8, 42]
- [29] M. Olshanii, “Atomic Scattering in the Presence of an External Confinement and a Gas of Impenetrable Bosons,” *Physical Review Letters*, vol. 81, pp. 938–941, Aug. 1998. [p. 8]
- [30] E. Haller, M. J. Mark, R. Hart, J. G. Danzl, L. Reichsöllner, V. Melezhik, P. Schmelcher, and H.-C. Nägerl, “Confinement-Induced Resonances in Low-Dimensional Quantum Systems,” *Physical Review Letters*, vol. 104, p. 153203, Apr. 2010. [p. 8]
- [31] E. H. Lieb, “Exact Analysis of an Interacting Bose Gas. 2. The Excitation Spectrum,” *Phys.Rev.*, vol. 130, pp. 1616–1624, 1963. [p. 9, 13]
- [32] F. Franchini, “The Lieb-Liniger Model,” in *An Introduction to Integrable Techniques for One-Dimensional Quantum Systems* (F. Franchini, ed.), Lecture

- Notes in Physics, pp. 19–45, Cham : Springer International Publishing, 2017. [p. 11, 16]
- [33] J. Dubail, ““Generalized” HydroDynamics (GHD) : A short introduction,” Sept. 2017. [p. 11, 16, 33]
- [34] M. Ishikawa and H. Takayama, “Solitons in a One-Dimensional Bose System with the Repulsive Delta-Function Interaction,” *Journal of the Physical Society of Japan*, vol. 49, pp. 1242–1246, Oct. 1980. [p. 14]
- [35] C. N. Yang and C. P. Yang, “Thermodynamics of a One-Dimensional System of Bosons with Repulsive Delta-Function Interaction,” *Journal of Mathematical Physics*, vol. 10, pp. 1115–1122, July 1969. [p. 15, 16]
- [36] Y. B. Fang, *Equilibrium and Nonequilibrium Behaviours of 1D Bose Gases*. Theses, Institut d’Optique Graduate School, Oct. 2014. [p. 16, 39, 63, 65, 68, 70, 82, 135, 136, 144]
- [37] N. D. Mermin and H. Wagner, “Absence of Ferromagnetism or Antiferromagnetism in One- or Two-Dimensional Isotropic Heisenberg Models,” *Physical Review Letters*, vol. 17, pp. 1133–1136, Nov. 1966. [p. 16]
- [38] P. C. Hohenberg, “Existence of Long-Range Order in One and Two Dimensions,” *Physical Review*, vol. 158, pp. 383–386, June 1967.
- [39] S. Coleman, “There are no Goldstone bosons in two dimensions,” *Communications in Mathematical Physics*, vol. 31, pp. 259–264, Dec. 1973. [p. 16]
- [40] T. Jacqmin, B. Fang, T. Berrada, T. Roscilde, and I. Bouchoule, “Momentum distribution of one-dimensional Bose gases at the quasicondensation crossover : Theoretical and experimental investigation,” *Physical Review A*, vol. 86, p. 043626, Oct. 2012. [p. 16, 20, 80]
- [41] K. V. Kheruntsyan, D. M. Gangardt, P. D. Drummond, and G. V. Shlyapnikov, “Pair Correlations in a Finite-Temperature 1D Bose Gas,” *Physical Review Letters*, vol. 91, p. 040403, July 2003. [p. 17]
- [42] T. Jacqmin, *Probing Correlations in a One-Dimensional Gas of Bosons on an Atom Chip*. Theses, Université Paris Sud - Paris XI, Nov. 2012. [p. 18, 20, 39, 49, 51, 53, 54, 66, 68, 80, 81, 163]
- [43] Y. Castin, “Simple theoretical tools for low dimension Bose gases,” *Journal de Physique IV (Proceedings)*, vol. 116, pp. 89–132, Oct. 2004. [p. 21, 23, 30]

- [44] M. A. Cazalilla, R. Citro, T. Giamarchi, E. Orignac, and M. Rigol, “One dimensional bosons : From condensed matter systems to ultracold gases,” *Reviews of Modern Physics*, vol. 83, pp. 1405–1466, Dec. 2011. [p. 21]
- [45] N. Bogolubov, “On the theory of superfluidity,” *J. Phys*, p. 10, 1946. [p. 21]
- [46] C. Mora and Y. Castin, “Extension of Bogoliubov theory to quasicondensates,” *Physical Review A*, vol. 67, p. 053615, May 2003. [p. 21, 23, 31]
- [47] T.-L. Ho and M. Ma, “Quasi 1 and 2d Dilute Bose Gas in Magnetic Traps : Existence of Off-Diagonal Order and Anomalous Quantum Fluctuations,” *Journal of Low Temperature Physics*, vol. 115, pp. 61–70, Apr. 1999. [p. 27]
- [48] D. S. Petrov, G. V. Shlyapnikov, and J. T. M. Walraven, “Regimes of Quantum Degeneracy in Trapped 1D Gases,” *Physical Review Letters*, vol. 85, pp. 3745–3749, Oct. 2000. [p. 27]
- [49] L. Salasnich, A. Parola, and L. Reatto, “Effective wave equations for the dynamics of cigar-shaped and disk-shaped Bose condensates,” *Physical Review A*, vol. 65, p. 043614, Apr. 2002. [p. 28]
- [50] E. Gerbier, “Quasi-1D Bose-Einstein condensates in the dimensional crossover regime,” *EPL (Europhysics Letters)*, vol. 66, p. 771, June 2004. [p. 28]
- [51] J. N. Fuchs, X. Leyronas, and R. Combescot, “Hydrodynamic modes of a one-dimensional trapped Bose gas,” *Physical Review A*, vol. 68, p. 043610, Oct. 2003. [p. 28]
- [52] S. P. Cockburn, D. Gallucci, and N. P. Proukakis, “Quantitative study of quasi-one-dimensional Bose gas experiments via the stochastic Gross-Pitaevskii equation,” *Physical Review A*, vol. 84, p. 023613, Aug. 2011. [p. 29]
- [53] W. Bao, D. Jaksch, and P. A. Markowich, “Numerical solution of the Gross–Pitaevskii equation for Bose–Einstein condensation,” *Journal of Computational Physics*, vol. 187, pp. 318–342, May 2003. [p. 30, 156]
- [54] J. De Nardis, D. Bernard, and B. Doyon, “Hydrodynamic Diffusion in Integrable Systems,” *Physical Review Letters*, vol. 121, p. 160603, Oct. 2018. [p. 35]
- [55] B. Doyon, T. Yoshimura, and T. Yoshimura, “A note on generalized hydrodynamics : Inhomogeneous fields and other concepts,” *SciPost Physics*, vol. 2, p. 014, Apr. 2017. [p. 35]

- [56] K. Mølmer and Y. Castin, “Monte Carlo wavefunctions in quantum optics,” *Quantum and Semiclassical Optics : Journal of the European Optical Society Part B*, vol. 8, no. 1, p. 49, 1996. [p. 36]
- [57] J. Dalibard, Y. Castin, and K. Mølmer, “Wave-function approach to dissipative processes in quantum optics,” *Physical Review Letters*, vol. 68, pp. 580–583, Feb. 1992. [p. 36]
- [58] H.-P. Breuer, W. Huber, and F. Petruccione, “Stochastic wave-function method versus density matrix : A numerical comparison,” *Computer Physics Communications*, vol. 104, pp. 46–58, Aug. 1997. [p. 37]
- [59] A. Johnson, *One-Dimensional Bose Gases on an Atom Chip : Correlations in Momentum Space and Theoretical Investigation of Loss-Induced Cooling*. Theses, Université Paris-Saclay, Dec. 2016. [p. 39, 40, 41, 63, 65, 68, 82]
- [60] J. Armijo, C. L. Garrido Alzar, and I. Bouchoule, “Thermal properties of AlN-based atom chips,” *The European Physical Journal D*, vol. 56, p. 33, Nov. 2009. [p. 40]
- [61] J.-B. Trebbia, C. L. Garrido Alzar, R. Cornelussen, C. I. Westbrook, and I. Bouchoule, “Roughness Suppression via Rapid Current Modulation on an Atom Chip,” *Physical Review Letters*, vol. 98, p. 263201, June 2007. [p. 41, 45]
- [62] E. Majorana, “Atomi orientati in campo magnetico variabile,” *Il Nuovo Cimento (1924-1942)*, vol. 9, pp. 43–50, Feb. 1932. [p. 42]
- [63] R. Folman, P. Krüger, J. Schmiedmayer, J. Denschlag, and C. Henkel, “Microscopic atom optics : From wires to an atom chip,” *Advances in Atomic Molecular and Optical Physics*, vol. 48, pp. 263–356, 2002. [p. 42, 60, 62]
- [64] W. Wing, “On neutral particle trapping in quasistatic electromagnetic fields,” *Progress in Quantum Electronics*, vol. 8, pp. 181–199, Jan. 1984. [p. 42]
- [65] T. Schumm, *Bose-Einstein Condensates in Magnetic Double Well Potentials*. Theses, Université Paris Sud - Paris XI, Feb. 2006. [p. 44]
- [66] S. Kraft, A. Günther, H. Ott, D. Wharam, C. Zimmermann, and J. Fortágh, “Anomalous longitudinal magnetic field near the surface of copper conductors,” *Journal of Physics B : Atomic, Molecular and Optical Physics*, vol. 35, no. 21, p. L469, 2002. [p. 45]
- [67] T. Schumm, J. Estève, C. Figl, J.-B. Trebbia, C. Aussibal, H. Nguyen, D. Mailly, I. Bouchoule, C. I. Westbrook, and A. Aspect, “Atom chips in the real world :

- The effects of wire corrugation,” *The European Physical Journal D - Atomic, Molecular, Optical and Plasma Physics*, vol. 32, pp. 171–180, Feb. 2005. [p. 45]
- [68] D.-W. Wang, M. D. Lukin, and E. Demler, “Disordered Bose-Einstein Condensates in Quasi-One-Dimensional Magnetic Microtraps,” *Physical Review Letters*, vol. 92, p. 076802, Feb. 2004. [p. 45]
- [69] J. Estève, C. Aussibal, T. Schumm, C. Figl, D. Mailly, I. Bouchoule, C. I. Westbrook, and A. Aspect, “Role of wire imperfections in micromagnetic traps for atoms,” *Physical Review A*, vol. 70, p. 043629, Oct. 2004. [p. 45]
- [70] P. Krüger, L. M. Andersson, S. Wildermuth, S. Hofferberth, E. Haller, S. Aigner, S. Groth, I. Bar-Joseph, and J. Schmiedmayer, “Potential roughness near lithographically fabricated atom chips,” *Physical Review A*, vol. 76, p. 063621, Dec. 2007. [p. 45]
- [71] J.-B. Trebbia, *Study of Degenerate Bose Gases in the Quasi-One Dimensional Regime Confined by an Atom Chip*. Theses, Université Paris Sud - Paris XI, Oct. 2007. [p. 45, 65, 84]
- [72] I. Bouchoule, J.-B. Trebbia, and C. L. Garrido Alzar, “Limitations of the modulation method to smooth wire-guide roughness,” *Physical Review A*, vol. 77, p. 023624, Feb. 2008. [p. 47]
- [73] J. M. McGuirk, D. M. Harber, J. M. Obrecht, and E. A. Cornell, “Alkali-metal adsorbate polarization on conducting and insulating surfaces probed with Bose-Einstein condensates,” *Physical Review A*, vol. 69, p. 062905, June 2004. [p. 57]
- [74] K. S. Chan, M. Siercke, C. Hufnagel, and R. Dumke, “Adsorbate Electric Fields on a Cryogenic Atom Chip,” *Physical Review Letters*, vol. 112, p. 026101, Jan. 2014. [p. 57]
- [75] C. Hermann-Avigliano, R. C. Teixeira, T. L. Nguyen, T. Cantat-Moltrecht, G. Nogues, I. Dotsenko, S. Gleyzes, J. M. Raimond, S. Haroche, and M. Brune, “Long coherence times for Rydberg qubits on a superconducting atom chip,” *Physical Review A*, vol. 90, p. 040502, Oct. 2014. [p. 57]
- [76] J. A. Sedlacek, E. Kim, S. T. Rittenhouse, P. F. Weck, H. R. Sadeghpour, and J. P. Shaffer, “Electric Field Cancellation on Quartz by Rb Adsorbate-Induced Negative Electron Affinity,” *Physical Review Letters*, vol. 116, p. 133201, Mar. 2016. [p. 57]
- [77] S. Magnusson, “Design and construction of a pyramidal Magneto-Optical Trap for laser cooling of rubidium atoms,” tech. rep., Lund Technical University, Lund Reports in Atomic Physics, 2005. [p. 57]

- [78] P. B. Wigley, P. J. Everitt, A. van den Hengel, J. W. Bastian, M. A. Sooriyabandara, G. D. McDonald, K. S. Hardman, C. D. Quinlivan, P. Manju, C. C. N. Kuhn, I. R. Petersen, A. N. Luiten, J. J. Hope, N. P. Robins, and M. R. Hush, “Fast machine-learning online optimization of ultra-cold-atom experiments,” *Scientific Reports*, vol. 6, May 2016. [p. 58]
- [79] A. D. Tranter, H. J. Slatyer, M. R. Hush, A. C. Leung, J. L. Everett, K. V. Paul, P. Vernaz-Gris, P. K. Lam, B. C. Buchler, and G. T. Campbell, “Multiparameter optimisation of a magneto-optical trap using deep learning,” *arXiv:1805.00654 [physics, physics :quant-ph]*, May 2018. [p. 58]
- [80] T. Lausch, M. Hohmann, F. Kindermann, D. Mayer, F. Schmidt, and A. Widera, “Optimizing quantum gas production by an evolutionary algorithm,” *Applied Physics B*, vol. 122, p. 112, May 2016. [p. 58]
- [81] W. Rohringer, R. Bücker, S. Manz, T. Betz, C. Koller, M. Göbel, A. Perrin, J. Schmiedmayer, and T. Schumm, “Stochastic optimization of a cold atom experiment using a genetic algorithm,” *Applied Physics Letters*, vol. 93, p. 264101, Dec. 2008. [p. 58, 59]
- [82] H. Mühlenbein and D. Schlierkamp-Voosen, “Predictive Models for the Breeder Genetic Algorithm I. Continuous Parameter Optimization,” *Evolutionary Computation*, vol. 1, pp. 25–49, Mar. 1993. [p. 59]
- [83] S. Bali, K. M. O’Hara, M. E. Gehm, S. R. Granade, and J. E. Thomas, “Quantum-diffractive background gas collisions in atom-trap heating and loss,” *Physical Review A*, vol. 60, pp. R29–R32, July 1999. [p. 60]
- [84] S. Wildermuth, S. Hofferberth, I. Lesanovsky, S. Groth, I. Bar-Joseph, P. Krueger, and J. Schmiedmayer, “Sensing electric and magnetic fields with Bose-Einstein Condensates,” *Applied Physics Letters*, vol. 88, p. 264103, June 2006. [p. 61]
- [85] S. Wildermuth, S. Hofferberth, I. Lesanovsky, E. Haller, L. M. Andersson, S. Groth, I. Bar-Joseph, P. Krüger, and J. Schmiedmayer, “Bose-Einstein condensates : Microscopic magnetic-field imaging,” *Nature*, vol. 435, p. 440, May 2005. [p. 61]
- [86] C. Henkel, S. Pötting, and M. Wilkens, “Loss and heating of particles in small and noisy traps,” *Applied Physics B*, vol. 69, pp. 379–387, Dec. 1999. [p. 62]
- [87] B. E. Schultz, “Measurement of the rubidium D2 natural transition linewidth,” *Ph.D. Thesis*, 2010. [p. 66]

- [88] G. Reinaudi, T. Lahaye, Z. Wang, and D. Guéry-Odelin, “Strong saturation absorption imaging of dense clouds of ultracold atoms,” *Optics Letters*, vol. 32, pp. 3143–3145, Nov. 2007. [p. 68]
- [89] S. Dettmer, D. Hellweg, P. Ryytty, J. J. Arlt, W. Ertmer, K. Sengstock, D. S. Petrov, G. V. Shlyapnikov, H. Kreutzmann, L. Santos, and M. Lewenstein, “Observation of Phase Fluctuations in Elongated Bose-Einstein Condensates,” *Physical Review Letters*, vol. 87, p. 160406, Oct. 2001. [p. 70]
- [90] A. Imambekov, I. E. Mazets, D. S. Petrov, V. Gritsev, S. Manz, S. Hofferberth, T. Schumm, E. Demler, and J. Schmiedmayer, “Density ripples in expanding low-dimensional gases as a probe of correlations,” *Physical Review A*, vol. 80, p. 033604, Sept. 2009. [p. 70, 73]
- [91] S. Manz, R. Bücker, T. Betz, C. Koller, S. Hofferberth, I. E. Mazets, A. Imambekov, E. Demler, A. Perrin, J. Schmiedmayer, and T. Schumm, “Two-point density correlations of quasicondensates in free expansion,” *Physical Review A*, vol. 81, p. 031610, Mar. 2010. [p. 70]
- [92] T. Jacqmin, J. Armijo, T. Berrada, K. V. Kheruntsyan, and I. Bouchoule, “Sub-Poissonian Fluctuations in a 1D Bose Gas : From the Quantum Quasicondensate to the Strongly Interacting Regime,” *Physical Review Letters*, vol. 106, p. 230405, June 2011. [p. 70, 78]
- [93] J. Armijo, T. Jacqmin, K. Kheruntsyan, and I. Bouchoule, “Mapping out the quasicondensate transition through the dimensional crossover from one to three dimensions,” *Physical Review A*, vol. 83, p. 021605, Feb. 2011. [p. 70, 79]
- [94] D. Hellweg, S. Dettmer, P. Ryytty, J. Arlt, W. Ertmer, K. Sengstock, D. Petrov, G. Shlyapnikov, H. Kreutzmann, L. Santos, and M. Lewenstein, “Phase fluctuations in Bose-Einstein condensates,” *Applied Physics B*, vol. 73, pp. 781–789, Dec. 2001. [p. 78]
- [95] A. Vogler, R. Labouvie, F. Stubenrauch, G. Barontini, V. Guarrera, and H. Ott, “Thermodynamics of strongly correlated one-dimensional Bose gases,” *Physical Review A*, vol. 88, p. 031603, Sept. 2013. [p. 78]
- [96] I. Shvarchuck, C. Buggle, D. S. Petrov, K. Dieckmann, M. Zielonkowski, M. Kemmann, T. G. Tiecke, W. von Klitzing, G. V. Shlyapnikov, and J. T. M. Walraven, “Bose-Einstein Condensation into Nonequilibrium States Studied by Condensate Focusing,” *Physical Review Letters*, vol. 89, p. 270404, Dec. 2002. [p. 80]
- [97] M. J. Davis, P. B. Blakie, A. H. van Amerongen, N. J. van Druten, and K. V. Kheruntsyan, “Yang-Yang thermometry and momentum distribution of a trapped

- one-dimensional Bose gas," *Physical Review A*, vol. 85, p. 031604, Mar. 2012. [p. 80]
- [98] B. Fang, G. Carleo, A. Johnson, and I. Bouchoule, "Quench-Induced Breathing Mode of One-Dimensional Bose Gases," *Physical Review Letters*, vol. 113, p. 035301, July 2014. [p. 80, 89]
- [99] B. Fang, A. Johnson, T. Roscilde, and I. Bouchoule, "Momentum-Space Correlations of a One-Dimensional Bose Gas," *Physical Review Letters*, vol. 116, p. 050402, Feb. 2016. [p. 80]
- [100] S. Trotzky, Y.-A. Chen, A. Flesch, I. P. McCulloch, U. Schollwöck, J. Eisert, and I. Bloch, "Probing the relaxation towards equilibrium in an isolated strongly correlated one-dimensional Bose gas," *Nature Physics*, vol. 8, pp. 325–330, Apr. 2012. [p. 86]
- [101] M. Cheneau, P. Barmettler, D. Poletti, M. Endres, P. Schauß, T. Fukuhara, C. Gross, I. Bloch, C. Kollath, and S. Kuhr, "Light-cone-like spreading of correlations in a quantum many-body system," *Nature*, vol. 481, pp. 484–487, Jan. 2012.
- [102] C.-L. Hung, V. Gurarie, and C. Chin, "From Cosmology to Cold Atoms : Observation of Sakharov Oscillations in a Quenched Atomic Superfluid," *Science*, p. 1237557, Aug. 2013. [p. 98]
- [103] T. Langen, R. Geiger, M. Kuhnert, B. Rauer, and J. Schmiedmayer, "Local emergence of thermal correlations in an isolated quantum many-body system," *Nature Physics*, vol. 9, pp. 640–643, Oct. 2013. [p. 88, 93, 95]
- [104] J.-C. Jaskula, G. B. Partridge, M. Bonneau, R. Lopes, J. Ruaudel, D. Boiron, and C. I. Westbrook, "Acoustic Analog to the Dynamical Casimir Effect in a Bose-Einstein Condensate," *Physical Review Letters*, vol. 109, p. 220401, Nov. 2012.
- [105] L. Xia, L. A. Zundel, J. Carrasquilla, A. Reinhard, J. M. Wilson, M. Rigol, and D. S. Weiss, "Quantum distillation and confinement of vacancies in a doublon sea," *Nature Physics*, vol. 11, pp. 316–320, Apr. 2015.
- [106] J. P. Ronzheimer, M. Schreiber, S. Braun, S. S. Hodgman, S. Langer, I. P. McCulloch, F. Heidrich-Meisner, I. Bloch, and U. Schneider, "Expansion Dynamics of Interacting Bosons in Homogeneous Lattices in One and Two Dimensions," *Physical Review Letters*, vol. 110, p. 205301, May 2013.
- [107] U. Schneider, L. Hackermüller, J. P. Ronzheimer, S. Will, S. Braun, T. Best, I. Bloch, E. Demler, S. Mandt, D. Rasch, and A. Rosch, "Fermionic transport

- and out-of-equilibrium dynamics in a homogeneous Hubbard model with ultracold atoms,” *Nature Physics*, vol. 8, pp. 213–218, Mar. 2012.
- [108] N. Strohmaier, Y. Takasu, K. Günter, R. Jördens, M. Köhl, H. Moritz, and T. Esslinger, “Interaction-Controlled Transport of an Ultracold Fermi Gas,” *Physical Review Letters*, vol. 99, p. 220601, Nov. 2007. [p. 86]
- [109] J. M. Deutsch, “Quantum statistical mechanics in a closed system,” *Physical Review A*, vol. 43, pp. 2046–2049, Feb. 1991. [p. 86]
- [110] M. Srednicki, “Chaos and quantum thermalization,” *Physical Review E*, vol. 50, pp. 888–901, Aug. 1994.
- [111] M. Rigol, V. Dunjko, and M. Olshanii, “Thermalization and its mechanism for generic isolated quantum systems,” *Nature*, vol. 452, pp. 854–858, Apr. 2008. [p. 86, 87]
- [112] J. Eisert, M. Friesdorf, and C. Gogolin, “Quantum many-body systems out of equilibrium,” *Nature Physics*, vol. 11, pp. 124–130, Feb. 2015. [p. 86]
- [113] A. Polkovnikov, K. Sengupta, A. Silva, and M. Vengalattore, “Colloquium : Nonequilibrium dynamics of closed interacting quantum systems,” *Reviews of Modern Physics*, vol. 83, pp. 863–883, Aug. 2011.
- [114] A. Mitra, “Quantum Quench Dynamics,” *Annual Review of Condensed Matter Physics*, vol. 9, no. 1, pp. 245–259, 2018. [p. 86]
- [115] J. M. Deutsch, “Eigenstate thermalization hypothesis,” *Reports on Progress in Physics*, vol. 81, no. 8, p. 082001, 2018. [p. 86]
- [116] T. Palmai and R. M. Konik, “Quasilocal charges and the generalized Gibbs ensemble in the Lieb-Liniger model,” *Physical Review E*, vol. 98, p. 052126, Nov. 2018. [p. 87]
- [117] T. Langen, S. Erne, R. Geiger, B. Rauer, T. Schweigler, M. Kuhnert, W. Rohringer, I. E. Mazets, T. Gasenzer, and J. Schmiedmayer, “Experimental observation of a generalized Gibbs ensemble,” *Science*, vol. 348, pp. 207–211, Apr. 2015. [p. 87]
- [118] M. Kollar, F. A. Wolf, and M. Eckstein, “Generalized Gibbs ensemble prediction of prethermalization plateaus and their relation to nonthermal steady states in integrable systems,” *Physical Review B*, vol. 84, p. 054304, Aug. 2011. [p. 88]
- [119] J. Berges, S. Borsányi, and C. Wetterich, “Prethermalization,” *Physical Review Letters*, vol. 93, p. 142002, Sept. 2004.

- [120] M. Eckstein, M. Kollar, and P. Werner, “Thermalization after an Interaction Quench in the Hubbard Model,” *Physical Review Letters*, vol. 103, p. 056403, July 2009.
- [121] M. Moeckel and S. Kehrein, “Interaction Quench in the Hubbard Model,” *Physical Review Letters*, vol. 100, p. 175702, May 2008. [p. 88]
- [122] J.-S. Caux and R. M. Konik, “Constructing the Generalized Gibbs Ensemble after a Quantum Quench,” *Physical Review Letters*, vol. 109, p. 175301, Oct. 2012. [p. 88]
- [123] J. De Nardis, B. Wouters, M. Brockmann, and J.-S. Caux, “Solution for an interaction quench in the Lieb-Liniger Bose gas,” *Physical Review A*, vol. 89, p. 033601, Mar. 2014.
- [124] P. Calabrese and P. L. Doussal, “Interaction quench in a Lieb–Liniger model and the KPZ equation with flat initial conditions,” *Journal of Statistical Mechanics : Theory and Experiment*, vol. 2014, no. 5, p. P05004, 2014.
- [125] M. Collura, M. Kormos, and P. Calabrese, “Stationary entanglement entropies following an interaction quench in 1D Bose gas,” *Journal of Statistical Mechanics : Theory and Experiment*, vol. 2014, no. 1, p. P01009, 2014.
- [126] M. A. Cazalilla and M.-C. Chung, “Quantum quenches in the Luttinger model and its close relatives,” *Journal of Statistical Mechanics : Theory and Experiment*, vol. 2016, no. 6, p. 064004, 2016.
- [127] T. Świsłocki and P. Deuar, “Quantum fluctuation effects on the quench dynamics of thermal quasicondensates,” *Journal of Physics B : Atomic, Molecular and Optical Physics*, vol. 49, p. 145303, July 2016.
- [128] J. De Nardis, M. Panfil, A. Gambassi, L. Cugliandolo, R. Konik, and L. Foini, “Probing non-thermal density fluctuations in the one-dimensional Bose gas,” *SciPost Physics*, vol. 3, p. 023, Sept. 2017.
- [129] T. Langen, T. Schweigler, E. Demler, and J. Schmiedmayer, “Double light-cone dynamics establish thermal states in integrable 1D Bose gases,” *New Journal of Physics*, vol. 20, no. 2, p. 023034, 2018.
- [130] G. I. Martone, P.-E. Larré, A. Fabbri, and N. Pavloff, “Momentum distribution and coherence of a weakly interacting Bose gas after a quench,” *arXiv :1810.01362 [cond-mat, physics :gr-qc]*, Oct. 2018.

- [131] P.-E. Larré, D. Delande, and N. Cherroret, “Postquench prethermalization in a disordered quantum fluid of light,” *Physical Review A*, vol. 97, p. 043805, Apr. 2018.
- [132] P.-E. Larré and I. Carusotto, “Propagation of a quantum fluid of light in a cavityless nonlinear optical medium : General theory and response to quantum quenches,” *Physical Review A*, vol. 92, p. 043802, Oct. 2015. [p. 88]
- [133] B. Rauer, S. Erne, T. Schweigler, F. Cataldini, M. Tajik, and J. Schmiedmayer, “Recurrences in an isolated quantum many-body system,” *Science*, p. eaan7938, Apr. 2018. [p. 88, 104, 106]
- [134] I. Bouchoule, S. S. Szigeti, M. J. Davis, and K. V. Kheruntsyan, “Finite-temperature hydrodynamics for one-dimensional Bose gases : Breathing-mode oscillations as a case study,” *Physical Review A*, vol. 94, p. 051602, Nov. 2016. [p. 89]
- [135] E. H. Lieb and D. W. Robinson, “The Finite Group Velocity of Quantum Spin Systems,” in *Statistical Mechanics : Selecta of Elliott H. Lieb* (B. Nachtergaele, J. P. Solovej, and J. Yngvason, eds.), pp. 425–431, Berlin, Heidelberg : Springer Berlin Heidelberg, 2004. [p. 91]
- [136] B. Nachtergaele, H. Raz, B. Schlein, and R. Sims, “Lieb-Robinson Bounds for Harmonic and Anharmonic Lattice Systems,” *Communications in Mathematical Physics*, vol. 286, pp. 1073–1098, Mar. 2009. [p. 91]
- [137] T. Langen, *Non-Equilibrium Dynamics of One-Dimensional Bose Gases*. Springer Theses, Cham : Springer International Publishing, 2015. [p. 93]
- [138] B. Rauer, *Non-Equilibrium Dynamics beyond Dephasing : Recurrences and Loss Induced Cooling in One-Dimensional Bose Gases*. PhD thesis, Technische Universität Wien. [p. 106, 138]
- [139] D. Guéry-Odelin and G. V. Shlyapnikov, “Excitation-assisted inelastic processes in trapped Bose-Einstein condensates,” *Physical Review A*, vol. 61, Dec. 1999. [p. 126]
- [140] J. Söding, D. Guéry-Odelin, P. Desbiolles, F. Chevy, H. Inamori, and J. Dalibard, “Three-body decay of a rubidium Bose-Einstein condensate,” *Applied Physics B*, vol. 69, pp. 257–261, Oct. 1999. [p. 126, 127, 128, 165]
- [141] S. P. Cockburn, A. Negretti, N. P. Proukakis, and C. Henkel, “A comparison between microscopic methods for finite temperature Bose gases,” *Physical Review A*, vol. 83, Apr. 2011. [p. 151]

- [142] P. B. Blakie, A. S. Bradley, M. J. Davis, R. J. Ballagh, and C. W. Gardiner, “Dynamics and statistical mechanics of ultra-cold Bose gases using c-field techniques,” *Advances in Physics*, vol. 57, pp. 363–455, Sept. 2008. [p. 151]
- [143] Y. Tang, W. Kao, K.-Y. Li, S. Seo, K. Mallayya, M. Rigol, S. Gopalakrishnan, and B. L. Lev, “Thermalization near Integrability in a Dipolar Quantum Newton’s Cradle,” *Physical Review X*, vol. 8, p. 021030, May 2018. [p. 156, 162]
- [144] C. Li, T. Zhou, I. Mazets, H.-P. Stimming, Z. Zhu, Y. Zhai, W. Xiong, X. Zhou, X. Chen, and J. Schmiedmayer, “Dephasing and Relaxation of Bosons in 1D : Newton’s Cradle Revisited,” *arXiv:1804.01969 [cond-mat, physics:physics, physics:quant-ph]*, Apr. 2018. [p. 156]
- [145] A. S. Campbell, D. M. Gangardt, and K. V. Kheruntsyan, “Sudden Expansion of a One-Dimensional Bose Gas from Power-Law Traps,” *Physical Review Letters*, vol. 114, p. 125302, Mar. 2015. [p. 162]
- [146] S. Whitlock, S. Whitlock, P. Wicke, and N. J. van Druten, “Controlling spin motion and interactions in a one-dimensional Bose gas,” in *CLEO/Europe and EQEC 2011 Conference Digest (2011), Paper EC1_1*, p. EC1_1, Optical Society of America, May 2011. [p. 162]
- [147] E. G. M. van Kempen, S. J. J. M. F. Kokkelmans, D. J. Heinzen, and B. J. Verhaar, “Interisotope Determination of Ultracold Rubidium Interactions from Three High-Precision Experiments,” *Physical Review Letters*, vol. 88, p. 093201, Feb. 2002. [p. 165]
- [148] E. Braaten, H.-W. Hammer, and G. P. Lepage, “Lindblad Equation for the Inelastic Loss of Ultracold Atoms,” *Physical Review A*, vol. 95, Jan. 2017. [p. 169]

Titre : Dynamique hors équilibre des gaz bosoniques unidimensionnels

Résumé : Cette thèse contient plusieurs études expérimentales centrées sur la dynamique des bosons dans une dimension (1D). En utilisant une expérience de type puce atomique, nous créons des géométries de piègeage très allongées pour des atomes de ^{87}Rb . Cela conduit à geler deux dimensions et à créer un gaz 1D avec des interactions de contact qui est décrit par le modèle de Lieb-Liniger. Le manuscrit contient trois études expérimentales indépendantes : La première étude traite de la dynamique hors équilibre suite à une trempe des interactions. Nous observons l'évolution temporelle des modes de Bogoliubov comprimés et montrons que cette dynamique continue sur des temps qui ne seraient pas observable sur la fonction de corrélation d'ordre un. La deuxième étude montre que les pertes à trois-corps refroidissent un gaz de Bose 1D dans le régime quasi-condensat. Ce travail est accompagné d'une étude théorique qui prédit ce refroidissement pour les pertes à j -corps. La troisième étude est la première étude expérimentale d'une nouvelle théorie des systèmes intégrables, nommé HydroDynamics Généralisé (HDG). Nous montrons que HDG est la seule théorie «simple» qui décrit correctement les résultats expérimentaux. En particulier, l'approche de l'HydroDynamique Conventiennelle (HDC) ne reproduit pas l'observation expérimentale. Contrairement au HDG, HDC ne prend pas en compte l'intégrabilité du système.

Mots clés : atomes froids, expérience de puce atomique, modèle de Lieb-Liniger, systèmes intégrables, trempe des interactions, pertes à trois corps, hydrodynamique généralisée,

Title : Out-of-equilibrium dynamics in 1D Bose gases

Abstract : This thesis contains several experimental studies centered around the dynamics of bosons in one dimension (1D). With the use of an atomchip setup we create very elongated trapping geometries for ^{87}Rb . This leads to the freeze-out of two dimensions and the creation of a 1D gas with contact interactions, described the Lieb-Liniger model. The manuscript contains three independent experimental studies : The first one investigates the out-of-equilibrium dynamics after an interaction quench. We observe the time evolution of squeezed Bogoliubov modes and show that this dynamics continues on times which cannot be observed on the first order correlation function. The second study shows that three-body losses cool a 1D Bose gas in the quasi-condensate regime. This work is accompanied by a theoretical study, which predicts this cooling for j -body losses. The third study consists of the first experimental study of a new theory in integrable systems – the Generalized HydroDynamics (GHD). We show that GHD is the only "simple" theory which correctly describes the experimental results. In particular, the Conventional HydroDynamics (CHD) approach fails to reproduce the experimental observation. In contrast to GHD, CHD does not take into account the integrability of the system.

Keywords : cold atoms, atomchip experiment, Lieb-Liniger model, integrable systems, three-body losses, interaction quench, generalized hydrodynamics.

